Metallicity dependence of late-O and B supergiant winds in the Milky Way and Magellanic Clouds

Thaer Alkousa

Department of Physics and Astronomy

The University of Sheffield



A dissertation submitted in candidature for the degree of Doctor of Philosophy at the University of Sheffield

12th August 2026

“ Let the beauty
of what you love
be what you do. ”

— Jalal al-Din Rumi

Declaration

I declare that, unless otherwise stated, the work presented in this thesis is my own.

No part of this thesis has been accepted or is currently being submitted for any other qualification at the University of Sheffield or elsewhere.

The following chapters are based wholly or in part on previous publications:

- Chapter 3 (OB supergiants in the LMC): Alkousa et al. (2025) + Alkousa et al. (2026a)
- Chapter 4 (OB supergiants in the SMC): Alkousa et al. (2026b)

Acknowledgements

This thesis would not have been possible without the guidance and contributions of several individuals who played key roles in my academic and personal lives. No amount of thanks could express the gratitude to those who made this possible for me. However, I will give it a go.

I am indebted to my supervisor, Paul Crowther, whose expertise and support were a cornerstone of my academic development and completion of this thesis. I must also acknowledge my appreciation to Paul for his style of supervision, which gave me the freedom to set the objectives of my thesis and to maintain a healthy work-life balance. I would be remiss not to thank Paul for the decaf lattes he provided every Friday morning during our group meetings, and for the many rounds of pints at the University Arms pub and other establishments on the many "conference" trips we shared. I would like to acknowledge Joachim Bestenlehner's role in aiding me through the daunting task of understanding CMFGEN and radiative transfer in massive stars. You have always provided help when I needed and gave invaluable advice. I also have to extend my thanks to Andy Pollock, whose passion for massive stars and vast knowledge of X-ray astronomy inspire me to go back to the topic of colliding-wind binaries and to pursue research in that area.

I would also like to thank all of my teachers that have played an crucial role in my career. I would like to thank my previous supervisor, Igor I. Antokhin, for his dedicated supervision and for encouraging me to apply for this PhD position. I must also

express my gratitude to my undergraduate lecturer Oleg P. Polyakov, who recognised my seriousness in pursuing a career in physics and showed great support during the difficult first year of my undergraduate degree.

Additionally, I would like to extend my thanks to my friends and colleagues. I consider myself extremely lucky to have met such a unique group of weirdos like me. Coming to work felt like a pleasure thanks to you. Our office, E18, was the scene of some of the funniest and most ridiculous moments in my life. I appreciate your tolerance of my occasionally baffling behaviour and takes. I would like to extend a special thanks to my friend Adam Singleton, who was on the receiving end of most of my silliness. I also give special thanks to Summer McLaughlin, who was someone I could always turn to for venting and moral support. I thank you all for making my experience in Sheffield exponentially better.

Lastly, I would like to dedicate this thesis to my family. My mother, Thawra Youssef, thank you for enduring my fiery nature and for being a beacon of support and care to me in smooth and rough waters. My father, Bassam Alkousa, thank you for being my moral compass and a mountain of support that I can always fall back on. Thank you both for the safe, warm, and open-minded environment your created for our family. Everything you have done is the reason why I am here. To my little brother, Wajd Alkousa, my partner in crime and close confidant. You have been with me in every step I have taken so far and for that I cannot thank you enough. You are truly the best.

Public summary

Stars, the tiny lights that can be seen across the sky on a clear night, can be described as (semi-)spherical bodies of hot, gravitationally bound plasma. Stars are highly efficient engines that fuse different atoms in their cores throughout their lifetimes, producing enormous amounts of energy in the form of electromagnetic radiation (photons). Photons from stars traverse long distances to reach our telescopes, allowing us to examine their properties. The electromagnetic signal from stars can be interpreted using photometric methods in terms of colours, or split into dark absorption lines within a continuous spectrum, revealing the flux intensity per unit wavelength as a function of wavelength. The motion of stars relative to our position also provides insight into their evolutionary histories and the histories of the host galaxies, which can be studied using astrometry.

This thesis investigates a subcategory of stars, known as massive stars. As the name suggests, massive stars hold much more matter than solar-type stars, making them extremely hot and bright as they quickly burn through the nuclear fuel provided by their own bodies, evolving relatively quickly and shortening their lifespan. Massive stars are thought to be the source of the first ionising photons, playing a major role in making the universe transparent to electromagnetic radiation, allowing us to observe the cosmos using various techniques. The interiors of massive stars are highly efficient factories that produce heavy nuclei, most notably carbon, oxygen and nitrogen, all of which are key ingredients needed to initiate life. Massive stars end their lives in a cataclysmic collapse, usually followed by a violent explosion known as a core-collapse supernova, which shapes the evolution of host galaxies by unleashing copious amounts of matter and energy into the galactic medium. Therefore, the importance of massive stars in the evolution of the universe and the emergence of life cannot be overstated, making them essential for unlocking the secrets of the cosmos and the mysteries of human existence.

Abstract

Blue supergiants (BSGs) are hot, luminous, and evolved massive stars that produce significant chemical, radiative, and mechanical feedback in their surroundings. BSGs possess line-driven winds, whose properties play a crucial role in determining their evolution and fate. Studying the properties of BSGs across multiple metallicity environments provides significant insight into the effect of metallicity on wind properties. In this thesis, we conduct a combined ultraviolet and optical spectroscopic study of late-O and B supergiants in the Milky Way (MW) and the Magellanic Clouds using the model atmosphere code CMFGEN.

We present the properties of 20, 16, and 26 OB supergiants between O9 and B8 in the Small Magellanic Cloud (SMC), Large Magellanic Cloud (LMC), and the MW, respectively. We find a strong metallicity dependence in mass-loss rates ($\dot{M}$) and in the wind momentum-luminosity relation. We derive a fully empirical mass-loss recipe as an alternative to the numerical recipe commonly used in stellar-evolution models. Our results show that these numerical recipes do not predict the behaviour of mass loss for stars near the terminal-age main sequence and in the Hertzsprung gap. We do not find any evidence of an increase in $\dot{M}$ or a decrease in the ratio of terminal wind velocity to escape velocity ($v_\infty/v_{\rm esc}$) that is associated with the bi-stability jump around 25-21 kK, with both decreasing monotonically with temperature.

We investigate the evolutionary history of our sample using single-star evolutionary models. We find that many stars lie in the Hertzsprung gap, showing enhanced helium and nitrogen abundances and slow rotation rates, suggesting that they may be products of binary interaction, such as stellar mergers. We find that the evolutionary mass is generally higher than the spectroscopically derived mass, with 40% of the SMC and MW stars exhibiting a significant mass discrepancy.

Contents

1 Introduction **1**
- 1.1 Massive stars across cosmic and human history . . . 1
  - 1.1.1 Observational properties of massive stars . . . 1
  - 1.1.2 Feedback from massive stars . . . 2
  - 1.1.3 Classification of massive stars . . . 6
  - 1.1.4 Introducing blue supergiants and their role in modern astrophysics 8
- 1.2 Evolution of massive stars . . . 9
  - 1.2.1 The main sequence . . . 9
  - 1.2.2 Post-main sequence evolution . . . 13
  - 1.2.3 Core-Collapse Supernova . . . 19
  - 1.2.4 Stellar evolution codes . . . 22
  - 1.2.5 Binary evolution . . . 28
- 1.3 Mass loss and Stellar winds . . . 31
  - 1.3.1 Solar winds . . . 32
  - 1.3.2 The line-driven winds of massive stars . . . 33
  - 1.3.3 Mass loss recipes and the bi-stability jump . . . 37
  - 1.3.4 Effect of metallicity . . . 39
  - 1.3.5 Wind signatures and wind density measurement . . . 42
- 1.4 Unanswered questions . . . 49
  - 1.4.1 Mass loss . . . 49
  - 1.4.2 Multiplicity and binary evolution . . . 53
  - 1.4.3 Massive stars in the early universe . . . 54
- 1.5 The purpose and outline of this thesis . . . 55

2 Methods **57**
- 2.1 Radiative transfer in CMFGEN . . . 58
  - 2.1.1 The radiative transfer equations . . . 59
  - 2.1.2 Why nLTE? . . . 62
  - 2.1.3 The inner workings of CMFGEN . . . 65
- 2.2 The CMFGEN grids . . . 69
  - 2.2.1 Velocity and clumping laws . . . 69
  - 2.2.2 Fundamental grid parameters . . . 70

2.2.3 Atomic data and X-rays . . . 75
2.3 Analysis procedure . . . 79
2.3.1 Summary of the fitting procedure . . . 80
2.3.2 Effective temperature and helium abundance . . . 81
2.3.3 Effective surface gravity . . . 88
2.3.4 Luminosity . . . 90
2.3.5 Line-broadening parameters . . . 93
2.3.6 Terminal wind velocity . . . 94
2.3.7 Wind density parameters . . . 96
2.3.8 He and CNO abundances . . . 97

3 OB supergiants in the LMC **100**
3.1 Observations . . . 100
3.1.1 Sample . . . 102
3.1.2 Ultraviolet spectroscopy . . . 102
3.1.3 Optical data (XShootU) . . . 104
3.1.4 Auxiliary data (MIKE) . . . 105
3.1.5 Photometry . . . 106
3.1.6 UV normalisation . . . 106
3.2 Results . . . 109
3.2.1 Hertzsprung-Russell diagram . . . 109
3.2.2 Stellar masses . . . 112
3.2.3 Wind properties . . . 114
3.2.4 Line-broadening parameters . . . 123
3.2.5 He and CNO abundances . . . 124
3.3 Discussion . . . 130
3.3.1 Bi-stability jump . . . 131
3.3.2 Comparison to previous empirical studies . . . 133
3.3.3 Comparison to numerical mass-loss rate recipes . . . 142
3.3.4 Metallicity effect . . . 144
3.4 Summary . . . 147

4 OB supergiants in the SMC **150**
4.1 Observations . . . 151
4.1.1 Sample . . . 151
4.1.2 Utraviolet and optical spectroscopy . . . 153
4.1.3 Photometry . . . 153
4.1.4 MIKE spectroscopy . . . 153
4.2 Results . . . 155
4.2.1 Hertzsprung-Russell diagram . . . 155
4.2.2 Stellar masses . . . 159
4.2.3 Wind properties . . . 162
4.2.4 Rotation . . . 168
4.2.5 Chemical composition . . . 170

4.3 Discussion . . . 174
4.3.1 Metallicity effect . . . 175
4.3.2 Bi-stability jump . . . 180
4.3.3 Implications for the population of blue supergiants . . . 184
4.3.4 Comparison to literature . . . 185
4.4 Summary . . . 188

5 OB supergiants in the Milky Way **191**
5.1 Observations . . . 192
5.1.1 Ultraviolet spectroscopy . . . 192
5.1.2 Optical spectroscopy . . . 194
5.1.3 Photometry and distances . . . 195
5.2 Results . . . 199
5.2.1 Hertzsprung-Russell diagram . . . 199
5.2.2 Stellar masses . . . 203
5.2.3 Wind properties . . . 205
5.2.4 Rotation . . . 215
5.2.5 Chemical composition . . . 218
5.3 Discussion . . . 220
5.3.1 Comparison to literature . . . 220
5.3.2 Bi-stability jump . . . 223
5.4 Summary . . . 227

6 Conclusions **229**
6.1 Mass-loss rate recipe . . . 231
6.2 Wind momentum-luminosity relation . . . 235
6.3 Implications for the evolution of BSGs . . . 239
6.4 Implications on the bi-stability jump . . . 241
6.5 Summary . . . 244
6.6 Future Work . . . 245

A LMC appendix **276**
A.1 Omitted objects . . . 276
A.2 $v_{\rm black}$ and $v_{\rm edge}$ . . . 277
A.3 Comparison to literature . . . 279
A.4 Comments on fitting issues . . . 282
A.5 Spectral energy distribution (SED) . . . 286
A.6 Line fitting for individual stars . . . 289
A.7 Overall spectral fits . . . 306
A.8 FM90 parameters . . . 323

B SMC Appendix **324**
B.1 $v_{\rm black}$ and $v_{\rm edge}$ . . . 324
B.2 Comparison to literature . . . 326
B.3 Comments on fitting issues . . . 329

B.4 Spectral energy distribution (SED) 333
B.5 Line fitting for individual stars 337
B.6 Overall spectral fits 358
B.7 FM90 parameters 379

C Milky Way **381**
C.1 $v_{\rm black}$ and $v_{\rm edge}$ 381
C.2 Comparison to literature 383
C.3 Comments on individual stars 386
C.4 Spectral energy distribution (SED) 391
C.5 Line fitting for individual stars 396
C.6 Overall spectral fits 423

Figures

1.1 The Hertzsprung-Russell diagram of the observed population of massive stars in the star-forming region 30 Doradus in the LMC. The solid and dashed black lines represent the non-rotating stellar evolutionary tracks and isochrones from Brott et al. (2011) and Köhler et al. (2015). The dot-dashed line in the top right shows the HumphreysDavidson (HD) limit. Different markers shown in the legend indicate the spectral type of the stars. The data used to create this HRD are drawn from multiple studies and compiled by Schneider et al. (2018). In the legend, the number of stars of each class that are in the final sample and those where not all observables can be reproduced by the stellar models simultaneously are provided in parentheses. This figure was adapted from Schneider et al. (2018). 10

1.2 Comparison between classical stellar interior composition diagrams (left) and diagrams produced with a Tool for Understanding the Lives, Interiors, and Physics of Stars (TULIPS, Laplace, 2022), containing the same information (right). The diagrams are for the case of 16 $M_{\odot}$ immediately before core collapse. Only isotopes with maximum mass fractions greater than 10^{-4} are shown. The upper and lower panels depict the stellar chemical composition as a function of mass and radial coordinate (on a logarithmic scale), respectively. From the centre, moving outward, these circles represent 0.25, 0.5, 0.75, and 1 times the total mass of the star. The radial direction is proportional to the mass fraction of the isotope in each of the 4 layers. This figure was adapted from Laplace (2022) 20

1.3 Remnant type of rotating massive star models as a function of initial mass and metallicity. The initial rotation rates $v_{\rm rot}$ are assumed to be equal to $0.4v_{\rm crit}$, where $v_{\rm crit} = \frac{3}{2}\sqrt{\frac{GM}{R_{\rm pb}}}$, and $R_{\rm pb}$ is the polar radius. The solid white lines are evolutionary tracks of rotating single stars. PISN: Pair-instability supernova with no remnant (grey region), PPISN: Pulsational pair-instability supernova with no remnant (salmon region), BH: Black hole remnant from direct collapse (black region), NS(BH): Neutron star remnant expected with the possibility of BH (orange region). BH(NS): Black holes via failed supernovae are expected, with the possibility of a successful explosion leading to a NS remnant (brown region). NS: Neutron star remnant with successful explosion (yellow region). This figure was adopted from Hirschi et al. (2025). 23
1.4 Illustration of mass transfer via RLO scenario in massive binaries. The parameters labelled on the diagram as T, N, and ν represent the characteristic lifetime of the evolutionary stage, the estimated number of binary systems in that particular evolutionary phase currently existing in our Galaxy, and the birth rate (formation frequency) of systems entering that specific evolutionary stage in the Galaxy. Credit: (Postnov & Yungelson, 2006). 30
1.5 Grotrian diagrams of Fe III (top panel) and Fe IV (bottom panel). The abscissa shows the values of the total angular momentum quantum number J while the ordinate shows energy levels in electron volts (eV). We include all lines (solid grey lines) between 912 and 3000 Å. The diagrams were produced using the graphical tool available on the website of the National Institute of Standards and Technology's Atomic Spectra Database. 38
1.6 The observed wind momentum-luminosity relation obtained by Mokiem et al. (2007, solid lines) compared to predictions from Vink et al. (2000, 2001). Top, middle and bottom lines correspond to Galactic, LMC and SMC, respectively. This figure was taken from Mokiem et al. (2007). . . . 41
1.7 Cartoon depicting the process of P Cygni profile formation in the atmospheres of massive stars. Credit: Stan Owocki. 43

2.1 Illustration of the specific intensity. 59
2.2 Flowchart of the CMFGEN program. 67
2.3 A slice of the model grid in the $T_{\rm eff}$-$\log g$ parameter space. Grey triangles show the grid points. The overlaid lines are isochrones taken from Brott et al. (2011). 71

2.4 Examples of the normalisation and fits to UV from the LMC sample, with the line identification for the UV lines. For illustration purposes, an offset of one was added. The coloured lines show the observations. The black lines show the model fits for each of the respective stars. Stellar features are indicated in black line labels, whereas green line labels indicate interstellar features. The gap at ≈ 1300 in the spectra of Sk 69° 52, Sk 68° 8 is due to appending observations from COS G130M and COS G160M. The gap at 1600 Å is due to appending observations from COS G160M and COS G185M. 78
2.5 O I $\lambda\lambda\lambda 7772 - 7774 - 7775$ and O II $\lambda 4254$ lines of the B8 supergiant Sk −67° 195 (black line). Red line: the preferred model, the temperature of which ($T_{\rm eff}$ = 12.5 kK) was obtained from fitting He I $\lambda 4471$ and Mg II $\lambda 4481$, and a comparison with higher $T_{\rm eff}$ = 14.0 kK. 83
2.6 Examples of the effect of varying $T_{\rm eff}$ on the Balmer jump. The best-fitting model is shown with the solid red line. Comparison model: blue solid line ($\Delta T_{\rm eff}$ = 500 kK). Observed XShootU spectrum: black solid line. 84
2.7 Examples of the effect of varying $T_{\rm eff}$ on the quality of the fit. The best-fitting model is shown with the solid red line. Comparison model: blue solid line ($\Delta T_{\rm eff}$ = 700 kK). Observed XShootU spectrum: black solid line. a-b: Sk −71° 41 (O9.5 Ib). c-d: Sk −68° 52 (B0 Ia). e-f: Sk −67° 78 (B3 Ia). 87
2.8 Examples of the effect of varying $\log g$ on the quality of the fit. The best-fitting model is shown with the solid red line. Comparison model: blue solid line. Observed XShootU spectrum: black solid line. a: Sk −66° 171 (O9 Ia) ($\Delta \log g = 0.05$). b: Sk −67° 5 (B0 Ib) ($\Delta \log g = 0.1$). 89
2.9 Example of a saturated P Cygni profile in the blue component of the resonance line Si IV $\lambda\lambda 1394 - 1403$ of the B supergiant Sk −68° 155. Marked in red squares are the positions of the measured black velocity ($v_{\rm black}$) and edge velocity ($v_{\rm edge}$). 94

3.1 Normalised XShootU spectra (Sana et al., 2024, DR1) in the blue optical range of the sample with identifications for a subset of the optical lines. For illustration purposes, we added an arbitrary offset of 0.5 for each spectrum. The fits to the violet, yellow, and red spectra for all stars are presented in Appendix A.7. 101
3.2 Hertzsprung-Russell diagram for our sample. The non-rotating isochrones for different ages (≈ [0 − 10] Myr) are overlaid as solid black lines, and the evolutionary tracks for stellar masses in the range ≈ [10 − 60] $M_\odot$ with a rotational velocity of 50 km s^{-1} are shown as dashed black lines. The isochrones and evolutionary tracks were adopted from Brott et al. (2011). 110
3.3 Spectroscopic Hertzsprung-Russell diagram for our sample. The evolutionary tracks (solid black lines) and the isochrones (dashed black lines) are the same as in Fig. 3.2, which are taken from Brott et al. (2011). The Encoding of the luminosity classes is the same as in Fig. 3.2 111

3.4 Blue circles show the spectroscopically obtained mass from our analysis $M_{\rm spec}$ vs. the mass produced by BONNSAI (Schneider et al., 2014a) applied to evolutionary tracks from Brott et al. (2011) $M_{\rm evo}$. Red circles overlaid onto the blue points depict stars that have a significant discrepancy between their $M_{\rm spec}$ and $M_{\rm evo}$. 113
3.5 v_∞ vs. $T_{\rm eff}$ for LMC supergiants. Green dots: results from this work, green line: linear fit of our results, yellow line: v_∞-$T_{\rm eff}$ relation from Hawcroft et al. (2024a), pink triangles: v_∞ calculated velocities from Vink & Sander (2021) recipe, violet diagonal cross: v_∞ calculated velocities from (Krtička et al., 2021) recipe. 116
3.6 Spectral fits to Hα for our sample of OB supergiants. Black line: observations, red line: model fit 118
3.7 $\dot{M}$ vs. $\Gamma_{\rm e}^{\rm spec}$. The green triangles indicate the objects Sk -67° 195 and Sk -70° 16, the mass-loss rates of which are considered upper limits. The red points correspond to the hypergiants Sk -67° 279 and Sk -68° 135. . 119
3.8 Hα of Sk -67° 78 from MIKE observations (dashed black line) overlaid on Hα from XShootU (solid black line) with our best-fitting model (solid red line) and the preferred fit for MIKE observations (solid blue line). . . 120
3.9 Best-fitting model $\beta = 2.2$ (solid red line) vs. two other models with $\beta = 2.5$ (solid blue line) and $\beta = 2.0$ (solid green line) for Hα of Sk -68° 140 (solid black line) 122
3.10 Line formation region (ζ vs. $\log(r/R_*)$) of Hα (solid blue line), He I λ4471 (solid red line), and a line from the dominating nitrogen ion (solid green line) for Sk -66° 171 ($T_{\rm eff}$ = 29.9 kK, left panel), Sk -68° 140 ($T_{\rm eff}$ = 24.1 kK, middle panel), and Sk -68° 8 ($T_{\rm eff}$ = 14.1 kK, right panel). The grey shaded region indicates the photosphere. 123
3.11 Nitrogen abundance (by number) vs. $v_{\rm rot} \sin i$. The colour scheme corresponds to the value of $\log g$, and the evolutionary tracks are computed for initial masses of 30 $M_\odot$, 40 $M_\odot$ and 50 $M_\odot$ (red, brown, and orange solid lines respectively) for initial rotational velocities of 50, 110, 170, 220, 270 380 km s^{-1} (Brott et al., 2011), which we multiplied by a factor of $\pi/4$ to take into account the inclination of the rotation axis (Hunter et al., 2008b). The black dashed line represents the LMC baseline nitrogen abundance. . . . 126
3.12 Each column shows from left to right Sk -66° 171 ($T_{\rm eff}$ = 29.9 kK), Sk -68° 140 ($T_{\rm eff}$ = 24.1 kK), and Sk -68° 8 ($T_{\rm eff}$ = 14.1 kK). *a*, *b*, and *c*: Wind velocity as a function of radius in stellar radii units $\log(r/R_*)$. *d*, *e*, and *f*: Ionisation structure (relative ionic density $\log(N(i^{n+})/N(i_{\rm tot}))$ vs. $\log(r/R_*)$) of helium. *g*, *h*, *i*: Ionisation structure of nitrogen. *j*, *k*, and *l*: Ionisation structure of iron. i^0 (orange), i^+ (green), i^{2+} (red), i^{3+} (blue), i^{4+} (magenta), i^{5+} (black), and i^{6+} (grey) where i is the element. 128
3.13 $\log$ N/C vs. $\log$ N/O of our sample (grey triangles, blue circles, and red squares). The upper and lower boundaries (dashed black lines) are adopted from Maeder et al. (2014). The sample is divided into three groups depending on their N/C and N/O values, similar to Menon et al. (2024). 129

3.14 Wind efficiency ($\eta = \frac{\dot{M} v_\infty}{L_{\rm bol}/c}$) in terms of effective temperature. 131
3.15 Ratio ($v_\infty/v_{\rm esc}$) as a function of temperature. The black dashed line is the relation presented in Krtička et al. (2021). The filled red lines represent the ratios from Lamers et al. (1995). The green filled line is the average relation for stars of spectral type earlier than B1 from Hawcroft et al. (2024a). The colour gradient correlates with the value of $\Gamma_e^{\rm evo}$. Red circles indicate stars the v_∞ of which is inferred as $v_{\rm edge} \times \langle v_\infty/v_{\rm edge} \rangle_{\rm LMC}$. 132
3.16 Comparison of our obtained $T_{\rm eff}$ to previous studies. We present on the x-axis our effective temperature for each star and the comparison $T_{\rm eff}$ from previous analyses on the y-axis. Blue triangles: Comparison to values obtained by Verhamme et al. (2024), Red circles: Comparison to values obtained by Brands et al. (2025). Green filled crosses: Comparison to values obtained by Evans et al. (2004). Black square: Comparison to values obtained by Gvaramadze et al. (2018). Magenta diamond: Comparison to values obtained by Ramachandran et al. (2018). Cyan star: Our $T_{\rm eff}$ to the effective temperatures from Urbaneja et al. (2017). Yellow hexagon: Comparison to values obtained by McEvoy et al. (2015). 134
3.17 Comparison of our obtained $\log g$ to previous studies. The symbols follow the same encoding as in Fig. 3.16. 135
3.18 Comparison of our derived $\dot{M}$ to previous studies. The symbols follow the same encoding as in Fig. 3.16. 136
3.19 Comparison of our derived $\log L_{\rm bol}$ to previous studies. The symbols follow the same encoding as in Fig. 3.16. 137
3.20 Mass-loss rates as a function of $T_{\rm eff}$, comparing our derived $\dot{M}$ (green circles) to mass-loss rates that we calculated via various numerical recipes. Pink squares: $\dot{M}$ from Vink et al. (2001) recipe. Yellow triangles: $\dot{M}$ from Björklund et al. (2023). Violet crosses: $\dot{M}$ from Krtička et al. (2024). . . 143
3.21 Modified wind momentum-luminosity distribution of LMC (blue symbols) supergiants from this work and SMC (red symbols) supergiants from Bernini-Peron et al. (2024). Objects with $\log(L_{\rm bol}/L_\odot) < 5$ are excluded from the linear fits for the LMC and SMC samples. The symbols for the SMC sample (red) follow the same encoding of the LMC sample (blue), where each luminosity class is given a unique symbol. 145

4.1 Hertzsprung-Russell diagram for our sample. Overlaid in solid black lines are non-rotating SMC isochrones for different ages ($\approx 0-10$ Myr). Dashed black lines are the SMC rotating evolutionary tracks for stellar masses in the range of $\approx 10-60\ M_\odot$ with a rotational velocity of 110 $\rm km\,s^{-1}$. Both the isochrones and evolutionary tracks are adopted from Brott et al. (2011). The shaded area is defined by the HD limit (Humphreys & Davidson, 1979a; Smith et al., 2004; Davies et al., 2018). 158

4.2 The spectroscopic Hertzsprung-Russell diagram for our sample. The evolutionary tracks (dashed black lines) and the isochrones (solid black lines) are the same as in Fig. 3.2, which are taken from Brott et al. (2011). The encoding of the luminosity classes is the same as in Fig. 3.2. 160
4.3 Relative (percentage) difference of the evolutionary and spectroscopic masses $(M_{\rm evo} - M_{\rm spec})/M_{\rm spec}$. $M_{\rm evo}$ was obtained using a Bayesian inference method applied to SMC evolutionary models of Brott et al. (2011). The diagonal black crosses indicate the presence of a mass discrepancy. . 161
4.4 Best fits (solid red lines) to XShootU Hα (+ C II λ6578) profiles (solid black lines). Magellan/MIKE spectra are also shown (dashed blue lines), where available, to illustrate line variability. 163
4.5 $\Delta \log \dot{M}$ vs $T_{\rm eff}$. $\Delta \log \dot{M}$ is the difference between our derived $\Delta \log \dot{M}$ and those obtained from numerical recipes from Vink & Sander (2021) (yellow dots), Björklund et al. (2023) (blue dots), and Krtička et al. (2024) (red dots). 164
4.6 v_∞ vs $T_{\rm eff}$. The green dots represent our results. The green line is the linear fit. The dashed magenta line is the Z-dependent v_∞-$T_{\rm eff}$ relation from Hawcroft et al. (2024a). The solid magenta line was obtained from fitting Hawcroft et al. (2024a) results for O and B supergiants only. The solid blue line was obtained from fitting the results of Bernini-Peron et al. (2024). The grey crosses are v_∞ calculated from Vink & Sander (2021) recipe. The black triangles represent v_∞, calculated from the recipe in Krtička et al. (2021). 166
4.7 $\epsilon_{\rm N}$ vs $v_{\rm rot} \sin i$. The colour scheme corresponds to the value of $\Gamma_{\rm e}$. The solid pink, brown, orange, and red lines represent SMC evolutionary tracks for initial masses of 12 $M_\odot$, 25 $M_\odot$, 40 $M_\odot$, and 60 $M_\odot$, respectively, with initial rotational velocities of 110, 250, 350 km s^{-1} (Brott et al., 2011). We multiplied by a factor of $\pi/4$ to take into account the inclination of the rotation axis (Hunter et al., 2008b). The dashed black line represents the baseline $\epsilon_{\rm N}$ in the SMC (Vink et al., 2023). The dots along the evolutionary tracks represent time steps of 0.1 Myr 171
4.8 log N/C vs log N/O. The red triangles show the distribution of our sample. The stars for which the oxygen abundance was obtained from fitting the O I $\lambda\lambda\lambda$7772−7774−7775 multiplet are shown in blue squares. The dashed black lines represent the upper and lower boundaries adopted from Maeder et al. (2014). 173
4.9 $D_{\rm mom}$ vs log $L_{\rm bol}$. The green symbols represent the SMC sample. The yellow symbols represent the LMC sample from Chapter 3. Circles indicate stars with reliable UV and optical wind diagnostics. Triangles indicate upper limits. Solid lines are fits to the circles, in which the triangles (upper limits) are not used. Dash-dotted lines are fits for the entire sample. 176
4.10 v_∞ vs $T_{\rm eff}$. The symbol and colour encoding are the same as in Fig. 4.9. . 177

4.11 $\log \dot{M}$ vs $\log L_{\rm bol}$. The green symbols represent the SMC sample. The yellow symbols represent the LMC sample from Chapter 3. Circles indicate stars with reliable UV and optical wind diagnostics. Triangles indicate upper limits. Solid lines are fits to the circles. Upper limits (triangles) are not included in the linear fits. 178
4.12 $\log \dot{M}$ versus $T_{\rm eff}$. The solid blue line is a simple linear fit to the entire sample. The colour gradient correlates with the value of Γ_e. 180
4.13 $\log \dot{M}_{\rm t}$ versus $T_{\rm eff}$. The symbol and colour encoding are the same as in Fig. 4.12. 181
4.14 Ratio $(v_\infty/v_{\rm esc})$ as a function of temperature. The solid green line represents the linear fit to our sample. The dashed black line is the relation presented in Krtička et al. (2021). The dotted red lines represent the ratios from Lamers et al. (1995). The dot-dashed blue line represents the ratios from Hawcroft et al. (2024a). The colour gradient correlates with the value of Γ_e. Red circles indicate stars the v_∞ of which is inferred as $v_{\rm edge} \times \langle v_\infty/v_{\rm edge} \rangle_{\rm SMC}$. 182
4.15 Wind efficiency $\eta = \frac{\dot{M} v_\infty}{L_{\rm bol}/c}$ in terms of $T_{\rm eff}$. 183
4.16 Comparison of our derived parameters to literature values. a: $T_{\rm eff}$ comparison, b: $\log g$ comparison, c: $L_{\rm bol}$ comparison, d: $\log \dot{M}$ comparison, e: $\log \dot{M}_{\rm smooth}$ comparison. Pink triangles: comparison to Backs et al. (2024). Green squares: comparison to Bernini-Peron et al. (2024). Blue Xs: comparison to Trundle et al. (2004a) and Trundle & Lennon (2005a). Grey diamonds: comparison to values obtained from LIME Sundqvist et al. (2025). 187

5.1 Top panel: top-down view of the MW. The black triangles represent our sample. The Sun's position is indicated as a red circle. Bottom panel: side-on view of the MW with our stars overlaid. 198
5.2 Hertzsprung-Russell diagram for our sample. Overlaid in solid black lines are rotating Galactic isochrones for different ages ($\approx 0-10$ Myr). Dashed black lines are the Galactic rotating evolutionary tracks for stellar masses in the range of $\approx 10-60\ M_\odot$ with a rotational velocity of 100 $\rm km\,s^{-1}$. Both the isochrones and evolutionary tracks are adopted from Brott et al. (2011). The shaded area is defined by the HD limit (Humphreys & Davidson, 1979a; Smith et al., 2004; Davies et al., 2018). 202
5.3 The spectroscopic Hertzsprung-Russell diagram for our sample. The evolutionary tracks (dashed black lines) and the isochrones (solid black lines) are the same as in Fig. 5.2, which are taken from Brott et al. (2011). The encoding of the luminosity classes is the same as in Fig. 5.2. 204
5.4 Relative (percentage) difference of the evolutionary and spectroscopic masses $(M_{\rm evo} - M_{\rm spec})/M_{\rm spec}$. $M_{\rm evo}$ was obtained using a Bayesian inference method applied to Galactic evolutionary models of Brott et al. (2011). The diagonal black crosses indicate the presence of a mass discrepancy. 206

5.5 Best fits (solid red lines) to the observed Hα (+ C II λ6578) profiles (solid black lines). 208
5.6 $\log \dot{M}$ vs $\log \Gamma_{\rm e}^{\rm spec}$. Blue circles indicate stars that have reliably obtained $\dot{M}$ from observed Hα emission components and reliable v_∞ measurements. Green triangles indicate an upper limit on $\dot{M}$. 209
5.7 $\Delta \log \dot{M}$ vs $T_{\rm eff}$. $\Delta \log \dot{M}$ is the difference between our derived $\Delta \log \dot{M}$ and those obtained from numerical recipes from Vink & Sander (2021) (yellow dots), Björklund et al. (2023) (blue dots), and Krtička et al. (2024) (red dots). 211
5.8 Relative (percentage) difference terminal wind velocity obtained by this study $v_{\infty,\ \rm this\ study}$ and those of previous empirical measurements and predictions from recipes $v_{\infty,\ \rm other}$. Grey crosses: Vink & Sander (2021) numerical recipe. Black triangles: Krtička et al. (2021) numerical recipe. Green circles: Hawcroft et al. (2024a) empirical recipe (O and B supergiants only). Red squares: Direct measurements from Prinja et al. (1990). Yellow diamonds: direct measurements from Howarth et al. (1997). . . . 212
5.9 $\epsilon_{\rm N}$ vs $v_{\rm rot} \sin i$. The colour scheme corresponds to the value of $\Gamma_{\rm e}$. The solid pink, brown, orange, and red lines represent Galactic evolutionary tracks for initial masses of 10 $M_\odot$, 25 $M_\odot$, 40 $M_\odot$, and 60 $M_\odot$, respectively, with initial rotational velocities of 110, 220, 320, 420 km s^{-1} (Brott et al., 2011). We multiplied by a factor of $\pi/4$ to take into account the inclination of the rotation axis (Hunter et al., 2008b). The dashed black line represents the baseline $\epsilon_{\rm N}$ in the MW (Asplund et al., 2005). The dots along the evolutionary tracks represent time steps of 0.1 Myr 216
5.10 $\log$ N/C vs $\log$ N/O. The red triangles show the distribution of our sample. The dashed black lines represent the upper and lower boundaries adopted from Maeder et al. (2014). 219
5.11 Comparison of our derived parameters to literature values. a: $T_{\rm eff}$ comparison, b: $\log g$ comparison, c: $L_{\rm bol}$ comparison, d: $\log \dot{M}_{\rm smooth}$ comparison. Cyan diagonal crosses: comparison to Crowther et al. (2006). Black crosses: comparison to Lefever et al. (2007). Pink triangles: comparison to Searle et al. (2008). Yellow circles: comparison to Haucke et al. (2018). Grey tri-diagonals: comparison to Rubio-Díez et al. (2022). Green squares: comparison to Bernini-Peron et al. (2023). 221
5.12 Ratio ($v_\infty/v_{\rm esc}$) as a function of temperature. The solid green line represents the linear fit to our sample. The dashed black line is the relation presented in Krtička et al. (2021). The dotted red lines represent the ratios from Lamers et al. (1995). The colour gradient correlates with the value of Γ_e. Red circles indicate stars the v_∞ of which is inferred as $v_{\rm edge} \times \langle v_\infty/v_{\rm edge} \rangle_{\rm MW}$. 224
5.13 $\log \dot{M}$ versus $T_{\rm eff}$. The colour scale corresponds to $\Gamma_e^{\rm evo}$. 226

6.1 Residuals between the predicted and observed mass loss rates. The shaded area indicates the 1σ root-mean-square dispersion from the fitting routine for each galaxy, adjusted for the bias. The circles represent stars included in our fitting routine (reliable $\dot{M}$ and v_∞ diagnostics). Triangles indicate stars excluded from the fitting procedure. Black circles indicate the hypergiants. 232
6.2 $D_{\rm mom}$ vs $\log L_{\rm bol}$. The salmon symbols represent the MW sample. The yellow and green symbols represent the LMC and SMC samples, respectively. Circles indicate stars with reliable $\dot{M}$ and v_∞ diagnostics. Triangles indicate upper limits. Solid lines are fits to the circle only. Upper limits (triangles) are not included in the linear fits. 236
6.3 Z-dependent modified wind momentum relation. The solid colored lines show predictions from our $\log D_{\rm mom}$ recipe for the MW, LMC, and SMC metallicities. The dashed and dash-dotted black and grey lines indicate the modified wind momentum relations from Backs et al. (2024) and Mokiem et al. (2007). 238

A.1 Spectral energy distribution for all the stars in our sample. Red solid line: model SED, Black solid line: observed SED. The photometric points are indicated as blue circles. 287
A.1 continued 288
A.2 Individual line fits for Sk -66° 171. Black solid line: observed spectrum. Red solid line: spectrum of the best fitting model. The observed spectrum is corrected for $v_{\rm rad} = 410 {\rm km\,s^{-1}}$ 290
A.3 Individual line fits for Sk -68° 155. Black solid line: observed spectrum. Red solid line: spectrum of the best fitting model. The observed spectrum is corrected for $v_{\rm rad} = 240 {\rm km\,s^{-1}}$ 291
A.4 Individual line fits for Sk -69° 279. Black solid line: observed spectrum. Red solid line: spectrum of the best fitting model. The observed spectrum is corrected for $v_{\rm rad} = 230 {\rm km\,s^{-1}}$ 292
A.5 Individual line fits for Sk -71° 41. Black solid line: observed spectrum. Red solid line: spectrum of the best fitting model. The observed spectrum is corrected for $v_{\rm rad} = 260 {\rm km\,s^{-1}}$ 293
A.6 Individual line fits for Sk -68° 135. Black solid line: observed spectrum. Red solid line: spectrum of the best fitting model. The observed spectrum is corrected for $v_{\rm rad} = 270 {\rm km\,s^{-1}}$ 294
A.7 Individual line fits for Sk -67° 5. Black solid line: observed spectrum. Red solid line: spectrum of the best fitting model. The observed spectrum is corrected for $v_{\rm rad} = 295 {\rm km\,s^{-1}}$ 295
A.8 Individual line fits for Sk -68° 52. Black solid line: observed spectrum. Red solid line: spectrum of the best fitting model. The observed spectrum is corrected for $v_{\rm rad} = 255 {\rm km\,s^{-1}}$ 296

A.9 Individual line fits for Sk −69° 43. Black solid line: observed spectrum. Red solid line: spectrum of the best fitting model. The observed spectrum is corrected for $v_{\rm rad} = 255 {\rm km\,s^{-1}}$ 297
A.10 Individual line fits for Sk −68° 140. Black solid line: observed spectrum. Red solid line: spectrum of the best fitting model. The observed spectrum is corrected for $v_{\rm rad} = 260 {\rm km\,s^{-1}}$ 298
A.11 Individual line fits for Sk −67° 2. Black solid line: observed spectrum. Red solid line: spectrum of the best fitting model. The observed spectrum is corrected for $v_{\rm rad} = 320 {\rm km\,s^{-1}}$ 299
A.12 Individual line fits for Sk −67° 14. Black solid line: observed spectrum. Red solid line: spectrum of the best fitting model. The observed spectrum is corrected for $v_{\rm rad} = 300 {\rm km\,s^{-1}}$ 300
A.13 Individual line fits for Sk −69° 52. Black solid line: observed spectrum. Red solid line: spectrum of the best fitting model. The observed spectrum is corrected for $v_{\rm rad} = 260 {\rm km\,s^{-1}}$ 301
A.14 Individual line fits for Sk −67° 78. Black solid line: observed spectrum. Red solid line: spectrum of the best fitting model. The observed spectrum is corrected for $v_{\rm rad} = 310 {\rm km\,s^{-1}}$ 302
A.15 Individual line fits for Sk −70° 16. Black solid line: observed spectrum. Red solid line: spectrum of the best fitting model. The observed spectrum is corrected for $v_{\rm rad} = 265 {\rm km\,s^{-1}}$ 303
A.16 Individual line fits for Sk −68° 8. Black solid line: observed spectrum. Red solid line: spectrum of the best fitting model. The observed spectrum is corrected for $v_{\rm rad} = 250 {\rm km\,s^{-1}}$ 304
A.17 Individual line fits for Sk −67° 195. Black solid line: observed spectrum. Red solid line: spectrum of the best fitting model. The observed spectrum is corrected for $v_{\rm rad} = 300 {\rm km\,s^{-1}}$ 305
A.18 An overall view of the best fit (red solid line) to key regions of the observed spectrum (black solid line) of Sk −66° 171. From the top, the first panel is the FUV FUSE range, containing interstellar features such as $Ly\delta$ λ950, $Ly\gamma$ λ973, and $Ly\beta$ λ1026. Second and third panels are STIS E140M FUV and STIS E230M NUV spectral ranges, respectively, and we note some interstellar features: $Ly\alpha$ λ1216, O I + P II λ1302, C II λ1335, Si II λ1527, and Al IIλ1671. The rest of the panels are the UBV and VIS XShooter spectra, with the break between the two arms at ≈ 5600 Å. The lines Ca II H + K and Na I D are interstellar features. For this star, we fit the absorption profiles for $Ly\alpha$ through $Ly\eta$, which were calculated using H I column density $\log N(HI) = 20.7$ cm^{-2} (Fitzpatrick, 1985). 307

A.19 An overall view of the best fit (red solid line) to key regions of the observed spectrum (black solid line) of Sk −68° 155. From the top, the first panel is the FUV FUSE range, containing interstellar features such as *Lyδ* λ950, *Lyγ* λ973, and *Lyβ* λ1026. The second and third panels are the COS G130M+G160M FUV and STIS E230M NUV spectral ranges, respectively, and we note some interstellar features: *Lyα* λ1216, O I + P II λ1302, C II λ1335, Si II λ1527, and Al IIλ1671. The rest of the panels are the UBV and VIS XShooter spectra, with the break between the two arms at ≈ 5600 Å. The lines Ca II H + K and Na I D are interstellar features. . . 308
A.20 An overall view of the best fit (red solid line) to key regions of the observed spectrum (black solid line) of Sk −69° 279. From the top, the first panel is the FUV FUSE range, containing interstellar features such as *Lyδ* λ950, *Lyγ* λ973, and *Lyβ* λ1026. Second and third panels are STIS E140M FUV and STIS E230M NUV spectral ranges, respectively, and we note some interstellar features: *Lyα* λ1216, O I + P II λ1302, C II λ1335, Si II λ1527, and Al IIλ1671. The rest of the panels are the UBV and VIS XShooter spectra, with the break between the two arms at ≈ 5600 Å. The lines Ca II H + K and Na I D are interstellar features. 309
A.21 An overall view of the best fit (red solid line) to key regions of the observed spectrum (black solid line) of Sk −71° 41. From the top, the first panel is the FUV FUSE range, containing interstellar features such as *Lyδ* λ950, *Lyγ* λ973, and *Lyβ* λ1026. Second panel is STIS E140M FUV, and we note some interstellar features: *Lyα* λ1216, O I + P II λ1302, C II λ1335, Si II λ1527, and Al IIλ1671. The rest of the panels are the UBV and VIS XShooter spectra, with the break between the two arms at ≈ 5600 Å. The lines Ca II H + K and Na I D are interstellar features. 310
A.22 An overall view of the best fit (red solid line) to key regions of the observed spectrum (black solid line) of Sk −68° 135. From the top, the first panel is the FUV FUSE range, containing interstellar features such as *Lyδ* λ950, *Lyγ* λ973, and *Lyβ* λ1026. Second and third panels are STIS E140M FUV and STIS E230M NUV spectral ranges, respectively, and we note some interstellar features: *Lyα* λ1216, O I + P II λ1302, C II λ1335, Si II λ1527, and Al IIλ1671. The rest of the panels are the UBV and VIS XShooter spectra, with the break between the two arms at ≈ 5600 Å. The lines Ca II H + K and Na I D are interstellar features. 311
A.23 An overall view of the best fit (red solid line) to key regions of the observed spectrum (black solid line) of Sk −67° 5. From the top, the first panel is the FUV FUSE range, containing interstellar features such as *Lyδ* λ950, *Lyγ* λ973, and *Lyβ* λ1026. Second and third panels are STIS E140M FUV and STIS E230M NUV spectral ranges, respectively, and we note some interstellar features: *Lyα* λ1216, O I + P II λ1302, C II λ1335, Si II λ1527, and Al IIλ1671. The rest of the panels are the UBV and VIS XShooter spectra, with the break between the two arms at ≈ 5600 Å. The lines Ca II H + K and Na I D are interstellar features. 312

A.24 An overall view of the best fit (red solid line) to key regions of the observed spectrum (black solid line) of Sk −68° 52. From the top, the first panel is the FUV FUSE range, containing interstellar features such as *Lyδ* λ950, *Lyγ* λ973, and *Lyβ* λ1026. Second and third panels are STIS E140M FUV and STIS E230M NUV spectral ranges, respectively, and we note some interstellar features: *Lyα* λ1216, O I + P II λ1302, C II λ1335, Si II λ1527, and Al IIλ1671. The rest of the panels are the UBV and VIS XShooter spectra, with the break between the two arms at ≈ 5600 Å. The lines Ca II H + K and Na I D are interstellar features. 313
A.25 An overall view of the best fit (red solid line) to key regions of the observed spectrum (black solid line) of Sk −69° 43. From the top, the first panel is the FUV FUSE range, containing interstellar features such as *Lyδ* λ950, *Lyγ* λ973, and *Lyβ* λ1026. Second and third panels are STIS E140M FUV and STIS E230M NUV spectral ranges, respectively, and we note some interstellar features: *Lyα* λ1216, O I + P II λ1302, C II λ1335, Si II λ1527, and Al IIλ1671. The rest of the panels are the UBV and VIS XShooter spectra, with the break between the two arms at ≈ 5600 Å. The lines Ca II H + K and Na I D are interstellar features. 314
A.26 An overall view of the best fit (red solid line) to key regions of the observed spectrum (black solid line) of Sk −68° 140. From the top, the first panel is the FUV FUSE range, containing interstellar features such as *Lyδ* λ950, *Lyγ* λ973, and *Lyβ* λ1026. Second and third panels are COS G130M+G160M FUV and STIS E230M NUV spectral ranges, respectively, and we note some interstellar features: *Lyα* λ1216, O I + P II λ1302, C II λ1335, Si II λ1527, and Al IIλ1671. The rest of the panels are the UBV and VIS XShooter spectra, with the break between the two arms at ≈ 5600 Å. The lines Ca II H + K and Na I D are interstellar features. . . 315
A.27 An overall view of the best fit (red solid line) to key regions of the observed spectrum (black solid line) of Sk −67° 2. From the top, the first panel is the FUV FUSE range, containing interstellar features such as *Lyδ* λ950, *Lyγ* λ973, and *Lyβ* λ1026. Second and third panels are STIS E140M FUV and STIS E230M NUV spectral ranges, respectively, and we note some interstellar features: *Lyα* λ1216, O I + P II λ1302, C II λ1335, Si II λ1527, and Al IIλ1671. The rest of the panels are the UBV and VIS XShooter spectra, with the break between the two arms at ≈ 5600 Å. The lines Ca II H + K and Na I D are interstellar features. 316

A.28 An overall view of the best fit (red solid line) to key regions of the observed spectrum (black solid line) of Sk −67° 14. From the top, the first panel is the FUV FUSE range, containing interstellar features such as *Lyδ* λ950, *Lyγ* λ973, and *Lyβ* λ1026. Second and third panels are COS G130M+G160M FUV and STIS E230M NUV spectral ranges, respectively, and we note some interstellar features: *Lyα* λ1216, O I + P II λ1302, C II λ1335, Si II λ1527, and Al II λ1671. The rest of the panels are the UBV and VIS XShooter spectra, with the break between the two arms at ≈ 5600 Å. The lines Ca II H + K and Na I D are interstellar features. . . 317

A.29 An overall view of the best fit (red solid line) to key regions of the observed spectrum (black solid line) of Sk −69° 52. From the top, the first panel is the FUV FUSE range, containing interstellar features such as *Lyδ* λ950, *Lyγ* λ973, and *Lyβ* λ1026. Second and third panels are COS G130M+G160M FUV and STIS E230M NUV spectral ranges, respectively, and we note some interstellar features: *Lyα* λ1216, O I + P II λ1302, C II λ1335, Si II λ1527, and Al II λ1671. The rest of the panels are the UBV and VIS XShooter spectra, with the break between the two arms at ≈ 5600 Å. The lines Ca II H + K and Na I D are interstellar features. . . 318

A.30 An overall view of the best fit (red solid line) to key regions of the observed spectrum (black solid line) of Sk −67° 78. From the top, the first panel is the FUV FUSE range, containing interstellar features such as *Lyδ* λ950, *Lyγ* λ973, and *Lyβ* λ1026. Second and third panels are COS G130M+G160M FUV and STIS E230M NUV spectral ranges, respectively, and we note some interstellar features: *Lyα* λ1216, O I + P II λ1302, C II λ1335, Si II λ1527, and Al II λ1671. The rest of the panels are the UBV and VIS XShooter spectra, with the break between the two arms at ≈ 5600 Å. The lines Ca II H + K and Na I D are interstellar features. . . 319

A.31 An overall view of the best fit (red solid line) to key regions of the observed spectrum (black solid line) of Sk −70° 16. From the top, the first and second panels are COS G130M+G160M FUV and COS G160M+G185M NUV spectral ranges, respectively, and we note some interstellar features: *Lyα* λ1216, O I + P II λ1302, C II λ1335, Si II λ1527, and Al II λ1671. The rest of the panels are the UBV and VIS XShooter spectra, with the break between the two arms at ≈ 5600 Å. The lines Ca II H + K and Na I D are interstellar features. 320

A.32 An overall view of the best fit (red solid line) to key regions of the observed spectrum (black solid line) of Sk −68° 8. From the top, the first and second panels are COS G130M+G160M FUV and STIS E230M NUV spectral ranges, respectively, and we note some interstellar features: *Lyα* λ1216, O I + P II λ1302, C II λ1335, Si II λ1527, and Al II λ1671. The rest of the panels are the UBV and VIS XShooter spectra, with the break between the two arms at ≈ 5600 Å. The lines Ca II H + K and Na I D are interstellar features. 321

A.33 An overall view of the best fit (red solid line) to key regions of the observed spectrum (black solid line) of Sk −67° 195. From the top, the first and second panels are COS G130M+G160M FUV and STIS E230M NUV spectral ranges, respectively, and we note some interstellar features: $Ly\alpha$ λ1216, O I + P II λ1302, C II λ1335, Si II λ1527, and Al IIλ1671. The rest of the panels are the UBV and VIS XShooter spectra, with the break between the two arms at $\approx$ 5600 Å. The lines Ca II H + K and Na I D are interstellar features. 322

B.1 Spectral energy distribution for all the stars in our sample. Red solid line: model SED, Black solid line: observed SED. The photometric points are indicated as blue circles. 334
B.1 continued 335
B.1 continued 336
B.2 Individual line fits for AzV 469 (O9 Iab(f)). Black solid line: observed spectrum. Red solid line: spectrum of the best fitting model. 338
B.3 Individual line fits for AzV 372 (O9.2 Iab). Black solid line: observed spectrum. Red solid line: spectrum of the best fitting model. 339
B.4 Individual line fits for AzV 456 (O9.5 Iab). Black solid line: observed spectrum. Red solid line: spectrum of the best fitting model. 340
B.5 Individual line fits for AzV 327 (O9.7 Ib). Black solid line: observed spectrum. Red solid line: spectrum of the best fitting model. 341
B.6 Individual line fits for AzV 235 (B0 Ia). Black solid line: observed spectrum. Red solid line: spectrum of the best fitting model. 342
B.7 Individual line fits for AzV 215 (B0 Ia). Black solid line: observed spectrum. Red solid line: spectrum of the best fitting model. 343
B.8 Individual line fits for AzV 104 (B0.5 Ia). Black solid line: observed spectrum. Red solid line: spectrum of the best fitting model. 344
B.9 Individual line fits for AzV 410 (B0.7 Iab). Black solid line: observed spectrum. Red solid line: spectrum of the best fitting model. 345
B.10 Individual line fits for AzV 242 (B0.5 Ia). Black solid line: observed spectrum. Red solid line: spectrum of the best fitting model. 346
B.11 Individual line fits for AzV 96 (B1 Iab). Black solid line: observed spectrum. Red solid line: spectrum of the best fitting model. 347
B.12 Individual line fits for AzV 264 (B1 Ia). Black solid line: observed spectrum. Red solid line: spectrum of the best fitting model. 348
B.13 Individual line fits for AzV 175 (B1.5 Ib). Black solid line: observed spectrum. Red solid line: spectrum of the best fitting model. 349
B.14 Individual line fits for Sk 191 (B1.5 Ia). Black solid line: observed spectrum. Red solid line: spectrum of the best fitting model. 350
B.15 Individual line fits for AzV 18 (B2 Ia). Black solid line: observed spectrum. Red solid line: spectrum of the best fitting model. 351
B.16 Individual line fits for NGC330 ELS 04 (B2.5 Ib). Black solid line: observed spectrum. Red solid line: spectrum of the best fitting model. . . . 352

B.17 Individual line fits for AzV 187 (B2.5 Ia). Black solid line: observed spectrum. Red solid line: spectrum of the best fitting model. 353
B.18 Individual line fits for AzV 22 (B3 Ia). Black solid line: observed spectrum. Red solid line: spectrum of the best fitting model. 354
B.19 Individual line fits for AzV 393 (B3 Ia$^+$). Black solid line: observed spectrum. Red solid line: spectrum of the best fitting model. 355
B.20 Individual line fits for AzV 343 (B8 Iab). Black solid line: observed spectrum. Red solid line: spectrum of the best fitting model. 356
B.21 Individual line fits for AzV 324 (B8 Ib). Black solid line: observed spectrum. Red solid line: spectrum of the best fitting model. 357
B.22 An overall view of the best fit (red solid line) to key regions of the observed spectrum (black solid line) of AzV 469 (O9 Iab(f)). From the top, the first panel displays the FUV FUSE range, which contains interstellar features such as *Lyδ* λ950, *Lyγ* λ973, and *Lyβ* λ1026. The second panel is the STIS E140M FUV range. We note some interstellar features: *Lyα* λ1216, O I + P II λ1302, C II λ1335, Si II λ1527, and Al IIλ1671. The rest of the panels are the UBV and VIS XShooter spectra, with the break between the two arms at ≈ 5600 Å. The lines Ca II H + K and Na I D are interstellar features. 359
B.23 An overall view of the best fit (red solid line) to key regions of the observed spectrum (black solid line) of AzV 372 (O9.2 Iab). From the top, the first panel displays the FUV FUSE range, which contains interstellar features such as *Lyδ* λ950, *Lyγ* λ973, and *Lyβ* λ1026. The second and third panels are STIS E140M FUV and STIS E230M UV, respectively. We note some interstellar features: *Lyα* λ1216, O I + P II λ1302, C II λ1335, Si II λ1527, and Al IIλ1671. The rest of the panels are the UBV and VIS XShooter spectra, with the break between the two arms at ≈ 5600 Å. The lines Ca II H + K and Na I D are interstellar features. 360
B.24 An overall view of the best fit (red solid line) to key regions of the observed spectrum (black solid line) of AzV 456 (O9.5 Iab). From the top, the first panel displays the FUV FUSE range, which contains interstellar features such as *Lyδ* λ950, *Lyγ* λ973, and *Lyβ* λ1026. The second and third panels are STIS E140M FUV and STIS E230M UV, respectively. We note some interstellar features: *Lyα* λ1216, O I + P II λ1302, C II λ1335, Si II λ1527, and Al IIλ1671. The rest of the panels are the UBV and VIS XShooter spectra, with the break between the two arms at ≈ 5600 Å. The lines Ca II H + K and Na I D are interstellar features. 361

B.25 An overall view of the best fit (red solid line) to key regions of the observed spectrum (black solid line) of AzV 327 (O9.7 Ib). From the top, the first panel displays the FUV FUSE range, which contains interstellar features such as $Ly\delta$ λ950, $Ly\gamma$ λ973, and $Ly\beta$ λ1026. The second and third panels are COS G130M + Cos G160M FUV and STIS E230M UV, respectively. We note some interstellar features: $Ly\alpha$ λ1216, O I + P II λ1302, C II λ1335, Si II λ1527, and Al IIλ1671. The rest of the panels are the UBV and VIS XShooter spectra, with the break between the two arms at $\approx$ 5600 Å. The lines Ca II H + K and Na I D are interstellar features. . . 362
B.26 An overall view of the best fit (red solid line) to key regions of the observed spectrum (black solid line) of AzV 235 (B0 Ia). From the top, the first panel displays the FUV FUSE range, which contains interstellar features such as $Ly\delta$ λ950, $Ly\gamma$ λ973, and $Ly\beta$ λ1026. The second and third panels are STIS E140M FUV and STIS E230M UV, respectively. We note some interstellar features: $Ly\alpha$ λ1216, O I + P II λ1302, C II λ1335, Si II λ1527, and Al IIλ1671. The rest of the panels are the UBV and VIS XShooter spectra, with the break between the two arms at $\approx$ 5600 Å. The lines Ca II H + K and Na I D are interstellar features. 363
B.27 An overall view of the best fit (red solid line) to key regions of the observed spectrum (black solid line) of AzV 215 (B0 Ia). From the top, the first panel displays the FUV FUSE range, which contains interstellar features such as $Ly\delta$ λ950, $Ly\gamma$ λ973, and $Ly\beta$ λ1026. The second and third panels are STIS E140M FUV and STIS E230M UV, respectively. We note some interstellar features: $Ly\alpha$ λ1216, O I + P II λ1302, C II λ1335, Si II λ1527, and Al IIλ1671. The rest of the panels are the UBV and VIS XShooter spectra, with the break between the two arms at $\approx$ 5600 Å. The lines Ca II H + K and Na I D are interstellar features. 364
B.28 An overall view of the best fit (red solid line) to key regions of the observed spectrum (black solid line) of AzV 104 (B0.5 Ia). From the top, the first panel displays the FUV FUSE range, which contains interstellar features such as $Ly\delta$ λ950, $Ly\gamma$ λ973, and $Ly\beta$ λ1026. The second and third panels are STIS E140M FUV and STIS E230M UV, respectively. We note some interstellar features: $Ly\alpha$ λ1216, O I + P II λ1302, C II λ1335, Si II λ1527, and Al IIλ1671. The rest of the panels are the UBV and VIS XShooter spectra, with the break between the two arms at $\approx$ 5600 Å. The lines Ca II H + K and Na I D are interstellar features. 365
B.29 An overall view of the best fit (red solid line) to key regions of the observed spectrum (black solid line) of AzV 410 (B0.7 Iab). From the top, the first and second panels are STIS E140M FUV and COS G230MLB UV, respectively. We note some interstellar features: $Ly\alpha$ λ1216, O I + P II λ1302, C II λ1335, Si II λ1527, and Al IIλ1671. The rest of the panels are the UBV and VIS XShooter spectra, with the break between the two arms at $\approx$ 5600 Å. The lines Ca II H + K and Na I D are interstellar features. . . 366

B.30 An overall view of the best fit (red solid line) to key regions of the observed spectrum (black solid line) of AzV 242 (B0.7 Ia). From the top, the first panel displays the FUV FUSE range, which contains interstellar features such as *Lyδ* λ950, *Lyγ* λ973, and *Lyβ* λ1026. The second and third panels are STIS E140M FUV and STIS E230M UV, respectively. We note some interstellar features: *Lyα* λ1216, O I + P II λ1302, C II λ1335, Si II λ1527, and Al IIλ1671. The rest of the panels are the UBV and VIS XShooter spectra, with the break between the two arms at ≈ 5600 Å. The lines Ca II H + K and Na I D are interstellar features. 367
B.31 An overall view of the best fit (red solid line) to key regions of the observed spectrum (black solid line) of AzV 96 (B1 Iab). From the top, the first panel displays the FUV FUSE range, which contains interstellar features such as *Lyδ* λ950, *Lyγ* λ973, and *Lyβ* λ1026. The second and third panels are STIS E140M FUV and STIS E230M UV, respectively. We note some interstellar features: *Lyα* λ1216, O I + P II λ1302, C II λ1335, Si II λ1527, and Al IIλ1671. The rest of the panels are the UBV and VIS XShooter spectra, with the break between the two arms at ≈ 5600 Å. The lines Ca II H + K and Na I D are interstellar features. 368
B.32 An overall view of the best fit (red solid line) to key regions of the observed spectrum (black solid line) of AzV 264 (B1 Ia). From the top, the first panel displays the FUV FUSE range, which contains interstellar features such as *Lyδ* λ950, *Lyγ* λ973, and *Lyβ* λ1026. The second and third panels are STIS E140M FUV and STIS E230M UV, respectively. We note some interstellar features: *Lyα* λ1216, O I + P II λ1302, C II λ1335, Si II λ1527, and Al IIλ1671. The rest of the panels are the UBV and VIS XShooter spectra, with the break between the two arms at ≈ 5600 Å. The lines Ca II H + K and Na I D are interstellar features. 369
B.33 An overall view of the best fit (red solid line) to key regions of the observed spectrum (black solid line) of AzV 175 (B1.5 Ib). From the top, the first panel displays the FUV FUSE range, which contains interstellar features such as *Lyδ* λ950, *Lyγ* λ973, and *Lyβ* λ1026. The second panel is the COS G130M + COS G160M FUV. We note some interstellar features: *Lyα* λ1216, O I + P II λ1302, C II λ1335, Si II λ1527, and Al IIλ1671. The rest of the panels are the UBV and VIS XShooter spectra, with the break between the two arms at ≈ 5600 Å. The lines Ca II H + K and Na I D are interstellar features. 370

B.34 An overall view of the best fit (red solid line) to key regions of the observed spectrum (black solid line) of Sk 191 (B1.5 Ia). From the top, the first panel displays the FUV FUSE range, which contains interstellar features such as *Lyδ* λ950, *Lyγ* λ973, and *Lyβ* λ1026. The second and third panels are STIS E140M FUV and STIS E230M UV, respectively. We note some interstellar features: *Lyα* λ1216, O I + P II λ1302, C II λ1335, Si II λ1527, and Al IIλ1671. The rest of the panels are the UBV and VIS XShooter spectra, with the break between the two arms at ≈ 5600 Å. The lines Ca II H + K and Na I D are interstellar features. 371
B.35 An overall view of the best fit (red solid line) to key regions of the observed spectrum (black solid line) of AzV 18 (B2 Ia). From the top, the first panel displays the FUV FUSE range, which contains interstellar features such as *Lyδ* λ950, *Lyγ* λ973, and *Lyβ* λ1026. The second and third panels are STIS E140M FUV and STIS E230M UV, respectively. We note some interstellar features: *Lyα* λ1216, O I + P II λ1302, C II λ1335, Si II λ1527, and Al IIλ1671. The rest of the panels are the UBV and VIS XShooter spectra, with the break between the two arms at ≈ 5600 Å. The lines Ca II H + K and Na I D are interstellar features. 372
B.36 An overall view of the best fit (red solid line) to key regions of the observed spectrum (black solid line) of NGC330 ELS 04 (B2.5 Ib). From the top, the first panel and second panels are STIS E140M FUV and STIS E230M UV, respectively. We note some interstellar features: *Lyα* λ1216, O I + P II λ1302, C II λ1335, Si II λ1527, and Al IIλ1671. The rest of the panels are the UBV and VIS XShooter spectra, with the break between the two arms at ≈ 5600 Å. The lines Ca II H + K and Na I D are interstellar features. 373
B.37 An overall view of the best fit (red solid line) to key regions of the observed spectrum (black solid line) of AzV 187 (B2.5 Ia). From the top, the first panel displays the FUV FUSE range, which contains interstellar features such as *Lyδ* λ950, *Lyγ* λ973, and *Lyβ* λ1026. The second and third panels are COS G130M + COS G160M FUV and STIS E230M UV, respectively. We note some interstellar features: *Lyα* λ1216, O I + P II λ1302, C II λ1335, Si II λ1527, and Al IIλ1671. The rest of the panels are the UBV and VIS XShooter spectra, with the break between the two arms at ≈ 5600 Å. The lines Ca II H + K and Na I D are interstellar features. . . 374
B.38 An overall view of the best fit (red solid line) to key regions of the observed spectrum (black solid line) of AzV 22 (B3 Ia). From the top, the first and second panels are the STIS E140M FUV and STIS E230M UV, respectively. We note some interstellar features: *Lyα* λ1216, O I + P II λ1302, C II λ1335, Si II λ1527, and Al IIλ1671. The rest of the panels are the UBV and VIS XShooter spectra, with the break between the two arms at ≈ 5600 Å. The lines Ca II H + K and Na I D are interstellar features. . . 375

B.39 An overall view of the best fit (red solid line) to key regions of the observed spectrum (black solid line) of AzV 393 (B3 Ia$^+$). From the top, the first panel is the FUV FUSE range, containing interstellar features such as *Lyδ* λ950, *Lyγ* λ973, and *Lyβ* λ1026. The second and third panels are COS G130M + COS G160M FUV and STIS E230M UV, respectively. We note some interstellar features: *Lyα* λ1216, O I + P II λ1302, C II λ1335, Si II λ1527, and Al IIλ1671. The rest of the panels are the UBV and VIS XShooter spectra, with the break between the two arms at ≈ 5600 Å. The lines Ca II H + K and Na I D are interstellar features. 376
B.40 An overall view of the best fit (red solid line) to key regions of the observed spectrum (black solid line) of AzV 343 (B8 Iab). From the top, the first panel and second panels are COS G130M + COS G160M FUV and STIS E230M UV, respectively. We note some interstellar features: *Lyα* λ1216, O I + P II λ1302, C II λ1335, Si II λ1527, and Al IIλ1671. The rest of the panels are the UBV and VIS XShooter spectra, with the break between the two arms at ≈ 5600 Å. The lines Ca II H + K and Na I D are interstellar features. 377
B.41 An overall view of the best fit (red solid line) to key regions of the observed spectrum (black solid line) of AzV 324 (B8 Ib). From the top, the first and second panels are COS G130M + COS G160M FUV and STIS E230M UV, respectively. We note some interstellar features: *Lyα* λ1216, O I + P II λ1302, C II λ1335, Si II λ1527, and Al IIλ1671. The rest of the panels are the UBV and VIS XShooter spectra, with the break between the two arms at ≈ 5600 Å. The lines Ca II H + K and Na I D are interstellar features. 378

C.1 Spectral energy distribution for all the stars in our Galactic sample. Red solid line: model SED, Black solid line: observed SED. The photometric points are indicated as blue circles. 392
C.1 continued 393
C.1 continued 394
C.1 continued 395
C.2 Individual line fits for HD30614 (O9 Ia). Black solid line: observed spectrum. Red solid line: spectrum of the best fitting model. 397
C.3 Individual line fits for HD210809 (O9 Iab). Black solid line: observed spectrum. Red solid line: spectrum of the best fitting model. 398
C.4 Individual line fits for HD209975 (O9 Ib). Black solid line: observed spectrum. Red solid line: spectrum of the best fitting model. The observed spectrum is corrected for 399
C.5 Individual line fits for HD154368 (O9.2 Iab). Black solid line: observed spectrum. Red solid line: spectrum of the best fitting model. The observed spectrum is corrected for 400
C.6 Individual line fits for HD76968 (O9.2 Ib). Black solid line: observed spectrum. Red solid line: spectrum of the best fitting model. The observed spectrum is corrected for 401

C.7 Individual line fits for HD105056 (ON9.7 Ia$^+$). Black solid line: observed spectrum. Red solid line: spectrum of the best fitting model. The observed spectrum is corrected for 402
C.8 Individual line fits for HD37128 (B0 Ia). Black solid line: observed spectrum. Red solid line: spectrum of the best fitting model. The observed spectrum is corrected for 403
C.9 Individual line fits for HD209975 (B0.2 Iab). Black solid line: observed spectrum. Red solid line: spectrum of the best fitting model. The observed spectrum is corrected for 404
C.10 Individual line fits for HD38771 (B0.5 Ia). Black solid line: observed spectrum. Red solid line: spectrum of the best fitting model. 405
C.11 Individual line fits for HD192422 (B0.5 Ib). Black solid line: observed spectrum. Red solid line: spectrum of the best fitting model. 406
C.12 Individual line fits for HD190066 (B0.7 Ib). Black solid line: observed spectrum. Red solid line: spectrum of the best fitting model. 407
C.13 Individual line fits for HD169454 (B1 Ia$^+$). Black solid line: observed spectrum. Red solid line: spectrum of the best fitting model. 408
C.14 Individual line fits for HD13854 (B1 Iab). Black solid line: observed spectrum. Red solid line: spectrum of the best fitting model. 409
C.15 Individual line fits for HD24398 (B1 Ib). Black solid line: observed spectrum. Red solid line: spectrum of the best fitting model. 410
C.16 Individual line fits for HD190603 (B1.5 Ia$^+$). Black solid line: observed spectrum. Red solid line: spectrum of the best fitting model. 411
C.17 Individual line fits for HD13841 (B1.5 Ib). Black solid line: observed spectrum. Red solid line: spectrum of the best fitting model. 412
C.18 Individual line fits for HD41117 (B2 Ia). Black solid line: observed spectrum. Red solid line: spectrum of the best fitting model. 413
C.19 Individual line fits for HD206165 (O9 Ia). Black solid line: observed spectrum. Red solid line: spectrum of the best fitting model. 414
C.20 Individual line fits for HD198478 (B2.5 Ia). Black solid line: observed spectrum. Red solid line: spectrum of the best fitting model. 415
C.21 Individual line fits for HD42087 (B2.5 Ib). Black solid line: observed spectrum. Red solid line: spectrum of the best fitting model. 416
C.22 Individual line fits for HD53138 (B3 Ib). Black solid line: observed spectrum. Red solid line: spectrum of the best fitting model. 417
C.23 Individual line fits for HD51309 (B3 Ib). Black solid line: observed spectrum. Red solid line: spectrum of the best fitting model. 418
C.24 Individual line fits for HD58350 (B5 Ia). Black solid line: observed spectrum. Red solid line: spectrum of the best fitting model. 419
C.25 Individual line fits for HD199478 (B7 Ia). Black solid line: observed spectrum. Red solid line: spectrum of the best fitting model. 420
C.26 Individual line fits for HD34085 (B8 Ia). Black solid line: observed spectrum. Red solid line: spectrum of the best fitting model. 421

C.27 Individual line fits for HD12301 (B8 Ib). Black solid line: observed spectrum. Red solid line: spectrum of the best fitting model. 422
C.28 An overall view of the best fit (red solid line) to key regions of the observed spectrum (black solid line) of HD30614. From top to bottom, the first two panels show the IUE SWP FUV range. We note some interstellar features: *Lyα* λ1216, O I + P II λ1302, C II λ1335, Si II λ1527, and Al IIλ1671. The remaining panels show the Mercator/HERMES spectrum from the Melchiors spectroscopic library. The lines Ca II H + K and Na I D are interstellar features. 424
C.29 An overall view of the best fit (red solid line) to key regions of the observed spectrum (black solid line) of HD210809. From top to bottom, the first two panels show the IUE SWP FUV range. We note some interstellar features: *Lyα* λ1216, O I+P II λ1302, C II λ1335, Si II λ1527, and Al IIλ1671. The remaining panels show the Mercator/HERMES spectrum from the Melchiors spectroscopic library. The lines Ca II H + K and Na I D are interstellar features. 425
C.30 An overall view of the best fit (red solid line) to key regions of the observed spectrum (black solid line) of HD209975. From top to bottom, the first two panels show the IUE SWP FUV range. We note some interstellar features: *Lyα* λ1216, O I + P II λ1302, C II λ1335, Si II λ1527, and Al IIλ1671. The remaining panels show the Mercator/HERMES spectrum from the IACOB spectroscopic library. The lines Ca II H + K and Na I D are interstellar features. 426
C.31 An overall view of the best fit (red solid line) to key regions of the observed spectrum (black solid line) of HD154368. From top to bottom, the first two panels show the IUE SWP FUV range. We note some interstellar features: *Lyα* λ1216, O I + P II λ1302, C II λ1335, Si II λ1527, and Al IIλ1671. The remaining panels show the MPG/FEROS spectrum from the IACOB spectroscopic library. The lines Ca II H + K and Na I D are interstellar features. 427
C.32 An overall view of the best fit (red solid line) to key regions of the observed spectrum (black solid line) of HD76968. From top to bottom, the first two panels show the IUE SWP FUV range. We note some interstellar features: *Lyα* λ1216, O I + P II λ1302, C II λ1335, Si II λ1527, and Al IIλ1671. The remaining panels show the MPG/FEROS spectrum from the IACOB spectroscopic library. The lines Ca II H + K and Na I D are interstellar features. 428
C.33 An overall view of the best fit (red solid line) to key regions of the observed spectrum (black solid line) of HD105056. From top to bottom, the first two panels show the IUE SWP FUV range. We note some interstellar features: *Lyα* λ1216, O I + P II λ1302, C II λ1335, Si II λ1527, and Al IIλ1671. The remaining panels show the VLT/UVES spectrum from the UVES-POP spectroscopic library. The lines Ca II H + K and Na I D are interstellar features. 429

C.34 An overall view of the best fit (red solid line) to key regions of the observed spectrum (black solid line) of HD37128. From top to bottom, the first two panels show the IUE SWP FUV range. We note some interstellar features: *Lyα* λ1216, O I + P II λ1302, C II λ1335, Si II λ1527, and Al IIλ1671. The remaining panels show the Mercator/HERMES spectrum from the IACOB spectroscopic library. The lines Ca II H + K and Na I D are interstellar features. 430
C.35 An overall view of the best fit (red solid line) to key regions of the observed spectrum (black solid line) of HD204172. From top to bottom, the first two panels show the IUE SWP FUV range. We note some interstellar features: *Lyα* λ1216, O I + P II λ1302, C II λ1335, Si II λ1527, and Al IIλ1671. The remaining panels show the NOT/FIES spectrum from the IACOB spectroscopic library. The lines Ca II H + K and Na I D are interstellar features. 431
C.36 An overall view of the best fit (red solid line) to key regions of the observed spectrum (black solid line) of HD38771. From top to bottom, the first two panels show the IUE SWP FUV range. We note some interstellar features: *Lyα* λ1216, O I + P II λ1302, C II λ1335, Si II λ1527, and Al IIλ1671. The remaining panels show the Mercator/HERMES spectrum from the IACOB spectroscopic library. The lines Ca II H + K and Na I D are interstellar features. 432
C.37 An overall view of the best fit (red solid line) to key regions of the observed spectrum (black solid line) of HD192422. From top to bottom, the first two panels show the IUE SWP FUV range. We note some interstellar features: *Lyα* λ1216, O I + P II λ1302, C II λ1335, Si II λ1527, and Al IIλ1671. The remaining panels show the Mercator/HERMES spectrum from the IACOB spectroscopic library. The lines Ca II H + K and Na I D are interstellar features. 433
C.38 An overall view of the best fit (red solid line) to key regions of the observed spectrum (black solid line) of HD190066. From top to bottom, the first two panels show the IUE SWP FUV range. We note some interstellar features: *Lyα* λ1216, O I + P II λ1302, C II λ1335, Si II λ1527, and Al IIλ1671. The remaining panels show the NOT/FIES spectrum from the IACOB spectroscopic library. The lines Ca II H + K and Na I D are interstellar features. 434
C.39 An overall view of the best fit (red solid line) to key regions of the observed spectrum (black solid line) of HD169454. From top to bottom, the first two panels show the IUE SWP FUV range. We note some interstellar features: *Lyα* λ1216, O I+P II λ1302, C II λ1335, Si II λ1527, and Al IIλ1671. The remaining panels show the Mercator/HERMES spectrum from the Melchiors spectroscopic library. The lines Ca II H + K and Na I D are interstellar features. 435

C.40 An overall view of the best fit (red solid line) to key regions of the observed spectrum (black solid line) of HD13854. From top to bottom, the first two panels show the IUE SWP FUV range. We note some interstellar features: *Lyα* λ1216, O I + P II λ1302, C II λ1335, Si II λ1527, and Al IIλ1671. The remaining panels show the Mercator/HERMES spectrum from the IACOB spectroscopic library. The lines Ca II H + K and Na I D are interstellar features. 436
C.41 An overall view of the best fit (red solid line) to key regions of the observed spectrum (black solid line) of HD24398. From top to bottom, the first two panels show the IUE SWP FUV range. We note some interstellar features: *Lyα* λ1216, O I + P II λ1302, C II λ1335, Si II λ1527, and Al IIλ1671. The remaining panels show the Mercator/HERMES spectrum from the Melchiors spectroscopic library. The lines Ca II H + K and Na I D are interstellar features. 437
C.42 An overall view of the best fit (red solid line) to key regions of the observed spectrum (black solid line) of HD190603. From top to bottom, the first two panels show the IUE SWP FUV range. We note some interstellar features: *Lyα* λ1216, O I + P II λ1302, C II λ1335, Si II λ1527, and Al IIλ1671. The remaining panels show the Mercator/HERMES spectrum from the IACOB spectroscopic library. The lines Ca II H + K and Na I D are interstellar features. 438
C.43 An overall view of the best fit (red solid line) to key regions of the observed spectrum (black solid line) of HD13841. From top to bottom, the first two panels show the IUE SWP FUV range. We note some interstellar features: *Lyα* λ1216, O I + P II λ1302, C II λ1335, Si II λ1527, and Al IIλ1671. The remaining panels show the Mercator/HERMES spectrum from the IACOB spectroscopic library. The lines Ca II H + K and Na I D are interstellar features. 439
C.44 An overall view of the best fit (red solid line) to key regions of the observed spectrum (black solid line) of HD41117. From top to bottom, the first two panels show the IUE SWP FUV range. We note some interstellar features: *Lyα* λ1216, O I + P II λ1302, C II λ1335, Si II λ1527, and Al IIλ1671. The remaining panels show the NOT/FIES spectrum from the IACOB spectroscopic library. The lines Ca II H + K and Na I D are interstellar features. 440
C.45 An overall view of the best fit (red solid line) to key regions of the observed spectrum (black solid line) of HD206165. From top to bottom, the first two panels show the IUE SWP FUV range. We note some interstellar features: *Lyα* λ1216, O I + P II λ1302, C II λ1335, Si II λ1527, and Al IIλ1671. The remaining panels show the NOT/FIES spectrum from the IACOB spectroscopic library. The lines Ca II H + K and Na I D are interstellar features. 441

C.46 An overall view of the best fit (red solid line) to key regions of the observed spectrum (black solid line) of HD198478. From top to bottom, the first two panels show the IUE SWP FUV range. We note some interstellar features: *Lyα* λ1216, O I + P II λ1302, C II λ1335, Si II λ1527, and Al IIλ1671. The remaining panels show the Mercator/HERMES spectrum from the IACOB spectroscopic library. The lines Ca II H + K and Na I D are interstellar features. 442
C.47 An overall view of the best fit (red solid line) to key regions of the observed spectrum (black solid line) of HD42087. From top to bottom, the first two panels show the IUE SWP FUV range. We note some interstellar features: *Lyα* λ1216, O I + P II λ1302, C II λ1335, Si II λ1527, and Al IIλ1671. The remaining panels show the Mercator/HERMES spectrum from the IACOB spectroscopic library. The lines Ca II H + K and Na I D are interstellar features. 443
C.48 An overall view of the best fit (red solid line) to key regions of the observed spectrum (black solid line) of HD53138. From top to bottom, the first two panels show the IUE SWP FUV range. We note some interstellar features: *Lyα* λ1216, O I + P II λ1302, C II λ1335, Si II λ1527, and Al IIλ1671. The remaining panels show the Mercator/HERMES spectrum from the IACOB spectroscopic library. The lines Ca II H + K and Na I D are interstellar features. 444
C.49 An overall view of the best fit (red solid line) to key regions of the observed spectrum (black solid line) of HD51309. From top to bottom, the first two panels show the IUE SWP FUV range. We note some interstellar features: *Lyα* λ1216, O I + P II λ1302, C II λ1335, Si II λ1527, and Al IIλ1671. The remaining panels show the Mercator/HERMES spectrum from the IACOB spectroscopic library. The lines Ca II H + K and Na I D are interstellar features. 445
C.50 An overall view of the best fit (red solid line) to key regions of the observed spectrum (black solid line) of HD58350. From top to bottom, the first two panels show the IUE SWP FUV range. We note some interstellar features: *Lyα* λ1216, O I + P II λ1302, C II λ1335, Si II λ1527, and Al IIλ1671. The remaining panels show the Mercator/HERMES spectrum from the Melchiors spectroscopic library. The lines Ca II H + K and Na I D are interstellar features. 446
C.51 An overall view of the best fit (red solid line) to key regions of the observed spectrum (black solid line) of HD199478. From top to bottom, the first two panels show the IUE SWP FUV range. We note some interstellar features: *Lyα* λ1216, O I + P II λ1302, C II λ1335, Si II λ1527, and Al IIλ1671. The remaining panels show the Mercator/HERMES spectrum from the IACOB spectroscopic library. The lines Ca II H + K and Na I D are interstellar features. 447

C.52 An overall view of the best fit (red solid line) to key regions of the observed spectrum (black solid line) of HD34085. From top to bottom, the first two panels show the IUE SWP FUV range. We note some interstellar features: *Lyα* λ1216, O I + P II λ1302, C II λ1335, Si II λ1527, and Al IIλ1671. The remaining panels show the Mercator/HERMES spectrum from the IACOB spectroscopic library. The lines Ca II H + K and Na I D are interstellar features. 448
C.53 An overall view of the best fit (red solid line) to key regions of the observed spectrum (black solid line) of HD12301. From top to bottom, the first two panels show the IUE SWP FUV range. We note some interstellar features: *Lyα* λ1216, O I + P II λ1302, C II λ1335, Si II λ1527, and Al IIλ1671. The remaining panels show the Mercator/HERMES spectrum from the IACOB spectroscopic library. The lines Ca II H + K and Na I D are interstellar features. 449

Tables

2.1 Parameters of the CMGEN grids. 70
2.2 Metal abundances adopted in the model grids. $\epsilon_X = \log X/H + 12$ by number. In the reference columns, A05 is Asplund et al. (2005), H08 is Hunter et al. (2008b), and V23 is Vink et al. (2023). 73
2.3 Ions and number of important levels (IL), super-levels (SL), full levels (FL), and transitions (T) considered per ion, which constitutes the atomic model (M) used by the code to synthesise the spectrum. 76
2.3 Continued. 77
2.4 Properties of the PYPHOT filter functions (Fouesneau, 2025). 90
2.5 Line diagnostics for determination of CNO elemental abundances. 99

3.1 Targets in our sample. The last three columns are the wavelengths (in Å) of the UV ranges and the corresponding instruments that were used for observations. The literature spectral types were adopted from Vink et al. (2023). The revised classifications were adopted from Bestenlehner et al. (2025). 103
3.2 Photometric data. References: 1 Cioni et al. (2011), 2 Cutri et al. (2003), 3 Massey (2002), 4 Schmidt-Kaler et al. (1999), 5 Ardeberg et al. (1972), 6 Isserstedt (1975). 105
3.3 Derived stellar parameters based on the best fitting CMFGEN model. Presented uncertainties for effective temperatures $T_{\rm eff}$ are double the model uncertainty. In the uncertainties of centrifugal force-corrected surface gravity $\log g_c$, we take into account the model uncertainty of $\log g$ and the uncertainty of the projected rotational velocity $v_{\rm rot} \sin i$ and the radius R_*. The uncertainty in the derived luminosities is $\Delta \log L_{\rm bol} = 0.1$ The uncertainty in radial velocity $v_{\rm rad}$ measurements is dominated by the velocity resolution of the UBV part of the spectrum, which is $\Delta v \approx 45$ km s^{-1}. The relative extinction R_V ($\Delta R_V \approx 0.3$ mag), colour excess $E(B-V)$ ($\Delta E(B-V) \approx 0.05$ mag), absolute V-band magnitude M_V, and bolometric correction BC_V are produced from the SED fits that are shown in Appendix A.5. $\Gamma_e^{\rm spec}$ is subject to uncertainties of $\Delta\Gamma_e^{\rm spec} \approx 0.18$ which takes into account the uncertainties of $M_{\rm spec}$ and $\log L_{\rm bol}$ 107

3.4 Evolutionary parameters of our sample. $M_{\rm init}$, $M_{\rm evo}$, and ages of the stars are derived using an updated Bayesian inference method (Bronner et al. in prep) that is similar to BONNSAI (Schneider et al., 2014a) applied to Brott et al. (2011) evolutionary tracks. 108
3.5 Wind parameters for our targets. The mass-loss rates of Sk −70° 16 and Sk −67° 195 are upper limits. The escape velocities are adjusted for $\Gamma_{\rm e}$. v_∞ values with the superscript ‡ indicate that v_∞ was inferred as $v_{\rm edge} \times \langle v_{\rm black}/v_{\rm edge}\rangle_{\rm LMC}$. 115
3.6 Slopes, a, and offsets, b, of the linear fits to the terminal wind velocity equation (Equation 3.2) of this study and Hawcroft et al. (2024a) 115
3.7 Comparison of our broadening parameters with those obtained via IACOB-BROAD (Simón-Díaz & Herrero, 2014a) applied to high-resolution MIKE data. 124
3.8 Best-fitting photospheric abundances $\epsilon_{\rm X}$. The final two columns list the cumulative CNO abundances relative to the LMC baseline (Vink et al., 2023) and solar (Asplund et al., 2005). The adopted uncertainty on the CNO abundances is ±0.3 125
3.9 Slopes, x, and offsets, $\log D_0$, of the linear fits to the modified wind momentum equation (Equation 3.4) of this study, Mokiem et al. (2007), and Backs et al. (2024) 146

4.1 List of the stars included in our analysis and the respective wavelength coverage. The spectral types are based on XShootU observations (Bestenlehner et al., 2025) 152
4.2 Photometric data. References: 1 Cioni et al. (2011), 2 Cutri et al. (2003), 3 Massey (2002), 4 Azzopardi et al. (1975), 5 Ardeberg & Maurice (1977), 6 Ardeberg (1980), 7 Evans et al. (2006). 154
4.3 Derived stellar parameters based on the best fitting CMFGEN model. The uncertainties of the best fitting parameters are derived similarly to those in Table 3.3 of Chapter 3/ 156
4.4 Inferred evolutionary masses M_{init}, $M_{\rm evo}$, and ages of the stars. These were derived using an updated Bayesian inference method (Bronner et al. in prep) that is similar to BONNSAI (Schneider et al., 2014a) applied to Brott et al. (2011) SMC evolutionary tracks. 157
4.5 Derived wind parameters. $\log \dot{M}$ with † in the superscript indicates an upper limit. v_∞ values with the superscript ‡ indicate that v_∞ was inferred as $v_{\rm edge} \times \langle v_{\rm black}/v_{\rm edge}\rangle_{\rm SMC}$. 162
4.6 Fitting parameter a (slope) and b (intercept) for Equation 4.1. 167
4.7 Comparison of our adopted broadening parameters with those obtained via IACOB-BROAD (Simón-Díaz & Herrero, 2014b) applied to high-resolution MIKE data. 169

4.8 Best-fitting helium (Y, by mass) and CNO (ϵ_X, by number) abundances. The uncertainties of the helium mass fraction are 10% . The adopted uncertainty of CNO abundances is ±0.3 dex. The last two columns represent the cumulative CNO mass fraction relative to the cumulative CNO SMC baseline and solar baseline, respectively. Oxygen abundance values with the asterisk subscript were obtained from fitting the O I $\lambda\lambda\lambda 7772 - 7774 - 7775$ multiple, and are considered lower limits. . . 170
4.9 Slopes, x, and vertical offsets, $\log D_0$, of Equation 4.2 of this study and from Chapter 3. 175
4.10 Fitting parameter of Equation 4.3. 179

5.1 List of the stars included in our analysis and the respective wavelength coverage. The number of IUE observations is included for each individual star. The spectral types (SpT) are taken from Negueruela et al. (2024) for B supergiants and Holgado et al. (2018) for O supergiants. 193
5.2 Photometric data and distances. B-J: Bailer-Jones et al. (2021); Bailer-Jones (2023, *GAIA* DR3), V-L: van Leeuwen (2007, *Hipparcos*), S-S: Sánchez-Sanjuán et al. (2024, cluster association using *GAIA* DR3) . . . 196
5.3 Derived stellar parameters based on the best fitting CMFGEN model. The uncertainties of the best fitting parameters are derived similarly to those in Table 3.3 of Chapter 3. 200
5.4 Inferred evolutionary masses M_{init}, $M_{\rm evo}$, and ages of the stars. These were derived using an updated Bayesian inference method (Bronner et al. in prep) that is similar to BONNSAI (Schneider et al., 2014a) applied to Brott et al. (2011) Galactic evolutionary tracks. 201
5.5 Derived wind parameters. $\log \dot{M}$ with † in the superscript indicates an upper limit. $\log \dot{M}$ is subject to an average uncertainty of 0.4 dex. $v_{\rm esc}$ is the escape velocity at the photosphere. v_∞ values with the superscript ‡ indicate that v_∞ was inferred as $v_{\rm edge} \times \langle v_{\rm black}/v_{\rm edge}\rangle_{\rm MW}$. 207
5.6 Comparison of our derived broadening parameters with those obtained via IACOB-BROAD (Simón-Díaz & Herrero, 2014b) from same data set and rotational properties drawn from Simón-Díaz & Herrero (2014a) and de Burgos et al. (2024b) (SD14 and DB24, respectively). Simón-Díaz & Herrero (2014a) and de Burgos et al. (2024b) adopt global uncertainties for $v_{\rm rot} \sin i$ and $v_{\rm mac}$ of 15 and 20 km s^{-1}, respectively. 214
5.7 Best-fitting helium (Y, by mass) and CNO (ϵ_X, by number) abundances. The uncertainty in the helium mass fraction is 10%. The adopted uncertainty of CNO abundances is ±0.3 dex. The last column represents the cumulative CNO mass fraction relative to the cumulative CNO solar baseline. 217

5.8 Absolute means of the difference between our derived values of $T_{\rm eff}$ [kK], $\log g/{\rm cm\,s^{-2}}$, $\log L_{\rm bol}/L_\odot$, and $\log \dot{M}_{\rm smooth}/M_\odot\,{\rm yr^{-1}}$, and those obtained by Crowther et al. (2006, C06), Lefever et al. (2007, L07), Searle et al. (2008, S08), Haucke et al. (2018, H18), Rubio-Díez et al. (2022, RD22), and Bernini-Peron et al. (2023, BP23). 222

6.1 Fitting parameters of Equation 6.1. In the first column, "reliable" indicates that the fit was performed using stars with reliably determined mass-loss rates, i.e., these stars show an emission component in Hα and have reliable v_∞ measurements from UV P Cygni profiles. N in the second column represents the number of stars. 231
6.2 Comparison of the metallicity dependence of the mass-loss rates from various recipes. e is the metallicity scaling factor from Equation 6.1. The two values from Vink & Sander (2021) are for stars on the hot and cool side of the bi-stability jump, respectively. 234

A.1 $v_{\rm black}$ for the stars in our sample. 278
A.2 Comparison of derived parameters to previous studies. 280
A.2 Continued 281
A.3 Fitting parameters of the UV reddening law. 323

B.1 $v_{\rm edge}$ and $v_{\rm black}$ for the stars in our sample. 325
B.2 Comparison of derived parameters to previous studies. 327
B.2 Continued. 328
B.2 Continued. 329
B.3 Fitting parameters of the UV reddening law. 380

C.1 $v_{\rm black}$ for the stars in our Galactic sample. 382
C.2 Comparison of derived parameters to previous studies. 384
C.2 Continued. 385

Acronyms and Abbreviations

BC	bolometric correction
DM	distance modulus
BH	black hole
BSG	blue supergiants
DAC	discrete absorption components
EUV	extreme ultraviolet
FUV	far ultraviolet
FWHM	full-width at half-maximum
HD	Humphreys-Davidson
HRD	Hertzsprung-Russell diagram
HST	Hubble Space Telescope
IMF	initial mass function
IUE	International Ultraviolet Explorer
LBVs	Luminous Blue Variables
LMC	Large Magellanic Cloud
LTE	local thermodynamic equilibrium
MCs	Magellanic Clouds
MK	Morgan-Keenan classification scheme
MS	main sequence
MW	Milky Way
NAC	narrow absorption components
nLTE	non-local thermodynamic equilibrium
NS	neutron star
Pop III	Population III

RSG	red supergiants
RT	radiative transfer
RTE	radiative transfer equations
SED	spectral energy distribution
SEI	Sobolev with exact integration
SMC	Small Magellanic Cloud
TAMS	terminal-age main sequence
TE	Thermodynamic equilibrium
ULLYSES	Ultraviolet Legacy Library of Young Stars as Essential Standards
UV	ultraviolet
VLT	Very Large Telescope
WLR	wind momentum-luminosity relation
WR	Wolf-Rayet
ZAMS	zero-age main sequence

Chapter 1

Introduction

1.1 Massive stars across cosmic and human history

1.1.1 Observational properties of massive stars

Massive stars are generally defined as stars with masses starting at 8 $M_{\odot}$, and reaching up to a few hundred $M_{\odot}$ in some extreme cases (Crowther et al., 2010). They are rare by absolute numbers, making up $\leq 2\%$ of the initial mass function (IMF). The effective surface temperatures $T_{\rm eff}$ of hot and young massive stars on the main sequence (MS) exceed 20 kK, whereas evolved cool massive stars can reach temperatures as low as 3 kK. Due to their high $T_{\rm eff}$ and radii, massive stars are extremely bright, with luminosities ranging from a few tens of thousands up to millions of $L_{\odot}$, making them some of the brightest objects in their host galaxies. Visually, their colour appears to be blue, if not heavily reddened by dust. Their lifespans are short ($\tau_{\rm life} \approx 10$ Myr for a 20 $M_{\odot}$ star), of which they spend $\approx 90\%$ on the main sequence. The death of a massive star signals a cataclysmic collapse of its core, and may end in an explosive event, known as a core-collapse supernova. After their death, massive stars leave behind exotic remnants, which could be a stellar mass black hole (BH) or a neutron star (NS).

One of the most interesting features of massive stars is the powerful winds through which they lose large amounts of their mass during their life. Morton (1967) was the first to recognise mass loss from massive stars. Their discovery was enabled by analysing some of the earliest ultraviolet (UV) spectroscopic data. They noticed blueshifted absorption lines in the UV spectra of OB stars in Orion. This was interpreted as being due to photon absorption in atmospheric UV lines, where an outward force is exerted on ions as the exciting photons are travelling outwards. This causes the accelerated ions to couple with the other particles through scattering and electrostatic forces, leading to outflows extending from the atmosphere (Lucy & Solomon, 1970a; Castor et al., 1975a).

Over the last few decades, with the advancement in observational capabilities, large-scale spectroscopic surveys aiming at characterising the multiplicity of massive stars have reached a consensus: massive stars are mostly binaries. Studies find a binary fraction of 20-70% in different environments and evolutionary phases (Sana et al., 2008, 2012; Britavskiy et al., 2025; Villaseñor et al., 2025). However, in some studies, these are lower limits that do not account for observational biases like spectroscopic binary systems that are missed because of specific orbital configurations (low inclination, high eccentricity), long orbital periods, undetected low-mass companions, and single lined spectroscopic binaries that can only be confirmed as binaries with high-resolution spectroscopy (SB1). Therefore, it could be the case that binary massive stars are more common than we observe.

1.1.2 Feedback from massive stars

Radiative feedback

The spectral energy distribution (SED) of massive stars peaks in the UV due to their high temperatures, making them the dominating source of Lyman continuum in most star-forming galaxies – if not heavily obscured by dust – and dictating the thermal

and ionisation state of the ISM (Kennicutt, 1998). The far ultraviolet (FUV) photons ($\approx 6.0 < h\nu < 13.6$ eV) emitted from massive stars or clusters can penetrate deep into their host molecular clouds, leading to the photodissociation of certain atomic and molecular species, most notably molecular hydrogen, and forming photodissociation regions. The emission of the more energetic extreme ultraviolet (EUV) Lyman photons ($h\nu \geq 13.6$ eV) leads to the formation of H II regions where the gas is heated to $\approx 10^4$ K. This photoionisation drives thermal expansion of the host nebulae into the colder and neutral surrounding, leading to the destruction of the natal molecular cloud. O-type stars emit hydrogen-ionizing fluxes of $Q_{\rm H} \approx 10^{47}$–$10^{49.5}$ s^{-1} (Martins et al., 2005a). While B-type stars are significantly more numerous, their individual output is orders of magnitude lower ($Q_{\rm H} \approx 10^{45}$–$10^{47}$ s^{-1} for early B-types), creating only smaller, localized H II regions (Sternberg et al., 2003). In contrast, Wolf-Rayet (WR) stars possess extremely hard ionising spectra due to their high effective temperatures ($T_{\rm eff} \gtrsim 40$ kK). A single WR star can emit $Q_{\rm H} \approx 10^{49}$-$10^{50}$ s^{-1}, but they are uniquely distinguished by their production of helium-ionising photons. While O and B stars produce negligible He II-ionizing flux ($h\nu > 54.4$ eV), WR stars can emit $Q_{\rm HeII} \approx 10^{46}$–$10^{47}$ s^{-1} (Garnett et al., 1991; Crowther, 2007; Sander & Vink, 2020), significantly altering the ionization structure and temperature profile of the surrounding nebula.

Beyond the UV regime, massive stars contribute significantly to the X-ray background. Soft X-rays ($0.1 - 2$ keV) are generated intrinsically by shocks embedded within stellar winds (Owocki et al., 1988) or by wind-wind collisions in binary systems (Cherepashchuk, 1976; Stevens et al., 1992). Additionally, High-Mass X-ray Binaries (HMXBs) produce hard X-rays ($E > 2$ keV) via accretion onto the compact component. This generates hard X-ray luminosities that can exceed 10^{38} erg s^{-1} (Grimm et al., 2003; Mineo et al., 2012). Unlike UV photons, which are absorbed at the ionisation front, these X-rays have small photoionisation cross-sections, allowing them to penetrate deep into the neutral gas, heating and partially ionising the warm neutral medium far from the

star itself. This is why X-rays from massive stars have been invoked to explain nebular He II emission in nearby star-forming regions (Senchyna et al., 2020) and the heating and ionisation of the early universe (Mirabel et al., 2011).

Furthermore, the first stars that formed in the early universe are thought to have been extremely hot and massive. These stars are called Population III (Pop III) stars, and are characterised by their extremely low or even lack of metal content, which reflects the conditions in the early universe. As such, massive stars are thought to have had extreme ionising fluxes (Barkana & Loeb, 2001), which could have played an essential role in re-ionising the universe (Haiman & Loeb, 1997). Early predictions showed that the temperatures of Pop III stars exceed 10^5 K, with masses that range from a few hundred solar masses to potentially thousands of solar masses (Abel et al., 2002), which are known as very massive stars (VMS). More recent studies show that Pop III stars are more diverse than previously thought, and could be low-mass stars ($M \approx$ 0.1-0.8 $M_\odot$ Stacy & Bromm, 2014), intermediate-mass stars ($M \approx$ 0.8-10 $M_\odot$ Susa et al., 2014), or even supermassive stars (10^5-10^6 $M_\odot$ Woods et al., 2017).

Compact remnant binaries, such as NS-NS, NS-BH, and BH-BH, are thought to be the offspring of massive binaries. Components of these binaries may eventually spiral down and merge, producing some of the most energetic events in the universe. The feedback of these events is felt across the cosmos as gravitational radiation, which we can detect as gravitational waves that ripple through the space-time continuum. This has been confirmed by the landmark GW150914 event, which saw the merger of two heavy stellar-mass black holes (Abbott et al., 2016), and the NS-NS merger GW170817, which was the first gravitational-wave source to be successfully observed across the electromagnetic spectrum (Abbott et al., 2017).

Mechanical feedback

Massive stars are also a source of mechanical feedback, which is represented by the injection of momentum and kinetic energy into the ISM via their continuous stellar winds and the explosive input from CCSNe. Massive stars can experience different rates of mass loss, depending on their evolutionary stage, reaching upwards of 10^{-4} $M_{\odot}\,yr^{-1}$. Their winds reach supersonic terminal velocities, ranging between a few hundred and a few thousand $km\,s^{-1}$, which is a function of their temperature and evolutionary stage. The combination of the extreme ionising fluxes and energetic winds leads to significant perturbations in the ISM, creating local low-density regions (voids) that are surrounded by the perturbed, high-density shells (Castor et al., 1975b; Weaver et al., 1977). This is a potential triggering mechanism of star formation, where the perturbations disturb the structure of the gas, causing it to collapse on itself, initiating star formation.

Following the exhaustion of nuclear fuel, the feedback cycle concludes with a CCSN, which produces shock waves that carry immense amounts of energy ($\approx 10^{51}$ erg) (Smith, 2014). The resulting blast accelerates the surrounding gas, generating large-scale turbulence and shocks that can disrupt molecular clouds and regulate the galaxy-scale star formation rate (Thornton et al., 1998; Hopkins et al., 2014).

Chemical feedback

Due to efficient internal mixing, winds from massive stars become enriched in heavy elements up to iron. These elements may get transported to the surrounding environment via stellar winds, a process that is particularly efficient during the WR phase (Maeder & Meynet, 2000; Crowther, 2007). This leads to the chemical enrichment of the ISM with these elements, which in turn has a significant impact on the chemical evolution of the parent galaxy. Additionally, carbon and oxygen that are carried to the surrounding environment by stellar winds increase the opacity of the ISM, which allows heat to dis-

sipate via radiation, causing the gas to cool down and collapse more efficiently, increasing the star formation rate.

The final enrichment event occurs during the CCSN explosion. The bulk of the chemical yields from CCSNe is in the form of He, C and O isotopes, with a smaller contribution from α-capture elements like Ne and Mg (Hirschi et al., 2005). Additionally, the explosive nucleosynthesis in CCSNe yields elements heavier than iron via rapid-neutron capture (r-process) (Woosley & Weaver, 1995; Romano et al., 2010). The yields of these events are highly sensitive to the initial stellar mass, metallicity, rotation, and explosion energy, and drive the chemical evolution on the galactic scale (Limongi & Chieffi, 2018).

1.1.3 Classification of massive stars

Stars are classified into different categories based on the properties of their spectra. The most commonly used scheme is the Harvard Spectral Classification Scheme, which was created by Annie Jump Cannon. In this scheme, stars are given a letter from O, B, A, F, G, K or M, where O indicates the hottest and intrinsically bluest spectral type, and M indicates the coolest and reddest stars. The star is also assigned a number from 0 to 9, indicating its spectral subtype, with 0 denoting the earliest stars, which present the highest ionisation stages in their spectra, and 9 denoting the latest objects, which present the lowest ionisation stages.

The star is assigned a Roman numeral between I and V, which indicates its luminosity class. This scheme is commonly known as the Morgan-Keenan classification scheme (MK), following Morgan, Keenan and Kellman (Morgan et al., 1943). Main-sequence stars are given the numeral V, subgiants the numeral IV, giants and bright giants the numerals III and II, respectively, and supergiants the numeral I. Stars are assigned a luminosity class based on the morphology of certain absorption lines, usually Balmer

lines, which is determined by the pressure-broadened wings of these lines. This means that stars with very strong and broad absorption lines will be labelled as a luminosity class "V", or a dwarf star. On the other hand, stars with weak and narrow Balmer lines will be given a luminosity class "I", or a supergiant, even if the star is a main sequence, core-hydrogen burning star.

The MK system for O and early B stars was defined by Walborn (1971). The classification of O and early B supergiants is based on ionised and neutral helium lines, as well as on triply, doubly, and singly ionised silicon. Historically, the lines used for classifying the subtypes of these stars are: He II λ4542, He I λ4471, Si IV $\lambda\lambda 4089-4116$, Si III λ4552, and Si II $\lambda 4128-4130$. O stars are characterised by the presence of He II λ4542, with the ratio of line equivalent widths of He I λ4471 to He II λ4542 increasing with lower temperature, and therefore at later spectral subtypes. The B star regime begins when He II λ4542 becomes very weak/completely absent and He I lines dominate, as Si IV lines begin to weaken. The classification of the earliest B-subtypes (B0 to B1.5) is given based on the line ratio of Si III to Si IV. For mid B-subtypes (B2-B5), the classification is based on the ratio of Si II to Si III. The classification of late B supergiants relate to the strength of Si II $\lambda 4128-4130$ to He I λ4121 and Mg II λ4481 to He I λ4471, where silicon and magnesium lines becoming stronger at later subtypes (Walborn & Fitzpatrick, 1990). The scheme has been updated to include optical CNO lines to aid in the classification (e.g. Negueruela et al., 2024). Additionally, this scheme has been revised in subsolar metallicities (Lennon, 1997; Evans & Howarth, 2003).

The supergiant luminosity class I is also subdivided from most to least luminous into a^+, a, ab, b. Moreover, additional interesting features or peculiarities observed in the optical or ultraviolet spectrum of the star can be denoted after the spectral type. Examples of this are fast rotators, which are denoted by "n" for their broad lines, and O stars that show He II λ4686 and the triplet N III $\lambda 4634-40-42$ in emission, which are denoted with an "f". These categories are compiled in the digital atlases of Walborn &

Fitzpatrick (1990) and Walborn & Fitzpatrick (2000). We also refer to Table 3 in Sota et al. (2011) for a complete and modern compilation of all sub-classifications.

1.1.4 Introducing blue supergiants and their role in modern astrophysics

Massive stars can be divided into a hot and cool branch. Hot massive stars include MS stars of O and early B spectral types, O, B, and early A supergiants, Luminous Blue Variables (LBVs), WRs, and helium stars. The cool branch contains red supergiants (RSG) of K and M spectral type, and the less common yellow supergiants. Each of these objects presents a potential evolutionary stage that massive stars pass through during their lives. This thesis work is focused on the analysis of blue supergiants (BSG), in particular late-O and B supergiants.

BSG temperatures range from ≈ 8 to 60 kK, and their luminosities between $10^{4.3}$ and $10^{6.2}\ L_{\odot}$, with the higher luminosity end being reserved for the most extreme supergiants, known as hypergiants (luminosity subclass Ia^{+}). Their surface gravities $\log g/(\mathrm{cm\,s^{-2}})$ are usually the lowest among other luminosity classes, falling between 1.5 and 3.5.

BSGs, particularly the luminous B and A supergiants, have been used as distance indicators primarily due to their high intrinsic luminosity and relatively well-defined characteristics. Their extreme brightness means they can be observed across vast interstellar and intergalactic distances. By comparing their observed apparent magnitudes m with their known intrinsic absolute magnitudes - which can be estimated from their bolometric correction (BC) - one can apply the distance modulus formula ($m - M = 5\log_{10}(d) - 5$) to determine the distance d to the star and, by extension, the cluster or galaxy in which it resides (Kudritzki et al., 1995). A more refined method for deriving distances from late-B and A supergiants involves the flux-weighted gravity g_F, a spectroscopic quantity defined as $g_F = g/T_{eff}^4$ (Kudritzki et al., 2003; Urbaneja et al., 2008). This parameter is

the basis of the flux-weighted gravity-luminosity relationship (FGLR) observed in BSGs. Because BSGs are extremely bright and the FGLR shows a predictable behaviour, they can act as a type of standard candle for accurately determining extragalactic distances out to megaparsecs (Kudritzki et al., 2013).

The presence of B-type supergiants is used to age-date starburst populations to the window immediately following the exhaustion of the most massive O-type stars, specifically between 10 and 20 million years. While O-stars dominate the ultraviolet spectrum with strong P Cygni profiles in N V $\lambda\lambda$1238−242 and C IV $\lambda\lambda$1548−1551 during the first few million years, the emergence of B supergiants marks the disappearance of these highest-ionization lines and the simultaneous strengthening of Si IV $\lambda\lambda$1394 − 1403. This spectral transition is critical for dating young post-starburst regions that are too old to contain ionising O-stars or Wolf-Rayet stars ($>$ 6 Myr) but are not yet old enough ($<$ 100 Myr) to be dominated by A-type stars (Leitherer et al., 2001).

B and A stars have also been used successfully as diagnostics of heavy-metal abundances (Urbaneja et al., 2005; Przybilla et al., 2006; Kudritzki et al., 2024). This is due to the significant number of lines of various metal species in their optical spectra. Additionally, the UV spectrum of late O and B stars contains dense forests of highly ionised iron absorption and emission lines, known as the iron forest. The iron forest can provide valuable constraints on the iron abundance if paired with radiative transfer codes that take into account line blanketing in the UV.

1.2 Evolution of massive stars

1.2.1 The main sequence

Perhaps the best way to understand stellar evolution is by using the Hertzsprung-Russell diagram (HRD), named after its founders Ejnar Hertzsprung and Henry Norris Russell.

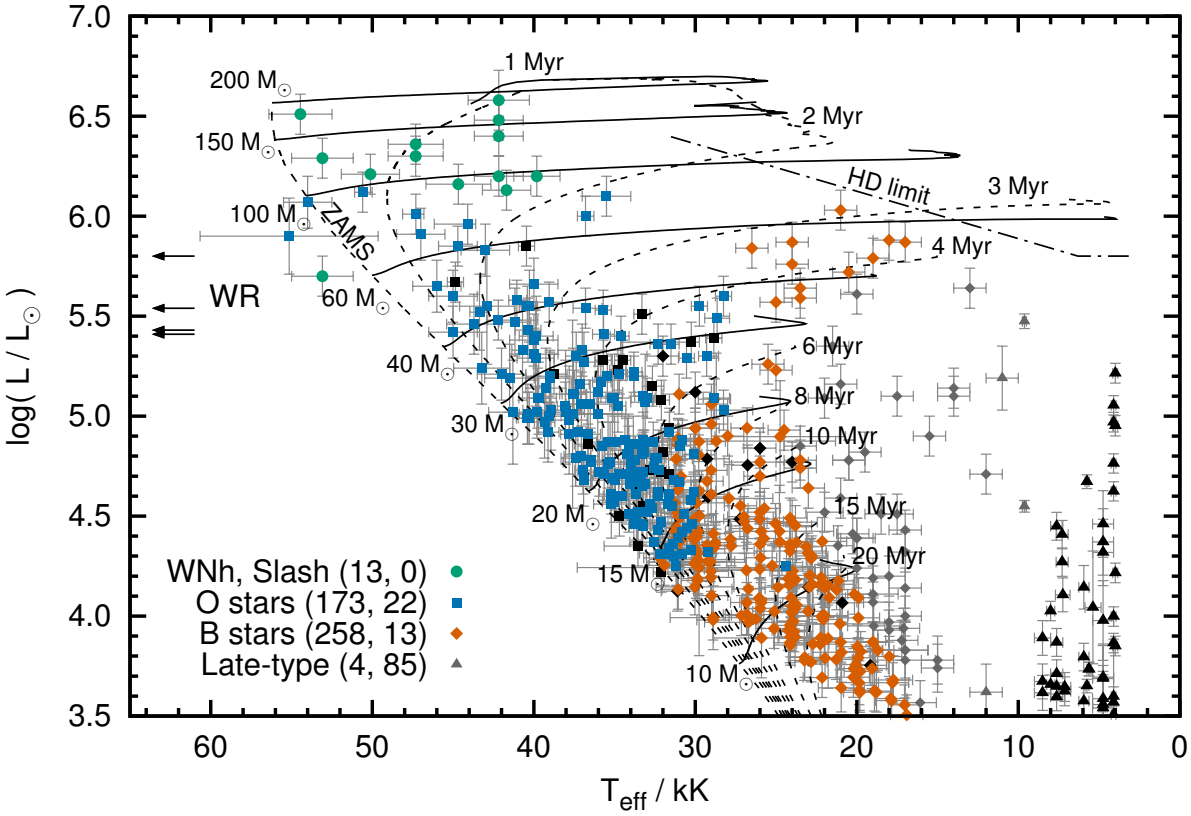


Figure 1.1: The Hertzsprung-Russell diagram of the observed population of massive stars in the star-forming region 30 Doradus in the LMC. The solid and dashed black lines represent the non-rotating stellar evolutionary tracks and isochrones from Brott et al. (2011) and Köhler et al. (2015). The dot-dashed line in the top right shows the HumphreysDavidson (HD) limit. Different markers shown in the legend indicate the spectral type of the stars. The data used to create this HRD are drawn from multiple studies and compiled by Schneider et al. (2018). In the legend, the number of stars of each class that are in the final sample and those where not all observables can be reproduced by the stellar models simultaneously are provided in parentheses. This figure was adapted from Schneider et al. (2018).

The HRD represents the stellar luminosity as a function of the effective surface temperature. An example of the HRD is shown in Fig. 1.1. In this part , we focus on the evolution of stars in the initial mass range ($15 \leq M_{\rm ZAMS}/M_{\odot} \leq 40$), which is representative of the majority of the stars analysed in this thesis work. For now, we ignore the role of internal mixing processes and mass loss on evolution.

The evolutionary pathway of stars in the 15-40 $M_{\odot}$ range differs significantly from the commonly referenced Conti scenario (Conti, 1975). In the Conti scenario, stars with sufficiently high $M_{\rm ZAMS}$ ($\geq$ 60 $M_{\odot}$) strip their hydrogen envelope during the MS or immediate post-MS via strong wind-driven mass loss or by the LBV stage. In such stars, the RSG phase can be completely circumvented due to the wind-driven mass loss or by an LBV phase. The Conti scenario for solar metallicity can be summarised by the following diagram:

$$\mathrm{M_{init}} \geq 60\ \mathrm{M_{\odot}}:\ \ \mathrm{O} \rightarrow \mathrm{WNh} \rightarrow \mathrm{LBV?} \rightarrow \mathrm{WN} \rightarrow \mathrm{WC} \rightarrow \mathrm{SN}.$$

In contrast, single stars in the 15–40$M_{\odot}$ regime generally retain a significant portion of their mass during their evolution on the MS (and post-MS), which begins at the zero-age main sequence (ZAMS) and ends at the terminal-age main sequence (TAMS). The main sequence phase is defined by burning hydrogen in the convective core of the star via the CNO process. This changes the interior structure of the star and its chemical composition, increasing the mean molecular weight in the core as helium is converted into hydrogen. To maintain hydrostatic and thermal equilibrium, the core contracts slowly (increasing its temperature and density) and the envelope slightly expands. Throughout this phase, the star evolves horizontally across the HR diagram towards cooler temperatures at nearly constant luminosity Maeder & Meynet (2000).

Nucleosynthesis: hydrogen burning

In early evolutionary stages of massive stars on the main sequence, the core temperature is about 3.5×10^7 K (Woosley & Janka, 2005), which is sufficient for the carbon, nitrogen, and oxygen nuclei to overcome their strong Coulomb barrier. Therefore, hydrogen burning in massive stars is dominated by the fast CNO cycle. This is in contrast to cool stars, where the proton-proton cycle dominates hydrogen fusion in their cooler cores. The CNO cycle has multiple branches, some with higher probability than others. The main branch is the C-N cycle, also known as the Bethe-Weizsacker cycle (Bethe, 1939), in which the carbon-12 isotope that is used in the first reaction is regenerated in the last reaction following the chain

$$\begin{aligned}
{}^{12}_{6}\mathrm{C} + {}^{1}_{1}\mathrm{H} &\longrightarrow {}^{13}_{7}\mathrm{N} + \gamma && + 1.94 \text{ MeV} \\
{}^{13}_{7}\mathrm{N} &\longrightarrow {}^{13}_{6}\mathrm{C} + e^{+} + \nu_e && + 2.22 \text{ MeV} - 0.71 \text{ MeV} \\
{}^{13}_{6}\mathrm{C} + {}^{1}_{1}\mathrm{H} &\longrightarrow {}^{14}_{7}\mathrm{N} + \gamma && + 7.55 \text{ MeV} \\
{}^{14}_{7}\mathrm{N} + {}^{1}_{1}\mathrm{H} &\longrightarrow {}^{15}_{8}\mathrm{O} + \gamma && + 7.29 \text{ MeV} \\
{}^{15}_{8}\mathrm{O} &\longrightarrow {}^{15}_{7}\mathrm{N} + e^{+} + \nu_e && + 2.75 \text{ MeV} - 1.00 \text{ MeV} \\
{}^{15}_{7}\mathrm{N} + {}^{1}_{1}\mathrm{H} &\longrightarrow {}^{12}_{6}\mathrm{C} + {}^{4}_{2}\mathrm{He} && + 4.96 \text{ MeV}.
\end{aligned} \tag{1.1}$$

A branch of the main CNO cycle is the O-N cycle, which produces N^{14}_{7} following

$$\begin{aligned}
{}^{15}_{7}\mathrm{N} + {}^{1}_{1}\mathrm{H} &\longrightarrow {}^{16}_{8}\mathrm{O} + \gamma && + 12.13 \text{ MeV} \\
{}^{16}_{8}\mathrm{O} + {}^{1}_{1}\mathrm{H} &\longrightarrow {}^{17}_{9}\mathrm{F} + \gamma && + 0.60 \text{ MeV} \\
{}^{17}_{9}\mathrm{F} &\longrightarrow {}^{17}_{8}\mathrm{O} + e^{+} + \nu_e && + 2.76 \text{ MeV} - 0.94 \text{ MeV} \\
{}^{17}_{8}\mathrm{O} + {}^{1}_{1}\mathrm{H} &\longrightarrow {}^{14}_{7}\mathrm{N} + {}^{4}_{2}\mathrm{He} && + 1.19 \text{ MeV} \\
{}^{14}_{7}\mathrm{N} + {}^{1}_{1}\mathrm{H} &\longrightarrow {}^{15}_{8}\mathrm{O} + \gamma && + 7.35 \text{ MeV} \\
{}^{15}_{8}\mathrm{O} &\longrightarrow {}^{15}_{7}\mathrm{N} + e^{+} + \nu_e && + 2.75 \text{ MeV}.
\end{aligned} \tag{1.2}$$

In the C-N and O-N chains, the reaction with the lowest probability is the proton capture by N_7^{14} nucleus to produce O_8^{15}, making it the slowest step in the CNO cycle. In other words, the input reaction to nitrogen is faster than the rate of its consumption. This acts as a bottleneck, where most of the CNO elements are converted into nitrogen, making it the most abundant nucleus among the CNO catalysts by the end of the hydrogen-burning phase. Therefore, a massive star that has recently evolved into a WR is likely to be classified as a nitrogen-rich WR, or a WN star, until it sheds all of its CNO-processed material via mass-loss.

1.2.2 Post-main sequence evolution

As the star leaves the main sequence, core hydrogen burning ceases. The abrupt end of nuclear burning causes the core to rapidly contract, as it can no longer support the overlying layers through energy generated by nuclear fusion alone. This leads to an increase in core temperature and density, and subsequently affects the overall structure of the star. On the HRD, this manifests itself as the brief excursion towards a higher effective temperature in the form of a blueward hook, which is caused by the overall contraction of the star, marking the TAMS.

The contraction of the star heats the layers immediately surrounding the inert helium core. This eventually ignites hydrogen burning in the thin shell overlying the core, which halts the contraction of the star. This pushes the star towards the red part of the HRD, a phase known as the Hertzsprung gap. This gap is not due to forbidden physics, but rather a result of the low probability of observing stars in this transitional phase. The reason for this low probability lies within the timescales of various physical processes taking place in the inner structure of the star.

The nuclear timescale ($\tau_{\rm nuc} \approx E_{\rm nuc}/L$) describes the time required to deplete the available nuclear fuel. For massive stars, the MS $\tau_{\rm nuc}$ is on the order of 10^6–10^7 years

($\tau_{\rm nuc}$ decreases with higher mass). However, the structure of hydrogen shell-burning stars readjusts its structure to maintain thermal equilibrium. This adjustment occurs on the Kelvin-Helmholtz timescale of the envelope ($\tau_{\rm KH} \approx GM^2/RL$), which is the time required for the star to radiate its thermal energy. In massive stars, $\tau_{KH} \ll \tau_{nuc}$, as the main-sequence lasts for millions of years, the transit time across the Hertzsprung gap happens in a few thousand to tens of thousands of years. This timescale difference explains why the transition region on the HRD appears to be empty in observational surveys.

For most stars in the $15-25 M_{\odot}$ range, helium burning commences after the transit across the Hertzsprung gap ends. For higher mass stars, helium burning may start while the star is still in the gap. Helium burning provides a new stable source of nuclear energy, restoring thermal equilibrium. The bulk of helium burning takes place on the red supergiant branch (Levesque, 2017). This puts the evolution back on the long, nuclear burning timescale, albeit being much shorter for helium burning than it is for hydrogen burning on the main sequence $\tau_{\rm He} \approx 10\%\ \tau_{\rm H}$ (Kippenhahn & Weigert, 1990). Stars in the 15-25 $M_{\odot}$ range are expected to remain as RSGs until core collapse, upon which they explode as Type II-P supernovae. The P stands for the "plateau" in the light curve, which appears due to the recombination of the thick hydrogen envelope retained by the single star. For the upper mass range (30-40$M_{\odot}$), if the wind mass loss is particularly strong (high metallicity environment), the hydrogen envelope may be depleted to $< 2 M_{\odot}$ at the time of explosion (Heger et al., 2003). This may result in Type II-L (Linear) or Type IIb spectra, distinguishing them from the standard plateau events (Eldridge & Tout, 2004; Yoon & Cantiello, 2010).

For single stars in this mass domain and assuming solar metallicity, this evolutionary trajectory can be summarised with the following diagram:

$$20 \leq \mathrm{M_{init}} \leq 40\ \mathrm{M_{\odot}}:\ \mathrm{O(MS)} \rightarrow \mathrm{BSG} \rightarrow \mathrm{YSG(transient)} \rightarrow \mathrm{RSG} \rightarrow \mathrm{SNII-P/L}.$$

Crowther (2007) provides an alternative scenario following:

$$20 \leq \mathrm{M_{init}} \leq 40\ \mathrm{M_{\odot}}:\ \mathrm{O} \rightarrow \mathrm{LBV/RSG} \rightarrow \mathrm{WN} \rightarrow \mathrm{SN},.$$

In this scenario, after the MS, stars might become unstable due to approaching the Eddington limit and could experience extreme eruption episodes. This is known as a Luminous Blue Variable, characterised by high variability in temperature and wind properties, with a relatively constant luminosity during the dormant phase and increased luminosity during episodes of eruption. These giant eruptions can shed significant mass ($\approx 10^{-3}$ to $1M_{\odot}$ per event) over very short timescales (Smith, 2014). This causes the star to efficiently shed its hydrogen envelope, subsequently zooming across the HRD to the blue, and forming a nitrogen-rich WR star, or a WN. This scenario has been invoked to explain the observed large number of luminous non-binary WR stars in low metallicity environments, which is in contention with predictions from evolutionary models and the low observed mass loss rates of BSGs (Hainich et al., 2015; Schootemeijer et al., 2024). Alternative scenarios place the LBV phase as an immediate precursor to CCSNe. This hypothesis is supported by the detection of LBV-like progenitors for Type IIn SN, which show signs of interaction with dense, recently ejected CSM material (Smith et al., 2011).

Additionally, the eruptive-dormant (hot phase-cool phase) cycle has been used to explain the absence of observed high luminosity red supergiants above the limit of ≈ 5.5 as a result of the large mass loss (Davies et al., 2018). This limit was first observed by Humphreys & Davidson (1979b), and is known as the Humphreys-Davidson (HD) limit. On the HRD (Fig. 1.1), the zone of avoidance is defined by a horizontal border tracing the HD limit and a diagonal slope that follows the position of dormant LBVs and LBV candidates on the HRD (Smith et al., 2004).

These scenarios are a basic description of massive star evolution. In reality, many questions remain unanswered regarding the physical processes that can affect these evolu-

tionary pathways. For example, it is still a matter of debate whether all blue supergiants are MS core-hydrogen burning stars, or if some blue supergiants, in particular B supergiants, are post-MS stars, albeit close to the TAMS and shell-hydrogen burning. Also, the LBV phase remains shrouded in mystery. The mechanism of inducing the extreme eruptions is poorly understood from a theoretical point of view. Additionally, the small sample of potential LBVs makes it difficult to conduct statistically significant studies of the properties of LBVs.

Nucleosynthesis: Helium and metal burning

When hydrogen is exhausted, the abrupt halt of fusion energy generation and the buildup of helium in the core cause it to contract and become denser. This heats the core, and upon reaching a temperature of $\approx 1.8 \times 10^8$ K (Woosley & Janka, 2005), hydrogen burning begins in the overlaying shell, followed by core-helium burning, marking the TAMS. During the helium burning phase, the triple alpha process fuses three helium nuclei to create stable carbon-12, following

$$\begin{aligned} {}^4_2\mathrm{He} + {}^4_2\mathrm{He} &\longrightarrow {}^8_4\mathrm{Be} && -0.09\ \mathrm{MeV} \\ {}^8_4\mathrm{Be} + {}^4_2\mathrm{He} &\longrightarrow {}^{12}_6\mathrm{C}^* && -0.29\ \mathrm{MeV} \\ {}^{12}_6\mathrm{C}^* &\longrightarrow {}^{12}_6\mathrm{C} + \gamma && +7.57\ \mathrm{MeV}. \end{aligned} \tag{1.3}$$

Once carbon-12 is formed, oxygen-16 and heavier elements up to iron-52 are created by the single α-capture process, following

$$\begin{aligned}
{}^{12}_{6}\mathrm{C} + {}^{4}_{2}\mathrm{He} &\longrightarrow {}^{16}_{8}\mathrm{O} + \gamma && + 7.16\ \mathrm{MeV} \\
{}^{16}_{8}\mathrm{O} + {}^{4}_{2}\mathrm{He} &\longrightarrow {}^{20}_{10}\mathrm{Ne} + \gamma && + 4.73\ \mathrm{MeV} \\
{}^{20}_{10}\mathrm{Ne} + {}^{4}_{2}\mathrm{He} &\longrightarrow {}^{24}_{12}\mathrm{Mg} + \gamma && + 9.32\ \mathrm{MeV} \\
{}^{24}_{12}\mathrm{Mg} + {}^{4}_{2}\mathrm{He} &\longrightarrow {}^{28}_{14}\mathrm{Si} + \gamma && + 9.98\ \mathrm{MeV} \\
{}^{28}_{14}\mathrm{Si} + {}^{4}_{2}\mathrm{He} &\longrightarrow {}^{32}_{16}\mathrm{S} + \gamma && + 6.95\ \mathrm{MeV} \\
{}^{32}_{16}\mathrm{S} + {}^{4}_{2}\mathrm{He} &\longrightarrow {}^{36}_{18}\mathrm{Ar} + \gamma && + 6.64\ \mathrm{MeV} \\
{}^{36}_{18}\mathrm{Ar} + {}^{4}_{2}\mathrm{He} &\longrightarrow {}^{40}_{20}\mathrm{Ca} + \gamma && + 7.04\ \mathrm{MeV} \\
{}^{40}_{20}\mathrm{Ca} + {}^{4}_{2}\mathrm{He} &\longrightarrow {}^{44}_{22}\mathrm{Ti} + \gamma && + 5.13\ \mathrm{MeV} \\
{}^{44}_{22}\mathrm{Ti} + {}^{4}_{2}\mathrm{He} &\longrightarrow {}^{48}_{24}\mathrm{Cr} + \gamma && + 7.70\ \mathrm{MeV} \\
{}^{48}_{24}\mathrm{Cr} + {}^{4}_{2}\mathrm{He} &\longrightarrow {}^{52}_{26}\mathrm{Fe} + \gamma && + 7.94\ \mathrm{MeV},
\end{aligned} \tag{1.4}$$

where in each step, energy is lost due to the release of electromagnetic radiation (photons).

During helium burning, the predominant nuclei in the core are carbon-12 and oxygen-16. Helium burning produces neutrons by α-capture, where N^{14}_{7} is converted into Mg^{25}_{12} by the α-capture via the following chain:

$$\begin{aligned}
{}^{14}_{7}\mathrm{N} + {}^{4}_{2}\mathrm{He} &\longrightarrow {}^{18}_{9}\mathrm{F} + \gamma && + 4.415\ \mathrm{MeV} \\
{}^{18}_{9}\mathrm{F} &\longrightarrow {}^{18}_{8}\mathrm{O} + e^{+} + \nu_e && + 0.632\ \mathrm{MeV} \\
{}^{18}_{8}\mathrm{O} + {}^{4}_{2}\mathrm{He} &\longrightarrow {}^{22}_{10}\mathrm{Ne} + \gamma && + 9.668\ \mathrm{MeV} \\
{}^{22}_{10}\mathrm{Ne} + {}^{4}_{2}\mathrm{He} &\longrightarrow {}^{25}_{12}\mathrm{Mg} + n && - 0.479\ \mathrm{MeV}
\end{aligned} \tag{1.5}$$

This is the main source of neutrinos for slow (s-)processes in massive stars. This is known as the weak s-process, which creates elements heavier than iron nuclei up to A$\approx$ 90 by slowly adding neutrons to seed nuclei, followed by beta decay (Nishimura et al., 2017).

The exhaustion of helium in the core causes it to contract again, leading to another increase in temperature to $\approx 10^9$ K. In the most massive or metal-rich stars, this signals the onset of carbon burning, where C_6^{12} starts reacting with itself, following:

$$\begin{aligned} {}^{12}_{6}\mathrm{C} + {}^{12}_{6}\mathrm{C} &\longrightarrow {}^{24}_{12}\mathrm{Mg} + \gamma && + 13.93 \text{ MeV} \\ &\longrightarrow {}^{23}_{11}\mathrm{Na} + {}^{1}_{1}\mathrm{H} && + 2.24 \text{ MeV} \\ &\longrightarrow {}^{20}_{10}\mathrm{Ne} + {}^{4}_{2}\mathrm{He} && + 4.62 \text{ MeV} \\ &\longrightarrow {}^{23}_{12}\mathrm{Mg} + \mathrm{n} && - 2.61 \text{ MeV} \\ &\longrightarrow {}^{16}_{8}\mathrm{O} + 2{}^{4}_{2}\mathrm{He} && - 0.11 \text{ MeV} \end{aligned} \tag{1.6}$$

This produces a core that is dominated by O_8^{16}. At this stage, neutrinos become the dominant source of energy loss instead of electromagnetic radiation. Since neutrinos have an extremely long mean free path, they can escape the star's core almost instantly after they are produced, carrying a large amount of energy with them. The energy produced by fusion processes cannot compensate for the energy loss via neutrinos, forcing the star to contract and raising the core pressure and temperature, thereby reducing the evolutionary timescales.

When the temperature reaches $\approx 1.6 \times 10^9$ (Woosley & Janka, 2005), neon-burning starts and follows the chain

$$\begin{aligned} {}^{20}_{10}\mathrm{Ne} + {}^{4}_{2}\mathrm{He} &\longrightarrow {}^{24}_{12}\mathrm{Mg} + \gamma && + 9.316 \text{ MeV} \\ {}^{24}_{12}\mathrm{Mg} + {}^{4}_{2}\mathrm{He} &\longrightarrow {}^{28}_{14}\mathrm{Si} + \gamma && + 9.984 \text{ MeV} \end{aligned} \tag{1.7}$$

which is followed by oxygen-burning when the temperature reaches $\approx 2 \times 10^9$, where

oxygen reacts with itself, creating a silicon-dominated core via the following chain:

$$\begin{aligned} {}^{16}_{8}\mathrm{O} + {}^{16}_{8}\mathrm{O} &\longrightarrow {}^{32}_{16}\mathrm{S} + \gamma \quad &+ 16.54 \text{ MeV} \\ &\longrightarrow {}^{31}_{15}\mathrm{P} + {}^{1}_{1}\mathrm{H} \quad &+ 7.68 \text{ MeV} \\ &\longrightarrow {}^{31}_{16}\mathrm{S} + \mathrm{n} \quad &+ 1.46 \text{ MeV} \\ &\longrightarrow {}^{28}_{16}\mathrm{S} + {}^{4}_{2}\mathrm{He} \quad &+ 9.59 \text{ MeV} \end{aligned} \tag{1.8}$$

In Fig. 1.2, we present a depiction of the pre-supernova structure of the stellar interior of a 16 $M_\odot$ evolved massive star, which was generated by A Tool for Understanding the Lives, Interiors, and Physics of Stars (TULIPS Laplace, 2022), based on numerical calculations from MESA stellar evolution code. The structure resembles the layers of an onion, where heavier elements dominate the composition of each shell as one moves to the surface.

1.2.3 Core-Collapse Supernova

During the final stages of evolution, the core of a massive star becomes dominated by iron-peak elements. The core is surrounded by shells, starting with silicon, then oxygen, neon, carbon, helium, and the outermost layer of hydrogen. The core is supported by electron degeneracy pressure. In the immediate overlying shell, silicon burning continues for a very brief time, adding iron ash to the core until it reaches the effective Chandrasekhar mass $\approx 1.4 M_\odot$. As a result, the core contracts and heats up. At this point, the core cannot sustain the internal pressure using nuclear energy. This is due to the endothermic nature of the reactions involving the stable nuclei of iron-peak elements. Due to the extremely high temperatures ($\approx 10^{10}$ K), the core begins to produce gamma-rays. Gamma rays lead to the photodisintegration of iron nuclei into alpha particles. i.e.

$$\gamma + \mathrm{Fe}^{56}_{26} \rightarrow 13\mathrm{He}^{4}_{2} + 4\mathrm{n}, \tag{1.9}$$

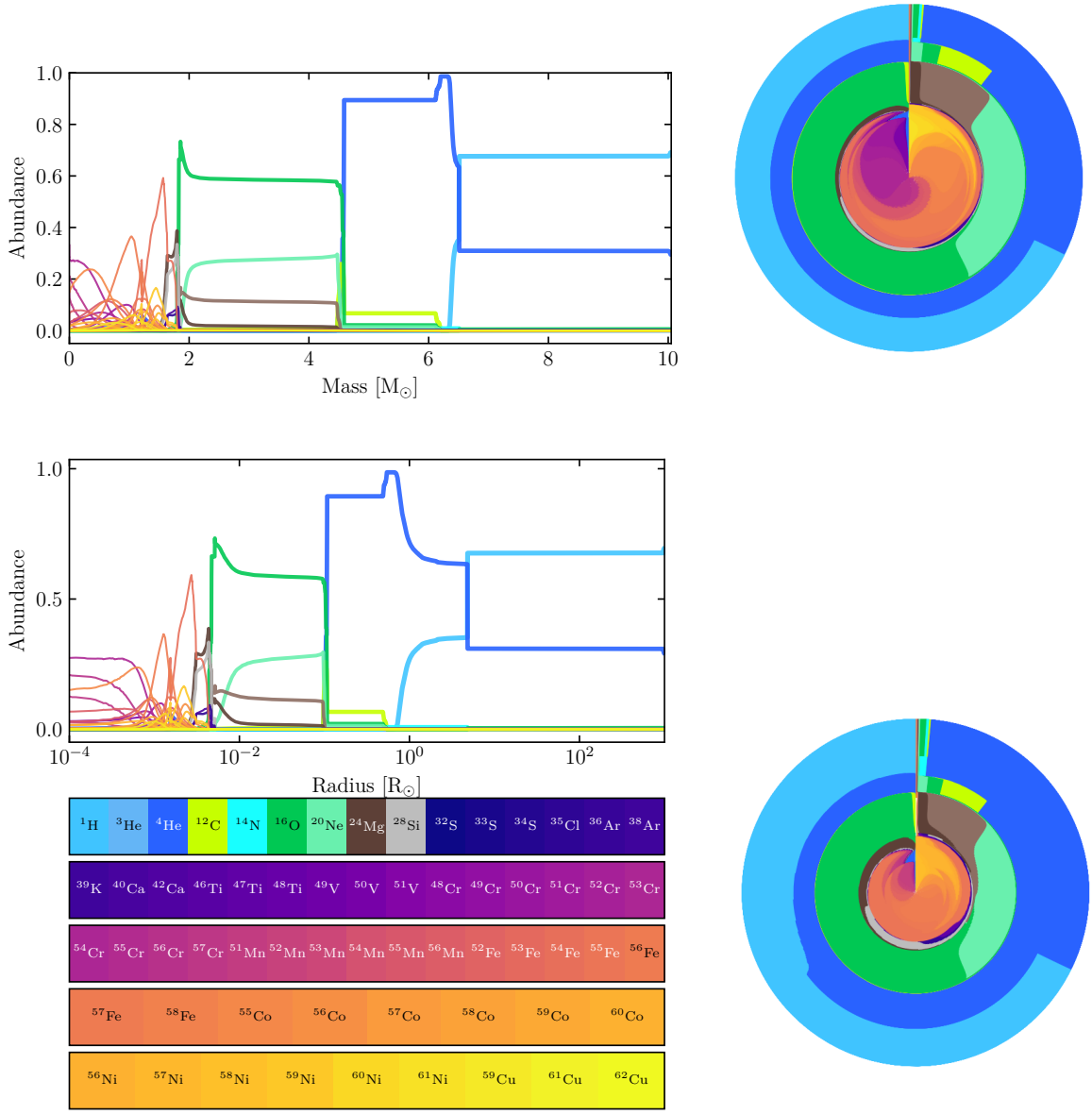


Figure 1.2: Comparison between classical stellar interior composition diagrams (left) and diagrams produced with a Tool for Understanding the Lives, Interiors, and Physics of Stars (TULIPS, Laplace, 2022), containing the same information (right). The diagrams are for the case of 16 $M_{\odot}$ immediately before core collapse. Only isotopes with maximum mass fractions greater than 10^{-4} are shown. The upper and lower panels depict the stellar chemical composition as a function of mass and radial coordinate (on a logarithmic scale), respectively. From the centre, moving outward, these circles represent 0.25, 0.5, 0.75, and 1 times the total mass of the star. The radial direction is proportional to the mass fraction of the isotope in each of the 4 layers. This figure was adapted from Laplace (2022)

which then decay into a soup of neutrons and protons following:

$$\gamma + \mathrm{He}_2^4 \rightarrow 2\mathrm{n} + 2\mathrm{p}, \tag{1.10}$$

The protons and heavy nuclei capture electrons, forming neutrons and releasing neutrinos. The pressure exerted by electrons gets significantly reduced, accelerating the collapse. This leads to the formation of an unstable, degenerate, atomic nucleus density core. The collapse is abruptly halted by the repulsive component of the strong nuclear forces. Consequently, a shockwave at the outer boundary of the core forms, which moves outward into the infalling material carrying with it enormous amounts of energy ($\approx 10^{51}$ erg). It is thought that if the remaining amount of infalling material is sufficiently small ($\leq 0.4\ M_\odot$), the shockwave can reach the outer envelope with enough energy to cause a direct explosion (Baron et al., 1985). However, established simulations indicate that this prompt shock stalls within milliseconds. The energy of the shock is depleted by the photodissociation of heavy nuclei (Bethe, 1990). Successful explosion requires the revival of this accretion shock by other mechanisms, such as neutrino-heating (Bethe & Wilson, 1985) or high magnetic fields in rapid rotators (Janka, 2012).

Observationally, CCSNe are classified primarily by the behaviour of their light curves and the appearance of lines of certain elements in their emerging spectra (Minkowski, 1941). If hydrogen lines are present in the spectrum, the CCSN is designated as a type II supernova. The absence of hydrogen in the spectrum hints towards the stripping of the H-envelope that happens during the WR phase through radiatively driven winds (Crowther, 2007) or binary interaction (Zapartas et al., 2017). Stripped-envelope supernovae are classified as type Ib if helium lines are present, or Ic if the spectrum lacks both helium and hydrogen lines. Between these extremes lie transitional classes such as Type IIb, which retain only a residual hydrogen shell.

The most common progenitors of CCSNe are RSGs, which are linked to Type II-P

(Plateau) supernovae. Upon explosion, the shock ionises this envelope; as the ejecta expands and cools, it recombines, maintaining a constant temperature and producing the characteristic luminosity plateau that persists for roughly 100 days (Smartt, 2009). BSGs can also explode into a CCSN, and present a more compact progenitor profile and are associated with Type II-pec (Peculiar) supernovae. The most famous example is SN 1987A, the progenitor of which is a B3 supergiant. Podsiadlowski et al. (1992) invoked a merger scenario, which is required to prevent the star from remaining in the red supergiant phase and keep it in the blue part of the HRD.

When massive stars end their lives, they leave behind a compact remnant. One scenario suggests that the pre-SN core remains intact as a neutron star or a pulsar after a CCSN takes place. Another scenario suggests that, if the mass of material falling onto the neutron core is large enough, the gravitational forces could overpower the pressure from the degenerate neutrons, causing the core to collapse even further into a stellar mass black hole, preventing a supernova (known as a failed-CCSN, O'Connor & Ott, 2011). The conditions for the formation of these remnants are yet to be fully understood. Although it is clear that the fate is mass dependent and that the physical processes which impact the pre-CCSN evolution of massive stars also play a major role in the determination of the type of CCSN and the remnant. Hirschi et al. (2025) provides useful schematics of types of remnants as a function of initial mass and metallicity for rotating single massive star models, which is presented in Fig. 1.3.

1.2.4 Stellar evolution codes

Our understanding of stellar evolution is heavily reliant on theory and numerical simulations. There are many stellar evolution codes, such as GENEC (Eggenberger et al., 2008), MESA (Paxton et al., 2011), BEC (Brott et al., 2011), and STARS (Eggleton, 1971; Pols et al., 1995; Eldridge et al., 2008). These models infer the properties of stars

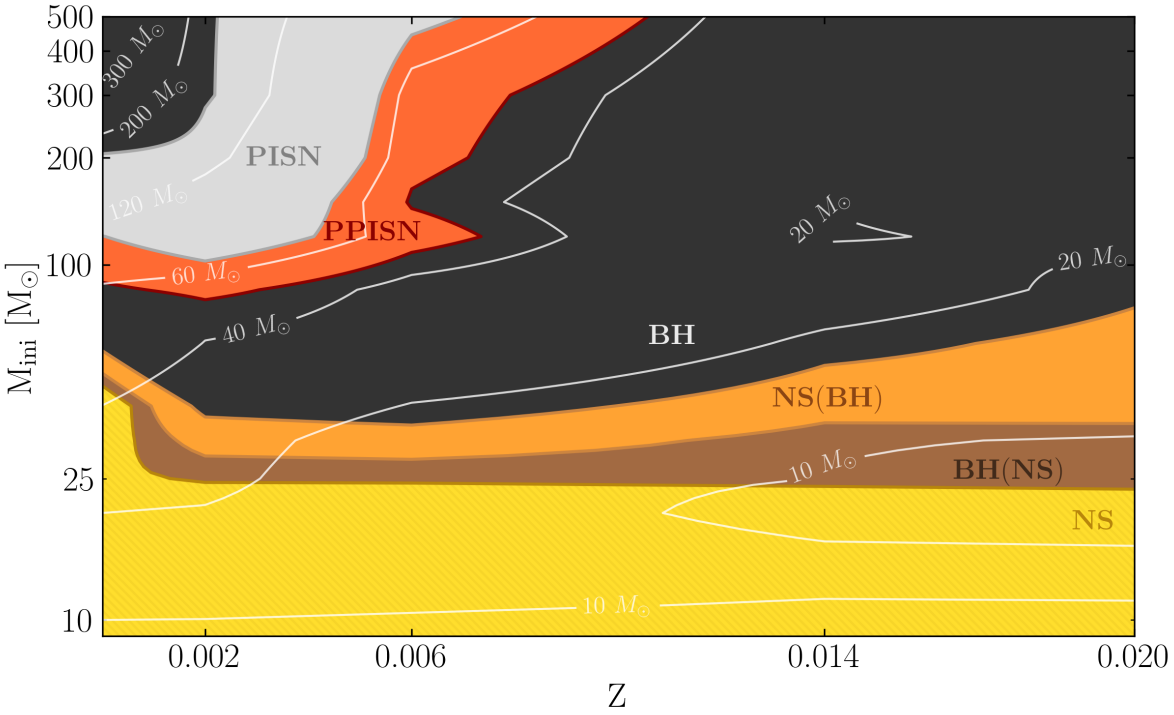


Figure 1.3: Remnant type of rotating massive star models as a function of initial mass and metallicity. The initial rotation rates $v_{\rm rot}$ are assumed to be equal to $0.4v_{\rm crit}$, where $v_{\rm crit} = \frac{3}{2}\sqrt{\frac{GM}{R_{\rm pb}}}$, and $R_{\rm pb}$ is the polar radius. The solid white lines are evolutionary tracks of rotating single stars. PISN: Pair-instability supernova with no remnant (grey region), PPISN: Pulsational pair-instability supernova with no remnant (salmon region), BH: Black hole remnant from direct collapse (black region), NS(BH): Neutron star remnant expected with the possibility of BH (orange region). BH(NS): Black holes via failed supernovae are expected, with the possibility of a successful explosion leading to a NS remnant (brown region). NS: Neutron star remnant with successful explosion (yellow region). This figure was adopted from Hirschi et al. (2025).

by solving the stellar structure equations in hydrostatic equilibrium. Although valuable insight can be obtained from these models, there are several key aspects that remain highly uncertain. In this thesis work, the Brott et al. (2011) tracks were employed, which are based on BEC. Therefore, these aspects will be discussed in the framework of the Brott et al. (2011) models.

Convection and internal mixing

One of the most impactful aspects of stellar models is the internal mixing and treatment of the boundaries between different layers of the stellar interior. Mixing processes dominate the lives of stars in the $15 - 30\ M_{\odot}$ range. On the MS, the cores of massive stars are convectively unstable due to the temperature gradient, which arises from the energy generated from the CNO-cycle, which in turn increases the temperature of the core relative to the radiative overlying layers. In most stellar evolution codes, convection is treated using the mixing length theory (MLT, Böhm-Vitense, 1958). This theory entails that, if the energy produced from nuclear burning is transported to the outer layers through convection (due to the adiabatic temperature gradient of the moving particles being smaller than the radiative temperature gradient of its surroundings, known as the Schwarzschild criterion for convection Schwarzschild & Härm, 1958), angular momentum and processed material is also transported through the layers of the star due to the movement of particles. A result of this theory is that the moving particles stop precisely where the adiabatic temperature gradient equals the radiative temperature gradient and the convective acceleration becomes zero, which is also known as the Schwarzschild boundary. This induces efficient convective mixing in the core.

In reality, convection may carry those particles beyond the Schwarzschild boundary. This phenomenon is known as core overshooting (Shaviv & Salpeter, 1973). The BEC implements a step overshooting treatment, where the fully mixed convective core is extended by a distance equal to $\alpha_{\rm ov} H_p$, where $\alpha_{\rm ov}$ is the overshooting parameter and

H_p is the pressure scale height. Brott et al. (2011) used a value of $\alpha_{\rm ov} = 0.335$[1], which is significantly higher than those typically used in other contemporary grids, such as the Geneva models, which adopt a more moderate overshoot parameter of $\alpha_{\rm ov} = 0.1$ (Ekström et al., 2012). This relatively large value is observationally motivated and is calibrated to reproduce the width of the MS ($\tau_{\rm H}$ increases with $\alpha_{\rm ov}$) observed by the Very Large Telescope (VLT)-FLAMES survey in the Magellanic Clouds (MCs) and the Milky Way (MW) (Evans et al., 2006; Hunter et al., 2008a, 2009).

While nuclear fuel is being burnt in the core, the mass of the fuel decreases. This, combined with the processed material, creates varying molecular weight gradients in the stellar interior. If this is taken into account as in the Schwarzschild criterion as a stabilising gradient to the adiabatic gradient, one considers the Ledoux criterion for convection (Ledoux, 1947). In convectionally (Schwarzschild) unstable layers that have such a stabilising molecular weight gradient, no convective mixing takes place. Therefore, mixing is less efficient compared to mixing in the convective core, and takes place via vibrational instabilities, which have been described by Kato (1966). Semiconvection is used to describe the mixing in the zone between the two extremes of fully convective and non-convective layers.

In Brott et al. (2011) models, mixing in semiconvective zones is treated by a diffusion process, which is scaled by an efficiency parameter $\alpha_{\rm sc}$ (Langer et al., 1983). They adopt $\alpha_{\rm sc} = 1.0$, resulting in an efficient semiconvection. This high efficiency allows for significant species transport through the semiconvective layers (Langer et al., 1985).

Rotational mixing

The centrifugal forces generated by the rotation of the star lead to the oblateness of the star, causing the temperature to depend upon the latitude, where the equatorial

[1]Recent studies, such as Schootemeijer et al. (2019), claim that there is some evidence suggestive of a mass-dependent overshooting parameter.

regions are cooler and less luminous than the polar regions (von Zeipel, 1924). This latitudinal temperature gradient creates an anisotropic stellar wind, such that the mass loss is predicted to be enhanced over the hotter poles (Maeder, 2002).

Additionally, this imbalance between the pole and equator in a rotating star drives meridional currents, also known as the Eddington-Sweet circulation (Eddington, 1925; Sweet, 1950), which is the dominant rotational mixing process. Moreover, as the star rotates, the stellar layers may rotate at different rates. The friction resulting between those layers induces turbulence. This is known as shear instability (Zahn, 1992).

These rotational instabilities transport momentum in the stellar interior and induce mixing from the core to the surface, and vice versa. This has the effect of enhancing the outer layers of the stars with products of the CNO cycle. Moreover, the cores in rotating models are more extended and massive than in non-rotating models. This is similar to the effect of convective overshooting, which increases $\tau_{\rm H}$ and the luminosity. In the BEC model, the efficiency of rotational mixing is calibrated via a parameter f_c, which scales the contribution of the inhibiting mean molecular weight gradient. Brott et al. (2011) adopt $f_c = 0.0228$, a value calibrated to match the observed nitrogen enrichment in B-type stars from the VLT-FLAMES survey (Hunter et al., 2008b, 2009).

If the star is rotating above a critical rate $v_{\rm crit} = \sqrt{\frac{GM}{R}(1-\Gamma_e)}$, where G is the gravitational constant, M is the mass of the star, R is the stellar radius, and Γ_e is the Eddington parameter, it may evolve as chemically-homogeneous star. In this case, the star never builds up a hydrogen-rich envelope and does not expand to become an RSG. Instead, it evolves directly towards higher temperatures and luminosities, remaining compact and blue and directly going into the WR phase, completely avoiding the red part of the HRD. While rare in the Galactic metallicity range due to strong wind braking, this channel is significant at lower metallicities and is considered a primary progenitor for long Gamma-Ray Bursts (Yoon et al., 2006).

Mass loss and metallicity

The wind-driven mass loss in stars is intertwined with the rotation of the star. The integrated mass loss during the MS for stars in the lower end of the 15-40 $M_{\odot}$ range is relatively modest compared to stars on upper end, typically losing only a few solar masses in the Small Magellanic Cloud (SMC) and upwards of half their mass in the MW for stars in the upper end of the range, which is a result of the strong line-dirven winds in metal rich environments (Renzo et al., 2017). However, the wind carries away material with high angular momentum, which efficiently spins down the star – a process known as wind braking (Langer, 1998).

Generally, evolutionary codes do not consistently solve the full hydrodynamical equations for stellar winds along with stellar structure. Instead, they rely on empirical and theoretical prescriptions of mass loss that vary according to the evolutionary stage and surface properties of the star. In the Brott et al. (2011) models for O and early B stars, the Vink et al. (2001) mass loss recipe is adopted, which explicitly accounts for the bi-stability jump. For the RSG phase, where the Vink et al. (2001) mass-loss rates are no longer applicable, the empirically derived mass loss recipe of Nieuwenhuijzen & de Jager (1990) is used. Should the star strip its hydrogen envelope, the code switches to the WR mass loss prescription of Hamann et al. (1995), the rates from which are divided by a factor of ten to account for the impact of wind clumping (Yoon et al., 2006).

The radiation-driven nature of winds of massive stars makes metallicity a key for determining the efficiency of the wind, impacting the evolutionary pathway that the star takes. Mainly, due to the lower mass-loss rates, metal-poor stars undergo less efficient wind breaking. According to Maeder & Meynet (2000), this results in maintaining rapid rotation for longer fractions of their lifetimes compared to their Galactic counterparts. This trend is confirmed observationally by the Hunter et al. (2008b), who found that the distribution of the projected rotational velocity of B stars peaks at ≈ 170 km s^{-1} in the

SMC and $\approx$ 100 km s^{-1} in the Large Magellanic Cloud (LMC), which are higher than what was observed in the MW $\approx$ 60 km s^{-1} (Simón-Díaz & Herrero, 2014a).

Furthermore, the reduced mass loss makes it more difficult for a single metal-poor star to strip its hydrogen envelope. Consequently, the minimum initial mass required to form a Wolf-Rayet star via the single-star channel increases significantly with decreasing metallicity (Maeder, 1992). Moreover, the weaker winds allow metal-poor stars to retain a larger fraction of their initial mass by the time they reach core collapse, directly influencing the mass and type of the resulting compact remnant (Belczynski et al., 2010).

1.2.5 Binary evolution

This thesis work focuses on single massive stars. Nevertheless, the effect of binarity on the evolution of massive stars is too significant to ignore. Historically, before the development of the theory of line-driven winds, it was thought that the binary evolutionary channel was the sole way to produce WR stars (Paczyński, 1971). The introduction of line-driven wind theory as the primary source of mass loss in massive stars shifted the consensus towards single-star evolution. However, in the past few decades, with the advancement of observational capabilities, the binary evolution scenario has again been invoked to explain some of the observed properties of massive star populations that do not abide by the predictions of single-star evolutionary models.

Binarity can impact the evolution of massive stars in multiple ways. Direct interaction in the form of mass exchange or mergers is thought to be very common among short-period massive binaries. It is estimated that $\approx$ 50-70% of massive stars in short-period binaries will interact with their companions at some stage during their lives (Sana et al., 2012; Kiminki & Kobulnicky, 2012). To be more specific, it is thought that in a given population of massive stars, $\approx$ 25% merge into a single star as binary interaction products, $\approx$ 33% will be stripped of their hydrogen envelopes to form WR stars through

binary interaction, $\approx 14\%$ will accrete mass and form disks, which increase the angular momentum and spin up the emission line stars (Be and Oe stars). This leaves only about 25% of massive stars evolve as single stars, albeit with the possibility that even these single stars could be in very wide, non-interacting binary systems.

Fig 1.4 depicts one of the possible scenarios involving mass transfer via Roche lobe overflow (RLO). As the primary evolves, it expands to the point where it fills its Roche lobe, where the hydrogen envelope of the primary becomes gravitationally unbound. Subsequently, and due to variations in pressure at the inner Lagrange point (L1), matter from the primary (donor) starts flowing through L1 and is captured and accreted by the secondary star (gainer). The rate of mass loss through binary interaction of the primary exceeds the mass loss via winds by a few orders of magnitude. Therefore, it is not surprising that the mechanism that dominates mass loss in massive stars – and WR formation – is mass transfer via RLO.

A possible scenario that is particularly important for close binaries is the common envelope (CE) phase. CE is typically triggered when a donor star expands rapidly and initiates unstable mass transfer that engulfs its companion (Paczynski, 1976). This may occur while the primary is crossing the Hertzsprung Gap (with a radiative envelope) or ascending the giant branch (with a convective envelope). The details of CE evolution are highly uncertain. However, CE is important for the formation of compact binary mergers, as it provides the necessary decay of orbital energy via dynamical friction (Bondi & Hoyle, 1944), thereby reducing the orbital separation.

The binary evolution channel has been invoked to explain the discrepancy between single-star evolutionary predictions and empirically derived HRDs, which involve the presence of stellar objects within the Hertzsprung gap. Podsiadlowski et al. (1992) showed that if mass transfer takes place during hydrogen-shell burning phase (Case B) or core-helium burning (Case C), the mass that is accreted by the secondary may lead to it becoming the more massive and luminous star of the system by the time the original

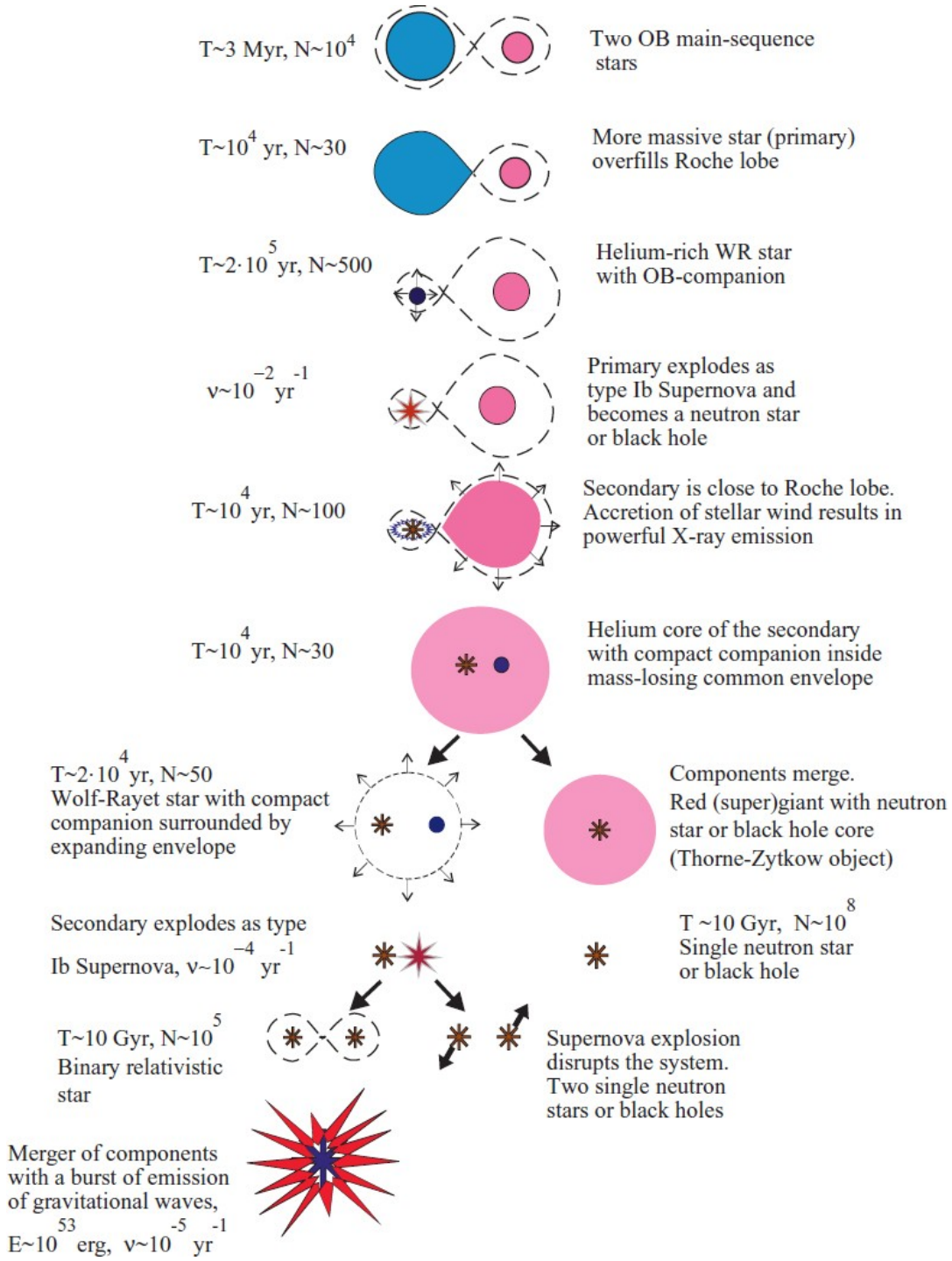


Figure 1.4: Illustration of mass transfer via RLO scenario in massive binaries. The parameters labelled on the diagram as T, N, and ν represent the characteristic lifetime of the evolutionary stage, the estimated number of binary systems in that particular evolutionary phase currently existing in our Galaxy, and the birth rate (formation frequency) of systems entering that specific evolutionary stage in the Galaxy. Credit: (Postnov & Yungelson, 2006).

primary explodes, leaving the star in the blue part of the HR diagram before it explodes in a CCSN.

The merger of two MS stars, which is thought to be the consequence of contact binaries or unstable mass transfer (Case A), results in the formation of a single, more massive star. These merger products are often identified as "Blue Stragglers" (Mateo et al., 1990). Such stars may exhibit anomalous chemical properties and luminosities that situate them near or within the high-temperature boundary of the Hertzsprung Gap (Schneider et al., 2014b). Additionally, Menon et al. (2024) was able to successfully reproduce the properties of B-type supergiants (anomalously high helium enrichment and N/C and N/O ratios), such as the ones analysed in this thesis, with models of evolved stellar mergers (Case B or C mass transfer).

In the previous part of this section, we discussed how studies of the rotational properties of OB stellar populations show that the rotation rate distributions generally peak at velocities < 200 km s^{-1}. Nevertheless, the same studies indicate a non-trivial population of massive stars with projected rotational velocities $v \sin i > 300$km s^{-1}, which presents a significant challenge to single-star models. Binarity presents two pathways for the generation of these rapid rotators. The first pathway is the accretion-induced rotational acceleration experienced by rejuvenated gainer stars due to the formation of circumstellar disks with high angular momentum (Packet, 1981). The second pathway involved a merger event, in which the resulting star may lack a mechanism for efficient removal of the newly acquired high angular momentum and therefore is formed with high rotational velocity (de Mink et al., 2014).

1.3 Mass loss and Stellar winds

Stellar winds are defined as the continuous outflow that is ejected from the atmosphere of a star. All stars, by one mechanism or another, produce winds. The more massive

the star, the more likely that its winds will be stronger. The winds of massive stars can be extremely powerful, draining the star of matter at high rates. This has significant consequences for the evolution of the star and the circumstellar medium. In this section, a basic physical description of winds in solar-type stars will be provided, and then the focus will shift to the main focal point of this thesis work: the winds of massive stars.

1.3.1 Solar winds

Solar-type winds are launched due to disequilibrium in the physical conditions between the star's photosphere and the overlaying corona (Parker, 1958). Let us take the Sun as an example; the temperature of the Sun's photosphere is $\approx$ 5800 K, whereas the temperature of its corona ranges from 10^6 to 10^7 K. This large difference in temperatures causes matter to flow from the high-pressure photosphere to the relatively low-pressure corona, producing supersonic winds from the stellar surface. The mass loss that is induced in this process has a typical rate of 10^{-14} $M_\odot\,yr^{-1}$ (Noble & Scarf, 1963).

In addition to the quasi-steady, thermally driven winds, solar-type stars experience eruptive, violent mass loss episodes known as coronal mass ejections (CMEs) (Vourlidas et al., 2010). CMEs are thought to be triggered by the interaction between the magnetic field lines and the coronal material via magnetic reconnection and instabilities in the stellar atmosphere caused by stellar rotation (Priest & Forbes, 2002; Vourlidas et al., 2010). CMEs are relatively minor contributors to mass loss, yielding a cumulative rate of just 10^{-16} to $10^{-15} M_\odot$ yr^{-1} (Odert et al., 2017).

Assuming that the lifespan of the Sun on the MS is about 10 billion years, then the total mass it loses via winds is $\approx 0.01\%$ of its initial mass. To put this into perspective, the mass that the Sun would lose by burning nuclear fuel and radiating light is about an order of magnitude larger than mass loss via solar winds. This is by no means a full description of the properties of solar winds, but it serves to show that – in contrast to

massive stars – the evolution and fate of low- and intermediate-mass stars $M < 8\mathrm{M}_{\odot}$ is mostly predetermined by their initial mass and chemical composition.

Although solar-type stars lose a negligible fraction of their mass on the MS, the mass loss – as in massive stars – becomes much more significant during late evolutionary phases. On the red giant branch and asymptotic giant branch, stars experience high mass-loss rates between 10^{-7}-10^{-4} $M_{\odot}\,\mathrm{yr}$ (Vassiliadis & Wood, 1993). This intensified mass loss is thought to be driven by radiation pressure that acts on dust grains, similar to the mechanism of RSG mass loss (Höfner & Olofsson, 2018).

1.3.2 The line-driven winds of massive stars

Following some of the first UV observations of OB stars by Morton (1967), Lucy & Solomon (1970b) introduced the idea that to overcome gravity, the acceleration due to radiation pressure acting on free electrons has to be combined with the so-called "line driving". The idea behind line driving, in its simplest form, is that momentum and energy are transferred by the photons that are radiated from the stellar interior to heavy species, like iron, forcing them out of the photosphere via radiative acceleration. This momentum is then shared with the surrounding ions. Hence, the designation of line driving, which describes the mechanism of the launching of the winds of massive stars, is caused by the radiative acceleration that is generated due to momentum transfer via spectral lines.

To understand line driving, we need to tackle a few concepts. For a time-independent stellar wind with a constant mass-loss rate, the amount of gas passing through a spherical surface of radius r is constant. This is expressed in the equation for the conservation of mass

$$\dot{M} = 4\pi r^2 \rho(r) v(r), \tag{1.11}$$

where $\rho(r)$ and $v(r)$ are the density and velocity of the wind at radius r.

We consider a simplified case in which the radiative force can be described by the frequency-independent scattering of free electrons. In this case, the radiative flux can be expressed as $L/4\pi r^2$, and the momentum flux as $L/4\pi r^2 c$, where c is the speed of light. The opacity can be defined as a constant $\kappa_e = \sigma_e/\mu_e$, where σ_e is the Thompson scattering cross section and μ_e is the mean atomic mass. From these equations, we can express the radiative acceleration in the wind due to free electron scattering as follows:

$$g_e(r) = \frac{\kappa_e L}{4\pi r^2 c} \tag{1.12}$$

Then, by comparing Equation 1.12 to the star's gravitational acceleration $g = GM/r^2$, where G is the gravitational constant and M is the mass of the star, we obtain the Eddington parameter

$$\Gamma_e = \frac{\kappa_e L}{4\pi G M c}, \tag{1.13}$$

which expresses the limits at which the radiative forces overcome the force of gravity. Hot massive stars approach the limit $\Gamma_e = 1$, whereas for lower mass stars, such as the Sun, the value hovers around 10^{-5}.

In reality, stars are driven more efficiently by absorption and scattering in spectral lines. Milne (1926) introduced the idea that, due to the Doppler effect, an atom that is launched outwards in the stellar atmosphere with a discrete velocity, will start to absorb photons of the same atom at rest in the blue wing of the absorption line (local line resonance). This means that the line is able to resonate with higher energies, leading to positive feedback. The simplest way to explain this is by adopting the Sobolev approximation (Sobolev, 1960), which assumes that the width of the resonance region $v_{\rm th}/(dv/dr)$, which depends on the velocity gradient dv/dr and the thermal broadening of the line $v_{\rm th}$ and is known as the Sobolev length, is infinitely narrow. In a supersonic medium, such as the wind of massive stars, the Sobolev length is of order $v_{\rm th}/(dv/dr) \ll 1$. Given this condition, line scattering can be described by the local density ρ, and line opacity κ, and

the optical depth at a given resonance can be expressed as

$$\tau = \frac{\kappa \rho v_{\rm th}}{dv/dr}, \tag{1.14}$$

As a line becomes optically thick (higher κ), the force is reduced. This can be expressed by modifying the optically thin acceleration by the escape probability, expressed as $(1 - e^{-\tau})/\tau$, which leads to the expression of line acceleration of:

$$g_{\rm line} = g_{\rm thin} \left(\frac{1 - e^{-\tau}}{\tau} \right). \tag{1.15}$$

If we consider the optically thin limit ($\tau \ll 1$), Equation 1.15 resembles the case of pure electron scattering, following:

$$g_{\rm thin} = \frac{\kappa v_{\rm th} v_0 L_\nu}{4\pi r^2 c^2} = g_e \frac{\kappa}{\kappa_e} \frac{v_{\rm th}}{c}, \tag{1.16}$$

where the first expression is approximate by assuming that the line frequency v_0 is close to the peak luminosity ($v_0 L_\nu \approx L$). In the optically thick limit $\tau \gg 1$, line acceleration takes the form

$$g_{\rm thick} = \frac{g_{\rm thin}}{\tau} = \frac{L}{4\pi r^2 \rho c^2} \frac{dv}{dr} = \frac{L}{\dot{M} c^2} v \frac{dv}{dr}, \tag{1.17}$$

where the definition of the mass-loss rate from Equation 1.11 is used. This shows that the acceleration from an optically thick line is independent of the opacity and is proportional to the velocity gradient.

The picture becomes more complex when considering that stellar winds are driven by a large number of optically thick lines. Castor et al. (1975a, CAK) provided a self-consistent solution of the stellar wind properties, by using the Sobolev approximation (high velocity gradient) and assuming that the star is a point source such that all radiation is radially streaming. Their formalism includes the use of a power law to represent

the flux-weighted number distribution of lines in the line opacity κ, and can be expressed as

$$\frac{dN}{d\kappa} = \frac{1}{\kappa_0}\left(\frac{\kappa}{\kappa_0}\right)^{\alpha-2}, \tag{1.18}$$

where κ_0 is a constant defined such that $\kappa_0(dN/d\kappa) = 1$ and the value of the power law index is between $\alpha = 0$ (optically thin) and $\alpha = 1$ (optically thick), and is known as the force multiplier parameter. In order to obtain the total force from these lines, we need to integrate the single-line results (Equation 1.15) over this opacity distribution.

The momentum equation for a gas that is driven by continuum opacity g_e and line opacity $g_{\rm line}$ can be expressed as:

$$v\frac{dv}{dr} = \frac{1}{\rho}\frac{dP}{dr} - g_{\rm grav} + g_e + g_{\rm line} = g_{\rm line} - \frac{GM}{r^2}(1-\Gamma_e) \tag{1.19}$$

where $g_{\rm grav} = GM/r^2$ and $g_e = g_{\rm grav}\Gamma_e$ (from Equation 1.12 and 1.13). From CAK theory, which neglects gas pressure ($dP/dr = 0$), we obtain the velocity law

$$v(r) = v_\infty\left(1 - \frac{R_*}{r}\right)^{\beta}, \tag{1.20}$$

where $\beta = 1/2$ and the terminal velocity is

$$v_\infty = v_{\rm esc}\sqrt{\frac{\alpha}{1-\alpha}}, \tag{1.21}$$

where the effective escape velocity $v_{\rm esc} = \sqrt{2GM(1-\Gamma_e)/R}$. Additionally, Castor et al. (1975a) derived a scaling relation for the mass-loss rate.

Unfortunately, predictions from CAK theory fall short. By way of example, for a hot O-type star, CAK theory often uses a value of $\alpha = 0.7$, which predicts v_∞ and $\dot{M}$ to be $\approx 1500\,{\rm km\,s^{-1}}$ and $\approx 10^{-5.2}\ {\rm M_\odot\,yr^{-1}}$ respectively. This implies that for such a star $v_\infty/v_{\rm esc} \approx 1.2$. This is much lower than observed values. For example, Prinja et al.

(1990) finds a mean value of $v_\infty/v_{\rm esc} \approx 2.4$ from a large sample of O stars and early B supergiants.

The shortcomings of CAK theory have been addressed by subsequent studies by avoiding the assumptions made in the original CAK theory, allowing for multiple scattering of overlapping lines (Beckman & Crivellari, 1985) and adopting a finite angular extension of the stellar disk (Friend & Abbott, 1986; Kudritzki et al., 1989). This led to the revision of wind parameter predictions, where v_∞ increased by a factor of 2–3, which led to an increase in the $v_\infty/v_{\rm esc}$ to ≈ 2.6 (Kudritzki & Puls, 2000). Additionally, β increased to 0.8–1.0, and $\dot{M}$ was reduced by nearly a factor of two. However, due to the use of the Sobolev approximation, CAK-based models are valid only in the supersonic outer parts of the wind but fail in the subsonic inner regions near the photosphere. One way to resolve this issue is to adapt the comoving frame when solving the radiative transfer equations (Mihalas et al., 1975). This is discussed in the context of the radiative transfer code CMFGEN in the following subsection.

1.3.3 Mass loss recipes and the bi-stability jump

The term bi-stability jump describes a phenomenon of a steep jump in stellar wind density around $T_{\rm eff} \approx 25{-}21$ kK, and it was first coined by Pauldrach & Puls (1990) in a spectroscopic analysis of the LBV P Cygni in which two solutions were possible. The first solution has a high temperature (the “hot" side of the jump) and involves higher ionisation levels that would produce a faster and relatively low-density wind. The second solution has a lower temperature (the “cool" side of the jump), in which the wind recombines to lower ionisation stages. This results in a significant drop in the terminal velocity and in denser wind.

Later, Lamers et al. (1995) observed a jump in the ratio $v_\infty/v_{\rm esc}$ from ≈ 2.6 for supergiants earlier than B1 (≈ 25 kK) to $v_\infty/v_{\rm esc} \approx 1.3$ for supergiants of types later than

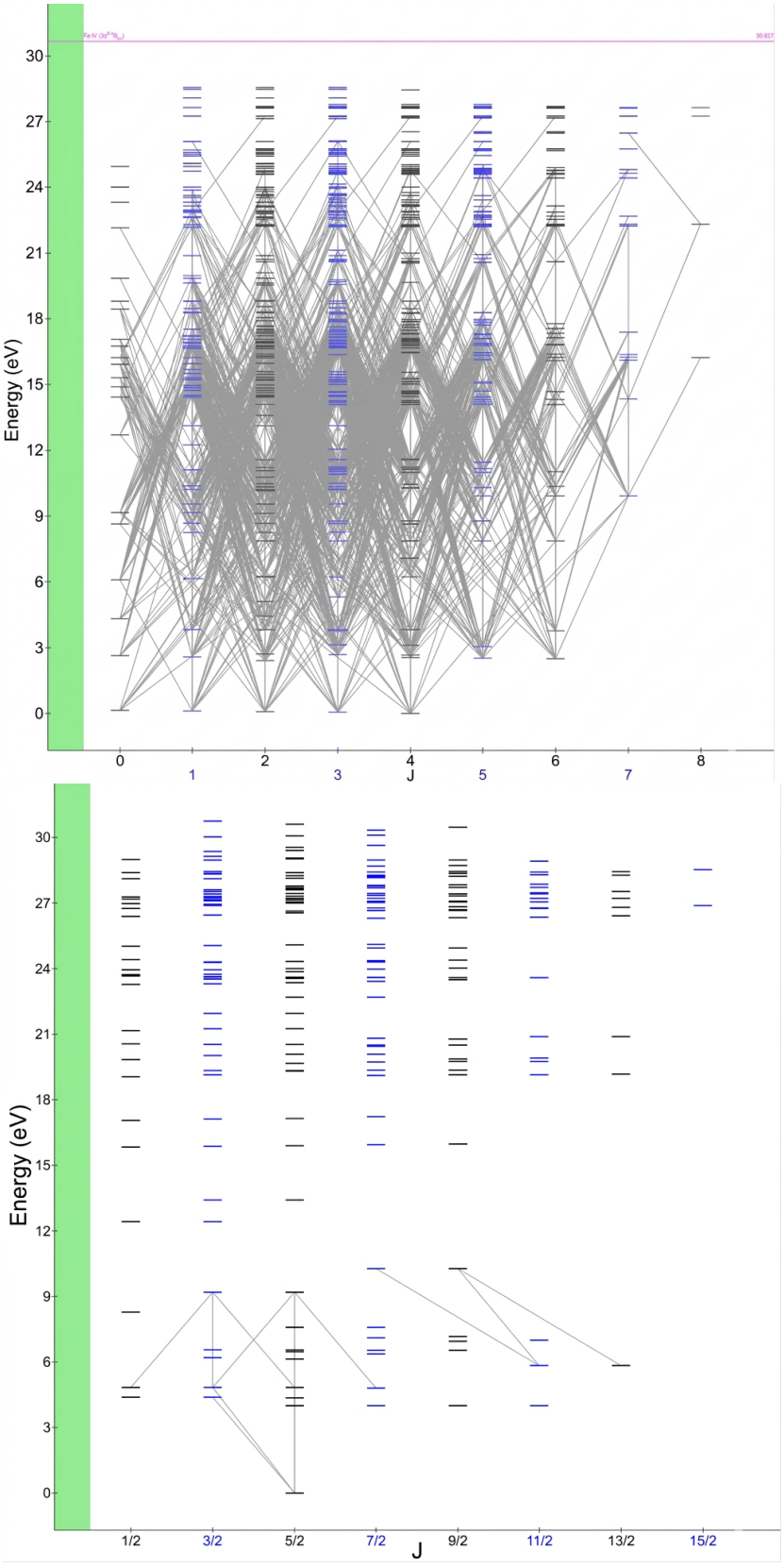


Figure 1.5: Grotrian diagrams of Fe III (top panel) and Fe IV (bottom panel). The abscissa shows the values of the total angular momentum quantum number J while the ordinate shows energy levels in electron volts (eV). We include all lines (solid grey lines) between 912 and 3000 Å. The diagrams were produced using the graphical tool available on the website of the National Institute of Standards and Technology's Atomic Spectra Database.

B1 (Kudritzki & Puls, 2000). The reason for this jump is attributed to the recombination of Fe IV to Fe III, as explained by Vink et al. (2000), since these lines dominate the acceleration in the subsonic part of the wind (Vink et al., 1999). Fe III has far more lines in the UV region close to the peak of the SED than Fe IV. Thus, more momentum is transmitted to the material, and a much higher mass loss is produced. For reference, we present the Grotian diagrams of Fe IV to Fe III in Fig. 1.5, which show the extreme difference in the number of lines in the wavelength range 912-3000 Å.

Vink et al. (2001) provided a numerically derived mass-loss prescription, where the temperature of the jump that divides the range into cool and hot depends on the Eddington parameter Γ_e and the metallicity. The introduction of the bi-stability jump might increase the mass-loss rate by a factor of seven for the cool compared to the hot solution for stars that are located roughly around the bi-stability jump. On the other hand, newer mass-loss prescriptions using a different approach for calculating the radiative acceleration, such as Björklund et al. (2021) and Krtička et al. (2021), did not predict such a steep increase in the mass-loss rates. There have been multiple efforts to explore the behaviour of the wind of blue supergiants around the bi-stability jump in the Milky Way (Crowther et al., 2006; Benaglia et al., 2007; de Burgos et al., 2024a) and in the LMC (Verhamme et al., 2024) and SMC (Bernini-Peron et al., 2024). In this thesis, a new investigation of this phenomenon in the LMC, SMC, and MW is conducted.

1.3.4 Effect of metallicity

In the stellar atmosphere, the most abundant species are hydrogen and helium. Due to the high effective temperatures, hydrogen and helium are either fully or partially ionised, with little contribution to the overall radiative acceleration. This is because the bulk of the radiation in massive stars is emitted in the UV and FUV, where hydrogen and helium have a relatively small number of absorption lines. Metals account for the majority of

line driving, due to the complexity of their ionic structure and the large number of absorption lines in the UV spectral range, which increases with heavier elements. This is particularly important for iron-group elements, with each of their ions possessing millions of line transitions in the UV. This leads to the conclusion that, in the framework of the theory of line-driven winds, the metal content of the star, or the metallicity (Z), plays an important role in determining the properties of the winds (Abbott, 1982).

The theory of line-driven wind and its implications for the Z-dependence of wind properties have been studied in the literature. It is taken into account in the various numerical mass-loss recipes (e.g., Vink et al., 1999, 2001; Krtička et al., 2021). The Z-dependence of mass-loss and wind velocity has also been well established observationally (e.g., Kudritzki et al., 1987; Prinja & Crowther, 1998a; Mokiem et al., 2007; Ramachandran et al., 2019; Hawcroft et al., 2024a; Backs et al., 2024; Pauli et al., 2025). Nevertheless, there is a persistent discrepancy between the Z-dependence that is predicted in theory and what is empirically derived from observations of blue supergiants in low-Z environments (Krtička et al., 2024).

The wind momentum-luminosity relation

The concept of a wind momentum-luminosity relation (WLR) was first proposed by (Kudritzki et al., 1995) implying that the mechanical momentum of the flow $\dot{M}v_\infty$ strongly depends on the stellar luminosity. Recalling Section 1.1.4, the FGLR method for determining distances heavily relies on the reliable calibration of the WLR.

The WLR has become a staple in investigating the metallicity dependence of wind parameters, with many studies having published values for modified wind momenta ($D_{\rm mom}$) when deriving the parameters of massive stars (see e.g., Repolust et al., 2005; Markova et al., 2005; Trundle et al., 2004b; Trundle & Lennon, 2005b; Urbaneja et al.,

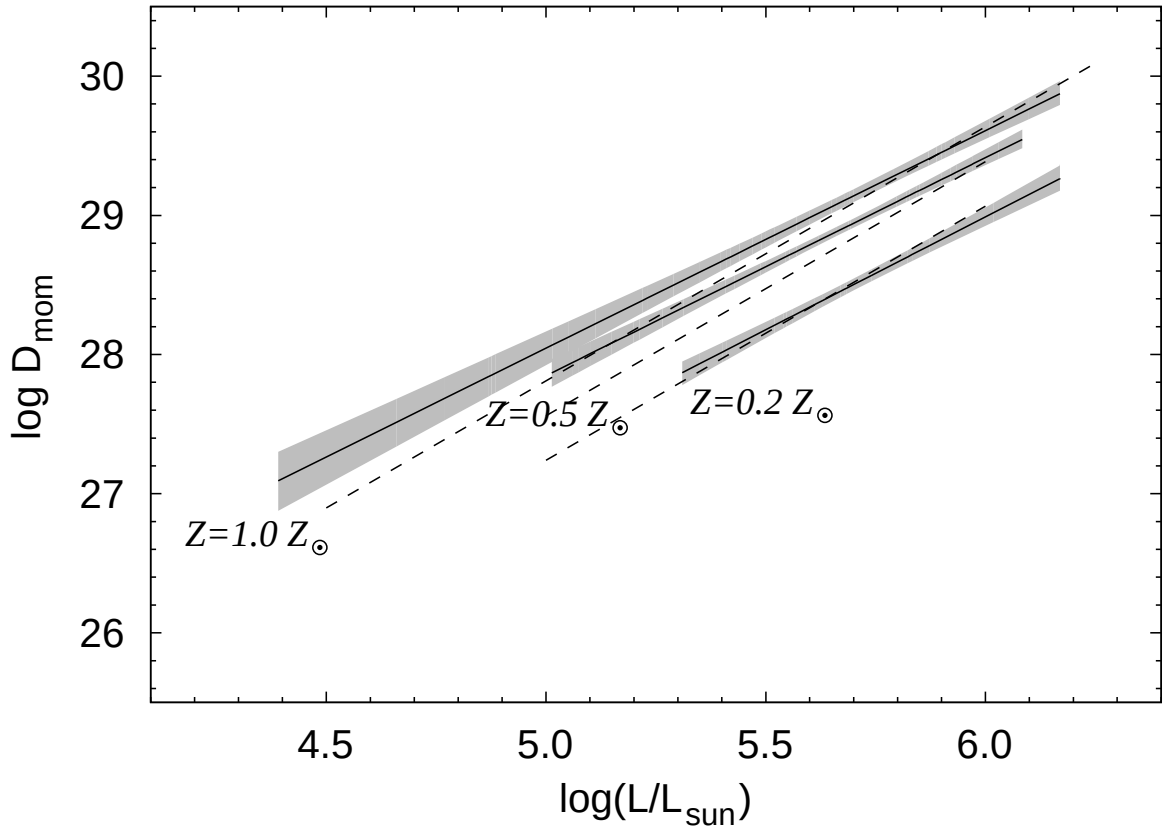


Figure 1.6: The observed wind momentum-luminosity relation obtained by Mokiem et al. (2007, solid lines) compared to predictions from Vink et al. (2000, 2001). Top, middle and bottom lines correspond to Galactic, LMC and SMC, respectively. This figure was taken from Mokiem et al. (2007).

2017; Verhamme et al., 2024; Bernini-Peron et al., 2024; Backs et al., 2024), such that

$$D_{\rm mom} = \dot{M} v_\infty \sqrt{R/R_\odot} \tag{1.22}$$

Then, assuming a WLR of the form

$$\log D_{\rm mom} = \log D_0 + \log L, \tag{1.23}$$

one can constrain the coefficients $\log D_0$ and x. Fig. 1.6 shows the results from Mokiem et al. (2007), who empirically established that O stars in the MW systematically possess

higher log $Dmom$ than in the LMC, which in turn are higher than in the SMC, indicating a metallicity dependence of wind parameters. They provide a metallicity scaling of $\dot{M} \propto Z^{0.83\pm0.16}$, which agrees with predictions from models based on CAK theory, which show $\dot{M} \propto Z^{0.69\pm0.10}$ (Vink et al., 1999).

Since the seminal work of Mokiem et al. (2007), efforts have been made to constrain the metallicity-dependence of wind properties and to produce empirical recipes for mass loss and wind momentum (for recent studies see e.g., Marcolino et al., 2022; Backs et al., 2024; Pauli et al., 2025). These recipes, although very insightful, suffer from different issues. In particular, these recipes are produced using assumptions inferred from numerical recipes (Leitherer et al., 1992; Vink et al., 2001; Krtička et al., 2021; Björklund et al., 2023). Furthermore, luminosity classes are not taken into account in these recipes. Lastly, empirical recipes usually use results from the literature, which use different atmosphere codes and various datasets, some UV and optical, and some only optical, subjecting the derived parameters to a large variance (Sander et al., 2024).

1.3.5 Wind signatures and wind density measurement

Wind lines are easily distinguished from spectral lines formed in the photosphere by their broad width, or Doppler-shifted profile, signifying an outflow.

P Cygni profiles

The most distinct signature of a stellar wind is the P Cygni profile, where the spectral lines have both a blueshifted absorption and redshifted emission. A schematic of the formation of a P Cygni profile is presented in Fig 1.7. Ions moving through the column of gas directly in front of the stellar disk scatter photospheric photons out of the line of sight. Because these Ions are moving toward the observer, the absorption is Doppler-shifted to shorter wavelengths (blue). Meanwhile, ions moving in the peripheral lobes of the wind surrounding the star can scatter photons into the line of sight. As the wind

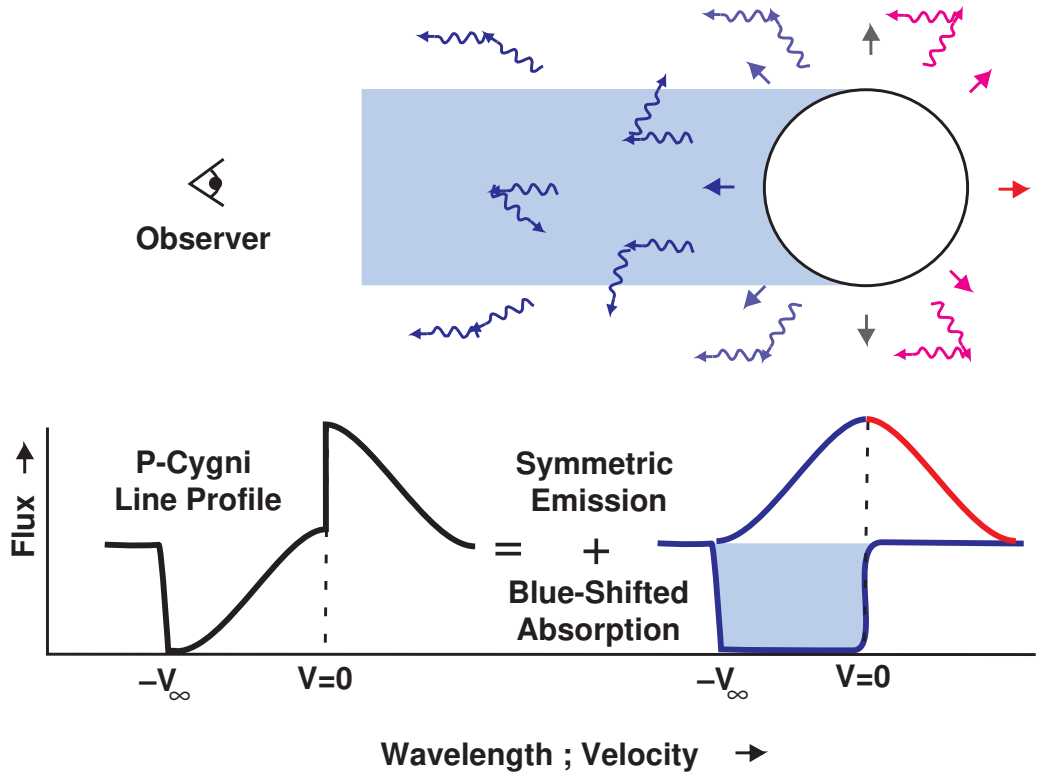


Figure 1.7: Cartoon depicting the process of P Cygni profile formation in the atmospheres of massive stars. Credit: Stan Owocki.

expands spherically, some of this material moves away from and toward the observer, producing a line that has both a blue and redshifted component. This results in the classic P Cygni profile seen in Fig. 1.7.

In reality, P Cygni profiles deviate from the classical shape presented in Fig. 1.7. This is thought to be a direct result of the line-driven instability (LDI, Lucy & Solomon, 1970b; Owocki et al., 1988), also known as the line-deshadowing instability, which leads to the fragmentation of the wind into slow-moving dense clumps that are separated by high-velocity, rarefied gas, resulting in a highly structured, non-monotonic velocity field (Owocki et al., 1988; Feldmeier, 1995). Photons propagating through such a non-monotonic wind encounter multiple resonance zones where the same Doppler-shifted velocity is repeated along the line of sight. This multi-resonance structure increases the effective line optical depth across a wide range of velocities (Puls et al., 1993; Sundqvist et al., 2010; Sundqvist & Owocki, 2013; Sundqvist et al., 2014). This broad absorption heavily suppresses the emerging stellar flux well below the terminal velocity, flattening the narrow classical blue absorption wing into an extended, flat-bottomed trough of near-zero flux (Lucy, 1983).

In late-O and B supergiants, typical examples of P Cygni profiles in OB supergiant spectra are UV resonance transitions connected to the ground level, such as C IV $\lambda\lambda 1548 - 1551$ and Si IV $\lambda\lambda 1394 - 1403$. These lines are sensitive to the wind velocity structure, which is why saturated P Cygni profiles have been used to measure the terminal velocity v_∞ of the wind by fitting the blue edge of the absorption trough (Prinja et al., 1990). This velocity is known as the black velocity $v_{\rm black}$. If the P Cygni profile is unsaturated, then measuring the terminal velocity is not possible. However, the maximum velocity achieved by the wind $v_{\rm edge}$ can be measured at the point where the blue edge of the absorption trough rejoins the continuum.

Mass-loss rates can be inferred from P Cygni profiles from UV line synthesis code using the Sobolev with exact integration (SEI) method (Lamers et al., 1987). However,

mass-loss rates determined by this method suffer from a few non-trivial caveats. Saturated P Cygni profiles are not sensitive to the changes in density and mass-loss rates, making the mass-loss rates derived from such lines upper limits. Another serious issue for obtaining mass-loss rates from P Cygni modelling is that the fractional population of each ion must be well known. There have been several attempts at modelling the ionisation structure of the winds for OB stars (e.g., Massa et al., 2003), but values of the ionisation fractions of ions of various species, such as Si IV and Al III, are highly contentious (Prinja et al., 2005). Furthermore, these mass-loss rates are subject to large uncertainties due to the high intrinsic variability of wind lines (Prinja et al., 2002; Massa et al., 2024), in addition to degeneracies caused by the X-rays that are generated via shocks in the wind (Puls et al., 2008).

Recombination lines

Unlike resonance scattering, recombination is a collisional process. The collision of an ion in the stellar wind with a free electron can result in recombination, normally to the ground state. However, an electron can recombine to an excited state, upon which it will de-excite and cascade down to lower states. A line photon is produced from each de-excitation, meaning that recombination is an important source of line photons in the wind. The strength of the recombination line is dependent on the ion and electron density in the wind; as such, these lines are known as density-squared (ρ^2). Examples of such lines are Hα and He II λ4686 (for stars earlier than B1). While resonance lines primarily trace velocity, recombination lines are the primary diagnostic for wind density and the mass-loss rate (Klein & Castor, 1978).

These lines may be observed in emission, which is a spectroscopic characteristic of hot BSGs with strong winds. For cooler stars with strong winds, Hα may begin to display a P Cygni profile. The amplitude of the line indicates the degree of mass loss in the wind, whereas the line morphology can be used to constrain the velocity law β. In stars

with modest mass-loss rates, the photospheric component dominates the Hα line profile. However, the resulting line profile is shallower in absorption than a solely photospheric component due to emission from the stellar wind, which fills in the line. In this case, one cannot constrain β, and the derived mass-loss rates can be considered upper limits.

Electron scattering and wind inhomogeneity

Electron scattering (also known as Thompson scattering) is the process in which electromagnetic radiation (photons) interacts and is scattered by free electrons. For low-energy photons, the electrons kinetic energy and the frequency of light are unchanged after scattering. For high-energy photons, i.e. photons with energy greater than the rest mass energy of an electron, relativistic corrections are required as the frequency of the light changes or the free electron is accelerated to relativistic speeds.

Electron scattering shapes the wings of strong emission lines, particularly the Balmer series and He II lines (Hillier, 1984, who employed He II λ5411 in their calculations owing to it being an isolated line). As line photons traverse the wind, they undergo incoherent scattering by high-velocity thermal electrons, redistributing flux from the core into the wings. This effect is a defining characteristic of WR stars, where high wind densities create significant electron scattering optical depths τ_e; conversely, in OB supergiants, the effect is much less significant due to their lower wind densities and mass-loss rates (Puls et al., 2006).

Historically, a major discrepancy arose when modelling WR spectra: models assuming a homogeneous (smooth) wind required very high mass-loss rates to match the intensity of recombination emission lines ($\propto \rho^2$). However, these high rates predicted electron scattering wings ($\propto \rho$) that were far stronger than observed. To resolve this, micro-clumping approximations were introduced (Hillier, 1991; Hamann & Koesterke, 1998). By assuming the wind consists of optically thin, dense clumps occupying a small volume filling factor, models could reproduce the strong recombination emission (formed

in the dense clumps) while maintaining a lower global mass-loss rate, thereby fitting the weaker observed electron scattering wings. This clumping formalism is also essential for accurately reproducing P Cygni profiles, particularly in scaling the strength of the red emission component relative to the blue absorption trough (Crowther et al., 2002).

Mass loss from IR and radio

Another method for measuring the mass loss rates of massive stars involves using the infrared, sub-mm, and radio continua. The idea is to measure the excess flux produced by bound-free and free-free (Bremsstrahlung) emission in the wind and compare it to the amount of flux predicted by photospheric model atmospheres. (Wright & Barlow, 1975) and Panagia & Felli (1975) independently came to the conclusion that the continuum flux S_ν depends on the frequency ν, such that $S_\nu \propto \nu^{0.6}$. This solution was derived by assuming that S_ν is being generated by homogeneous and isothermal winds that are expanding at a constant velocity v_∞. They also showed that the emergent flux strongly depends on the distance to the star d, $\dot{M}$ and v_∞, in addition to a weak dependence on the electron temperature of the wind, which is formulated as

$$S_\nu \propto \left(\frac{\dot{M}}{v_\infty}\right)^{4/3} \frac{\nu^{0.6}}{d^2}. \tag{1.24}$$

Combined with infrared excesses, this constitutes a robust method for deriving $\dot{M}$, since it is based on well-understood physics of atomic processes and radiation transfer, avoiding the complexity of radiative transfer models, such as line blanketing, non-local thermodynamic equilibrium (nLTE) effects, and line broadening. However, the caveat is that early-type stars are very faint in these wavelengths, which limits the use of this method to studies of nearby galactic objects (Barlow & Cohen, 1977; Puls et al., 2006; Benaglia et al., 2007). Additionally, this method is hindered by the inverse square law, which dictates that the observed flux (F) from a source decreases with the square of the

distance (d): $F = \frac{L}{4\pi d^2}$, making the radio fluxes of extragalactic OB stars very small.

Mass-loss rate discrepancy

The mass-loss rate discrepancy stems from how different spectral lines respond to the density (ρ) of the stellar wind. UV resonance lines formed by line scattering of stellar continuum are linearly dependent on the density ($\propto \rho$) and probe a wide region of the stellar wind. Recombination lines (such as Hα) have a quadratic density dependence ($\propto \rho^2$), making them highly sensitive to local density variation in a narrow region of the inner wind near the photosphere. Free-free emission (radio and sub-mm excess) also depends on the square of the density ($\propto \rho^2$); however, it probes the outermost, accelerating-free region of the wind. Therefore, when assuming a smooth, homogeneous wind, different spectral regions yield vastly different mass-loss rates ($\dot{M}$) (Fullerton et al., 2006).

To reconcile this dissonance, the micro-clumping approximation (Hamann & Koesterke, 1998), which we discussed earlier, was introduced. However, attempts to fully resolve the discrepancy between P Cygni and recombination-line mass-loss rates using only micro-clumping led to scaling down the Hα mass-loss rates by factors of more than 10 and up to 100 (Fullerton et al., 2006). Reducing mass-loss rates by this magnitude contradicts stellar evolution models and creates a "weak-wind" problem (see Section 1.4) across the majority of O-type stars.

This problem was relaxed by the introduction of the macro-clumping approximation, where clumps are assumed to be optically thick, and photons can avoid interacting with them by travelling through the relatively empty porous channels (gaps) between the clumps (Owocki et al., 2004). This effect of leaking light makes the stellar wind more transparent to UV photons than a smooth wind of the same mass would be. Consequently, UV resonance lines appear weaker, mimicking a lower mass-loss rate. Furthermore, because stellar winds are rapidly accelerating, clumping also occurs in ve-

locity space (Owocki, 2008; Sundqvist et al., 2014). Since the Doppler shift changes continuously as the wind expands, a photon only interacts with gas at a specific resonant velocity. If the dense gas is clustered into discrete velocity packets, large gaps are left in velocity space where the wind is effectively transparent(Massa et al., 2003). This velocity-porosity (vorosity) further weakens the absorption profiles of UV resonance lines (for a comprehensive description and visualisation of the effect of vorosity see, Brands et al., 2022). We further discuss the uncertainties in mass loss estimates that stem from wind variability and structure in the next section.

1.4 Unanswered questions

1.4.1 Mass loss

Post-MS winds

Unlike steady mass loss via radiation-driven winds, Eddington limit-driven mass loss, such as LBV eruptions, remains shrouded in mystery. A major question involves the underlying physics and whether these eruptions are a purely photospheric phenomenon or if they are triggered by internal instabilities. Radiation hydrodynamic simulations from Jiang et al. (2018) show that instabilities in high-opacity helium could lead to the reduction in temperature observed in LBVs, and consequently, the eruptive mass loss. Another hypothesis is linked with the role of strange mode instabilities, which occur in the iron ionisation zones, affecting the iron-bump opacity and therefore the strength of winds (Smith, 2014).

From observations, RSGs are enveloped by circumstellar dust, which is condensed from their stellar wind. Albeit, the driving mechanism of RSG winds remains poorly understood (Smith, 2014). One of the mechanisms that contributes to wind driving involves pulsations at the surface of the RSG, which produce perturbations in the loosely

bound atmospheres, leading to mass loss (Owocki et al., 2022). Additionally, radiation driving through the absorption of the continuum by dust grains, which is known as dust-driven winds, is also thought to contribute to the mass loss in RSGs (Sedlmayr & Dominik, 1995; Zhang, 2018).

The lack of knowledge on the mechanisms of wind driving in these phases makes the mass loss in the post-MS phase highly uncertain. Consequently, issues such as the metallicity dependence remain unclear. This in turn introduces uncertainties in single-star evolution, questioning the range at which isolated stars can self-strip (remove their hydrogen envelopes) and become WR stars, especially at lower metallicity (Hainich et al., 2015)

Wind structure and variability

Another issue that introduces large uncertainties to the empirically determined $\dot{M}$ is wind inhomogeneity. In Section 2.1.3, we discussed the implementation of clumping in CMFGEN (micro-clumping). Other implementations have been used in radiative transfer (RT) codes. One example of this is the macro-clumping approximation, where the inter-clump medium is not treated as a void, but rather a low-density medium, producing what is known as the velocity-porosity effect (see e.g., Sundqvist et al., 2014; Brands et al., 2022). However, these implementations are rough approximations, which are necessitated by the 1-D nature of RT codes, and may be regarded as nonphysical fudge parameters that merely aid in producing better spectroscopic fits for wind lines.

Furthermore, the clumping paradox refers to a challenge in the theory of radiation-driven winds that is centred on the discrepancy in the spatial scales of the clumps. On the one hand, the constant appearance of UV and optical spectral line profiles hints towards the idea that the wind must be composed of a large population of "micro-clumps" (Puls et al., 2008). On the other hand, the dramatic variability seen in the X-ray lightcurves of accreting HMXB suggests the presence of large-scale density structure

capable of producing flares of X-ray emission (Walter & Zurita Heras, 2007; Martínez-Núñez et al., 2017). Owocki & Cohen (2006) claim that this paradox points towards a variable structure, where small-scale instabilities eventually coalesce into larger, more massive structures further out in the wind.

While clumping deals with small-scale stochastic structures, discrete absorption components (DAC) and narrow absorption components (NAC) represent large-scale variability and are linked to changes in the star itself (Prinja & Crowther, 1998b). DACs are seen in UV P Cygni profiles as absorption features that migrate from low to high velocities, which has been linked to the rotation of the star (Prinja, 1988). Cranmer & Owocki (1996) claim that this could be attributed to the variance in the velocity of wind components, resulting in the formation of spiral-like structures, known as corotating interaction regions. The asymptotic velocity evolution of DACs towards the blue edge of the unsaturated P Cygni profile results in the formation of localised NACs that are seen in single UV "snapshot" observations of OB stars (Lamers et al., 1982; Howarth & Prinja, 1989; Kaper et al., 1996).

However, our understanding of clumping and wind variability – and mass loss in general – depends on the models we use, which are full of simplifications and nonphysical parameterisations, which makes our observationally derived $\dot{M}$ and v_∞ highly uncertain (Oskinova et al., 2007), especially when considering the intrinsic variability of wind line profiles (Massa et al., 2024). Unified 3D time-dependent models that capture all types of variability in the winds remain a holy grail of stellar astrophysics that is yet to be found.

The weak wind problem

The "weak wind problem" represents a significant discrepancy between empirically derived mass-loss rates derived from UV and optical wind diagnostics and theoretical predictions. This was first discovered in Galactic late-O dwarfs by Martins et al. (2005a),

who noted a transition in wind properties near $\log L/L_{\odot} = 5.2$, in which stars exhibit observed mass-loss rates that are one to two orders of magnitude lower than those predicted by standard line-driven wind theory (Marcolino et al., 2009).

This was initially thought to be an effect of metallicity, where non-solar He and CNO abundances could contribute to this discrepancy in line driving. However, further investigation concluded that this cannot be fully explained by metallicity, as this problem persisted in other environments, such as the SMC (Martins et al., 2005b). This problem was later suspected to encompass O dwarfs across all spectral types and metallicities (Ramachandran et al., 2019).

Several other remedies to this problem have been suggested. Puls et al. (2008) argued that the lack of clumping could be the culprit, where smooth wind assumptions in CAK-based models overestimate the mass-loss rates, and empirical mass-loss rates derived using RT codes that implement clumping are underestimated, leading to this large discrepancy. It has also been suggested that new CAK-based simulations show that the force multiplier parameters used in older models may overcount the number of lines contributing to the radiation pressure, which leads to producing unrealistically large mass-loss rates (Muijres et al., 2012).

Although it is tempting to blame this problem solely on theory and models, as we discussed previously, different methods for empirically deriving mass-loss rates yield vastly different values. From X-ray spectroscopy, Huenemoerder et al. (2012) derived a mass-loss rate for the Galactic O dwarf μ Col that is six times higher than the one obtained from classical UV and optical diagnostics. Similarly, in the case of the late-O dwarf 10 Lac, Law et al. (2024) derived a mass-loss rate ten times higher from forbidden high-ionisation fine-structure mid-infrared lines. These examples are evidence that our current approaches, sophisticated as they may be, will have to be revised.

1.4.2 Multiplicity and binary evolution

Identifying the multiplicity of massive star systems is a challenging task, primarily due to limitations on the observational capabilities and the extreme brightness of the massive components, which drown out the light of smaller companions. To accurately determine whether a star is single, binary, or higher-order, one must go beyond the use of photometry and ideally employ multi-epoch spectroscopy to identify possible radial velocity variations and quantitatively analyse the components. A recent example is the discovery of a massive companion to R136a1, which was previously thought to be a 300 $M_{\odot}$ single WR star (Crowther et al., 2010). This led to the downward revision of the mass of the primary component R136a1A to $\approx 170 - 230$ $M_{\odot}$ (Kalari et al., 2022), with an estimated companion mass of $\approx 40 - 70$ $M_{\odot}$. The existence of a massive companion in R136a1 at < 1000 au has recently been confirmed using VLT/GRAVITY+ observations of R136a (priv. comm. with Sarah Brands, see press release). Another example comes from Ramachandran et al. (2024), who found that the O8 SMC supergiant Sk -71° 35 is actually made up of an O6.5 stripped star and an early emission line B0-1 dwarf. These examples serve to show that stellar properties and evolutionary status of systems inferred from photometry or spectral-type calibrations under the single-star assumption can be highly contentious.

In stellar evolution theory, the common envelope stage is the most critical phase for creating tight binary systems, yet it remains the least understood due to its short duration and high gas density, which makes it difficult to observe directly. In this case, according to Ivanova et al. (2013), whether the stars merge or the envelope gets ejected due to sufficiently high energy (mainly orbital) is not well understood. This is primarily due to the simplistic formalism in describing this process, which relies on a fudge parameter known as the efficiency parameter, the value of which is not constrained observationally. This problem is mirrored in the physics of RLOF, where the efficiency

of mass transfer, i.e. the mass that is actually accreted onto the companion compared to the mass that is lost, drastically alters the resulting orbital periods, mass ratios, and the type of SN and remnant (de Mink et al., 2014; Shao & Li, 2019).

Observationally, these uncertainties extend to the RSG problem: the lack of RSGs with luminosities higher that $\log L/L_{\odot} \approx 5.5$, even though they are predicted in models, questions whether massive stars above that luminosity threshold are dominated by binary stripping of if they collapse directly into black holes as failed SN before reaching the red part of the HRD (Smartt, 2015; Davies et al., 2018). This is also complicated by the difficulty in distinguishing truly single stars that are not a post-binary interaction product and that do not currently have a faint companion that has eluded detection. Furthermore, models struggle in explaining the spins and masses of black hole binaries observed via gravitational waves, which forced the reevaluation of the mechanisms of angular momentum transport and internal mixing (Marchant et al., 2016; Abbott et al., 2023).

1.4.3 Massive stars in the early universe

The discovery of high N/O ratios in galaxies at high redshifts $z > 5$ poses a challenge for chemical evolution models. An example of this is GN-z11, which exhibits strong semi-forbidden N III and N IV lines compared to O III and O II lines, implying super-solar N/O ratios. Some studies have suggested that this enrichment stems from the winds of a dense population of WR stars or the presence of a 1000 $M_{\odot}$ supermassive star, which is supported by the Lyman emission observed in the spectrum of this galaxy (Bunker et al., 2023; Cameron et al., 2023).

The observation of extremely low metallicity galaxies with enhanced nitrogen abundances has led to questioning the validity of universal initial mass functions, with some theoretical studies suggesting that metal-poor galaxies may transition into a top-heavy

IMF (Chon et al., 2021). This has also raised speculations on the nature of stars in the early universe and whether pristine Pop III star formation could reproduce the observables (Cullen et al., 2025).

1.5 The purpose and outline of this thesis

In view of the various questions presented in the previous sections, this thesis is focused mainly on two aspects of the physics of massive stars:

- Winds of late-O and B supergiants:

  Here, we have conducted three quantitative spectroscopic studies of early-O and B supergiants in the Galaxy and Magellanic Clouds, using a detailed analysis method that employs the RT code CMFGEN. The studies include investigations into the mass-loss rates, wind velocities, the bi-stability jump, the fundamental photospheric parameters, and the elemental abundance of stars. We have tested our results by comparing them to theoretical predictions and to results from archival studies.

- Metallicity scaling of wind parameters:

  The studies in the LMC, SMC, and MW were conducted in a global effort to constrain the metallicity dependence of wind parameters, calibrate the modified wind momentum - luminosity relation, and enhance the constraints on the mass loss rates of late-O and B supergiants.

The manuscript is organised as follows:

- Chapter 2: This chapter provides a general description of CMFGEN, the model grids used in the analysis, and the fitting routine from which we derive the physical and wind parameters of the stars in our samples.

- Chapter 3: In this chapter, we present the first study of a sample of 16 supergiants in the LMC, with subtypes ranging from O9 to B8. Here, we focus on many aspects of the bi-stability jump and provide detailed discussions on the commonly used numerical mass-loss rate recipes.

- Chapter 4: In this chapter, we present our second study, which includes a sample of 20 SMC supergiants in the same spectral type range. The focus of this chapter is to investigate the metallicity dependence of wind parameters in the Magellanic Clouds by contrasting the results of this study with those of its LMC counterpart.

- Chapter 5: This chapter extends the analysis to the MW. This provides the necessary baseline to produce fully empirical mass-loss rate and wind momentum recipes using homogeneously obtained results in the three environments with different metallicities.

- Chapter 6: This is the concluding chapter where we discuss the metallicity dependence of wind parameters and the new empirical mass-loss rate recipe. We also discuss the implications of our results on the evolutionary status of the stars in our samples. We present a summary of the results and future work.

Chapter 2

Methods

In this chapter, we aim to provide a description of (i) the interplay between matter and radiation in the atmospheres of massive stars as the basis of radiative transfer codes, (ii) the code we used in our analysis and the reasons behind our choice, and (iii) the analysis methods used to derive the stellar and wind properties of the stars in our samples. In Section 2.1, we present and discuss the radiative transfer and statistical rate equations and their link to the macro- and micro-physics of radiation-driven winds. We also summarise the complex inner workings of CMFGEN, explaining the concepts of the co-moving frame and spherical symmetry required to solve the radiative transfer equations in tandem with the statistical rate equations. In Section 2.2, we introduce the CMFGEN grids used for our analysis and discuss the underlying assumptions included in our models. In Section 2.3, we present our analysis methods and fitting techniques and provide a detailed account of the fitting procedure, the diagnostic lines used in our analysis, and the uncertainties resulting from our approach and assumptions.

2.1 Radiative transfer in CMFGEN

The most reliable method for deriving the fundamental wind and photospheric parameters of hot, massive stars with strong winds is to use multiple lines in their spectra. To do this, we compare the observed spectral lines with spectra synthesised by codes that rely on radiative transfer calculations. In this study, we used the code CMFGEN (Hillier, 1990; Hillier & Miller, 1998) to model the stars. The main function of CMFGEN is to determine the structure of the stellar atmosphere. In other words, it determines the stratification of temperature and density, and the ionisation structure, in the photosphere and wind, as well as the populations of energy levels in atoms and ions.

Currently, apart from CMFGEN, there are two other unified-atmosphere codes (i.e., codes that take into account the effects of the stellar wind and the star's radiation field simultaneously) that are commonly used in spectroscopic analysis of BSGs: PoWR (Gräfener et al., 2002a; Hamann & Gräfener, 2003a) and FASTWIND (Puls et al., 2005). PoWR is similar to CMFGEN, solving the radiative transfer equation in spherical geometry in the co-moving frame for all transitions (lines and continuum), fully accounting for blanketing using the super-levels approach, and assuming radiative equilibrium to determine the temperature stratification.

FASTWIND deals with line transfer either in the co-moving frame (for explicit elements such as H, He, C, N, O, and Si) or using the Sobolev approximation with continuum (primarily used for background elements, such as the iron-group elements). It also includes an approximate treatment of line blanketing. The main difference between this code and the other two is that it allows for a consistent treatment of incoherent electron scattering.

Derived stellar and wind parameters obtained by each of these codes can vary greatly. This is due to differences between these codes in the physics implemented and the numerical treatments. Sander et al. (2024) compared results obtained from CMFGEN,

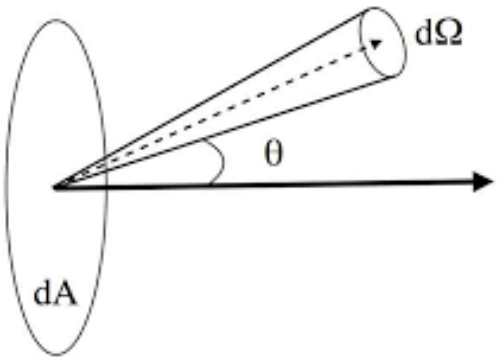


Figure 2.1: Illustration of the specific intensity.

PoWR and FASTWIND of three O-type stars in the Magellanic Clouds in an attempt to quantify the spread that is to be expected when using different model atmosphere codes (see Section 3.3.2 for discussion of the results from Sander et al. (2024)).

An important practical distinction between CMFGEN and PoWR on the one hand, and FASTWIND on the other, is that FASTWIND is suitable for large-scale grid modelling (e.g., Simón-Díaz et al., 2011c) or automated pipeline fitting (e.g., Bestenlehner et al., 2024; Brands et al., 2022), as models converge in minutes to a couple of hours thanks to its approximations and optimised numerical schemes. Due to the rigorous approaches used by CMFGEN and PoWR, models take from several hours to days to converge. The high time and computational demand make these codes more suitable for tailored analysis of small samples.

2.1.1 The radiative transfer equations

The macroscopic interplay between matter and radiation is described by the radiative transfer equations (RTE), which governs changes in the specific intensity I_ν. Fig. 2.1 illustrates the definition of the specific intensity. For a beam of light from a source point, the specific intensity is defined as the beams energy that passes through surface

area dA at an angle of θ to the surface normal $\mathbf{n}_0$ within a solid angle $d\Omega$, in time dt and frequency range $[\nu, \nu + d\nu]$. Mathematically, this is formulated as:

$$I_\nu = \frac{dE_\nu}{\cos\theta \, dA \, dt \, d\Omega \, d\nu}. \tag{2.1}$$

A unique property of the specific intensity is its invariance along a ray path in a vacuum, making it the preferred quantity for observing surface brightness independent of distance. From Equation 2.1, the energy dE_ν oriented in direction $\mathbf{n}$ (such that $\cos\theta = \mathbf{n} \cdot \mathbf{n}_0$) is formulated as:

$$dE_\nu = I_\nu(\mathbf{r}, \mathbf{n}, t) \cos\theta \, dA \, dt \, d\Omega \, d\nu. \tag{2.2}$$

As radiation passes through a medium, its energy changes due to absorption and emission processes, such that the difference between the initial specific energy I_ν^{init} and observed specific energy I_ν^{obs} it must be equal to the difference between the energy gained by emission processes dE^{em} and the energy lost due to absorption processes dE^{abs}. This can be expressed as:

$$(I_\nu^{\text{obs}} - I_\nu^{\text{init}}) \cos\theta \, dA \, dt \, d\Omega \, d\nu = dE^{\text{em}} - dE^{\text{abs}}, \tag{2.3}$$

where

$$dE^{\text{em}} = \eta_\nu \cos\theta \, dA \, dt \, d\Omega \, d\nu, \tag{2.4}$$

and

$$dE^{\text{abs}} = \chi_\nu \, I_\nu^{\text{init}} \cos\theta \, dA \, dt \, d\Omega \, d\nu, \tag{2.5}$$

and η_ν and χ_ν are the terms of emissivity and extinction, respectively. In the observer's frame, this is formulated as:

$$\frac{1}{c}\frac{\partial I_\nu}{\partial t} + \mathbf{n} \cdot \nabla I_\nu = \eta_\nu - \chi_\nu I_\nu^{\text{init}}, \tag{2.6}$$

where $\mathbf{n} \cdot \nabla I_\nu$ is the change in specific intensity at the frequency ν along the direction vector $\mathbf{n}$

For the atmospheres of hot massive stars, it is more convenient to transform Equations 2.3 and 2.6 from this general formulation into the comoving frame (CMF) in spherical coordinates in the form of

$$\mu \frac{\partial I_\nu}{\partial r} + \frac{(1-\mu^2)}{r} \frac{\partial I_\nu}{\partial \mu} - \left[\frac{\nu_0 v(r)}{rc}\right] \left[(1-\mu^2) + \mu^2 \left(\frac{d \ln v(r)}{d \ln r}\right)\right] \frac{\partial I_\nu}{\partial \nu} = \chi_\nu (S_\nu - I_\nu). \quad (2.7)$$

This represents the simplest form of the RTE in the CMF, where all time-dependent terms are eliminated (quasi-static), and the flow of material is assumed to be homologous, i.e. $v(r) \propto r$ (For detailed derivations and discussions on the solution of the RTE in the spherically symmetric configuration in the CMF see Mihalas et al., 1975, 1976a,b,c; Mihalas & Kunasz, 1978). From Equation 2.7, radiation propagates in the direction $\mu = \cos\theta$ (θ is the angle between the normal to the atmosphere and the direction of the beam of radiation) to the radius vector r, and $v(r)$ is the velocity of the expanding atmosphere at position r, and c is the speed of light. The term S_ν is equal to η_ν/χ_ν and is known as the source function, which describes the emission of photons with frequency ν over an optical path length of the medium. The spherical geometry is necessitated by the fact that the atmospheres of hot massive stars are extended and therefore cannot be considered a thin layer relative to the stellar radius, i.e., the atmospheric pressure scale-height is no longer negligible. In the CMF formulation, η and χ can be assumed as isotropic, meaning that the Doppler shift due to the movement of the medium does not need to be considered, but rather only the frequencies in the immediate neighbourhood of ν_0 are calculated when transferred to the observer's frame. This simplifies numerical calculations of scattering, redistribution, and emission processes.

Stellar atmosphere models that solve the RTE in plane-parallel geometry have been successfully used for determining the physical properties and chemical abundances of

early-type stars with weak winds (e.g., Hunter et al., 2007; Przybilla et al., 2008), which have included late-B supergiants (Przybilla et al., 2006). Plane-parallel models offer significant advantages over spherically symmetric models, particularly in computational efficiency, simplicity, and numerical stability, especially for stars with relatively thin atmospheres, such as dwarfs and subgiants. However, such models should be used with caution when analysing hot giants and supergiants, as the lack of curvature can significantly affect line formation and absorption-line strengths. This is especially important for the Balmer lines, which are used to determine the surface gravity $\log g$ (for more on the effect of sphericity in hot stars, see e.g., Kubat, 1996; Kubát, 1999).

2.1.2 Why nLTE?

Thermodynamic equilibrium (TE) is the most idealised state, where a system is assumed to be an isotropic medium that is isothermal, homogeneous, and enclosed, or a black body. This means that every process in the system is in detailed balance, i.e. every microscopic process (like an atom emitting a photon) is exactly balanced by its reverse process (an atom absorbing a photon) at the same rate. Macroscopically, this means that there is no net flow of energy or matter, and the radiation field is Planckian.

In this case, the populations of energy levels can be described by the Boltzmann distribution

$$\frac{n_{i,j}}{n_{1,j}} = \frac{g_{i,j}}{g_{1,j}} e^{-\Delta E_{i,j}^{\text{excitation}}/k_B T}. \tag{2.8}$$

The ionisation balance in the medium can be determined by Saha's equation

$$\frac{n_{1,j+1} n_e}{n_{1,j}} = 2 \left(\frac{2\pi m_e k_B T}{h^2} \right)^{3/2} \frac{g_{1,j+1}}{g_{1,j}} e^{-\Delta E_{i,j}^{\text{ionisation}}/k_B T}. \tag{2.9}$$

In these equations, $n_{i,j}$ is the number density of the equilibrium population. n_e is the electron number density. $g_{i,j}$ in Boltzmann's equation are the statistical weights of the

i-th level of the j-th ionisation state. In Saha's equation, $g_{i,j}$ represents the partition functions of the j-th and the $j+1$-th ions. $\Delta E_{i,j}^{\text{excitation}}$ is the excitation energy of the i-th level measured from the ground state. $\Delta E_{i,j}^{\text{ionisation}}$ is the ionisation energy of the ground state of the j-th ionisation state. T is the temperature. k_B is the Boltzmann constant, m_e is the electron mass, and h is the Planck constant.

The velocity of the particles is described by the Maxwell distribution. In TE, all the physical properties of the gas (i.e., pressure, emissivity, and opacity) are completely described by two parameters: the total particle number density and temperature, and, subsequently, the pressure scale height or the surface gravity. Unfortunately, the simple case of TE is not applicable in either stellar interiors or stellar atmospheres.

In local thermodynamic equilibrium (LTE), the situation is less restrictive. In this case, the energy is assumed to be flowing, albeit very slowly, allowing the TE assumption to hold in small (local) regions, even though the radiation field is no longer constant. This holds when collisional processes dominate over radiative processes, such as in the stellar interior. In this case, photons are scattered isotropically by ions and free electrons with no change in frequency, and the source function is equal to the mean intensity ($S_\nu = J_\nu$).

In reality, the atmospheres of massive stars are open media with extreme radiation fields, experiencing energy and matter loss and deviating from LTE. Therefore, in nLTE, we must describe every state that departs from LTE while preserving the Maxwellian velocity distribution of particles. Due to the extreme radiation field and relatively low densities in the wind, the level populations in nLTE are described by the departure coefficient:

$$b_i = n_{i,j}/n_{i,j}^*, \tag{2.10}$$

where $n_{i,j}^*$ is the LTE population. The case $b_i = 1$ indicates LTE, and the farther from unity, the stronger the departure from LTE. In massive stars, using departure coefficients is essential for accurate abundance determinations, as both line opacity and

source functions depend on level populations.

From the Saha-Boltzmann equations, we can deduce that stellar parameters, such as the temperature, luminosity and surface gravity, determine the structure and ionisation of the stellar atmosphere. By defining the stellar radius (R_*) and mass (M_*), CMFGEN establishes a density scale through the equation of state ($P_{gas} = \rho k_B T/\mu m_H$, where P_{gas}, ρ, and T are the pressure the mass density, and the absolute temperature of the gas, μ is the mean molecular weight, and m_H is the mass of a hydrogen atom). These parameters dictate the local temperature and electron density (n_e), which the Saha-Boltzmann equations use to calculate the initial distribution of atoms across various ionisation stages and excitation levels.

The atmospheric structure is calculated using hydrodynamic equations, ensuring consistency between the radiation field and the gas dynamics. In CMFGEN, the mass continuity equation ($\dot{M} = 4\pi r^2 \rho v$) is strictly preserved. The density stratification $\rho(r)$ is then calculated by superimposing a velocity law, usually in the form of a β-power law. The momentum equation is also preserved and solved in the hydrostatic layers near the photosphere to determine the density scale height.

Unlike the continuity and momentum equations, the full hydrodynamic energy equation is generally not preserved or solved self-consistently in CMFGEN. Instead, the temperature stratification is calculated iteratively under the assumption of radiative equilibrium. This means that the temperature structure is determined by balancing the energy absorbed from the radiation field with the energy emitted ($\int \kappa_\nu J_\nu d\nu = \int \eta_\nu d\nu$). In other words, the energy (luminosity) at the inner boundary (photosphere) is assumed to be approximately equal to that at the outer boundary (what is seen on the surface from the observer's perspective).

2.1.3 The inner workings of CMFGEN

CMFGEN is a nLTE, radiative transfer code. It was initially developed to study the thick winds of WR stars, but was later extended to study the atmospheres of OB stars and LBVs (Hillier, 1990; Hillier & Miller, 1999). The model also has a time-dependent mode used to study SNe (Dessart & Hillier, 2010).

CMFGEN simultaneously solves the 1-D radiative transfer equation and the statistical equilibrium equation, which can be expressed as:

$$\sum n_i(R_{ij} + C_{ij}) = \sum n_j(R_{ji} + C_{ji}) \tag{2.11}$$

where i and j are the atomic levels of the specific transition, n_j and n_i are electron populations of the levels, R_{ij} and C_ij are the radiative and collisional rates our of the i-th level into the j-th, respectively. This means that we assume that for each level of an atom, the amount of (rate of) electrons departing from and arriving at that level is equal.

To accurately model the emerging flux from a massive star, we require large atomic models containing thousands of levels. For simple atoms like hydrogen and helium, discretely solving the rate equation for all transitions is acceptable. However, for ions of heavier elements, the large number of line transitions to be considered makes this exhaustive from a numerical standpoint. One reason for choosing CMFGEN is its sophisticated method for accounting for blanketing, which is especially important in the UV, where most of the flux is and therefore where most of the driving takes place.

CMFGEN accounts for the influence of extreme-UV line blanketing on the wind populations and ionisation structure that is the result of thousands of overlapping lines. It does so with a detailed treatment using super-levels, pioneered by Anderson (1985, 1989), in which several levels with similar energies and properties are treated as a single super-level. The idea of super-levels is of tremendous importance for the iron-group

elements. An individual ionisation stage can have hundreds of levels and line transitions that must be considered in the full model atom, but applying the super-levels method significantly reduces the number of statistical equilibrium equations to be solved in the nLTE treatment, thereby drastically reducing the computation time in the CMF.

The nLTE RT equation and the statistical equilibrium equation are coupled and highly nonlinear. In other words, the radiation field depends on the level populations, which in turn depend on the radiation field, which introduces a "chicken and egg" effect. Subsequently, an iterative method is required to solve these equations. The iterative method used in CMFGEN relies on linearising all equations, from which corrections to the temperature and atomic-level populations are obtained (Mihalas et al., 1975).

Numerically, this scheme starts by solving the RT equation for the radiation field, assuming a set of known (input) parameters (such as the temperature, gravity, mass-loss rates, electron and ion number populations from a previous model, etc.), and then the SE equations are evaluated with the new radiation field. In most cases, the SE equations will not be satisfied by the first iteration. To estimate the error in the known variables so that the boundary conditions are satisfied, a generalised Newton-Raphson technique is used. These corrections are then used to redistribute the atomic populations, such that the SE equations are satisfied. The new level populations are then used to re-solve the RT equation and update the radiation field. This iteration is repeated until convergence in the radiation field and populations is achieved.

The advantage of the CMF formulation is that the opacity and emissivity can be treated isotropically, and physical changes between neighbouring depth points, such as the winds density and velocity field, are minimal. Additionally, the (quasi-)hydrostatic (subsonic) structure in the layers near the photosphere can be solved consistently. The desired temperature in the (quasi-)hydrostatic (subsonic) layers of the atmosphere is determined by the enforcement of the radiative equilibrium condition in the co-moving

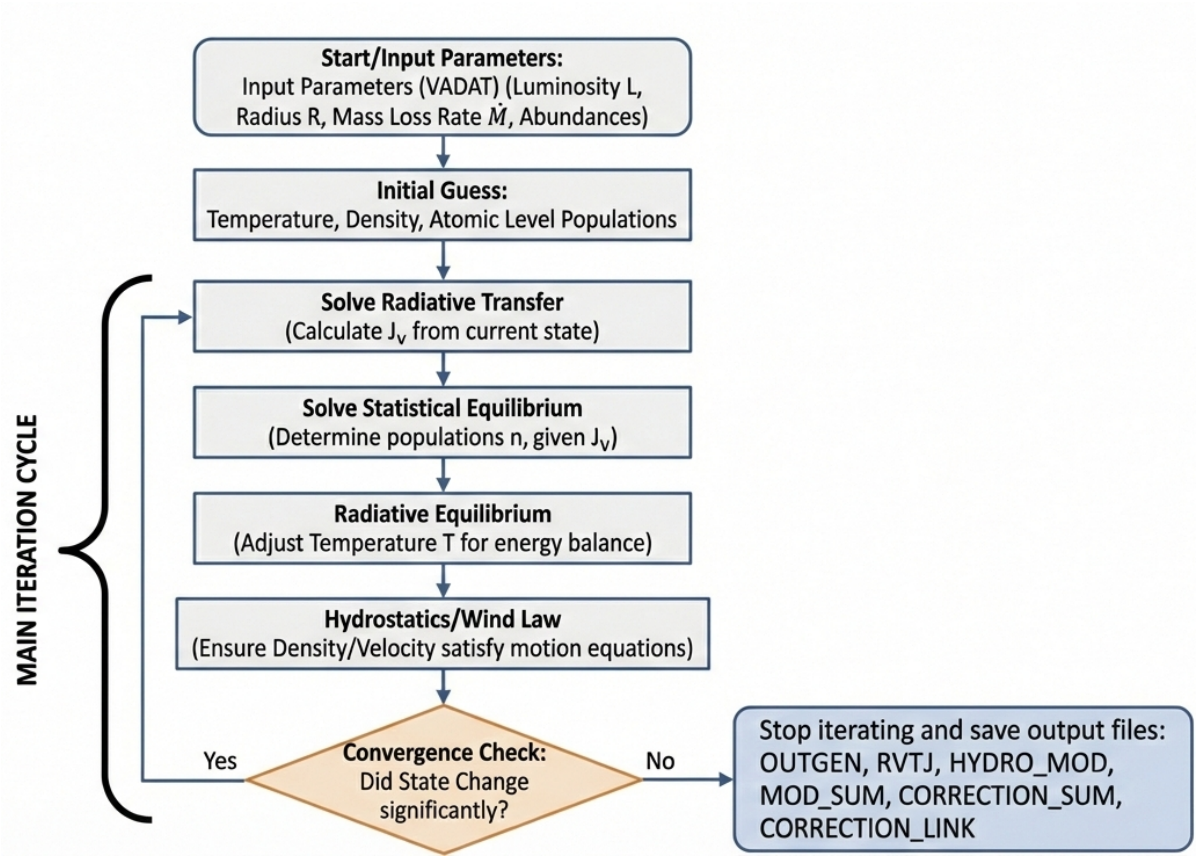


Figure 2.2: Flowchart of the CMFGEN program.

frame. This condition can be simply formulated as

$$\int \chi_\nu \left[J\left(\nu\right) - S\left(\nu\right) \right] = 0. \tag{2.12}$$

This condition is solved using a flux-correction technique (Hillier, 1990), in which the flux is kept constant with depth via a flux-conservation iteration until the desired temperature is reached. Fig 2.2 illustrates a simplified flowchart of the main functions of CMFGEN.

CMFGEN does not calculate the velocity field stratification with radiative acceleration. Instead, as we explained before, the density (velocity) structure of the extended atmosphere is established through the continuity equation by a parametrised velocity law $v(r)$ on top of a solution of the hydrostatic equation from a connection velocity to the inner photosphere (e.g., Martins et al., 2012). Additionally, wind inhomogeneities are considered under the "optically thin clumping" approximation, or micro-clumping, assuming that these optically thin clumps are smaller than the mean free path of the photons (Hillier, 1996), and that the medium between the clumps is completely void of matter (Hillier, 1997; Hillier & Miller, 1999).

Once a model is converged, one can obtain the formal solution of the RT equation. CMF_FLUX is a 1-D code that employs the output from CMFGEN to compute the emerging spectrum in the observers frame. In short, CMF_FLUX reads in the level populations and ionisation structure from CMFGEN and converts the opacities and emissivities from the CMF to the observer's frame, by allowing only for the Doppler effect. It also adds additional depth points along each radial ray when calculating the formal integral. This method of computing the synthetic spectrum avoids numerical inaccuracies arising from sparse sampling of the space-frequency parameter space, leading to broader lines.

2.2 The CMFGEN grids

2.2.1 Velocity and clumping laws

In our grids, we used the simple modified β velocity law that was introduced by Castor & Lamers (1979)

$$v(r) = v_0 + (v_\infty - v_0)\left(1 - \frac{R_*}{r}\right)^\beta, \tag{2.13}$$

where v_∞ is the terminal wind velocity, v_0 is the velocity at which the photosphere connects to the base of the wind, which is estimated as two thirds the speed of sound $\approx 10\ \mathrm{km\,s^{-1}}$, and $R_{\tau=100}$ is the radius of the star R_*, which is defined at Rosseland optical depth $\tau = 100$. We adopt a fixed value of $\beta = 1$, which is later treated as a free parameter in the fine-tuning stage. This is important for reproducing the overall morphology of $H\alpha$.

In CMFGEN, clumping is treated in the optically thin clumping approximation, also known as micro-clumping, assuming a void inter-clump medium and a volume-filling factor f_{vol}. To solve the radiative transfer equation under the micro-clumping assumption, the clump size is assumed to be smaller than the photon mean free path (Hillier, 1996). The treatment of wind inhomogeneities in CMFGEN has been extensively discussed in the literature (Hillier, 1997; Hillier & Miller, 1998, 1999).

In the grids, we adopt a velocity-dependent clumping law that was introduced for O stars in Hillier et al. (2003)

$$f(r) = f_{\mathrm{vol},\infty} + (1 - f_{\mathrm{vol},\infty})\exp\left(-\frac{v(r)}{v_{\mathrm{cl}}}\right), \tag{2.14}$$

where $f_{\mathrm{vol},\infty}$ is the terminal volume-filling factor, v_{cl} is the onset clumping velocity, and $v(r)$ is the velocity of the wind at a given radius r. In its essence, $f_{\mathrm{vol},\infty}$ determines the degree of clumping in the wind, where smaller values of $f_{\mathrm{vol},\infty}$ indicate a more highly clumped wind at $r \to \infty$. v_{cl} determines the location (depth) at which clumping starts.

Table 2.1: Parameters of the CMGEN grids.

Iterated parameters		
parameter	Values	Step
$\log(T_{\rm eff}/{\rm K})$	$4.150 \cdots 4.600$	0.025
$\log(g/{\rm cm\,s^{-2}})$	$1.7 \cdots 3.9$	0.2
$\log(\dot{M}/M_\odot\,{\rm yr^{-1}})$	$-7.0 \cdots -5.5$	0.3
$\log R_t$	$1.6 \cdots 3.2$	N/A
$\log Q$	$-14.1 \cdots -11.9$	N/A
Fixed parameters		
parameter	Value	
$\log(L/L_\odot)$	5.8	
β	1.0	
$f_{\rm vol,\infty}$	0.1	
$v_{\rm mic,\infty}$ [km s^{-1}]	100	
$v_{\rm mic,\,phot}$ [km s^{-1}]	10	
Dependent parameters		
parameter	Value	
$v_\infty(T_{\rm eff}, Z)$	Recipe from Hawcroft et al. (2024a)	

This means that Equation 2.14, describes winds that become smoother as $v(r)$ becomes lower approaching the photosphere, and become rapidly more clumped at larger radii. In our grid, we fix $f_{\rm vol,\infty}$ to a value of 0.1. Later in the fine-tuning procedure, $f_{\rm vol,\infty}$ is treated as a free parameter. This is essential for obtaining satisfactory fits to the electron-scattering wings of Hα and to unsaturated P Cygni resonance lines.

2.2.2 Fundamental grid parameters

In Table 2.1, we present the properties of the fundamental parameters in the grids. To build the grids, the luminosity in the models was fixed to $\log(L/L_\odot) = 5.8$ and

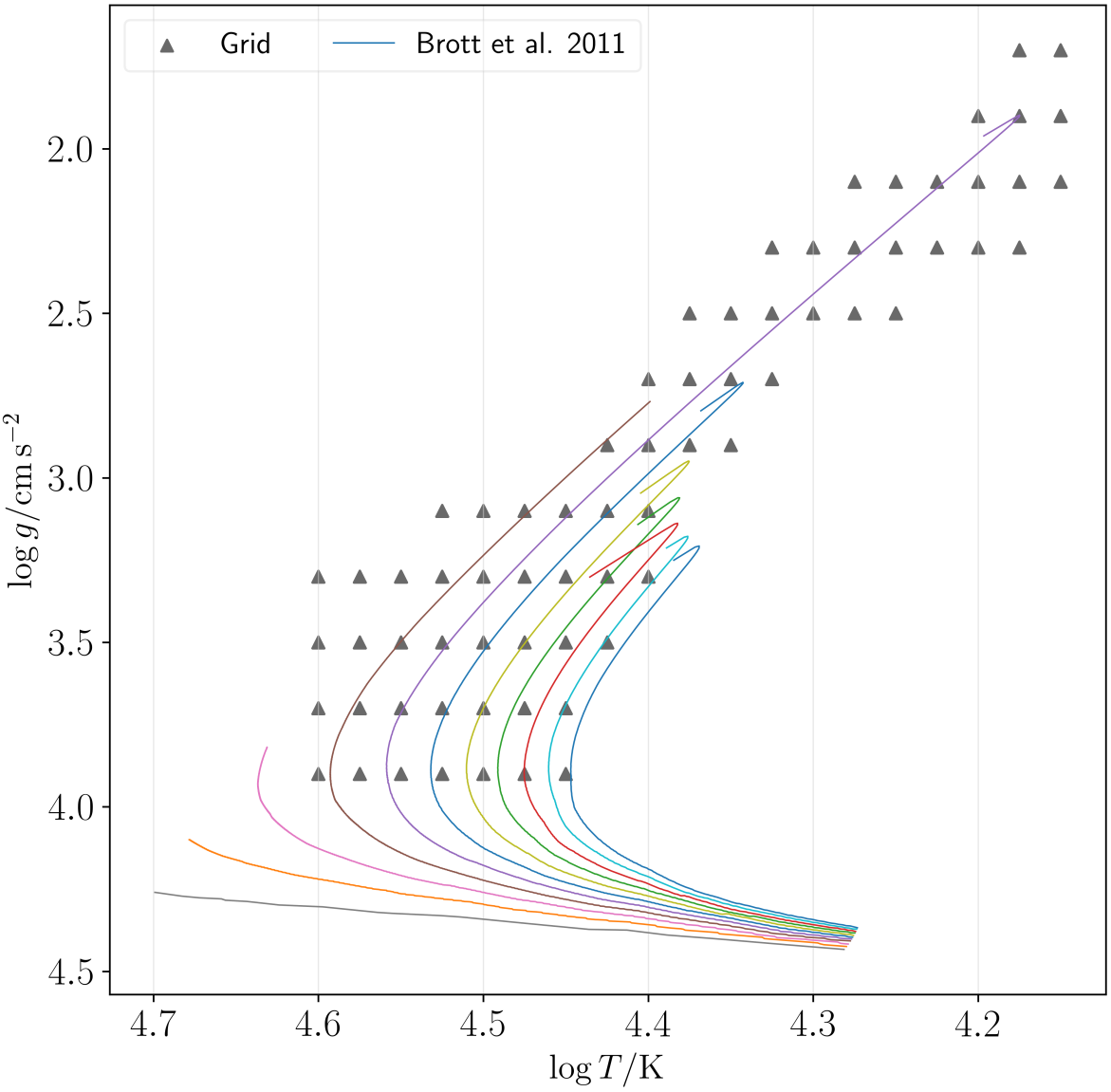


Figure 2.3: A slice of the model grid in the $T_{\rm eff}$-$\log g$ parameter space. Grey triangles show the grid points. The overlaid lines are isochrones taken from Brott et al. (2011).

$\log(T_{\rm eff}/{\rm K})$ was varied in the range $\approx [4.15, 4.60]$ and $\log(g/{\rm cm\,s^{-2}})$ in the range $\approx [1.7, 3.9]$ depending on the temperature, in steps of 0.025 dex for $\log(T_{\rm eff}/{\rm K})$ and 0.2 dex for $\log(g/{\rm cm\,s^{-2}})$. This procedure yielded a 2-D grid in the temperature-gravity parameter space, which is presented in Fig. 2.3.

We employed the empirical temperature and metallicity-dependent terminal wind velocity recipe from Hawcroft et al. (2024a)

$$v_\infty\ ({\rm km\,s^{-1}}) = [0.092\,(\pm0.003)\,T_{\rm eff}\ ({\rm K}) - 1040\,(\pm100)]\ \ (Z/Z_\odot)^{(0.22\pm0.03)}, \qquad (2.15)$$

where $Z \approx 0.43 Z_\odot$ for the LMC, and $Z \approx 0.2 Z_\odot$ for the SMC (Vink et al., 2023). In Hawcroft et al. (2024a), Sobolev with Exact Integration (SEI) modelling was employed to measure the terminal wind velocities for objects no later than B1.5 spectral types, using the C IV $\lambda\lambda 1548-1551$ resonance doublet, with radial velocities adopted from the UV.

In Table 2.2, we present the values of metal abundances $\log {\rm X/H} + 12$ (by number) adopted in the model grid. Henceforth, we substitute $\log {\rm X/H} + 12$ with the notation $\epsilon_{\rm X}$. In the SMC and MW grids, we adopt baseline chemical abundances for all species from Vink et al. (2023) and Asplund et al. (2005), respectively. The abundances presented in Vink et al. (2023) are obtained by averaging abundances from archival studies of supernova remnants (Dopita et al., 2019), H II regions (Kurt & Dufour, 1998; Garnett, 1999; Peimbert, 2003; Tsamis et al., 2003; Lebouteiller et al., 2008; Toribio San Cipriano et al., 2017), B stars (Korn et al., 2005; Trundle et al., 2007; Hunter et al., 2007, 2009; Dufton et al., 2018), A stars (Venn, 1999), and RSGs (Hill et al., 1995, 1997; Hill, 1997, 1999; Andrievsky et al., 2001).

For the LMC grid, rather than adopting baseline CNO abundance values for metals such as the one compiled in Vink et al. (2023), we chose to adopt CNO processed abundances correlating to low luminosity B stars in the LMC from Hunter et al. (2008b),

Table 2.2: Metal abundances adopted in the model grids. $\epsilon_X = \log X/H+12$ by number. In the reference columns, A05 is Asplund et al. (2005), H08 is Hunter et al. (2008b), and V23 is Vink et al. (2023).

Element	ϵ_X^{LMC}	Reference	ϵ_X^{SMC}	Reference	ϵ_X^{MW}	Reference
C	7.51	H08	7.42	V23	8.39	A05
N	7.50	H08	6.66	V23	7.78	A05
O	8.33	H08	8.05	V23	8.66	A05
Ne	7.70	V23	7.23	V23	7.84	A05
Mg	7.13	V23	6.72	V23	7.53	A05
Al	6.20	V23	5.59	V23	6.37	A05
Si	7.06	V23	6.72	V23	7.51	A05
P	5.11	V23	5.11	V23	5.36	A05
S	6.88	V23	6.36	V23	7.14	A05
Ca	6.10	V23	5.61	V23	6.31	A05
Fe	7.23	V23	6.80	V23	7.45	A05
Ni	5.90	V23	5.37	V23	6.23	A05

that show nitrogen enhancement of $\Delta\epsilon_{\rm N} \approx +0.47$ dex, compared to the LMC baseline in Vink et al. (2023), and at the expense of carbon and oxygen deficiencies of $\Delta\epsilon_{\rm C} \approx -0.5$ dex and $\Delta\epsilon_{\rm O} \approx -0.07$ dex. Since Hunter et al. (2008b) excludes B supergiants, we checked the validity of these values for luminous B supergiants (which might be expected to show the greatest N enhancements) by resorting to the work of McEvoy et al. (2015), in which TLUSTY non-LTE model atmosphere calculations have been used to determine atmospheric parameters and nitrogen abundances for 34 single and 18 binary supergiants. Their analysis shows a nitrogen enrichment value of ≈ 0.5 dex relative to Vink et al. (2023), which is very close to our grid's nitrogen abundance. For other key elements in our grids, such as silicon, magnesium, and iron, we adopted baseline LMC abundances from Vink et al. (2023). Abundances of metals heavier than oxygen are not modified during the fitting procedure.

Lastly, we covered the temperature-gravity-wind density parameter space. We did that by iterating over the mass-loss rates $\log(\dot{M}/M_\odot\,{\rm yr}^{-1})$ in the range $\approx [-5.5, -7.0]$ in steps of 0.3 dex for each of the points from grid$_{base}$. The final grid is 3-D in the temperature-gravity-wind-density space. Since the strength of emission features scales not only with the mass-loss rate but also with the volume-filling factor ($f_{\rm vol}$), terminal velocity, and stellar radius, it is convenient to compress these parameters into a single parameter when compartmentalising the model grids. To spectroscopically quantify mass-loss rates of hot massive stars using scaling relations, we chose to adopt the transformed radius (Schmutz et al., 1989)

$$R_t = R_* \left[\frac{v_\infty}{2500\ {\rm km\,s^{-1}}} \Big/ \frac{\dot{M}}{10^{-4}\ M_\odot {\rm yr}^{-1}\sqrt{f_{\rm vol}}} \right]^{2/3}, \tag{2.16}$$

which was originally used for optically thick winds of Wolf-Rayet stars (WR), where the line equivalent width is preserved. In Table 2.1, we present the range of $\log R_t$ covered by each grid, with smaller values relating to denser winds. This $\log R_t$ range corresponds

to an optical depth-invariant wind-strength parameter $\log Q = \log \dot{M}/(R_* v_\infty)^{3/2}$ (Puls et al., 1996) range that is presented in Table 2.1, where larger values of $\log Q$ correspond to denser winds. We employ R_t to scale $\dot{M}$ to the derived bolometric luminosity of the star.

2.2.3 Atomic data and X-rays

In Table 2.3, we present the detailed underlying atomic structure used in our CMFGEN models. We divide our model grid into a 'cool' ($< \ 25 \ kK$) and a 'hot' ($> \ 25 \ kK$) sections, which correspond to different ions. "all" in the models column means that this ion was included in the hot and cool sections of our grid. We included 14 species and 50 different ions in our models. We excluded higher ionisation stages for the cooler models and included the lower ionisation stages. This is particularly important for iron lines, which dominate the UV in the B-star regime. This also helps with the convergence of cooler models.

X-rays can be included in CMFGEN using X-ray emissivities from collisional plasma models (Smith et al., 2001), where the source of this emission is assumed to be shocks forming in the winds (Pauldrach et al., 1994). The detailed approach used in CMFGEN is described in Hillier & Miller (1998). The general spectral appearance is not affected by X-rays, although the highest ionisation UV lines can be enhanced at the expense of lower ionisation lines (Baum et al., 1992) at relatively low stellar temperatures due to Auger processes. We elect to exclude X-rays from our analysis because the ad hoc addition of X-rays in CMFGEN does not provide a phenomenological description of the physical shock parameters and reduces the number of unconstrained parameters in the fitting procedure.

The main drawback of excluding X-rays in our models is that, in some cases, satisfactory fits to high-ionisation UV P Cygni lines are difficult to obtain. This could

Table 2.3: Ions and number of important levels (IL), super-levels (SL), full levels (FL), and transitions (T) considered per ion, which constitutes the atomic model (M) used by the code to synthesise the spectrum.

Ion	IL	SL	FL	T	M
H I	20	20	30	435	all
He I	45	45	69	905	all
He II	22	22	30	435	all
C I	52	52	100	10204	$< 25\ kK$
C II	40	40	92	8017	all
C III	51	51	84	5528	all
C IV	64	64	64	1446	all
C V	0	35	67	2196	$> 25\ kK$
N I	44	44	104	855	$< 25\ kK$
N II	45	45	85	7879	all
N III	104	104	164	6710	all
N IV	107	107	202	6943	all
N V	45	45	67	1664	$> 25\ kK$
O I	53	53	133	2138	$< 25\ kK$
O II	54	54	123	8937	all
O III	788	88	170	6561	all
O IV	78	78	154	7599	all
O V	32	32	56	2324	all
O VI	25	25	31	1475	$> 25\ kK$
Mg I	36	36	56	3511	$< 25\ kK$
Mg II	27	27	60	1993	all
Mg III	0	39	175	3052	all
Mg IV	0	36	169	5706	$> 25\ kK$
Ca I	0	66	88	3976	$< 25\ kK$
Ca II	0	39	46	1736	$< 25\ kK$
Ca III	0	29	88	3497	$< 25\ kK$
Ca IV	0	30	123	8532	$< 25\ kK$

Table 2.3: Continued.

Ion	IL	SL	FL	T	M
Al I	54	54	82	4985	$< 25\ kK$
Al II	0	40	67	3490	$< 25\ kK$
Al III	0	37	60	2011	all
Al IV	0	56	163	3052	$> 25\ kK$
Si II	22	22	43	2294	all
Si III	33	33	33	1639	all
Si IV	22	22	33	1090	all
P III	0	59	128	5576	$> 25\ kK$
P IV	0	30	90	2537	$> 25\ kK$
P V	0	16	62	561	$> 25\ kK$
S II	0	21	65	8208	all
S III	0	24	44	6193	all
S IV	0	51	142	3598	all
S V	0	31	98	3462	all
Fe I	100	100	297	141821	$< 25\ kK$
Fe II	0	318	2430	21544	$< 25\ kK$
Fe III	104	104	1433	136060	all
Fe IV	74	74	540	72223	all
Fe V	50	50	220	71983	$> 25\ kK$
Fe VI	44	44	433	185392	$> 25\ kK$
Fe VII	29	29	153	86504	$> 25\ kK$
Ni II	0	42	433	51707	$< 25\ kK$
Ni III	0	46	849	66486	all
Ni IV	0	36	200	72898	all
Ni V	0	69	305	75541	$> 25\ kK$
Ni VI	0	65	314	79169	$> 25\ kK$

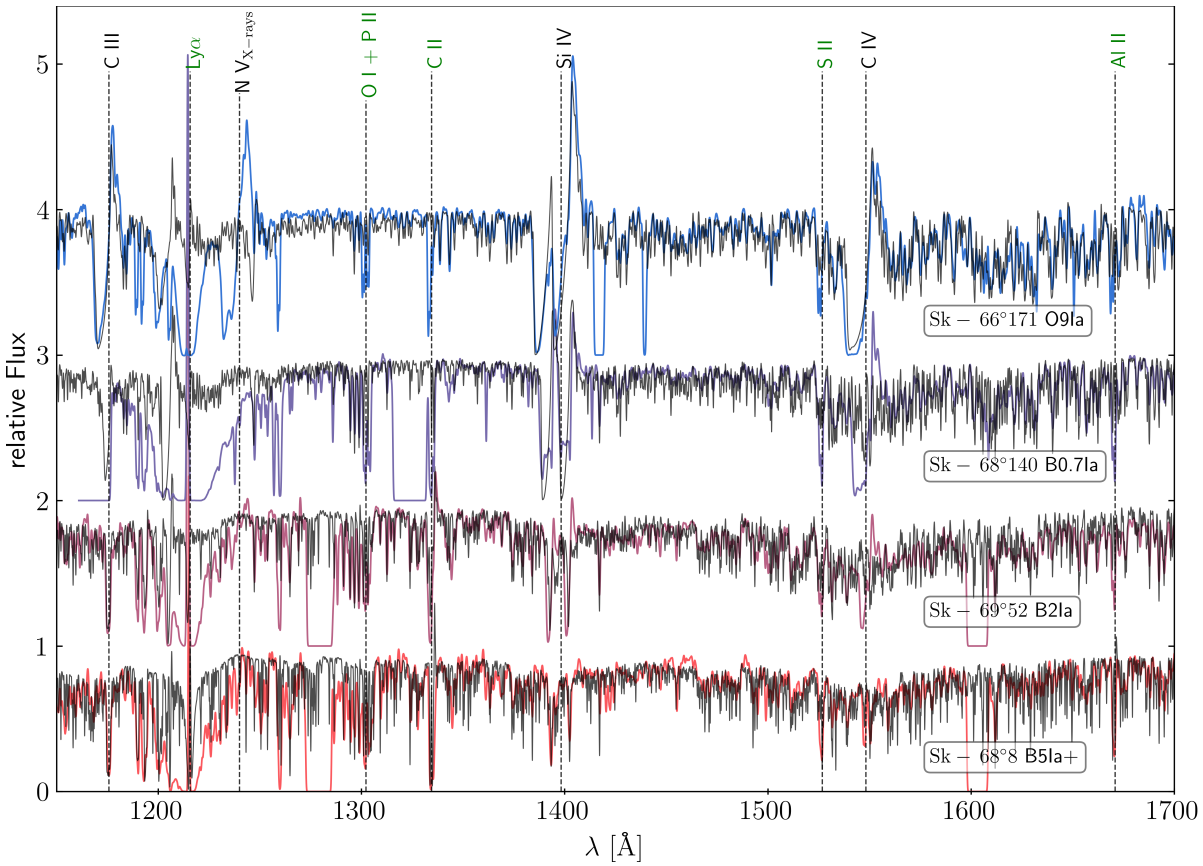


Figure 2.4: Examples of the normalisation and fits to UV from the LMC sample, with the line identification for the UV lines. For illustration purposes, an offset of one was added. The coloured lines show the observations. The black lines show the model fits for each of the respective stars. Stellar features are indicated in black line labels, whereas green line labels indicate interstellar features. The gap at ≈ 1300 in the spectra of Sk 69° 52, Sk 68° 8 is due to appending observations from COS G130M and COS G160M. The gap at 1600 Å is due to appending observations from COS G160M and COS G185M.

potentially lead to overestimating the mass-loss rates. Bernini-Peron et al. (2023), who included X-rays in their CMFGEN models, found that their mass-loss rates for Galactic B supergiants are lower by a factor of two compared to the mass-loss rates obtained by Crowther et al. (2006) and Searle et al. (2008), who exclude X-rays. In Fig. 2.4, the discrepancy between the predicted and observed P Cygni N V $\lambda\lambda 1238-1242$ line in Sk -66° 171 is due to the lack of X-rays in the model. This is also the case for the P Cygni C IV $\lambda\lambda 1548-1551$ profile in Sk -68° 140 and Sk -69° 52. Additionally, the inclusion of X-ray emission in low wind-density models is crucial for deriving accurate mass-loss rates from UV lines. Therefore, cooler B supergiants in our samples are affected by the exclusion of X-rays. However, this effect is reduced due to combining optical and UV wind diagnostics.

2.3 Analysis procedure

Underlying systematic errors arise from our grid and fitting procedure. The most notable are the inclusion of a limited number of species and ions, fixing certain parameters like the micro- and macro-turbulent velocities, and fixing the abundances of elements heavier than oxygen. An important part of our analysis is wind clumping, which can vary greatly depending on the treatment used in the model (e.g., Brands et al., 2022). Finally, the finite spectral resolution of the observation adds another layer of uncertainty to the overall analysis. We estimate the model uncertainties (parameters with superscript notation 'm'), the derived physical parameters and wind properties. By 'model uncertainty' we simply mean the smallest variation in a given input parameter that would produce a noticeable change in the quality of the fit.

2.3.1 Summary of the fitting procedure

Since CMFGEN is time and resource-intensive, we are limited by a small number of models relative to the number of parameters that we have to extract from the stellar spectra. Therefore, as a first-order approximation (initial pinpoint), we use the results of the LMC and SMC analysis done using the pipeline that was introduced in Bestenlehner et al. (2024), which is a grid-based χ^2- minimisation algorithm that uses the entire optical spectrum rather than selected diagnostic lines. This allows us to analyse a wider range of temperatures from B to early-O stars.

The grid of synthetic spectra used by Bestenlehner et al. (2025) was computed with the non-LTE stellar atmosphere and radiative transfer code FASTWIND (Puls et al., 2005), which is efficient and quick but lacks a detailed treatment of the iron forest in the UV range. This pipeline provides a first approximation of $T_{\rm eff}$, $\log g$, $v_{\rm rot} \sin i$ using only the optical XShootU data, which we then refine using the UV range provided by our CMFGEN grid, and then produce a fine-tuned model for the entire spectrum based on the best fitting grid model.

In the case of the MW sample, the first approximation was obtained by performing a simple minimisation routine of the equivalent width ratio of $T_{\rm eff}$ diagnostics. To obtain $\log g$, we minimised the quantity FW3414 Hγ, which is defined as the difference between the width of the Hγ line measured at three-quarters and one-quarter of the line depth.

To summarise, our entire procedure consists of the following steps:

- 1$^{\rm st}$ step: Approximation of $T_{\rm eff}$ and $\log g$ from the optical spectrum using the model de-idealisation pipeline introduced in Bestenlehner et al. (2024) for the LMC and SMC samples, and using the simple minimisation routine for the MW sample. The first approximation is then used to pinpoint the closest fitting model from our grids in $T_{\rm eff}$-$\log g$-$\dot{M}$ parameter space.

- 2$^{\rm nd}$ step: Fine-tune the values of $T_{\rm eff}$, $\log g$, v_∞ and the helium abundance of the

model from the previous step.

- 3$^{\rm rd}$ step: Fine-tune wind parameters $\dot{M}$, β-law, $f_{\rm vol}$ and clumping on-set velocity $v_{\rm cl}$.
- 4$^{\rm th}$ step: Refine CNO- surface abundances.

The second, third and fourth steps are done iteratively, and take on average 6 to 8 tailored models in total to obtain a satisfactory fit. We use the expression "fine-tuning" to describe the iterative process of varying the stellar and wind parameters in the model to achieve a satisfactory fit to the line diagnostics. The quality of the fit is assessed by eye.

2.3.2 Effective temperature and helium abundance

After we derived a rough estimate of the stellar and wind parameters from our grid, we started fine-tuning the model parameters to reproduce the observed spectrum. In order to do that, we first vary the temperature, which has a large impact on the morphology of the spectrum for different spectral classes. Consequently, obtaining an accurate temperature determines the overall quality of the fit and of the other estimated stellar and wind parameters. In our fitting procedure, $T_{\rm eff}$ is derived using the ionisation balance of helium (He) and silicon (Si). In practice, lines from successive ions of the same elements must be observed.

The most reliable late O star diagnostics for the determination of $T_{\rm eff}$ are He II and He I, and historically He II λ4542 and He I λ4471 have been used (Martins, 2011), which is what we used for the O stars in our sample as primary diagnostics. Additionally we use He II λ5411 and He I λ4922 as a sanity check. For B stars, the main diagnostic is the silicon ionisation balance (McErlean et al., 1999; Trundle et al., 2004b; Trundle & Lennon, 2005b). For the earliest B stars (B0 - B2) spanning a temperature range

$T_{\rm eff} \approx 28{-}21$ kK we use Si IV $\lambda\lambda 4089 - 4116$ [1] and Si III $\lambda\lambda\lambda 4553 - 4568 - 4575$ as our main diagnostics. For mid-B stars (B3-B5) in the temperature range $T_{\rm eff} \approx 20{-}14$ kK Si III $\lambda\lambda\lambda 4553 - 4568 - 4575$ and Si II $\lambda\lambda 4128 - 4131$ are used. For late-B stars (B6-B8), we resort to fitting He I $\lambda 4471$ and Mg II $\lambda 4481$, which is not as reliable as fitting consecutive ions of the same species.

An alternative indicator of $T_{\rm eff}$ in late-B stars is the ratio of O II to O I line. By way of example, in Fig. 2.5 we show the triplet O I $\lambda\lambda\lambda 7772 - 7774 - 7775$ (upper panel) and O II $\lambda 4254$ (lower panel). The preferred model (red solid line) for the B8 supergiant Sk -67° 195, the temperature of which was obtained from fitting He I $\lambda 4471$ and Mg II $\lambda 4481$, reproduces the O I $\lambda\lambda\lambda 7772{-}7774{-}7775$ and O II $\lambda 4254$ lines relatively well. For comparison, we display another model that differs from the preferred model only in its temperature with $\Delta T_{\rm eff} = 1500$ K (blue solid line). We select this model as it is the nearest model on the grid to our preferred model in the temperature parameter-space that presents O II lines. This fit implies that decreasing the oxygen abundance in the comparison model could produce a better match to both lines. This could be used either as a primary diagnostic for $T_{\rm eff}$ or as a sanity check in late-B supergiants.

By way of a sanity check, we compared the predicted Balmer jump strengths to observations (Kudritzki et al., 2008; Urbaneja et al., 2017). We find that, for the most part, the strength of the predicted Balmer jumps – the $T_{\rm eff}$ of which was obtained from line diagnostics – are in good agreement with observations. Nevertheless, a few hundred K higher temperatures produce a better match for a subset of mid- to late-B supergiants, albeit within the quoted uncertainties. This check was performed only for the LMC and SMC samples, as the lack of flux-calibrated data for the MW sample makes this method impractical. Fig. 2.6 shows an example of fitting the Balmer jump strength, where the

[1] The Si IV absorption line at $\lambda = 4089$ Å is actually a blend of Si IV and O II (de Burgos et al., 2024b). Considering models with extended O II atomic levels, we find that the O II component contributes $\approx 9\%$, 10%, 62% to the equivalent width of the combined line at $T_{\rm eff} = 30$, 25, 20 kK, respectively, with both lines being very weak in the low $T_{\rm eff}$ case

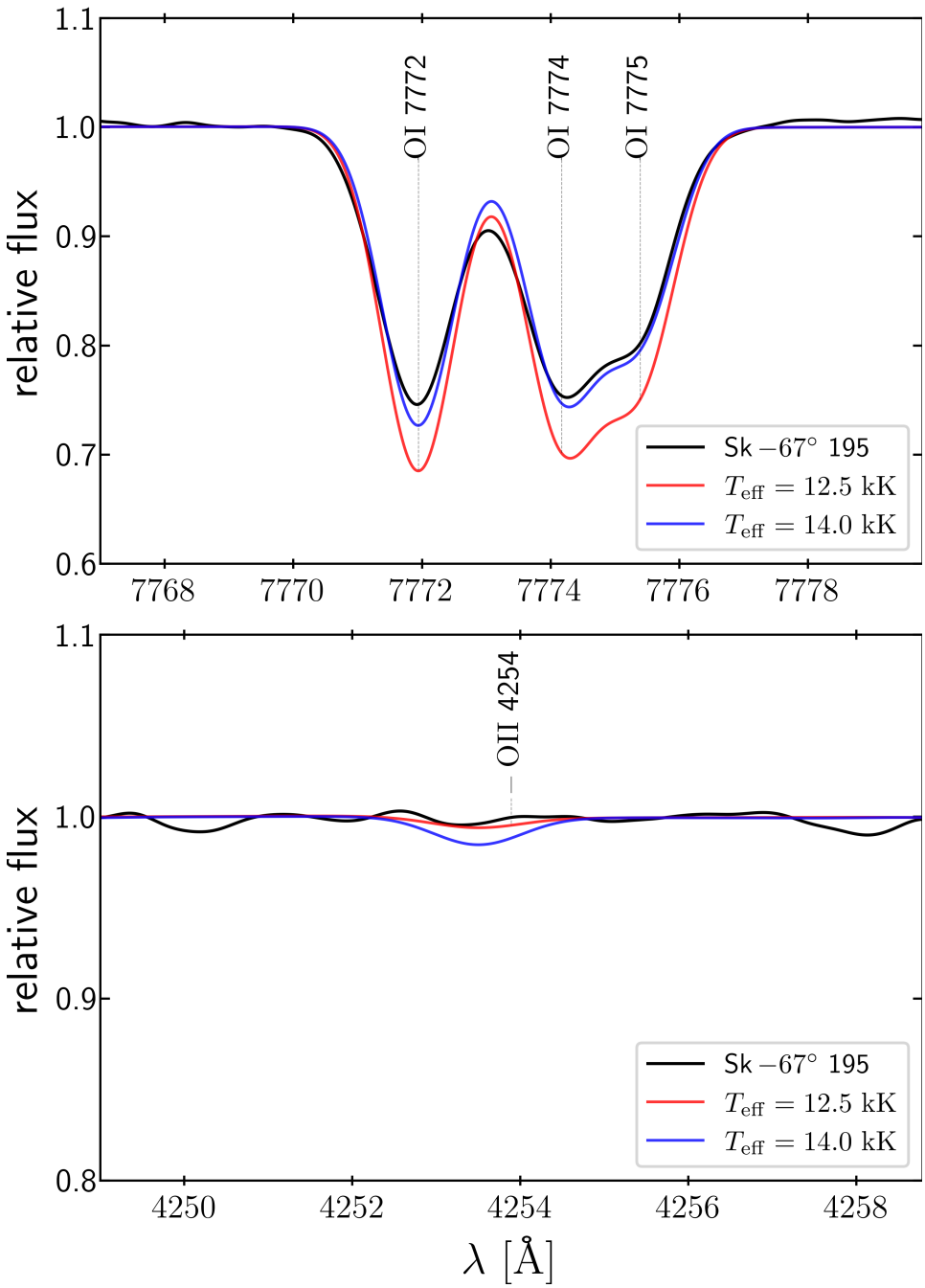


Figure 2.5: O I λλλ7772−7774−7775 and O II λ4254 lines of the B8 supergiant Sk −67° 195 (black line). Red line: the preferred model, the temperature of which ($T_{\rm eff}$ = 12.5 kK) was obtained from fitting He I λ4471 and Mg II λ4481, and a comparison with higher $T_{\rm eff}$ = 14.0 kK.

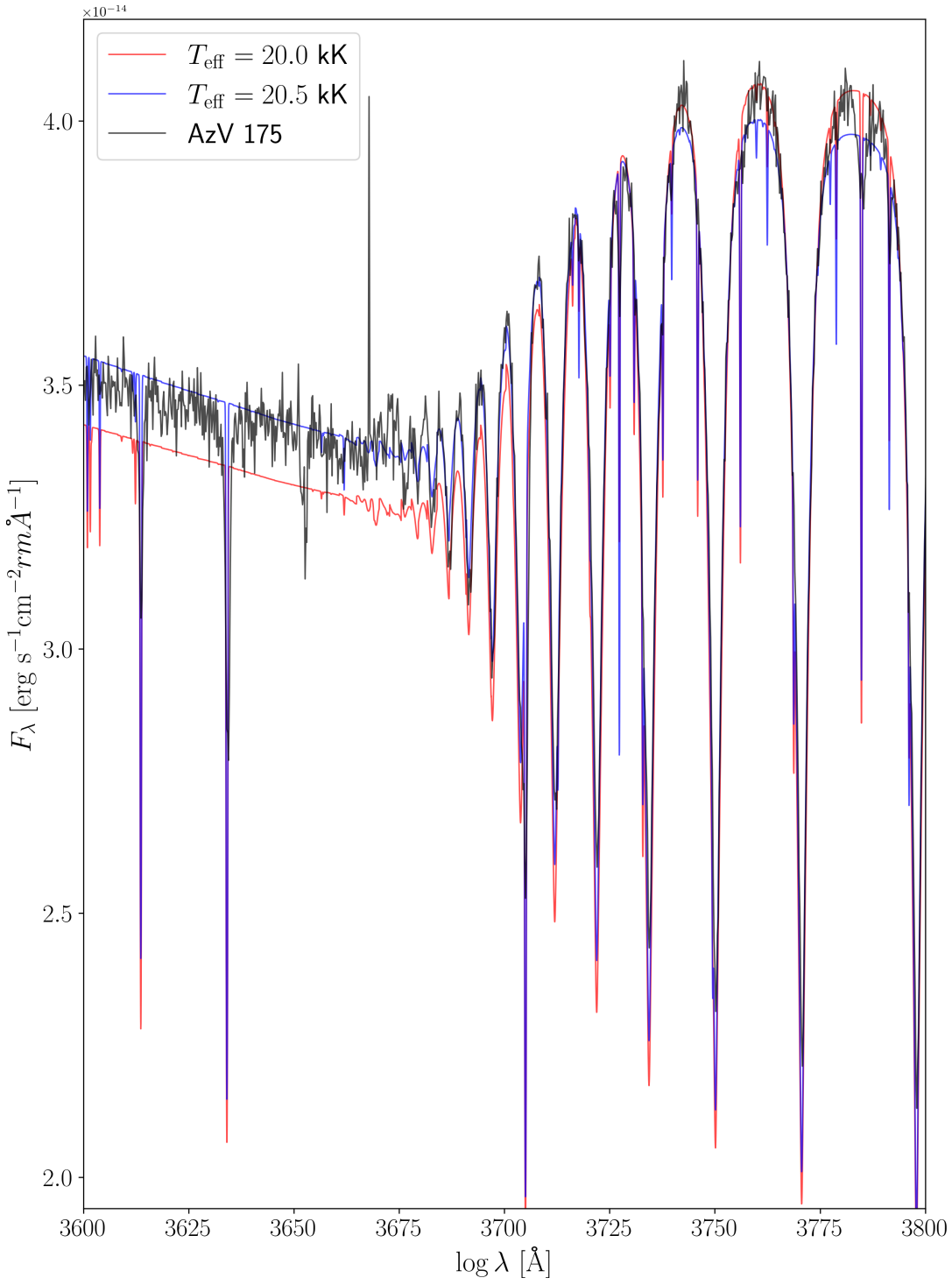


Figure 2.6: Examples of the effect of varying $T_{\rm eff}$ on the Balmer jump. The best-fitting model is shown with the solid red line. Comparison model: blue solid line ($\Delta T_{\rm eff}$ = 500 kK). Observed XShootU spectrum: black solid line.

preferred model of the supergiant AzV 175 with $T_{\rm eff} = 20.0$ kK is compared to a hotter model with $T_{\rm eff} = 20.5$ kK. We can see that the predicted strength of the Balmer jump in the comparison model is a better match to the observations than our preferred model.

The earliest B stars (B0-B0.7) in the temperature range $T_{\rm eff} \approx 25{-}22$ kK show weak He II lines, so we use He I λ4471 and He II λ4542 as a sanity check when fine-tuning the temperature for such objects. There is also a temperature range $T_{\rm eff} \approx 20{-}17$ kK at which silicon lines of all three ionisation stages (Si IV, Si III, and Si II) are present. In those cases, we attempted to fit all lines but focused mainly on the stronger consecutive pair.

Since silicon is an alpha-process element, its abundance is determined by the environment and not heavily influenced by the evolution of the star in the supergiant phase. To explain this, we use the LMC case as an example. Korn et al. (2005) obtained a value of $\epsilon_{\rm Si} = 7.07 \pm 0.3$ from fast-rotating B stars in the LMC, and Hunter et al. (2007) reported a silicon abundance $\epsilon_{\rm Si} = 7.19 \pm 0.07$ from narrow-line late-O and B stars in the LMC, whereas Dopita et al. (2019) derived a value $\epsilon_{\rm Si} = 7.11 \pm 0.04$ from supernova remnants in the LMC. The low variance between these values caused us to fix the silicon abundance. For these reasons, we did not attempt to fit the silicon line strength by varying the silicon abundance during fine-tuning. We also do not change the abundance of magnesium during our fine-tuning stage. Similar to silicon, this is motivated by the low variance in magnesium abundance values reported across different methods in the literature. LMC $\epsilon_{\rm Mg}$ values from the literature are as follows: $\epsilon_{\rm Mg} = 7.15 \pm 0.3$ from Korn et al. (2005), and $\epsilon_{\rm Mg} = 7.06 \pm 0.09$ from Hunter et al. (2007), and $\epsilon_{\rm Mg} = 7.19 \pm 0.09$ from Dopita et al. (2019). One could make a similar case for the SMC when comparing silicon and magnesium abundances obtained from the analysis B stars (e.g. Hunter et al., 2007, 2009), A supergiants Venn (1999), and supernova remnants (e.g. Dopita et al., 2019; Maggi et al., 2019).

For O stars, the helium abundance is essential for an accurate temperature estim-

ate. Changing the helium abundance at the expense of hydrogen modifies the ionisation structure in the atmosphere, which, in turn, affects the shape and strength of Hα, especially when it is in emission. This holds for the majority of targets in our sample. It is therefore important to also obtain an accurate helium abundance for the O and B stars. In our fitting procedure, as we are fitting temperature line diagnostics, we simultaneously fine-tune abundances of helium and hydrogen before attempting to fit wind lines such as Hα.

It is important to understand that small variations in $T_{\rm eff}$ can have different effects on the quality of the fit, depending on the model's temperature range. To illustrate this, we show in Fig. 2.7 the effect of varying the temperature of the best fitting model (red solid line) by $\Delta T_{\rm eff} = -700$ K with all other parameters fixed. The top panels shows the fits to He II λ4542 and He I λ4471 (panels *a* and *b* respectively in Fig. 2.7) for the O9.5 Ib supergiant Sk -71° 41, where the best fitting model has a $T_{\rm eff} = 29.2$ kK and we can see that while the model with a lower temperature does not yield a noticeably different fit for He I λ4471, He II λ4542 is significantly changed. The equivalent widths (EW) ratio of He I λ4471 to He II λ4542 in the observations is $\approx 3.20 \pm 0.05$. our preferred model yield an EW ratio of $\approx 3.15 \pm 0.05$ compared to an EW ratio $\approx 3.45 \pm 0.05$ for the comparison model with the higher $T_{\rm eff}$.

Panels *c* and *d* in Fig. 2.7 show the comparison of the fits of Si IV $\lambda\lambda 4088 - 4116$ and Si III $\lambda\lambda\lambda 4553 - 4568 - 4575$, respectively, for the B0 Ia supergiant Sk -68° 52 (best fitting model $T_{\rm eff} = 26.0$ kK). In this case, lowering the temperature by $\Delta T_{\rm eff} = 700$ K slightly worsens the quality of the fits for both sets of lines. The EW ratio of Si III λ4552 to Si IV λ4088 in the observed spectrum of Sk -68° 52 is $\approx 0.55 \pm 0.05$. Our preferred model yields an EW ratio of $\approx 0.51 \pm 0.05$ compared to an EW ratio of 0.45 ± 0.05 for the comparison model with the lower $T_{\rm eff}$.

In panels *e* and *f* of Fig. 2.7, we show the fits of the B3 Ia supergiant Sk -67° 78 for Si III $\lambda\lambda\lambda 4553 - 4568 - 4575$ and Si II $\lambda\lambda 4128 - 4131$, respectively, where the best

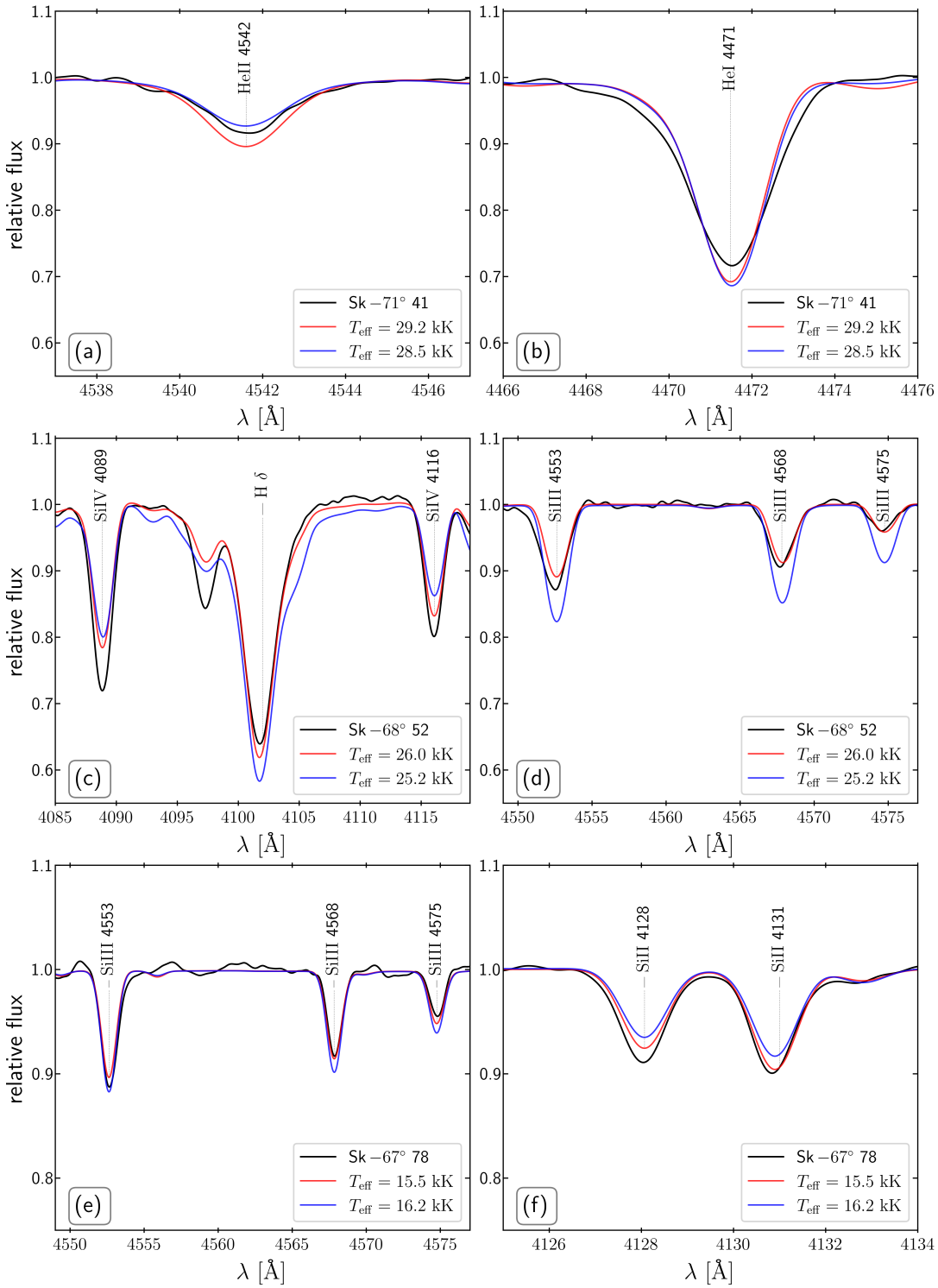


Figure 2.7: Examples of the effect of varying $T_{\rm eff}$ on the quality of the fit. The best-fitting model is shown with the solid red line. Comparison model: blue solid line ($\Delta T_{\rm eff}$ = 700 kK). Observed XShootU spectrum: black solid line. a-b: Sk −71° 41 (O9.5 Ib). c-d: Sk −68° 52 (B0 Ia). e-f: Sk −67° 78 (B3 Ia).

fitting model has $T_{\rm eff}$ = 15.5 kK. We observe that raising the model temperature by $\Delta T_{\rm eff}$ = 700 K noticeably degrades the fit quality. The EW ratio of Si II λ4128 to Si IV λ4552 in the observed spectrum of Sk −67° 78 is $\approx 0.60 \pm 0.05$. Our preferred model yields an EW ratio of $\approx 0.62 \pm 0.05$ compared to an EW ratio 0.53 ± 0.05 for the comparison model with the higher $T_{\rm eff}$. We estimate the uncertainty of the model from the spectral fitting as $\Delta T_{\rm eff}^{m} \approx \pm 500-1000$ K depending on the quality of the fit, and we estimate a more conservative and realistic uncertainty as double the uncertainty of the model in an attempt to take into account the limitations of the model atmosphere code, giving us $\Delta T_{\rm eff} \approx \pm 1000-2000$ K.

2.3.3 Effective surface gravity

The surface gravity ($\log g$) is obtained via fitting the wings of Balmer lines. Balmer lines are broadened by collisional processes and are most sensitive to Stark broadening (linear Stark broadening affects the wings of the H and, to a lesser extent, He II lines; indeed, this effect is mainly used to constrain the surface gravity), which is related to gas pressure, and in turn, gas pressure is intimately connected to electron pressure ($P_{\rm e} = N_{\rm e}KT$) in hot stars. This means that Balmer lines are broader in higher gravity stars. Degeneracies arising in fitting Balmer lines are alleviated when temperature diagnostic lines are included (fitting $\log g$ and $T_{\rm eff}$ simultaneously and iteratively).

We use Hγ as the primary indicator because it is usually in absorption and its wings are largely uncontaminated by wind emission or blending with other lines. Hη and Hζ are used as a sanity check. These Balmer lines are usually strong and well resolved (Simón-Díaz, 2020; Martins, 2011), but in the cases of the LMC O hypergiants Sk −68° 135 and Sk −69° 279, the SMC B hypergiant AzV 393, and the MW hypergiants HD105056, HD169454, and HD190603, we resorted to fitting Hη as our primary surface gravity diagnostic due to wind contamination in all the lower Balmer lines.

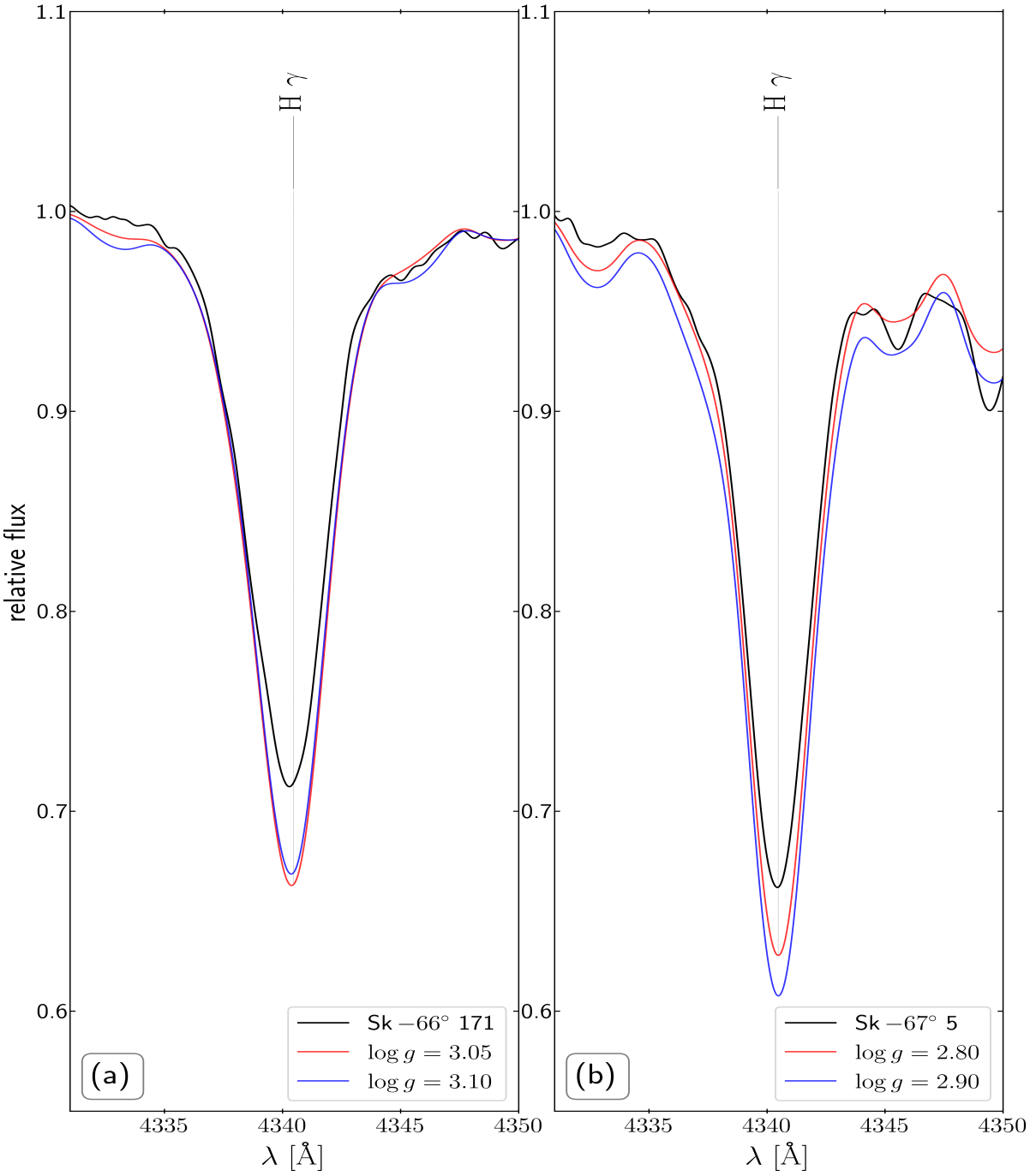


Figure 2.8: Examples of the effect of varying $\log g$ on the quality of the fit. The best-fitting model is shown with the solid red line. Comparison model: blue solid line. Observed XShootU spectrum: black solid line. a: Sk −66° 171 (O9 Ia) ($\Delta \log g = 0.05$). b: Sk −67° 5 (B0 Ib) ($\Delta \log g = 0.1$).

Table 2.4: Properties of the PYPHOT filter functions (Fouesneau, 2025).

filter	$\lambda_{\rm central}$	$\lambda_{\rm pivot}$	$\lambda_{\rm effective}$	Vega
	Å	Å	Å	
B	4347.526	4296.702	4316.312	20.512
V	5504.666	5469.853	5438.689	21.099
K_S	21655.864	21638.169	21521.413	25.921

To show the level of sensitivity of the model to modest changes in $\log g$, we present two cases of fitting Hγ. For the O9 Ia supergiant Sk -66° 171 (panel (a) in Fig. 2.8), the best fitting model (red solid line) was computed with $\log(g/\mathrm{cm\,s^{-2}}) = 3.05$ dex and the comparison model (blue solid line) with $\log(g/\mathrm{cm\,s^{-2}}) = 3.10$ dex. Both models were computed with the same $T_{\rm eff} = 29.9$ kK and with all other parameters held constant; as shown, the two fits are very similar. The second case (panel (b) in Fig. 2.8) is for the B0 Ib supergiant Sk -67° 5, where the best fitting model and the comparison model were computed for $\log(g/\mathrm{cm\,s^{-2}}) = 2.8$ dex and 2.9, respectively, and the same $T_{\rm eff} = 25.6$ kK. In contrast to the previous case, a $\Delta\log(g/\mathrm{cm\,s^{-2}}) = 0.1$ dex dramatically changes the quality of the fit.

We estimate the model uncertainty at $\Delta\log g^m = \pm 0.05 - 0.10$ dex and adopt a conservative uncertainty $\Delta\log g_c = \pm 0.2 - 0.25$ dex which takes into account the additional uncertainty of $v_{\rm rot}\sin i$ and R_* and the quality of the normalisation (a 1% change in the wings due to normalisation can lead to a $\log g$ difference of 0.1 dex).

2.3.4 Luminosity

For the determination of the bolometric luminosities $L_{\rm bol}$ of our stars, we use the flux from the model computations, which was computed for a fixed luminosity of $\log(L_{\rm model}/L_\odot) = 5.8$. We select the Vega magnitude system photometric zero-point. First, we apply suitable filter functions from PYPHOT (Fouesneau, 2025) using the effective wavelengths

of the filters, and we obtain the BVK_S fluxes of the model using the function get_flux ($F_B^{\rm m}$, $F_V^{\rm m}$ and $F_{K_S}^{\rm m}$), and from the fluxes we calculate the magnitudes of the model ($B^{\rm m}$, $V^{\rm m}$ and $K_S^{\rm m}$) as $-2.5 \log F_{BVK_S} - m_{BVK_S}^{\rm vega}$. The filter function properties and Vega magnitudes are presented in Table 2.4.

For the LMC and SMC samples, we apply the reddening law from Gordon et al. (2003) and Gordon et al. (2024) and fit the relative extinction $R_{\rm V}$. We also fit additional parameters, following Fitzpatrick & Massa (1990, FM90), to match the observed UV shape of the SED. In addition to $R_{\rm V}$ and $E(B-V)$, the FM90 parametrisation includes 6 parameters that determine the shape of the UV extinction curve. c_1 is the intercept of the linear background term, c_2 determines the slope of the linear background term, c_3 controls the strength of the 2175 Å bump, and c_4 determines the amplitude and slope of the FUV tail. The last two parameters x_o and γ are part of the Drude function, and determine the position of the 2175 Å bump and the full-width at half-maximum (FWHM) of the 2175 Å bump, respectively. None of these six parameters is considered a physically motivated value, as their sole function is to reproduce the shape of the UV part of the SED.

For the MW sample, we apply the reddening law from Fitzpatrick et al. (2019), which is based on the simple two-parameter ($R_{\rm V}$ and $E(B-V)$) approach of Cardelli et al. (1989). In contrast to LMC and SMC, Galactic dust attenuation is much more significant. Therefore, we do not determine $E(B-V)$ from the model magnitudes, but rather fit $E(B-V)$ and $R_{\rm V}$ as free parameters and in relation to one another.

The model SED is then scaled to the observed SED using a factor equal to $F_{K_S}^{\rm m}/F_{K_S}$. Using the model magnitudes, the colour excess $E(B-V)$ is calculated as $(B-V) - (B^{\rm m}-V^{\rm m})$. We calculate the bolometric correction of the visual magnitude of the model $BC_{\rm V}^{\rm m}$ with the equation $BC_V^{\rm m} = -2.5 \log L_{\rm model} + 4.74 - V^{\rm m}$. Finally, the bolometric luminosity is calculated via $BC_V^{\rm m}$, the apparent visual magnitude of star m_V, and the distance modulus (DM) as $\log L_{\rm bol} = (DM + A_V - BC_V^{\rm m} - m_V + 4.74)/2.5$, where A_V

is the total extinction and is equal to $E(B-V)\,R_V$. The absolute visual magnitude is calculated as $M_V = m_V - DM - A_V$.

We adopt DM values of 18.50 ± 0.02 mag for the LMC (Alves, 2004) and 18.96 for the SMC (Scowcroft et al., 2016). For the Galactic sample, DM is calculated from the distances d as $DM = 5\log(d/10)$. The distances d are the photogeometric distances, which were drawn from Bailer-Jones et al. (2021) and were obtained using a Bayesian inference method that combines GAIA parallaxes with a 3D stellar spatial distribution prior of the Milky Way and a photometric, colour-dependent prior on the star's absolute magnitude. If the star is not included in Bailer-Jones et al. (2021), we calculated the distance as the inverse of the parallax. We found that in the latter case, the stars are extremely bright and close, rendering GAIA observations unreliable due to saturation. Therefore, we resorted to using the re-reduced and improved archival HIPPARCOS parallaxes (van Leeuwen, 2007) in our calculations.

With this procedure, we simultaneously obtain the extinction parameter R_V and the colour excess $E(B-V)$. This method relies on the relation of the B and V bands to the K_S band, and since the extinction is minimal in the K_S, the obtained bolometric luminosities are highly reliable. The uncertainty in the derived bolometric luminosity is dominated by the uncertainty in the target's distance, for which we adopt a random error of 0.1 dex in the distance moduli of the LMC and SMC. For the Galactic sample, the uncertainty in distance is the range $\Delta DM \approx 0.02$-0.07 dex. Additionally, the SED fitting method (by eye) results in an uncertainty in the A_V, which is inherited by the bolometric luminosity. Finally, the 2MASS photometry formal errors range from 0.01 to 0.1, averaging ≈ 0.03. Therefore, we adopt a global uncertainty in the derived luminosity of $\Delta \log L_{\rm bol} \approx 0.15$ dex.

2.3.5 Line-broadening parameters

Out of all parameters that cause spectral line-broadening (macro-turbulent velocity $v_{\rm mac}$, micro-turbulent velocity $v_{\rm mic}$, and projected rotational velocity $v_{\rm rot}\sin i$), we elected to include only $v_{\rm rot}\sin i$ as part of the fitting procedure. When calculating the formal integral using CMF_FLUX, we fix the $v_{\rm mic}$ in the photosphere to 10 km s^{-1} and the maximum $v_{\rm mic}$ in the wind to 100km s^{-1} (see Table 2.1).

Changing $v_{\rm mic}$ in the photosphere has little effect on wind lines, but the changes in line opacities do affect photospheric lines (primarily metal but also He I lines). This produces a degeneracy between $v_{\rm mic}$ and chemical abundances. Therefore, increasing $v_{\rm mic}$ could lead to an underestimation of the abundances and temperatures (Brands et al., 2022), and we therefore excluded $v_{\rm mic}$ from our fitting procedure. This degeneracy can be alleviated by simultaneously fitting $v_{\rm mic}$ and the abundances using multiplet lines. A common diagnostic of $v_{\rm mic}$ in B stars is the depth of the components of Si III $\lambda\lambda\lambda 4553-4568-4575$, which are sensitive and react differently to changes in $v_{\rm mic}$ (McErlean et al., 1998).

The values of macro-turbulent velocities on OB stars range from a few km s^{-1} for dwarfs up to a few tens of km s^{-1} for supergiants. We fix $v_{\rm mac}$ at 20 km s^{-1} in our fitting procedure. Fixing $v_{\rm mac}$ is appropriate for our sample, especially when taking into account the velocity resolution of the UBV and VIS arms of X-shooter that are $\approx$ 45 and 25 km s^{-1}, respectively. Although the resolution of the Galactic data is almost twice that of the LMC and SMC ($\approx$ 10 km s^{-1}), which would allow for disentangling $v_{\rm mac}$ and $v_{\rm rot}\sin i$, we keep $v_{\rm mac}$ fixed at 20 km s^{-1} for the sake of uniformity and homogeneity in the analysis procedure. However, we investigate the line-broadening characteristics of our MW sample and of subsamples of our LMC and SMC stars with high-resolution MIKE data, using the IACOB-BROAD tool (Simón-Díaz & Herrero, 2014a).

The main diagnostic line for O stars is O III 5592. For early-B stars O III 5592 is also

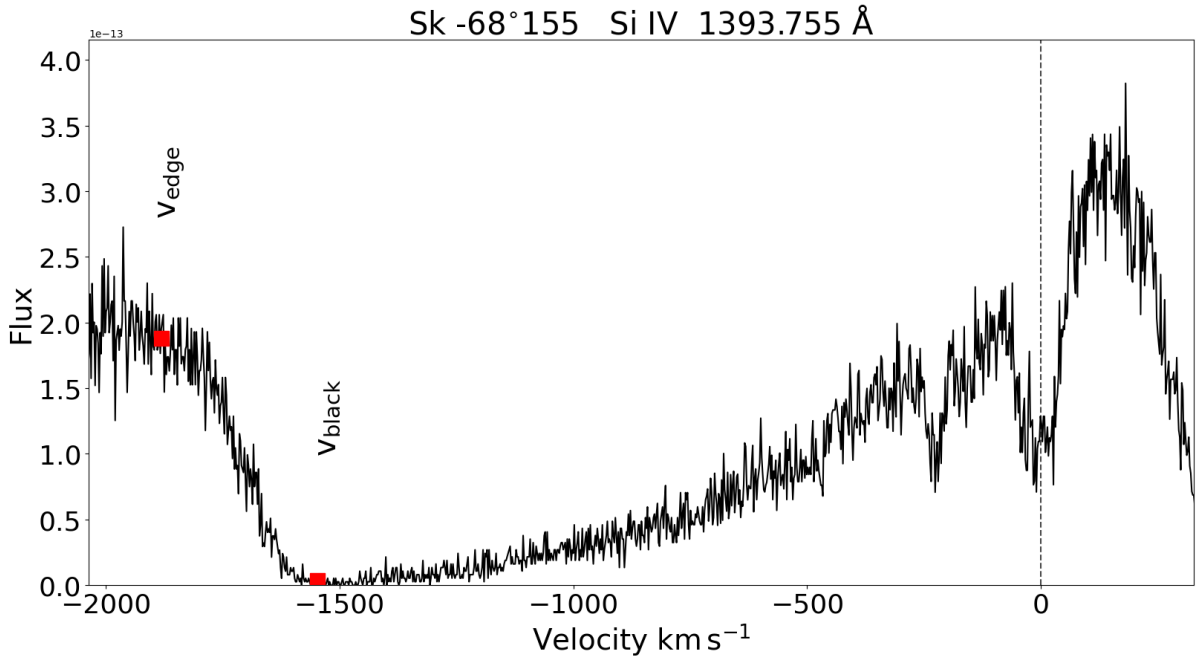


Figure 2.9: Example of a saturated P Cygni profile in the blue component of the resonance line Si IV $\lambda\lambda 1394 - 1403$ of the B supergiant Sk $-68°$ 155. Marked in red squares are the positions of the measured black velocity ($v_{\rm black}$) and edge velocity ($v_{\rm edge}$).

used and as a sanity check we fit C III $\lambda 4267$, Si IV $\lambda\lambda 4089 - 4116$, and Si III $\lambda\lambda\lambda 4553 - 4568 - 4575$. for mid- to late-B stars we fit the Mg II 4481 line and as a sanity check we use C II and Si II lines. The uncertainty in $v_{\rm rot} \sin i$ measurements is dominated by the velocity resolution of the UBV arm of X-shooter (Vernet et al., 2011) $\Delta v \approx 45$ km s^{-1}.

2.3.6 Terminal wind velocity

The black velocity $v_{\rm black}$ is the velocity measured at the bluest extent of fully saturated P Cygni absorption (Prinja et al., 1990). This is thought to provide a more robust estimate of the wind terminal velocity than the edge velocity $v_{\rm edge}$, which is measured at the point where the blue trough of the P Cygni profile intersects the local continuum (Beckman & Crivellari, 1985). The difference $v_{\rm edge} - v_{\rm black}$ arises from the turbulence in the velocity field of the wind. An example of these measurements is shown in Fig. 2.9.

We obtained $v_{\rm edge}$ and $v_{\rm black}$ using direct measurements of all the viable P Cygni

resonance lines in the range $\approx [1200, 2900]$ Å, with the advantage of accurate radial velocity estimates for each object from the optical metal lines. $v_{\rm edge}$ and $v_{\rm black}$ were determined as the mean value of all velocities obtained from the individual resonance lines. From the stars from which we were able to measure both $v_{\rm edge}$ and $v_{\rm black}$, we calculate the mean ratio of $v_{\rm black}$ to $v_{\rm edge}$ across each sample $\langle v_{\rm black}/v_{\rm edge}\rangle_{\rm sample}$. The resonance lines used are Si IV $\lambda\lambda 1394-1403$, C IV $\lambda\lambda 1548-1551$, Al III $\lambda\lambda 1855-1863$, and Mg II $\lambda\lambda 2796-2803$.

Stars at low metallicity are well known for having absorption profiles that may not reach zero intensity; consequently, it is sometimes not possible to obtain an accurate measurement of $v_{\rm black}$. For stars with unsaturated P Cygni profiles, where $v_{\rm black}$ cannot be directly observed, we measured $v_{\rm edge}$ and derived the terminal velocity by scaling it by the respective sample average, following: $v_\infty = v_{\rm edge} \times \langle v_{\rm black}/v_{\rm edge}\rangle_{\rm sample}$.

Another established empirical diagnostic that allows for direct measurement of v_∞ is to use NACs (see Section 1.4.1). Because these narrow absorption features accumulate near the asymptotic limit of the wind velocity law, their central velocities offer an independent, direct tracer of v_∞ (Kaper et al., 1996; Prinja & Crowther, 1998a). However, in some cases, unsaturated P Cygni profiles do not present with a NAC, and in other cases it is challenging to correctly identify NACs due to the complexity of the P Cygni profile shape. Therefore, for the sake of consistency, we only use the method that employs $\langle v_{\rm black}/v_{\rm edge}\rangle_{\rm sample}$ for measuring v_∞ for stars with unsaturated P Cygni profiles.

The uncertainty in v_∞ is calculated as the quadrature of (i) the uncertainty of single velocity measurements from each line, which is dominated by the spectral resolution of UV observations $\Delta v \approx 15$ km s^{-1}, the uncertainty in the radial velocity correction which is also dominated by the resolution of the optical spectra $\Delta v \approx 30$ km s^{-1}, and (iii) the spread of the mean velocity determined from multiple P Cygni profiles which is either directly calculated from multiple $v_{\rm black}$ or from the spread on the mean ratio of $v_{\rm black}/v_{\rm edge}$. Δv_∞ ranges between 60 and 100 km s^{-1}, and therefore we adopt a conservative global

uncertainty $\Delta v_\infty = 100$ km s^{-1}.

2.3.7 Wind density parameters

The primary optical diagnostic line used to constrain the wind mass-loss rate is Hα, and in the case of O supergiants, He II 4686 is used to a lesser extent. Hα is formed relatively close to the photosphere ($\approx 1-2\ R_*$), and since it is a recombination line, it is very sensitive to wind density ($\sim \rho^2$). The wind density is itself a function of the mass-loss rate and the velocity-field structure. Therefore, the parameters we try to fit that affect the strength and the morphology of Hα within the framework of CMFGEN are wind terminal velocity v_∞, mass-loss rate $\dot{M}$, β and clumping parameters (volume-filling factor $f_{\rm vol}$ and the onset clumping velocity $v_{\rm cl}$). UV lines are used to further constrain the density and to break degeneracies of clumping and mass-loss. The most consistently available lines in our sample, which we use to constrain the mass-loss rate and clumping, are the unsaturated P Cygni sulphur doublet S IV $1063-1073$, plus C III $\lambda1176$ and Si IV $\lambda\lambda1394-1403$ if it is not fully saturated. We also use C IV $\lambda\lambda1548-1551$ for O stars as a sanity check and for late-B stars we use Al III $\lambda1856-1862$ and Mg II $\lambda2796-2803$.

In our fine-tuned model, we adopt a value for the onset clumping velocity $v_{\rm cl}$ equal to double the sound speed of the model, which comes to a value in the range $\approx 25-35$ km s^{-1} depending mainly on the temperature and helium abundance. This is a common procedure in the analysis of OB stars (Marcolino et al., 2009; Puebla et al., 2016). Since the connection velocity in our models is set by default to 10 km s^{-1}, the adopted values of $v_{\rm cl}$ indicate that the clumping becomes significant in the base of the supersonic winds, rather than in the subsonic layers or the photosphere. However, recent 2-D global simulations of O stars indicate that wind inhomogeneities could originate from photospheric turbulence in the iron opacity peak zone, driven by the unstable nature of convection (Debnath et al., 2024).

Having acquired R_* (from the derived $L_{\rm bol}$ and $T_{\rm eff}$), v_∞ and model mass-loss rate ($\dot{M}^m$), we derive the luminosity-adjusted mass-loss rate ($\dot{M}$) by scaling $\dot{M}^m$ to the transformed radius $R_{\rm t}$ via Eq. 2.16. We estimate uncertainties in the wind parameters in a manner suitable for our analysis. For v_∞ that is determined as $v_{\rm black}$, we calculate the uncertainty by quadrature of the systematic and stochastic errors. The systematic errors stem from the instrument's resolution, and the stochastic errors are the sum of the standard deviation of the mean v_∞ and the mean radial velocity $v_{\rm rad}$. For v_∞ that is calculated as a fraction of $v_{\rm edge}$, other than the resolution and the dispersion of the mean $v_{\rm edge}$ and $v_{\rm rad}$, we additionally take into account in quadrature the standard deviation of the mean of $v_\infty/v_{\rm edge}$ over our sample, which yields relatively higher v_∞ errors for stars that do not show saturated P Cygni profiles in their UV spectra.

It is quite difficult to quantify the uncertainty of β, but by varying beta in our model and adjusting the mass-loss rate accordingly, we were able to get a general idea of the range of beta that would reproduce a fit with a similar quality for Hα, which is defined by the uncertainty $\Delta\beta = \pm 0.2$ (an example is given later in Section 3.2.3). The model uncertainty of the mass-loss rate $\Delta \log \dot{M}^m = \pm 0.05$ to 0.1 dex depending on the quality of the fit. Using Eq. 2.16 we calculate the uncertainty in the scaled mass-loss rates as

$$\Delta \log \dot{M} = \sqrt{\left(\frac{4}{3}\frac{\Delta T_{\rm eff}}{T_{\rm eff}}\right)^2 + \left(\frac{2}{\ln 10}\cdot\frac{\Delta \dot{M}^m}{\dot{M}^m}\right)^2 + \left(\frac{\Delta v_\infty}{v_\infty}\right)^2}. \tag{2.17}$$

We obtain $\Delta \log \dot{M}$ between 0.30 and 0.45 dex. Therefore, we adopt a conservative global uncertainty $\Delta \log \dot{M} \approx 0.5$ dex.

2.3.8 He and CNO abundances

The accurate determination of the effective temperature and surface gravity depends on the helium abundance in the model, especially for O stars, because of the way the

temperature is gauged by He I to He II equivalent widths ratio. To restrict the helium mass fraction (Y), we fix the mass fraction of all included elements except for hydrogen, which means that increasing or decreasing the mass fraction of helium in the model would respectively deplete or enrich the model with hydrogen. We use the following Helium line diagnostics: He I λ4026, He I λ4471,He I λ4922, (He I λ6678), (He I λ7065), (He I λ7281), He II λ4542, He II λ5411.

Since CMFGEN is used in the present study, we acknowledge larger uncertainties in the derived CNO abundances relative to other analyses. Nevertheless, after obtaining the stellar and wind parameters, we try to fit multiple lines that adhere to different ionisation levels of CNO elements. The lines depend on the spectral type of the star, but the primary lines that we use to refine the CNO abundances are presented in Table 2.5.

The triplet N III $\lambda 4634 - 4641$ is usually in emission and is notoriously difficult to fit (Rivero González et al., 2011). In some objects C III λ5696 is also in emission. We leave fitting CNO abundances as the last step in our fitting procedure since it does not affect other diagnostic lines that are used to gauge other parameters. He I and O I lines quoted above in parentheses were not part of the analysis and are only used as supplementary diagnostics.

The CNO abundances presented in the following chapters are subject to large uncertainties, for which we adopt a value of $\approx \pm 0.3$ dex. This is due to the high sensitivity of metal lines to changes in $T_{\rm eff}$ and $\log g$, in addition to changes in $v_{\rm mic}$. We are more confident in our helium abundances, and we determine our uncertainties based on the way we varied the helium mass fraction in our models (in steps of 10% of the baseline grid abundance), so we adopt a 20% uncertainty in the mass fraction, which translates to 0.09 dex for the helium abundance by number $\epsilon_{\rm He} = \log \frac{\rm He}{\rm H} + 12$.

Table 2.5: Line diagnostics for determination of CNO elemental abundances.

line	Sp. T.
C IV $\lambda\lambda 5801 - 5811$	O9-B0
C III $\lambda\lambda 4647 - 4650$	O9-B3
C III $\lambda 5696$	O9-B3
C II $\lambda 4070$	B0-B8
C II $\lambda 4267$	B0-B8
C II $\lambda\lambda 6578 - 6582$	B0-B8
N III $\lambda 4097$	O9-B0.5
N III $\lambda\lambda 4379$	O9-B0.5
N III $\lambda\lambda 4510 - 4515$	O9-B0
N III $\lambda\lambda 4634 - 4641$	O9-B0
N II $\lambda 3995$	B1-B8
N II $\lambda 4447$	B1-B8
N II $\lambda\lambda\lambda 4601 - 4607 - 4614$	B1-B8
N II $\lambda 4630$	B1-B8
O III $\lambda\lambda 3261 - 3265$	O9-B1
O III $\lambda 3760$	O9-B1
O III $\lambda 5592$	O9-B1
O II $\lambda 4254$	B0-B6
O II $\lambda 4367$	B0-B6
O II $\lambda\lambda 4415 - 4417$	B0-B6
O II $\lambda\lambda 4638 - 4641$	B0-B6
(O I $\lambda\lambda\lambda 7772 - 7774 - 7775$)	B7-B8

Chapter 3

OB supergiants in the LMC

In this chapter, we present our study of LMC late-O and B supergiants. The importance of the LMC for the purposes of this PhD thesis stems from its chemical content, which is moderately metal-deficient with respect to the solar neighbourhood. The LMC can be considered a bridge between the state of the modern universe and the state of the early universe. The first goal of this chapter is to provide new estimates of the stellar and wind properties of a late-O and B supergiant sample in the LMC using the methods discussed in Chapter 2. The second goal of this chapter is to investigate the bi-stability jump in the LMC. The final aim is to check the validity of mass-loss rates predicted by numerical recipes by comparing them to our empirically derived mass-loss rates.

In Section 3.1, we present a detailed account of the observational data used in the study. In Section 3.2, we present our results, including the values of the physical and wind parameters obtained through our pipeline. In Section 3.3, we compare our results to previous empirical studies and numerical predictions, and we discuss the implications of our findings on the bi-stability jump and the effect of metallicity on wind parameters.

3.1 Observations

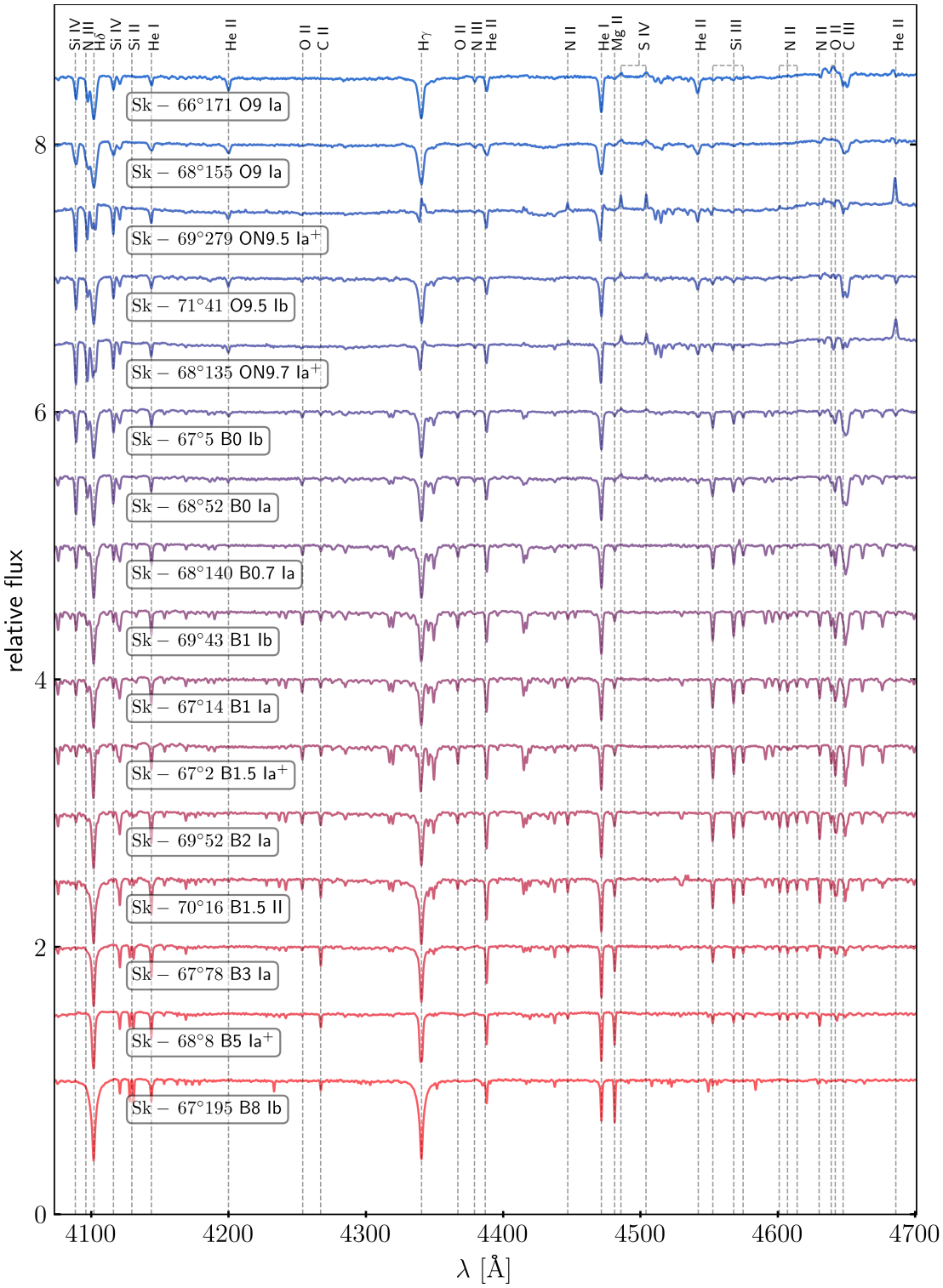


Figure 3.1: Normalised XShootU spectra (Sana et al., 2024, DR1) in the blue optical range of the sample with identifications for a subset of the optical lines. For illustration purposes, we added an arbitrary offset of 0.5 for each spectrum. The fits to the violet, yellow, and red spectra for all stars are presented in Appendix A.7.

3.1.1 Sample

We initially identified 22 LMC supergiants in the spectral type range O7-B9 from the ULLYSES sample, the classification of which was obtained from various sources and compiled in Vink et al. (2023). Of the original sample, four stars (Sk −67° 197, Sk −66° 152, Sk −67° 168, and Sk −70° 50) were excluded due to odd features in the morphology of optical wind-lines (Hα and He II λ4686) that could hint toward a circumstellar discs. Another two stars (Sk −69° 83 and Sk −66° 50) were excluded due to signs of binarity. The end result is a sample of 16 OB supergiants in the spectral range O9-B8, including multiple luminosity subclasses (Ia$^+$, Ia, Iab, and Ib) in each spectral bin, covering a wide temperature range that includes the bi-stability jump (theoretically predicted to be around B1 spectral type). We further discuss each of the omitted objects in Appendix A.1.

In Table 3.1, we provide the updated spectral type taken from Bestenlehner et al. (2025), in which the classification was determined using O star templates from Sota et al. (2011) and B star templates from Negueruela et al. (2024). In the revised classification, the luminosity class of Sk −70° 16 was changed from a low luminosity supergiant (Ib) to a bright giant (II).

3.1.2 Ultraviolet spectroscopy

The Ultraviolet Legacy Library of Young Stars as Essential Standards (ULLYSES) programme (Roman-Duval et al., 2025) made use of two instruments aboard the Hubble Space Telescope (HST); namely, the Cosmic Origins Spectrograph (COS, Green et al., 2012) in the G130M/1291, G160M/1611, and G185M/1953 wavelength settings, achieving a minimum spectral resolving power of $R \approx 12,000$, $R \approx 13,000$, and $R \approx 16,000$, respectively, and the Space Telescope Imaging Spectrograph (STIS, Woodgate et al., 1998) E140M/1425 ($R \approx 46,000$), and E230M/1978 ($R \approx 30,000$) gratings in the far-

Table 3.1: Targets in our sample. The last three columns are the wavelengths (in Å) of the UV ranges and the corresponding instruments that were used for observations. The literature spectral types were adopted from Vink et al. (2023). The revised classifications were adopted from Bestenlehner et al. (2025).

Sk −	HDE	SpT (revised)	SpT (literature)	(900 − 1160)	(1150 − 1700)	(1700 − 2370)
66° 171	269889	O9 Ia	O9 Ia	FUSE	STIS E140M	STIS E230M
68° 155	-	O9 Ia	B0.5 I	FUSE	COS G130M+G160M	STIS E230M
69° 279	-	ON9.5 Ia$^+$	O9.2 Iaf	FUSE	STIS E140M	STIS E230M
71° 41	-	O9.5 Ib	O9.7 Iab	FUSE	STIS E140M	-
68° 135	-	ON9.7 Ia$^+$	ON9.7 Ia$^+$	FUSE	STIS E140M	STIS E230M
67° 5	268605	B0 Ib	O9.7 Ib	FUSE	STIS E140M	STIS E230M
68° 52	269050	B0 Ia	B0 Ia	FUSE	STIS E140M	STIS E230M
69° 43	268809	B1 Ib	B0.5 Ia	FUSE	STIS E140M	STIS E230M
68° 140	-	B0.7 Ia	B0.7 Iab	FUSE	COS G130M+G160M	STIS E230M
67° 2	270754	B1.5 Ia$^+$	B1 Ia$^+$	FUSE	STIS E140M	STIS E230M
67° 14,	268685	B1 Ib	B1.5 Ia	FUSE	COS G130M+G160M	STIS E230M
69° 52,	268867	B2 Ia	B2 Ia	FUSE	COS G130M+G160M	STIS E230M
67° 78,	269371	B3 Ia	B3 Ia	FUSE	COS G130M+G160M	STIS E230M
70° 16	-	B1.5 II	B4 I	-	COS G130M+G160M	COS G185M
68° 8	268729	B5 Ia$^+$	B5 Ia$^+$	-	COS G130M+G160M	STIS E230M
67° 195	-	B8 Ib	B6 I	-	COS G130M+G160M	STIS E230M

and near-UV. New COS and STIS spectra were obtained for a subset of our targets between July 2020 and Sept 2022 during HST cycles 27 - 29, and were combined with archival HST spectra drawn from GO 7437 (P.I. Lennon), GO 9116 (P.I. Lennon), GO 12581 (P.I. Roman-Duval), GO 13778 (P.I. Jenkins), and GO 15837 (P.I. Oskinova) obtained between Oct 2001 and Jun 2020. A subset of HST spectra has previously been presented by Walborn et al. (2000) and Evans et al. (2004).

Those new spectra were combined with suitable existing spectra (previously obtained with *FUSE* and/or *HST*). Far Ultraviolet Spectroscopic Explorer (FUSE) spectra cover the wavelength $\approx 900 - 1160$ Å with a resolving power of $\approx 15,000$ (Moos et al., 2000).

Archival spectra from the Far Ultraviolet Spectroscopic Explorer (FUSE, Moos et al., 2000) cover the wavelength range of $\approx 900 - 1160$ Å through the $4'' \times 20''$ (MDRS) or $30'' \times 30''$ (LWRS) apertures for our sample, providing $R \approx 15,000$. These are drawn from various Principal Investigator Team and Guest Investigator programmes obtained between May 2000 and July 2003. FUSE spectroscopy of a subset of the current sample has previously been presented by Walborn et al. (2002).

3.1.3 Optical data (XShootU)

To complement the UV spectra, high-quality optical/NIR spectroscopy was carried out with the X-shooter instrument (Vernet et al., 2011), which is mounted on the VLT. This slit-fed ($11''$ slit length) spectrograph provides simultaneous coverage of the wavelength region between $3000 - 10200$ Å, across two arms: UVB ($3000 \leq \lambda \leq 5600$ Å), VIS ($5600 \leq \lambda \leq 10000$ Å). X-shooters wide wavelength coverage made it the instrument of choice to build an optical legacy dataset (Vink et al., 2023). The XShootU dataset was observed with the following settings: $0.8''$ slit width for the UBV arm achieving spectra resolution $R \approx 6700$, and $0.7''$ for the VIS arm ($R \approx 11400$). Fig. 3.1 shows the optical spectra, which were combined, flux calibrated, corrected for telluric contamination, and

Table 3.2: Photometric data. References: 1 Cioni et al. (2011), 2 Cutri et al. (2003), 3 Massey (2002), 4 Schmidt-Kaler et al. (1999), 5 Ardeberg et al. (1972), 6 Isserstedt (1975).

Sk −	U	B	V	Ref.	J	H	K	Ref.
66° 171	11.02	12.04	12.19	6	12.62	12.57	12.62	1,2
68° 155	11.84	12.74	12.75	3	12.63	12.64	12.60	1,2
69° 279	12.00	12.84	12.79	6	12.62	12.58	12.50	1,2
71° 41	11.78	12.75	12.82	3	12.94	12.98	12.91	1,2
68° 135	10.50	11.36	11.36	5	11.46	11.24	11.16	1,2
67° 5	10.27	11.22	11.34	5	11.81	11.61	11.68	1,2
68° 52	10.69	11.66	11.72	4	11.84	11.75	11.72	1,2
69° 43	10.96	11.90	11.98	4	12.22	12.13	12.15	1,2
68° 140	11.99	12.84	12.79	3	12.51	12.43	12.41	1,2
67° 2	10.49	11.30	11.26	4	11.02	11.00	11.01	2
67° 14	10.51	11.42	11.52	5	12.08	11.78	11.90	1,2
69° 52	10.73	11.55	11.50	5	11.73	11.57	11.58	1,2
67° 78	10.49	11.22	11.26	5	11.60	11.45	11.35	1,2
70° 16	12.19	13.04	13.10	3	13.33	13.34	13.34	1,2
68° 8	10.39	11.09	11.02	4	10.86	10.87	11.16	2
67° 195	12.21	12.82	12.84	3	12.81	12.73	12.68	1,2

normalised by Sana et al. (2024, DR).

3.1.4 Auxiliary data (MIKE)

Another complementary spectroscopic optical dataset was collected using the Magellan Inamori Kyocera Echelle (MIKE) spectrograph, which is mounted on the Magellan Clay Telescope, for known slow-rotating ULLYSES stars. The higher spectral resolution ($R \approx 35000 - 40000$) and the wide wavelength coverage ($3350 - 5000$ Å blue arm and $4900 - 9500$ Å red arm) are needed to resolve spectral features and determine their rotation rates using metal lines (Crowther, 2024). Four of the stars in our analysed sample are also included in the Magellan/MIKE sample Sk −67° 78, Sk −70° 16, Sk −68° 8, and Sk −67° 195.

3.1.5 Photometry

The photometric data are presented in Table 3.2. The photometric magnitudes we used in the SED fitting to obtain the bolometric luminosities of the targets were taken from various sources and compiled in Vink et al. (2023). The UBV photometry are drawn from Ardeberg et al. (1972); Isserstedt (1975); Schmidt-Kaler et al. (1999) and Massey (2002).

The infrared JK_S photometry are preferably taken from the *VISTA near-infrared* YJK_S *survey of the Magellanic System* (VMC, Cioni et al., 2011), with H-band photometry taken from the *Two Micron All Sky Survey* (2MASS, Cutri et al., 2003; Skrutskie et al., 2006). For very bright sources that are saturated in VMC (Cioni et al., 2011) we use the J and K_S photometry provided in 2MASS (Skrutskie et al., 2006).

3.1.6 UV normalisation

The UV spectra require normalisation, which is challenging due to the iron forest that heavily contaminates the continuum. Fig. 2.4 shows normalised UV spectra of a subset of our sample. The quality of the fits to the UV lines is highly dependent on the quality of the normalisation of the observed spectrum. On average, we obtained very good normalised UV and far UV spectra for the targets by using the SED fitting explained later in Section 2.3.4 to obtain the bolometric luminosities of the targets. In essence, we apply the reddening law to the normalised synthetic spectrum of the best-fitting model and scale it to the flux levels of the observed spectrum using the K_S magnitude, then simply divide the observed spectrum by the extincted and scaled continuum of the model to obtain a normalised spectrum with relative flux values.

Table 3.3: Derived stellar parameters based on the best fitting CMFGEN model. Presented uncertainties for effective temperatures $T_{\rm eff}$ are double the model uncertainty. In the uncertainties of centrifugal force-corrected surface gravity $\log g_c$, we take into account the model uncertainty of $\log g$ and the uncertainty of the projected rotational velocity $v_{\rm rot} \sin i$ and the radius R_*. The uncertainty in the derived luminosities is $\Delta \log L_{\rm bol} = 0.1$ The uncertainty in radial velocity $v_{\rm rad}$ measurements is dominated by the velocity resolution of the UBV part of the spectrum, which is $\Delta v \approx 45$ km s^{-1}. The relative extinction $R_{\rm V}$ ($\Delta R_{\rm V} \approx 0.3$ mag), colour excess $E(B-V)$ ($\Delta E(B-V) \approx 0.05$ mag), absolute V-band magnitude $M_{\rm V}$, and bolometric correction $BC_{\rm V}$ are produced from the SED fits that are shown in Appendix A.5. $\Gamma_{\rm e}^{\rm spec}$ is subject to uncertainties of $\Delta\Gamma_{\rm e}^{\rm spec} \approx 0.18$ which takes into account the uncertainties of $M_{\rm spec}$ and $\log L_{\rm bol}$

Sk −	$T_{\rm eff}$	Diag.	$\log g_c$	R_*	$\log L_{\rm bol}$	$R_{\rm V}$	$E(B-V)$	$M_{\rm V}$	$BC_{\rm V}$	$v_{\rm rad}$	$v_{\rm rot} \sin i$	$M_{\rm spec}$	$\Gamma_{\rm e}^{\rm spec}$
	kK		cm s^{-2}	$R_\odot$	$L_\odot$		mag	mag	mag	km s^{-1}	km s^{-1}	$M_\odot$	
66° 171	29.9±1.0	He I – He II	3.11±0.20	25	5.67	1.9	0.16	−6.6	−2.83	410	75	31^{+18}_{-11}	0.36
68° 155	29.0±1.0	He I – He II	3.06±0.20	26	5.64	2.9	0.29	−6.6	−2.76	240	80	29^{+17}_{-11}	0.36
69° 279	28.5±2.0	He I – He II	2.95±0.25	27	5.63	2.6	0.34	−6.6	−2.76	230	40	24^{+14}_{-9}	0.45
71° 41	29.2±1.0	He I – He II	3.12±0.20	23	5.53	2.8	0.25	−6.3	−2.77	260	45	25^{+15}_{-9}	0.35
68° 135	26.9±1.5	He I – He II	2.82±0.24	51	6.10	2.8	0.28	−7.9	−2.60	270	45	65^{+38}_{-24}	0.48
67° 5	25.6±1.0	He I – He II	2.81±0.20	45	5.89	2.2	0.17	−7.5	−2.46	295	65	47^{+28}_{-17}	0.38
68° 52	26.0±1.0	Si III – Si IV	2.85±0.20	42	5.87	2.9	0.22	−7.4	−2.51	255	50	46^{+27}_{-17}	0.41
69° 43	22.4±1.0	Si III – Si IV	2.71±0.21	40	5.55	2.5	0.19	−7.0	−2.14	255	50	29^{+17}_{-11}	0.31
68° 140	24.1±1.0	Si III – Si IV	2.81±0.21	33	5.52	3.1	0.34	−6.7	−2.32	260	50	26^{+15}_{-9}	0.33
67° 2	18.8±1.0	Si III – Si IV	2.31±0.21	71	5.76	2.7	0.27	−7.9	−1.73	320	45	38^{+22}_{-14}	0.36
67° 14	21.1±1.0	Si III – Si IV	2.51±0.21	46	5.58	1.6	0.16	−7.2	−2.00	300	50	25^{+15}_{-9}	0.38
69° 52	18.8±1.0	Si III – Si IV	2.31±0.21	59	5.60	1.9	0.28	−7.5	−1.73	260	50	26^{+15}_{-10}	0.36
67° 78	15.5±1.0	Si II – Si III	2.10±0.21	75	5.47	2.2	0.17	−7.6	−1.33	310	30	26^{+15}_{-10}	0.29
70° 16	18.4±1.0	Si II – Si III	2.61±0.21	27	4.88	1.9	0.19	−5.8	−1.70	265	30	11^{+6}_{-4}	0.18
68° 8	14.1±1.0	Si II – Si III	1.81±0.21	102	5.57	2.4	0.25	−8.1	−1.13	250	35	24^{+14}_{-9}	0.37
67° 195	12.6±1.0	He I – Mg II	2.11±0.22	44	4.65	2.9	0.14	−6.1	−0.83	300	25	9^{+5}_{-3}	0.12

Table 3.4: Evolutionary parameters of our sample. $M_{\rm init}$, $M_{\rm evo}$, and ages of the stars are derived using an updated Bayesian inference method (Bronner et al. in prep) that is similar to BONNSAI (Schneider et al., 2014a) applied to Brott et al. (2011) evolutionary tracks.

Sk −	$T_{\rm eff}$	$\log g_c$	$\log L_{\rm bol}$	$M_{\rm init}$	$M_{\rm evo}$	Age	$\Gamma_{\rm e}^{\rm evo}$
	kK	$\rm cm\,s^{-2}$	$L_\odot$	$M_\odot$	$M_\odot$	My	
66° 171	29.9	3.11	5.67	35^{+9}_{-4}	30^{+8}_{-2}	$5.2^{+0.7}_{-1.0}$	$0.37^{+0.1}_{-0.03}$
68° 155	29.0	3.06	5.64	34^{+8}_{-8}	30^{+8}_{-5}	$5.5^{+0.2}_{-1.0}$	$0.35^{+0.1}_{-0.05}$
69° 279	28.5	2.95	5.63	34^{+7}_{-3}	30^{+8}_{-1}	$4.2^{+0.6}_{-0.4}$	$0.35^{+0.09}_{-0.03}$
71° 41	29.2	3.12	5.53	33^{+5}_{-3}	30^{+5}_{-2}	$4.2^{+0.6}_{-0.3}$	$0.29^{+0.05}_{-0.02}$
68° 135	26.9	2.82	6.10	61^{+17}_{-7}	52^{+15}_{-5}	$3.3^{+0.7}_{-0.7}$	$0.60^{+0.17}_{-0.06}$
67° 5	25.6	2.81	5.89	44^{+9}_{-5}	38^{+6}_{-4}	$4.8^{+0.3}_{-1.0}$	$0.47^{+0.08}_{-0.05}$
68° 52	26.0	2.85	5.87	50^{+7}_{-8}	45^{+7}_{-6}	$3.4^{+0.5}_{-0.3}$	$0.42^{+0.07}_{-0.06}$
69° 43	22.4	2.71	5.55	32^{+4}_{-4}	29^{+4}_{-2}	$5.2^{+0.4}_{-0.7}$	$0.31^{+0.04}_{-0.03}$
68° 140	24.1	2.81	5.52	30^{+4}_{-3}	29^{+4}_{-3}	$5.2^{+0.6}_{-0.7}$	$0.29^{+0.04}_{-0.03}$
67° 2	18.8	2.31	5.76	42^{+8}_{-3}	37^{+6}_{-2}	$4.2^{+0.4}_{-0.5}$	$0.38^{+0.07}_{-0.03}$
67° 14	21.1	2.51	5.58	40^{+3}_{-6}	36^{+2}_{-4}	$4.8^{+0.4}_{-0.4}$	$0.27^{+0.02}_{-0.03}$
69° 52	18.8	2.31	5.60	41^{+6}_{-2}	36^{+4}_{-1}	$4.4^{+0.3}_{-0.2}$	$0.27^{+0.04}_{-0.02}$
67° 78	15.5	2.10	5.47	29^{+4}_{-4}	28^{+3}_{-4}	$5.5^{+1.0}_{-0.6}$	$0.27^{+0.03}_{-0.04}$
70° 16	18.4	2.61	4.88	16^{+1}_{-1}	16^{+1}_{-1}	$10.4^{+1.6}_{-1.1}$	$0.12^{+0.01}_{-0.01}$
68° 8	14.1	1.81	5.57	32^{+5}_{-4}	23^{+5}_{-5}	$5.2^{+0.7}_{-0.8}$	$0.31^{+0.06}_{-0.06}$
67° 195	12.6	2.11	4.65	13^{+1}_{-1}	13^{+1}_{-0}	$13.9^{+1.7}_{-1.9}$	$0.08^{+0.01}_{-0.01}$

3.2 Results

We present below an overview of the results obtained using the methods presented in Chapter 2 and compare them to other theoretical and empirical results that used the combined UV and optical or the optical range alone. Best-fitting physical parameters are presented in Table 3.3. In Table 3.4, we present the inferred evolutionary masses and ages from BONNSAI (Schneider et al., 2014a) applied to Brott et al. (2011) rotating single-star evolutionary models for LMC metallicity. The details of v_∞ measurements are presented in Appendix A.2. The table containing the literature values can be found in Appendix A.3. The quality of our analysis is described for each star individually in Appendix A.4. The SED fits, individual line fits, and overall spectral fits are presented in Appendix A.5, A.6 and A.7, respectively. Finally, the FM90 UV SED fitting parameters are presented in A.8.

3.2.1 Hertzsprung-Russell diagram

Fig. 3.2 shows the location of our targets on a Hertzsprung-Russell diagram (HRD). Our sample spans a range of temperatures $\log(T_{\rm eff}/{\rm K}) \approx 4.1-4.5$, while luminosities cover a broad range of $\log(L_{\rm bol}/L_\odot) \approx 4.50-6.10$ (see Table 3.3). The extremely luminous star is the hypergiant Sk -68° 135 with $\log(L_{\rm bol}/L_\odot) \approx 6.1$.

The majority of our sample exceeds $\log(L_{\rm bol}/L_\odot) \approx 5.4$, except for Sk -70° 16, which is a bright giant (II), and Sk -67° 195, which is a B8 Ib supergiant, according to Bestenlehner et al. (2025). Overall, the majority of the sample lies between the ZAMS and the terminal-age main sequence (TAMS), according to the evolutionary models of Brott et al. (2011), but several targets, assuming a single-star evolutionary scenario, are located beyond the TAMS and would therefore be identified as post-main-sequence stars.

Fig. 3.3 shows the location of our targets on the spectroscopic Hertzsprung-Russell diagram (sHRD, Langer & Kudritzki, 2014). $\mathcal{L} = T_{\rm eff}^4/g$ is a distance-independent para-

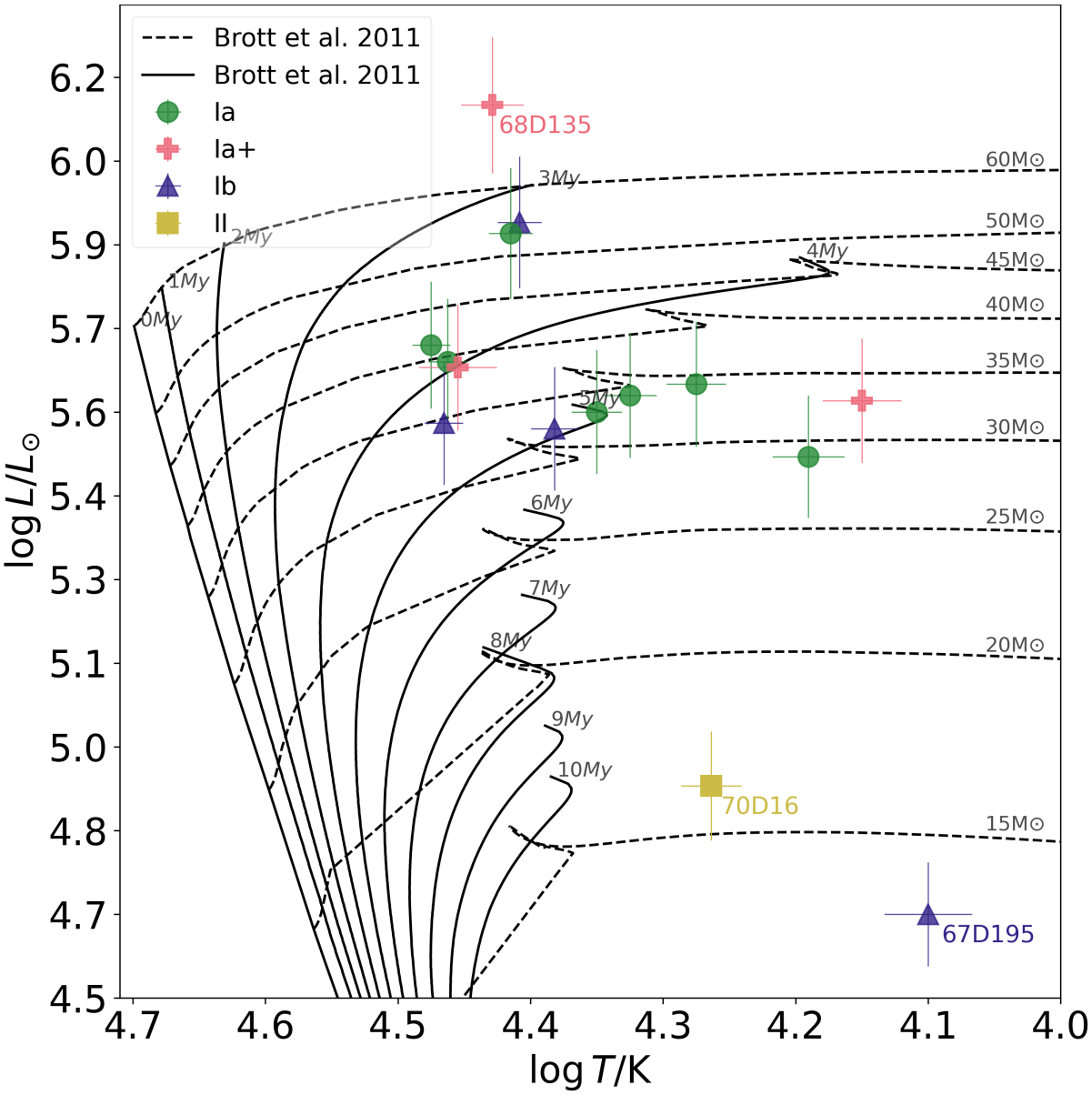


Figure 3.2: Hertzsprung-Russell diagram for our sample. The non-rotating isochrones for different ages ($\approx [0-10]$ Myr) are overlaid as solid black lines, and the evolutionary tracks for stellar masses in the range $\approx [10-60]$ $M_{\odot}$ with a rotational velocity of 50 km s^{-1} are shown as dashed black lines. The isochrones and evolutionary tracks were adopted from Brott et al. (2011).

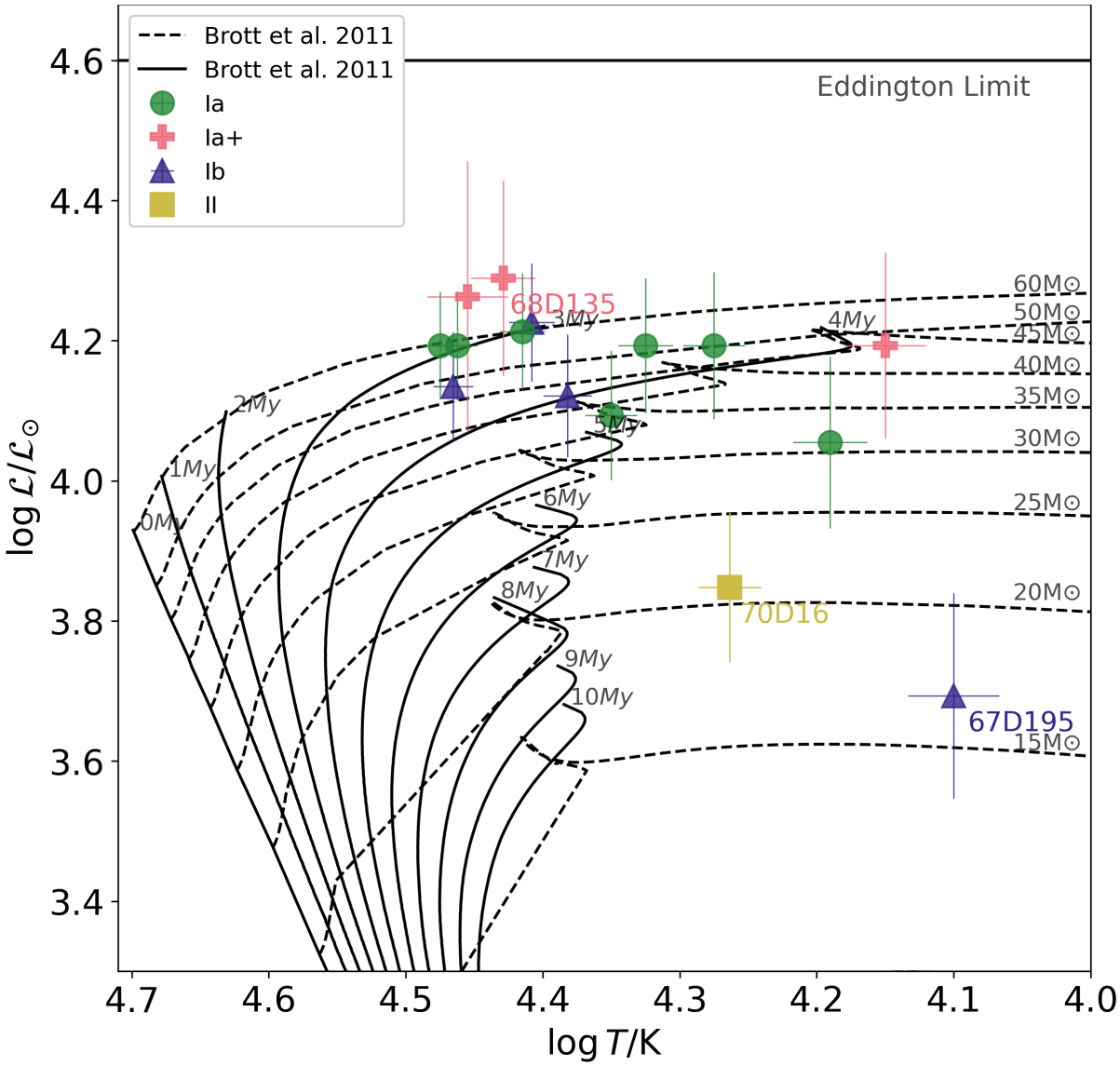


Figure 3.3: Spectroscopic Hertzsprung-Russell diagram for our sample. The evolutionary tracks (solid black lines) and the isochrones (dashed black lines) are the same as in Fig. 3.2, which are taken from Brott et al. (2011). The Encoding of the luminosity classes is the same as in Fig. 3.2

meter, that is proportional to the luminosity-to-mass ratio, i.e. the Eddington factor. Therefore, the sHRD is helpful for direct comparison with the HRD and also shows the proximity of the star to the Eddington limit, giving insight into stellar evolution without prior information about the distance. $\mathcal{L}_\odot \approx 10.6\ \mathrm{k^4\,s^2\,cm^{-1}}$ is calculated assuming solar values of $T_{\rm eff} = 5777$ K and $\log(g/\mathrm{cm\,s^{-2}}) = 4.44$. The majority of our stars fall in the $\log \mathcal{L}/\mathcal{L}_\odot$ range of 4.0−4.3. We find that the hypergiants are the closest to the Eddington limit of $\log \mathcal{L}/\mathcal{L}_\odot \approx 4.6$ (assuming a hydrogen mass fraction of 0.73). As expected, the low-luminosity supergiant Sk −67° 195 and the bright giant Sk −70° 16 are also farthest away from the Eddington limit, with $\log \mathcal{L}/\mathcal{L}_\odot$ equal to 3.68 and 3.82, respectively.

We also compare a calibration of the bolometric correction in the visual band $BC_{\rm V}$ versus $T_{\rm eff}$ to the calibration obtained by Lanz & Hubeny (2007a) from TLUSTY non-LTE plane-parallel models of B stars. A simple fit to our dataset reveals

$$BC_{\rm V}/\mathrm{mag} = 21.00 - 5.33 \log(T_{\rm eff}/\mathrm{K}), \tag{3.1}$$

with a standard deviation of ≈ 0.1 mag, which support the results of Lanz & Hubeny (2007a) for the LMC, who find: $BC_{\rm V}/\mathrm{mag} = 21.08 - 5.36 \log(T_{\rm eff}/\mathrm{K})$. As to be expected for a UV-bright sample, extinctions are relatively low with an average colour excess $E(B-V) = 0.23 \pm 0.06$ mag, and an average total extinction in the V-band $A_{\rm V}^{\rm average} = 0.6 \pm 0.4$ mag. This agrees with the findings of Gordon et al. (2003).

3.2.2 Stellar masses

Evolutionary masses ($M_{\rm evo}$) presented in Table 3.4 are derived via a Bayesian inference method that is similar to Bonnsai (Schneider et al., 2014a) with updated techniques (Bronner et al. in prep) applied to LMC tracks from Brott et al. (2011) with $L_{\rm bol}$, $T_{\rm eff}$, $\log g$, $v_{\rm rot} \sin i$, and $\log \frac{\rm He}{\rm H} + 12$ as input parameters. Our sample spans a wide range from ($M_{\rm evo}$) of $13.20^{+1.17}_{-0.10}\ M_\odot$ (Sk −67° 195) to $52.35^{+14.90}_{-4.63}\ M_\odot$ (Sk −68° 135). Table 3.3

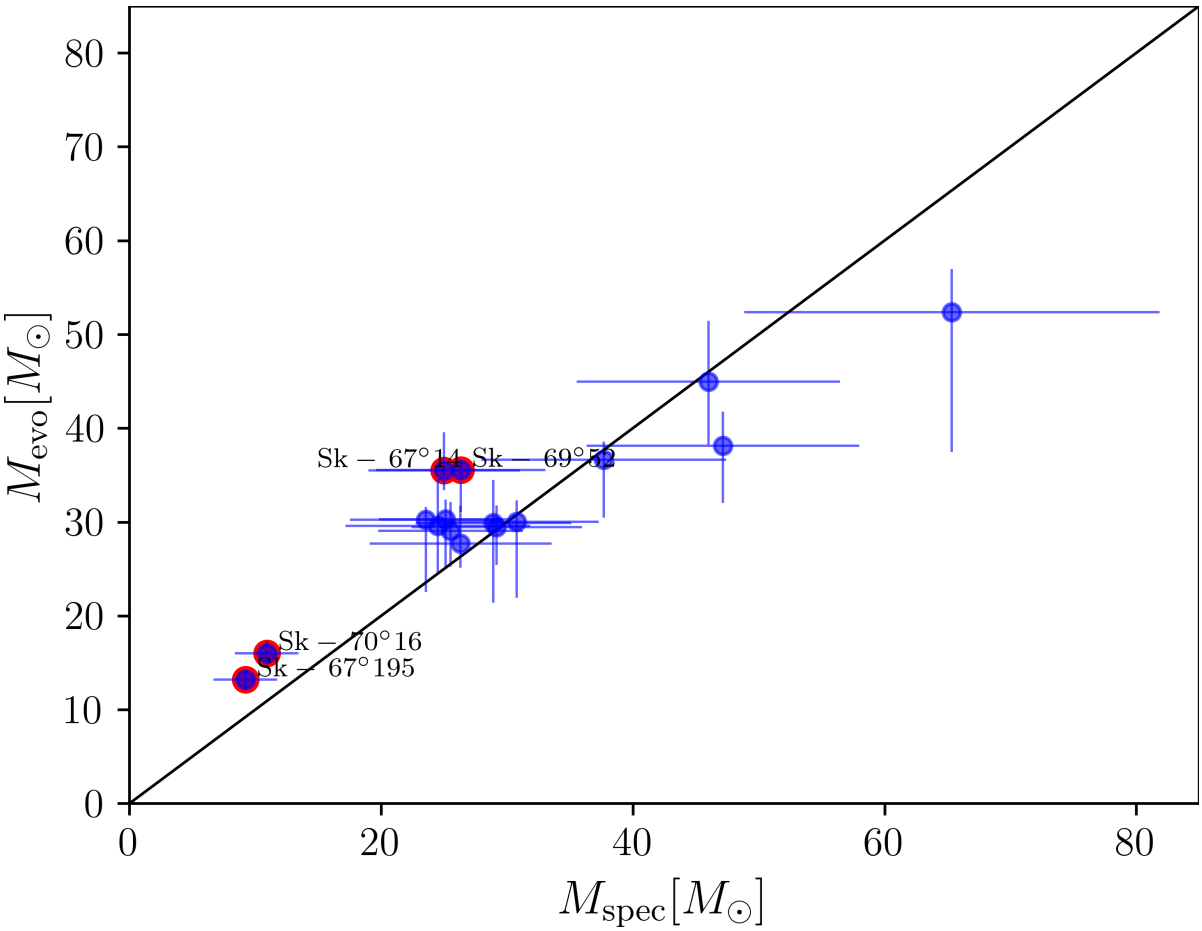


Figure 3.4: Blue circles show the spectroscopically obtained mass from our analysis $M_{\rm spec}$ vs. the mass produced by BONNSAI (Schneider et al., 2014a) applied to evolutionary tracks from Brott et al. (2011) $M_{\rm evo}$. Red circles overlaid onto the blue points depict stars that have a significant discrepancy between their $M_{\rm spec}$ and $M_{\rm evo}$.

also includes stellar ages that range from $3.40^{+0.45}_{-0.34}$ Myr (Sk −68° 135) to $13.94^{+1.70}_{-1.87}$ Myr (Sk −67° 195).

In Table 3.3 we present our values of the true surface effective gravity $\log\,(g_c/{\rm cm\,s^{-2}}) = \log\,(g_{\rm model} + v_{\rm rot}\sin i^2/R_*)$, where R_* is obtained from StefanBoltzmann law. g_c takes into account the centrifugal force due to stellar rotation (Herrero et al., 1992). Our values range from $\log g_c \approx 1.8$ to 3.1 due to the stars possessing large radii ($R_* > 20\ R_\odot$), which is expected for a sample that consists of evolved OB stars.

We derive the spectroscopic masses ($M_{\rm spec}$) from the gravities via $g = G\,M/R_*^2$. Therefore, we derive relative uncertainties of $25\% - 40\%$, which mainly depend on the

uncertainties of $\log g$, which is largely affected by the quality of normalisation. To put this into perspective, a difference in the wings of the Balmer lines of 1% can potentially lead to a $\log g$ difference up to ≈ 0.1 dex. Such a difference leads to a relative uncertainty of $\Delta M_{\rm spec} \approx 20\%$.

Spectroscopic masses are compared to evolutionary masses in Fig. 3.4. This shows that, for most of the stars, $M_{\rm spec}$ and $M_{\rm evo}$ are consistent within the uncertainties, similar to what Schneider et al. (2018) finds in a large sample of OB stars. For some of the stars (red circles in Fig. 3.4), the mass discrepancy that was established for Galactic O supergiants by Herrero et al. (1992), and later expanded to SMC O stars by Trundle et al. (2004b) and further to Galactic B supergiants in Crowther et al. (2006) persists. We find that the spectroscopic masses for these stars are significantly lower than the masses produced by evolutionary models. The Eddington parameter $\Gamma_{\rm e}^{\rm evo}$ presented in Table 3.4 is derived using the evolutionary masses and it ranges from $\Gamma_{\rm e}^{\rm evo} = 0.08^{+0.01}_{-0.01}$ (Sk -67° 195) to $0.60^{+0.17}_{-0.06}$ (Sk -68° 135).

3.2.3 Wind properties

Terminal wind velocity v_∞

Measured wind velocities are presented in Table 3.5. In Fig. 3.5 we compare our $v_\infty - (T_{\rm eff})$ to the empirical recipe of Hawcroft et al. (2024a), adopting a simple linear fit of the form

$$v_\infty [\mathrm{km\,s^{-1}}] = a T_{\rm eff} [\mathrm{K}] \; - \; b. \tag{3.2}$$

In Table 3.6 we present the parameters of the linear fit in Equation 3.2. We find that our v_∞-$T_{\rm eff}$ relation agrees with the relation obtained by Hawcroft et al. (2024a) within the uncertainties. We note that the two outliers are the hypergiants Sk -69° 279 and Sk -68° 135, which have abnormally low v_∞ compared to stars of similar temperatures.

We also compare our results to numerical predictions of wind velocity from Vink

Table 3.5: Wind parameters for our targets. The mass-loss rates of Sk −70° 16 and Sk −67° 195 are upper limits. The escape velocities are adjusted for Γ_e. v_∞ values with the superscript ‡ indicate that v_∞ was inferred as $v_{edge} \times \langle v_{black}/v_{edge} \rangle_{LMC}$.

Target	L_{bol}	$\log \dot{M}$	v_∞	$v_{esc,(1-\Gamma_e)}$	β	f_{vol}	v_{cl}
Sk −	$L_\odot$	$M_\odot\,yr^{-1}$	$km\,s^{-1}$	$km\,s^{-1}$			$km\,s^{-1}$
66° 171	5.67	−6.07	1775	537	1.7	0.03	30
68° 155	5.64	−6.19	1520	524	1.5	0.03	30
69° 279	5.63	−5.70	630	467	2.7	0.1	30
71° 41	5.53	−6.03	1390	548‡	1.2	0.1	35
68° 135	6.10	−5.70	880	440	2.3	0.1	35
67° 5	5.89	−6.05	1230	460	1.3	0.1	30
68° 52	5.87	−6.28	1140	488	2.0	0.03	35
69° 43	5.55	−6.49	825	440	2.0	0.1	30
68° 140	5.52	−6.46	1000	456	2.2	0.1	30
67° 2	5.76	−6.21	435	355	3.0	0.14	30
67° 14	5.58	−6.33	810	390	2.0	0.1	30
69° 52	5.60	−6.62	465	352	2.5	0.14	25
67° 78	5.47	−6.70	380	311‡	3.0	0.2	30
70° 16	4.88	−7.60	235	366‡	1.0	0.1	25
68° 8	5.57	−6.50	210	253‡	1.0	0.1	25
67° 195	4.65	−7.50	210	269	1.0	0.1	25

Table 3.6: Slopes, a, and offsets, b, of the linear fits to the terminal wind velocity equation (Equation 3.2) of this study and Hawcroft et al. (2024a)

LMC	a	b
	K	$km\,s^{-1}$
This study	0.076 ± 0.011	884 ± 260
Hawcroft et al. (2024a)	0.085 ± 0.050	1150 ± 170

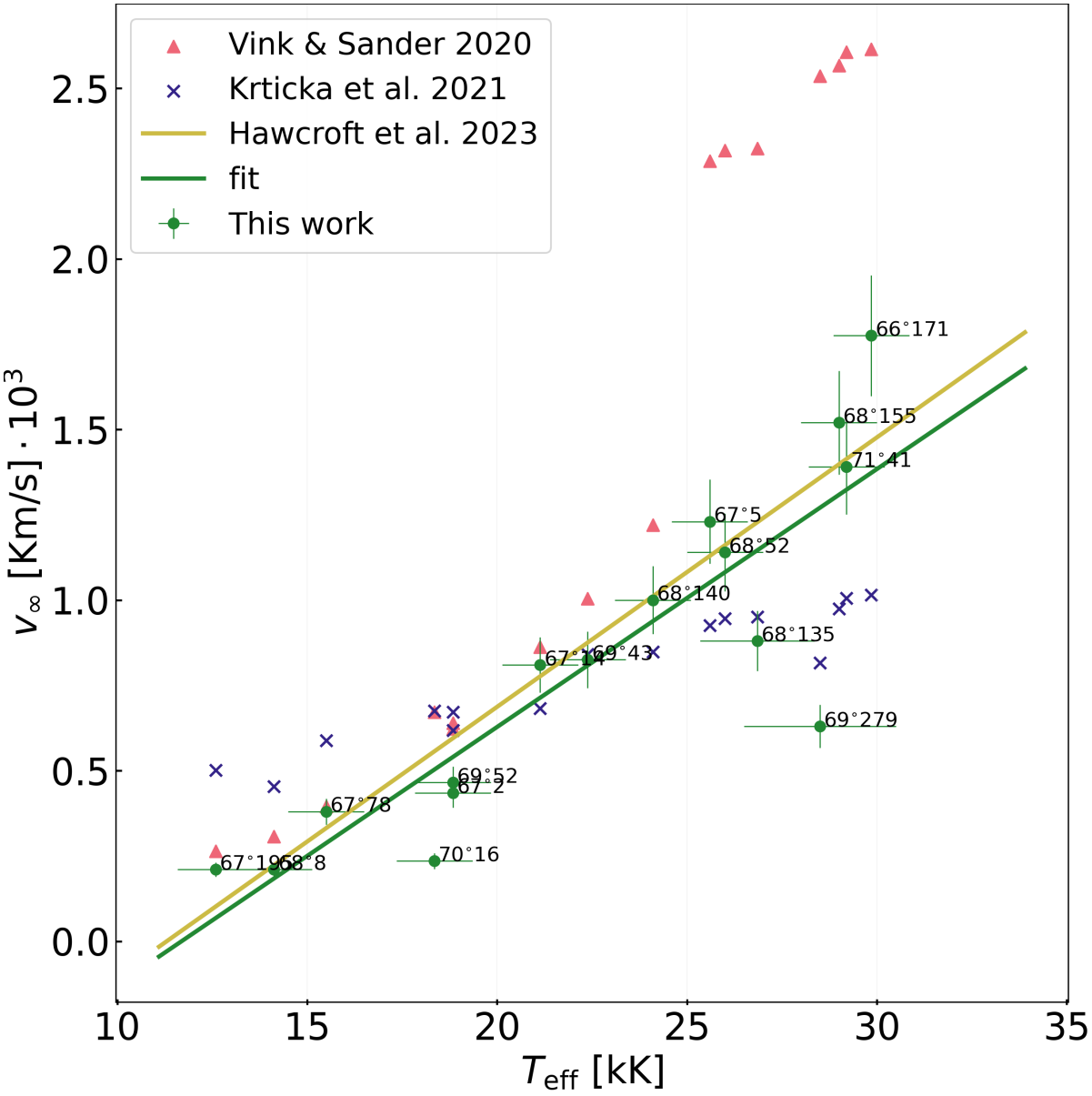


Figure 3.5: v_∞ vs. $T_{\rm eff}$ for LMC supergiants. Green dots: results from this work, green line: linear fit of our results, yellow line: v_∞-$T_{\rm eff}$ relation from Hawcroft et al. (2024a), pink triangles: v_∞ calculated velocities from Vink & Sander (2021) recipe, violet diagonal cross: v_∞ calculated velocities from (Krtička et al., 2021) recipe.

& Sander (2021) and Krtička et al. (2024). The velocities calculated using the recipe provided in Vink & Sander (2021), which was obtained using a locally consistent Monte Carlo radiative transfer model (Müller & Vink, 2008), agree with our measurements for stars located at the 'cool' side of the bi-stability jump predicted in Vink et al. (2001) (< 25 kK), where as we find large discrepancies in the wind velocities of the objects that are located above the 'hot' edge of the bi-stability jump. As for the velocities calculated by the recipe presented in Krtička et al. (2024), we find that there is a discrepancy in the general trend, but just as in our results, there is a lack of a downward jump in the temperature range $T_{\rm eff} \approx 25{-}21$ kK.

We also calculate the values of the escape velocity of each star (see Table 3.5) using the evolutionary mass obtained via BONNSAI as explained in Section 3.2.2. We discuss the implications of our findings later in Section 3.3.1.

Mass loss and clumping

Fig. 3.6 presents the spectral fits to Hα for all the stars in our sample. Aside from a few peculiar cases, our models well reproduce the overall shape and intensity of the emission feature in Hα. The results for the true mass-loss rates that are scaled to the transformed radius and volume-filling factor are presented in Table 3.5.

A good indicator of wind strength is the Eddington ratio ($\Gamma_{\rm e} = L_{\rm bol}/L_{\rm edd}$), and it is expected that objects with higher $\Gamma_{\rm e}$ will have a greater mass-loss rate (Vink et al., 2011; Bestenlehner et al., 2014). In Fig. 3.7 a correlation between $\Gamma_{\rm e}$ and $\dot{M}$ is revealed.

Our method revolves around applying the spectral fitting techniques described in Chapter 2 to a single XShootU observation, completely disregarding the intrinsic variability of wind diagnostics (Massa et al., 2024). To display the effect of wind variability on optical wind diagnostics, we present the Magellan/MIKE (Crowther, 2024) Hα spectrum of Sk -67° 78 in Fig. 3.8 and compare it to the XShootU spectrum of Hα.

Hα in this case is significantly weaker in MIKE observations with respect to XShootU.

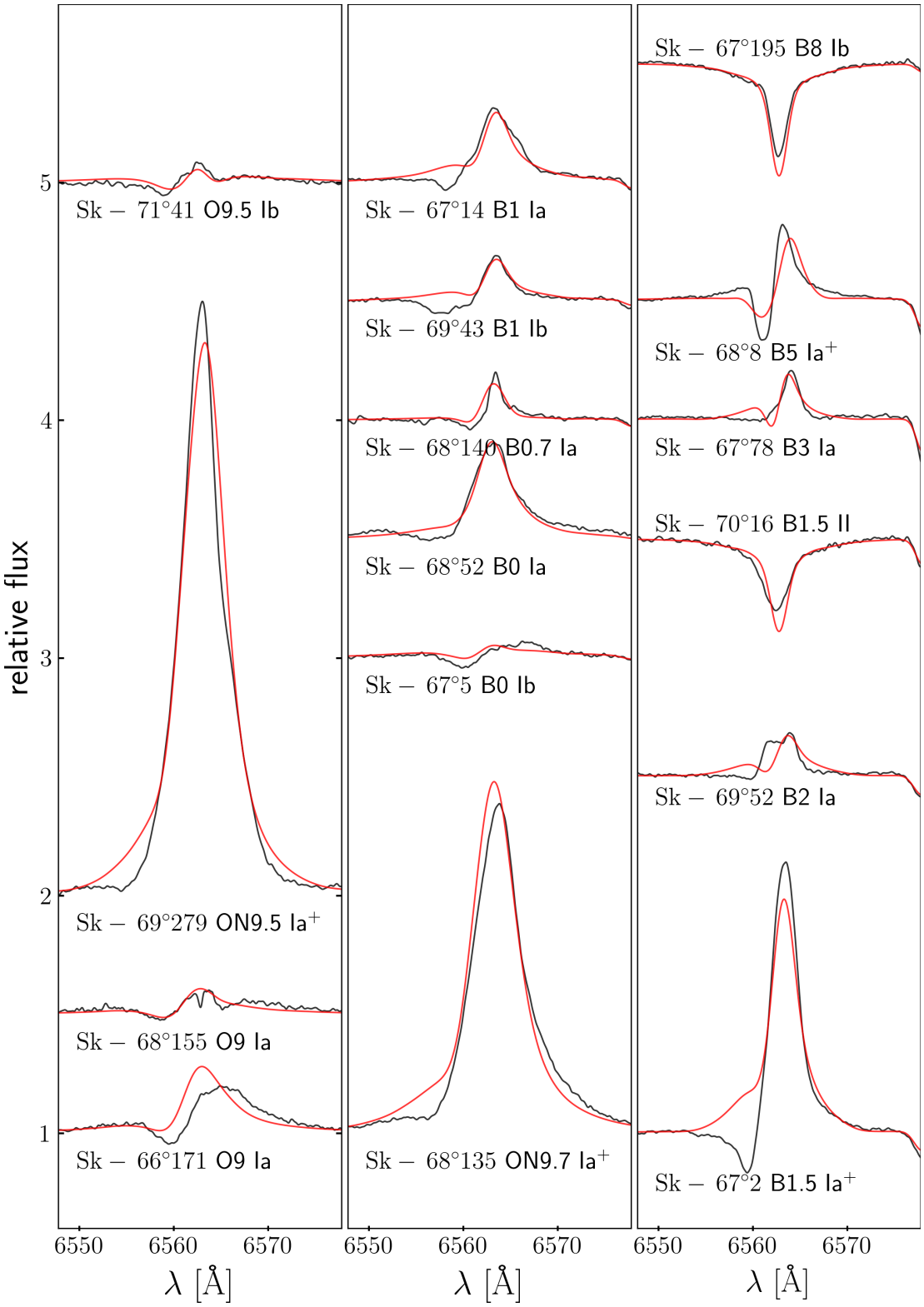


Figure 3.6: Spectral fits to Hα for our sample of OB supergiants. Black line: observations, red line: model fit

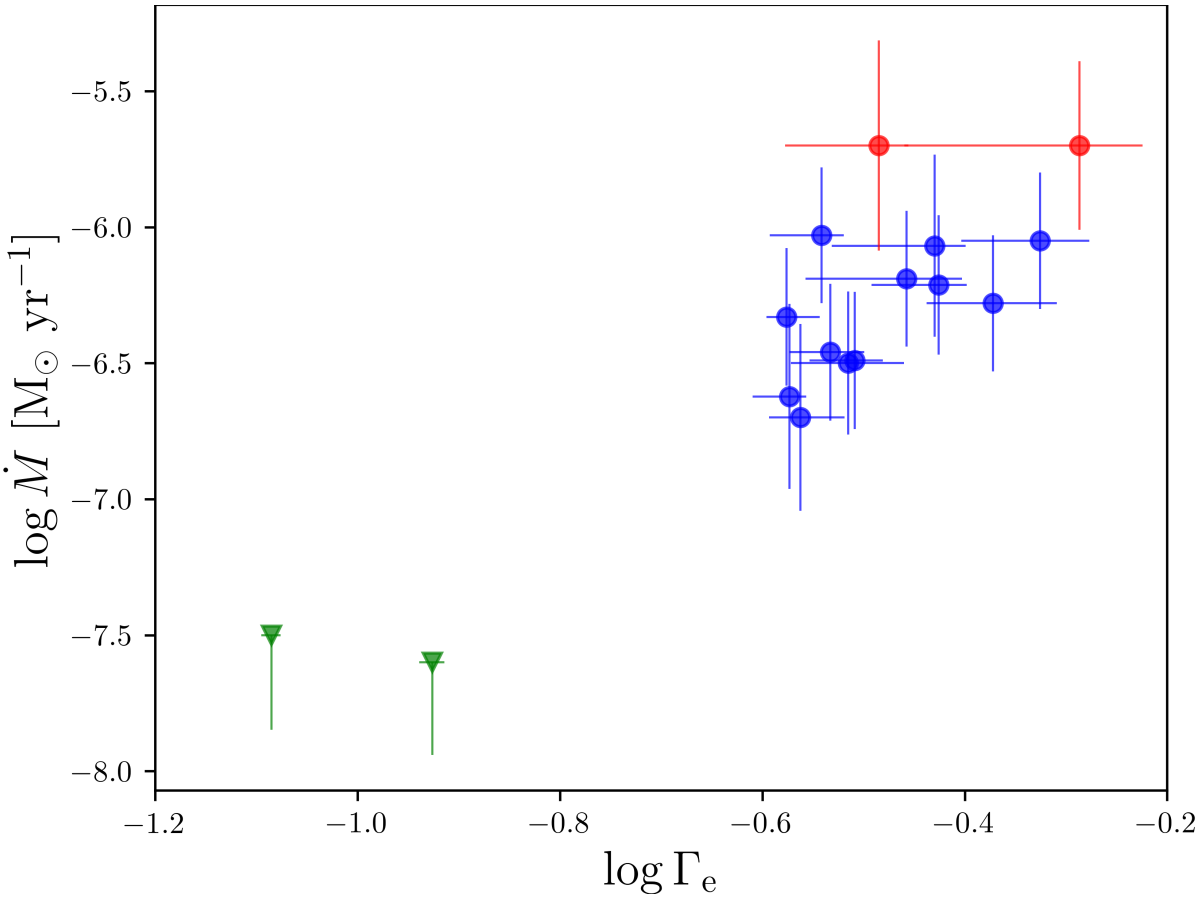


Figure 3.7: $\dot{M}$ vs. Γ_e^{spec}. The green triangles indicate the objects Sk −67° 195 and Sk −70° 16, the mass-loss rates of which are considered upper limits. The red points correspond to the hypergiants Sk −67° 279 and Sk −68° 135.

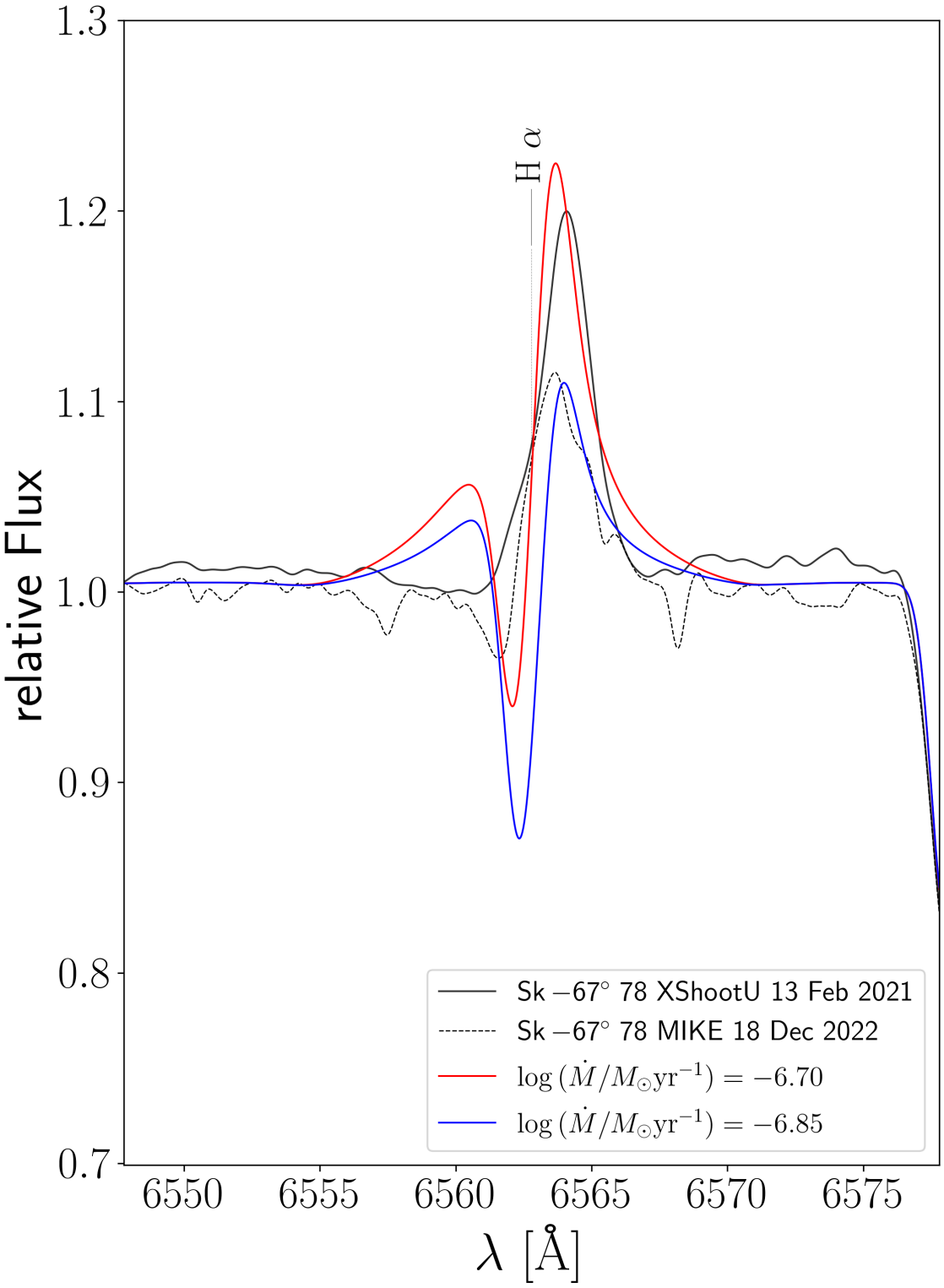


Figure 3.8: Hα of Sk −67° 78 from MIKE observations (dashed black line) overlaid on Hα from XShootU (solid black line) with our best-fitting model (solid red line) and the preferred fit for MIKE observations (solid blue line).

This would lead to different $\dot{M}$, β and $f_{\rm vol}$ if we were to apply our fitting to MIKE data. Our tests showed that fitting the MIKE Hα requires a $\log \dot{M}$ that is lower by 0.15 dex. Therefore, we include a factor of 2 in the uncertainties of the model mass-loss rates to take into account the possible variation in Hα and the additional error from having non-simultaneous UV and optical observations. This puts the uncertainty for the derived mass loss rates in the range $\Delta \log \dot{M} \approx \pm 0.2 - 0.4$ dex, which falls within our global uncertainty of $\Delta \log \dot{M} = 0.5$ dex.

For Sk -70° 16 and Sk -67° 195 we adopt $\beta = 1.0$ due to Hα being fully in absorption. For the rest of our sample, we find that higher $\beta = 2.0 \pm 0.6$ are preferred to achieve a satisfactory fit for Hα. This is in agreement with Crowther et al. (2006) in which CMFGEN was used to model cool Galactic B supergiants, and they find that an average value of 2.0 for β is necessary to achieve a good fit. This is also in agreement with Haucke et al. (2018), in which they analysed Galactic B supergiants using FASTWIND and find that the suitable average value for β is also $\approx 2.0 \pm 0.5$. We present our β values in Table 3.5.

Fig. 3.9 demonstrates the effect of varying β for Sk -68° 140. In the middle panel of Fig. 3.10, we present the line-formation region of Hα (blue solid line) for Sk -68° 140. The peak is at $\log (r/R_*) \approx 0.2 - 0.4$ (r is measured from the photosphere where $\tau_{ross} = 100$), which is well into the sonic regime of the atmosphere, and is averaged over a wide range of $v_{\rm wind}$ ($\log (r/R_*) \approx 0.1 - 0.8$). From Equation 2.13 it is clear that increasing β lowers the acceleration of the wind. This leads to lower wind velocities at the Hα line-formation region, where the wind has not yet reached its terminal velocity, resulting in higher densities at this region. This yields narrower red-shifted emission and blue-shifted absorption in Hα with less extended wings

In Fig. 3.9, although the model with $\beta = 2.5$ (the blue solid line on Fig. 3.9) fits the blue shifted absorption better its emission is weaker than the observation, and the model with $\beta = 2.0$ (green solid line), fits the extended red wing of the emission but has

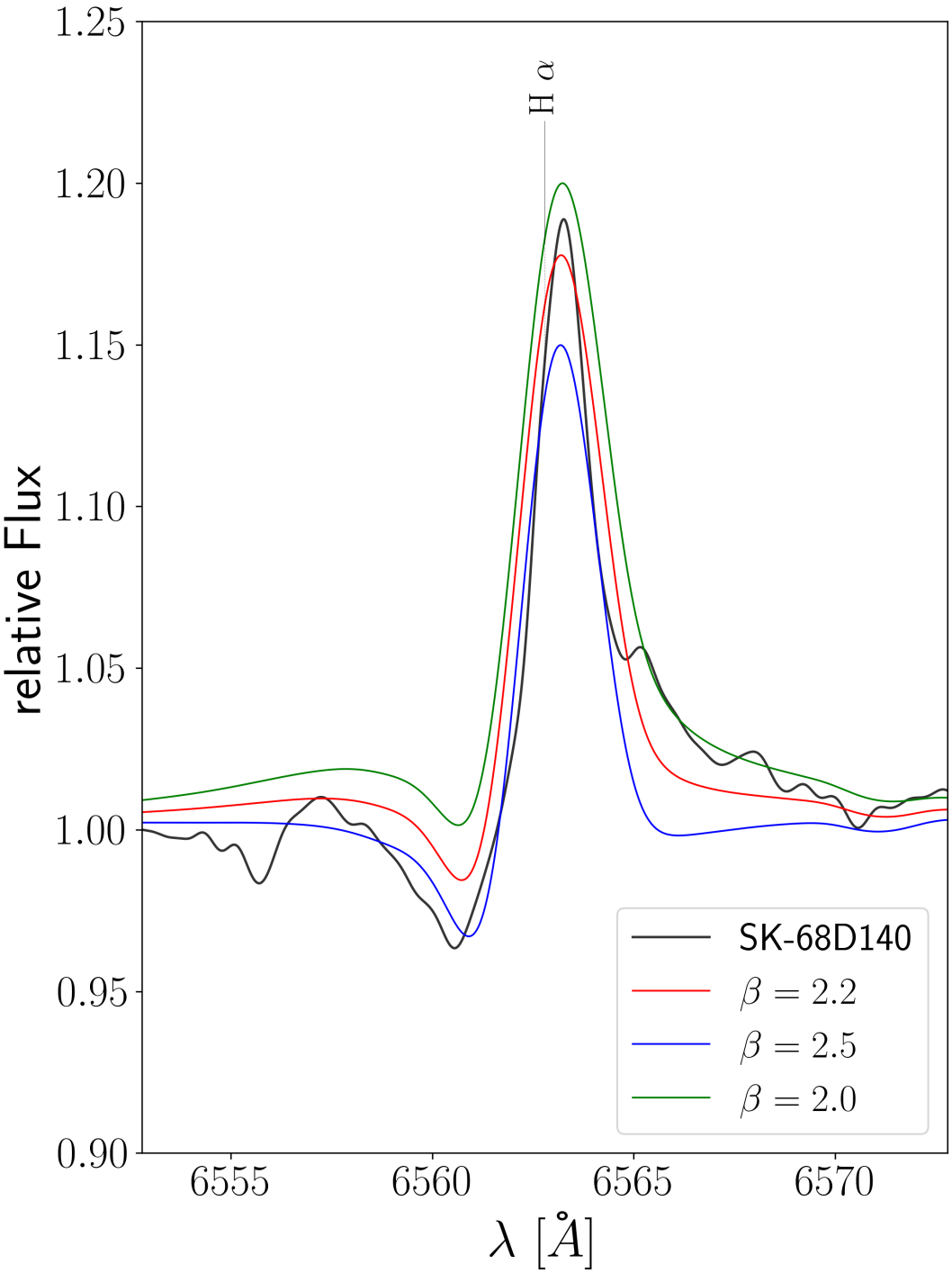


Figure 3.9: Best-fitting model $\beta = 2.2$ (solid red line) vs. two other models with $\beta = 2.5$ (solid blue line) and $\beta = 2.0$ (solid green line) for Hα of Sk $-68°$ 140 (solid black line)

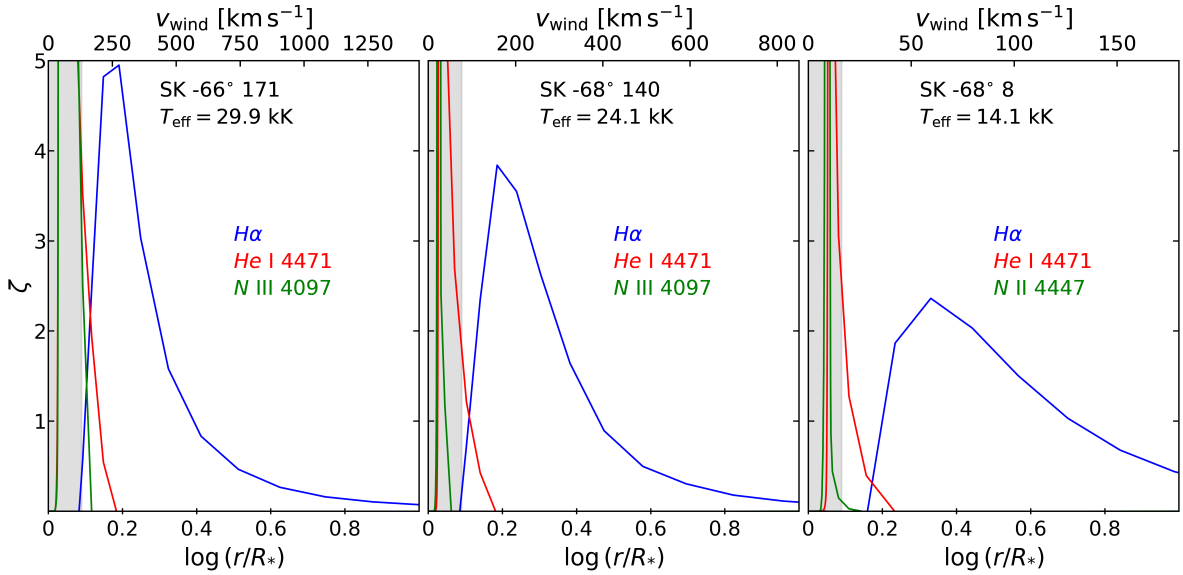


Figure 3.10: Line formation region (ζ vs. $\log(r/R_*)$) of Hα (solid blue line), He I λ4471 (solid red line), and a line from the dominating nitrogen ion (solid green line) for Sk -66° 171 ($T_{\rm eff}$ = 29.9 kK, left panel), Sk -68° 140 ($T_{\rm eff}$ = 24.1 kK, middle panel), and Sk -68° 8 ($T_{\rm eff}$ = 14.1 kK, right panel). The grey shaded region indicates the photosphere.

an overly extended blue wing and is stronger than the observed emission. Therefore, we select the model with $\beta = 2.2$ (red solid line), which matches the observed emission and fits the overall morphology of the line.

3.2.4 Line-broadening parameters

In Table 3.3 we include $v_{\rm rot} \sin i$, the values of which are within reasonable agreement with the spectroscopic pipeline results from Bestenlehner et al. (2025). The values of $v_{\rm rot} \sin i$ we obtain for our stars are in the range $\approx 25{-}80$ km s^{-1}.

In Table 3.7 we compare our derived $v_{\rm rot} \sin i$, which were obtained with the assumption of $v_{\rm mac} = 20$ km s^{-1}, to the $v_{\rm rot} \sin i$ and $v_{\rm mac}$ that were obtained by applying the IACOB-BROAD (Simón-Díaz & Herrero, 2014a) tool to a subsample of the stars with high-resolution MIKE data. IACOB-BROAD is a procedure based on a combined Fourier transform and goodness of fit approach that allows for the extraction of

Table 3.7: Comparison of our broadening parameters with those obtained via IACOB-BROAD (Simón-Díaz & Herrero, 2014a) applied to high-resolution MIKE data.

Sk −	XShootU		IACOB-BROAD		MIKE
	$v_{\rm rot} \sin i$	$v_{\rm mac}$	$v_{\rm rot} \sin i$	$v_{\rm mac}$	line
	km s^{-1}	km s^{-1}	km s^{-1}	km s^{-1}	
67° 2	45	20	46^{+10}_{-15}	40^{+17}_{-20}	Si III λ4552
67° 78	30	20	39^{+10}_{-29}	23^{+33}_{-22}	Si III λ4552
70° 16	35	20	40^{+10}_{-25}	35^{+13}_{-17}	Si III λ4552
68° 8	40	20	38^{+7}_{-15}	22^{+22}_{-20}	Si III λ4552
67° 195	30	20	28^{+8}_{-14}	28^{+14}_{-16}	Si II λ6347

line-broadening parameters from a single snapshot of OB-type star spectra.

We used Si III λ4552 for all stars in the subsample except for the late supergiant Sk −67° 195, for which we use Si II λ6347. We find that our derived $v_{\rm rot} \sin i$ are in good agreement with those obtained from IACOB-BROAD. On the other hand, we systematically underestimate $v_{\rm mac}$ by $\approx$ 10 km s^{-1}. This implies that we could potentially be underestimating the CNO abundances in our sample, albeit this underestimation is well within our adopted uncertainties of 0.3 dex.

3.2.5 He and CNO abundances

Table 3.8 presents the results for the chemical abundances of He and CNO elements. The analysis shows an overall boost in helium at the expense of hydrogen relative to the LMC baseline helium mass fraction of $Y = 0.25$ (Brott et al., 2011). This is to be expected for a sample of evolved stars. We would also expect nitrogen enrichment at the expense of oxygen and carbon, which are depleted due to CNO-cycle processing. Indeed, nitrogen abundances are significantly higher than the LMC baseline (Fig. 3.11), with a mean enhancement of 1 dex and a spread of 0.5 dex. We also note that our sample is mostly carbon and oxygen depleted, with the exception of Sk −71° 41 and Sk −67° 2

Table 3.8: Best-fitting photospheric abundances ϵ_X. The final two columns list the cumulative CNO abundances relative to the LMC baseline (Vink et al., 2023) and solar (Asplund et al., 2005). The adopted uncertainty on the CNO abundances is ±0.3

Sk −	Y	ϵ_C	ϵ_N	ϵ_O	$\frac{\Sigma CNO}{\Sigma CNO_{LMC}}$	$\frac{\Sigma CNO}{\Sigma CNO_{\odot}}$
66° 171	0.43 ± 0.085	8.05	8.19	8.42	1.2	0.5
68° 155	0.43 ± 0.085	7.53	8.25	8.42	1.1	0.5
69° 279	0.36 ± 0.073	7.53	8.02	8.07	0.6	0.3
71° 41	0.30 ± 0.061	7.79	7.50	8.70	1.7	0.8
68° 135	0.36 ± 0.073	7.53	8.24	8.17	0.9	0.4
67° 5	0.47 ± 0.094	7.61	7.62	8.45	0.8	0.4
68° 52	0.30 ± 0.061	7.49	7.50	8.33	0.8	0.4
69° 43	0.30 ± 0.061	7.49	7.50	8.33	0.8	0.4
68° 140	0.30 ± 0.061	7.19	8.10	8.33	1.0	0.5
67° 2	0.43 ± 0.085	7.32	8.40	8.34	1.1	0.5
67° 14	0.36 ± 0.073	7.53	7.72	8.67	1.4	0.7
69° 52	0.43 ± 0.085	7.53	8.36	8.42	1.2	0.5
70° 16	0.30 ± 0.061	7.39	8.24	8.33	1.1	0.5
67° 78	0.30 ± 0.061	7.65	7.98	8.33	1.0	0.5
68° 8	0.40 ± 0.079	7.85	8.47	8.39	1.4	0.7
67° 195	0.36 ± 0.073	7.71	8.02	8.37	1.0	0.5

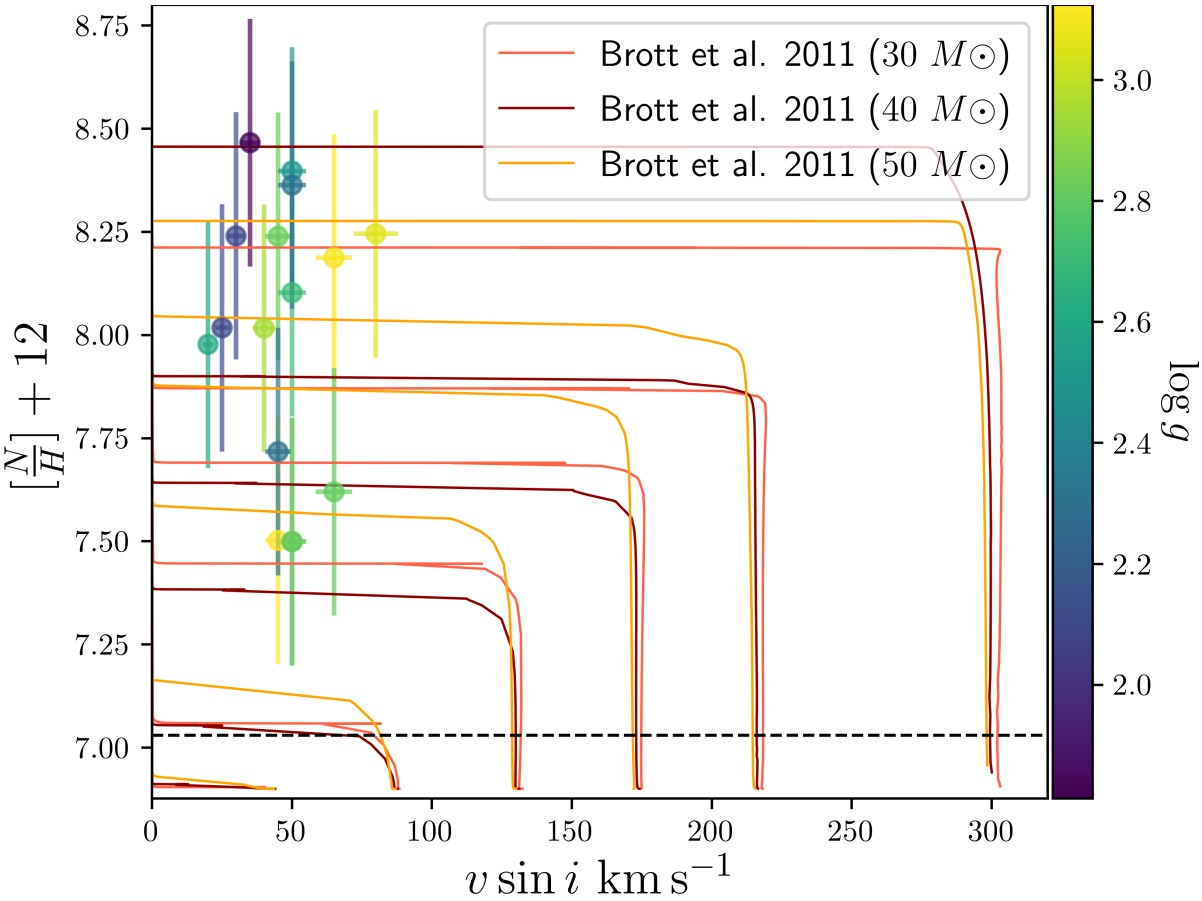


Figure 3.11: Nitrogen abundance (by number) vs. $v_{\rm rot} \sin i$. The colour scheme corresponds to the value of $\log g$, and the evolutionary tracks are computed for initial masses of 30 $M_\odot$, 40 $M_\odot$ and 50 $M_\odot$ (red, brown, and orange solid lines respectively) for initial rotational velocities of 50, 110, 170, 220, 270 380 km s^{-1} (Brott et al., 2011), which we multiplied by a factor of $\pi/4$ to take into account the inclination of the rotation axis (Hunter et al., 2008b). The black dashed line represents the LMC baseline nitrogen abundance.

where we find a 0.2 dex enhancement in oxygen.

Recalling Section 2.3.8, it is necessary to use lines of lower ionisation stages for B than for O stars. In panels *d*-*l* of Fig. 3.12, we use the best fitting models for Sk −66° 171, Sk −68° 140, and Sk −68° 8 (left to right, respectively), which corresponds to temperatures of 29.9, 24.1, and 14.1 kK, respectively, to plot the radial ionisation structure of helium, nitrogen and iron. This shows that the atmosphere is dominated by lines of different ionisation levels depending on the temperature, which illustrates the reason behind fitting lines of lower ionisation stages with lower $T_{\rm eff}$.

In Fig. 3.10, we show the line formation regions of different lines versus radius $v_{\rm wind}$, and we can see that photospheric lines like He I λ4471 (red solid lines), N III λ4097, and N II λ4447 (green solid lines) form around $v_{\rm wind} \approx 10 - 15$ km s^{-1}, which coincides with the transition point between the subsonic and super-sonic regimes, connecting the photosphere to the inner region of the stellar winds. On the topmost panels of Fig. 3.12, the transition point is where the velocity jumps from 0 km s^{-1} to $\approx$ 15 km s^{-1}.

Fig. 3.11 shows that the overall distribution of the observed nitrogen enhancement in our sample might be produced via evolutionary tracks that include rotational mixing (Brott et al., 2011). Extremely high initial rotational velocities disagree with what is observed for O stars and the findings of Ramírez-Agudelo et al. (2013), however, who obtained the rotational properties of a large sample of LMC O stars (216 stars) and concluded that the distribution of $v_{\rm rot} \sin i$ peaks at $\approx$ 80 km s^{-1}. We found no clear positive correlation between rotation rates and nitrogen enhancement either, which is similar to the findings of Hunter et al. (2008b).

In Fig. 3.13, we present the logarithm number ratios N/C and N/O of our sample (blue circles). Maeder et al. (2014) analytically obtains the upper and lower bounds (black dashed lines) from nuclear constraints (^{12}C is turned immediately into ^{14}N and the number of carbon atoms is constant throughout the CNO cycle) on the changes of N/C versus N/O ratios during the CNO cycle. We find that the majority of our stars

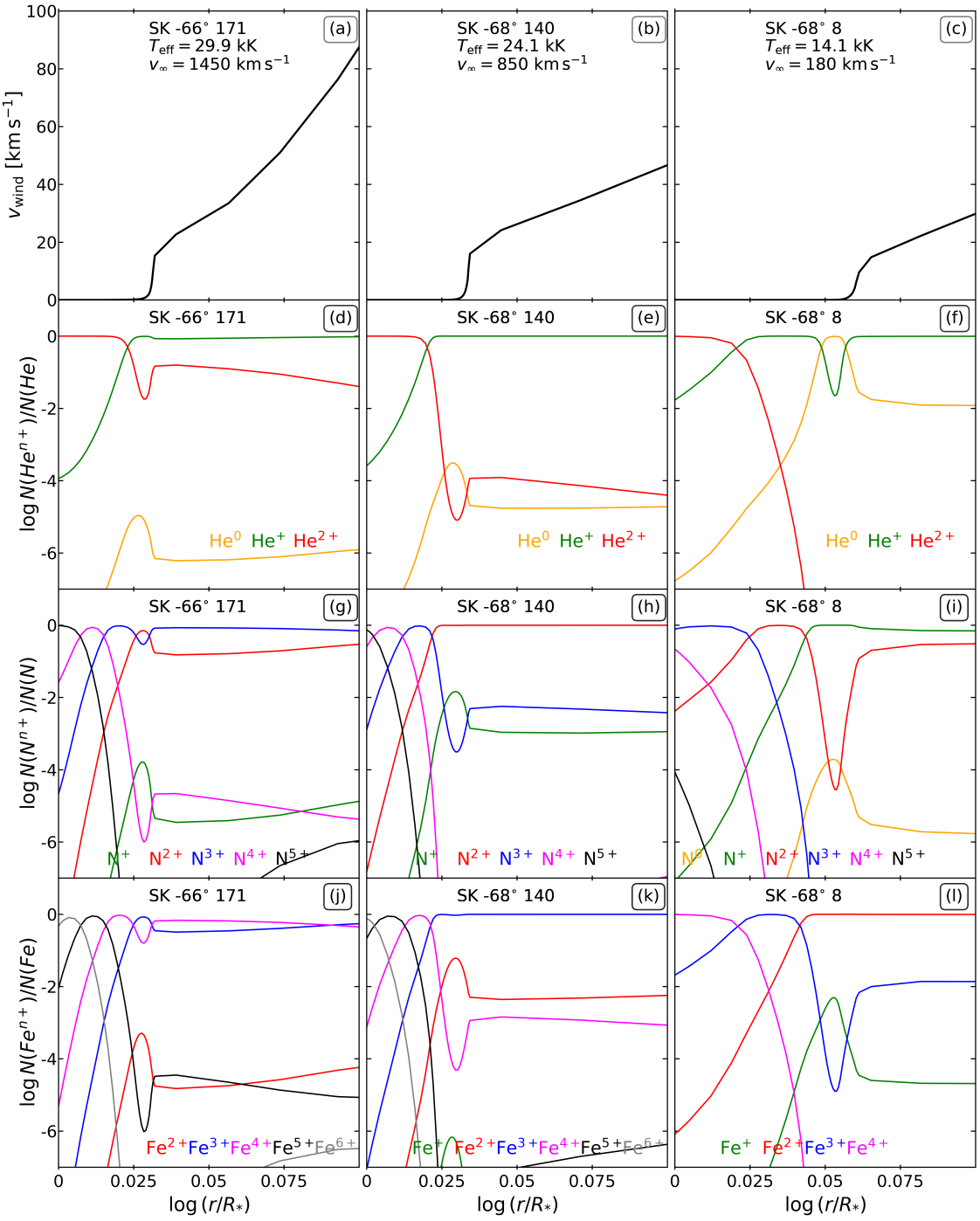


Figure 3.12: Each column shows from left to right Sk −66° 171 ($T_{\rm eff}$ = 29.9 kK), Sk −68° 140 ($T_{\rm eff}$ = 24.1 kK), and Sk −68° 8 ($T_{\rm eff}$ = 14.1 kK). *a*, *b*, and *c*: Wind velocity as a function of radius in stellar radii units log (r/R_*). *d*, *e*, and *f*: Ionisation structure (relative ionic density log $(N(i^{n+})/N(i_{\rm tot}))$ vs. log (r/R_*)) of helium. *g*, *h*, *i*: Ionisation structure of nitrogen. *j*, *k*, and *l*: Ionisation structure of iron. i^0 (orange), i^+ (green), i^{2+} (red), i^{3+} (blue), i^{4+} (magenta), i^{5+} (black), and i^{6+} (grey) where i is the element.

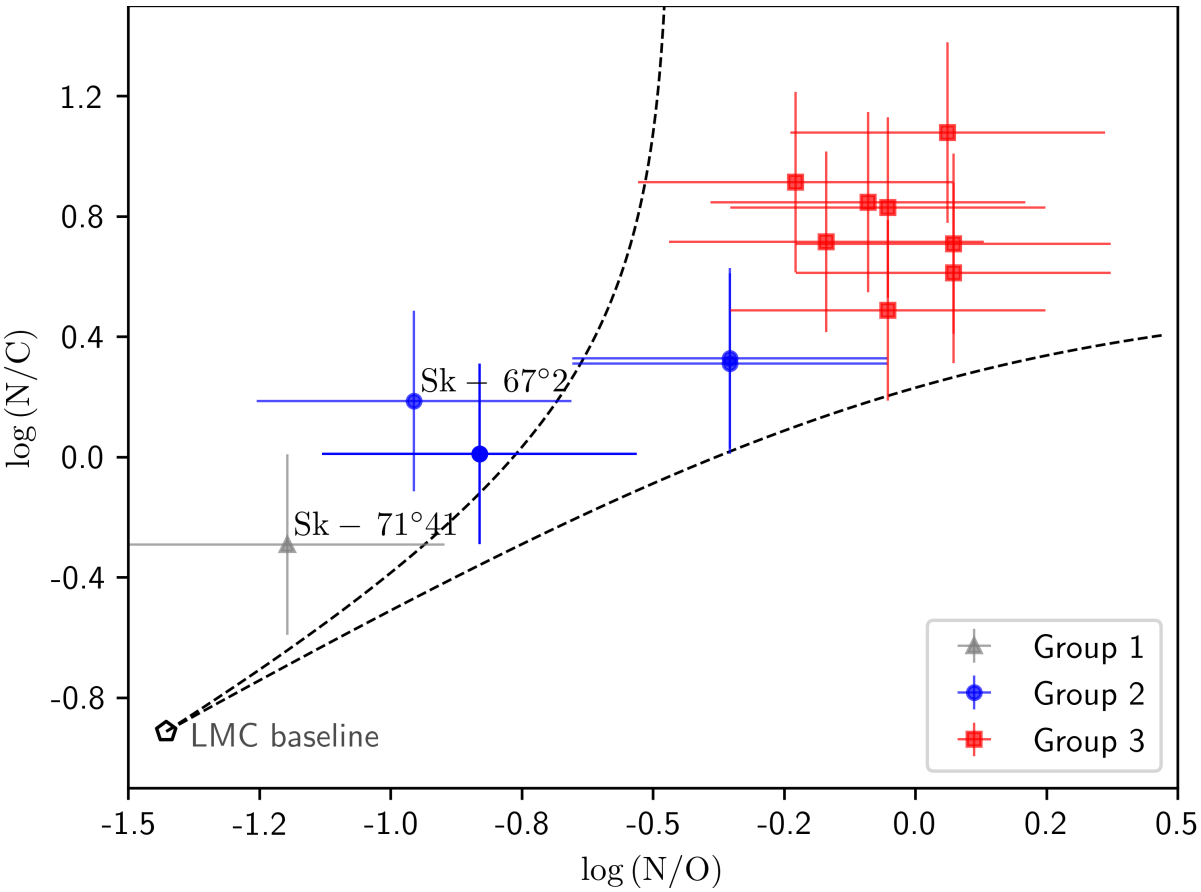


Figure 3.13: $\log \mathrm{N/C}$ vs. $\log \mathrm{N/O}$ of our sample (grey triangles, blue circles, and red squares). The upper and lower boundaries (dashed black lines) are adopted from Maeder et al. (2014). The sample is divided into three groups depending on their N/C and N/O values, similar to Menon et al. (2024).

are within those bounds. The exception are the stars Sk −71° 41, Sk −67° 5, Sk −68° 52, Sk −68° 140, which fall outside of the boundaries, but are within the uncertainties. In Fig. 3.13, we divide the stars into groups following the criteria introduced by Menon et al. (2024), who obtained the CNO abundances of 59 early-B supergiants in the LMC using FASTWIND. We find that only Sk −71° 41 is part of *Group 1*, which is the group whose number ratios can be explained by a single star evolutionary scenario. *Group 2*, whose number ratios can be obtained via blue loop models, fast-rotating ($v_{\rm init,rot} = 220 {\rm km\,s^{-1}}$) TAMS models, or merger models. The rest of the sample falls within *Group 3*, the number ratios of which can only be explained by merger scenarios.

Although it is expected for the combined mass fraction of CNO elements of any given star in our sample to stay constant throughout its evolution and to be similar to that of the LMC, we do find that, in some cases, the aggregate CNO mass fraction required to obtain a satisfactory fit to the designated CNO lines significantly diverges from the baseline CNO mass fraction of the LMC (ΣCNO/ΣCNO$_{\rm LMC}$ in Table 3.8). The most extreme examples of this are Sk −71° 41 and Sk −69° 279, with ratios of summed CNO mass fraction to LMC CNO mass fraction of $\approx$ 1.7 and 0.6, respectively, indicating that these objects have a respectively higher and lower cumulative CNO mass fraction. This likely arises from the sensitivity of abundances to other parameters, mainly $T_{\rm eff}$, $\log g$. Fixing $v_{\rm mic}$, as explained in Section 2.3.5, could be a contributing factor to this discrepancy.

3.3 Discussion

In Section 3.3.1 we discuss the existence of the bi-stability jump in our sample. In Section 3.3.2 we compare our results to previous empirical studies. In Section 3.3.3, we compare our results to various numerical predictions. Finally, in Section 3.3.4 we explore the dependence of wind properties on metallicity.

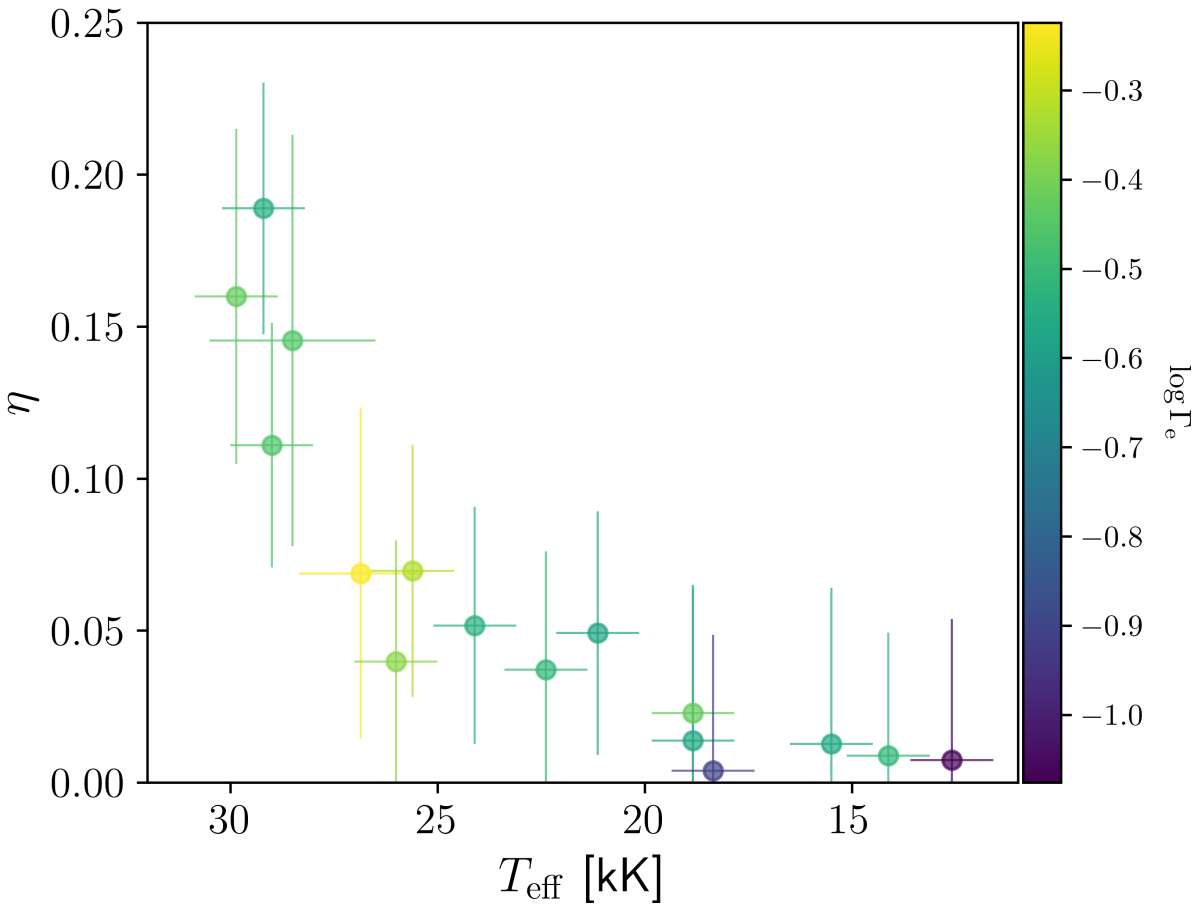


Figure 3.14: Wind efficiency ($\eta = \frac{\dot{M} v_\infty}{L_{\rm bol}/c}$) in terms of effective temperature.

3.3.1 Bi-stability jump

The main goal of this study is to explore the existence of the numerical mass-loss rate jump-like increase when going from the 'hot' regime to the 'cool' regime around $T_{\rm eff}$ = 25 kK. We attempted to alleviate the degeneracy of mass loss and clumping that plagues the recombination line emission in Hα by using the appropriate unsaturated P Cygni lines in the UV, as mentioned above. Fig. 3.14 shows our derived wind efficiency parameter ($\eta = \frac{\dot{M} v_\infty}{L_{\rm bol}/c}$) versus $T_{\rm eff}$. The downward trend in the overall sample is clear. This agrees with Benaglia et al. (2007), who derive the mass-loss rates for a sample of Galactic OB stars from thermal radio emission and find a similar monotonic downward trend in wind efficiency with lower temperatures.

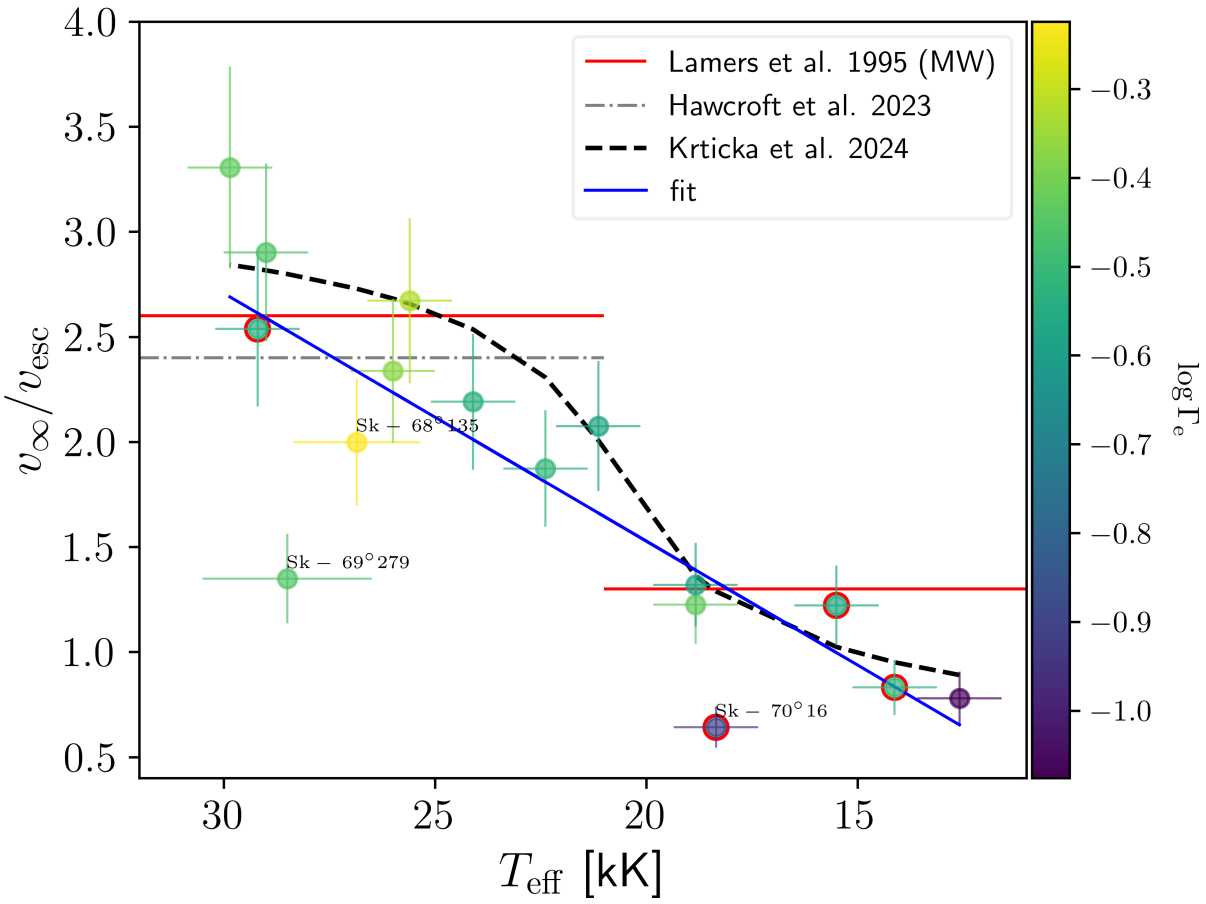


Figure 3.15: Ratio ($v_\infty/v_{\rm esc}$) as a function of temperature. The black dashed line is the relation presented in Krtička et al. (2021). The filled red lines represent the ratios from Lamers et al. (1995). The green filled line is the average relation for stars of spectral type earlier than B1 from Hawcroft et al. (2024a). The colour gradient correlates with the value of $\Gamma_e^{\rm evo}$. Red circles indicate stars the v_∞ of which is inferred as $v_{\rm edge} \times \langle v_\infty/v_{\rm edge} \rangle_{\rm LMC}$.

In Fig. 3.15, we compare the distribution of $v_\infty/v_{\rm esc}$ versus $T_{\rm eff}$ to empirical predictions from Lamers et al. (1995) (MW) and Hawcroft et al. (2024a) (LMC), plus the $v_{\rm esc}$-$T_{\rm eff}$ prediction from Krtička et al. (2021) which does not assume a bi-stability jump, but rather a smooth transition from high to low ratios. Our sample show a smooth decline in $v_\infty/v_{\rm esc}$ with lower temperatures and lacks signs of a bi-stability jump around the proposed $T_{\rm eff} \approx 25{-}21$ kK. The Krtička et al. (2021) recipe produces a smooth decrease in $v_\infty/v_{\rm esc}$, and our are in good agreement with their prediction. The outliers are the hypergiants Sk -68° 135 and Sk -69° 279, which have low $v_\infty/v_{\rm esc}$. This is due to abnormally slow winds relative to other objects with similar temperatures.

The vertical error bars in Fig. 3.15 include the uncertainties of v_∞ and the $v_{\rm esc}$. With a simple linear fit we obtain the relation

$$v_\infty/v_{\rm esc} = 5.6(\pm1.0)\log\left(T_{\rm eff}/{\rm K}\right) - 22.3(\pm4.5). \tag{3.3}$$

3.3.2 Comparison to previous empirical studies

Due to differences in radiative transfer codes, in analysis methods and in observational datasets, and above all the lack of a clear unified method for calculating model and true uncertainties, we are not comparing like-for-like. The reason for the comparison is to check if the collection of those comparison studies produces an observable bi-stability jump.

Sander et al. (2024) concludes that an average maximum spread in $T_{\rm eff}$, $\log g$, and $\log \dot{M}$ obtained with different methods applied to ULYSSES/XShootU data is $\Delta T_{\rm eff} \approx 3000$ kK, $\Delta \log\left(g/{\rm cm\,s^{-2}}\right) \approx 0.2$ and $\Delta \log\left(\dot{M}/{\rm M_\odot\,yr^{-1}}\right) \approx 0.4$. While the analysis conducted by Sander et al. (2024) is very revealing of the discrepancies between the different radiative transfer codes and a great attempt at parameterising the spread that could be expected when comparing results obtained by these codes, the sample was

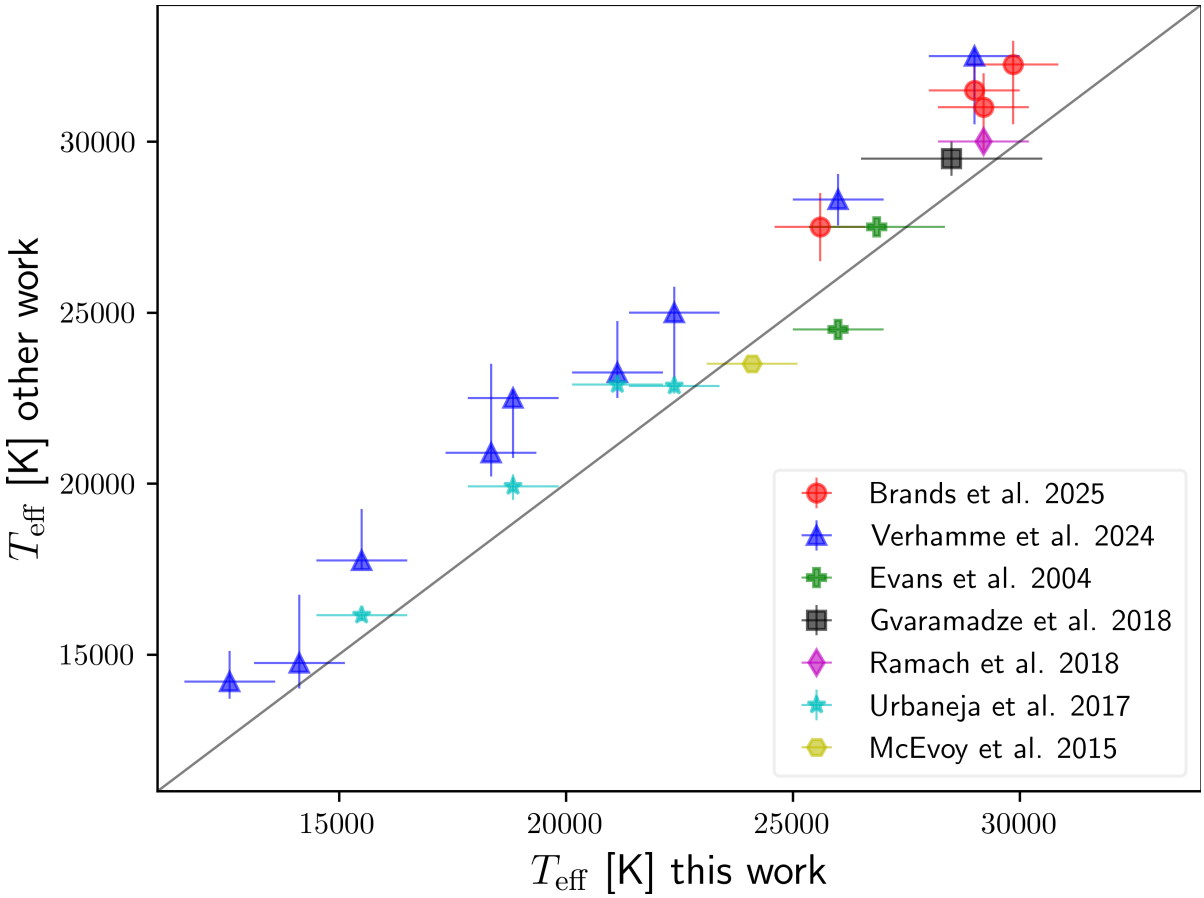


Figure 3.16: Comparison of our obtained $T_{\rm eff}$ to previous studies. We present on the x-axis our effective temperature for each star and the comparison $T_{\rm eff}$ from previous analyses on the y-axis. Blue triangles: Comparison to values obtained by Verhamme et al. (2024), Red circles: Comparison to values obtained by Brands et al. (2025). Green filled crosses: Comparison to values obtained by Evans et al. (2004). Black square: Comparison to values obtained by Gvaramadze et al. (2018). Magenta diamond: Comparison to values obtained by Ramachandran et al. (2018). Cyan star: Our $T_{\rm eff}$ to the effective temperatures from Urbaneja et al. (2017). Yellow hexagon: Comparison to values obtained by McEvoy et al. (2015).

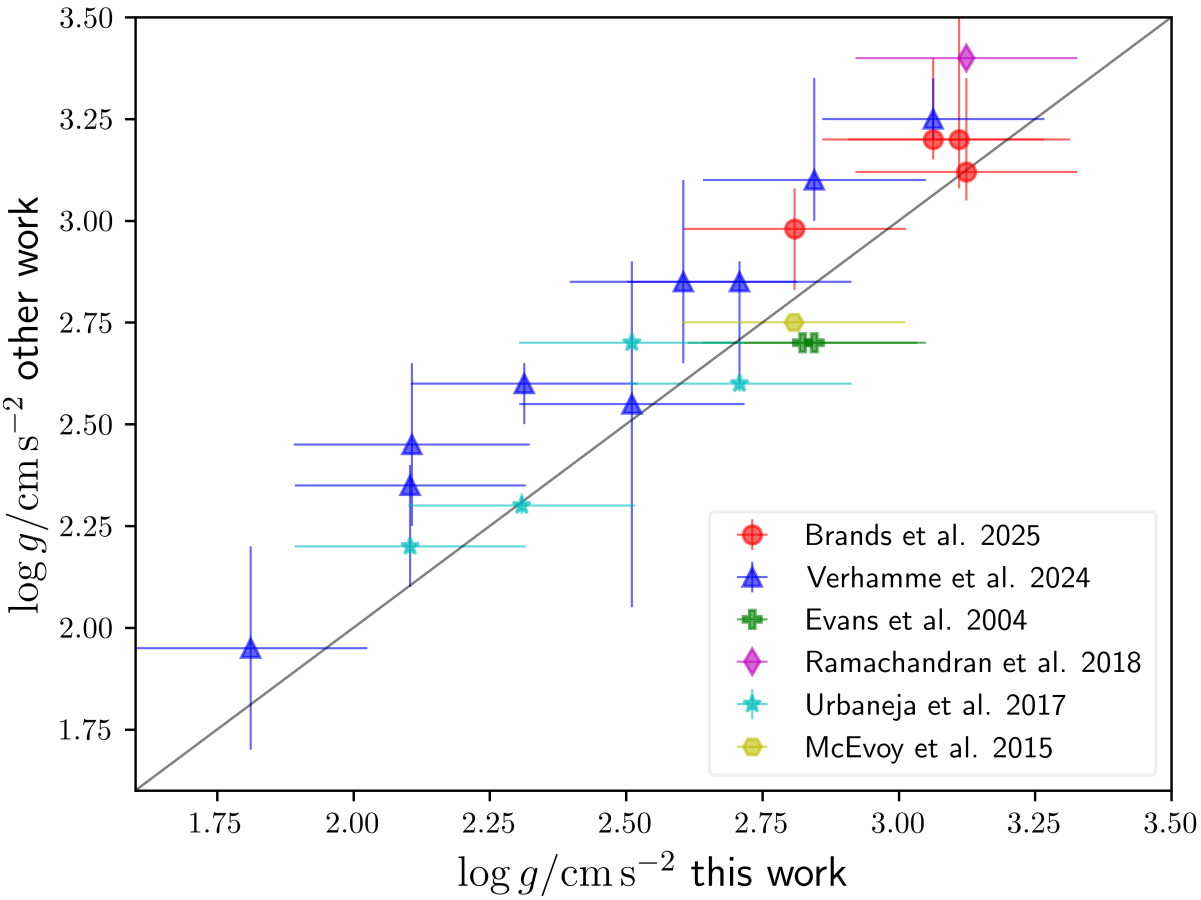


Figure 3.17: Comparison of our obtained $\log g$ to previous studies. The symbols follow the same encoding as in Fig. 3.16.

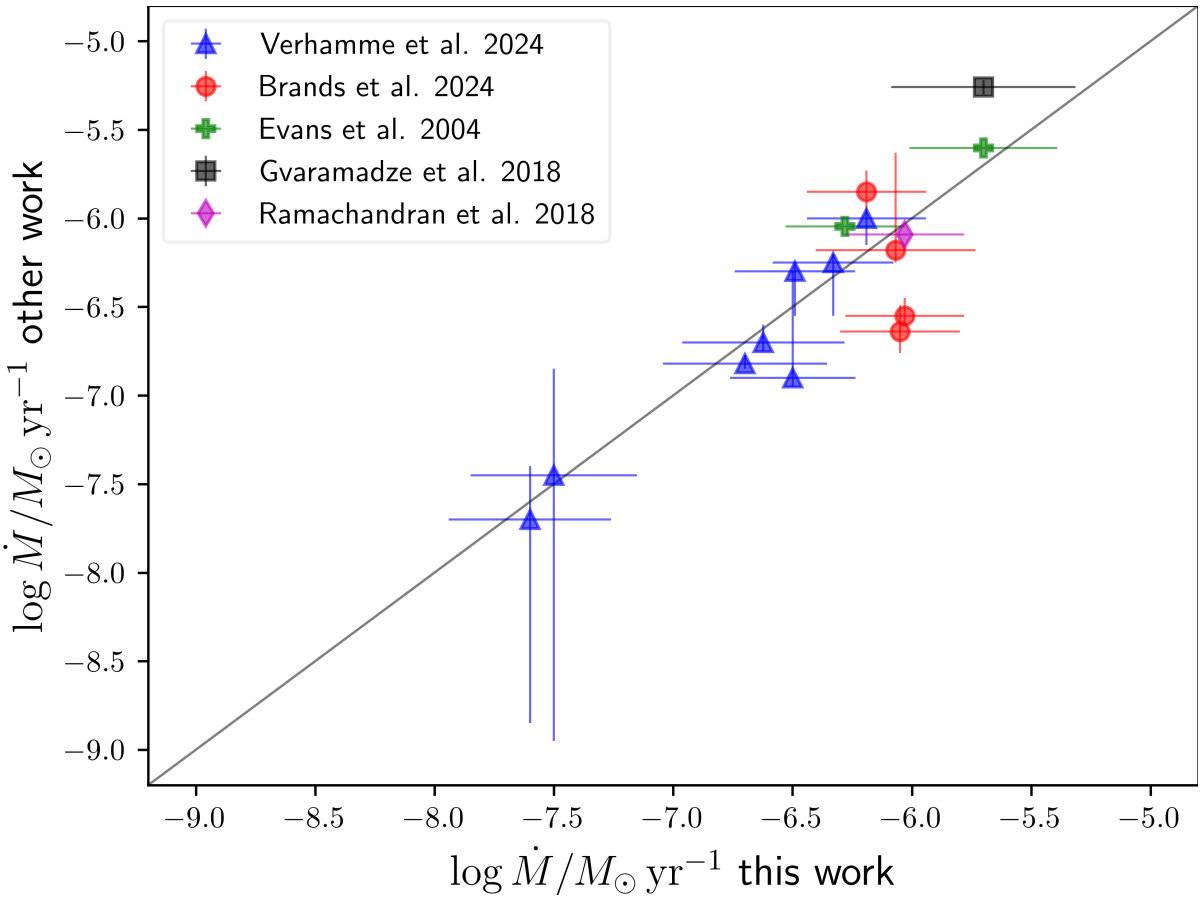


Figure 3.18: Comparison of our derived $\dot{M}$ to previous studies. The symbols follow the same encoding as in Fig. 3.16.

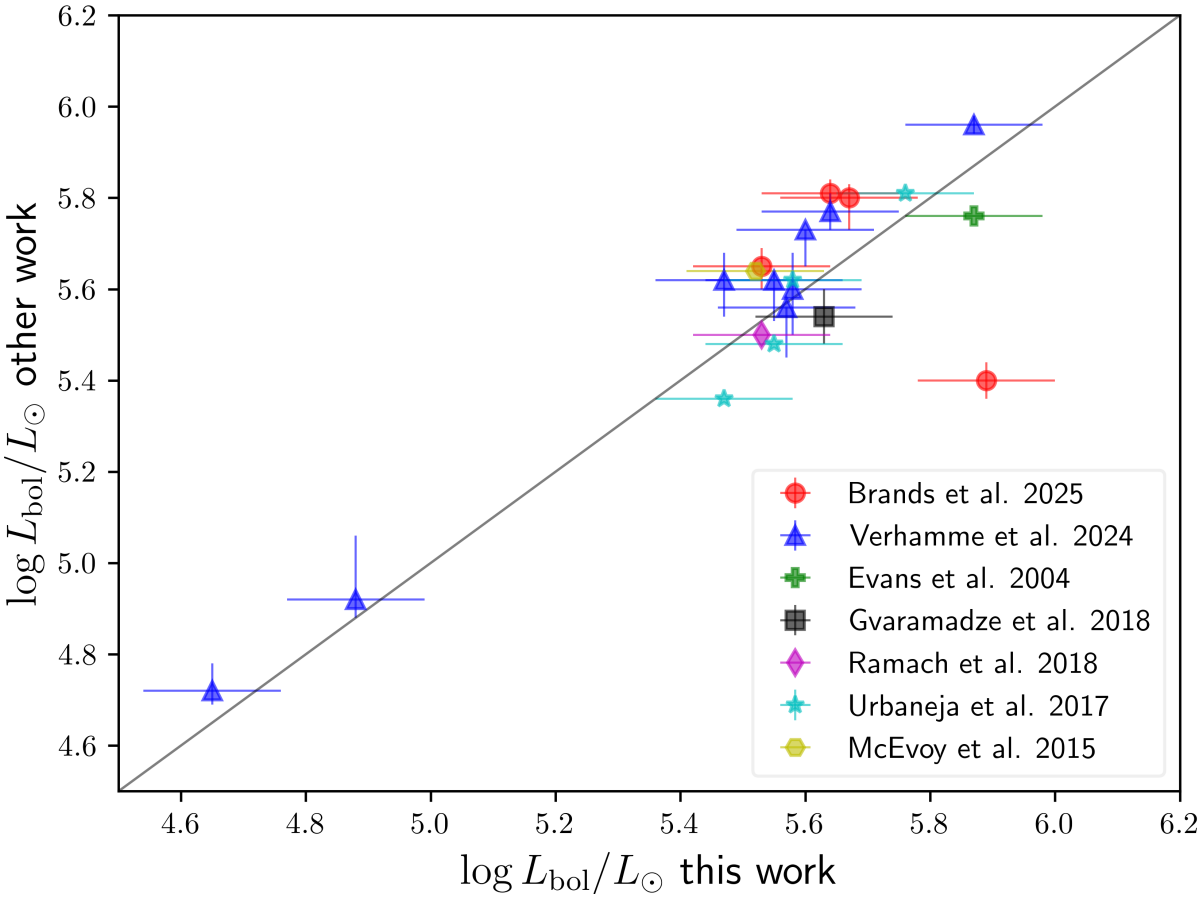


Figure 3.19: Comparison of our derived $\log L_{\rm bol}$ to previous studies. The symbols follow the same encoding as in Fig. 3.16.

limited to two LMC and one SMC O-type stars. Therefore, the spread of parameters obtained in that study is not significant from a statistical point of view.

We focus below on comparing $T_{\rm eff}$, $\log g$, and $\log \dot{M}$. In Sections 3.3.2 and 3.3.2, when comparing the mass-loss rates, we do not adjust the values to the equivalent "smoothed wind" values (for $f_{\rm vol} = 1$).

Fig. 3.16-3.19 compare our derived values of $T_{\rm eff}$, $\log g$, $\dot{M}$, and $\log L_{\rm bol}$ respectively, versus values derived in previous studies. We compile our derived $T_{\rm eff}$, $\log g$, $\log \dot{M}$, $\log L_{\rm bol}$, β, and $f_{\rm vol}$ alongside the results of various previous empirical studies in Table A.2 in Appendix A.3.

UV and optical studies

Evans et al. (2004) has two targets in common with the present study, and also employed CMFGEN. Their $T_{\rm eff}$ for the hypergiant Sk −68° 135 is 1500 K lower than ours and a $T_{\rm eff}$ for Sk −68° 52 is 800 K higher than our estimate, whereas their $\log g$ is lower than ours by 0.15 dex and 0.12 dex respectively. They provide two mass-loss rates for each object, one with the assumption of a smooth wind, and the other with the assumption of a generic volume-filling factor of 0.1, and we compare our mass-loss rates to the latter and we find that their mass-loss rates are higher by 0.23 dex and 0.10 dex for Sk −68° 52 and Sk −68° 135, respectively. This can be attributed to the difference in photospheric parameters, the difference in β-law, which they assume is 2.75 and 3.50, respectively, for Sk −68° 52 and Sk −68° 135, versus our β that we estimate at 2 and 2.3, and most significantly the large difference in the terminal wind velocity estimates, as we determine the wind velocities at 1140 km s^{-1} and 880 km s^{-1}, versus their v_∞ of 1400 km s^{-1} and 1350 km s^{-1} for Sk −68° 52 and Sk −68° 135, respectively, which they measure from the N III λ991 doublet in the FUV FUSE range. The luminosities obtained by Evans et al. (2004) are consistent within 0.1 dex of our luminosities.

We share Sk −71° 41 in common with Ramachandran et al. (2018), who analysed a

large sample of OB stars in the LMC N206 super bubble using the Potsdam WolfRayet (PoWR) code (Gräfener et al., 2002b; Hamann & Gräfener, 2003b; Sander et al., 2015). Their $T_{\rm eff}$ is slightly higher than ours (see Table A.2), but we do find a large discrepancy in $\log g$, where they estimate it to be ≈ 0.3 dex higher than ours. The source of this observed discrepancy is unclear, but could be due to the difference in datasets. The mass-loss rate obtained by them is consistent with our mass-loss rates, albeit slightly lower.

We have seven targets in common with Verhamme et al. (2024) and four targets with Brands et al. (2025), who conducted a UV+optical analysis for B supergiants and hot O supergiants, respectively, using the genetic algorithm Kiwi-GA, which uses FASTWIND non-LTE radiative transfer models. These studies both used the same spectroscopic dataset as this study (ULLYSES/XShootU dataset). We find that our effective temperatures are systematically lower than those of Verhamme et al. (2024) and Brands et al. (2025) by $1000 - 4000$ K (see Fig. 3.16). This could be attributed to the differences between CMFGEN and FASTWIND in the treatment of helium and silicon lines (Massey et al., 2013), and the different analysis methods (genetic algorithm versus manual by-eye fitting).

For the coolest star Sk -67° 195, Verhamme et al. (2024) obtained the temperature through the He I and Si II lines, whereas we obtain our temperature from fitting the He I and Mg II lines. FASTWIND suffers from known convergence problems below 15 kK (Lorenzo et al., 2025), therefore CMFGEN is more reliable. The higher temperatures of Verhamme et al. (2024) and Brands et al. (2025) lead to higher $\log g$ in comparison to our work. We find that our effective surface gravities are $0.1 - 0.25$ dex lower than theirs (see Fig. 3.17). The luminosities obtained by Verhamme et al. (2024) and Brands et al. (2025) are systematically higher than ours by $\Delta L_{\rm bol} = 0.02 - 0.12$ dex, albeit they are consistent within the uncertainties. The sole outlier is Sk -67° 5, for which the lumiosity derived by Brands et al. (2025) is lower than ours by approximately $\Delta \log L_{\rm bol} = 0.5$ dex.

This arises from adopting incorrect UBV photometry by Brands et al. (2025). The use of the correct photometry yields $\log L_{\rm bol} = 6.00^{+0.04}_{-0.04}$ for Sk −67° 5 (Brands et al., 2025, priv. comm.), which is in better agreement with our derived luminosity of $\log L_{\rm bol} = 5.89$. We do not notice any trend in the difference between our mass-loss rates and those obtained by Verhamme et al. (2024) and Brands et al. (2025) despite the different clumping parametrisation. We do note that mass-loss rates from Verhamme et al. (2024) and Brands et al. (2025) are consistent with our mass-loss rates within the uncertainties.

The advantages of our analysis methods compared to Verhamme et al. (2024) are the detailed treatment of line blanketing in the UV provided in CMFGEN (see Fig. 2.4), the robust velocity measurements from P Cygni profiles in the UV, and the employment of Mg II 4481 when measuring the temperature of the coolest B supergiants where Si III lines are no longer present. The main disadvantages of our method are the lack of robust calculations of statistical model errors. Unlike FASTWIND, the treatment of clumping in CMFGEN is limited to micro-clumping, which in some cases yields poor fits to the red emission in P Cygni profiles and requires unrealistically low volume-filling factors (or high clumping factors) to obtain good fits for the blue absorption. Muijres et al. (2011) describes how optically thin clumps increase the predicted mass-loss rates, while the optically thick clumps can display an opposite effect. This might have a differential effect on objects at either side of the bi-stability jump. This effect was recently explored by de Burgos et al. (2024a) in a large sample of Galactic OB stars, and they report a lack of evidence for a bi-stability jump. We found no correlation between the mass-loss rate and the clumping parameters, which agrees with Verhamme et al. (2024) and Brands et al. (2025).

Optical-only studies

Sk −68° 140 is in common with McEvoy et al. (2015), who obtained the atmospheric parameters and nitrogen abundances for a B supergiants in the LMC using TLUSTY

and SYNSPEC codes (Hubeny & Lanz, 1995). We find that our $T_{\rm eff}$ and $\log g$ are slightly higher compared to theirs (500 K and 0.05 dex respectively), which falls well within our uncertainties. The model grids they use are plane-parallel and do not provide a measure of the mass-loss rate.

We share 4 targets in common with Urbaneja et al. (2017), which is a photometric and spectroscopic (optical only) study for LMC OB supergiants using FASTWIND. We find that the effective temperatures are systematically larger than ours by $500-1500$ K, whereas for $\log g$ we do not identify any systematic trend. Since Urbaneja et al. (2017) conducted their study to specifically explore the gravityluminosity relation, mass-loss rates are not investigated. We find that our $T_{\rm eff}$ and $\log g$ are consistent with theirs within the uncertainties. We calculate $\log L_{\rm bol}$ from the total extinction values, bolometric corrections and apparent magnitudes provided in Urbaneja et al. (2017). We find that they are in agreement with our derived $\log L_{\rm bol}$ within the uncertainties.

Gvaramadze et al. (2018) performed a detailed optical only spectroscopic analysis using CMFGEN for the hypergiant Sk -69° 279. In comparison to our effective temperature and mass-loss rate, theirs are larger by 700 K and 0.4 dex, respectively. The difference in mass-loss is due to the difference in wind clumping, as they estimate $f_{\rm vol}$ at 0.5 versus 0.1 in our analysis and β-law, which they fix at a value of 3, whereas we estimate a value of $\beta = 2.7$. The different observational data used in Gvaramadze et al. (2018) and the variable nature of this object, which resembles a dormant Luminous Blue Variable (LBV, Weis et al., 1997), could also be a contributing factor to this discrepancy. Gvaramadze et al. (2018) do not provide the effective surface gravity used in their models therefore we cannot compare our results.

Comparing our results to Bestenlehner et al. (2025), we find that there is a good agreement in the $T_{\rm eff}$ and $\log g$. The exception to this are the late-O hypergiants Sk -68° 135 and Sk -69° 279, where we find large differences in temperature and gravity. The discrepancy in $T_{\rm eff}$ is likely due the weak He II λ4686 line, the region of which is clearly offset

from the continuum (see Figures A.22 and A.20). Additionally, all Balmer lines used by the pipeline in Bestenlehner et al. (2025) present heavy wind contamination (fully or partially in emission), making $\log g$ hard to constrain. Subsequently, all the parameters obtained from fitting those lines are not reliable. Unlike other FASTWIND-based studies, we do not notice a clear offset in $T_{\rm eff}$ and $\log g$. We find no major discrepancies in the luminosities. Despite the constant $\beta = 1$ and $f_{\rm vol} = 0.1$ in the grid that was used by the pipeline of Bestenlehner et al. (2025), their derived mass-loss rates are consistent with ours within the uncertainties.

3.3.3 Comparison to numerical mass-loss rate recipes

Here, we compare our derived mass-loss rates to those predicted by numerical recipes presented in Vink et al. (2001), Björklund et al. (2023), and Krtička et al. (2024). The mass-loss rate recipe produced by Vink et al. (2001) is based on predictions from unified Monte-Carlo models with consistency between radiative acceleration and mechanical acceleration in the overall structure of the wind. The prediction of the bi-stability jump and the mass-loss rates around $T_{\rm eff} = 25 - 21$ kK in those simulations is due to the recombination of Fe IV into Fe III, which has significantly more spectral lines, resulting in a boost in line-driving. In the bottommost row of Fig. 3.12, it is clear the dominant iron ions at the connection point marking the photosphere in Sk −66° 171, Sk −68° 140, and Sk −68° 8 are Fe V, Fe IV, and Fe III, respectively. This means that the shift from Fe IV to Fe III is indeed reflected in our results, with Fe III providing the majority of line-driving (Petrov et al., 2016), but as we discuss later, this is not accompanied by an increase in empirical mass-loss rates. Petrov et al. (2016) explores another bi-stability jump at $T_{\rm eff} \approx 10-8$ kK, which was discussed by Lamers et al. (1995) and Vink et al. (1999). This bi-stability jump is due to the change in ionisation balance between Fe III and Fe II, with Fe II becoming the source of most of the line acceleration.

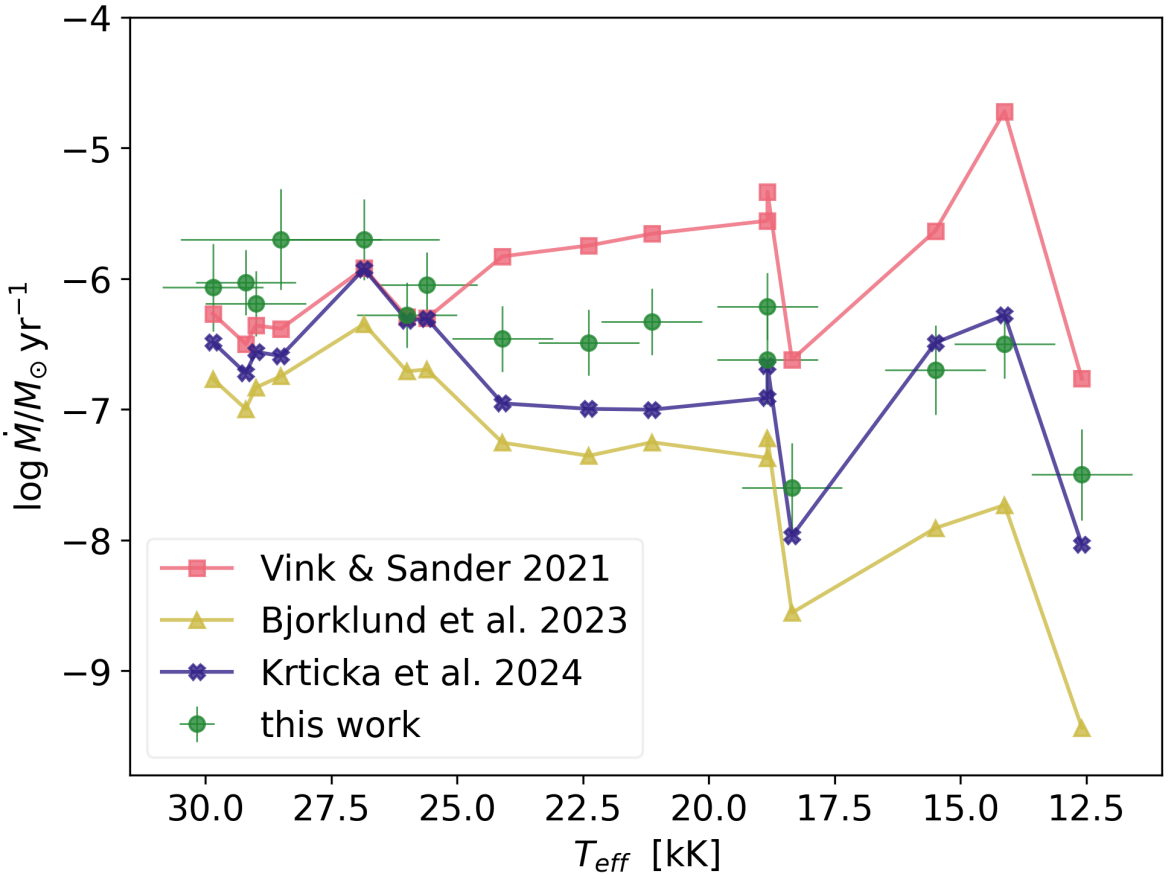


Figure 3.20: Mass-loss rates as a function of $T_{\rm eff}$, comparing our derived $\dot{M}$ (green circles) to mass-loss rates that we calculated via various numerical recipes. Pink squares: $\dot{M}$ from Vink et al. (2001) recipe. Yellow triangles: $\dot{M}$ from Björklund et al. (2023). Violet crosses: $\dot{M}$ from Krtička et al. (2024).

An important element in the calculation routine is the ratio of terminal velocity to escape velocity ($v_\infty/v_{\rm esc}$). For this, we adopt the v_∞ introduced in a later study (Vink & Sander, 2021). In Björklund et al. (2021, 2023), a locally self-consistent wind model FASTWIND that solves the radiative transfer equation in the co-moving frame is used. In this case, no sudden increase in the mass-loss rate is produced with decreasing $T_{\rm eff}$. In this recipe, the mass-loss rates decrease as a smooth function of stellar parameters. Finally, in Krtička et al. (2024), the mass-loss rates are derived using the global stellar atmosphere code METUJE that was introduced in Krtička & Kubát (2017), which calculates the velocity stratification with the radiative acceleration. This recipe predicts a much more moderate increase in the mass-loss rates compared to what is predicted by Vink et al. (2001) in the regime below $T_{\rm eff} = 20$ kK.

Fig. 3.20 compares our derived mass-loss rates with the predicted mass-loss rates calculated by numerical recipes assuming $Z/Z_\odot = 0.5$. We notice that for stars with temperatures above 25 kK, the Vink et al. (2001) and Krtička et al. (2024) mass-loss rate predictions are relatively consistent with our derived mass-loss rates. For stars cooler than 25 kK our derived mass-loss rates are situated between Vink et al. (2001) and Krtička et al. (2024) favouring the latter in values and overall trend. Predictions from Björklund et al. (2023) have a similar trend to those from Krtička et al. (2024), but are consistently lower by ≈ 1 dex. The dip in the mass-loss rates in our results and in all predictions between $T_{\rm eff} = 18 - 15$ kK is due to the object Sk -70° 16 not being a B4 blue supergiant (Ib), but rather a lower luminosity bright giant.

3.3.4 Metallicity effect

To explore the metallicity dependence of wind properties, we derive the modified wind momentum $D_{\rm mom}$-$L_{\rm bol}$ relation ($D_{\rm mom} = \dot{M}\, v_\infty \sqrt{R_*/R_\odot}$) (Kudritzki et al., 1995; Kudritzki & Puls, 2000), and we limit our fit to stars with $\log(L_{\rm bol}/L_\odot) > 5$. For lower luminosity

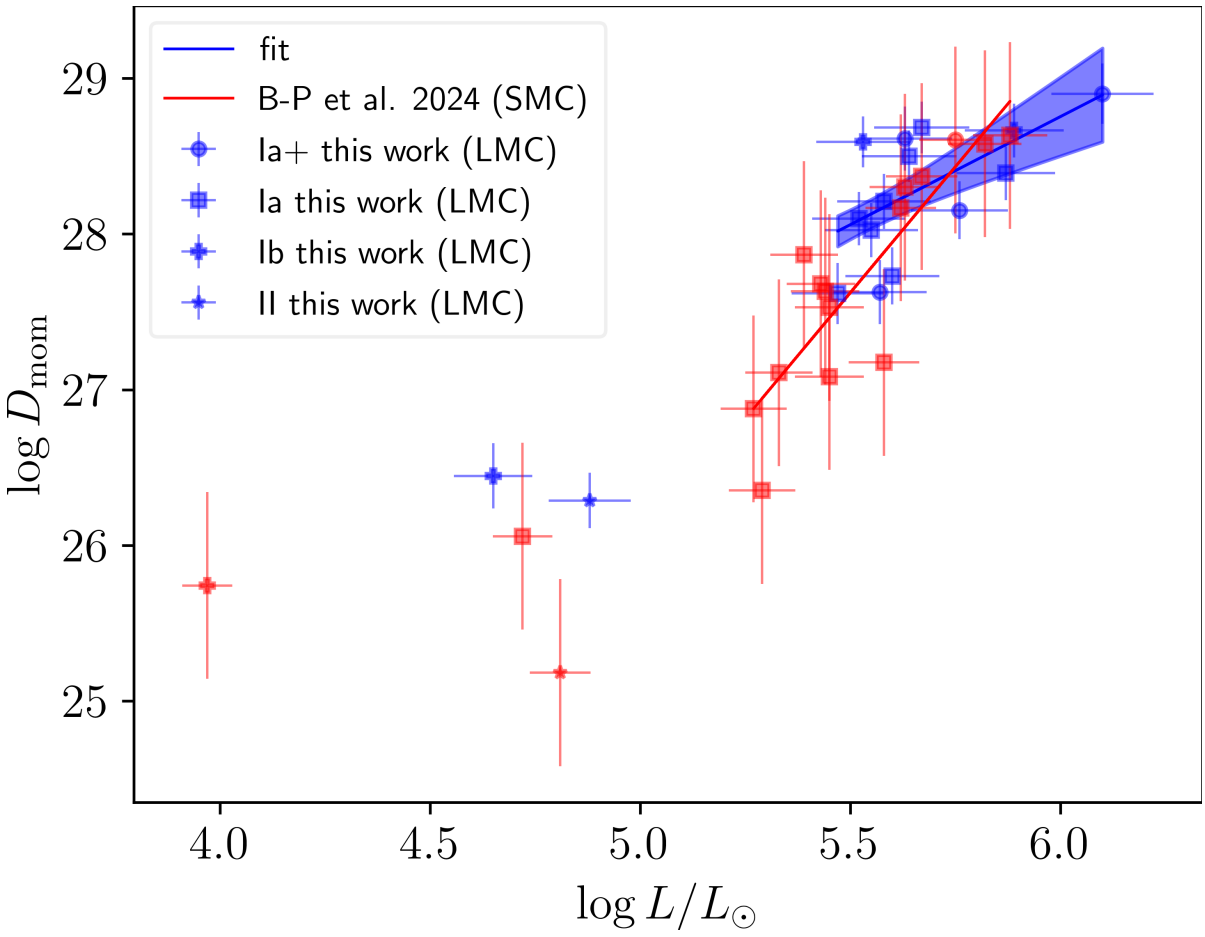


Figure 3.21: Modified wind momentum-luminosity distribution of LMC (blue symbols) supergiants from this work and SMC (red symbols) supergiants from Bernini-Peron et al. (2024). Objects with $\log(L_{\rm bol}/L_\odot) < 5$ are excluded from the linear fits for the LMC and SMC samples. The symbols for the SMC sample (red) follow the same encoding of the LMC sample (blue), where each luminosity class is given a unique symbol.

Table 3.9: Slopes, x, and offsets, $\log D_0$, of the linear fits to the modified wind momentum equation (Equation 3.4) of this study, Mokiem et al. (2007), and Backs et al. (2024)

LMC	x	$\log D_0$
This study	1.39 ± 0.54	20.4 ± 3.0
Mokiem et al. (2007)	1.49 ± 0.18	20.4 ± 1.0
Backs et al. (2024)	1.87 ± 0.11	18.03 ± 1.2

stars, the mass-loss rates we obtain are less reliable and can be considered upper limits due to Hα being fully in absorption and due to the lack of reliable P Cygni profiles for wind velocity measurements. We fit our derived values using a $D_{\rm mom}$-$L_{\rm bol}$ relation of the form

$$\log D_{\rm mom}^{\rm LMC} = x \log (L_{\rm bol}/L_{\odot}) + \log D_0 \tag{3.4}$$

Table 3.9 shows that our derived relation agrees well with the clumping-scaled relation derived by Mokiem et al. (2007) for LMC OB stars. Our $D_{\rm mom}$-$L_{\rm bol}$ relation is consistent with the findings of Backs et al. (2024) within the uncertainties; however, they obtain a steeper relation from an LMC sample that consists mostly of O giants and bright giants, and incorporates results from Brands et al. (2025).

We also compare our results to those of Bernini-Peron et al. (2024), the latest detailed ULLYSES/XShootU spectroscopic analysis of an SMC B supergiant sample using CMFGEN. The main differences between our results and those of Bernini-Peron et al. (2024) are that, whereas we include late-O stars, their sample is composed of B stars exclusively. Their method differs from ours in that X-rays are included and $v_{\rm mic}$ is a free parameter that is determined in their fitting procedure, which could lead to different temperature determination due to the change in opacity, which affects the depth of silicon lines. Higher $v_{\rm mic}$ at larger radii in the wind could potentially also lead to underestimating v_{∞}.

In Fig. 3.21, we compare our derived $D_{\rm mom}$-$L_{\rm bol}$ relation to that of Bernini-Peron et al. (2024). When fitting the results of their SMC sample, we obtain:

$$\log D_{\rm mom}^{\rm SMC} = 3.24(\pm0.50)\log\left(L_{\rm bol}/L_{\odot}\right) + 9.8(\pm2.8).$$

There is a clear difference in the vertical offset between the linear fit of our LMC sample and that of the SMC sample of Bernini-Peron et al. (2024) which could be attributed to the scaling of wind strength with metallicity, but unlike the findings of Mokiem et al. (2007), the two slopes greatly vary, which is not something predicted by previous studies exploring the metallicity dependence of wind properties in the LMC and SMC for neither O nor B stars (e.g. Crowther et al. (2006); Mokiem et al. (2007); Backs et al. (2024)), which generally find similar slopes when fitting each sample. Excluding low luminosity objects, the sample of Bernini-Peron et al. (2024) spans a range of $\log L_{\rm bol}/L_{\odot} \approx 5.2-5.9$, compared to the range of our sample $\log L_{\rm bol}/L_{\odot} \approx 5.5-6.1$. The sample of Bernini-Peron et al. (2024) was also almost exclusively composed of Ia supergiants, and the authors inferred a selection bias to strong winds, whereas our sample contains supergiants from Ib to Ia^{+}. These differences in the samples might be a major contributing factor to the difference in the dependence of the slope on the metallicity compared to previous studies.

3.4 Summary

We have applied a quantitative analysis using CMFGEN models to 16 LMC late-O and B supergiants. Here we summarise the conclusions drawn from this chapter in the following points:

- We compared our results to previous works, and we found that when the differences in the analysis methods and the quality of the data are taken into account,

our parameters are mostly consistent with previously derived values within the expected systematic variance, which we discussed in Sander et al. (2024).

- We found that the majority of the sample are main-sequence stars with a few that appear to have evolved beyond the TAMS into post-main-sequence stars, according to the rotating single-star evolutionary models of Brott et al. (2011).

- The spectroscopic masses we derived are broadly consistent with the evolutionary masses obtained from BONNSAI (Schneider et al., 2014a) within the uncertainties. Our results did not show the large mass discrepancy that was reported in previous studies (e.g., Herrero et al., 1992; Trundle et al., 2004b; Crowther et al., 2006).

- We obtained a velocity-temperature relation of

$$v_\infty/\mathrm{km\,s^{-1}} = 0.076\,(\pm0.011)\,T_\mathrm{eff}/\mathrm{K} - 884\,(\pm260)\,,$$

  which agrees with the relation obtained by Hawcroft et al. (2024a).

- We derived a wind momentum-luminosity relation of

$$\log D_\mathrm{mom}^\mathrm{LMC} = 1.39\,(\pm0.54)\log\left(L_\mathrm{bol}/L_\odot\right) + 20.4\,(\pm3.0)\,,$$

  which is very similar to the relation obtained for OB stars in the LMC by Mokiem et al. (2007).

- We investigated the existence of the bi-stability jump, and we found a lack of observational evidence in our sample that would support this boost in line-driving, and hence, in mass loss and momentum, despite the shift from Fe IV to Fe III. This agrees with the analysis of Verhamme et al. (2024), who analysed a similar ULLUSES/XShootU LMC sample. This also agrees with the results of de Burgos

et al. (2024a), who found no increase in the mass-loss rates over the bi-stability region in a large sample of Galactic blue supergiants.

- Our results showed a strong correlation between $v_\infty/v_{\rm esc}$ and $T_{\rm eff}$, and we obtained the relation

$$v_\infty/v_{\rm esc} = 4.1\,(\pm 0.8)\log\left(T_{\rm eff}/{\rm K}\right) - 16.3\,(\pm 3.5)\,.$$

  We found no evidence of a sharp drop in $v_\infty/v_{\rm esc}$, which might be attributed to the shift from the low-density and high-velocity wind regime to the high-density and low-velocity regime, which is associated with the theorised bi-stability jump (Pauldrach & Puls, 1990; Lamers et al., 1995; Vink et al., 2001; Petrov et al., 2016)

Chapter 4

OB supergiants in the SMC

In this chapter, we present the results of our analysis of late-O and B supergiants in the SMC. The SMC is close to what is expected to be observed in the early universe in terms of metallicity. Therefore, this chapter can be viewed as the logical next step towards our goal of homogeneously parametrising the metallicity scaling of BSG winds.

The principal motivation behind this chapter is to explore the metallicity dependence of wind parameters of late-O and B supergiants in the Magellanic Clouds. We aim to accomplish this by deriving stellar and wind properties of a sample of late-O and B SMC supergiants similar to the one analysed in Chapter 3 using the same methods (see Chapter 2). By comparing the results from this chapter to the results obtained for the LMC sample in Chapter 3, we aim to provide a new metallicity scaling for the wind momentum-luminosity relation. We also aim to investigate the bi-stability jump and the behaviour of the mass-loss rates predicted by numerical recipes.

In Section 4.1, we present the dataset that was used in this study, our sample, and our selection criteria. In Section 4.2, we introduce the results of our analysis. In Section 4.3, we discuss the effects of metallicity on wind parameters, the bi-stability jump, and the implications of our results in the context of the current picture of the massive star population in the SMC.

4.1 Observations

4.1.1 Sample

In Table 4.1, we present the stars in our sample, along with their classifications adopted from Bestenlehner et al. (2025). In this table, we also include the telescope, instrument, and wavelength coverage available for each star.

This sample was selected in such a way that it would cover a spectral range similar to that of Chapter 3. We cover a wide range of spectral classes, from O9 to B8, which includes the region of the theorised bi-stability jump. We attempted to include more than one star per spectral class, ideally with different luminosity classifications (Ia^+, Ia, Iab, Ib). This allowed us to explore the Z dependence of wind properties while avoiding selection bias, which we discussed in Chapter 3 when contrasting our results for the LMC sample with the results of Bernini-Peron et al. (2024) in the SMC, whose sample was made up almost exclusively of Ia supergiants. We have ten stars in common with Bernini-Peron et al. (2024), who include eight stars that are not covered in our study, while we include ten stars not covered in Bernini-Peron et al. (2024). That makes the two studies complementary, although with slightly varying modelling techniques (X-rays and micro-turbulence), and an excellent opportunity to compare the results in our overlapping samples.

Six stars in our sample have been included in the BLOeM survey (Shenar et al., 2024). Britavskiy et al. (2025) did not find evidence of significant radial velocity shifts across nine epochs of this subset, indicating that these stars are apparently single. They report that AzV 242 (BLOeM 4-078) and AzV 96 (BLOeM 8-008) show intrinsic line profile variability, with the possibility that AzV 242 is an SB1 spectroscopic binary.

Table 4.1: List of the stars included in our analysis and the respective wavelength coverage. The spectral types are based on XShootU observations (Bestenlehner et al., 2025)

Star	Alias	SpT	(900 – 1160) FUSE	(1150 – 1700) HST	(1700 – 2370) HST	Aux. Opt. Magellan
AzV 469	Sk 148	O9 Iab(f)	LWRS	STIS E140M	-	-
AzV 372	Sk 116	O9.2 Iab	LWRS	STIS E140M	STIS E230M	-
AzV 456	Sk 143	O9.5 Iab	LWRS	COS G130M+G160M	STIS E230M	-
AzV 327	R 28, BLOeM 1-066	O9.7 Ib	LWRS	STIS E140M	-	MIKE
AzV 235	R 17, Sk 82, BLOeM 7-064	B0 Ia	LWRS	STIS E140M	STIS E230M	-
AzV 215	Sk 76	B0 Ia	LWRS	STIS E140M	STIS E230M	-
AzV 104	-	B0.5 Ia	LWRS	STIS E140M	STIS E230M	MIKE
AzV 410	-	B0.7 Iab	-	STIS E140M	-	-
AzV 242	R 18, Sk 85, BLOeM 4-078	B0.7 Ia	LWRS	STIS E140M	STIS E230M	-
AzV 96	Sk 46, BLOeM 8-008	B1 Iab	LWRS	STIS E140M	STIS E230M	MIKE
AzV 264	Sk 94, BLOeM 1-009	B1 Ia	LWRS	STIS E140M	STIS E230M	MIKE
AzV 175	Sk 64	B1.5 Ib	LWRS	COS G130M+G160M	-	MIKE
Sk 191	-	B1.5 Ia	LWRS	STIS E140M	STIS E230M	-
AzV 18	Sk 13	B2 Ia	LWRS	STIS E140M	STIS E230M	MIKE
NGC330 ELS 4	Rob B37	B2.5 Ib	-	STIS E140M	STIS E230M	MIKE
AzV 187	Sk 68	B2.5 Ia	LWRS	COS G130M+G160M	STIS E230M	MIKE
AzV 22	2dFS 5015	B3 Ia	-	STIS E140M	STIS E230M	-
AzV 393	R 39, Sk 124	B3 Ia$^+$	LWRS	COS G130M+G160M	STIS E230M	MIKE
AzV 343	Sk 111	B8 Iab	-	COS G130M+G160M	STIS E230M	MIKE
AzV 324	BLOeM 1-062	B8 Ib	-	COS G130M+G160M	STIS E230M	-

4.1.2 Utraviolet and optical spectroscopy

The UV spectroscopy used in this chapter is drawn from the ULLYSES (Roman-Duval et al., 2025), the details of which can be viewed in Section 3.1. The only notable difference is in the FUSE data (Moos et al., 2000), which for our sample uniformly using only the LWRS ($30'' \times 30''$) aperture. We note that AzV 327 lies in a crowded region, such that other sources, including [M2002] SMC 55495, contribute to the FUSE spectrum (Danforth et al., 2002). Additionally, the complementary optical spectroscopy was also drawn from DR1 of the XShootU library (Sana et al., 2024), similar to the optical data presented in Chapter 3, with the exception of AzV 187. The optical data of AzV 187 were drawn from archival X-shooter spectroscopy from November 2013, which we normalised using a higher-order polynomial fit of points selected around regions of clean continuum.

4.1.3 Photometry

The photometric magnitudes used in this study are presented in Table 4.2 and were drawn from the compilation in Vink et al. (2023). The photometry is used to derive the bolometric luminosities by fitting the SED. The UBV photometry was taken from Ardeberg & Maurice (1977), Azzopardi et al. (1975), Ardeberg (1980), and Massey (2002), and the JKs photometry was drawn from the VISTA near-infrared YJK_S survey of the *Magellanic System* (VMC, Cioni et al., 2011), with H-band photometry taken from the *Two Micron All Sky Survey* (2MASS, Cutri et al., 2003; Skrutskie et al., 2006; Cutri et al., 2012).

4.1.4 MIKE spectroscopy

High-resolution optical spectroscopy used to extract the rotational properties of slow rotators was collected between December 2021 and December 2022 using the Magellan Inamori Kyocera Echelle (MIKE) spectrograph mounted on the Magellan Clay 6.5 m

Table 4.2: Photometric data. References: 1 Cioni et al. (2011), 2 Cutri et al. (2003), 3 Massey (2002), 4 Azzopardi et al. (1975), 5 Ardeberg & Maurice (1977), 6 Ardeberg (1980), 7 Evans et al. (2006).

Sk –	U	B	V	Ref.	J	H	Ks	Ref.
AzV 469	11.91	12.96	13.12	3	13.58	13.63	13.68	1,2
AzV 372	11.41	12.44	12.59	3	13.04	13.07	13.08	1,2
AzV 456	12.15	12.93	12.83	3	12.81	12.79	12.77	1,2
AzV 327	11.83	12.87	13.03	3	13.78	13.85	13.90	1,2
AzV 235	11.07	12.02	12.20	4	12.41	12.32	12.28	1,2
AzV 215	11.64	12.60	12.69	3	13.01	12.99	13.04	1,2
AzV 104	12.05	13.01	13.17	3	13.65	13.71	13.73	1,2
AzV 410	12.11	13.06	13.21	3	13.75	13.77	13.83	1,2
AzV 242	11.03	11.95	12.06	5	12.42	12.33	12.38	1,2
AzV 96	11.54	12.49	12.59	3	12.93	12.98	12.95	1,2
AzV 264	11.33	12.24	12.37	5	12.75	12.76	12.75	1,2
AzV 175	12.61	13.45	13.53	3	13.83	13.87	13.89	1,2
SK-191	10.97	11.82	11.86	5	12.03	11.96	11.90	1,2
AzV 18	11.70	12.49	12.46	5	12.47	12.36	12.32	1,2
NGC330-ELS-04	–	13.26	13.33	7	13.44	13.45	13.46	1,2
AzV 187	11.21	11.96	12.06	5	12.29	12.23	12.29	1,2
AzV 22	11.53	12.19	12.20	6	12.27	12.20	12.15	1,2
AzV 393	10.55	11.41	11.43	5	11.18	11.13	11.03	1
AzV 343	12.32	12.95	12.99	3	13.08	13.05	13.07	1,2
AzV 324	12.11	12.79	12.84	3	13.09	13.07	13.01	1,2

Telescope, covering the wavelengths 3350 to 5000 Å in the blue arm and 4900 to 9500 Å in the red arm, achieving $R \approx 35000 - 40000$ (Crowther, 2024).

4.2 Results

In this section, we present an overview of the results of our analysis. We compare our results with those from previous studies of SMC blue supergiants. In addition, we compare the derived wind parameters with predictions from numerical recipes. In Table 4.3, we present the derived physical parameters from our preferred CMFGEN models. In Table 4.4, we present the inferred evolutionary masses and ages. The details of v_∞ measurements are presented in Appendix B.1. The table containing the literature values can be found in Appendix B.2. The quality of our analysis is described for each star individually in Appendix B.3. The SED fits, individual line fits and overall spectral fits are presented in Appendix B.4, B.5 and B.6, respectively. Finally, the FM90 UV SED fitting parameters are presented in B.7.

4.2.1 Hertzsprung-Russell diagram

Fig. 4.1 shows the Hertzsprung-Russell diagram (HRD) for our sample, superimposed on SMC isochrones (solid black lines) and evolutionary models (dashed black lines, Brott et al., 2011). Our sample spans a wide range of $\log(L_{\rm bol}/L_\odot)$, from 4.65 (AzV 343) to 5.91 (AzV 456), and a $T_{\rm eff}$ range of 12.0 kK (AzV 343) to 32.0 kK (AzV 469). The shaded area in Fig. 4.1 is defined by the upper limit on the observed luminosities of SMC cool supergiants, also known as the Humphreys-Davidson (HD) limit (Humphreys & Davidson, 1979a; Smith et al., 2004; Davies et al., 2018).

As a sanity check on $T_{\rm eff}$, we compared the predicted Balmer jump strengths to observations (Kudritzki et al., 2008; Urbaneja et al., 2017). We find that the strength of the predicted Balmer jumps – the $T_{\rm eff}$ of which was obtained from the ionisation balance

Table 4.3: Derived stellar parameters based on the best fitting CMFGEN model. The uncertainties of the best fitting parameters are derived similarly to those in Table 3.3 of Chapter 3/

Star	$T_{\rm eff}$	Diag.	$\log g_c$	R_*	$\log L_{\rm bol}$	A_V	$M_{\rm V}$	$BC_{\rm V}$	$v_{\rm rad}$	$v_{\rm rot}\sin i$	$M_{\rm spec}$	$\Gamma_{\rm e}^{\rm spec}$
	kK		$\rm cm\,s^{-2}$	$R_\odot$	$L_\odot$	mag	mag	mag	$\rm km\,s^{-1}$	$\rm km\,s^{-1}$	$M_\odot$	
AzV 469	32.0 ± 1.0	He I – He II	3.30 ± 0.20	19	5.55	0.27	−6.11	−3.03	185	55	28^{+16}_{-10}	0.29
AzV 372	29.2 ± 1.0	He I – He II	3.00 ± 0.20	27	5.68	0.28	−6.65	−2.80	251	100	28^{+16}_{-10}	0.38
AzV 456	30.7 ± 1.0	He I – He II	3.35 ± 0.20	32	5.91	0.97	−7.10	−2.94	141	55	83^{+49}_{-31}	0.25
AzV 327	30.5 ± 1.0	He I – He II	3.32 ± 0.20	19	5.47	0.09	−6.02	−2.92	179	55	29^{+17}_{-11}	0.24
AzV 235	27.1 ± 1.0	Si III – Si IV	2.98 ± 0.20	39	5.86	0.52	−7.28	−2.64	165	60	53^{+31}_{-19}	0.35
AzV 215	27.1 ± 1.0	Si III – Si IV	2.95 ± 0.20	29	5.62	0.42	−6.69	−2.63	165	60	28^{+17}_{-10}	0.38
AzV 104	28.0 ± 1.0	Si III – Si IV	3.25 ± 0.20	22	5.42	0.28	−6.07	−2.72	140	65	31^{+18}_{-11}	0.22
AzV 410	25.1 ± 1.0	Si III – Si IV	3.10 ± 0.20	23	5.26	0.19	−5.94	−2.47	185	85	24^{+14}_{-9}	0.19
AzV 242	23.2 ± 1.0	Si III – Si IV	2.65 ± 0.20	44	5.71	0.35	−7.25	−2.25	177	55	33^{+19}_{-12}	0.40
AzV 96	21.7 ± 1.0	Si III – Si IV	2.65 ± 0.20	36	5.41	0.30	−6.67	−2.12	158	50	21^{+12}_{-8}	0.31
AzV 264	21.1 ± 1.0	Si III – Si IV	2.50 ± 0.20	39	5.44	0.23	−6.82	−2.04	131	45	18^{+11}_{-7}	0.36
AzV 175	20.0 ± 1.5	Si III – Si IV	2.80 ± 0.20	25	4.97	0.31	−5.74	−1.93	175	30	15^{+9}_{-6}	0.16
Sk 191	21.1 ± 1.0	Si III – Si IV	2.45 ± 0.20	51	5.67	0.52	−7.62	−2.06	127	65	28^{+16}_{-10}	0.40
AzV 18	18.5 ± 1.5	Si II – Si III	2.25 ± 0.20	52	5.45	0.66	−7.16	−1.73	150	50	18^{+11}_{-7}	0.37
NGC330-ELS-04	17.1 ± 1.5	Si II – Si III	2.35 ± 0.20	33	4.93	0.37	−6.00	−1.57	158	35	9^{+5}_{-3}	0.22
AzV 187	16.8 ± 1.0	Si II – Si III	2.20 ± 0.20	57	5.37	0.25	−7.15	−1.54	139	40	19^{+11}_{-7}	0.31
AzV 22	14.2 ± 1.0	Si II – Si III	1.80 ± 0.20	67	5.22	0.38	−7.14	−1.17	145	30	11^{+6}_{-4}	0.36
AzV 393	13.3 ± 1.0	He I – Mg II	1.60 ± 0.25	109	5.53	0.48	−8.01	−1.09	151	30	18^{+10}_{-7}	0.49
AzV 343	12.0 ± 1.0	He I – Mg II	1.98 ± 0.20	49	4.65	0.31	−6.14	−0.75	160	35	9^{+5}_{-3}	0.13
AzV 324	12.5 ± 1.0	He I – Mg II	2.20 ± 0.20	48	4.70	0.06	−6.18	−0.83	156	25	14^{+8}_{-5}	0.09

Table 4.4: Inferred evolutionary masses M_{init}, $M_{\rm evo}$, and ages of the stars. These were derived using an updated Bayesian inference method (Bronner et al. in prep) that is similar to BONNSAI (Schneider et al., 2014a) applied to Brott et al. (2011) SMC evolutionary tracks.

Star	$T_{\rm eff}$	$\log g_c$	$\log L_{\rm bol}$	M_{init}	$M_{\rm evo}$	Age	$\Gamma_{\rm e}^{\rm evo}$
	kK	cm s^{-2}	$L_\odot$	$M_\odot$	$M_\odot$	Myr	
AzV 469	32.0	3.30	5.55	32^{+8}_{-7}	30^{+9}_{-6}	$4.3^{+1.5}_{-0.6}$	$0.27^{+0.08}_{-0.06}$
AzV 372	29.2	3.00	5.68	37^{+6}_{-6}	35^{+7}_{-6}	$4.9^{+0.3}_{-1.1}$	$0.31^{+0.06}_{-0.05}$
AzV 456	30.7	3.35	5.91	50^{+6}_{-5}	47^{+6}_{-4}	$3.3^{+0.2}_{-0.3}$	$0.45^{+0.06}_{-0.04}$
AzV 327	30.5	3.32	5.47	30^{+4}_{-5}	29^{+3}_{-5}	$4.9^{+0.6}_{-0.8}$	$0.23^{+0.03}_{-0.04}$
AzV 235	27.1	2.98	5.86	48^{+5}_{-7}	46^{+4}_{-6}	$3.5^{+0.4}_{-0.3}$	$0.40^{+0.04}_{-0.06}$
AzV 215	27.1	2.95	5.62	35^{+5}_{-4}	33^{+5}_{-3}	$4.3^{+0.5}_{-0.5}$	$0.32^{+0.05}_{-0.03}$
AzV 104	28.0	3.25	5.42	28^{+3}_{-3}	27^{+3}_{-3}	$5.2^{+0.6}_{-0.5}$	$0.25^{+0.03}_{-0.03}$
AzV 410	25.1	3.10	5.26	23^{+2}_{-2}	23^{+2}_{-2}	$6.4^{+0.9}_{-0.7}$	$0.20^{+0.02}_{-0.02}$
AzV 242	23.2	2.65	5.71	39^{+5}_{-4}	38^{+4}_{-4}	$4.1^{+0.4}_{-0.3}$	$0.35^{+0.04}_{-0.04}$
AzV 96	21.7	2.65	5.41	28^{+2}_{-4}	27^{+2}_{-3}	$5.9^{+0.6}_{-0.7}$	$0.25^{+0.02}_{-0.03}$
AzV 264	21.1	2.50	5.44	28^{+4}_{-4}	27^{+4}_{-4}	$5.9^{+0.6}_{-1.0}$	$0.24^{+0.03}_{-0.03}$
AzV 175	20.0	2.80	4.97	17^{+2}_{-1}	17^{+2}_{-1}	$9.3^{+1.2}_{-1.0}$	$0.14^{+0.02}_{-0.01}$
Sk 191	21.1	2.45	5.67	43^{+4}_{-3}	41^{+3}_{-3}	$4.0^{+0.3}_{-0.2}$	$0.27^{+0.02}_{-0.02}$
AzV 18	18.5	2.25	5.45	28^{+4}_{-3}	27^{+3}_{-3}	$5.6^{+0.8}_{-0.6}$	$0.25^{+0.03}_{-0.03}$
NGC330-ELS-04	17.1	2.35	4.93	17^{+2}_{-1}	16^{+2}_{-1}	$9.8^{+1.3}_{-1.1}$	$0.13^{+0.01}_{-0.01}$
AzV 187	16.8	2.20	5.37	25^{+4}_{-4}	24^{+4}_{-4}	$6.0^{+1.4}_{-0.8}$	$0.25^{+0.05}_{-0.05}$
AzV 22	14.2	1.80	5.22	22^{+2}_{-2}	22^{+2}_{-2}	$7.2^{+0.9}_{-1.0}$	$0.18^{+0.02}_{-0.02}$
AzV 393	13.3	1.60	5.53	30^{+4}_{-4}	29^{+9}_{-10}	$5.2^{+0.8}_{-0.6}$	$0.30^{+0.09}_{-0.11}$
AzV 343	12.0	1.98	4.65	13^{+1}_{-1}	13^{+1}_{-1}	$13.3^{+2.0}_{-1.6}$	$0.08^{+0.01}_{-0.01}$
AzV 324	12.5	2.20	4.70	14^{+1}_{-1}	14^{+1}_{-1}	$12.5^{+1.8}_{-1.5}$	$0.09^{+0.01}_{-0.01}$

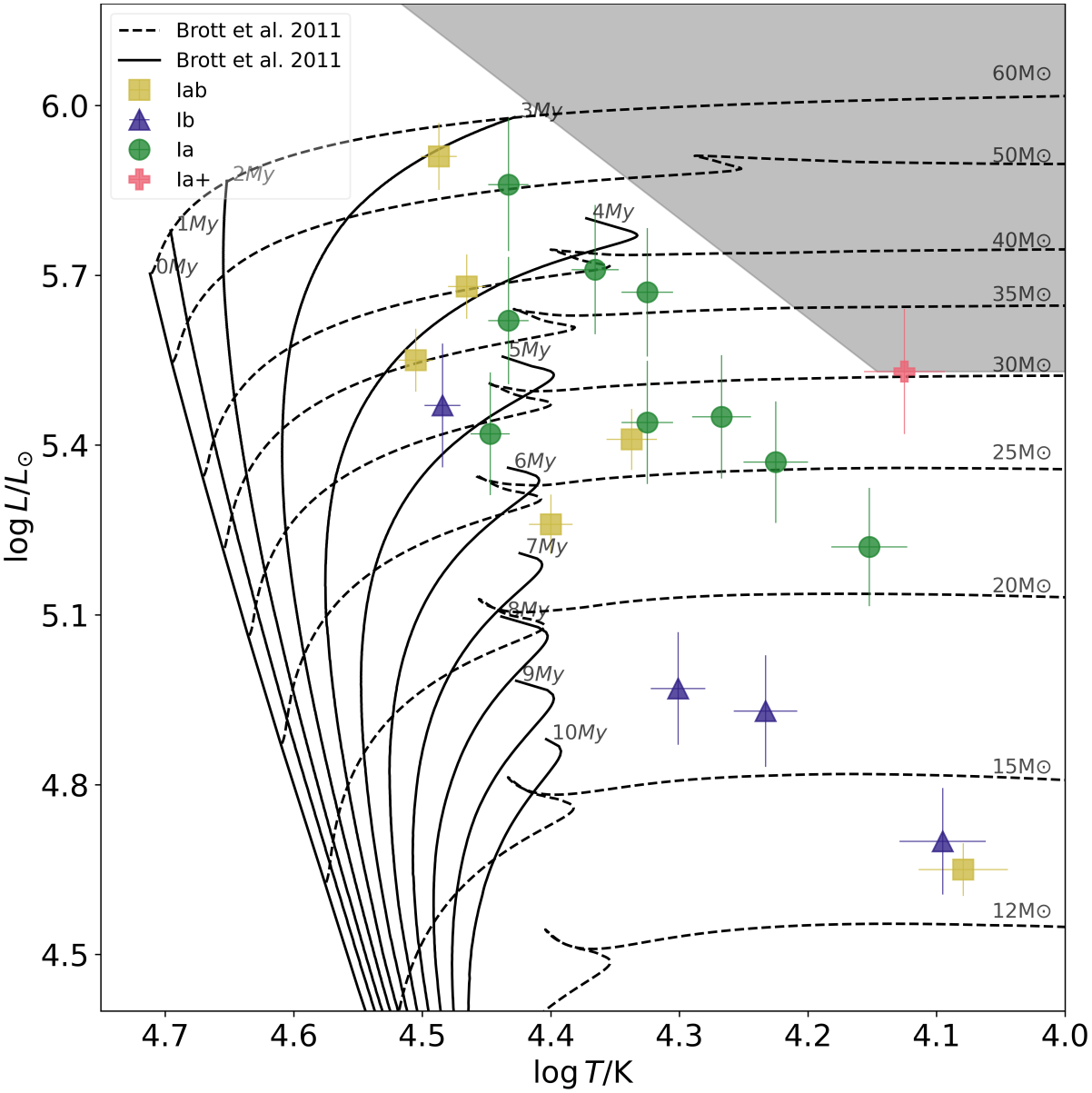


Figure 4.1: Hertzsprung-Russell diagram for our sample. Overlaid in solid black lines are non-rotating SMC isochrones for different ages ($\approx 0-10$ Myr). Dashed black lines are the SMC rotating evolutionary tracks for stellar masses in the range of $\approx 10-60\ M_{\odot}$ with a rotational velocity of 110 km s^{-1}. Both the isochrones and evolutionary tracks are adopted from Brott et al. (2011). The shaded area is defined by the HD limit (Humphreys & Davidson, 1979a; Smith et al., 2004; Davies et al., 2018).

and fits the line ratios of $T_{\rm eff}$ diagnostics best – agrees well with observations within a few hundred Kelvin.

The O supergiants in our sample occupy the region $\log T_{\rm eff}/{\rm kK} > 4.48$ (or $T_{\rm eff} > 30$ kK), and according to the isochrones of Brott et al. (2011), are still in their main-sequence (MS) phase. In contrast, the distribution of the cooler B supergiants ($\log T_{\rm eff}/{\rm kK} < 4.3$) on the HRD hints at them being post-MS objects, according to Brott et al. (2011) single-star evolutionary models. The evolutionary status of hot BSGs ($4.3 < \log T_{\rm eff}/{\rm kK} < 4.48$) remains ambiguous, as they are in close proximity to the terminal-age main sequence (TAMS).

Fig. 4.2 represents the spectroscopic Hertzsprung-Russell diagram (sHRD, Langer & Kudritzki, 2014, see Section 3.2.1 for the definition of sHRD). Our sample covers a $\log \mathcal{L}/\mathcal{L}_\odot$ range of 3.57 (AzV 343) to 4.29 (AzV 393). Similarly to the findings of Chapter 3, we find that the hypergiant AzV 393 is the closest to the Eddington limit of $\log \mathcal{L}/\mathcal{L}_\odot \approx 4.29$ (assuming a hydrogen mass fraction of 0.73).

4.2.2 Stellar masses

Spectroscopic masses, $M_{\rm spec}$, presented in Table. 4.3, were calculated via $g = G\,M/R_*^2$. Since our stars are generally slow rotators, the centrifugal-force corrected gravity, which is calculated via $\log\left(g_c/{\rm cm\,s^{-2}}\right) = \log\left(g + \left(v_{\rm rot}\sin i\right)^2/R_*\right)$ (Herrero et al., 1992), is very similar to $\log g$. By way of example, $\log g_c - \log g = 0.02$ dex for AzV 372, which has the largest $v_{\rm rot}\sin i$ of our sample (100 km s^{-1}). In Table 4.4, we present evolutionary masses, $M_{\rm evo}$, and ages, which were obtained using a Bayesian inference method (V. Bronner et al. in prep) that is similar to Bonnsai (Schneider et al., 2014a), applied to Brott et al. (2011) rotating single-star evolutionary models for SMC metallicity.

In Fig. 4.3 we present the difference between $M_{\rm spec}$ and $M_{\rm evo}$ for our sample. The error bars representing the uncertainties in Fig. 4.3 take into account in quadrature the

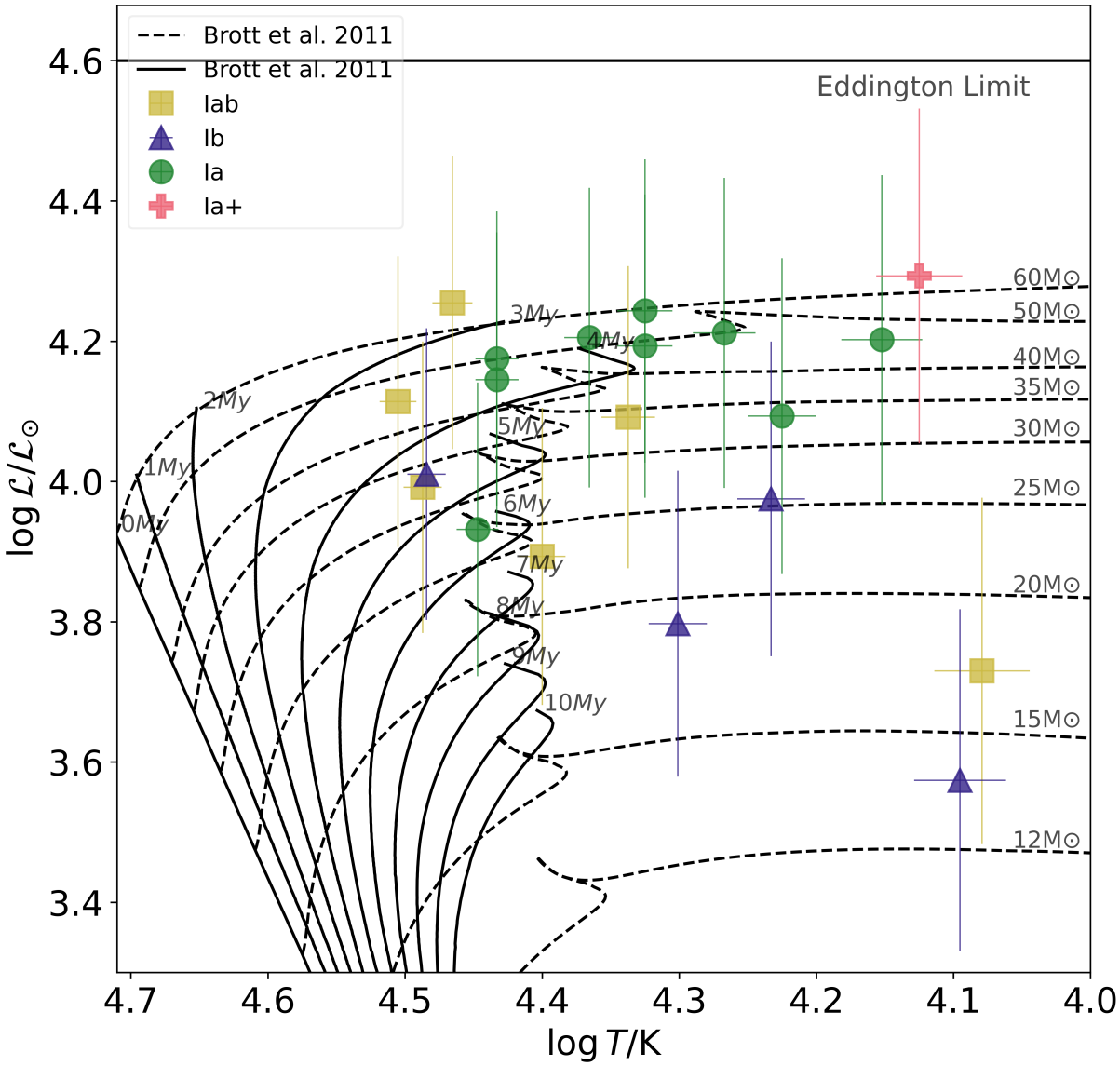


Figure 4.2: The spectroscopic Hertzsprung-Russell diagram for our sample. The evolutionary tracks (dashed black lines) and the isochrones (solid black lines) are the same as in Fig. 3.2, which are taken from Brott et al. (2011). The encoding of the luminosity classes is the same as in Fig. 3.2.

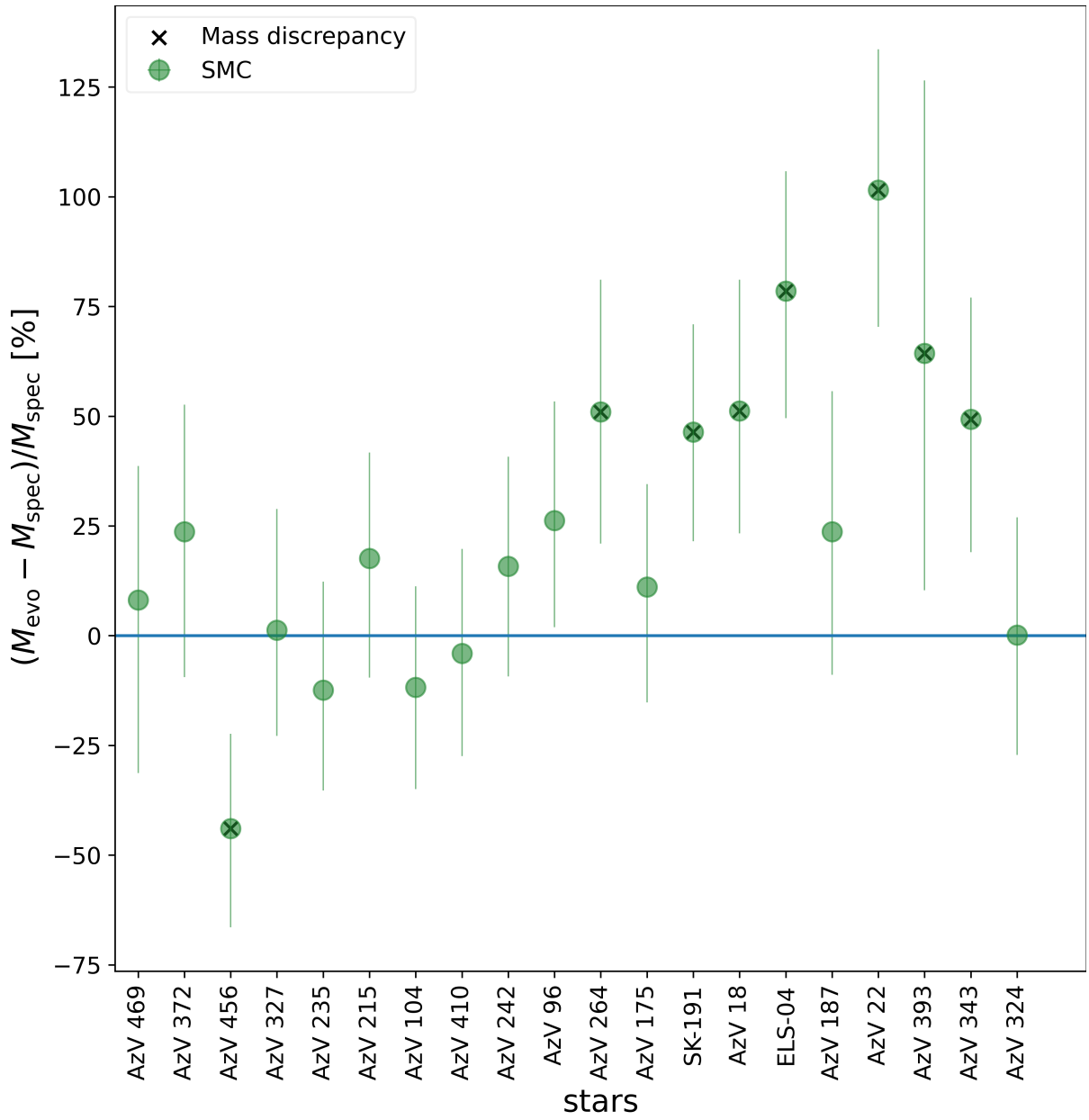


Figure 4.3: Relative (percentage) difference of the evolutionary and spectroscopic masses $(M_{evo} - M_{spec})/M_{spec}$. M_{evo} was obtained using a Bayesian inference method applied to SMC evolutionary models of Brott et al. (2011). The diagonal black crosses indicate the presence of a mass discrepancy.

Table 4.5: Derived wind parameters. $\log \dot{M}$ with † in the superscript indicates an upper limit. v_∞ values with the superscript ‡ indicate that v_∞ was inferred as $v_{\rm edge} \times \langle v_{\rm black}/v_{\rm edge}\rangle_{\rm SMC}$.

Star	$\log L_{\rm bol}$	$\log \dot{M}$	v_∞	$v_{\rm esc,1-\Gamma}$	β	$f_{\rm vol,\infty}$	$v_{\rm cl}$	
	$L_\odot$	$M_\odot\,{\rm yr}^{-1}$	$\rm km\,s^{-1}$	$\rm km\,s^{-1}$			$\rm km\,s^{-1}$	
AzV 469	5.55	-7.00	1800	628	1.0	0.2	30	
AzV 372	5.68	-6.76	1620	509	1.0	0.1	30	
AzV 456	5.91	-7.57	$1313^{\ddagger}$	740	1.0	0.1	30	
AzV 327	5.47	-8.12	$1551^{\ddagger}$	658	1.0	0.03	35	
AzV 235	5.86	-6.66	$1300^{\ddagger}$	553	1.5	0.05	30	
AzV 215	5.62	-7.17	$1585^{\ddagger}$	497	1.7	0.1	35	
AzV 104	5.42	-7.75	$996^{\ddagger}$	637	1.0	0.1	35	
AzV 410	5.26	$-7.65^{\dagger}$	$403^{\ddagger}$	564	1.0	0.1	30	
AzV 242	5.71	-7.47	$942^{\ddagger}$	424	3.1	0.03	30	[1]
AzV 96	5.41	-7.43	$758^{\ddagger}$	409	2.6	0.1	30	
AzV 264	5.44	-7.32	$656^{\ddagger}$	363	3.0	0.1	30	
AzV 175	4.97	$-7.55^{\dagger}$	$437^{\ddagger}$	498	1.0	0.2	30	
Sk 191	5.67	$-6.81^{\dagger}$	381	753	2.5	0.2	30	
AzV 18	5.45	-7.19	$388^{\ddagger}$	310	3.5	0.1	25	
NGC330-ELS-04	4.93	$-7.71^{\dagger}$	$301^{\ddagger}$	490	1.0	0.2	25	
AzV 187	5.37	$-7.77^{\dagger}$	$307^{\ddagger}$	627	1.0	0.2	25	
AzV 22	5.22	-6.75	$160^{\ddagger}$	220	2.5	0.1	25	
AzV 393	5.53	-5.94	$237^{\ddagger}$	206	2.5	0.1	25	
AzV 343	4.65	$-8.20^{\dagger}$	$200^{\ddagger}$	244	1.0	0.1	25	
AzV 324	4.70	$-8.05^{\dagger}$	$178^{\ddagger}$	310	1.0	0.1	25	

uncertainty of $M_{\rm evo}$, which was obtained from the Bayesian inference method, and the uncertainty of $M_{\rm spec}$, which in relative terms sits between 25% and 35%. Generally, $M_{\rm evo}$ is larger than $M_{\rm spec}$ in our sample. We find that 40% of our sample shows a significant discrepancy between $M_{\rm spec}$ and $M_{\rm evo}$. For these stars, $M_{\rm evo}$ is larger than $M_{\rm spec}$, except for AzV 456, for which we find that $M_{\rm spec}$ (83^{+49}_{-31} $M_\odot$) is significantly larger than $M_{\rm evo}$ ($\approx 47^{+6}_{-4}$ $M_\odot$).

4.2.3 Wind properties

[1] $\log \dot{M}$ is subject to an average uncertainty of 0.5 dex. $v_{\rm esc}$ is the escape velocity at the photosphere.

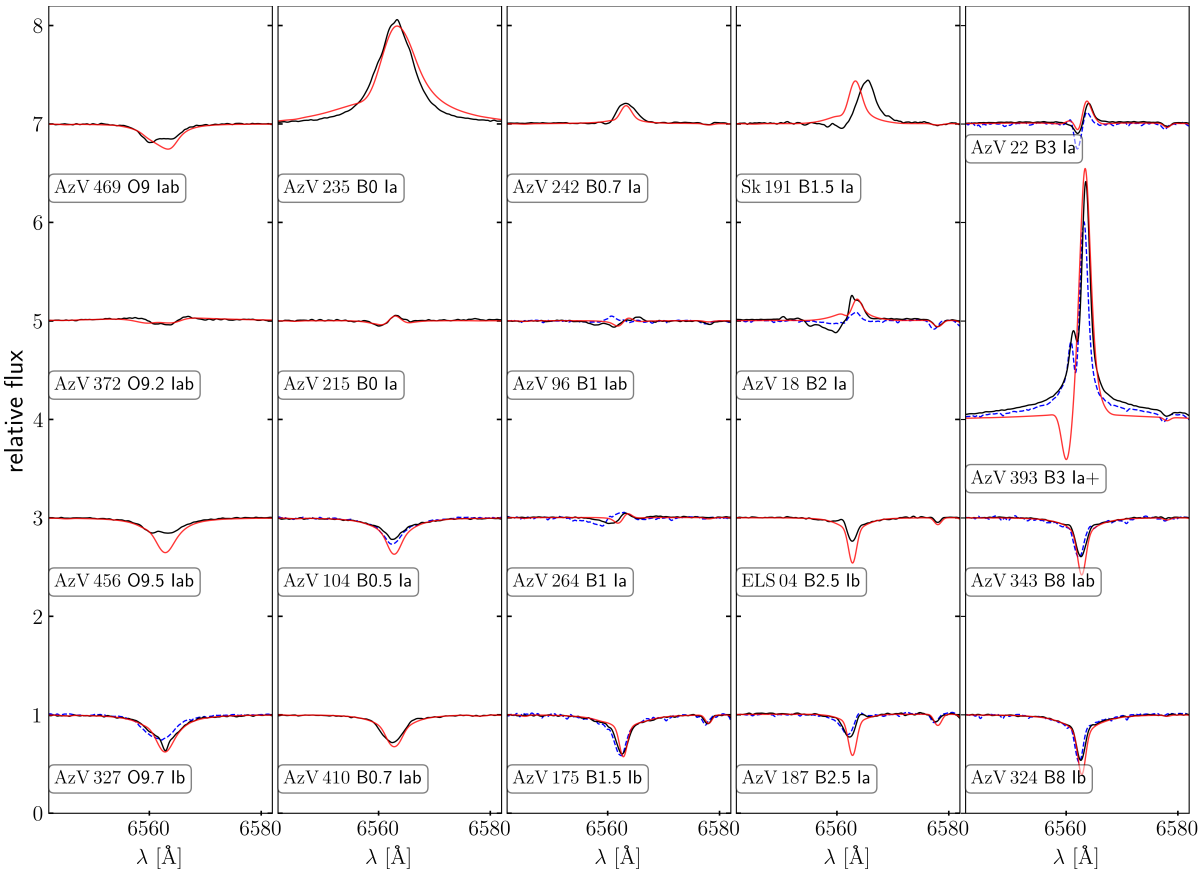


Figure 4.4: Best fits (solid red lines) to XShootU Hα (+ C II λ6578) profiles (solid black lines). Magellan/MIKE spectra are also shown (dashed blue lines), where available, to illustrate line variability.

In Table 4.5, we present the derived wind parameters for our sample. The diverse nature of our sample is shown in the variety of $\log \dot{M}/M_{\odot}\,\mathrm{yr}^{-1}$, covering a range of ≈ -8.20 to -5.94 dex. The highest mass-loss rate is attributed to the mid-B hypergiant AzV 393, and the lowest to the late-B supergiant AzV 343.

In Fig. 4.4, we present our best fits to (red solid line) Hα profiles from XShootU spectra (Sana et al., 2024, DR1). We also include Hα profiles from MIKE observations (Crowther, 2024) to illustrate the typical variability of this wind line. We quantify the $\log \dot{M}$ variability via test fits to MIKE Hα observations, and obtain $\Delta \log \dot{M}/M_{\odot}\,\mathrm{yr}^{-1} = \pm 0.15$ dex, which was taken into account when calculating the uncertainties of $\log \dot{M}$.

We obtain satisfactory fits for cases in which the Hα is fully or partially in emission,

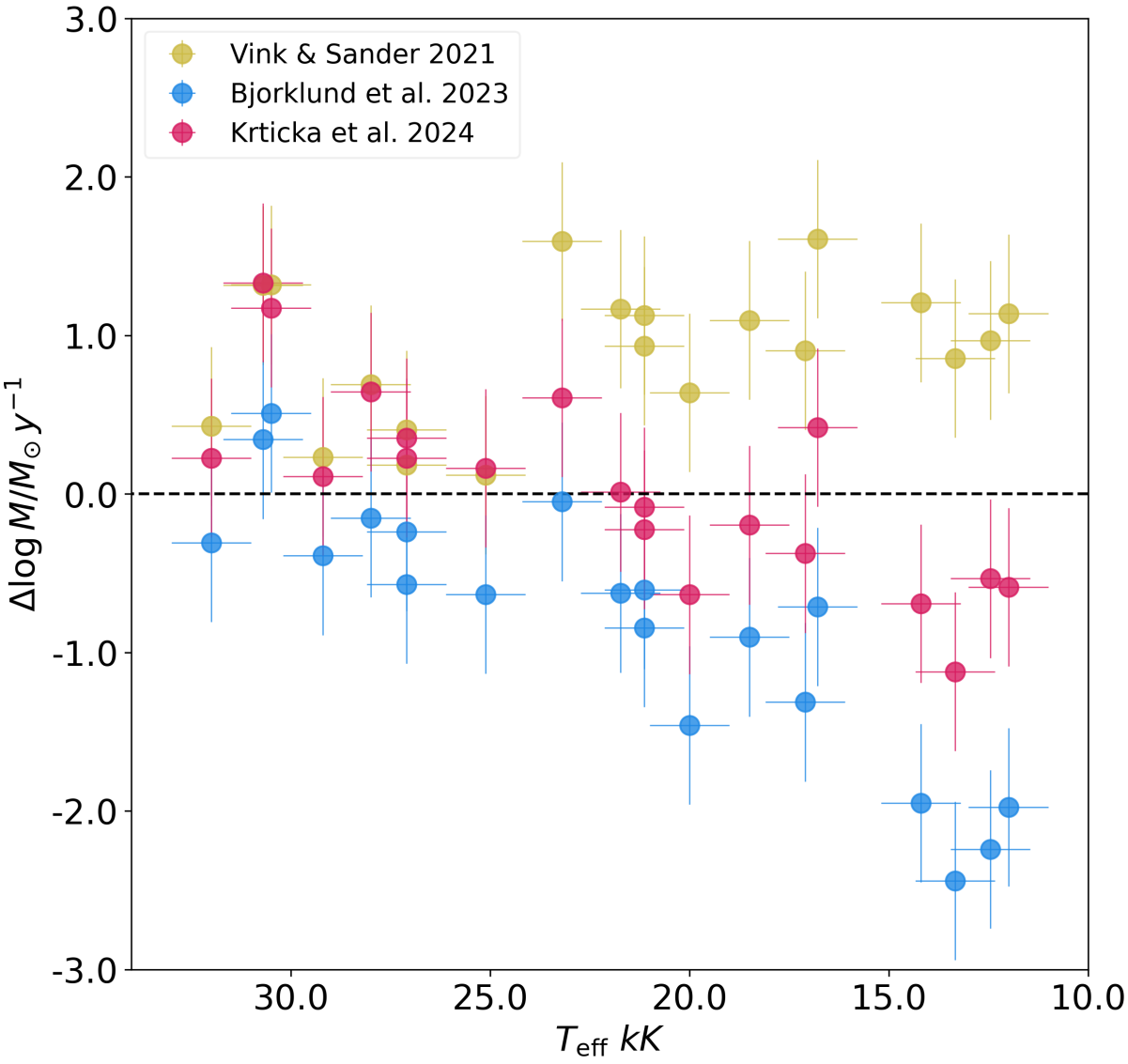


Figure 4.5: $\Delta \log \dot{M}$ vs $T_{\rm eff}$. $\Delta \log \dot{M}$ is the difference between our derived $\Delta \log \dot{M}$ and those obtained from numerical recipes from Vink & Sander (2021) (yellow dots), Björklund et al. (2023) (blue dots), and Krtička et al. (2024) (red dots).

except for Sk 191, the Hα of which shows a redward radial velocity shift that is not present in other photospheric lines. In the cases in which Hα is fully in absorption, we focus on fitting the wings. In any case, when determining $\dot{M}$, we take into account the level of saturation of P Cygni profiles. Nevertheless, for cases in which Hα is fully in absorption, we consider the $\log \dot{M}$ presented in Table 4.5 as an upper limit on mass loss.

In Fig. 4.5, we present a comparison between our derived $\log \dot{M}$ and the mass-loss rates predicted by the numerical recipe of Vink & Sander (2021), Björklund et al. (2023), and Krtička et al. (2024), assuming $Z = 0.2\ Z_{\odot}$. We find that for $T_{\rm eff} \gtrapprox 22$ kK all recipes perform well and match our derived $\log \dot{M}$ within the uncertainties. For $T_{\rm eff} \lessapprox 22$ kK, which is believed to be the region where the predicted bi-stability jump occurs (Vink et al., 2001), the $\log \dot{M}$ from the recipe of Vink & Sander (2021) predictably become much higher than ours by $\approx$ 1.5 dex. The recipe of Krtička et al. (2024) continues to perform well on the cool side of the bi-stability jump, whereas the values from the recipe of Björklund et al. (2023) gradually become much smaller than our measurements.

In general, $\dot{M}$ predictions from numerical recipes agree reasonably well with each other and with empirically derived $\dot{M}$ in the O star regime, but deviate greatly from one another and from empirical $\dot{M}$ in the B star regime. Recalling the discussion of the evolutionary status of our sample in Section 4.2.1, we conclude that predictions from numerical recipes are valid for O-type supergiants on the MS, where massive stars spend most of their lives and where most mass loss takes place. However, for post-MS stars, the empirical mass loss rates behave differently from what is predicted by these numerical recipes.

Our sample spans a wide range of $v_{\infty} \approx 160$–1800 km s^{-1}. In Fig. 4.6 we show v_{∞} versus $T_{\rm eff}$, with our results compared to the empirical recipe of Hawcroft et al. (2024a), results from Bernini-Peron et al. (2024), and velocities calculated from the numerical recipes of Vink & Sander (2021) and Krtička et al. (2021). We find a difference in the slopes with similar offsets. The main caveat of this comparison is that Hawcroft et al.

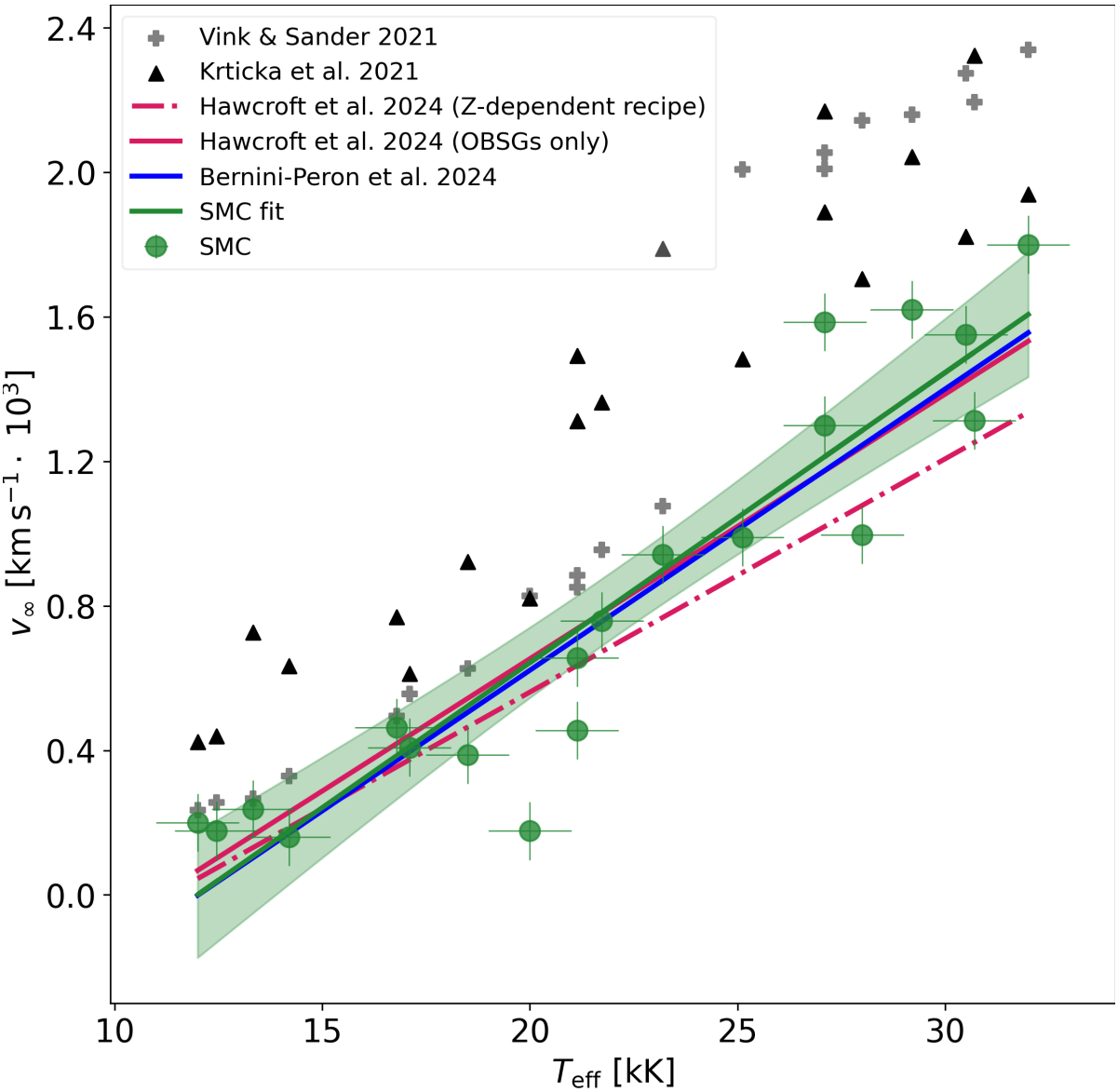


Figure 4.6: v_∞ vs $T_{\rm eff}$. The green dots represent our results. The green line is the linear fit. The dashed magenta line is the Z-dependent v_∞-$T_{\rm eff}$ relation from Hawcroft et al. (2024a). The solid magenta line was obtained from fitting Hawcroft et al. (2024a) results for O and B supergiants only. The solid blue line was obtained from fitting the results of Bernini-Peron et al. (2024). The grey crosses are v_∞ calculated from Vink & Sander (2021) recipe. The black triangles represent v_∞, calculated from the recipe in Krtička et al. (2021).

Table 4.6: Fitting parameter a (slope) and b (intercept) for Equation 4.1.

study	a	b
	kK	$\mathrm{km\,s^{-1}}$
This study	0.08 ± 0.01	963 ± 200
(Hawcroft et al., 2024a, entire sample)	0.09 ± 0.01	1560 ± 420
(Hawcroft et al., 2024a, OB SGs only)	0.07 ± 0.01	811 ± 300
(Bernini-Peron et al., 2024)	0.08 ± 0.02	936 ± 350

(2024a) obtained their results by employing the SEI method, fitting only the C IV λ1548 P Cygni for stars no later than B1 and with various luminosity classes. v_∞ prediction for $T_{\rm eff}$ values below 21 kK, therefore, should not be considered as reliable.

We fitted our results with a simple linear fit of the form

$$v_\infty[\mathrm{km\,s^{-1}}] = aT_{\rm eff}[\mathrm{kK}] \; - \; b[\mathrm{km\,s^{-1}}]. \tag{4.1}$$

In Table 4.6, we present the slope, a, and intercept, b, from Equation 4.1, and compare them to the results of Hawcroft et al. (2024a) and Bernini-Peron et al. (2024). We find that our derived fitting parameters are in excellent agreement with the parameters from (Hawcroft et al., 2024a) when considering only O and B supergiants. We also find excellent agreement with the results of Bernini-Peron et al. (2024).

Our velocities agree with predictions from the recipe of Vink & Sander (2021) below 25 kK, but are lower by $\approx 30\%$ for temperatures above that threshold. We also find that the recipe from Krtička et al. (2021) systematically overpredicts the velocities by an average of ≈ 500 $\mathrm{km\,s^{-1}}$.

Our results in Table 4.5 show that a high β ($\approx 2.5 \pm 0.6$) is preferred to obtain a satisfactory fit for Hα in the cases in which it is fully or partially in emission. This agrees with the findings of Bernini-Peron et al. (2024), who require $\beta > 2$ for most of their SMC sample. Similarly, Crowther et al. (2006) obtained an average $\beta = 2$ from a sample of early Galactic B supergiants.

Due to the weakness of the winds of SMC supergiants, and consequently the lack of broad saturated P Cygni profiles in the UV and Hα emission, we were able to constrain $f_{\rm vol,\infty}$ for only nine stars in our sample. We did not find any correlation between $f_{\rm vol,\infty}$ and $T_{\rm eff}$, $L_{\rm bol}$, or $\dot{M}$. This is similar to our findings in Chapter 3 and has been observed in recent studies that conduct UV and optical spectroscopic analyses of OB stars in multiple environments and utilise various codes with different clumping implementations (Hawcroft et al., 2024b; Bernini-Peron et al., 2024; Verhamme et al., 2024; Brands et al., 2025).

4.2.4 Rotation

In Table 4.3 we present $v_{\rm rot} \sin i$ of our sample. Our sample spans a range of $v_{\rm rot} \sin i$ from 25 km s^{-1} to 100 km s^{-1}, with a mean $v_{\rm rot} \sin i$ of 51 km s^{-1} and a standard deviation of 19 km s^{-1}. This agrees with the findings of Dufton et al. (2006), who analysed a sample of 24 SMC and Galactic B supergiants and found a linear correlation between $v_{\rm rot}$ and $T_{\rm eff}$ with a value of $v_{\rm rot} \sin i$ of $\approx$ 60 and 30 km s^{-1} for $T_{\rm eff}$ = 28 and 12 kK, respectively.

In Table 4.7, we compare our derived $v_{\rm rot} \sin i$ to the $v_{\rm rot} \sin i$ and $v_{\rm mac}$ that were obtained from the IACOB-BROAD tool, which employs a combined Fourier transform and goodness-of-fit approach that allows for the extraction of line-broadening parameters (Simón-Díaz & Herrero, 2014b). We applied IACOB-BROAD to a subsample of our stars with high-resolution MIKE data. The line we used to extract the rotational properties is Si III λ4552 for the entire subsample, except for the late B supergiants AzV 324 and AzV 343, for which we used Si II λ6347.

We find that our derived $v_{\rm rot} \sin i$ agree with those obtained from IACOB-BROAD within 10 km s^{-1}, except for AzV 104 and AzV 327, where the IACOB-BROAD $v_{\rm rot} \sin i$ is 15 and 20 km s^{-1} higher than ours, respectively. On the other hand, we tend to underestimate $v_{\rm mac}$ on average by $\approx$ 20 km s^{-1}. The largest difference in $v_{\rm mac}$ are observed

Table 4.7: Comparison of our adopted broadening parameters with those obtained via IACOB-BROAD (Simón-Díaz & Herrero, 2014b) applied to high-resolution MIKE data.

Star	by eye+XShootU		IACOB-BROAD+MIKE		
	$v_{\rm rot}\sin i$	$v_{\rm mac}$	$v_{\rm rot}\sin i$	$v_{\rm mac}$	line
	km s^{-1}	km s^{-1}	km s^{-1}	km s^{-1}	
AzV 327	55	20	64^{+35}_{-62}	87^{+42}_{-55}	Si III λ4552
AzV 104	65	20	80^{+19}_{-53}	45^{+63}_{-43}	Si III λ4552
AzV 96	50	20	52^{+16}_{-24}	59^{+23}_{-29}	Si III λ4552
AzV 264	45	20	45^{+15}_{-43}	33^{+39}_{-31}	Si III λ4552
AzV 18	50	20	43^{+11}_{-18}	44^{+20}_{-21}	Si III λ4552
NGC330-ELS-4	35	20	33^{+9}_{-18}	29^{+19}_{-19}	Si III λ4552
AzV 187	40	20	36^{+17}_{-34}	41^{+27}_{-35}	Si III λ4552
AzV 393	30	20	35^{+16}_{-32}	30^{+33}_{-28}	Si III λ4552
AzV 343	35	20	44^{+9}_{-21}	19^{+33}_{-17}	Si II λ6347
AzV 324	25	20	21^{+6}_{-9}	26^{+8}_{-10}	Si II λ6347

Table 4.8: Best-fitting helium (Y, by mass) and CNO (ϵ_X, by number) abundances. The uncertainties of the helium mass fraction are 10% . The adopted uncertainty of CNO abundances is ±0.3 dex. The last two columns represent the cumulative CNO mass fraction relative to the cumulative CNO SMC baseline and solar baseline, respectively. Oxygen abundance values with the asterisk subscript were obtained from fitting the O I $\lambda\lambda\lambda 7772 - 7774 - 7775$ multiple, and are considered lower limits.

Star	Y	ϵ_C	ϵ_N	ϵ_O	$\frac{\Sigma CNO}{\Sigma CNO_{SMC}}$	$\frac{\Sigma CNO}{\Sigma CNO_{\odot}}$
AzV 469	0.52	7.3	8.1	8.2	2.2	0.42
AzV 372	0.52	7.2	7.8	8.2	1.7	0.33
AzV 456	0.30	7.2	7.2	8.1	1.0	0.19
AzV 327	0.46	7.2	7.8	8.1	1.3	0.24
AzV 235	0.30	7.0	7.8	7.9	1.0	0.19
AzV 215	0.30	7.0	8.0	8.1	1.6	0.31
AzV 104	0.30	7.0	7.7	8.0	1.0	0.20
AzV 410	0.37	7.1	7.7	8.0	1.1	0.22
AzV 242	0.30	7.0	7.5	8.0	1.0	0.18
AzV 96	0.30	6.7	7.9	7.8	0.9	0.18
AzV 264	0.46	6.8	7.9	7.8	1.1	0.21
AzV 175	0.30	7.1	7.5	8.1	1.1	0.21
Sk 191	0.43	6.9	7.9	8.0	1.2	0.23
AzV 18	0.43	7.1	7.7	8.0	1.1	0.22
NGC330-ELS-04	0.40	7.0	7.9	7.9	1.2	0.23
AzV 187	0.30	7.2	7.5	8.0	0.9	0.18
AzV 22	0.46	6.9	8.0	8.0	1.4	0.27
AzV 393	0.30	6.9	7.8	8.0	1.1	0.21
AzV 343	0.40	7.6	7.9	7.5*	1.1	0.20
AzV 324	0.34	7.2	7.6	7.5*	0.6	0.11
Averages	0.37	7.0	7.8	7.9	1.1	0.23

in AzV 327 and AzV 96, for which the values obtained from IACOB-BROAD are higher by 67 and 39 km s^{-1}, respectively.

4.2.5 Chemical composition

We present the best-fitting chemical abundances for our sample in Table 4.8. We find moderate helium enhancement for our sample relative to the SMC baseline (Y∼0.25, Russell & Dopita, 1990), which is to be expected in a sample comprised of blue supergiants. Fig. 4.7 shows that all stars in our sample exhibit significant nitrogen enrichment.

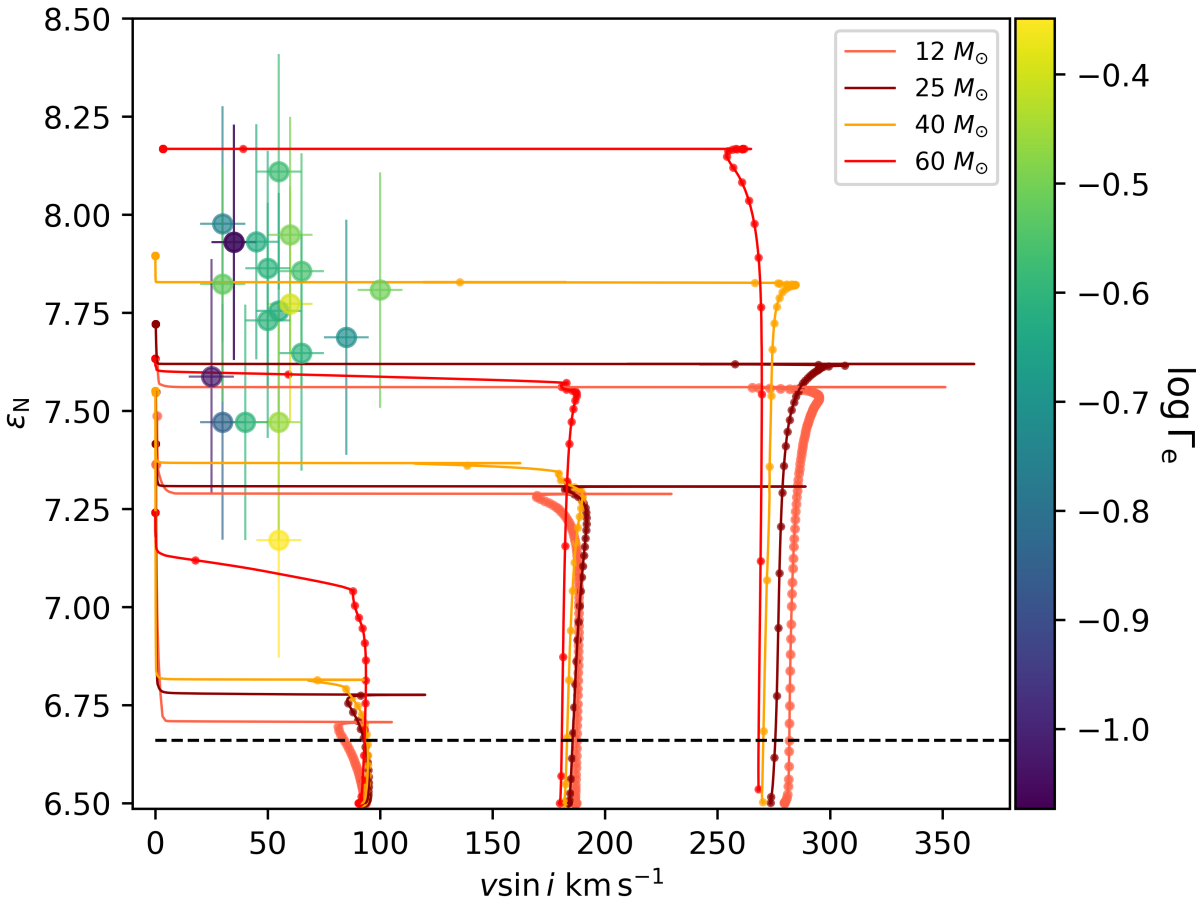


Figure 4.7: ϵ_N vs $v_{rot} \sin i$. The colour scheme corresponds to the value of Γ_e. The solid pink, brown, orange, and red lines represent SMC evolutionary tracks for initial masses of 12 $M_\odot$, 25 $M_\odot$, 40 $M_\odot$, and 60 $M_\odot$, respectively, with initial rotational velocities of 110, 250, 350 km s^{-1} (Brott et al., 2011). We multiplied by a factor of $\pi/4$ to take into account the inclination of the rotation axis (Hunter et al., 2008b). The dashed black line represents the baseline ϵ_N in the SMC (Vink et al., 2023). The dots along the evolutionary tracks represent time steps of 0.1 Myr

According to the rotating single-star evolutionary models of Brott et al. (2011) that include rotational mixing, this enrichment can be explained by the high initial rotational velocities ($v_{\rm rot} \sin i > 300$ km s^{-1}), which cause nitrogen synthesised in the interior of the star to be transported to the surface. However, Dufton et al. (2006) found that $v_{\rm rot} \sin i$ of SMC B supergiants falls in the range of $\approx$ 60–30 km s^{-1}, whereas Mokiem et al. (2006) found that $v_{\rm rot} \sin i$ falls in the range of $\approx$ 150–180 km s^{-1} from a diverse sample of SMC O and early B stars.

Spectroscopic studies of the rotational properties of O stars in the SMC, LMC, and the MW show that most early O stars, which are the progenitors of B supergiants, are not fast rotators. Ramachandran et al. (2019) find that $\approx$ 75% of SMC O stars have $v_{\rm rot} \sin i < 200$ km s^{-1}. In the Tarantula nebula, Ramírez-Agudelo et al. (2013) find that the distribution of $v_{\rm rot} \sin i$ of O stars peaks at $\approx$ 80 km s^{-1}. Similarly, (Holgado et al., 2022) find that the distribution of $v_{\rm rot} \sin i$ of O stars across all luminosity classes in the MW peaks at $\approx$ 80 km s^{-1}.

These observed distributions challenge the assumption that extremely high initial or current rotational velocities are the explanation for the nitrogen enhancement. Only about $\approx$ 25% of the massive stars are effectively single, with the overwhelming majority of the fastest rotators being the product of binary interaction (de Mink et al., 2013; Britavskiy et al., 2025; Villaseñor et al., 2025; Bodensteiner et al., 2025; Sana et al., 2025). Therefore, other processes should be considered to explain the nitrogen enhancement, such as binary interaction in the history of the star or the potential existence of a currently undetected companion.

Fig. 4.8 shows the ratio N/C versus N/O. Following the analytical solution of Maeder et al. (2014), the upper and lower CNO limits (dashed black lines) were calculated using the baseline CNO abundance averages of the SMC from Vink et al. (2023). The majority of our sample falls between the two boundaries and agrees with the expected yield of elements processed by the CNO cycle. The exceptions are AzV 324 and AzV 343, for

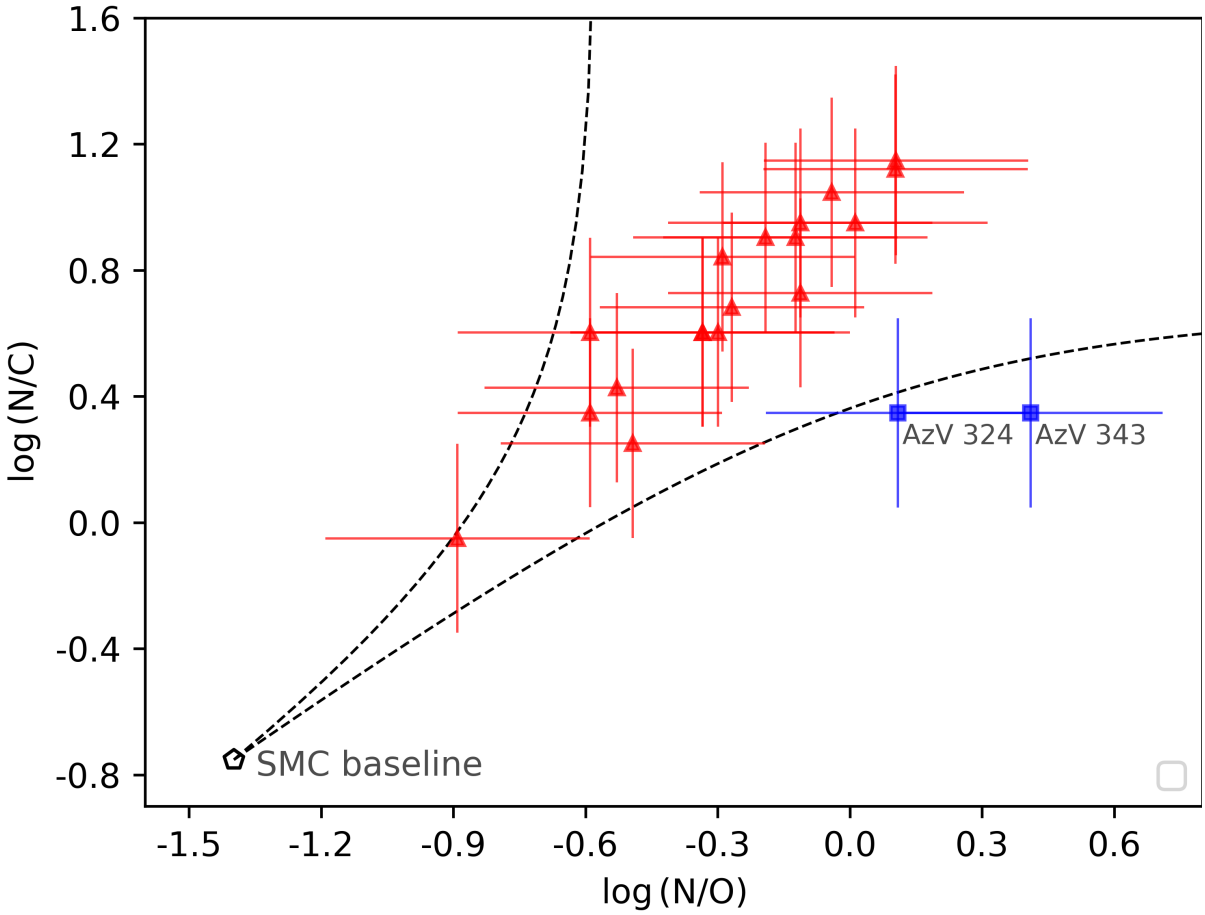


Figure 4.8: $\log \mathrm{N/C}$ vs $\log \mathrm{N/O}$. The red triangles show the distribution of our sample. The stars for which the oxygen abundance was obtained from fitting the O I $\lambda\lambda\lambda 7772 - 7774 - 7775$ multiplet are shown in blue squares. The dashed black lines represent the upper and lower boundaries adopted from Maeder et al. (2014).

which we obtained the oxygen abundance by fitting the O I $\lambda\lambda\lambda 7772 - 7774 - 7775$ multiplet, due to the absence of any other oxygen lines in the optical range. We found that a satisfactory fit to this complex line requires a reduction in the oxygen mass fraction in the model by a factor of four, which explains the high N/O ratios in Fig. 4.8 for these objects. As is explained in Chapter 3, the O I $\lambda\lambda\lambda 7772-7774-7775$ multiplet is extremely sensitive to $T_{\rm eff}$ variations at this range; therefore, the oxygen content obtained by fitting those lines is highly uncertain.

Our sample has two stars (AzV 469 and AzV 327) in common with Martins et al. (2024) , who employed CMFGEN to obtain the chemical abundances of a sample of SMC and LMC O stars using spectroscopy from ULLYSES and XShootU. We find that our obtained $\epsilon_{\rm N}$ for these stars agrees within 0.1 dex with their derived nitrogen abundances, whereas carbon and oxygen do not agree so well, though they match within the quoted uncertainties.

We find that the total CNO mass fraction is conserved for most of our sample, except AzV 469, AzV 372, and AzV 215. In the case of these stars, enhanced nitrogen abundances were required to obtain a satisfactory match to the diagnostic lines, and oxygen mass fractions slightly larger than baseline were also required to obtain satisfactory fits for oxygen lines. This explains the implausibly large ratio of cumulative CNO mass fraction to the cumulative solar CNO mass fraction, $\Sigma{\rm CNO}/\Sigma{\rm CNO}_{\odot}$. We use these examples as a reminder of the large uncertainties associated with the determination of abundances in supergiants from our approach, which are in part due to the sensitivity of the ionisation structure of CNO lines to variations in $T_{\rm eff}$ and $\log g$, but also the fixed micro-turbulent velocity, and the extent of the atomic model adopted in the calculation (number of important levels and superlevels), and the incompleteness of the atomic data.

4.3 Discussion

Table 4.9: Slopes, x, and vertical offsets, $\log D_0$, of Equation 4.2 of this study and from Chapter 3.

Galaxy	x	$\log D_0$	Sp. T.	Lum. Cl.	num. stars
SMC	1.73 ± 1.00	17.8 ± 5.62	O9-B3	I	9
LMC	1.39 ± 0.54	20.42 ± 3.04	O9-B3	I	14

4.3.1 Metallicity effect

Fig. 4.9 shows the modified wind momentum, which was introduced by Kudritzki et al. (1999) as $D_{\rm mom} = \dot{M} v_\infty \sqrt{R_*/R_\odot}$, as a function of $L_{\rm bol}$. We fitted our derived values using the relation

$$\log D_{\rm mom}^{\rm SMC} = \log D_0 + x \log \frac{L_{\rm bol}}{L_\odot}. \tag{4.2}$$

In Fig. 4.9, solid lines are fits to the stars (circles) that show both P Cygni profiles in the UV and Hα in emission, making their determined wind parameters the most reliable. We can see that including stars with Hα in absorption (triangles) in the linear fit slightly changes the slope of the fit for the LMC sample from Chapter 3 (dash-dotted green line). Doing the same for our SMC sample decreases the vertical offset of the fit (dash-dotted yellow line), albeit very slightly.

In Table 4.9, we present the best fitting parameters of Equation 4.2 (slopes, x, and offsets, $\log D_0$). Comparing the $D_{\rm mom}$ of the current SMC sample to the LMC sample analysed in Chapter 3, we find that the slope of the SMC is slightly steeper than the LMC, albeit quite similar. We also find a large difference in the intercepts between the two samples, which can be attributed to the Z dependence of wind properties.

In Figure 4.10, we show v_∞ as a function of $T_{\rm eff}$ of the present study compared to the results from Chapter 3. Figure 4.11 shows $\log \dot{M}$ vs $\log L_{\rm bol}$ from this study compared to Chapter 3. v_∞ does not show signs of Z dependence, whereas $\log \dot{M}$ shows a clear offset between the two samples, indicating a strong Z dependence. Therefore, we can assume that the Z dependence of $D_{\rm mom}$ is dominated by the Z dependence of $\dot{M}$.

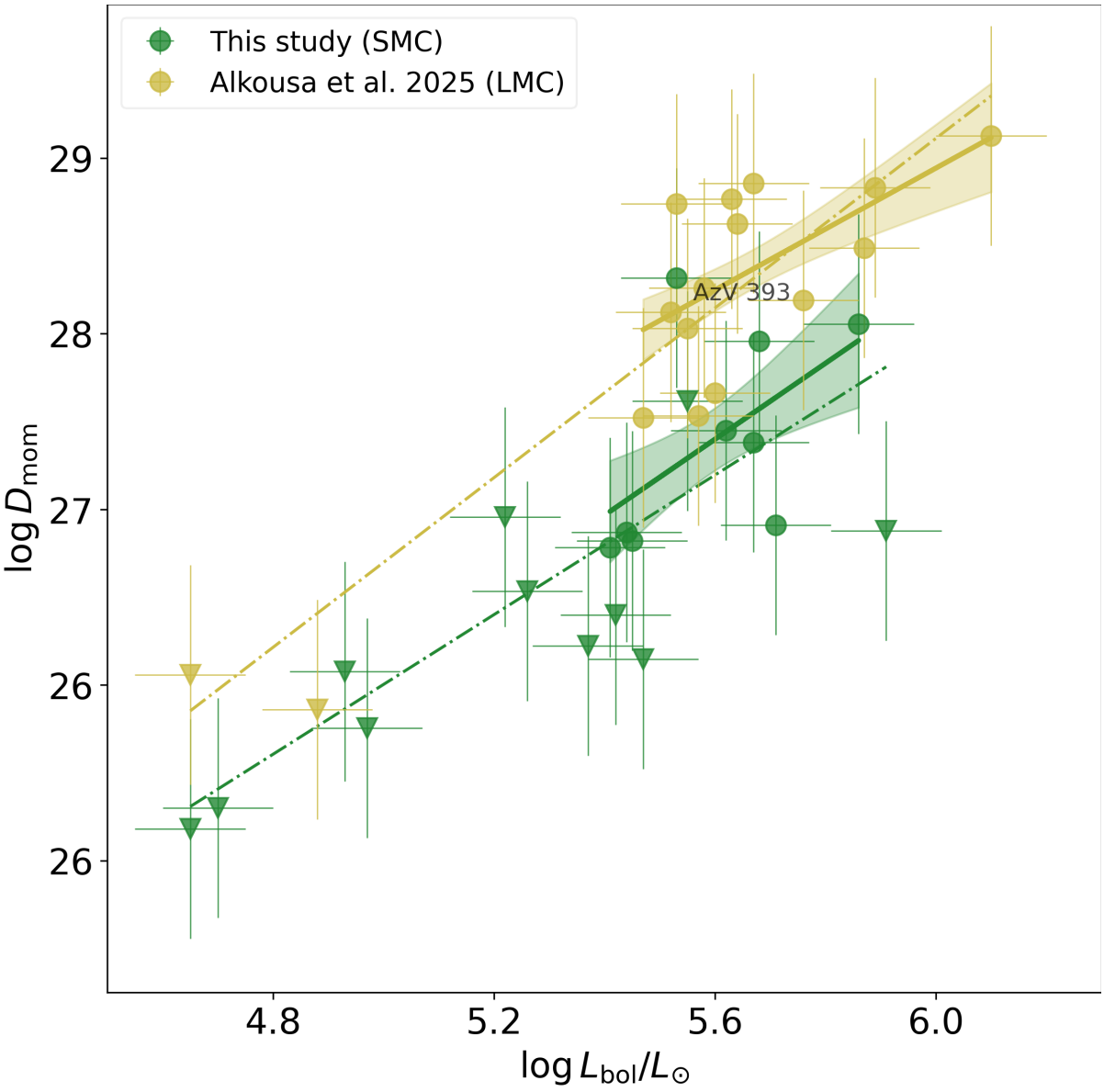


Figure 4.9: $D_{\rm mom}$ vs $\log L_{\rm bol}$. The green symbols represent the SMC sample. The yellow symbols represent the LMC sample from Chapter 3. Circles indicate stars with reliable UV and optical wind diagnostics. Triangles indicate upper limits. Solid lines are fits to the circles, in which the triangles (upper limits) are not used. Dash-dotted lines are fits for the entire sample.

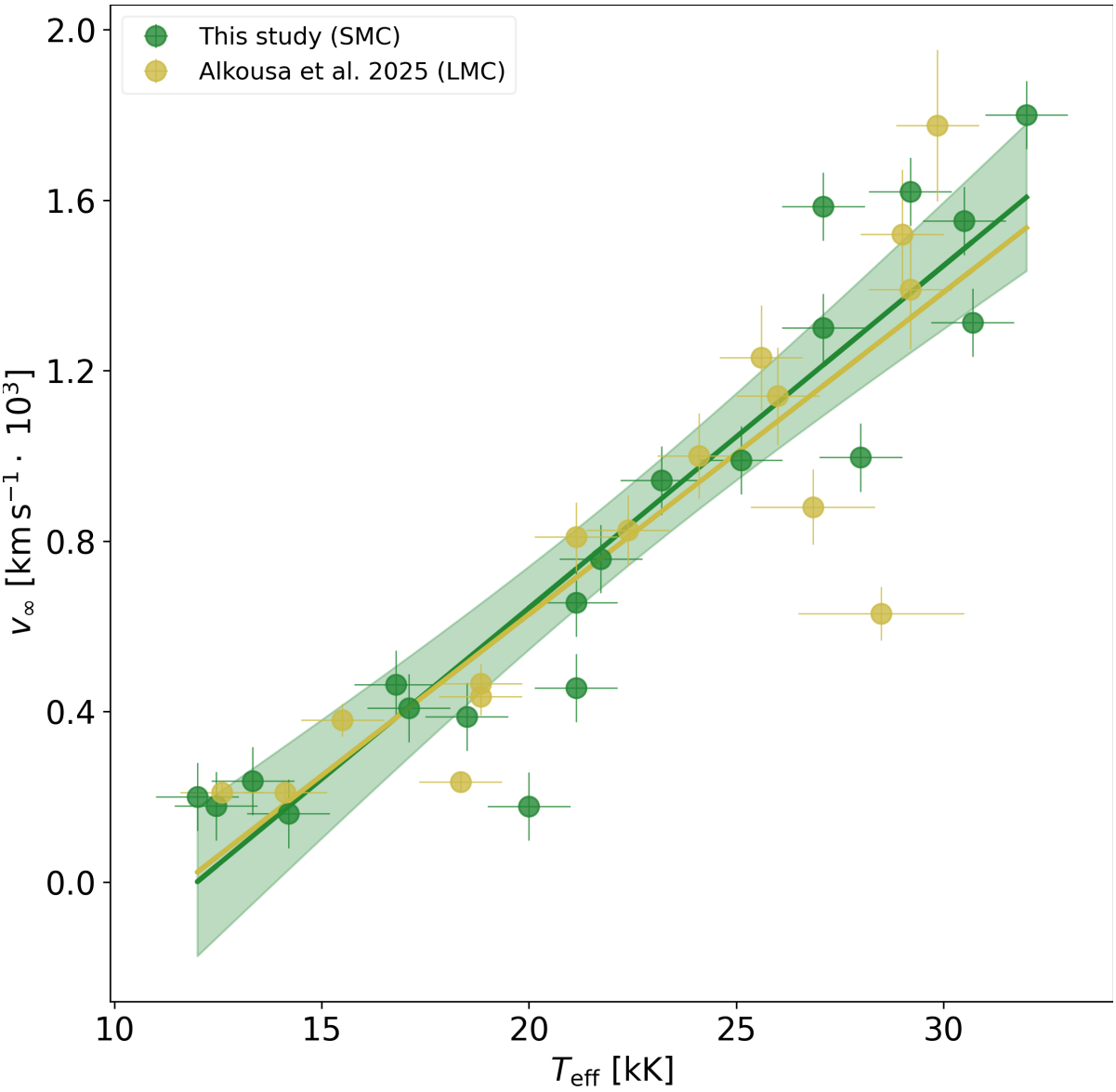


Figure 4.10: v_∞ vs $T_{\rm eff}$. The symbol and colour encoding are the same as in Fig. 4.9.

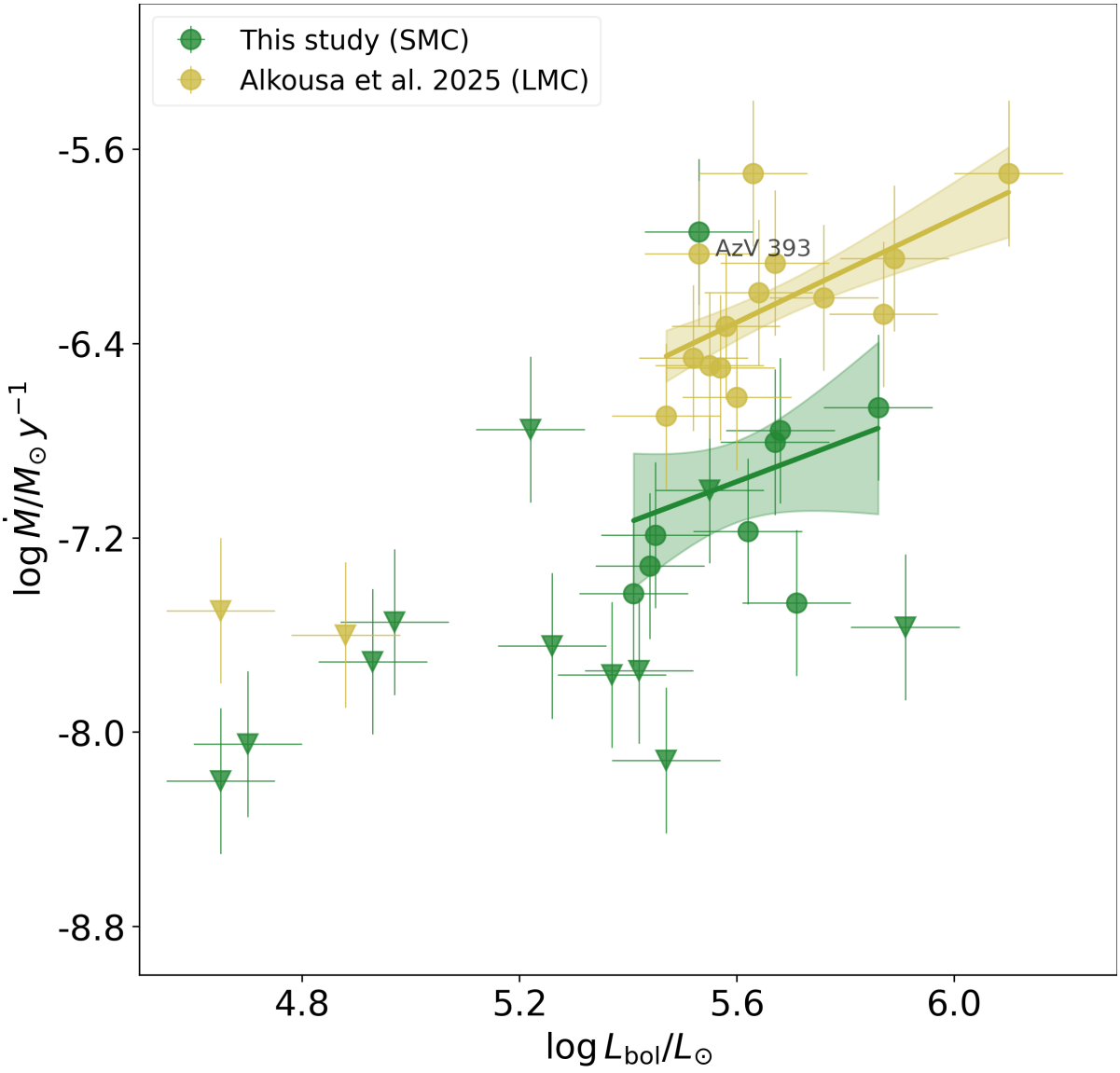


Figure 4.11: $\log \dot{M}$ vs $\log L_{\rm bol}$. The green symbols represent the SMC sample. The yellow symbols represent the LMC sample from Chapter 3. Circles indicate stars with reliable UV and optical wind diagnostics. Triangles indicate upper limits. Solid lines are fits to the circles. Upper limits (triangles) are not included in the linear fits.

Table 4.10: Fitting parameter of Equation 4.3.

parameter	This study	Backs et al. (2024)
a	1.16 ± 0.48	0.64
b	-0.75 ± 1.14	-2.84
c	1.38 ± 4.03	0.71
d	29.17 ± 6.39	29.27

Following Krtička & Kubát (2018) and Backs et al. (2024), we obtained an equation for the Z-dependent $\log D_{\rm mom}$ of the form

$$\log D_{\rm mom} = (a + b \log \frac{Z}{Z_\odot}) \log \frac{L_{\rm bol}}{10^6 L_\odot} + c \log \frac{Z}{Z_\odot} + d, \tag{4.3}$$

where from Equation 4.2 $x = a + b \log \frac{Z}{Z_\odot}$, $\log D_0 = c \log \frac{Z}{Z_\odot} + d$, and a, b, c, and d are fitting parameters. The results of the fitting are presented in Table 4.10, assuming that $Z_{\rm LMC} = 0.5 Z_\odot$ and $Z_{\rm SMC} = 0.2 Z_\odot$. We also include values from Backs et al. (2024) in Table 4.10.

In parallel with the present study, Verhamme et al. (2025) have analysed a sample of ULLYSES/XShootU SMC B supergiants using FASTWIND and KIWI-GA. They find broadly comparable mass-loss rates and wind momenta relative to LMC B supergiants (Verhamme et al., 2024), in contrast to our results, despite having 13 stars in common with our sample. This surprising result could be attributed to several issues. Firstly, the determination of robust wind parameters for late-B supergiants in the SMC is particularly challenging due to the lack of wind diagnostics, and the current version of FASTWIND is known to exhibit convergence difficulties below 14 kK (de Burgos et al., 2024b). These issues could have skewed KIWI-GA solutions to higher $D_{\rm mom}$. This is confirmed when examining the Hα fits of Verhamme et al. (2025), where the preferred solution overpredicts Hα emission. In addition, their derived $T_{\rm eff}$ often deviates quite significantly from the usual spectral type – temperature scale of B supergiants (see e.g.

Lanz & Hubeny, 2007b; Trundle et al., 2007; Nieva, 2013). By way of example, Verhamme et al. (2025) obtained a lower $T_{\rm eff}$ for AzV 410 (B0.7 Iab) than NGC330 ELS 4 (B2.5 Ib).

4.3.2 Bi-stability jump

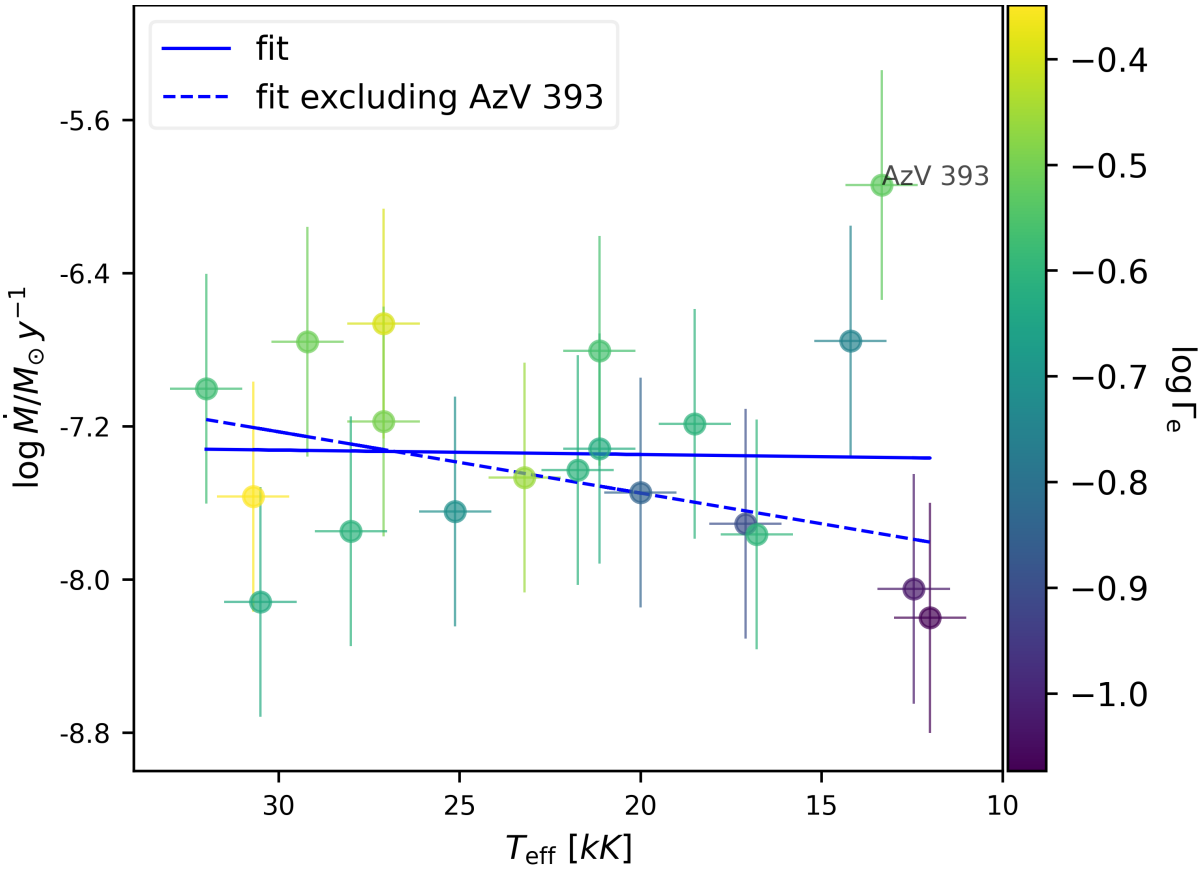


Figure 4.12: $\log \dot{M}$ versus $T_{\rm eff}$. The solid blue line is a simple linear fit to the entire sample. The colour gradient correlates with the value of Γ_e.

In Fig. 4.12, we present our derived $\log \dot{M}$ in terms of $T_{\rm eff}$. This confirms that AzV 393 possesses much higher $\dot{M}$, not just compared to objects with similar $T_{\rm eff}$, but even compared to the hotter OB supergiants in our sample. We do not find any sign of a large increase in $\dot{M}$ around 25-21 kK, which could be attributed to the bi-stability jump. Using a simple linear regression, we find that $\log \dot{M}$ is constant with $T_{\rm eff}$ (solid

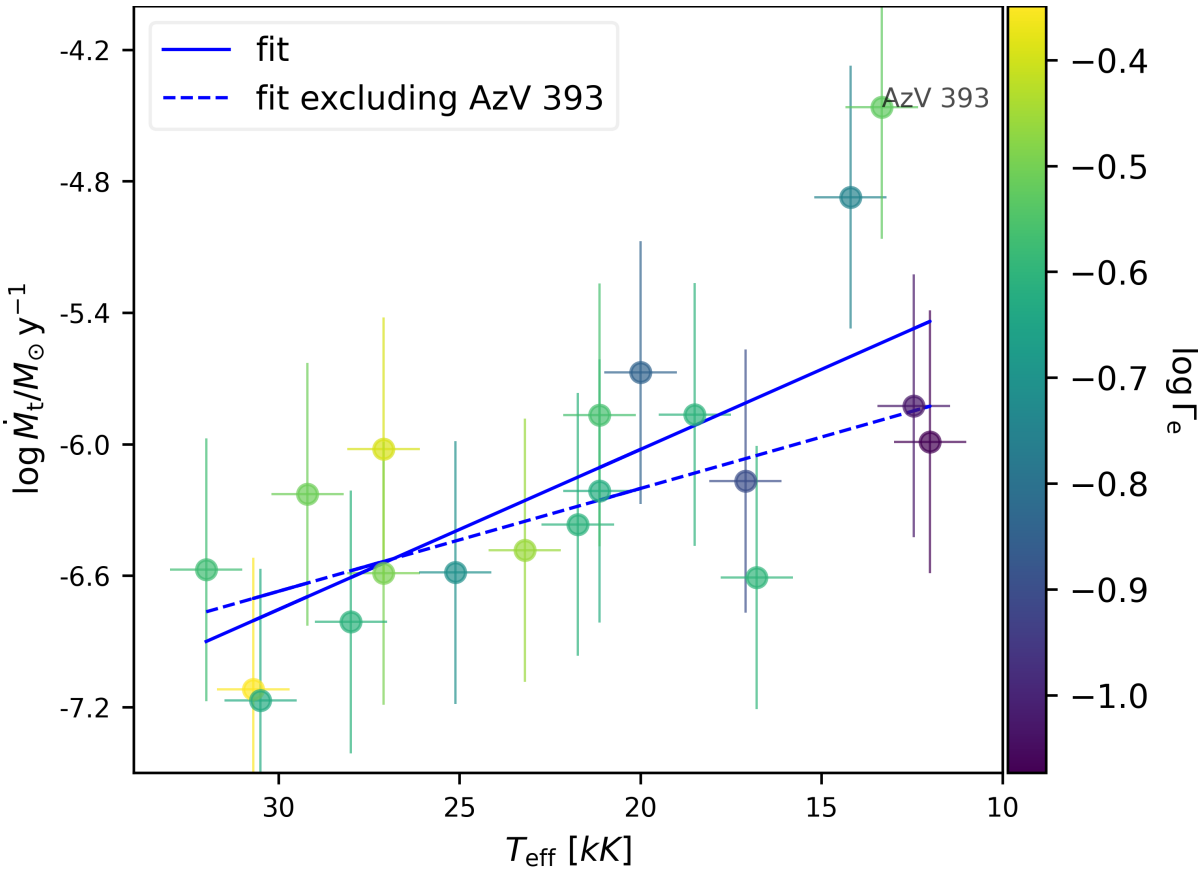


Figure 4.13: $\log \dot{M}_t$ versus $T_{\rm eff}$. The symbol and colour encoding are the same as in Fig. 4.12.

blue line). Excluding the hypergiant AzV 393 from the fit (dashed blue line), we find that $\log \dot{M}$ decreases with $T_{\rm eff}$.

To investigate the effect of luminosity, we calculated the transformed mass-loss rate, which is defined by Gräfener & Vink (2013) as

$$\dot{M}_t = \dot{M} \cdot f_{\rm vol,\infty}^{-1/2} \cdot (10^3 {\rm km\,s^{-1}}/v_\infty) \cdot (10^6 L_\odot/L_{\rm bol})^{3/4}. \quad (4.4)$$

In Fig. 4.13, we compare $\log \dot{M}_t$ to $T_{\rm eff}$. We find that when including or excluding AzV 393 in the linear fit, $\log \dot{M}_t$ increases with temperature. This is in contrast to the results of Bernini-Peron et al. (2024), which hint at a constant behaviour of the mass-loss rate with temperature. The reason for this trend could be our comparably low values

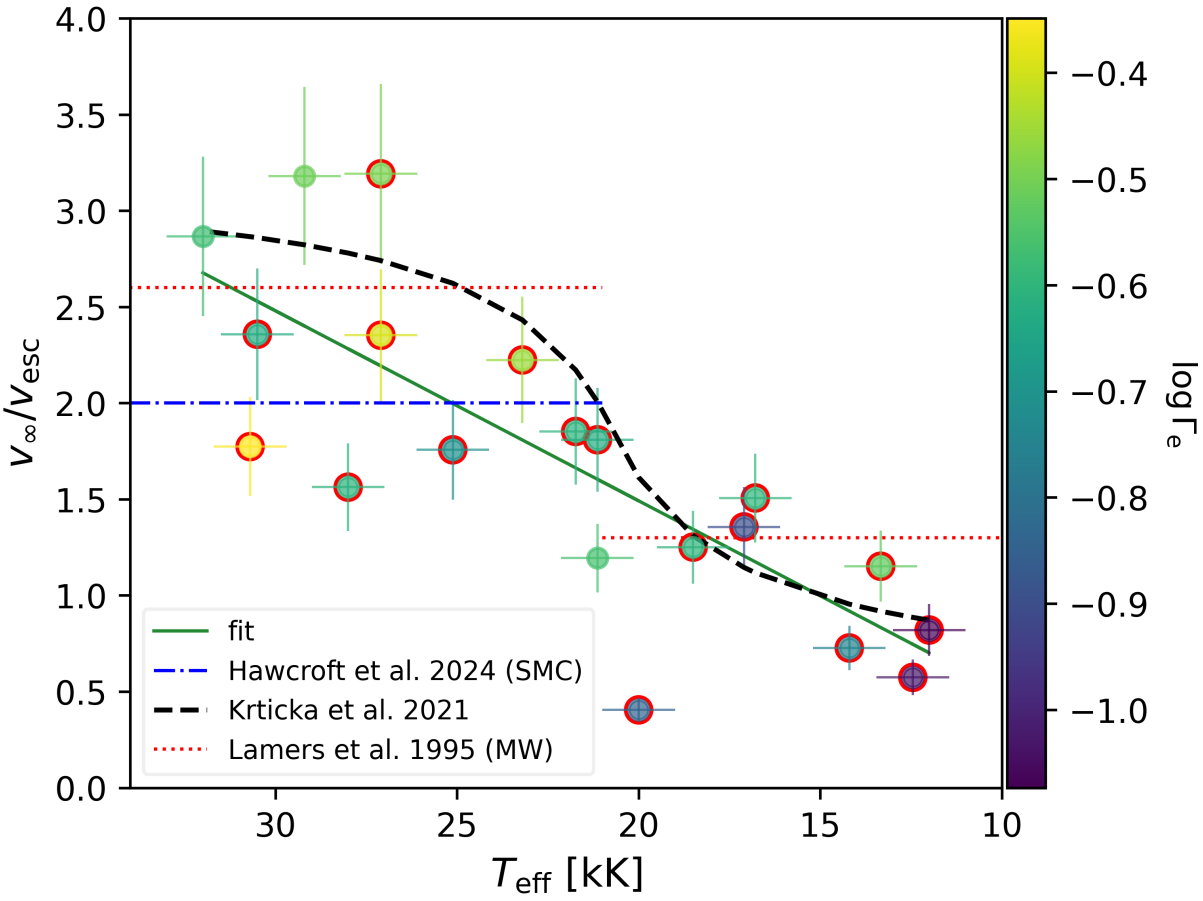


Figure 4.14: Ratio ($v_\infty/v_{\rm esc}$) as a function of temperature. The solid green line represents the linear fit to our sample. The dashed black line is the relation presented in Krtička et al. (2021). The dotted red lines represent the ratios from Lamers et al. (1995). The dot-dashed blue line represents the ratios from Hawcroft et al. (2024a). The colour gradient correlates with the value of Γ_e. Red circles indicate stars the v_∞ of which is inferred as $v_{\rm edge} \times \langle v_\infty/v_{\rm edge}\rangle_{\rm SMC}$.

of $f_{\rm vol,\infty} < 0.2$ (i.e. a high degree of clumping in the winds), which lowers the mass-loss rates required to obtain a satisfactory fit to Hα and to the UV P Cygni profiles.

In Fig. 4.14, we present the ratio v_∞ to the escape velocity $v_{\rm esc}$ as a function of $T_{\rm eff}$, which was calculated using $M_{\rm evo}$. From our results, we derive a relation of

$$v_\infty/v_{\rm esc} = 4.6(\pm0.9)\log(T_{\rm eff}/{\rm K}) - 18.3(\pm3.8), \tag{4.5}$$

where $v_{\rm esc} = \sqrt{2GM(1-\Gamma_{\rm e})/R_*}$, and $\Gamma_{\rm e}$ is the Eddington parameter, which was calcu-

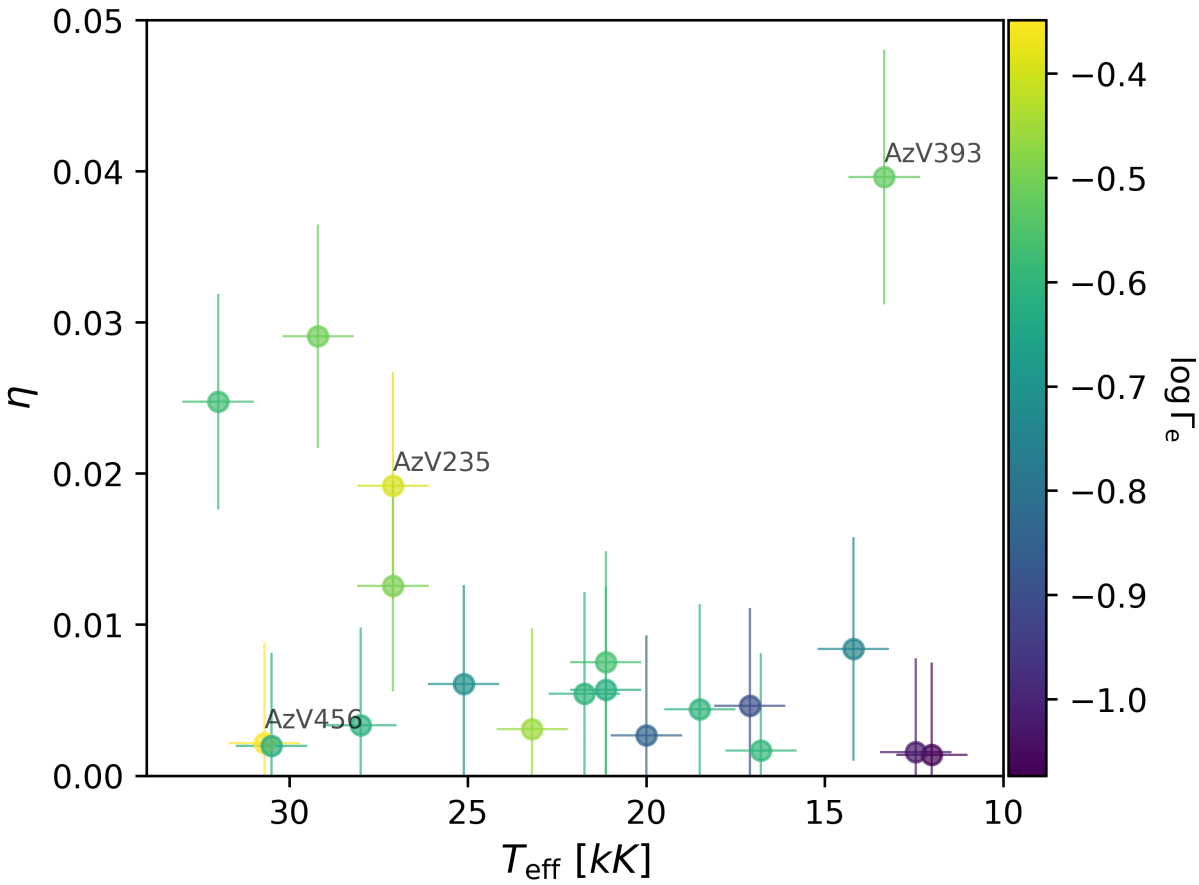


Figure 4.15: Wind efficiency $\eta = \frac{\dot{M} v_\infty}{L_{\rm bol}/c}$ in terms of $T_{\rm eff}$.

lated using $M_{\rm evo}$.

We do not notice any drastic decrease in $v_\infty/v_{\rm esc}$ below $T_{\rm eff}$ = 25-21 kK, indicative of the theorised bi-stability jump. We find that $v_\infty/v_{\rm esc}$ decreases monotonically with $T_{\rm eff}$. These results show a lack of evidence for the existence of the bi-stability jump, which is similar to the findings of Chapter 3, as well as the findings of de Burgos et al. (2024a) in the MW, and Verhamme et al. (2024) in the LMC. Bernini-Peron et al. (2024) also did not report any evidence of a bi-stability jump in their derived $\dot{M}$ in their sample of SMC B supergiants. However, they report that it is not clear whether the drop seen in their derived $v_\infty/v_{\rm esc}$ at $T_{\rm eff} \approx 25$ kK (see Fig. 18 in Bernini-Peron et al., 2024) is a sharp drop that is associated with the bi-stability jump, or a smooth decrease with a couple of outliers.

In Fig. 4.15, we show the wind efficiency parameter $\eta = \frac{\dot{M}v_\infty}{L_{\rm bol}/c}$ versus $T_{\rm eff}$. We find that η smoothly decreases with $T_{\rm eff}$. One extreme outlier is the hypergiant AzV 393, which has a very high $\dot{M}$. Another outlier is AzV 456, which has a very low η. This is due to its v_∞, which is lower by ≈ 300 km s^{-1} compared to AzV 327, which has a very similar $T_{\rm eff}$.

4.3.3 Implications for the population of blue supergiants

Recalling the HRD in Fig. 4.1, the shaded region is defined by the observed HD limit (Humphreys & Davidson, 1979a, 1994) in the SMC, which has a value of $\log L_{\rm bol}/L_\odot \approx 5.5$ (Davies et al., 2018). The diagonal blue edge of this region is inferred from the distribution of known luminous blue variables (LBVs) and LBV candidates on the HRD (Smith et al., 2004).

The HD limit suggests that the most massive stars with luminosities higher than $\log L_{\rm bol}/L_\odot \approx 5.5$ remain as blue supergiants, and end their lives as blue hypergiants and classical Wolf-Rayet (WR) stars, rather than evolving into luminous red supergiants. This means that, at least in theory, they should have sufficiently high mass-loss rates to shed their hydrogen-rich atmospheres and proceed to a classical WR phase. The existence of a considerable non-binary population of WRs in the SMC (e.g. Hainich et al., 2015; Schootemeijer et al., 2024) with high luminosity, for which Shenar et al. (2020) finds a non-binary fraction of $\approx$ 60-70%, in addition to a lower limit on WR luminosity of $\log L_{\rm bol}/L_\odot = 5.6$, which is comparable to the uppermost part of our sample and could, in principle, be seen as an argument for a self-stripping evolutionary scenario via extreme LBV eruptions.

However, aligning this evolutionary scenario with the mass-loss rates obtained in studies of blue supergiants in the SMC (This study, Bernini-Peron et al., 2024; Trundle & Lennon, 2005a; Trundle et al., 2004a) poses a challenge for explaining the formation

of WR stars from radiation-driven mass loss alone in the single-star regime. By way of example, AzV 242 has an evolutionary mass of $M_{\rm evo} = 38^{+5}_{-4}\ M_{\odot}$, a luminosity of $\log L_{\rm bol}/L_{\odot} = 5.71 \pm 0.1$, and a mass-loss rate of $\log \dot{M}/M_{\odot}\,{\rm yr}^{-1} = -7.47 \pm 0.4$. AzV 242 closely corresponds to the minimum initial mass of WR stars in the SMC (Shenar et al., 2020), yet the mass-loss rate of this supergiant is far too low to result in the stripping of the outer hydrogen-rich layers within its remaining ∼0.5 Myr lifetime.

The low current mass-loss rates, together with the observed properties of WR populations and the lack of luminous red supergiants in the SMC, lead to the following conclusion: to form a WR star via single-star evolution, luminous blue supergiants would need to lose copious amounts of mass during an LBV giant eruption (Smith, 2017; Jiang et al., 2018). This is supported by recent work from Pauli et al. (2026), who were able to replicate the observed properties of the WR and RSG populations – including the low-luminosity single WRs – in the SMC by incorporating LBV-like Eddington-limit-induced mass loss in evolutionary models. It is also probable that binarity, mass transfer via Roche lobe overflow, and common envelope evolution play a significant role in shaping the WR population (Schootemeijer & Langer, 2018).

4.3.4 Comparison to literature

Table A.2 contains our derived values for $T_{\rm eff}$, $\log g$, $L_{\rm bol}$, $\log \dot{M}$, β, and $f_{\rm vol,\infty}$, along with literature values from Trundle et al. (2004a), Trundle & Lennon (2005a), Bernini-Peron et al. (2024), Backs et al. (2024), and Bestenlehner et al. (2025). In addition to literature values, Table A.2 in includes $\log \dot{M}$ values obtained from LIME (Sundqvist et al., 2025). LIME is a user-friendly and fast online tool that allows for the estimation of the mass-loss rates of stars using an iterative semi-analytic approach using an extension of the CAK concept (Castor et al., 1975a). By including a detailed list of atomic lines, but avoiding a numerical solution for the equation of motion and the stellar atmosphere, the

tool can estimate $\dot{M}$ on the fly, in contrast to the recipes discussed in Section 4.2.3, which result from approximating sets of detailed numerical models. The input parameters we used for LIME are our derived $T_{\rm eff}$, $L_{\rm bol}$, $M_{\rm spec}$, mass fractions of H, He, C, N, O, and the mean mass fractions for elements heavier than oxygen presented in Vink et al. (2023).

In Fig. 4.16 we compare our obtained values $T_{\rm eff}$, $\log g$, $L_{\rm bol}$, $\log \dot{M}$, and $\log \dot{M}_{\rm smooth} = \log \dot{M}/\sqrt{f_{\rm vol,\infty}}$ (Schmutz, 1997; Hamann & Koesterke, 1998) to the values in the literature. We find that our $T_{\rm eff}$ values are consistent with values from the literature within the uncertainties. The only exception is AzV 18 for which Bestenlehner et al. (2025) find a value of $T_{\rm eff} = 23.7$ kK compared to our value of 18.5 kK. Similarly, our $\log g$ is generally in agreement with values from the aforementioned studies. We find that $\log g$ values obtained by Bestenlehner et al. (2025) are systematically lower than ours.

We find a similar picture for $L_{\rm bol}$, where our derived values are consistent with the values presented in the literature. The exception in this case is some of the values obtained by Bestenlehner et al. (2025), mainly for AzV 235, AzV 242, and AzV 18, for which we obtain $\log L_{\rm bol}/L_{\odot} = 5.86$, 5.71, 5.45, respectively, compared to 6.01, 5.28, 5.75 from Bestenlehner et al. (2025).

The $\dot{M}$ comparison tells a different story. We find that for the most part, the values of $\dot{M}$ are inconsistent, and our $\dot{M}$ is generally lower. The mean difference between our $\log \dot{M}$ and those from Bestenlehner et al. (2025), Backs et al. (2024), Bernini-Peron et al. (2024), Trundle et al. (2004a) and Trundle & Lennon (2005a), and LIME are $\approx -0.4, -0.7, -0.5, -0.9, -0.3$ dex, respectively. The immediate contributors to this inconsistency are the choice of clumping implementation (optically-thin vs optically-thick clumping and clumping law), the derived values for clumping parameters, and the derived/adopted values of β and v_{∞}. Furthermore, the differences in $T_{\rm eff}$, $\log g$, and $\epsilon_{\rm He}$ propagate to the estimated $\dot{M}$. Another obvious issue is the usage of various codes that implement different methods for solving the radiative transfer equations. Therefore, when all these issues are taken into account, differences up to a factor of 3 in $\dot{M}$ can be

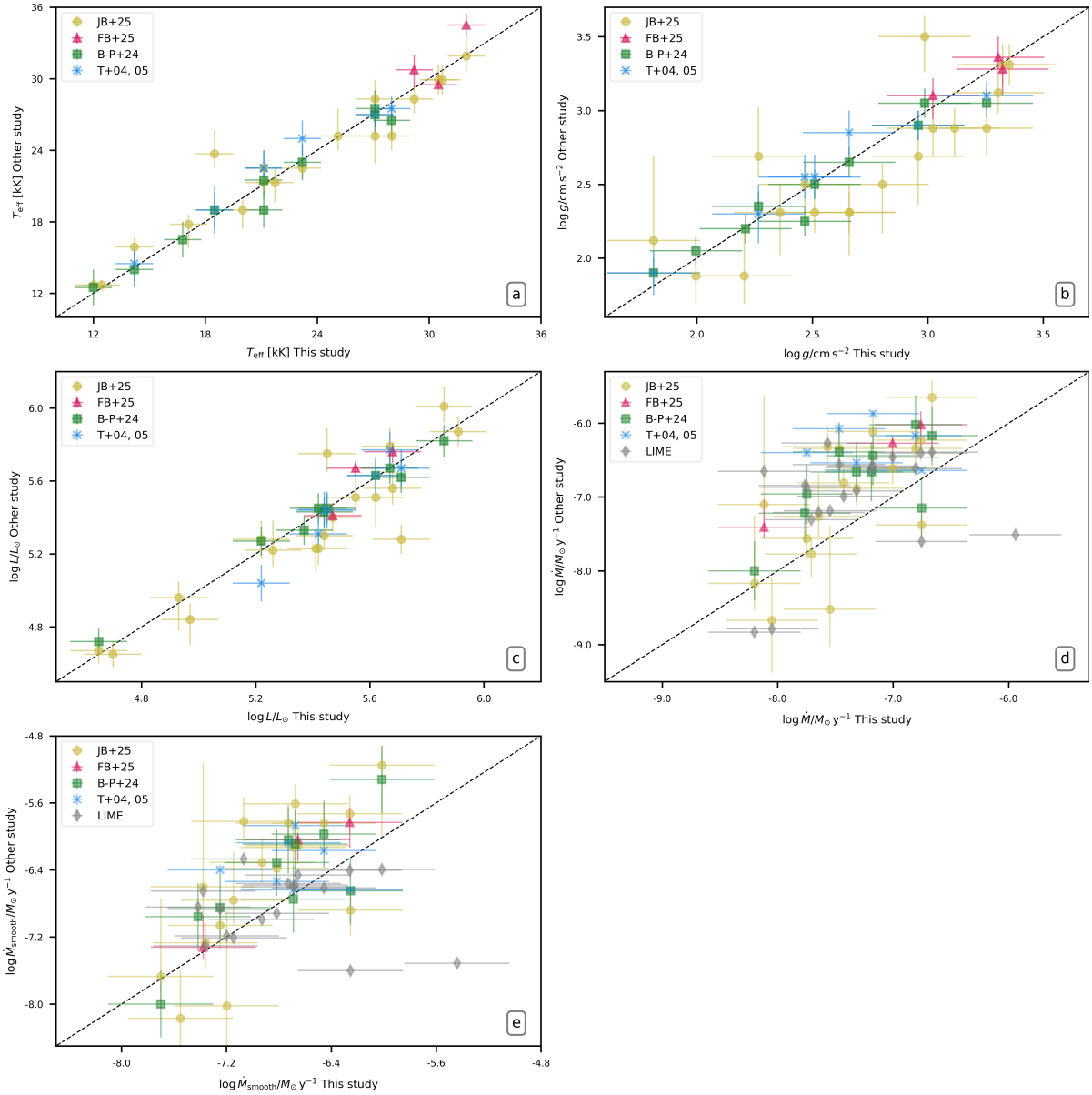


Figure 4.16: Comparison of our derived parameters to literature values. a: $T_{\rm eff}$ comparison, b: $\log g$ comparison, c: $L_{\rm bol}$ comparison, d: $\log \dot{M}$ comparison, e: $\log \dot{M}_{\rm smooth}$ comparison. Pink triangles: comparison to Backs et al. (2024). Green squares: comparison to Bernini-Peron et al. (2024). Blue Xs: comparison to Trundle et al. (2004a) and Trundle & Lennon (2005a). Grey diamonds: comparison to values obtained from LIME Sundqvist et al. (2025).

expected.

We can test if the values of clumping parameters are a major cause of the inconsistency in the mass-loss rates by comparing the 'smooth' mass-loss rates, $\dot{M}_{\rm smooth}$. This shows a similar trend; our $\dot{M}_{\rm smooth}$ is systematically lower than other studies, except for the values obtained from LIME, but now the mean difference between our $\dot{M}_{\rm smooth}$ and those from the literature are considerably lower and are $\approx -0.4, -0.4, -0.3, -0.4, 0.2$ dex, respectively. Therefore, the derived/adopted values of the clumping parameters can significantly affect the resulting mass-loss rates and are a major factor in the discrepancy observed in $\dot{M}$.

An interesting aspect of this comparison is that our derived $\dot{M}$ are systematically lower than those derived by Bernini-Peron et al. (2024), with the difference in some cases reaching almost an order of magnitude. A possible explanation could be related to clumping, as Bernini-Peron et al. (2024) derived significantly larger $f_{\rm vol,\infty}$ values, i.e. smoother, less clumped winds, for all but one of the stars in common with our sample. By comparing our derived $f_{\rm vol,\infty}$ with those derived by Bernini-Peron et al. (2024), we find that the mean of the difference $f_{\rm vol,\infty}^{\rm this\ study} - f_{\rm vol,\infty}^{\rm BP+24}$ is $\approx -0.33 \pm 0.34$. Recalling that $\rho \propto \dot{M}/\sqrt{f_{\rm vol,\infty}}$, the larger $f_{\rm vol,\infty}$ obtained by Bernini-Peron et al. (2024) translates to mass-loss rates that are higher by a factor of two on average, and upwards of a factor of ≈ 11.

4.4 Summary

We have completed a spectroscopic analysis of 20 late-O and B SMC supergiants, which employed CMFGEN (Hillier & Miller, 1998), using the UV (ULLYSES) and optical (XShootU) spectral ranges. We obtained stellar and wind parameters of the stars in our sample. Here we summarise the conclusions drawn from this chapter in the following points:

- By comparing our results to those obtained in Chapter 3 for the LMC, we find a clear Z dependence in wind momentum, which is shown in Fig. 4.9. We derived the wind momentum-luminosity relation presented in Equation 4.3. We also found a clear Z dependence in mass-loss rates, but did not find similar Z dependence in the terminal wind velocities.

- We compared our derived mass-loss rates to predictions from various numerical recipes Vink & Sander (2021); Björklund et al. (2023); Krtička et al. (2024). We found that the values of the numerical recipes differ from our mass-loss rates, with the recipe from Krtička et al. (2024) producing the values most closely aligned with ours, yet still showing a different trend with temperature.

- We also compared our results to literature values of the same stars (Trundle et al., 2004a; Trundle & Lennon, 2005a; Backs et al., 2024; Bernini-Peron et al., 2024; Bestenlehner et al., 2025). On the one hand, we find that the effective temperature, surface gravity, and luminosity generally agree with previous studies with modest variance. However, our derived mass-loss rates do not match previous estimates, with our values being generally lower than those previously obtained by previous studies.

- We do not find any sign of the theorised bi-stability jump. This is similar to the findings of de Burgos et al. (2024a), Verhamme et al. (2024), and our findings in Chapter 3. This means that within the current framework of radiative transfer codes used for modelling OB stars, the dramatic increase in mass loss at $T_{\rm eff}$ = 25-21 kK that is associated with the theorised bi-stability jump is not empirically supported.

- We also explored the evolutionary history of the stars within our sample. We employed an updated Bayesian inference method (V. Bronner et al., in prep.)

similar to BONNSAI (Schneider et al., 2014a) to obtain the evolutionary masses and ages using the rotating single-star evolutionary tracks of Brott et al. (2011). Evolutionary masses typically exceed spectroscopic masses, with 40% of our sample showing a mass discrepancy.

- Finally, we emphasise that mass-loss rates of supergiants exceeding the HD limit of $\log L_{\rm bol}/L_{\odot} = 5.5$ (Davies et al., 2018) are far too low to be able to strip the supergiants of their hydrogen-rich outer layers. Consequently, the high fraction of single WR stars observed in the SMC (Shenar et al., 2020) cannot be explained by the classical single star evolutionary regime, unless the supergiant is capable of losing an enormous amount of mass within its very short remaining lifespan. This possibly means that an intermediate LBV phase accompanied by extreme episodic eruptions and mass loss is required for the star to proceed into a WR phase.

Chapter 5

OB supergiants in the Milky Way

In this chapter, we present our study of a sample of late-O and B supergiants in the MW, the final step of a 3.5-year-long PhD endeavour. The MW provides a representative baseline of the conditions that dominate the local universe: high metal abundance ($Z = 0.0122$, see Table 2.2 Asplund et al., 2005).

The purpose of this chapter is to provide a Galactic baseline for analysing the metallicity dependence of wind parameters across the three environments studied in this thesis. We aim to derive the stellar and wind properties of a sample of late-O and B supergiants that is similar to those analysed in Chapter 3 and Chapter 4 by employing the techniques described in Chapter 2. We also aim to investigate the bi-stability jump in the context of the Galaxy and to compare our derived mass-loss rates to those predicted by numerical recipes.

In Section 5.1, we present the stars in our sample and the data used in this study. In Section 5.2, we introduce the results of our analysis. In Section 5.3, we present a detailed discussion of wind properties in relation to the metallicity. The purpose of this thesis is finally fulfilled by providing a fully empirical, homogeneously obtained mass-loss rate recipe. We also compare our results with previous studies of OB supergiants in the Galaxy.

5.1 Observations

In Table 5.1, we present the stars in our sample and list their spectral types and luminosity classes, which were drawn from Negueruela et al. (2024) for B supergiants and Holgado et al. (2018) for O supergiants. We also include the telescope, instrument, and wavelength coverage available for each star in the UV and optical.

The sample was selected to cover all spectral types from O9 to B8, similar to the samples presented in Chapter 3 and 4. We attempted to include all possible combinations of spectral type and luminosity subclasses (Ia^+, Ia, Iab, Ib) to avoid biases that could skew our results, particularly in WLR.

5.1.1 Ultraviolet spectroscopy

The UV data used in this study are drawn from the International Ultraviolet Explorer (IUE) archive [1]. The International Ultraviolet Explorer satellite (IUE Boggess et al., 1978) was equipped with a Short Wavelength Primary camera (SWP), a Long Wavelength Primary (LWP) camera, and replacement cameras (SWR and LWR), with wavelength coverage in the $\approx$ 1150-1950 Å and $\approx 1900-3250$ Å ranges, respectively. The IUE started its operations in 1978 and was decommissioned in 1996, during which the SWR camera was never used. The IUE was also equipped with high- and low-resolution spectrographs, achieving resolving powers of $R \approx 20000$ and $R \approx 300$, respectively. The observations were conducted in two modes: large aperture ($10'' \times 20''$ slot), which provided the best photometric accuracy and allowed for accurate flux calibration; and small aperture ($3''$ diameter circle), which was highly susceptible to pointing errors.

The high-resolution spectra of the bulk of our sample have been obtained with the SWP and LWP/LWR cameras in the large aperture configuration (indicated in Table 5.1 as /L). However, a few stars lack high-resolution observations with the large aperture; in

[1] https://sdc.cab.inta-csic.es/cgi-ines/IUEdbsMY

Table 5.1: List of the stars included in our analysis and the respective wavelength coverage. The number of IUE observations is included for each individual star. The spectral types (SpT) are taken from Negueruela et al. (2024) for B supergiants and Holgado et al. (2018) for O supergiants.

HD	aliases	SpT	Opt	1150-1970 Å	Num. Exp.	1850-3200 Å	Num. Exp.
30614	α Cam	O9 Ia	Melchiors/Mercator/HERMES	IUE/SWP/H/L	48	IUE/LWP+LWR/H/L	2
210809	-	O9 Iab	Melchiors/Mercator/HERMES	IUE/SWP/H/L	1	IUE/LWR/H/L	1
209975	19 Cep	O9 Ib	IACOB/Mercator/HERMES	IUE/SWP/H/L	50	-	-
154368	-	O9.2 Iab	IACOB/MPG/FEROS	IUE/SWP/H/L	7	IUE/LWP/H/L	6
76968	-	O9.2 Ib	IACOB/MPG/FEROS	IUE/SWP/H/L	1	IUE/LWP+LWR/H/L	2
105056	-	ON9.7 Ia+	UVES-POP/VLT/UVES	IUE/SWP/H/L	4	IUE/LWP/H/L	1
37128	ϵ Ori	B0 Ia	IACOB/Mercator/HERMES	IUE/SWP/H/L	10	IUE/LWR/S	8
204172	69 Cyg	B0.2 Iab	IACOB/NOT/FIES	IUE/SWP/H/L	36	-	-
38771	κ Ori	B0.5 Ia	IACOB/Mercator/HERMES	IUE/SWP/H/L	5	IUE/LWR/S	8
192422	-	B0.5 Ib	IACOB/Mercator/HERMES	IUE/SWP/H/L	1	-	-
190066	-	B0.7 Ib	IACOB/NOT/FIES	IUE/SWP/H/L	2	IUE/LWr/H/L	1
169454	-	B1 Ia+	Melchiors/Mercator/HERMES	IUE/SWP/H/L	4	IUE/LWP/H/L	2
13854	-	B1 Iab	IACOB/Mercator/HERMES	IUE/SWP/H/S	1	IUE/LWR/S	1
24398	ζ Per	B1 Ib	Melchiors/Mercator/HERMES	IUE/SWP/H/S	7	IUE/LWP/H/L	12
190603	-	B1.5 Ia+	IACOB/Mercator/HERMES	IUE/SWP/H/S	7	IUE/LWR/S	4
13841	-	B1.5 Ib	IACOB/Mercator/HERMES	IUE/SWP/H/L	1	-	-
41117	χ^2 Ori	B2 Ia	IACOB/NOT/FIES	IUE/SWP/H/S	2	IUE/LWP+LWR/H/S	2
206165	9 Cep	B2 Ib	IACOB/NOT/FIES	IUE/SWP/H/S	5	IUE/LWR/S	4
198478	55 Cyg	B2.5 Ia	IACOB/Mercator/HERMES	IUE/SWP/H/L	5	IUE/LWP/H/L	3
42087	3 Gem	B2.5 Ib	IACOB/Mercator/HERMES	IUE/SWP/H/L	1	IUE/LWP/H/L	2
53138	o^2 CMa	B3 Ia	IACOB/Mercator/HERMES	IUE/SWP/H/L	17	IUE/LWR/H/L	4
51309	ι CMa	B3 Ib	IACOB/Mercator/HERMES	IUE/SWP/H/L	1	IUE/LWR/H/L	1
58350	η CMa	B5 Ia	Melchiors/Mercator/HERMES	IUE/SWP/H/S	10	IUE/LWR/S	5
199478	-	B7 Ia	IACOB/Mercator/HERMES	IUE/SWP/H/L	2	IUE/LWR/H/L	4
34085	β Ori	B8 Ia	IACOB/Mercator/HERMES	IUE/SWP/H/L	16	IUE/LWP+LWR/H/L	16
12301	53 Cas	B8 Ib	IACOB/Mercator/HERMES	IUE/SWP/H/L	1	IUE/LWP+LWR/H/L	4

these cases, we used high-resolution spectra obtained in the small-aperture configuration (indicated in Table 5.1 as /S). Additionally, for those stars, we used the low-resolution spectra obtained with the large-aperture instrument, when available, for the SED fitting.

Single observations of our stars have an S/N of ≈ 3, measured in the wavelength ranges of 1600–1800 and 2500–2700 for SWP and LWP/LWR observations, respectively. For the stars in our sample observed multiple times with the IUE, we combined the individual observations to achieve higher S/N, since $S/N \propto \sqrt{N}$, where N is the number of exposures. Before combining, each snapshot was checked for quality (bad pixels) and variability, mainly in wind diagnostic lines. The observations exhibiting high variability or large errors were discarded. The remaining spectra were stacked using an exposure-time-weighted average.

5.1.2 Optical spectroscopy

The optical spectroscopic data used in the analysis are drawn from various sources. The majority of the sample is drawn from the private IACOB database (Simón-Díaz et al., 2011b,a, 2015). The IACOB database is a large, homogeneous set of high-resolution spectra of Galactic OB stars. The IACOB spectra in our sample were compiled between 2008 and Dec 2021. Northern IACOB targets were observed with the FIbre-fed Echelle Spectrograph (FIES, Telting et al., 2014) at the 2.56 m Nordic Optical Telescope (NOT) in the Roque de los Muchachos observatory in La Palma, Canary Islands, Spain; or the High Efficiency and Resolution Mercator Echelle Spectrograph (HERMES, Raskin et al., 2011) mounted on the 1.2 m Mercator semirobotic telescope. Southern IACOB targets were observed using the Fiber-fed Extended Range Optical Spectrograph (FEROS, Kaufer et al., 1999) at the 2.2 m MPG/ESO telescope located at the ESO La Silla Observatory, Chile. The resolving power achieved by these instruments for our sample range between of $R \approx 46000$ and 85000. The common spectral range covered by most

observations is 3800-9000 Å. However, some FIES spectra that were taken prior to the installation of the current CCD (30/09/2026) only cover up to 7200 Å. Furthermore, the FEROS spectra cover a wider range of 3500-9200 Å.

Optical spectra for those stars that are not included in IACOB were drawn from two sources: the UVES Paranal Observatory Project (UVES-POP, Bagnulo et al., 2003) for southern targets and the Mercator Library of High Resolution Stellar Spectroscopy (Melchiors, Royer et al., 2024) for northern targets. UVES-POP is a public spectroscopic library of 406 Galactic stars that were observed with the Ultraviolet and Visual Echelle Spectrograph (UVES, Dekker et al., 2000). The resolving power of the UVES-POP spectra is $R \approx 80000$, covering a spectral range of 3040-10400 Å across three arms. Similarly, Melchiors is a publicly available database, the spectra of which were obtained by the Mercator-HERMES instrument (Raskin et al., 2011) between 2010 and 2020, achieving $R \approx 85000$, and covering a spectral range of $\approx$ 3700- 8950 Å.

The signal-to-noise ratio S/N of all spectra ranges between 170 and 300. The IACOB, UVES-POP, and Melchiors libraries provide normalised spectra corrected for atmospheric telluric (molecular) absorption; however, they do not provide absolute flux-calibrated data. We note that, in our analysis, the high-resolution optical data are convolved with a Gaussian, intentionally degrading the spectra to match the resolution of the XShootU optical spectra (Sana et al., 2024). This was done to ensure uniformity in the analysis of the three environments and to mitigate potential effects of differences in data quality.

5.1.3 Photometry and distances

The photometric data used in this study are presented in Table 5.2 and were drawn from the catalogs of Ducati (2002) and Reed (2003). The photometry is used in the same way as in the previous chapters, mainly to derive the bolometric luminosities by fitting the

Table 5.2: Photometric data and distances. B-J: Bailer-Jones et al. (2021); Bailer-Jones (2023, *GAIA* DR3), V-L: van Leeuwen (2007, *Hipparcos*), S-S: Sánchez-Sanjuán et al. (2024, cluster association using *GAIA* DR3)

HD	U	B	V	J	H	K_S	distance	Ref.
	mag	mag	mag	mag	mag	mag	parsec	Ref.
30614	3.47	4.34	4.29	4.24	4.38	4.24	1695^{+386}_{-264}	B-J
210809	6.70	7.61	7.56	7.37	7.4	7.41	3730^{+494}_{-353}	B-J
209975	4.36	5.19	5.11	5.23	4.92	4.93	965^{+63}_{-59}	B-J
154368	6.10	6.63	6.13	5.02	4.85	4.75	1024^{+51}_{-47}	B-J
76968	6.53	7.33	7.21	6.75	6.76	6.66	2202^{+102}_{-91}	B-J
105056	6.57	7.31	7.34	7.16	7.14	7.05	2778^{+164}_{-126}	B-J
37128	0.48	1.51	1.69	2.19	2.41	2.27	422^{+11}_{-11}	S-S
204172	4.89	5.86	5.94	6.08	6.08	6.14	2038^{+150}_{-147}	B-J
38771	0.87	1.88	2.06	2.47	2.69	2.68	298^{+9}_{-9}	S-S
192422	7.13	7.61	7.10	5.92	5.84	5.75	2059^{+726}_{-561}	B-J
190066	6.07	6.78	6.60	6.07	6.12	6.1	1581^{+81}_{-72}	B-J
169454	7.39	7.61	6.71	4.44	3.96	3.84	1948^{+154}_{-115}	B-J
13854	6.10	6.76	6.48	5.78	5.70	5.61	2139^{+109}_{-103}	B-J
24398	2.19	2.97	2.85	2.6	2.62	2.6	262^{+35}_{-23}	B-J
190603	5.73	6.19	5.65	4.42	4.26	4.04	1925^{+166}_{-148}	B-J
13841	6.95	7.6	7.37	6.82	6.81	6.78	2268^{+117}_{-106}	B-J
41117	4.24	4.91	4.63	4.19	4.04	3.95	1278^{+201}_{-196}	B-J
206165	4.49	5.03	4.73	4.54	4.21	4.31	996^{+89}_{-79}	B-J
198478	4.83	5.28	4.86	4.18	4.05	3.95	1827^{+297}_{-234}	B-J
42087	5.33	5.96	5.75	5.39	5.21	5.12	2470^{+421}_{-289}	B-J
53138	2.14	2.94	3.02	3.33	3.28	3.34	1316^{+1094}_{-361}	B-J
51309	3.62	4.30	4.38	4.7	4.62	4.54	1109^{+407}_{-215}	B-J
58350	1.65	2.37	2.45	2.44	2.49	2.44	610^{+197}_{-120}	V-L
199478	5.79	6.12	5.64	4.73	4.50	4.34	2423^{+229}_{-215}	B-J
34085	−0.56	0.10	0.13	0.21	0.18	0.21	265^{+26}_{-22}	V-L
12301	5.69	5.93	5.61	4.74	4.65	4.53	905^{+40}_{-33}	B-J

SED spectral energy distribution. The Johnson broadband UBV photometry of our sample was taken from Hiltner (1956), Johnson et al. (1966), Schild (1966), Burnichon & Garnier (1976), Fernie (1983), Høg et al. (2000), Lasker et al. (2008). The $JHKs$ photometry was drawn the Two Micron All Sky Survey (2MASS, Cutri et al., 2003; Skrutskie et al., 2006; Cutri et al., 2012).

For all but four of the stars in our sample, the distances used for the bolometric luminosity calculation are the geophotometric distances obtained by Bailer-Jones et al. (2021) and Bailer-Jones (2023), who employed *Gaia* DR3 parallaxes. While Gaia Data Release 3 (Gaia DR3) provides unprecedented astrometric precision across billions of stars, its distance measurements for bright stars ($V \lesssim 6$) are limited by detector saturation. This is the case for HD37128, HD38771, HD58350, and HD34085, whose brightness exceeds the Gaia magnitude limit, leading to inferior astrometry (Lindegren et al., 2018). For HD58350 and HD34085, we used the revised *Hipparcos* parallax values (van Leeuwen, 2007). For HD37128 (ϵ Ori) and HD38771 (κ Ori), we used the distances to the respective sub-populations in the Orion Nebular Cloud reported in Sánchez-Sanjuán et al. (2024).

The upper panel of Fig 5.1 shows a top-down view of the MW, with our targets overlaid as black triangles. The lower panel of Fig. 5.1 shows the distance between the star and the Galactic Plane. Based on the spatial distribution of our sample shown in Fig 5.1, the assumption of a solar composition following Asplund et al. (2005) is well justified. The top panel in Fig 5.1 illustrates that our late O and B supergiants are concentrated within the solar neighbourhood, primarily clustered around the Solar Circle at a Galactocentric radius of ≈ 8.18 kpc (GRAVITY Collaboration et al., 2019). Given that the largest and smallest galactocentric distances in our sample are 10.6 (HD42087) and 6.3 kpc, applying the Galactic metallicity gradient of 0.07 dex kpc^{-1} as determined by observational studies (see e.g., Frankel et al., 2018; Willett et al., 2023), the maximum expected deviation in metallicity from solar values is roughly ± 0.16 dex, which is within

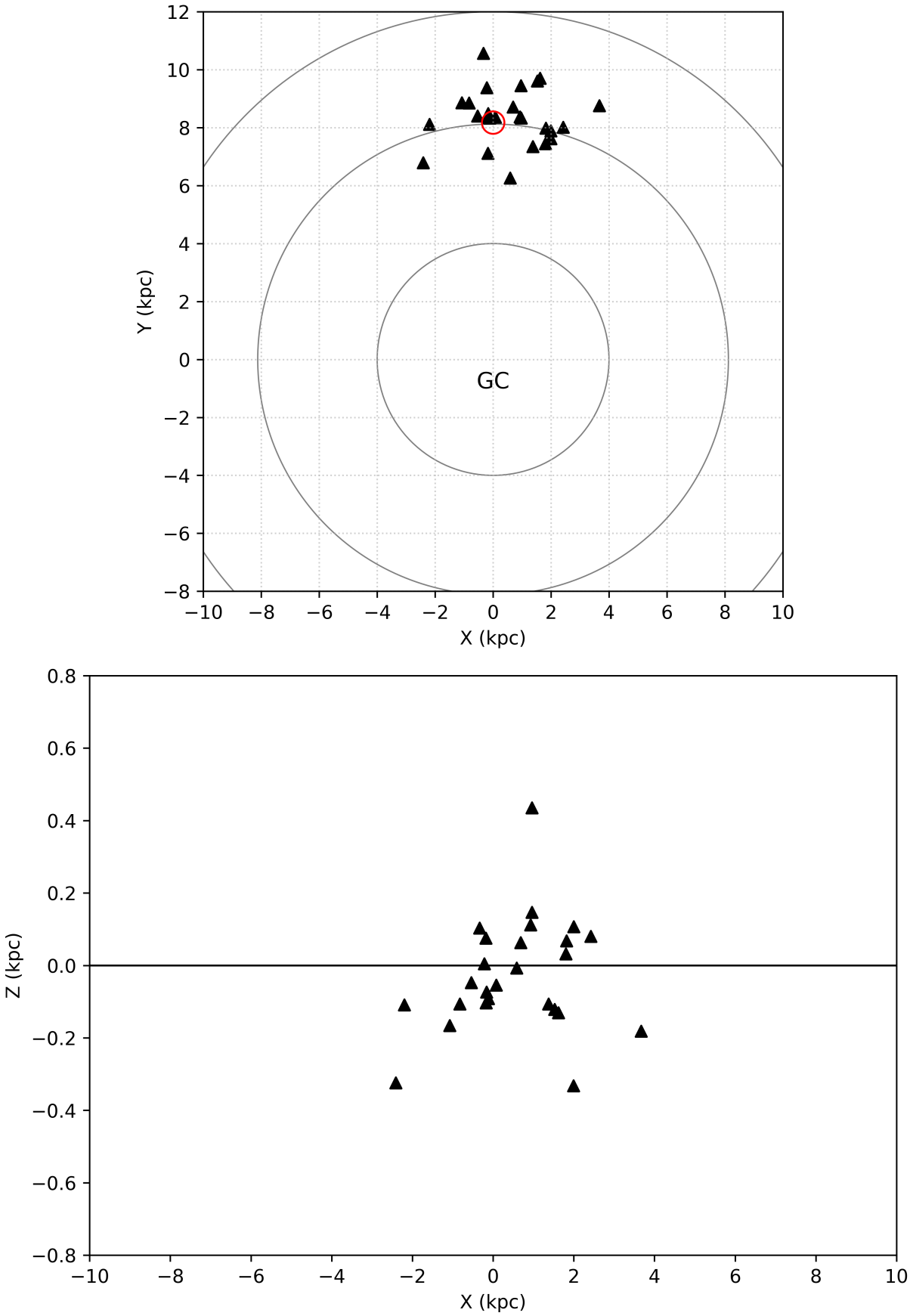


Figure 5.1: Top panel: top-down view of the MW. The black triangles represent our sample. The Sun's position is indicated as a red circle. Bottom panel: side-on view of the MW with our stars overlaid.

the uncertainty of our derived $\epsilon_{\rm CNO}$. Since most of the sample lies much closer to the Sun's orbital radius, the vast majority of these stars will exhibit even smaller deviations, making the adopted baseline chemical composition reliable for our sample.

5.2 Results

In this section, we provide an overview of the results of our analysis. In Table 5.3, we present the derived physical parameters from our preferred CMFGEN model. In Table 5.4, we present the inferred evolutionary masses and ages. The details of v_∞ measurements are presented in Appendix C.1. The table containing the literature values can be found in Appendix C.2. The quality of our analysis is described for each star individually in Appendix C.3. The SED fits, individual line fits and overall spectral fits are presented in Appendix C.4, C.5 and C.6, respectively.

5.2.1 Hertzsprung-Russell diagram

Fig. 5.2 shows the Hertzsprung-Russell diagram (HRD) for our sample, superimposed on Galactic isochrones of rotating stars (solid black lines) and evolutionary models (dashed black lines) (Brott et al., 2011). The sample covers a range of $\log(L_{\rm bol}/L_\odot)$ from 4.56 (HD12301) to 6.04 (HD30614), and spans a wide range of $T_{\rm eff}$, from 12.2 kK (HD34085) to 29.5 kK (HD210809). The shaded area in Fig. 5.2 is defined by the Humphreys-Davidson (HD) limit (Humphreys & Davidson, 1979a; Smith et al., 2004).

We note three stars that are located on the edge of the zone of avoidance on the edge: the B1 hypergiant HD169454, the B1.5 hypergiant HD190603, and the B2.5 Ia supergiant HD198478. However, the blue diagonal edge of the zone is an average of the position of Galactic and MC LBVs and LBV candidates (Smith et al., 2011), and is therefore an approximation. Therefore, considering the proximity of these stars to the LBV edge, we argue that these objects do not necessarily violate the HD limit.

Table 5.3: Derived stellar parameters based on the best fitting CMFGEN model. The uncertainties of the best fitting parameters are derived similarly to those in Table 3.3 of Chapter 3.

HD	$T_{\rm eff}$	Diag.	$\log g_c$	R_*	$\log L_{\rm bol}$	$R_{\rm V}$	$E(B-V)$	$M_{\rm V}$	$BC_{\rm V}$	$v_{\rm rad}$	$v_{\rm rot}\sin i$	$M_{\rm spec}$	$\Gamma_{\rm e}^{\rm spec}$
	kK		cm s^{-2}	$R_\odot$	$L_\odot$		mag	mag	mag	km s^{-1}	km s^{-1}	$M_\odot$	
30614	28.3 ± 1.0	He I – He II	2.95 ± 0.20	44	6.04	2.7	0.31	−7.69	−2.66	24	85	63^{+37}_{-23}	0.39
210809	29.5 ± 1.0	He I – He II	3.10 ± 0.20	22	5.51	2.9	0.34	−6.28	−2.75	−72	90	23^{+13}_{-8}	0.30
209975	29.2 ± 1.0	He I – He II	3.15 ± 0.20	18	5.32	2.9	0.35	−5.83	−2.73	−14	65	17^{+10}_{-6}	0.29
154368	28.2 ± 1.0	He I – He II	3.05 ± 0.20	23	5.47	3.0	0.78	−6.30	−2.64	27	70	22^{+13}_{-8}	0.30
76968	28.2 ± 1.0	He I – He II	3.05 ± 0.20	17	5.21	2.8	0.41	−5.65	−2.64	−18	70	12^{+7}_{-4}	0.30
105056	28.2 ± 2.0	He I – He II	3.10 ± 0.25	18	5.25	3.0	0.30	−5.74	−2.65	20	50	15^{+9}_{-5}	0.29
37128	29.5 ± 1.5	Si IV – Si III	3.22 ± 0.20	27	5.70	2.6	0.12	−6.75	−2.76	24	60	45^{+26}_{-17}	0.27
204172	28.3 ± 1.0	Si IV – Si III	3.15 ± 0.20	22	5.45	2.7	0.23	−6.23	−2.66	−20	75	26^{+15}_{-10}	0.26
38771	27.2 ± 1.5	Si IV – Si III	3.10 ± 0.20	17	5.16	2.5	0.11	−6.69	−2.56	21	60	14^{+8}_{-5}	0.25
192422	27.2 ± 1.0	Si IV – Si III	3.08 ± 0.20	30	5.64	2.7	0.80	−6.63	−2.56	−9	65	39^{+20}_{-12}	0.27
190066	24.2 ± 1.0	Si IV – Si III	2.95 ± 0.20	20	5.09	2.9	0.45	−5.70	−2.29	20	60	13^{+8}_{-5}	0.24
169454	19.4 ± 2.0	Si IV – Si III	2.40 ± 0.30	79	5.90	3.2	1.08	−8.25	−1.77	20	40	58^{+34}_{-21}	0.35
13854	20.9 ± 1.0	Si IV – Si III	2.60 ± 0.20	38	5.39	3.3	0.50	−6.82	−1.93	−38	50	21^{+12}_{-8}	0.29
24398	21.8 ± 1.0	Si IV – Si III	2.78 ± 0.20	18	4.80	2.8	0.36	−5.25	−2.02	20	50	7^{+4}_{-3}	0.21
190603	20.4 ± 1.5	Si IV – Si III	2.50 ± 0.25	75	5.94	2.9	0.81	−8.12	−1.87	24	50	65^{+34}_{-22}	0.32
13841	20.0 ± 1.0	Si IV – Si III	2.60 ± 0.20	24	4.92	2.7	0.50	−5.76	−1.81	−42	50	9^{+5}_{-3}	0.24
41117	19.3 ± 1.0	Si IV – Si III	2.28 ± 0.20	52	5.53	2.9	0.50	−7.35	−1.74	20	60	20^{+12}_{-7}	0.39
206165	17.8 ± 1.0	Si III – Si II	2.45 ± 0.20	44	5.25	2.9	0.50	−6.71	−1.57	−23	55	21^{+12}_{-7}	0.19
198478	15.9 ± 1.0	Si III – Si II	2.05 ± 0.20	90	5.67	2.7	0.61	−8.10	−1.34	−12	45	34^{+20}_{-13}	0.32
42087	17.6 ± 1.0	Si III – Si II	2.45 ± 0.20	61	5.51	2.8	0.45	−7.47	−1.56	20	45	39^{+23}_{-14}	0.20
53138	15.6 ± 1.0	Si III – Si II	2.10 ± 0.20	82	5.56	2.7	0.11	−7.87	−1.29	45	50	32^{+19}_{-12}	0.27
51309	15.8 ± 1.0	Si III – Si II	2.45 ± 0.20	38	4.92	3.0	0.13	−6.23	−1.34	41	40	15^{+9}_{-6}	0.13
58350	14.5 ± 1.0	Si III – Si II	2.10 ± 0.20	56	5.09	3.3	0.12	−6.87	−1.12	40	45	15^{+9}_{-5}	0.19
199478	12.6 ± 1.0	He I – Mg II	1.80 ± 0.25	113	5.46	2.9	0.63	−8.11	−0.80	−21	40	30^{+18}_{-11}	0.21
34085	12.2 ± 1.0	He I – Mg II	1.90 ± 0.20	80	5.11	2.9	0.11	−7.30	−0.73	13	35	19^{+11}_{-7}	0.16
12301	13.3 ± 1.0	He I – Mg II	2.25 ± 0.20	36	4.56	3.1	0.50	−5.72	−0.95	−20	35	8^{+5}_{-3}	0.11

Table 5.4: Inferred evolutionary masses M_{init}, $M_{\rm evo}$, and ages of the stars. These were derived using an updated Bayesian inference method (Bronner et al. in prep) that is similar to BONNSAI (Schneider et al., 2014a) applied to Brott et al. (2011) Galactic evolutionary tracks.

HD	$T_{\rm eff}$	$\log g_c$	$\log L_{\rm bol}$	M_{init}	$M_{\rm evo}$	Age	$\Gamma_{\rm e}^{\rm evo}$
	kK	$\rm cm\,s^{-2}$	$L_\odot$	$M_\odot$	$M_\odot$	Myr	
30614	28.3	2.95	6.04	81^{+12}_{-30}	57^{+9}_{-22}	$2.7^{+0.9}_{-0.3}$	$0.43^{+0.07}_{-0.17}$
210809	29.5	3.10	5.51	31^{+4}_{-4}	27^{+3}_{-3}	$5.4^{+0.7}_{-0.6}$	$0.25^{+0.02}_{-0.03}$
209975	29.2	3.15	5.32	26^{+3}_{-2}	24^{+2}_{-1}	$7.2^{+0.4}_{-1.1}$	$0.21^{+0.02}_{-0.01}$
154368	28.2	3.05	5.47	30^{+4}_{-2}	25^{+3}_{-1}	$6.9^{+0.2}_{-1.0}$	$0.26^{+0.03}_{-0.01}$
76968	28.2	3.05	5.21	22^{+2}_{-2}	21^{+2}_{-2}	$7.5^{+1.0}_{-1.0}$	$0.18^{+0.02}_{-0.02}$
105056	28.2	3.10	5.25	25^{+2}_{-2}	23^{+1}_{-2}	$7.4^{+0.8}_{-0.9}$	$0.18^{+0.01}_{-0.02}$
37128	29.5	3.22	5.70	40^{+31}_{-13}	34^{+22}_{-11}	$2.8^{+2.0}_{-0.3}$	$0.71^{+0.45}_{-0.22}$
204172	28.3	3.15	5.45	28^{+4}_{-2}	25^{+3}_{-1}	$7.1^{+0.3}_{-1.3}$	$0.27^{+0.04}_{-0.02}$
38771	27.2	3.10	5.16	18^{+1}_{-1}	18^{+1}_{-1}	$9.9^{+0.6}_{-1.8}$	$0.09^{+0.01}_{-0.01}$
192422	27.2	3.08	5.64	25^{+17}_{-5}	24^{+12}_{-4}	$7.4^{+0.5}_{-3.3}$	$0.38^{+0.19}_{-0.07}$
190066	24.2	2.95	5.09	21^{+2}_{-2}	20^{+2}_{-2}	$7.4^{+1.2}_{-0.8}$	$0.16^{+0.02}_{-0.01}$
169454	19.4	2.40	5.90	55^{+8}_{-5}	49^{+1}_{-8}	$3.0^{+0.5}_{-0.0}$	$0.42^{+0.02}_{-0.07}$
13854	20.9	2.60	5.39	26^{+2}_{-3}	24^{+2}_{-2}	$6.8^{+0.7}_{-0.9}$	$0.26^{+0.02}_{-0.02}$
24398	21.8	2.78	4.80	15^{+2}_{-1}	15^{+1}_{-1}	$11.6^{+1.7}_{-1.4}$	$0.10^{+0.01}_{-0.01}$
190603	20.4	2.50	5.94	45^{+12}_{-5}	33^{+8}_{-3}	$2.9^{+2.0}_{-0.0}$	$0.56^{+0.14}_{-0.05}$
13841	20.0	2.60	4.92	17^{+1}_{-1}	16^{+1}_{-1}	$10.1^{+1.5}_{-1.3}$	$0.13^{+0.01}_{-0.01}$
41117	19.3	2.28	5.53	42^{+11}_{-4}	32^{+4}_{-3}	$5.2^{+0.4}_{-1.1}$	$0.24^{+0.03}_{-0.03}$
206165	17.8	2.45	5.25	20^{+2}_{-2}	19^{+2}_{-2}	$8.1^{+1.3}_{-0.8}$	$0.19^{+0.02}_{-0.02}$
198478	15.9	2.05	5.67	43^{+4}_{-5}	32^{+2}_{-2}	$4.6^{+0.6}_{-0.3}$	$0.34^{+0.03}_{-0.03}$
42087	17.6	2.45	5.51	31^{+10}_{-2}	28^{+5}_{-1}	$5.3^{+0.6}_{-0.8}$	$0.28^{+0.05}_{-0.02}$
53138	15.6	2.10	5.56	65^{+3}_{-28}	32^{+16}_{-3}	$3.2^{+2.4}_{-0.3}$	$0.27^{+0.14}_{-0.03}$
51309	15.8	2.45	4.92	15^{+4}_{-4}	14^{+5}_{-3}	$10.3^{+3.9}_{-3.3}$	$0.14^{+0.05}_{-0.03}$
58350	14.5	2.10	5.09	19^{+4}_{-3}	18^{+3}_{-3}	$8.1^{+2.5}_{-1.4}$	$0.15^{+0.03}_{-0.03}$
199478	12.6	1.80	5.46	29^{+4}_{-3}	26^{+3}_{-2}	$5.5^{+1.0}_{-0.5}$	$0.25^{+0.03}_{-0.03}$
34085	12.2	1.90	5.11	20^{+2}_{-2}	19^{+2}_{-1}	$8.2^{+1.2}_{-0.9}$	$0.16^{+0.02}_{-0.02}$
12301	13.3	2.25	4.56	13^{+1}_{-1}	12^{+1}_{-1}	$15.5^{+2.3}_{-2.0}$	$0.08^{+0.01}_{-0.01}$

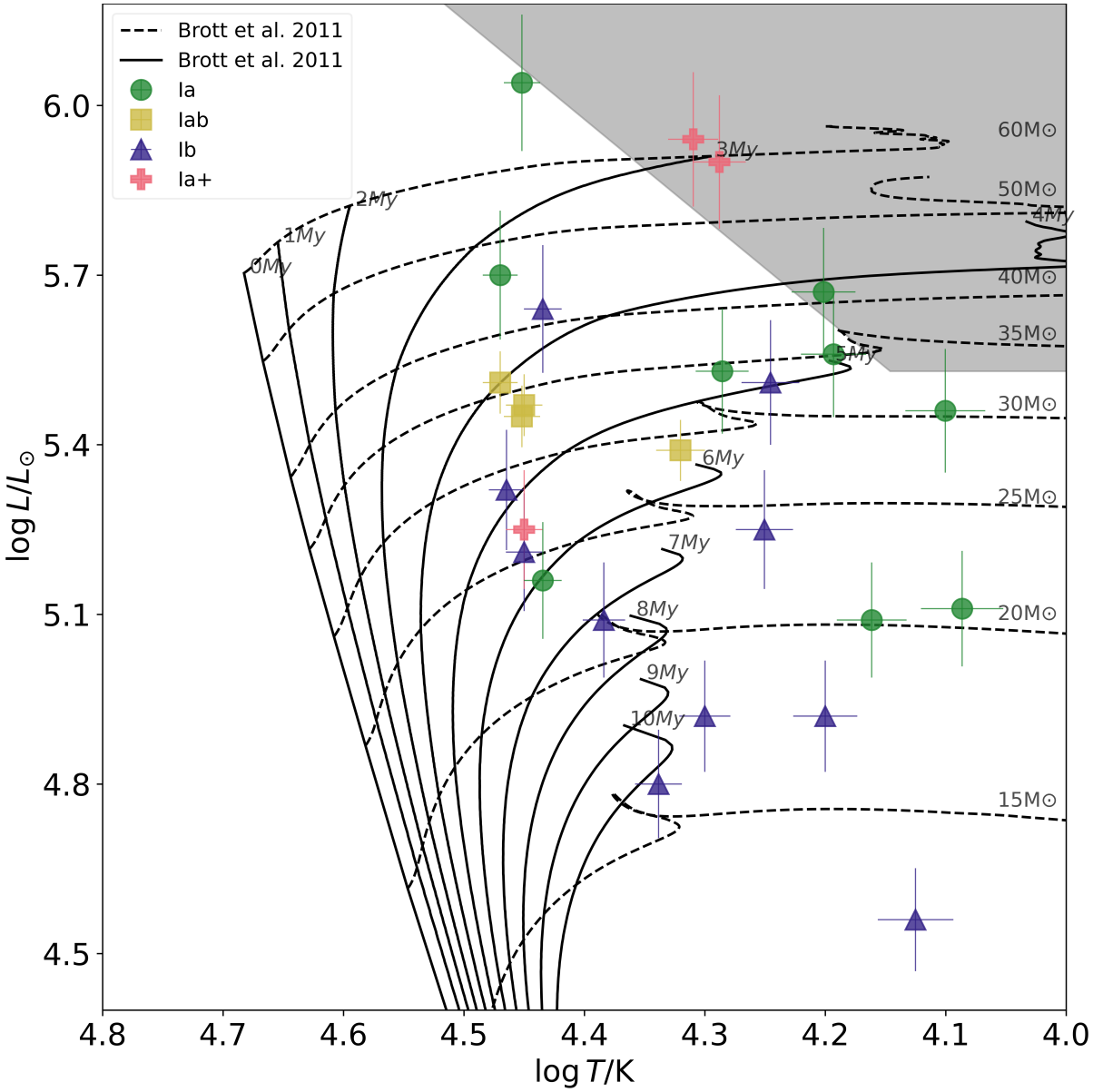


Figure 5.2: Hertzsprung-Russell diagram for our sample. Overlaid in solid black lines are rotating Galactic isochrones for different ages ($\approx 0-10$ Myr). Dashed black lines are the Galactic rotating evolutionary tracks for stellar masses in the range of $\approx 10-60\ M_{\odot}$ with a rotational velocity of 100 km s^{-1}. Both the isochrones and evolutionary tracks are adopted from Brott et al. (2011). The shaded area is defined by the HD limit (Humphreys & Davidson, 1979a; Smith et al., 2004; Davies et al., 2018).

According to Brott et al. (2011) single-star evolutionary models, seven BSGs, namely those with $\log T_{\rm eff}/{\rm K} < 4.3$, lie beyond the blue hook of the MS. Their position on the HRD suggests that they may be early post-MS objects, at the initial stages of the shell-hydrogen burning phase. Seven of the hot BSGs ($\log T_{\rm eff}/{\rm K} > 4.3$) are positioned in close proximity to the TAMS, making their evolutionary status ambiguous. The positions of the remaining hot BSGs, including all O stars, strongly suggest that they are MS, core-hydrogen-burning stars.

Fig. 5.3 represents the spectroscopic Hertzsprung-Russell diagram (sHRD) (Langer & Kudritzki, 2014, see Section 3.2.1 for the definition of sHRD). Our sample spans a $\log \mathcal{L}/\mathcal{L}_{\odot}$ range of 3.63 (HD12301) to 4.24 (HD30614). Unlike Chapter 3 and 4, we find that the O9.7 hypergiant HD105056 and the B hypergiants HD169454 and HD190603 are overtaken by the supergiant HD30614 in terms of proximity to the Eddington limit. Moreover, the luminosity and the spectroscopic luminosity of HD105056 are similar to those of other regular supergiants with similar temperatures.

5.2.2 Stellar masses

In Table 5.3, we present the spectroscopic masses, $M_{\rm spec}$, which were derived from $g = G\,M/R_*^2$. In Table 5.4 we present the evolutionary masses, $M_{\rm evo}$, and ages, which were obtained using the same method used in Chapter 4 (updated Bayesian inference method that is similar to Bonnsai, Schneider et al., 2014a), applied to Galactic rotating single-star evolutionary models of Brott et al. (2011).

$M_{\rm spec}$ of the stars in our sample ranges from 7^{+4}_{-3} (HD24398) to 63^{+37}_{-23} $M_{\odot}$ (HD30614). $M_{\rm evo}$ spans a smaller range between $12.37^{+0.95}_{-0.94}$ (HD12301) and $56.83^{+8.91}_{-22.00}$ $M_{\odot}$ (HD30614). We note that $M_{\rm spec}$ of HD24398 (7^{+4}_{-3} $M_{\odot}$) falls below the canonical $8M_{\odot}$ threshold for massive stars. However, this object remains consistent with a massive star origin within its uncertainties. Specifically, the upper bound of its mass estimate (11 $M_{\odot}$) extends

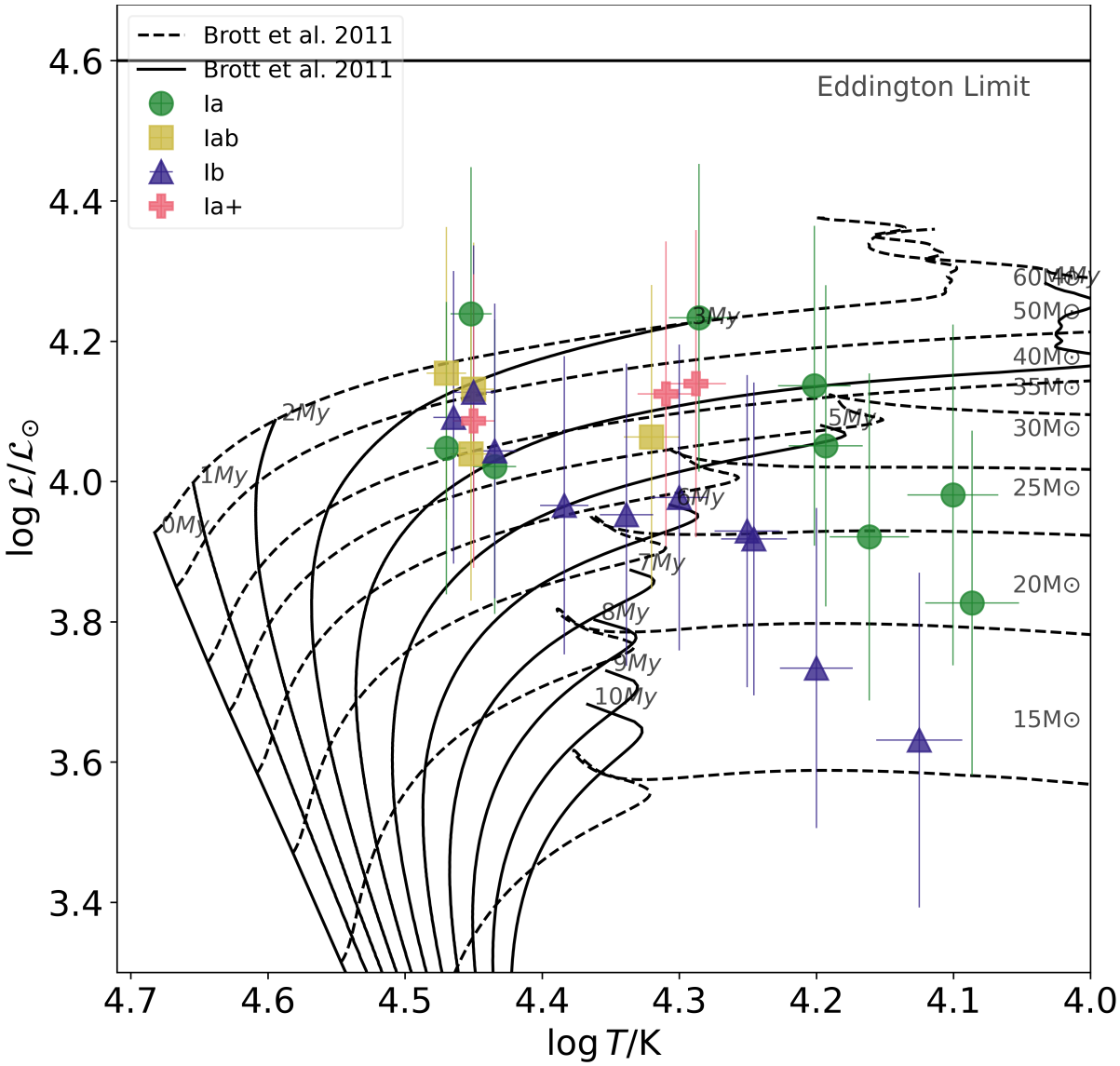


Figure 5.3: The spectroscopic Hertzsprung-Russell diagram for our sample. The evolutionary tracks (dashed black lines) and the isochrones (solid black lines) are the same as in Fig. 5.2, which are taken from Brott et al. (2011). The encoding of the luminosity classes is the same as in Fig. 5.2.

significantly into the high-mass regime. The low nominal masses are due to the relatively small radii that are derived from the Stefan-Boltzmann law $L_{\rm bol} = 4\pi R^2 \sigma_{sb} T^4$.

Fig. 5.4 shows a comparison between $M_{\rm evo}$ and $M_{\rm spec}$. The mass discrepancy is seen in $\approx 40\%$ of our sample, which is similar to our findings in Chapter 4. For the stars that show a significant mass discrepancy, $M_{\rm evo}$ is generally larger than $M_{\rm spec}$, with the exception of HD190603, for which $M_{\rm spec} > M_{\rm evo}$. The largest discrepancy in relative terms is seen in HD24398, the masses of which are $M_{\rm spec} = 7^{+4}_{-3}$ and $M_{\rm evo} = 15^{+1}_{-1}$.

5.2.3 Wind properties

In Table 5.5, we present the derived wind parameters for our sample. In Fig. 5.5, we present our best fits (red solid line) to the observed Hα (black solid line). Our sample covers a wide $\log \dot{M}/M_{\odot}\,{\rm yr}^{-1}$ range, from ≈ -7.31 (HD51309) to -5.56 dex (HD199478). The morphology of the observed Hα lines was successfully reproduced by our preferred models for all stars in our sample, except HD199478. We obtain satisfactory fits in cases where Hα is fully or partially in emission. Similar to our fitting approach in Chapter 3 and 4, in the cases in which Hα is fully in absorption, we focus on fitting the wings, and we consider the mass-loss rates obtained for these stars as upper limits.

We note the mismatch that is observed between C IV $\lambda\lambda$1548−1551 and Si IV $\lambda\lambda$1394−1403 line profiles in B0–B1 supergiants (e.g., Fig. C.12, C.11, and C.10). In these cases, the CMFGEN models consistently underpredict the C IV $\lambda\lambda 1548 - 1551$ optical depth, while overpredicting Si IV $\lambda\lambda 1394 - 1403$ depth. This could be indicative of overionisation of silicon and underionisation of carbon in CMFGEN model, which could be the direct results of excluding X-rays in our models (Bernini-Peron et al., 2023).

At effective temperatures of $T_{\rm eff} \approx 20$–30 kK, the photospheric radiation field lacks sufficient UV flux to thermally produce significant C^{3+} through direct ground-state photoionisation. Reproducing the observed optical depth of C IV $\lambda\lambda$1548, 1550 requires

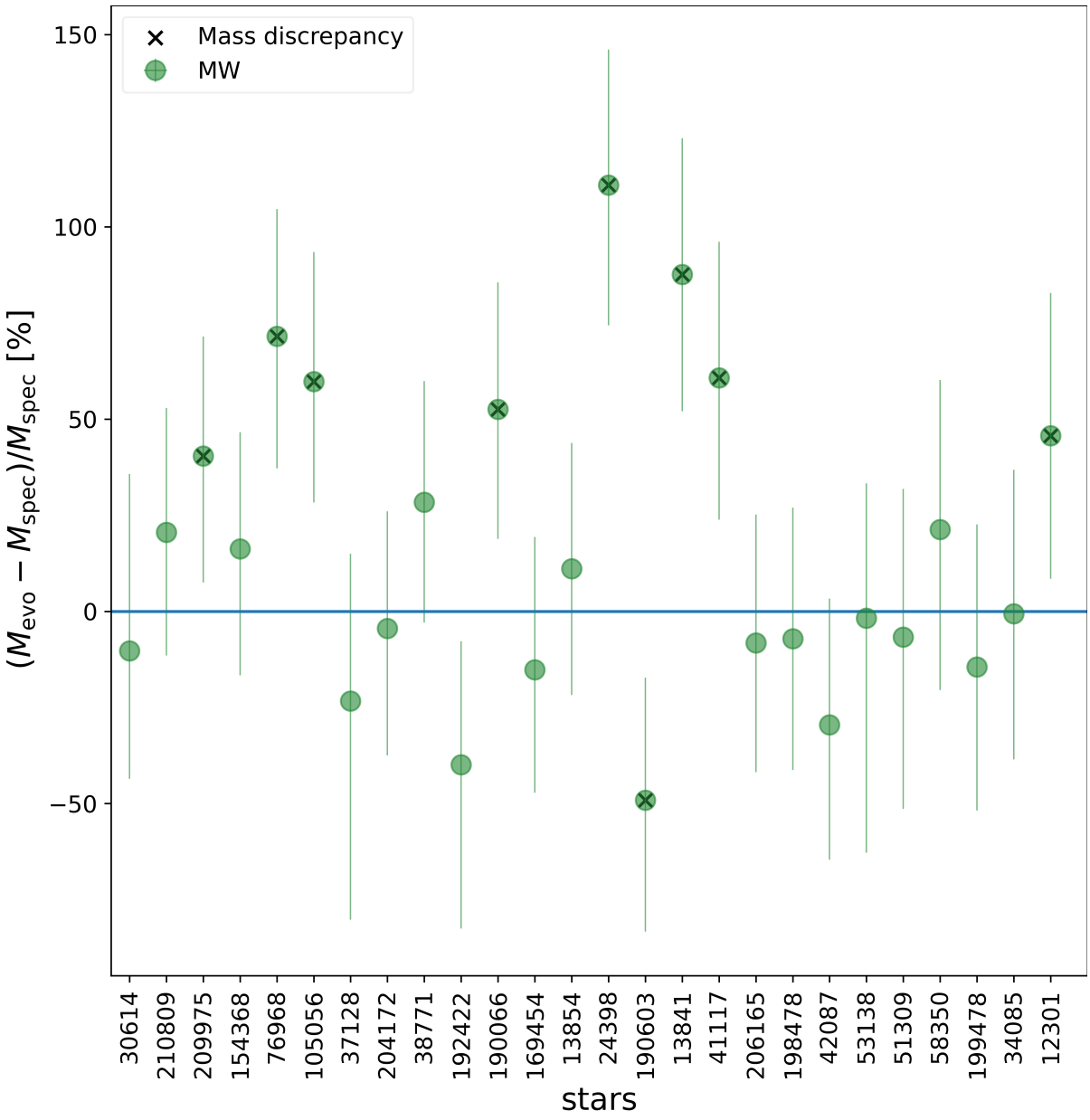


Figure 5.4: Relative (percentage) difference of the evolutionary and spectroscopic masses $(M_{evo} - M_{spec})/M_{spec}$. M_{evo} was obtained using a Bayesian inference method applied to Galactic evolutionary models of Brott et al. (2011). The diagonal black crosses indicate the presence of a mass discrepancy.

Table 5.5: Derived wind parameters. $\log \dot{M}$ with † in the superscript indicates an upper limit. $\log \dot{M}$ is subject to an average uncertainty of 0.4 dex. $v_{\rm esc}$ is the escape velocity at the photosphere. v_∞ values with the superscript ‡ indicate that v_∞ was inferred as $v_{\rm edge} \times \langle v_{\rm black}/v_{\rm edge} \rangle_{\rm MW}$.

HD	$\log L_{\rm bol}$	$\log \dot{M}$	v_∞	$v_{\rm esc,1-\Gamma}$	β	$f_{\rm vol,\infty}$	$v_{\rm cl}$
	$L_\odot$	$M_\odot\,{\rm yr}^{-1}$	$\rm km\,s^{-1}$	$\rm km\,s^{-1}$			$\rm km\,s^{-1}$
30614	6.04	−5.97	1540	553	1.0	0.10	35
210809	5.51	−6.08	1776‡	535	1.2	0.10	35
209975	5.32	−6.82†	1978	528	1.0	0.05	35
154368	5.47	−6.38	1793	513	1.5	0.10	35
76968	5.21	−6.53	1774‡	466	1.4	0.05	35
105056	5.25	−6.11	760‡	504	2.6	0.10	30
37128	5.70	−6.36	1532	640	1.3	0.10	30
204172	5.45	−6.61†	1723‡	562	1.0	0.10	30
38771	5.16	−6.42†	1231	490	1.0	0.10	30
192422	5.64	−6.51	1216‡	525	1.5	0.10	30
190066	5.09	−6.89	1294	457	1.0	0.20	30
169454	5.90	−5.73	704‡	401	3.0	0.50	30
13854	5.39	−6.68	902	394	3.0	0.20	30
24398	4.80	−7.22†	977‡	364	1.0	0.10	30
190603	5.94	−5.75	375	371	1.4	0.20	30
13841	4.92	−7.11†	1075	342	1.0	0.05	30
41117	5.53	−6.45	657‡	323	3.5	0.10	30
206165	5.25	−6.73†	631	366	1.0	0.10	30
198478	5.67	−6.74	540‡	304	4.3	0.10	25
42087	5.51	−6.97†	690‡	414	1.0	0.10	25
53138	5.56	−6.87	496‡	324	4.0	0.10	25
51309	4.92	−7.31†	607	358	1.0	0.10	25
58350	5.09	−6.48	355‡	287	2.5	0.10	25
199478	5.46	−5.56	286‡	273	1.0	0.10	25
34085	5.11	−6.38†	280‡	273	1.0	0.05	25
12301	4.56	−7.20†	470‡	286	1.0	0.10	25

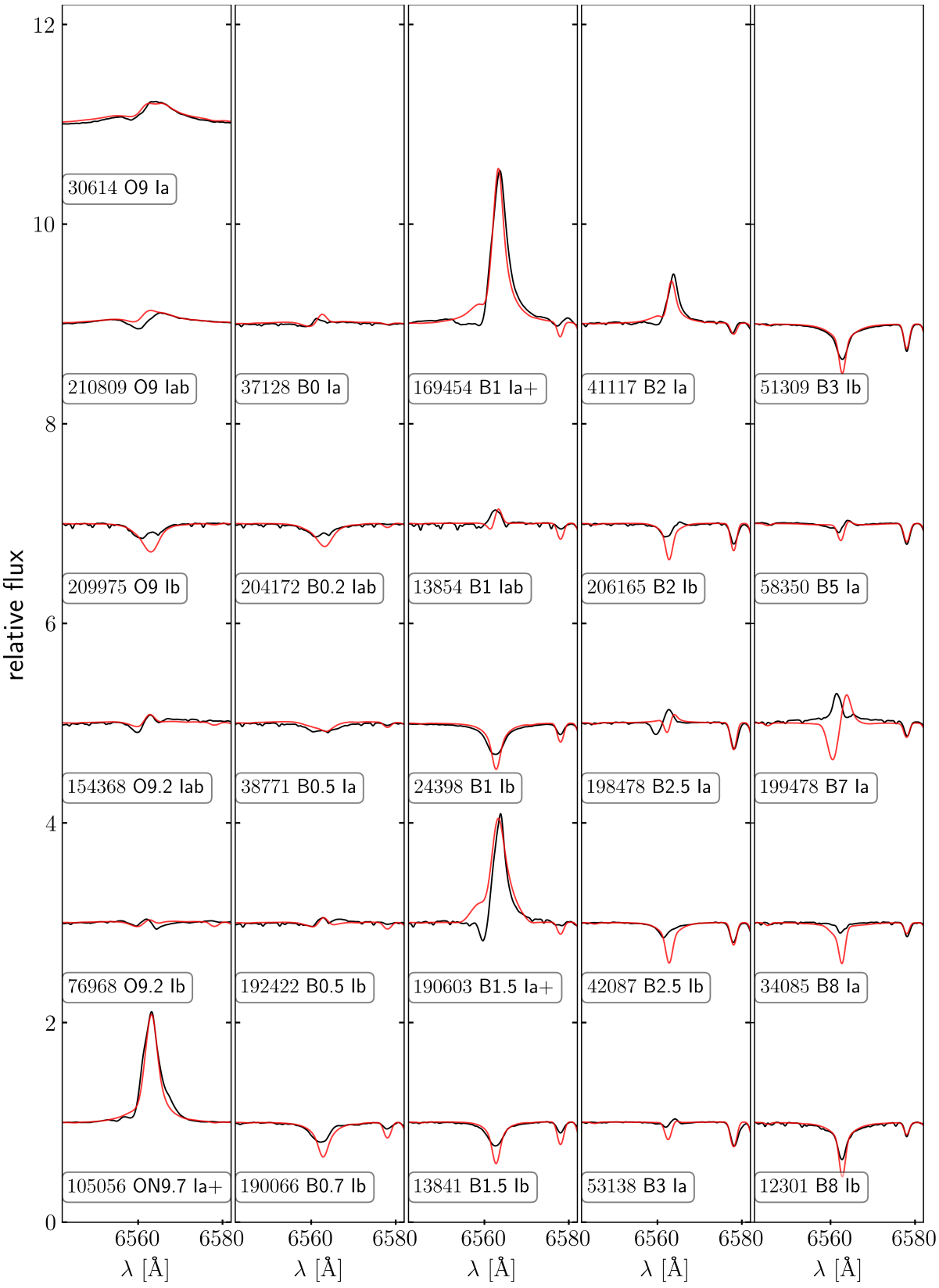


Figure 5.5: Best fits (solid red lines) to the observed Hα (+ C II λ6578) profiles (solid black lines).

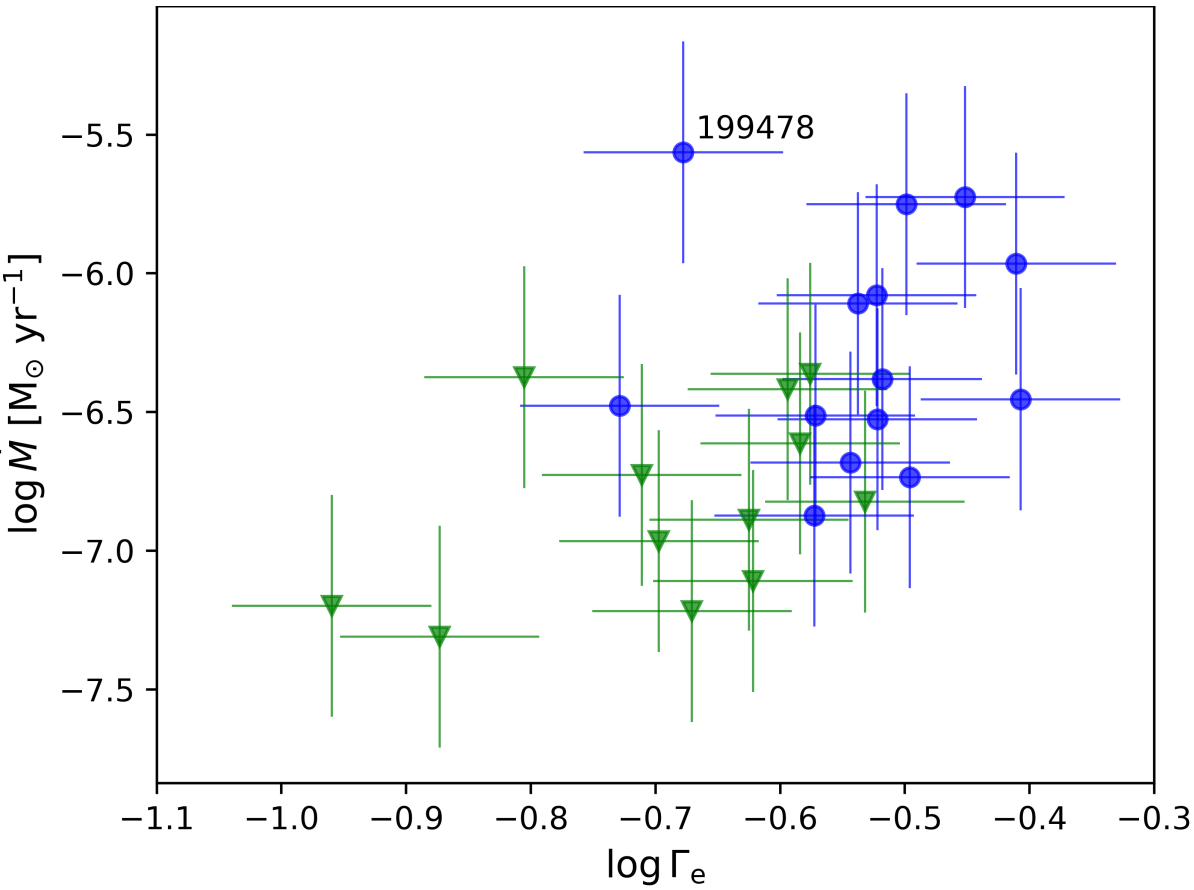


Figure 5.6: log $\dot{M}$ vs log Γ_e^{spec}. Blue circles indicate stars that have reliably obtained $\dot{M}$ from observed Hα emission components and reliable v_∞ measurements. Green triangles indicate an upper limit on $\dot{M}$.

accounting for superionisation driven by Auger ionisation from X-rays, which are generated in situ by line-driven wind instability shocks (see e.g., Cassinelli & Olson, 1979; Macfarlane et al., 1993, and Section 2.2.3). Models without these X-ray fields systematically underpredict C IV $\lambda\lambda$1548, 1550 (Bernini-Peron et al., 2023). Conversely, Si^{3+} is the dominant ionisation stage in early B stars with highly optically thick resonance transitions. Superionisation due to X-rays is accompanied by the depopulation of the thermally dominant ionisation stage, in this case Si^{3+}, which reduces the optical depth and therefore has the effect of desaturating the Si IV $\lambda\lambda1394-1403$ line profile (Bernini-Peron et al., 2023).

Fig. 5.6 shows the mass-loss rates as a function of the Eddington parameter Γ_e^{spec} in

logarithmic terms. We find a general trend of increasing $\log \dot{M}$ with $\log \Gamma_{\rm e}^{\rm spec}$. We note that the mass-loss rate we obtained for HD199478 is extremely high relative to other supergiants with similar $\log \Gamma_{\rm e}^{\rm spec}$. This is mainly due to its extremely large radius of $\approx 113\ R_{\odot}$, which is the result of this star's low $T_{\rm eff} = 12.6$ kK and high luminosity $\log L_{\rm bol}/L_{\odot} = 5.56$ (see Equation 2.16).

Ismailov & Ismayilova (2021) showed that HD199478 presents radial velocity variability in photospheric lines and Hα, with the lines being blue-shifted relative to the centre of mass of the system in a quasi-cyclical manner. This velocity shift is indeed seen in the observed Hα of HD199478 in Fig. 5.5. Ismailov & Ismayilova (2021) also reported an anti-correlation between the behaviour of the equivalent widths of the strong photospheric lines (Balmer lines) and the emission component of Hα, with both happening on similar timescales. They claimed that this phenomenon is indicative of large-scale stellar pulsations that lead to a cycle of photospheric expansion and compression. A slight blueshift is also observed in the Hα of HD198478, which is not present in other spectral lines.

Fig. 5.7 shows a comparison between our derived $\log \dot{M}$ and predictions from the numerical recipes of Vink & Sander (2021), Björklund et al. (2023), and Krtička et al. (2024), assuming $Z = Z_{\odot}$. We find that for $T_{\rm eff} \gtrapprox 22$ kK all recipes perform similarly well, generally matching our derived mass-loss rates. On the cool side of the bi-stability jump ($T_{\rm eff} \lessapprox 22$ kK), the $\log \dot{M}$ from the recipe of Vink & Sander (2021) dramatically increase and become much higher than ours, with $\Delta \log \dot{M}$ ranging from ≈ 0.8 to 2.3 dex. The recipe of Krtička et al. (2024) continues to produce the most similar predictions to our $\log \dot{M}$ on the cool side of the bi-stability jump. The recipe of Björklund et al. (2023) drastically under-predicts $\log \dot{M}$ for the majority of our sample with $T_{\rm eff} \lessapprox 22$ kK. These results are similar to our findings in Chapter 3 and Chapter 4.

Our sample spans a wide range of $v_{\infty} \approx 280$–1980 km s^{-1}. In Fig. 5.8 we show our measured v_{∞} compared to those predicted by the numerical recipes of Vink & Sander

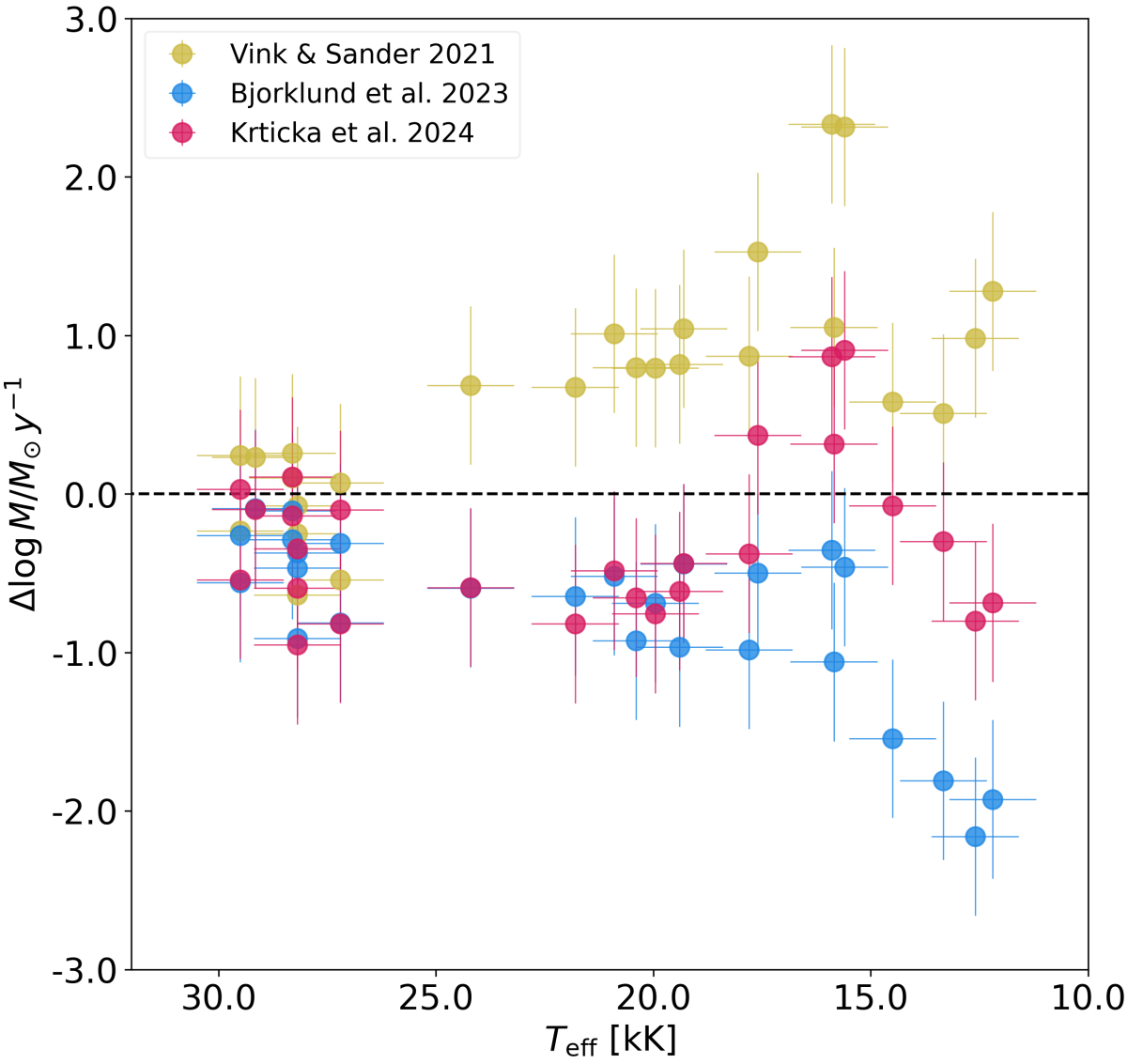


Figure 5.7: $\Delta \log \dot{M}$ vs $T_{\rm eff}$. $\Delta \log \dot{M}$ is the difference between our derived $\Delta \log \dot{M}$ and those obtained from numerical recipes from Vink & Sander (2021) (yellow dots), Björklund et al. (2023) (blue dots), and Krtička et al. (2024) (red dots).

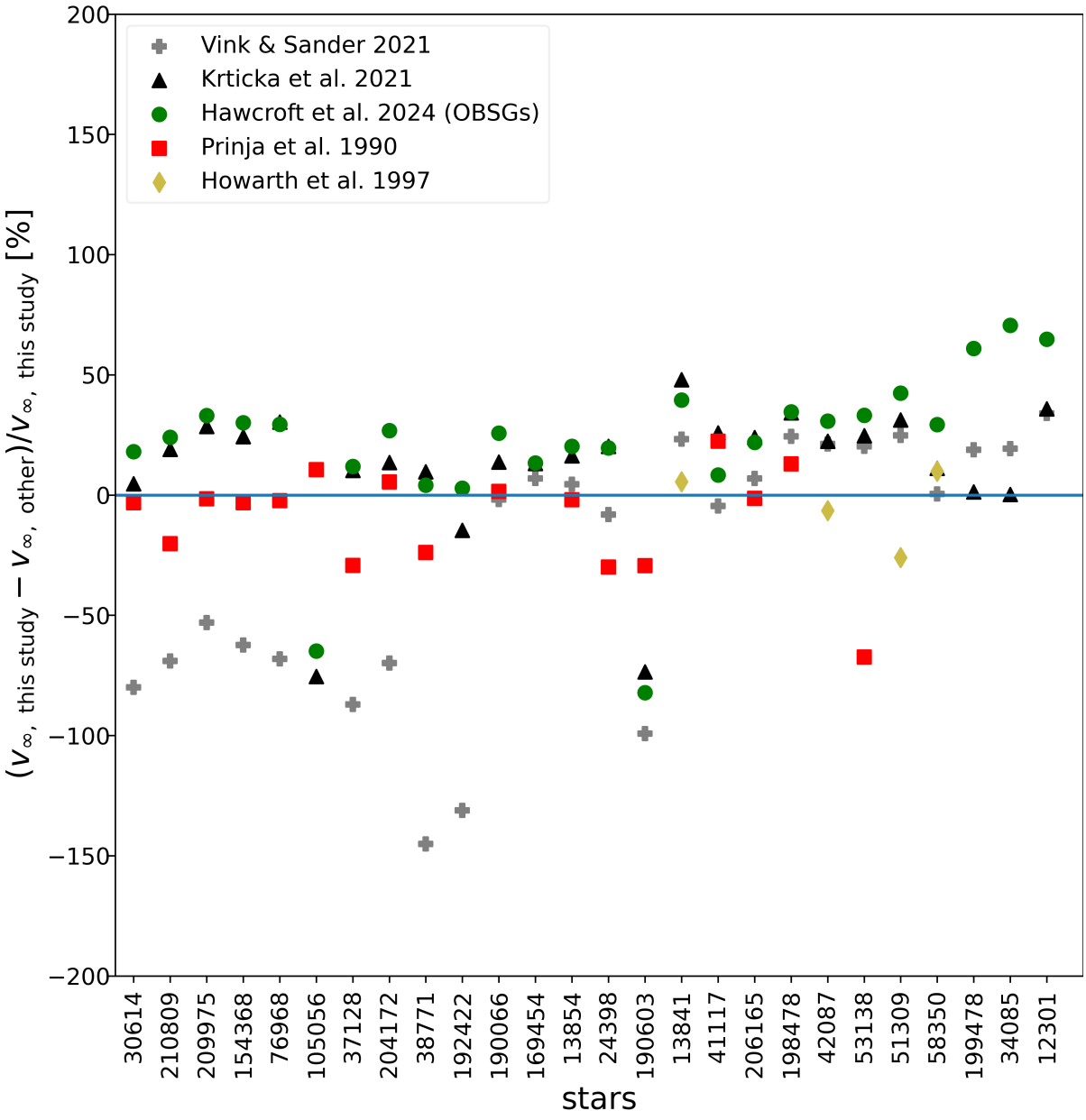


Figure 5.8: Relative (percentage) difference terminal wind velocity obtained by this study $v_{\infty,\ \text{this study}}$ and those of previous empirical measurements and predictions from recipes $v_{\infty,\ \text{other}}$. Grey crosses: Vink & Sander (2021) numerical recipe. Black triangles: Krtička et al. (2021) numerical recipe. Green circles: Hawcroft et al. (2024a) empirical recipe (O and B supergiants only). Red squares: Direct measurements from Prinja et al. (1990). Yellow diamonds: direct measurements from Howarth et al. (1997).

(2021) and Krtička et al. (2021), the empirically derived recipe of Hawcroft et al. (2024a), and archival measurements from Prinja et al. (1990) and Howarth et al. (1997). We find that the Vink & Sander (2021) theoretical prediction over-predicts the value of v_∞ by a factor of two for stars with $T_{\rm eff} \gtrsim 23$ kK. However, below that temperature, the predictions match our measured v_∞. The predictions from the Krtička et al. (2021) recipe generally match our v_∞, except in the cases of the hypergiants HD105056 and HD190603, both of which have slow winds (760 and 371 km s^{-1}, respectively) compared to objects with similar temperatures. This is a recurring theme across hypergiants in the MW, LMC, and SMC, and therefore could be considered a property of hypergiant winds. v_∞ calculations from the Hawcroft et al. (2024a) recipe agree with our measurements, but are generally lower, with the exception of the hypergiants HD105056 and HD190603. Finally, v_∞ of Prinja et al. (1990) and Howarth et al. (1997), which were uniformly determined from $v_{\rm black}$, are in reasonable agreement with our values, showing no systematic differences across our sample.

We fitted our results with a simple linear fit to derive the v_∞-$T_{\rm eff}$ relation. We derive

$$v_\infty[\mathrm{km\,s^{-1}}] = 0.08\,(\pm0.01)T_{\rm eff}[\mathrm{kK}] \;-\; 766\,(\pm182)[\mathrm{km\,s^{-1}}]. \tag{5.1}$$

Our results in Table 5.5 show that an average $\beta \approx 1.7 \pm 1.0$ is preferred to obtain a satisfactory fit for Hα in the cases in which it is fully or partially in emission. This is similar to our findings in Chapter 3 and 4, where we found an average β of 2.5 ± 0.6 and 2.0 ± 0.4, respectively. Additionally, we did not find any correlation between $f_{\rm vol,\infty}$ and $T_{\rm eff}$, $L_{\rm bol}$, or $\dot{M}$, which is the prevailing trend across the three environments studied in this thesis.

Table 5.6: Comparison of our derived broadening parameters with those obtained via IACOB-BROAD (Simón-Díaz & Herrero, 2014b) from same data set and rotational properties drawn from Simón-Díaz & Herrero (2014a) and de Burgos et al. (2024b) (SD14 and DB24, respectively). Simón-Díaz & Herrero (2014a) and de Burgos et al. (2024b) adopt global uncertainties for $v_{\rm rot}\sin i$ and $v_{\rm mac}$ of 15 and 20 km s^{-1}, respectively.

HD	by eye		IACOB-BROAD			SD14 + DB24		
	$v_{\rm rot}\sin i$	$v_{\rm mac}$	$v_{\rm rot}\sin i$	$v_{\rm mac}$	line	$v_{\rm rot}\sin i$	$v_{\rm mac}$	line
	km s^{-1}	km s^{-1}	km s^{-1}	km s^{-1}		km s^{-1}	km s^{-1}	
30614	85	20	97^{+34}_{-96}	85^{+78}_{-84}	O III λ5592	122	87	O III λ5592
210809	90	20	96^{+17}_{-44}	50^{+66}_{-49}	O III λ5592	102	75	O III λ5592
209975	65	20	65^{+17}_{-27}	64^{+30}_{-35}	O III λ5592	70	88	O III λ5592
154368	70	20	73^{+17}_{-25}	78^{+26}_{-28}	O III λ5592	65	75	O III λ5592
76968	70	20	52^{+18}_{-24}	65^{+30}_{-31}	O III λ5592	54	118	O III λ5592
105056	50	20	57^{+9}_{-14}	47^{+18}_{-21}	O III λ5592	-	-	-
37128	60	20	51^{+17}_{-14}	74^{+15}_{-13}	O III λ5592	52	84	O III λ5592
204172	75	20	68^{+15}_{-37}	41^{+50}_{-40}	O III λ5592	58	106	Si III λ4568
38771	60	20	57^{+12}_{-14}	64^{+15}_{-20}	Si III λ4553	47	86	Si III λ4568
192422	65	20	64^{+21}_{-33}	71^{+32}_{-39}	Si III λ4553	50	101	Si III λ4568
190066	60	20	70^{+11}_{-27}	59^{+41}_{-25}	Si III λ4553	60	84	Si III λ4568
169454	40	20	60^{+12}_{-16}	60^{+20}_{-22}	Si III λ4553	-	-	-
13854	50	20	55^{+14}_{-16}	72^{+16}_{-20}	Si III λ4553	55	70	Si III λ4568
24398	50	20	47^{+12}_{-13}	59^{+13}_{-18}	Si III λ4553	39	62	Si III λ4568
190603	50	20	49^{+9}_{-11}	73^{+10}_{-12}	Si III λ4553	-	-	Si III λ4568
13841	50	20	51^{+11}_{-17}	48^{+20}_{-20}	Si III λ4553	43	62	Si III λ4568
41117	60	20	47^{+7}_{-9}	51^{+9}_{-14}	Si III λ4553	47	48	Si III λ4568
206165	55	20	47^{+7}_{-9}	50^{+10}_{-11}	Si III λ4553	41	58	Si III λ4568
198478	45	20	40^{+7}_{-11}	43^{+14}_{-11}	Si III λ4553	36	47	Si III λ4568
42087	45	20	42^{+10}_{-13}	54^{+14}_{-14}	Si III λ4553	39	57	Si III λ4568
53138	50	20	44^{+8}_{-11}	49^{+12}_{-13}	Si III λ4553	36	64	Si III λ4568
51309	40	20	27^{+6}_{-7}	39^{+6}_{-8}	Si II λ6347	21	42	Si II λ6371
58350	45	20	41^{+6}_{-7}	38^{+9}_{-13}	Si II λ6347	32	54	Si II λ6371
199478	40	20	40^{+4}_{-4}	42^{+5}_{-5}	Si II λ6347	-	-	-
34085	35	20	38^{+2}_{-2}	50^{+2}_{-2}	Si II λ6347	-	-	-
12301	35	20	31^{+4}_{-5}	34^{+6}_{-7}	Si II λ6347	-	-	-

5.2.4 Rotation

Table 5.6 presents a comparison between our derived $v_{\rm rot} \sin i$, which were obtained by adopting $v_{\rm mac} = 20$ km s^{-1} and fitting by-eye the broadened profile of isolated metal lines from the degraded optical spectra ($R \approx 6800$), and the $v_{\rm rot} \sin i$ and $v_{\rm mac}$ values we obtained by applying the IACOB-BROAD (Simón-Díaz & Herrero, 2014b) to the same data with original resolution ($R \approx$ 46000–85000). The lines we used in the IACOB-BROAD procedure are: O III λ5592 for late-O supergiants, Si III λ4553 for early- and mid-B supergiants, and Si II λ6347 for late-B supergiants. We find that the projected rotational velocities obtained by the two methods agree excellently, and we derive a mean difference of ≈ 1 km s^{-1} with a spread of 8 km s^{-1}.

However, the results show that our adopted $v_{\rm mac} = 20$ km s^{-1} does not agree with those obtained using IACOB-BROAD. We find that the IACOB-BROAD $v_{\rm mac}$ are on average larger than our adopted value by ≈ 36 km s^{-1} with a spread of ≈ 13 km s^{-1}. This difference is much larger than what we obtained in the LMC and SMC (10 and 20 km s^{-1}, respectively). However, the LMC and SMC subsamples for which we conducted a similar investigation were smaller (five and ten stars, respectively) and limited by the availability of high-resolution spectra. Therefore, we acknowledge that the results obtained from the Galactic sample are likely more representative of the discrepancy between our adopted and measured values of $v_{\rm mac}$.

We also compare IACOB-BROAD $v_{\rm rot} \sin i$ and $v_{\rm mac}$ to those obtained by Simón-Díaz & Herrero (2014a) and de Burgos et al. (2024b) using the same tool and data. The main difference between our approach is the diagnostic lines, of which de Burgos et al. (2024b) used the Si III λ4568 component of the silicon triplet for early- and mid-B supergiants and the Si II λ6371 component of the silicon doublet for late-B supergiants. We find a mean difference in $v_{\rm rot} \sin i$ of ≈ 3 km s^{-1} with a spread 8 km s^{-1} We also find that our IACOB-BROAD $v_{\rm mac}$ measurements are on average 16 km s^{-1} lower than the

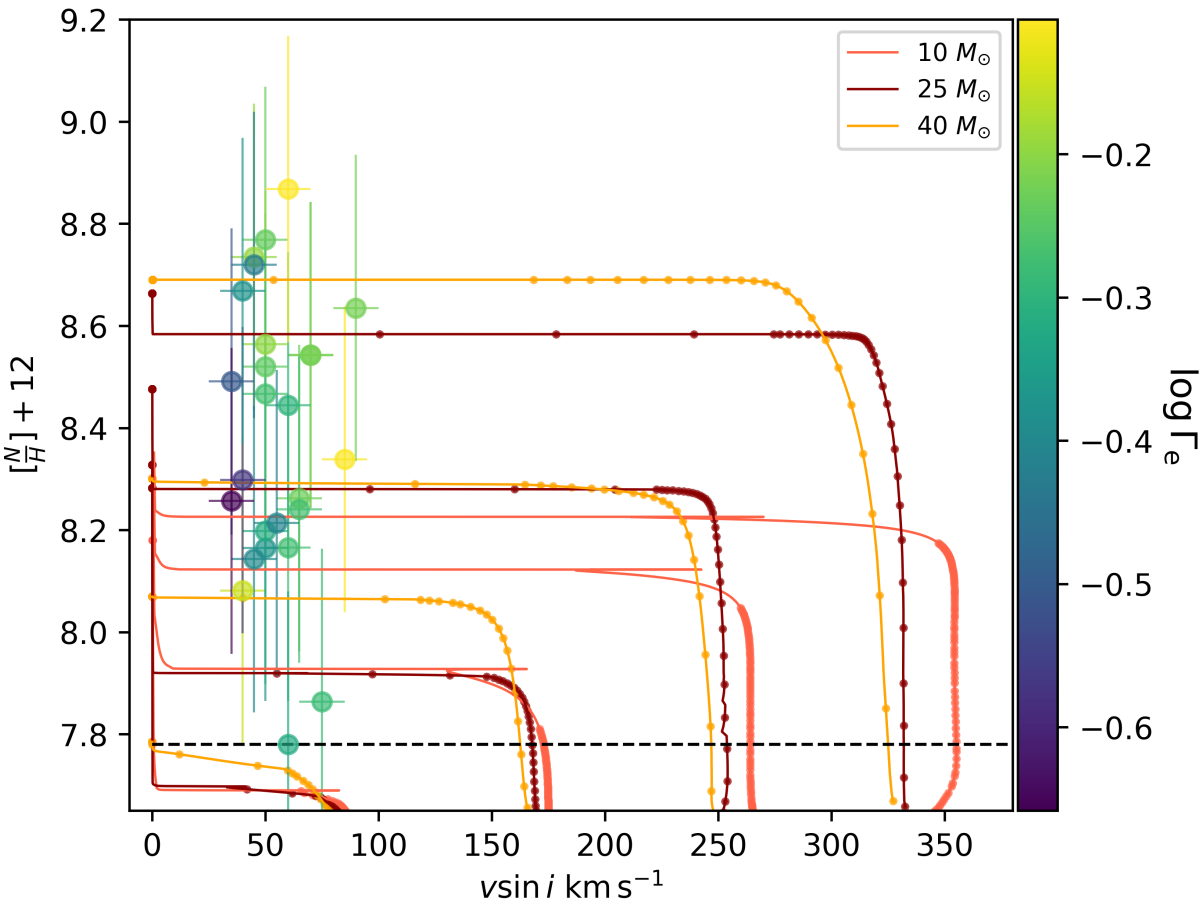


Figure 5.9: ϵ_N vs $v_{rot} \sin i$. The colour scheme corresponds to the value of Γ_e. The solid pink, brown, orange, and red lines represent Galactic evolutionary tracks for initial masses of 10 $M_\odot$, 25 $M_\odot$, 40 $M_\odot$, and 60 $M_\odot$, respectively, with initial rotational velocities of 110, 220, 320, 420 km s^{-1} (Brott et al., 2011). We multiplied by a factor of $\pi/4$ to take into account the inclination of the rotation axis (Hunter et al., 2008b). The dashed black line represents the baseline ϵ_N in the MW (Asplund et al., 2005). The dots along the evolutionary tracks represent time steps of 0.1 Myr

measurements of Simón-Díaz & Herrero (2014a) and de Burgos et al. (2024b), with a spread of 18 km s^{-1}. The mean differences for are within the global uncertainties adopted by Simón-Díaz & Herrero (2014a) and de Burgos et al. (2024b) of $\Delta v_{rot} \sin i = 15$ km s^{-1} and $\Delta v_{mac} = 20$ km s^{-1}, indicating that the use of different lines does not greatly alter the outcome of IACOB-BROAD.

Table 5.7: Best-fitting helium (Y, by mass) and CNO (ϵ_X, by number) abundances. The uncertainty in the helium mass fraction is 10%. The adopted uncertainty of CNO abundances is ±0.3 dex. The last column represents the cumulative CNO mass fraction relative to the cumulative CNO solar baseline.

HD	Y	ϵ_C	ϵ_N	ϵ_O	$\frac{\Sigma CNO}{\Sigma CNO_\odot}$
30614	0.51	8.55	8.34	8.82	1.03
210809	0.60	8.41	8.63	8.91	1.04
209975	0.42	8.36	8.26	8.74	0.98
154368	0.51	8.38	8.54	8.82	1.06
76968	0.51	8.55	8.54	8.67	0.97
105056	0.42	8.00	8.77	8.67	1.16
37128	0.42	8.40	8.17	8.74	0.96
204172	0.42	8.30	7.86	8.74	0.85
38771	0.39	8.15	8.44	8.72	1.02
192422	0.39	8.34	8.24	8.76	1.04
190066	0.30	8.39	7.78	8.66	0.93
169454	0.30	8.31	8.08	8.66	0.96
13854	0.36	8.18	8.52	8.70	1.10
24398	0.42	8.33	8.16	8.74	0.93
190603	0.42	8.00	8.56	8.74	1.05
13841	0.33	8.33	8.20	8.68	0.99
41117	0.48	7.87	8.87	8.45	0.97
206165	0.48	8.32	8.21	8.79	0.91
198478	0.45	8.32	8.73	8.73	1.21
42087	0.39	7.98	8.14	8.76	0.90
53138	0.42	8.36	8.47	8.72	1.05
51309	0.36	8.35	8.30	8.70	1.03
58350	0.51	8.25	8.72	8.78	1.10
199478	0.54	8.43	8.67	8.77	1.04
34085	0.45	8.39	8.49	8.77	1.08
12301	0.30	8.21	8.26	8.58	0.89
Averages	0.43	8.31	8.46	8.73	1.01

5.2.5 Chemical composition

We present the best-fitting chemical abundances for our sample in Table 5.7. We find that most of the stars in our show enhanced helium abundance relative to the MW baseline ($Y \approx 0.27$, Asplund et al., 2005), with an average $Y = 0.43$. Fig. 5.9 shows that most stars in our sample exhibit significant nitrogen enrichment, except for HD204172 and HD190066. According to the rotating single-star evolutionary models of Brott et al. (2011) that include rotational mixing, this enrichment can be explained by the high initial rotational velocities ($v_{\rm rot} \sin i > 320$ km s^{-1}), which cause nitrogen synthesised in the interior of the star to be transported to the surface.

This, however, is in contention with the observed rotational characteristics of Galactic O star populations. For example, Holgado et al. (2022) conducted a large-scale spectroscopic study of the rotational properties using the IACOB-BROAD tool (Simón-Díaz & Herrero, 2014a) of O stars in the MW using IACOB optical spectroscopy, and showed that most early O stars, which are the progenitors of B supergiants, are not fast rotators. They obtained a distribution of $v_{\rm rot} \sin i$ that peaks at ≈ 80 km s^{-1} for O stars across all luminosity classes in the MW. Additionally, Simón-Díaz & Herrero (2014a) found a single peak at ≈ 50 km s^{-1} in the $v_{\rm rot} \sin i$ distribution of Galactic B stars, which is in agreement with the findings of Dufton et al. (2006), who found that $v_{\rm rot} \sin i$ of Galactic B supergiants falls in the range of ≈ 60–30 km s^{-1}.

We can then conclude that invoking extremely high initial or current rotational velocities to explain the nitrogen enhancement is not supported by observational evidence. This is similar to our findings in the Magellanic Clouds. This could be a hint that other phenomena and evolutionary channels must be investigated, such as MS mergers (Menon & Heger, 2017; Menon et al., 2024) and mixing driven by internal gravitational waves and pulsations (Varghese et al., 2023; Morton et al., 2025), and possibly a combination of all mechanisms that affect the evolution and structure of the star.

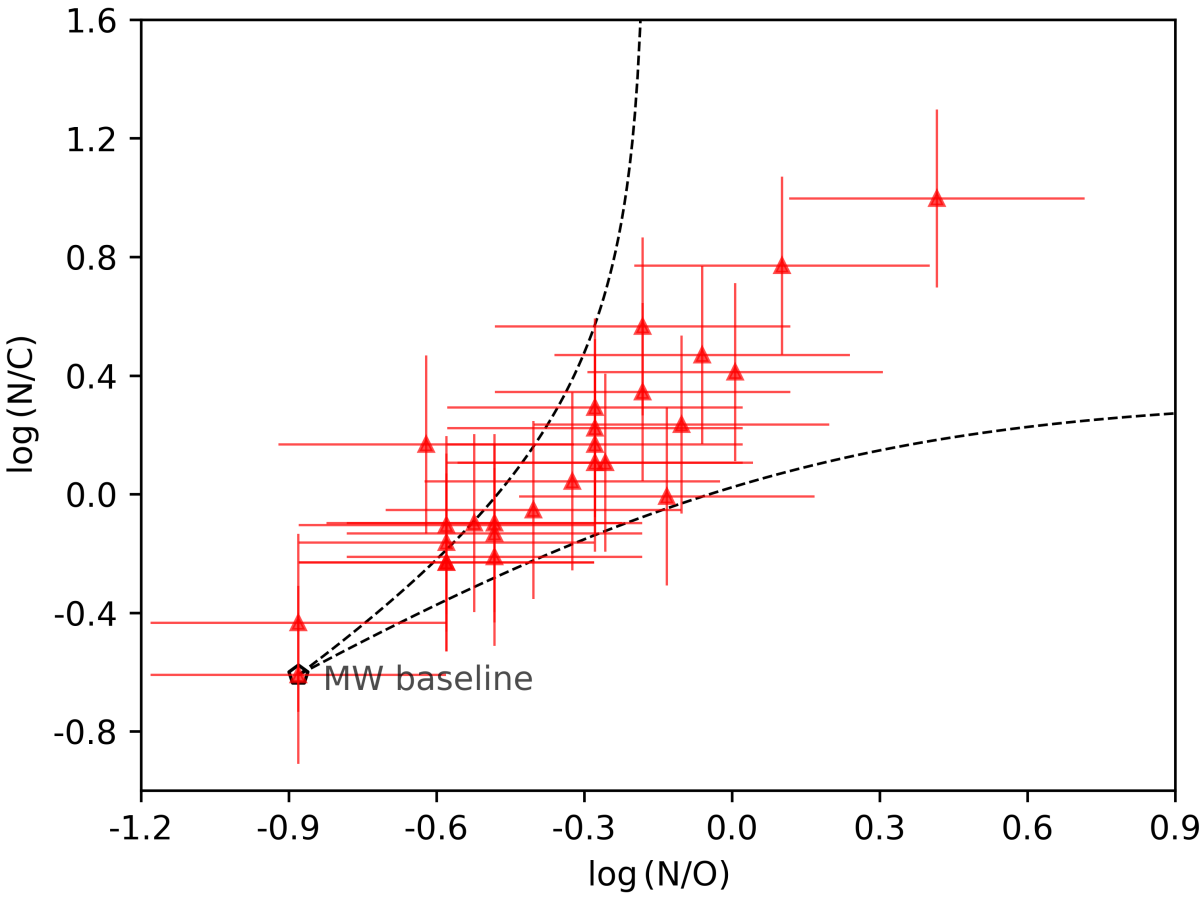


Figure 5.10: log N/C vs log N/O. The red triangles show the distribution of our sample. The dashed black lines represent the upper and lower boundaries adopted from Maeder et al. (2014).

Fig. 5.10 shows the ratio N/C versus N/O. Following the analytical solution of Maeder et al. (2014), the upper and lower CNO limits (dashed black lines) were calculated using the baseline CNO abundance averages of the SMC from Asplund et al. (2005). The majority of our sample falls between the two boundaries and agrees with the expected yield of elements processed by the CNO cycle. The last column in Table 5.7 shows that the CNO mass fraction is conserved for most of our sample.

5.3 Discussion

The discussion in this chapter will focus on comparing the derived fundamental parameters with those reported in the literature for the current Galactic BSG sample. Furthermore, we will discuss the implications of our results on the theorised bi-stability jump. Discussion of the overall metallicity scaling of wind parameters and the implications of our results for stellar evolution models is deferred to Chapter 6, where we will combine the results from the current Galactic sample with those from the LMC and SMC.

5.3.1 Comparison to literature

Our sample has eight, three, eleven, six, eight, and three stars in common with the samples of Crowther et al. (2006), Lefever et al. (2007), Searle et al. (2008), Haucke et al. (2018), Rubio-Díez et al. (2022), and Bernini-Peron et al. (2023), respectively. Crowther et al. (2006) and Searle et al. (2008) used a similar technique that employed TLUSTY and CMFGEN in their tailored UV and optical analysis of Galactic B supergiants. Lefever et al. (2007) and Haucke et al. (2018) conducted their studies on pulsating B supergiants and the variability of their fundamental parameters, which were derived from time-series optical spectroscopy using FASTWIND. Rubio-Díez et al. (2022) adopted the physical parameters of their sample from various sources to derive the mass loss and clumping properties of the winds from optical, infrared, and radio observa-

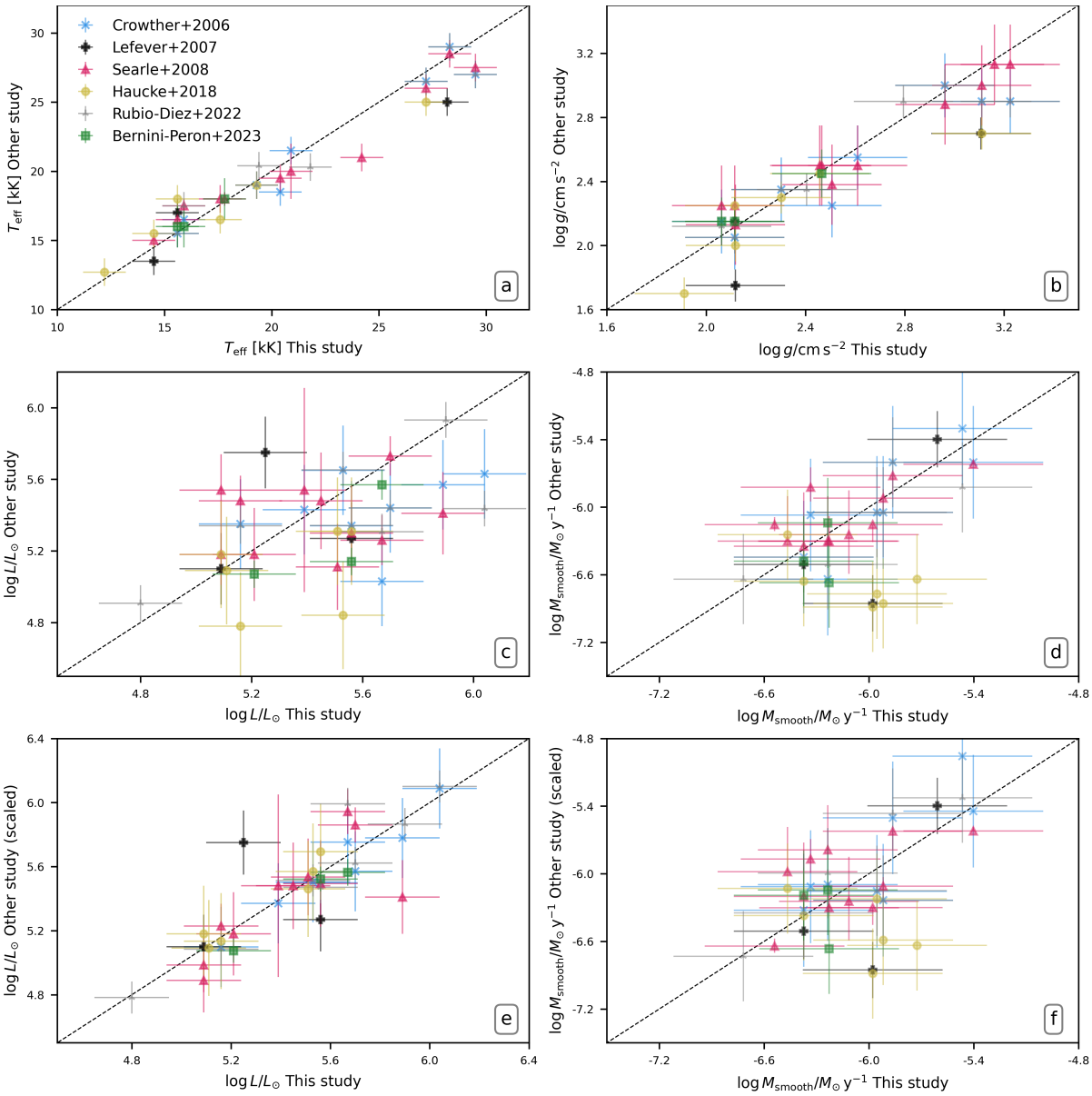


Figure 5.11: Comparison of our derived parameters to literature values. a: $T_{\rm eff}$ comparison, b: $\log g$ comparison, c: $L_{\rm bol}$ comparison, d: $\log \dot{M}_{\rm smooth}$ comparison. Cyan diagonal crosses: comparison to Crowther et al. (2006). Black crosses: comparison to Lefever et al. (2007). Pink triangles: comparison to Searle et al. (2008). Yellow circles: comparison to Haucke et al. (2018). Grey tri-diagonals: comparison to Rubio-Díez et al. (2022). Green squares: comparison to Bernini-Peron et al. (2023).

Table 5.8: Absolute means of the difference between our derived values of $T_{\rm eff}$ [kK], $\log g/{\rm cm\,s^{-2}}$, $\log L_{\rm bol}/L_\odot$, and $\log \dot{M}_{\rm smooth}/M_\odot\,{\rm yr^{-1}}$, and those obtained by Crowther et al. (2006, C06), Lefever et al. (2007, L07), Searle et al. (2008, S08), Haucke et al. (2018, H18), Rubio-Díez et al. (2022, RD22), and Bernini-Peron et al. (2023, BP23).

parameter	C06	L07	S08	H18	RD22	BP23
$\Delta T_{\rm eff}$	0.45 ± 1.12	0.93 ± 1.87	0.40 ± 1.33	0.05 ± 1.48	0.23 ± 1.26	0.23 ± 0.12
$\Delta \log g$	0.09 ± 0.14	0.25 ± 0.20	0.01 ± 0.10	0.10 ± 0.18	0.05 ± 0.14	0.04 ± 0.04
$\Delta \log L_{\rm bol}$	0.19 ± 0.27	0.07 ± 0.33	0.05 ± 0.29	0.24 ± 0.25	0.13 ± 0.26	0.22 ± 0.14
$\Delta \log \dot{M}$	0.03 ± 0.22	0.27 ± 0.45	0.05 ± 0.22	0.61 ± 0.43	0.10 ± 0.51	0.15 ± 0.22
	scaled to distance					
$\Delta \log L_{\rm bol}$	0.03 ± 0.07	0.07 ± 0.33	0.02 ± 0.19	0.03 ± 0.06	0.01 ± 0.13	0.09 ± 0.04
$\Delta \log \dot{M}$	0.09 ± 0.35	0.27 ± 0.45	0.07 ± 0.34	0.45 ± 0.50	0.19 ± 0.53	0.06 ± 0.27

tions using models based on the simulations of Puls et al. (2006). Bernini-Peron et al. (2023) employed CMFGEN in their analysis, and adopted similar techniques to the ones presented in this thesis, with some variations (primarily the inclusion of X-rays in their models), to investigate the clumping and X-ray properties of a small sample of Galactic B supergiants

Fig. 5.11 shows a comparison between our derived $T_{\rm eff}$, $\log g$, $L_{\rm bol}$, and $\log \dot{M}_{\rm smooth}$, and their counterparts from previous studies. In Table C.2, we list our values of the fundamental parameters and β in tandem with the values drawn from these previous studies. Our derived mass-loss rates that are used in Fig. 5.11 and listed in Table C.2 and those drawn from Bernini-Peron et al. (2023) are scaled by the derived $f_{\rm vol}$, i.e. $\dot{M}_{\rm smooth} = \dot{M}/\sqrt{f_{\rm vol}}$. Comparing smoothed mass-loss rates is preferred because most previous studies assumed smooth winds in their analyses. In Table 5.8, we present the means (and spread) of the difference between our values and the values in the literature for each parameter and for each previous study.

We find that our $T_{\rm eff}$ values agree well with those from previous studies within $\approx$ 2.0 kK, with the mean differences $\Delta T_{\rm eff} < 1.0$ kK across all studies. Similarly, $\log g$

values are in good agreement and $\Delta \log g/\mathrm{cm\,s^{-2}} < 0.25$. On the other hand, as seen in panel *c* of Fig 5.11, we find large discrepancies in the derived $\log L_{\rm bol}$. This is due to the use of incorrectly estimated distances in studies that lacked access to high-precision astrometry from *Gaia*. For a fair comparison, we scale the luminosities from these studies to modern distances using the inverse-square law, and compare them to our values in panel *e* of Fig. 5.11. This appears to alleviate the large discrepancies in $\log L_{\rm bol}$, as the distance-scaled luminosity $\log {L_{\rm bol}}^{\rm scaled}$ values from the literature are in good agreement with our derived values within the uncertainties. This is also reflected in the mean differences (and spread) presented in Table 5.8, where $\Delta \log {L_{\rm bol}}^{\rm scaled} < \Delta \log L_{\rm bol}$ for all comparison studies.

Finally, from the comparison shown in panel *d*, we find that our derived $\log \dot{M}^{\rm smooth}$ values generally agree with those reported in the literature within 0.5 dex, with a few exceptions. By scaling the literature $\log \dot{M}^{\rm smooth}$ to the respective distance-scaled luminosities, the comparison yields a similar picture. We underline that the uncertainties adopted in many of the literature studies appear to be very low. However, these uncertainties do not account for several crucial aspects that can make mass-loss rate estimates highly uncertain: the intrinsic variability of wind lines (Prinja, 1988; Massa et al., 2024), the inherent uncertainty in model-atmosphere calculations (Massey et al., 2013), and the propagation of errors from the parameters used to derive the true mass-loss rates. Therefore, when drawing comparisons, it is important to consider a wider range of uncertainties.

5.3.2 Bi-stability jump

Fig. 5.12 shows the ratio of the wind terminal velocity to the velocity of escape at the photosphere $v_\infty/v_{\rm esc}$ as a function of $T_{\rm eff}$, which shows that $v_\infty/v_{\rm esc}$ decreases with $T_{\rm eff}$. Two notable outliers are the hypergiants HD105056 and HD190603, both of which

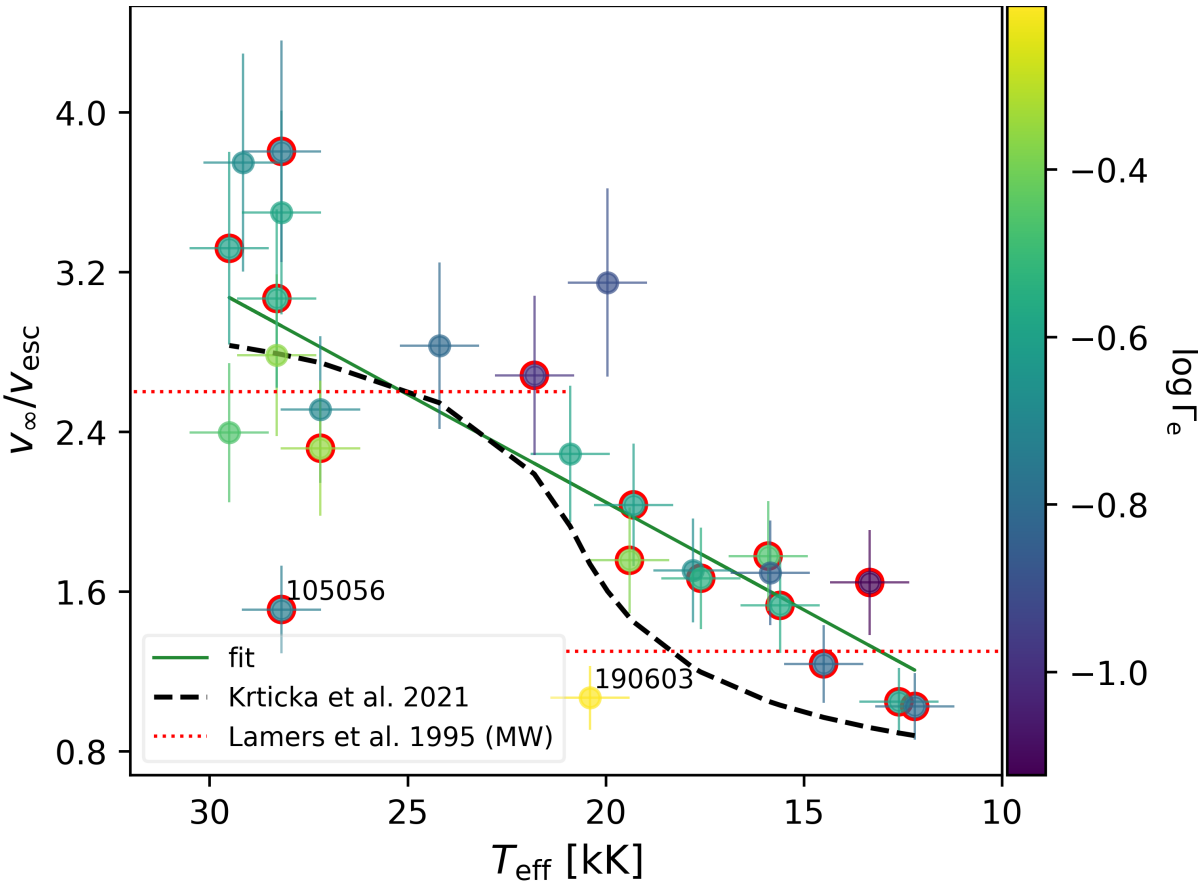


Figure 5.12: Ratio ($v_\infty/v_{\rm esc}$) as a function of temperature. The solid green line represents the linear fit to our sample. The dashed black line is the relation presented in Krtička et al. (2021). The dotted red lines represent the ratios from Lamers et al. (1995). The colour gradient correlates with the value of Γ_e. Red circles indicate stars the v_∞ of which is inferred as $v_{\rm edge} \times \langle v_\infty/v_{\rm edge}\rangle_{\rm MW}$.

have relatively low $v_\infty/v_{\rm esc}$ compared to stars with similar $T_{\rm eff}$. This is a result of their relatively slow winds with v_∞ of 760 km s^{-1} for HD105056 and 375 km s^{-1} for HD190603. From these results and the results presented in the previous chapters, one might draw the conclusion that hypergiants generally possess slower winds than what might be expected from a similar regular supergiant with the same temperature.

From a simple linear fit to our sample, we obtain:

$$v_\infty/v_{\rm esc} = 5.1(\pm0.9)\log(T_{\rm eff}/{\rm K}) - 19.8(\pm3.7), \tag{5.2}$$

where $v_{\rm esc} = \sqrt{2GM(1-\Gamma_{\rm e})/R_*}$, and $\Gamma_{\rm e}$ is the Eddington parameter, which was calculated using $M_{\rm evo}$. Our results do not support the claim of Vink et al. (2001) of a sudden decrease in $v_\infty/v_{\rm esc}$ in the region of the bi-stability jump around $T_{\rm eff} \approx 25$–21 kK.

In Fig. 5.13, which shows $\log \dot{M}$ as a function of $T_{\rm eff}$, there is a similar lack of evidence for an increase in mass loss around 25–21 kK, which could be attributed to the bi-stability jump. The lack of evidence supporting the existence of the bi-stability jump appears to be a recurring theme across our study of BSG wind properties, regardless of the environment and metallicity. This is consistent with results from the literature, in which empirically derived fundamental parameters of BSGs do not support the idea of increased line-driving around around $T_{\rm eff} \approx 25$–21 kK, that is associated with the shift in the ionisation structure from Fe IV to Fe III (see e.g., Crowther et al., 2006; Searle et al., 2008; Haucke et al., 2018; Bernini-Peron et al., 2024; Verhamme et al., 2024; de Burgos et al., 2024a).

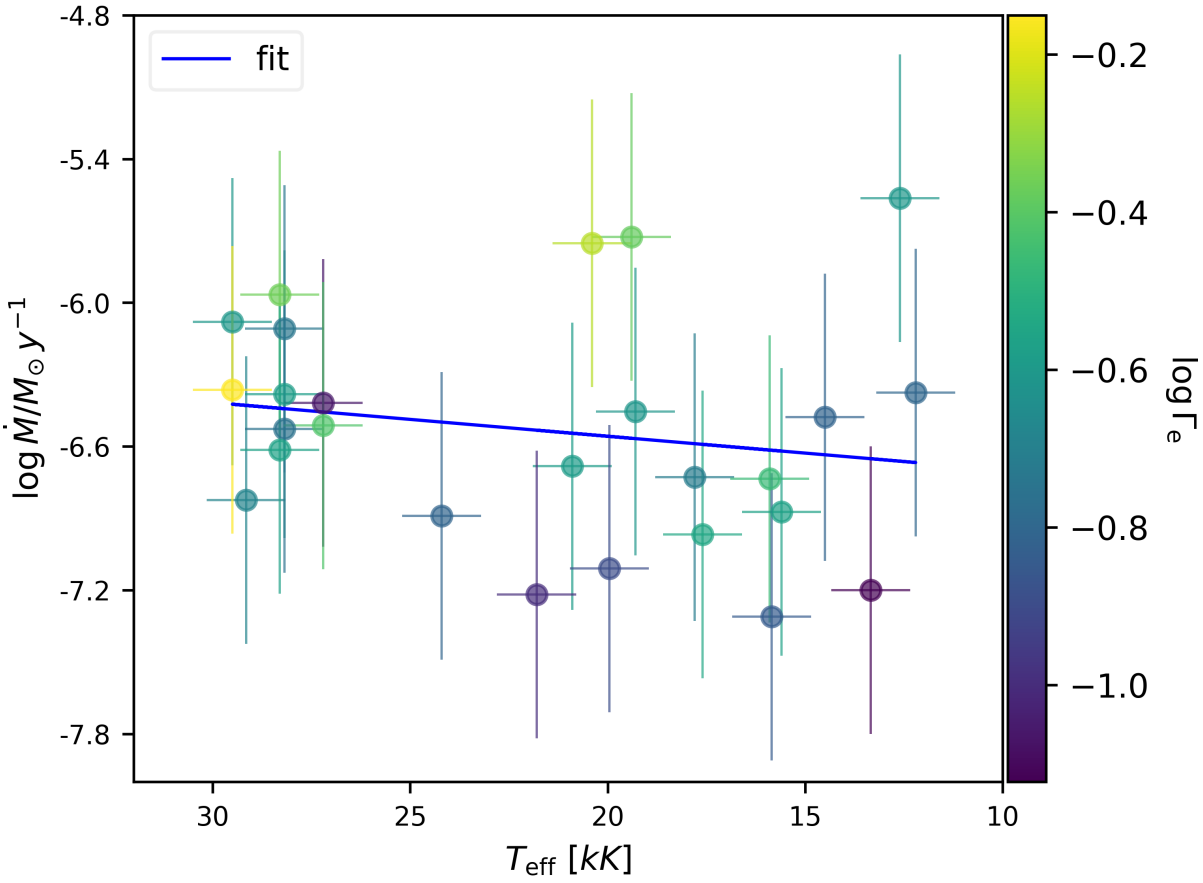


Figure 5.13: $\log \dot{M}$ versus $T_{\rm eff}$. The colour scale corresponds to $\Gamma_e^{\rm evo}$.

5.4 Summary

We have completed a spectroscopic analysis of 26 late-O and B Galactic supergiants, which employed CMFGEN (Hillier & Miller, 1998), using UV (IUE) and optical (IACOB, Melchiors, UVES-POP) spectral ranges. We obtained stellar and wind parameters of the stars in our sample. Here we summarise the conclusions drawn from this chapter in the following points:

- We compared our derived mass-loss rates to predictions from various numerical recipes Vink & Sander (2021); Björklund et al. (2023); Krtička et al. (2024). We found that the values of the numerical recipes differ from our mass-loss rates, with the recipe from Krtička et al. (2024) producing the values most closely aligned with ours, yet still showing a different trend with temperature, similar to the results in Chapters 3 and 4.

- We do not find any sign of the theorised bi-stability jump. This is similar to our findings in Chapters 3 and 4. This means that within the current framework of radiative transfer codes used for modelling OB stars, the dramatic increase in mass loss at $T_{\rm eff}$ = 25-21 kK that is associated with the theorised bi-stability jump is not empirically supported in any of the studied galaxies.

- We explored the evolutionary history of the stars within our sample. We employed an updated Bayesian inference method (V. Bronner et al., in prep.) similar to BONNSAI (Schneider et al., 2014a) to obtain the evolutionary masses and ages using the rotating single-star evolutionary tracks of Brott et al. (2011). Amongst our sample, $\approx 35\%$ of stars present with a mass discrepancy.

- We find that seven stars in our sample appear to have evolved beyond the TAMS according the rotating single-star evolutionary models of Brott et al. (2011). Out

of the remaining main-sequence stars, seven appear to be very close to the blue hook of TAMS.

- We also compared our results to literature values of the same stars (Crowther et al., 2006; Lefever et al., 2007; Searle et al., 2008; Haucke et al., 2018; Rubio-Díez et al., 2022; Bernini-Peron et al., 2023). We find that the effective temperature, surface gravity, and luminosity adjusted for modern distances generally agree with previous studies with modest variance. However, our derived smooth mass-loss rates broadly agree with previous estimates within the uncertainties, with no systemic trends to report.

Chapter 6

Conclusions

In this thesis, a combined UV and optical spectroscopic study of late-O and B supergiants in the MCs and the MW has been undertaken. The ULLYSES UV spectroscopic library and the complementary XShootU optical spectroscopy for the stars in the MCs have been introduced, along with comparable UV and optical spectroscopy for the Galactic targets. A new set of photospheric and wind parameters of 62 BSGs has been obtained. This is the first CMFGEN-based analysis of O9 to B8 supergiants that was applied homogeneously to three samples in environments of different metallicities.

The $T_{\rm eff}$, $\log g$, $\log L_{\rm bol}$, v_∞, and $\log \dot{M}$ values reported in previous studies of the same stars are compatible with those presented in this thesis. On the one hand, we find that our $T_{\rm eff}$, $\log g$, $\log L_{\rm bol}$, and v_∞ generally agree with previous studies with modest variance. On the other hand, our derived values of $\log \dot{M}$ do not exactly match previous estimates. However, when differences in analysis methods and data quality are accounted for, our mass-loss rates are generally consistent with previously derived values within the expected systematic uncertainty (Sander et al., 2024).

We employed an updated Bayesian inference method to infer evolutionary masses and ages from stellar evolution models, thereby exploring the stars' evolutionary histories. In the three environments, we found that the inferred evolutionary masses are generally

larger than spectroscopic masses. In the LMC, the spectroscopic masses we derived are broadly consistent with the evolutionary masses within the uncertainties. Our results did not reveal the large mass discrepancy reported in previous studies of OB stars in the LMC. However, we find significant mass discrepancies in approximately 40% of the SMC and MW samples.

Our results show that the mass-loss rates, terminal wind velocities, and the ratio of terminal wind velocity to the escape velocity decrease monotonically with temperature. We found no evidence for the theorised bi-stability jump (Vink et al., 2001), which is consistent with previous studies of OB stars in the MW and the MCs. This means that, within the current framework of radiative transfer codes used to model OB stars, the dramatic increase in mass loss and the corresponding decrease in wind velocities at $T_{\rm eff}$ = 25-21 kK associated with the theorised bi-stability jump is not empirically supported. This raises questions about the validity of numerical mass-loss rate recipes that exhibit bi-stability jumps across different temperature regions.

We compared our derived mass-loss rates to predictions from various numerical mass-loss rate recipes Vink & Sander (2021); Björklund et al. (2023); Krtička et al. (2024). We found that the predicted mass-loss rates in the O-star regime are generally consistent across the recipes and agree with our derived values. However, in the B-star regime, the predictions deviate greatly from one another and from our empirical $\dot{M}$. Therefore, we conclude that the numerical recipes are valid for main-sequence stars, where the majority of continuous mass-loss occurs prior to evolved phases (RSG, LBV, WR). Nevertheless, the predictive power of these recipes does not hold for stars nearing the end of the MS and in the post-MS phase. We found that the recipe from Krtička et al. (2024) yields values most closely aligned with ours, yet it still exhibits a different temperature dependence.

In Section 6.1 of this final chapter of this thesis, using the results presented in Chapters 3, 4, and 5, we derive and present a new metallicity-dependent mass-loss rate recipe. In Section 6.2, we discuss the metallicity scaling of the wind-momentum-

luminosity relation. In Section 6.3, we discuss the impact of our results on the evolution of hot massive stars. In Section 6.6, we discuss the prospective future projects to be undertaken.

6.1 Mass-loss rate recipe

To quantify the Z-dependence of mass-loss rates, we consider the three OB supergiant samples presented in this thesis. By preforming a χ^2-fit that takes into the account the uncertainties in $\dot{M}$, $L_{\rm bol}$, $M_{\rm evo}$, and $T_{\rm eff}$, we obtained a universal Z-dependent recipe for mass-loss rates for late-O and B supergiants following the formulation of Leitherer et al. (1992) as

$$\log\left(\frac{\dot{M}}{M_{\odot}\,\mathrm{yr}^{-1}}\right) = a + b\log\left(\frac{L_{\rm bol}}{L_{\odot}}\right) + c\log\left(\frac{M_{\rm evo}}{M_{\odot}}\right) + d\log\left(\frac{T_{\rm eff}}{\mathrm{K}}\right) + e\log\left(\frac{Z}{Z_{\odot}}\right). \quad (6.1)$$

Table 6.1 contains the values obtained for the fitting parameters of Equation 6.1. We performed the fitting routine to include only the stars with robust $\dot{M}$ estimates, assuming in one case that the winds are driven exclusively by iron, and by iron-group elements in another. We repeat this procedure to include the complete sample.

Here we will discuss the quality of the fit for the first case, where only stars with

Table 6.1: Fitting parameters of Equation 6.1. In the first column, "reliable" indicates that the fit was performed using stars with reliably determined mass-loss rates, i.e., these stars show an emission component in Hα and have reliable v_{∞} measurements from UV P Cygni profiles. N in the second column represents the number of stars.

	N	a	b	c	d	e
$Z_{\rm MW} = 1\ Z_{\odot,\rm Fe}$, $Z_{\rm LMC} = 0.5\ Z_{\odot,\rm Fe}$, $Z_{\rm SMC} = 0.2\ Z_{\odot,\rm Fe}$						
Reliable	39	-10.03 ± 3.32	1.26 ± 0.76	-0.30 ± 1.52	-0.61 ± 0.75	1.12 ± 0.26
Complete	62	-10.93 ± 2.18	1.48 ± 0.62	-0.65 ± 1.34	-0.60 ± 0.61	1.17 ± 0.20
$Z_{\rm MW} = 1\ Z_{\odot,\rm Fe-group}$, $Z_{\rm LMC} = 0.5\ Z_{\odot,\rm Fe-group}$, $Z_{\rm SMC} = 1/7\ Z_{\odot,\rm Fe-group}$						
Reliable	39	-9.83 ± 3.38	1.22 ± 0.74	-0.28 ± 1.49	-0.61 ± 0.76	0.95 ± 0.22
Complete	62	-10.93 ± 2.21	1.48 ± 0.56	-0.68 ± 1.21	-0.59 ± 0.62	0.98 ± 0.15

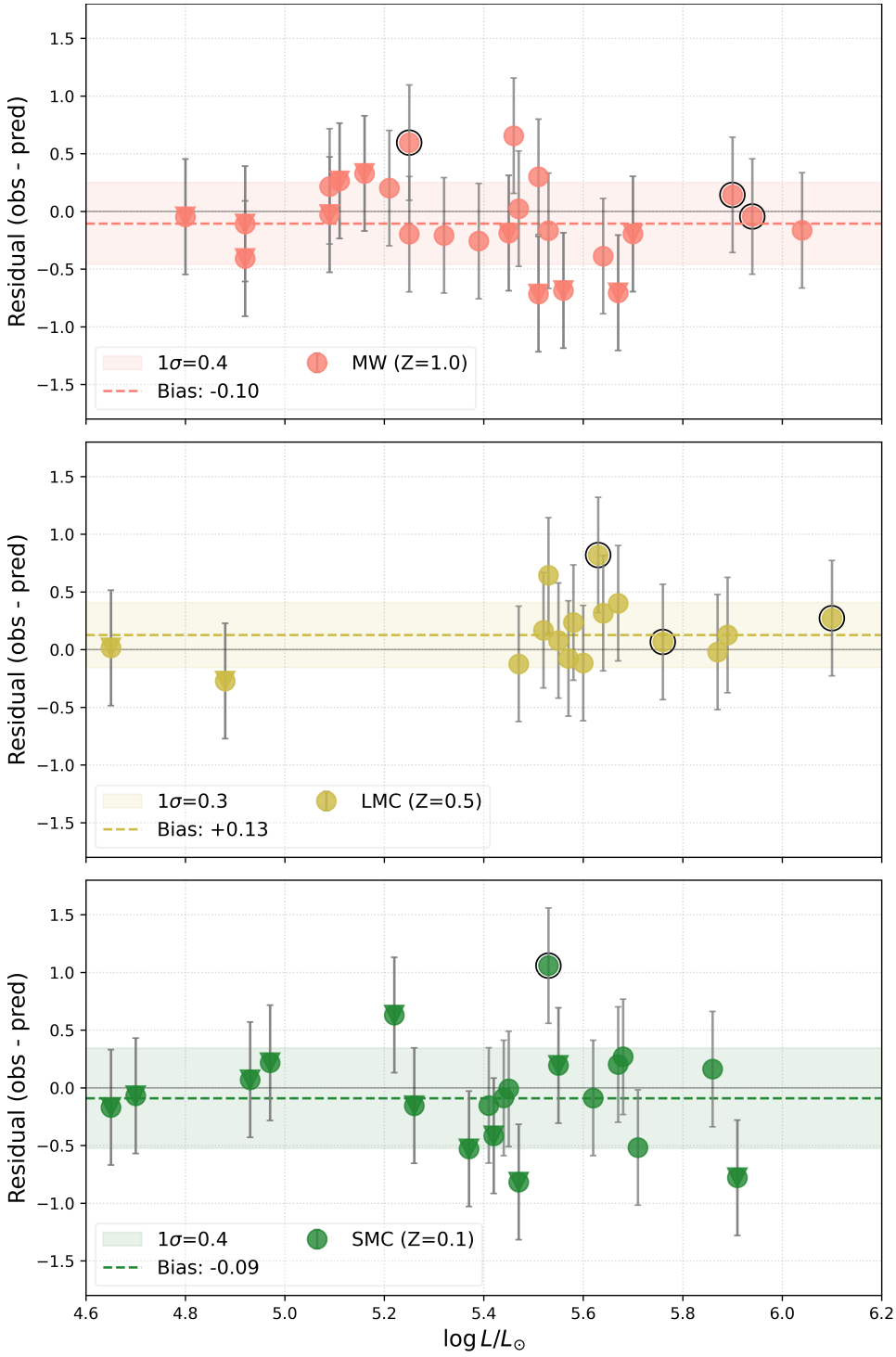


Figure 6.1: Residuals between the predicted and observed mass loss rates. The shaded area indicates the 1σ root-mean-square dispersion from the fitting routine for each galaxy, adjusted for the bias. The circles represent stars included in our fitting routine (reliable $\dot{M}$ and v_∞ diagnostics). Triangles indicate stars excluded from the fitting procedure. Black circles indicate the hypergiants.

reliable $\dot{M}$ are included, and iron is assumed to be the main source of wind driving, i.e. $Z_{\rm MW} = 1\ Z_{\odot}$, $Z_{\rm MW} = 0.5\ Z_{\odot}$, and $Z_{\rm MW} = 0.2\ Z_{\odot}$. In Fig 6.1, we present the residuals between the empirically derived mass-loss rates and those calculated from our scaling relation. The overall root-mean-square value (RMS) of the residuals is $\log \dot{M}/M_{\odot}\,{\rm yr}^{-1} = 0.42$. We find that the predicted $\log \dot{M}/M_{\odot}\,{\rm yr}^{-1}$ values are biased by -0.19, 0.07, and -0.24 for the MW, LMC, and SMC, respectively. Although this indicates a slight over-prediction of mass loss at $Z_{\rm MW}$ and $Z_{\rm SMC}$ by the scaling relation, it provides a consistent description of the mass-loss behaviour across a factor of ≈ 5 in Z.

By changing our assumption that the winds of massive stars are driven by the iron exclusively, i.e. $Z_{\rm SMC} = 0.2\ Z_{\odot,{\rm Fe}}$, to assuming that all iron-group elements contribute to line driving, i.e. $Z_{\rm SMC} = 1/7\ Z_{\odot,{\rm Fe-group}}$, the metallicity dependence coefficient e decreases from 1.12 ± 0.26 to 0.95 ± 0.22 (see Table 6.1). This example highlights the importance of the assumed metallicities, particularly the sensitivity of Z-dependent wind scaling relations to the adopted metallicity of the host galaxy.

In Table 6.1, under each the two line-driving assumptions ($Z_{\rm SMC} = 0.2\ Z_{\odot,{\rm Fe}}$ and $Z_{\rm SMC} = 1/7\ Z_{\odot,{\rm Fe-group}}$) , we provide the results of our χ^2-fitting excluding upper limits (identified as "reliable") and including the upper limits as regular values (identified as "complete"). By comparing the two results, we find that the slope (parametrised by the coefficients a, b, c, and d) and the intercept (parametrised by the coefficient e) of the fits of the complete sample and the sample excluding upper limits are in agreement within the fitting uncertainties. However, in the complete sample, we fit the upper limits as regular values (similar to our fits in Chapters 3 and 4), which is not strictly correct and may bias the slope. In the future, we intend to use a more robust fitting approach by swapping the χ^2-fitting to a least-square regression that allows for the accounting of upper limits, such as the Tobit regression (Tobin, 1958), which corrects the slope biases of the regular ordinary least-square fit-

Table 6.2: Comparison of the metallicity dependence of the mass-loss rates from various recipes. e is the metallicity scaling factor from Equation 6.1. The two values from Vink & Sander (2021) are for stars on the hot and cool side of the bi-stability jump, respectively.

e	Reference	Method	Regime
1.13 ± 0.26	this study	Empirical, UV+Opt	O9-B8 supergiants
1.03 ± 0.11	Pauli et al. (2025)	Empirical, Mixed	OB and WR stars
1.02 ± 0.30	Backs et al. (2024)	Empirical, UV+Opt	O3-O9.7 stars
0.5-0.8	Marcolino et al. (2022)	Empirical, UV+Opt	O3-B0.5 stars
0.83 ± 0.16	Mokiem et al. (2007)	Empirical, Opt	O2-B1 stars
0.60	Krtička et al. (2024)	nLTE RTE models	OB stars
$0.75 \cdots 1.87$	Björklund et al. (2023)	Hydro. nLTE RTE models	OB stars
0.42/0.83	Vink & Sander (2021)	Monte Carlo calculations	OB stars
0.85	Vink et al. (2001)	Monte Carlo Calculations	OB stars
0.94	Abbott (1982)	Modified CAK	OB stars

ting by using a modified maximum likelihood function that accounts for the probability of a data point falling at or above that upper threshold.

Some stars in our sample deviate significantly from the predictions. The largest deviations in the MW, LMC, and SMC are in HD42087 (-0.86 dex), Sk -69° 279 (0.74 dex), and AzV 327 (-0.98 dex), respectively. In most cases, outliers in all three galaxies are associated with stars that lack reliable $\dot{M}$ and/or v_∞ diagnostics (indicated as triangles in Fig. 6.1), and hypergiants (indicated with black circles).

In Table 6.2, we compare our empirical Z-dependence to results from previous studies based on empirical derivations (Pauli et al., 2025; Backs et al., 2024; Marcolino et al., 2022; Mokiem et al., 2007) . The Z-dependence estimates for $\dot{M}$ found in the literature range from 0.5 to 1.87. Our derived value of 1.13 ± 0.26 is steeper than those derived by Pauli et al. (2025), Backs et al. (2024), Marcolino et al. (2022), and Mokiem et al. (2007). However, Backs et al. (2024), Marcolino et al. (2022), and Mokiem et al. (2007) investigate the O-star regime, with stars in their samples no later than B1 spectral type and covering all luminosity classes. The Z-scaling relation from Pauli et al. (2025) was obtained from a large sample of OB and WR stars. Therefore, this difference is

not surprising, as we are not comparing like-for-like with respect to the dominant line-driving ions and evolutionary stages. However, when accounting for uncertainties, our derived scaling factor appears to be in agreement with the results of Pauli et al. (2025) and Backs et al. (2024), and significantly steeper than those derived by Marcolino et al. (2022) and Mokiem et al. (2007).

We also compare our results to those obtained from numerical simulations of various approaches. We find that our Z-scaling is significantly steeper than what is predicted by the numerical approaches of Abbott (1982), Vink et al. (2001), Vink & Sander (2021), and Krtička et al. (2024). This suggests that the efficiency of line-driving, specifically the number of effective driving lines, drops more steeply at low Z than current standard models predict.

6.2 Wind momentum-luminosity relation

Fig. 6.2 shows the modified wind momentum as a function of $L_{\rm bol}$. We obtain the following linear relation for the MW:

$$\log D_{\rm mom}^{\rm MW} = 22.42\,(\pm 1.46) + 1.06\,(\pm 0.27)\log \frac{L_{\rm bol}}{L_\odot}. \tag{6.2}$$

In Fig. 6.2, we show $\log D_{\rm mom}$ versus $L_{\rm bol}$ for our MW sample, and compare it to our results for the LMC and SMC. As in previous chapters, to obtain Equation 6.2, we fit only stars (circles) that exhibit both P Cygni profiles in the UV and an emission component in Hα, making the derived wind parameters the most reliable. Including the entire MW sample in the fit slightly changes the slope to 0.98 ± 0.19 and the intercept to 22.68 ± 1.01.

Combining our results for the MW, LMC and SMC, we updated the Z-dependent relation for $\log D_{\rm mom}$, which we presented in Chapter 4 for the Z-scaling only in the

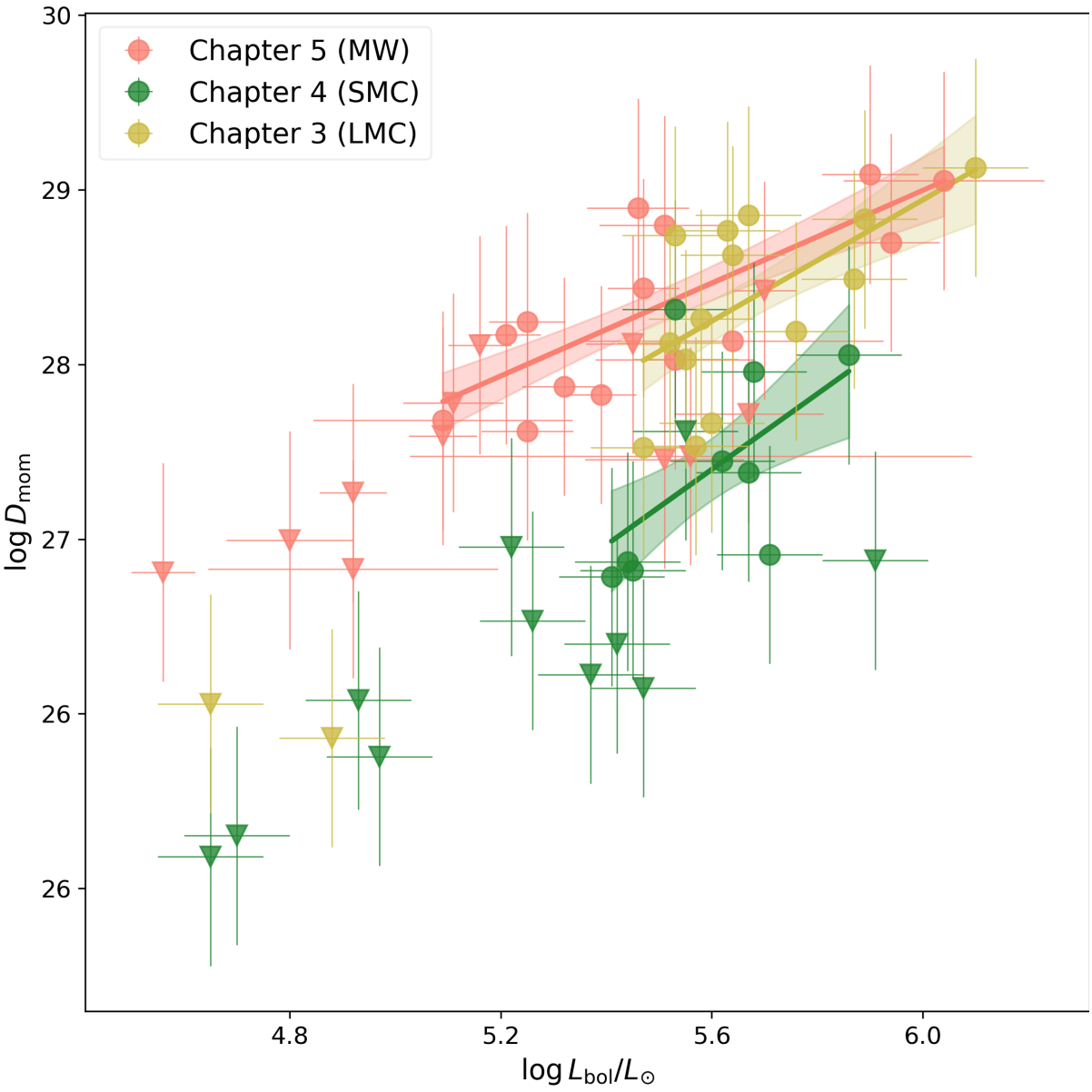


Figure 6.2: $D_{\rm mom}$ vs $\log L_{\rm bol}$. The salmon symbols represent the MW sample. The yellow and green symbols represent the LMC and SMC samples, respectively. Circles indicate stars with reliable $\dot{M}$ and v_∞ diagnostics. Triangles indicate upper limits. Solid lines are fits to the circle only. Upper limits (triangles) are not included in the linear fits.

Magellanic clouds (see Equation 4.3 and the fitting parameters in Table 4.10). We derive the relation as:

$$\log D_{\rm mom} = \left[1.15\,(\pm0.25) - 0.97\,(\pm1.25)\log\frac{Z}{Z_\odot}\right]\log\frac{L_{\rm bol}}{10^6 L_\odot} + 0.74\,(\pm1.03)\log\frac{Z}{Z_\odot} + 28.80\,(\pm2.07). \tag{6.3}$$

We find that, on average, the recipe slightly underestimates our derived $\log D_{\rm mom}$ for the MW and LMC samples and slightly overestimates it for our SMC stars.

The Z-dependence of $\log D_{\rm mom}$ is dominated by the Z-dependence of $\dot{M}$, with no significant contribution from v_∞. This conclusion is drawn from our investigation of the Z-dependence of the v_∞-$T_{\rm eff}$ relation, i.e. $v_\infty(T) \propto Z^n$. We obtain $n = 0.02 \pm 0.25$ when only fitting stars with precise v_∞ measurements. Including the complete sample decreases n to 0.01 ± 0.20. This indicates that v_∞ might be independent of Z in the BSG regime. This is contrary to the findings of Hawcroft et al. (2024a), who derived $n = 0.22 \pm 0.03$ for their complete sample, which is comprised of O2 to B1 stars of all luminosity classes. Additionally, Leitherer et al. (1992) found a more pronounced Z-dependence, with their theoretical models predicting $n \approx 0.13$. These deviating outcomes might suggest a more complex Z-dependence of v_∞ that is not well described by a simple power law.

We compare our derived relation to the empirical relation of Backs et al. (2024) and Mokiem et al. (2006). Backs et al. (2024) derived their Z-dependent relation from samples of Galactic (Hawcroft et al., 2024b), LMC (Brands et al., 2025), and SMC O-stars, which were analysed by applying the genetic fitting algorithm KIWI-GA to FASTWIND models. On the other hand, Mokiem et al. (2007) obtained $D_{\rm mom}$-$\log L_{\rm bol}$ fits for samples of O- and early B-stars across the three environments, drawing results from archival studies that used various fitting techniques and model atmosphere codes. Fig 6.3 shows this comparison, and we find that the relations of Backs et al. (2024) and Mokiem et al. (2006) perform very differently from ours. However, this is expected, as

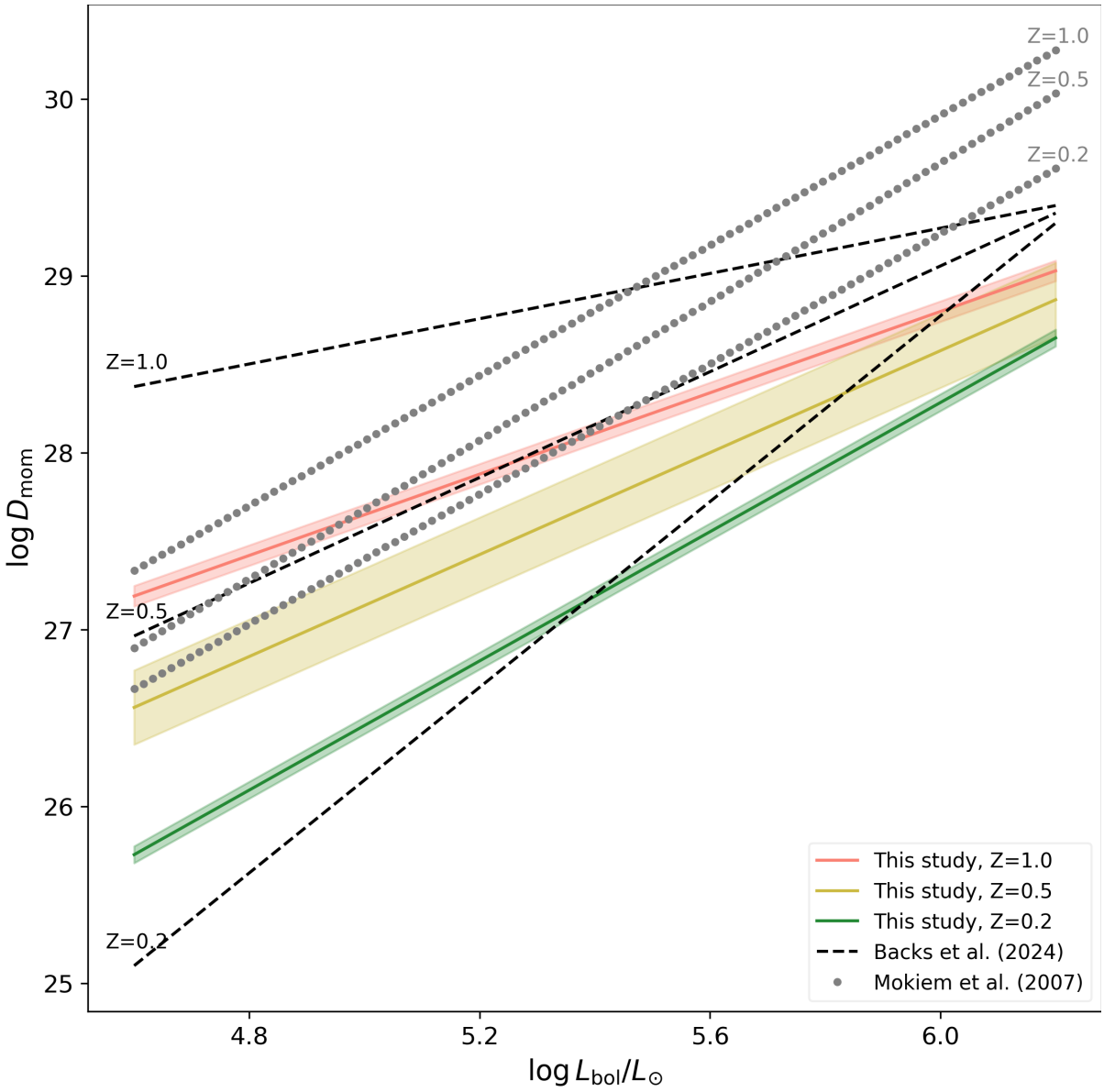


Figure 6.3: Z-dependent modified wind momentum relation. The solid colored lines show predictions from our $\log D_{\rm mom}$ recipe for the MW, LMC, and SMC metallicities. The dashed and dash-dotted black and grey lines indicate the modified wind momentum relations from Backs et al. (2024) and Mokiem et al. (2007).

both studies investigated the WLR primarily for O stars, whereas our study focuses on B supergiants.

6.3 Implications for the evolution of BSGs

The enhanced helium mass fraction and the nitrogen enhancement at the expense of carbon and oxygen that is observed in our stars indicate that our samples consist of evolved stars. The majority of the stars are main-sequence stars, according to the rotating single-star evolutionary models of Brott et al. (2011). However, a significant number of stars in our samples appear to have evolved beyond the main-sequence and may be in the shell-hydrogen-burning phase. On the HRD, these stars lie within the Hertzsprung gap. This phase is short-lived in single-star evolutionary models, which poses a challenge for explaining the presence of such stars. This problem becomes more significant when considering the discrepancy between $M_{\rm spec}$ and $M_{\rm evo}$, the nitrogen enrichment at the expense of carbon and oxygen, and the relatively slow rotation rates observed in our sample.

A possible explanation is that these stars may be products of binary mergers. Simulations suggest that stellar mergers in binary stars can lead to the formation of "rejuvenated" stars, effectively resetting the nuclear clock of the resulting star, causing it to reside in the Hertzsprung gap longer than a single star of equivalent luminosity would (Schneider et al., 2016). Simulations also show that binary-merger products may spend their entire core-helium burning phase as BSGs (Claeys et al., 2011; Justham et al., 2014). Binary merger models predict that these products may exhibit altered surface abundances, such as helium and nitrogen enrichment, and anomalous rotation rates that deviate from the expectations of single-star rotational mixing (de Mink et al., 2014). Bernini-Peron et al. (2023) found that tailored MESA models of merged stars can reproduce the observed luminosities, effective temperatures and surface gravities in their

core-helium burning stage, providing evidence that BSGs could be products of stellar mergers. However, the mass discrepancy was not resolved: they found that the $M_{\rm evo}$ predicted by the tailored models is significantly larger than $M_{\rm spec}$, as in single-star evolutionary models. An alternative scenario is stellar stripping, in which partially stripped stars may appear as blue supergiants (Götberg et al., 2017, 2018; Laplace et al., 2020). Simulations from Klencki et al. (2022) suggest that such objects would exhibit a lower $M_{\rm spec}$ relative to $M_{\rm evo}$, extreme helium enrichment, enhanced nitrogen and depleted carbon and oxygen abundances, and low $v_{\rm rot} \sin i$.

Although most stars in our sample exhibit these characteristics, neither evolutionary scenario (binary merger or stripping) can be confirmed, as none of the signatures observed in our sample is exclusive to any of the scenarios. This is primarily due to the possibility of an undetected companion in a close binary system. For the stars in our samples that lie in the Hertzsprung gap, there is no conclusive evidence of binarity. Nevertheless, the high luminosities of BSG-like stars can easily drown out the light from less luminous companions. Therefore, investigating the single-star status of our stars would require (i) high-resolution spectra of different epochs to check for any possible radial velocity shifts, and (ii) X-ray observations, which would allow the detection of high X-ray luminosities associated with mass accretion in HMXB or strong radiative shock in colliding-wind binaries.

The mass a single hot massive star loses near the TAMS and in the Hertzsprung gap is minute compared to that lost on the main sequence. However, because evolutionary codes implement a single mass-loss rate recipe from the MS through the RSG phase, and given the discrepancy between empirical and numerically predicted mass-loss rates, we conclude that the most accurate evolutionary tracks and, therefore, mass and age determinations, require the use of an empirical mass-loss rate recipe. The mass loss in this stage becomes more significant when considering the possibility of a stellar-merger origin for many BSGs, thereby prolonging their lifetime in this phase. This could be

done by combining empirical recipes tailored to different evolutionary stages, such as the one presented in this thesis and in Backs et al. (2024). This is not an easy task, as manual switching between those recipes is required. Another approach would be using a universal empirical mass-loss rate recipe, such as that provided by Pauli et al. (2025). However, if one chooses to employ numerical predictions, we recommend using the Krtička et al. (2024) recipe, as it yields the most reliable predictions and does not exhibit extreme increases in mass loss associated with bi-stability jumps, and performs similarly well for MS stars on the hot side of the bi-stability jump when compared to other numerical mass loss recipes.

The lack of observational evidence for a bi-stability jump makes explaining the properties of massive star populations more challenging. Particularly, our derived mass-loss rates of SMC supergiants exceeding the HD limit of $\log L_{\rm bol}/L_{\odot} = 5.5$ (Humphreys & Davidson, 1979a; Davies et al., 2018) are far too low to be able to strip the supergiants of their hydrogen-rich outer layers. Consequently, the high fraction of single WR stars observed in the SMC (Shenar et al., 2020) cannot be explained by the classical single star evolutionary regime, unless the supergiant is capable of losing an enormous amount of mass within its very short remaining lifespan. This may imply that an intermediate LBV phase accompanied by extreme episodic eruptions and mass loss is required for the star to transition to a WR phase.

6.4 Implications on the bi-stability jump

Results from Chapters 3, 4, and 5 do not support the existence of the theorised bi-stability jump (Lamers et al., 1995; Vink et al., 1999). This lack of a sudden increase in $\log \dot{M}$ that is accompanied by a sudden decrease in v_{∞} is in agreement with the findings of previous studies of OB stars in the MW, LMC, and SMC (e.g., Crowther et al., 2006; Searle et al., 2008; Verhamme et al., 2024; de Burgos et al., 2024a; Verhamme

et al., 2025). However, all spectroscopic studies of OB supergiants, including the work in this thesis, suffer similar issues related to the high uncertainty of empirically deriving mass-loss rates.

As discussed in previous chapters, we must consider that UV wind lines and optical recombination line diagnostics are heavily impacted by significant line-profile variability (Massa et al., 2024) and temporal optical-depth structure (such as NACs and DACs Prinja, 1988; Prinja et al., 2002). Unfortunately, current state-of-the-art spectral synthesis models used in spectroscopic analysis of massive stars are steady-state, and therefore do not capture the time variability of wind line diagnostics. This is complicated by the mass-loss rate discrepancy problem discussed in Section 1.3.5, where different diagnostics yield highly mismatched mass-loss rates.

Commonly used RT models include an extremely large number of parameters and prescriptions that are treated in varying approaches depending on the code. Many of these parameters represent rough approximations of multi-dimensional phenomena that cannot be sufficiently described by 1D models. An example of this is clumping, which is poorly described by current 1D approximations of micro- and macro-clumping (Hillier, 1991; Hamann & Koesterke, 1998; Owocki et al., 2004; Puls et al., 2008). The picture becomes even more complex when considering the time-dependent nature of the clumps and the inter-clump medium, which is seen in multi-dimensional unified atmosphere and wind simulations (see e.g., Moens et al., 2022; Debnath et al., 2024; Moens et al., 2025). It has been suggested that the bi-stability jump is masked by differences in macro-clumping properties on either side of the bi-stability jump. However, recent studies that have investigated the clumping properties of B supergiants using FASTWIND under the macro-clumping approximations did not report any trend in the properties of clumps or the inter-clump medium with temperature (Verhamme et al., 2024, 2025).

In addition to the time variability of winds, we also have to consider that the photosphere is not static and exhibits temperature variability. This variability affects the

ionisation structure and level populations (Prinja et al., 2005), which introduces temporal variability in the line-driving, iron-like elements that leads to variable mass-loss rates. Furthermore, the varying approaches and the large number of fudge parameters, such as clumping parameters and β-velocity laws, included in each code are a primary source of discrepancies seen in empirically derived stellar and wind parameters (Massey et al., 2013; Sander et al., 2024).

These complex issues make the complete rejection of the concept of a bi-stability jump unjustified and bring into question the reliability of empirically derived mass-loss rates. Moreover, spectroscopic studies of LBVs that exhibit temperatures around the region of the bi-stability jump ($T_{\rm eff} \approx 25$ kK) have reported on the existence of wind modulation. For example, Groh et al. (2009) and Groh et al. (2011) reported that during the S Doradus cycle (alternating between hot/faint minimum phases and cool/bright maximum phases) of AG Carinae, the mass-loss rate and wind terminal velocity undergo drastic changes over time, similar to those predicted by the bi-stability jump (Vink et al., 2001). Further investigation by Groh & Vink (2011) suggested that, given the large changes in temperature, the mechanism behind the observed LBV wind modulations is the same as in the bi-stability jump: changing their mass-loss properties as they traverse back and forth over the bi-stability limit due to changes in the ionisation of iron-group elements.

Additionally, a recent study by Vink et al. (2026) found that hydrodynamically consistent PoWR models predict a bi-stability jump at around $T_{\rm eff} \approx 25$ kK, similar to what is predicted by the Monte-Carlo predictions of Vink et al. (1999, 2000) and the CMFGEN predictions of Petrov et al. (2016). Therefore, we underline that, although our work and the work of many others report a lack of evidence of a bi-stability jump, the existence of opacity-induced wind modulations remains an open question, with the best empirical test being controlled experiments using stars that undergo temperature excursions at approximately fixed stellar parameters, such as known LBVs (Walborn

et al., 2017).

6.5 Summary

By combining the results from Chapters 3, 4, and 5, we present the following key points from this thesis

- We present a new, fully empirical mass-loss and wind momentum recipes, which were obtained from the consistently derived wind and stellar parameters of three homogenous samples in the MW, LMC, and SMC. We find that our metallicity scaling of mass loss is generally higher than predicted by numerical recipes (Abbott, 1982; Vink et al., 2001; Vink & Sander, 2021; Björklund et al., 2023; Krtička et al., 2024). We also find that our metallicity dependence is steeper than the previously derived empirical recipes of Mokiem et al. (2007) and Marcolino et al. (2022). Nonetheless, our derived value of the metallicity exponent agrees within the uncertainties with results from more recent studies of massive star winds (Backs et al., 2024; Pauli et al., 2025). We find that the wind velocity does not depend on the metallicity, which disagrees with the widely employed empirical wind velocity recipe of Hawcroft et al. (2024a). This might be a result of the our strictly O9 to B8 supergiant samples compared to the samples of Hawcroft et al. (2024a), which O2 to B2 stars of all luminosity classes.

- The numerical mass-loss rate recipe of Krtička et al. (2024) produces values most closely aligned with ours, yet still showing a different trend with temperature. Similar previous spectroscopic studies of OB supergiants have arrived to the same conclusion (Bernini-Peron et al., 2024; Verhamme et al., 2024, 2025). Therefore, we recommend using the Krtička et al. (2024) parametrisation of mass loss in evolutionary model calculations during the main-sequence and immediate post-

main-sequence phases.

- We do not find any sign of the theorised bi-stability jump, including the dramatic increase in mass loss and the decrease in the ratio $v_\infty/v_{\rm esc}$ at $T_{\rm eff}$ = 25-21 kK. However, this outcome does not entail the complete dismissal of the idea of a bi-stability jump, as the effects of the bi-stability jump could be masked by clumping and other wind-structure related phenomena, which are poorly parametrised in current radiative transfer models. One way to approach solving this mystery would be targeted studies that analyse the mass-loss properties of LBVs at different phases of their S Dor excursions. There have been a small number of this type of investigation (mainly AG Car and R127), all of which have reported modulations in the mass-loss rates of the LBVs (see e.g., Groh et al., 2009, 2011; Groh & Vink, 2011).

6.6 Future Work

A natural follow-up to this thesis work would be to extend the analysis to include additional OB supergiants in the MW and MCs, thereby increasing statistical significance and yielding tighter constraints on the mass-loss rate recipe. However, given the impressively large HST observing time dedicated to high-mass stars in ULLYSES (500 orbits, Vink et al., 2023), green-lighting a new project on a similar scale to ULLYSES to obtain UV spectroscopy of OB stars in the MCs does not seem likely. Therefore, this objective may be more attainable after the commissioning of future UV-capable missions. Furthermore, the analysis could be extended to samples in other metallicity regimes. An example of this is the irregular dwarf galaxy Sextans A, which is home to a significant number of extremely metal-poor OB supergiants ($Z < 1/10\ Z_\odot$, Lorenzo et al., 2022, 2025). It is also possible to expand the analysis to envelop environments with super-solar metallicities, such as M31, which has an overall metallicity of $Z = 1.5\ Z_\odot$ (Sanders et al.,

2012) and large populations of luminous blue stars (Humphreys et al., 1990).

The analysis can also be extended to a broader spectral range, particularly to O supergiants earlier than O9 and to A supergiants earlier than A3. On the one hand, applying our methods to O supergiants would be straightforward. However, nLTE radiative transfer models begin to break down at temperatures below 10 kK. Therefore, historically speaking, stars below that temperature threshold have been modelled using plane-parallel nLTE RT codes that do not include winds, such as the model atmosphere code TLUSTY (Hubeny & Lanz, 1995). However, recent updates to CMFGEN have enabled convergence of models at temperatures as low as 8 kK (priv. com. with Francisco Najarro).

The biggest logistical challenge facing these projects is the availability of suitable data. Luckily, suitable optical spectroscopy will be available from upcoming spectroscopic surveys, such as the 4MOST Milky Way Disc and Bulge High-Resolution Survey (4MIDABLE-HR, Bensby et al., 2019) and the 4MOST One Thousand and One Magellanic Fields (1001MC, Cioni et al., 2019), which will provide a complete sample of BSGs in the MW and MCs. Additionally, the soon-to-be-commissioned Extremely Large Telescope (ELT, Gilmozzi & Spyromilio, 2007), with its 39-meter mirror, will provide the necessary observational sensitivity to obtain data at unprecedented depth. The first-light instruments are MICADO and HARMONI. MICADO is a diffraction-limited near-infrared imager in the wavelength range 0.8-2.45 μm. HARMONI is a single-field near-infrared wide-band integral field spectrograph that will operate in the wavelength range 0.45-2.45 μm. These instruments will provide low- to medium-resolution ($R \approx$ 3200-20000) spectroscopy. The combination of the extremely high spatial resolution and the near-infrared wavelength range of MICADO and HARMONI provides a unique capability to pierce the dense dust that enshrouds massive star-forming regions, enabling studies of the formation histories of massive stars in heavily obscured environments, such as the Galactic centre. Furthermore, the ELT will break the confusion limit in dense clusters,

such as R136 in the LMC, thereby resolving previously unresolved individual massive stars. Additionally, the wavelength range covered by HARMONI, which includes Hα, would allow the investigation of wind properties of massive stars.

On the UV front, the situation appears somewhat less favourable in the near term. As the HST draws near the end of its life, the UV window is closing rapidly. There have been recent efforts at collecting UV spectroscopy of massive stars using HST instruments, such as the Treasury of Extremely Metal-Poor O Stars (TEMPOS, Telford et al., 2023). Although these efforts are commendable and very helpful to the massive star community, the sample sizes remain quite modest, especially compared to ULLYSES. The solution to this will be provided by future missions. In the early 2030s, the Ultraviolet Explorer (UVEX, Kulkarni et al., 2021) will provide FUV and NUV, space-based spectroscopy, albeit at low resolution ($R \approx$ 1000-3500). On a longer timescale, sometime in the 2040s, the Habitable Worlds Observatory (HWO), NASA's next flagship mission, will provide UV spectroscopy at high spatial resolution at distances not yet explored (Senchyna et al., 2025), mainly due to its large mirror array, which is comparable to that of the James Webb Space Telescope.

Bibliography

Abbott D. C., 1982, ApJ, 259, 282

Abbott B. P., et al., 2016, Phys. Rev. Lett., 116, 061102

Abbott B. P., et al., 2017, Phys. Rev. Lett., 119, 161101

Abbott R., et al., 2023, Physical Review X, 13, 011048

Abel T., Bryan G. L., Norman M. L., 2002, Science, 295, 93

Alkousa T., et al., 2025, A&A, 699, A314

Alkousa T., et al., 2026a, A&A, 707, C1

Alkousa T., et al., 2026b, A&A, 707, A253

Alves D. R., 2004, New Astron. Rev., 48, 659

Anderson L. S., 1985, ApJ, 298, 848

Anderson L. S., 1989, ApJ, 339, 558

Andrievsky S. M., Kovtyukh V. V., Korotin S. A., Spite M., Spite F., 2001, A&A, 367, 605

Ardeberg A., 1980, A&AS, 42, 1

Ardeberg A., Maurice E., 1977, A&AS, 30, 261

Ardeberg A., Brunet J. P., Maurice E., Prevot L., 1972, A&AS, 6, 249

Asplund M., Grevesse N., Sauval A. J., 2005, in Barnes III T. G., Bash F. N., eds, Astronomical Society of the Pacific Conference Series Vol. 336, Cosmic Abundances as Records of Stellar Evolution and Nucleosynthesis. p. 25

Azzopardi M., Vigneau J., Macquet M., 1975, A&AS, 22, 285

Backs F., et al., 2024, A&A, 692, A88

Bagnulo S., Jehin E., Ledoux C., Cabanac R., Melo C., Gilmozzi R., ESO Paranal Science Operations Team 2003, The Messenger, 114, 10

Bailer-Jones C. A. L., 2023, AJ, 166, 269

Bailer-Jones C. A. L., Rybizki J., Fouesneau M., Demleitner M., Andrae R., 2021, AJ, 161, 147

Barkana R., Loeb A., 2001, Phys. Rep., 349, 125

Barlow M. J., Cohen M., 1977, ApJ, 213, 737

Baron E., Cooperstein J., Kahana S., 1985, Phys. Rev. Lett., 55, 126

Baum E., Hamann W. R., Koesterke L., Wessolowski U., 1992, A&A, 266, 402

Beckman J. E., Crivellari L., 1985, Science, 230, 835

Belczynski K., Bulik T., Fryer C. L., Ruiter A., Valsecchi F., Vink J. S., Hurley J. R., 2010, ApJ, 714, 1217

Benaglia P., Vink J. S., Martí J., Maíz Apellániz J., Koribalski B., Crowther P. A., 2007, A&A, 467, 1265

Bensby T., et al., 2019, The Messenger, 175, 35

Bernini-Peron M., et al., 2023, A&A, 677, A50

Bernini-Peron M., et al., 2024, A&A, 692, A89

Bestenlehner J. M., et al., 2014, A&A, 570, A38

Bestenlehner J. M., Enßlin T., Bergemann M., Crowther P. A., Greiner M., Selig M., 2024, MNRAS, 528, 6735

Bestenlehner J. M., et al., 2025, A&A, 695, A198

Bethe H. A., 1939, Phys. Rev., 55, 434

Bethe H. A., 1990, Reviews of Modern Physics, 62, 801

Bethe H. A., Wilson J. R., 1985, ApJ, 295, 14

Björklund R., Sundqvist J. O., Puls J., Najarro F., 2021, A&A, 648, A36

Björklund R., Sundqvist J. O., Singh S. M., Puls J., Najarro F., 2023, A&A, 676, A109

Bodensteiner J., et al., 2025, A&A, 698, A38

Boggess A., et al., 1978, Nature, 275, 372

Böhm-Vitense E., 1958, Z. Astrophys., 46, 108

Bondi H., Hoyle F., 1944, MNRAS, 104, 273

Brands S. A., et al., 2022, A&A, 663, A36

Brands S. A., et al., 2025, A&A, 697, A54

Britavskiy N., et al., 2025, A&A, 698, A40

Brott I., et al., 2011, A&A, 530, A115

Bunker A. J., et al., 2023, A&A, 677, A88

Burnichon M. L., Garnier R., 1976, A&AS, 24, 89

Cameron A. J., et al., 2023, A&A, 677, A115

Cardelli J. A., Clayton G. C., Mathis J. S., 1989, ApJ, 345, 245

Cassinelli J. P., Olson G. L., 1979, ApJ, 229, 304

Castor J. I., Lamers H. J. G. L. M., 1979, ApJS, 39, 481

Castor J. I., Abbott D. C., Klein R. I., 1975a, ApJ, 195, 157

Castor J., McCray R., Weaver R., 1975b, ApJ, 200, L107

Cherepashchuk A. M., 1976, Soviet Astronomy Letters, 2, 138

Chon S., Omukai K., Schneider R., 2021, MNRAS, 508, 4175

Cioni M. R., et al., 2011, The Messenger, 144, 25

Cioni M. . R. L., et al., 2019, The Messenger, 175, 54

Claeys J. S. W., de Mink S. E., Pols O. R., Eldridge J. J., Baes M., 2011, A&A, 528, A131

Conti P. S., 1975, Memoires of the Societe Royale des Sciences de Liege, 9, 193

Cranmer S. R., Owocki S. P., 1996, ApJ, 462, 469

Crowther P. A., 2007, ARA&A, 45, 177

Crowther P. A., 2024, in Mackey J., Vink J. S., St-Louis N., eds, IAU Symposium Vol. 361, IAU Symposium. pp 15–25, doi:10.1017/S1743921322002435

Crowther P. A., Hillier D. J., Evans C. J., Fullerton A. W., De Marco O., Willis A. J., 2002, ApJ, 579, 774

Crowther P. A., Lennon D. J., Walborn N. R., 2006, A&A, 446, 279

Crowther P. A., Schnurr O., Hirschi R., Yusof N., Parker R. J., Goodwin S. P., Kassim H. A., 2010, MNRAS, 408, 731

Cullen F., et al., 2025, MNRAS, 540, 2176

Cutri R. M., et al., 2003, VizieR Online Data Catalog: 2MASS All-Sky Catalog of Point Sources (Cutri+ 2003), VizieR On-line Data Catalog: II/246. Originally published in: University of Massachusetts and Infrared Processing and Analysis Center, (IPAC/California Institute of Technology) (2003)

Cutri R. M., et al., 2012, VizieR Online Data Catalog: 2MASS 6X Point Source Working Database / Catalog (Cutri+ 2006), VizieR On-line Data Catalog: II/281. Originally published in: 2012yCat.2281....0C

Danforth C. W., Howk J. C., Fullerton A. W., Blair W. P., Sembach K. R., 2002, ApJS, 139, 81

Davies B., Crowther P. A., Beasor E. R., 2018, MNRAS, 478, 3138

Debnath D., Sundqvist J. O., Moens N., Van der Sijpt C., Verhamme O., Poniatowski L. G., 2024, A&A, 684, A177

Dekker H., D'Odorico S., Kaufer A., Delabre B., Kotzlowski H., 2000, in Iye M., Moorwood A. F., eds, Society of Photo-Optical Instrumentation Engineers (SPIE) Conference Series Vol. 4008, Optical and IR Telescope Instrumentation and Detectors. pp 534–545, doi:10.1117/12.395512

Dessart L., Hillier D. J., 2010, MNRAS, 405, 2141

Dopita M. A., Seitenzahl I. R., Sutherland R. S., Nicholls D. C., Vogt F. P. A., Ghavamian P., Ruiter A. J., 2019, AJ, 157, 50

Ducati J. R., 2002, VizieR Online Data Catalog: Stellar Photometry in Johnson's 11-color system (Ducati, 2002), VizieR On-line Data Catalog: II/237. Originally published in: Departement of Astronomy, University of Wisconsin, Madison WI 53706 (2002)

Dufton P. L., Ryans R. S. I., Simón-Díaz S., Trundle C., Lennon D. J., 2006, A&A, 451, 603

Dufton P. L., et al., 2018, A&A, 615, A101

Eddington A. S., 1925, The Observatory, 48, 73

Eggenberger P., Meynet G., Maeder A., Hirschi R., Charbonnel C., Talon S., Ekström S., 2008, Ap&SS, 316, 43

Eggleton P. P., 1971, MNRAS, 151, 351

Ekström S., et al., 2012, A&A, 537, A146

Eldridge J. J., Tout C. A., 2004, MNRAS, 353, 87

Eldridge J. J., Izzard R. G., Tout C. A., 2008, MNRAS, 384, 1109

Evans C. J., Howarth I. D., 2003, MNRAS, 345, 1223

Evans C. J., Crowther P. A., Fullerton A. W., Hillier D. J., 2004, ApJ, 610, 1021

Evans C. J., Lennon D. J., Smartt S. J., Trundle C., 2006, A&A, 456, 623

Feldmeier A., 1995, A&A, 299, 523

Fernie J. D., 1983, ApJS, 52, 7

Fitzpatrick E. L., 1985, ApJ, 299, 219

Fitzpatrick E. L., Massa D., 1990, ApJS, 72, 163

Fitzpatrick E. L., Massa D., Gordon K. D., Bohlin R., Clayton G. C., 2019, ApJ, 886, 108

Fouesneau M., 2025, pyphot, doi:10.5281/zenodo.14712174, https://doi.org/10.5281/zenodo.14712174

Frankel N., Rix H.-W., Ting Y.-S., Ness M., Hogg D. W., 2018, ApJ, 865, 96

Friend D. B., Abbott D. C., 1986, ApJ, 311, 701

Fullerton A. W., Massa D. L., Prinja R. K., 2006, ApJ, 637, 1025

GRAVITY Collaboration et al., 2019, A&A, 625, L10

Garnett D. R., 1999, in Chu Y. H., Suntzeff N., Hesser J., Bohlender D., eds, IAU Symposium Vol. 190, New Views of the Magellanic Clouds. p. 266

Garnett D. R., Kennicutt Jr. R. C., Chu Y.-H., Skillman E. D., 1991, ApJ, 373, 458

Gilmozzi R., Spyromilio J., 2007, The Messenger, 127, 11

Gordon K. D., Clayton G. C., Misselt K. A., Landolt A. U., Wolff M. J., 2003, ApJ, 594, 279

Gordon K. D., et al., 2024, ApJ, 970, 51

Götberg Y., de Mink S. E., Groh J. H., 2017, A&A, 608, A11

Götberg Y., de Mink S. E., Groh J. H., Kupfer T., Crowther P. A., Zapartas E., Renzo M., 2018, A&A, 615, A78

Gräfener G., Vink J. S., 2013, A&A, 560, A6

Gräfener G., Koesterke L., Hamann W. R., 2002a, A&A, 387, 244

Gräfener G., Koesterke L., Hamann W. R., 2002b, A&A, 387, 244

Green J. C., et al., 2012, ApJ, 744, 60

Grimm H.-J., Gilfanov M., Sunyaev R., 2003, MNRAS, 339, 793

Groh J. H., Vink J. S., 2011, A&A, 531, L10

Groh J. H., Hillier D. J., Damineli A., Whitelock P. A., Marang F., Rossi C., 2009, ApJ, 698, 1698

Groh J. H., Hillier D. J., Damineli A., 2011, ApJ, 736, 46

Gvaramadze V. V., Kniazev A. Y., Maryeva O. V., Berdnikov L. N., 2018, MNRAS, 474, 1412

Haiman Z., Loeb A., 1997, ApJ, 483, 21

Hainich R., Pasemann D., Todt H., Shenar T., Sander A., Hamann W. R., 2015, A&A, 581, A21

Hamann W. R., Gräfener G., 2003a, A&A, 410, 993

Hamann W. R., Gräfener G., 2003b, A&A, 410, 993

Hamann W.-R., Koesterke L., 1998, A&A, 335, 1003

Hamann W.-R., Koesterke L., Wessolowski U., 1995, A&A, 299, 151

Haucke M., Cidale L. S., Venero R. O. J., Curé M., Kraus M., Kanaan S., Arcos C., 2018, A&A, 614, A91

Hawcroft C., et al., 2024a, A&A, 688, A105

Hawcroft C., et al., 2024b, A&A, 690, A126

Heger A., Fryer C. L., Woosley S. E., Langer N., Hartmann D. H., 2003, ApJ, 591, 288

Herrero A., Kudritzki R. P., Vilchez J. M., Kunze D., Butler K., Haser S., 1992, A&A, 261, 209

Hill V., 1997, A&A, 324, 435

Hill V., 1999, A&A, 345, 430

Hill V., Andrievsky S., Spite M., 1995, A&A, 293, 347

Hill V., Barbuy B., Spite M., 1997, A&A, 323, 461

Hillier D. J., 1984, ApJ, 280, 744

Hillier D. J., 1990, A&A, 231, 116

Hillier D. J., 1991, A&A, 247, 455

Hillier D. J., 1996, in Vreux J. M., Detal A., Fraipont-Caro D., Gosset E., Rauw G., eds, Liege International Astrophysical Colloquia Vol. 33, Liege International Astrophysical Colloquia. p. 509

Hillier D. J., 1997, in Bedding T. R., Booth A. J., Davis J., eds, IAU Symposium Vol. 189, IAU Symposium. pp 209–216

Hillier D. J., Miller D. L., 1998, ApJ, 496, 407

Hillier D. J., Miller D. L., 1999, ApJ, 519, 354

Hillier D. J., Lanz T., Heap S. R., Hubeny I., Smith L. J., Evans C. J., Lennon D. J., Bouret J. C., 2003, ApJ, 588, 1039

Hiltner W. A., 1956, ApJS, 2, 389

Hirschi R., Meynet G., Maeder A., 2005, A&A, 433, 1013

Hirschi R., et al., 2025, MNRAS, 543, 2796

Höfner S., Olofsson H., 2018, A&ARv, 26, 1

Høg E., et al., 2000, A&A, 355, L27

Holgado G., et al., 2018, A&A, 613, A65

Holgado G., Simón-Díaz S., Herrero A., Barbá R. H., 2022, A&A, 665, A150

Hopkins P. F., Kereš D., Oñorbe J., Faucher-Giguère C.-A., Quataert E., Murray N., Bullock J. S., 2014, MNRAS, 445, 581

Howarth I. D., Prinja R. K., 1989, ApJS, 69, 527

Howarth I. D., Siebert K. W., Hussain G. A. J., Prinja R. K., 1997, MNRAS, 284, 265

Hubeny I., Lanz T., 1995, ApJ, 439, 875

Huenemoerder D. P., Oskinova L. M., Ignace R., Waldron W. L., Todt H., Hamaguchi K., Kitamoto S., 2012, ApJ, 756, L34

Humphreys R. M., Davidson K., 1979a, ApJ, 232, 409

Humphreys R. M., Davidson K., 1979b, ApJ, 232, 409

Humphreys R. M., Davidson K., 1994, PASP, 106, 1025

Humphreys R. M., Massey P., Freedman W. L., 1990, AJ, 99, 84

Hunter I., et al., 2007, A&A, 466, 277

Hunter I., Lennon D. J., Dufton P. L., Trundle C., Simón-Díaz S., Smartt S. J., Ryans R. S. I., Evans C. J., 2008a, A&A, 479, 541

Hunter I., et al., 2008b, ApJ, 676, L29

Hunter I., et al., 2009, A&A, 496, 841

Ismailov N. Z., Ismayilova S. K., 2021, MNRAS, 502, 157

Isserstedt J., 1975, A&AS, 19, 259

Ivanova N., et al., 2013, A&ARv, 21, 59

Janka H.-T., 2012, Annual Review of Nuclear and Particle Science, 62, 407

Jiang Y.-F., Cantiello M., Bildsten L., Quataert E., Blaes O., Stone J., 2018, Nature, 561, 498

Johnson H. L., Mitchell R. I., Iriarte B., Wisniewski W. Z., 1966, Communications of the Lunar and Planetary Laboratory, 4, 99

Justham S., Podsiadlowski P., Vink J. S., 2014, ApJ, 796, 121

Kalari V. M., Horch E. P., Salinas R., Vink J. S., Andersen M., Bestenlehner J. M., Rubio M., 2022, ApJ, 935, 162

Kaper L., Henrichs H. F., Nichols J. S., Snoek L. C., Volten H., Zwarthoed G. A. A., 1996, A&AS, 116, 257

Kato S., 1966, PASJ, 18, 374

Kaufer A., Stahl O., Tubbesing S., Nørregaard P., Avila G., Francois P., Pasquini L., Pizzella A., 1999, The Messenger, 95, 8

Kennicutt Jr. R. C., 1998, ARA&A, 36, 189

Kiminki D. C., Kobulnicky H. A., 2012, ApJ, 751, 4

Kippenhahn R., Weigert A., 1990, Stellar Structure and Evolution

Klein R. I., Castor J. I., 1978, ApJ, 220, 902

Klencki J., Istrate A., Nelemans G., Pols O., 2022, A&A, 662, A56

Köhler K., et al., 2015, A&A, 573, A71

Korn A. J., Nieva M. F., Daflon S., Cunha K., 2005, ApJ, 633, 899

Krtička J., Kubát J., 2017, A&A, 606, A31

Krtička J., Kubát J., 2018, A&A, 612, A20

Krtička J., Kubát J., Krtičková I., 2021, A&A, 647, A28

Krtička J., Kubát J., Krtičková I., 2024, A&A, 681, A29

Kubat J., 1996, in Adelman S. J., Kupka F., Weiss W. W., eds, Astronomical Society of the Pacific Conference Series Vol. 108, M.A.S.S., Model Atmospheres and Spectrum Synthesis. pp 165–169

Kubát J., 1999, New Astron., 4, 157

Kudritzki R.-P., Puls J., 2000, ARA&A, 38, 613

Kudritzki R. P., Pauldrach A., Puls J., 1987, A&A, 173, 293

Kudritzki R. P., Pauldrach A., Puls J., Abbott D. C., 1989, A&A, 219, 205

Kudritzki R. P., Lennon D. J., Puls J., 1995, in Walsh J. R., Danziger I. J., eds, Science with the VLT. p. 246

Kudritzki R. P., Puls J., Lennon D. J., Venn K. A., Reetz J., Najarro F., McCarthy J. K., Herrero A., 1999, A&A, 350, 970

Kudritzki R. P., Bresolin F., Przybilla N., 2003, ApJ, 582, L83

Kudritzki R.-P., Urbaneja M. A., Bresolin F., Przybilla N., Gieren W., Pietrzyński G., 2008, ApJ, 681, 269

Kudritzki R.-P., Urbaneja M. A., Gazak Z., Macri L., Hosek Jr. M. W., Bresolin F., Przybilla N., 2013, ApJ, 779, L20

Kudritzki R.-P., Urbaneja M. A., Bresolin F., Macri L. M., Yuan W., Li S., Anand G. S., Riess A. G., 2024, ApJ, 977, 217

Kulkarni S. R., et al., 2021, arXiv e-prints, p. arXiv:2111.15608

Kurt C. M., Dufour R. J., 1998, in Dufour R. J., Torres-Peimbert S., eds, Revista Mexicana de Astronomia y Astrofisica Conference Series Vol. 7, Revista Mexicana de Astronomia y Astrofisica Conference Series. p. 202

Lamers H. J. G. L. M., Gathier R., Snow Jr. T. P., 1982, ApJ, 258, 186

Lamers H. J. G. L. M., Cerruti-Sola M., Perinotto M., 1987, ApJ, 314, 726

Lamers H. J. G. L. M., Snow T. P., Lindholm D. M., 1995, ApJ, 455, 269

Langer N., 1998, A&A, 329, 551

Langer N., Kudritzki R. P., 2014, A&A, 564, A52

Langer N., Fricke K. J., Sugimoto D., 1983, A&A, 126, 207

Langer N., El Eid M. F., Fricke K. J., 1985, A&A, 145, 179

Lanz T., Hubeny I., 2007a, ApJS, 169, 83

Lanz T., Hubeny I., 2007b, ApJS, 169, 83

Laplace E., 2022, Astronomy and Computing, 38, 100516

Laplace E., Götberg Y., de Mink S. E., Justham S., Farmer R., 2020, A&A, 637, A6

Lasker B. M., et al., 2008, AJ, 136, 735

Law D. R., Hawcroft C., Smith L. J., Fullerton A. W., Evans C. J., Gordon K. D., Kumari N., Leitherer C., 2024, ApJ, 976, L25

Lebouteiller V., Bernard-Salas J., Brandl B., Whelan D. G., Wu Y., Charmandaris V., Devost D., Houck J. R., 2008, ApJ, 680, 398

Ledoux P., 1947, ApJ, 105, 305

Lefever K., Puls J., Aerts C., 2007, A&A, 463, 1093

Leitherer C., Robert C., Drissen L., 1992, ApJ, 401, 596

Leitherer C., Leão J. R. S., Heckman T. M., Lennon D. J., Pettini M., Robert C., 2001, ApJ, 550, 724

Lennon D. J., 1997, A&A, 317, 871

Levesque E. M., 2017, Astrophysics of Red Supergiants, doi:10.1088/978-0-7503-1329-2.

Limongi M., Chieffi A., 2018, ApJS, 237, 13

Lindegren L., et al., 2018, A&A, 616, A2

Lorenzo M., Garcia M., Najarro F., Herrero A., Cerviño M., Castro N., 2022, MNRAS, 516, 4164

Lorenzo M., Garcia M., Castro N., Najarro F., Cerviño M., Herrero A., Simón-Díaz S., 2025, MNRAS, 537, 1197

Lucy L. B., 1983, ApJ, 274, 372

Lucy L. B., Solomon P. M., 1970a, ApJ, 159, 879

Lucy L. B., Solomon P. M., 1970b, ApJ, 159, 879

Macfarlane J. J., Waldron W. L., Corcoran M. F., Wolff M. J., Wang P., Cassinelli J. P., 1993, ApJ, 419, 813

Maeder A., 1992, A&A, 264, 105

Maeder A., 2002, A&A, 392, 575

Maeder A., Meynet G., 2000, ARA&A, 38, 143

Maeder A., Przybilla N., Nieva M.-F., Georgy C., Meynet G., Ekström S., Eggenberger P., 2014, A&A, 565, A39

Maggi P., et al., 2019, A&A, 631, A127

Marchant P., Langer N., Podsiadlowski P., Tauris T. M., Moriya T. J., 2016, A&A, 588, A50

Marcolino W. L. F., Bouret J. C., Martins F., Hillier D. J., Lanz T., Escolano C., 2009, A&A, 498, 837

Marcolino W. L. F., Bouret J. C., Rocha-Pinto H. J., Bernini-Peron M., Vink J. S., 2022, MNRAS, 511, 5104

Markova N., Puls J., Scuderi S., Markov H., 2005, A&A, 440, 1133

Martínez-Núñez S., et al., 2017, Space Sci. Rev., 212, 59

Martins F., 2011, Bulletin de la Societe Royale des Sciences de Liege, 80, 29

Martins F., Schaerer D., Hillier D. J., 2005a, A&A, 436, 1049

Martins F., Schaerer D., Hillier D. J., Meynadier F., Heydari-Malayeri M., Walborn N. R., 2005b, A&A, 441, 735

Martins F., Mahy L., Hillier D. J., Rauw G., 2012, A&A, 538, A39

Martins F., et al., 2024, A&A, 689, A31

Massa D., Fullerton A. W., Sonneborn G., Hutchings J. B., 2003, ApJ, 586, 996

Massa D., Prinja R. K., Oskinova L. M., 2024, ApJ, 971, 166

Massey P., 2002, ApJS, 141, 81

Massey P., Neugent K. F., Hillier D. J., Puls J., 2013, ApJ, 768, 6

Mateo M., Harris H. C., Nemec J., Olszewski E. W., 1990, AJ, 100, 469

McErlean N. D., Lennon D. J., Dufton P. L., 1998, A&A, 329, 613

McErlean N. D., Lennon D. J., Dufton P. L., 1999, A&A, 349, 553

McEvoy C. M., et al., 2015, A&A, 575, A70

Menon A., Heger A., 2017, MNRAS, 469, 4649

Menon A., et al., 2024, ApJ, 963, L42

Mihalas D., Kunasz P. B., 1978, ApJ, 219, 635

Mihalas D., Kunasz P. B., Hummer D. G., 1975, ApJ, 202, 465

Mihalas D., Kunasz P. B., Hummer D. G., 1976a, ApJ, 203, 647

Mihalas D., Kunasz P. B., Hummer D. G., 1976b, ApJ, 206, 515

Mihalas D., Kunasz P. B., Hummer D. G., 1976c, ApJ, 210, 419

Milne E. A., 1926, MNRAS, 86, 459

Mineo S., Gilfanov M., Sunyaev R., 2012, MNRAS, 419, 2095

Minkowski R., 1941, PASP, 53, 224

Mirabel I. F., Dijkstra M., Laurent P., Loeb A., Pritchard J. R., 2011, A&A, 528, A149

Moens N., Poniatowski L. G., Hennicker L., Sundqvist J. O., El Mellah I., Kee N. D., 2022, A&A, 665, A42

Moens N., Debnath D., Verhamme O., Backs F., Van der Sijpt C., Sundqvist J. O., Sander A. A. C., 2025, A&A, 704, A121

Mokiem M. R., et al., 2006, A&A, 456, 1131

Mokiem M. R., et al., 2007, A&A, 473, 603

Moos H. W., et al., 2000, ApJ, 538, L1

Morgan W. W., Keenan P. C., Kellman E., 1943, An atlas of stellar spectra, with an outline of spectral classification

Morton D. C., 1967, ApJ, 147, 1017

Morton J., Guillet T., Baraffe I., Morison A., Le Saux A., Vlaykov D. G., Goffrey T., Pratt J., 2025, MNRAS, 537, 154

Muijres L. E., de Koter A., Vink J. S., Krtička J., Kubát J., Langer N., 2011, A&A, 526, A32

Muijres L. E., Vink J. S., de Koter A., Müller P. E., Langer N., 2012, A&A, 537, A37

Müller P. E., Vink J. S., 2008, A&A, 492, 493

Negueruela I., Simón-Díaz S., de Burgos A., Casasbuenas A., Beck P. G., 2024, A&A, 690, A176

Nieuwenhuijzen H., de Jager C., 1990, A&A, 231, 134

Nieva M. F., 2013, A&A, 550, A26

Nishimura N., Hirschi R., Rauscher T., St. J. Murphy A., Cescutti G., 2017, MNRAS, 469, 1752

Noble L. M., Scarf F. L., 1963, ApJ, 138, 1169

O'Connor E., Ott C. D., 2011, ApJ, 730, 70

Odert P., Leitzinger M., Hanslmeier A., Lammer H., 2017, MNRAS, 472, 876

Oskinova L. M., Hamann W.-R., Feldmeier A., 2007, A&A, 476, 1331

Owocki S. P., 2008, in Hamann W.-R., Feldmeier A., Oskinova L. M., eds, Clumping in Hot-Star Winds. p. 121

Owocki S. P., Cohen D. H., 2006, ApJ, 648, 565

Owocki S. P., Castor J. I., Rybicki G. B., 1988, ApJ, 335, 914

Owocki S. P., Gayley K. G., Shaviv N. J., 2004, ApJ, 616, 525

Owocki S. P., Shultz M. E., ud-Doula A., Chandra P., Das B., Leto P., 2022, MNRAS, 513, 1449

Packet W., 1981, A&A, 102, 17

Paczyński B., 1971, ARA&A, 9, 183

Paczynski B., 1976, in Eggleton P., Mitton S., Whelan J., eds, IAU Symposium Vol. 73, Structure and Evolution of Close Binary Systems. p. 75

Panagia N., Felli M., 1975, A&A, 39, 1

Parker E. N., 1958, ApJ, 128, 664

Pauldrach A. W. A., Puls J., 1990, A&A, 237, 409

Pauldrach A. W. A., Kudritzki R. P., Puls J., Butler K., Hunsinger J., 1994, A&A, 283, 525

Pauli D., et al., 2025, A&A, 697, A114

Pauli D., et al., 2026, A&A, 707, A11

Paxton B., Bildsten L., Dotter A., Herwig F., Lesaffre P., Timmes F., 2011, ApJS, 192, 3

Peimbert A., 2003, ApJ, 584, 735

Petrov B., Vink J. S., Gräfener G., 2016, MNRAS, 458, 1999

Podsiadlowski P., Joss P. C., Hsu J. J. L., 1992, ApJ, 391, 246

Pols O. R., Tout C. A., Eggleton P. P., Han Z., 1995, MNRAS, 274, 964

Postnov K. A., Yungelson L. R., 2006, Living Reviews in Relativity, 9, 6

Priest E. R., Forbes T. G., 2002, A&ARv, 10, 313

Prinja R. K., 1988, MNRAS, 231, 21P

Prinja R. K., Crowther P. A., 1998a, MNRAS, 300, 828

Prinja R. K., Crowther P. A., 1998b, MNRAS, 300, 828

Prinja R. K., Barlow M. J., Howarth I. D., 1990, ApJ, 361, 607

Prinja R. K., Massa D., Fullerton A. W., 2002, A&A, 388, 587

Prinja R. K., Massa D., Searle S. C., 2005, A&A, 430, L41

Przybilla N., Butler K., Becker S. R., Kudritzki R. P., 2006, A&A, 445, 1099

Przybilla N., Nieva M.-F., Butler K., 2008, ApJ, 688, L103

Puebla R. E., Hillier D. J., Zsargó J., Cohen D. H., Leutenegger M. A., 2016, MNRAS, 456, 2907

Puls J., Owocki S. P., Fullerton A. W., 1993, A&A, 279, 457

Puls J., et al., 1996, A&A, 305, 171

Puls J., Urbaneja M. A., Venero R., Repolust T., Springmann U., Jokuthy A., Mokiem M. R., 2005, A&A, 435, 669

Puls J., Markova N., Scuderi S., Stanghellini C., Taranova O. G., Burnley A. W., Howarth I. D., 2006, A&A, 454, 625

Puls J., Vink J. S., Najarro F., 2008, A&ARv, 16, 209

Ramachandran V., Hamann W. R., Hainich R., Oskinova L. M., Shenar T., Sander A. A. C., Todt H., Gallagher J. S., 2018, A&A, 615, A40

Ramachandran V., et al., 2019, A&A, 625, A104

Ramachandran V., et al., 2024, A&A, 692, A90

Ramírez-Agudelo O. H., et al., 2013, A&A, 560, A29

Raskin G., et al., 2011, A&A, 526, A69

Reed B. C., 2003, AJ, 125, 2531

Renzo M., Ott C. D., Shore S. N., de Mink S. E., 2017, A&A, 603, A118

Repolust T., Puls J., Hanson M. M., Kudritzki R. P., Mokiem M. R., 2005, A&A, 440, 261

Rivero González J. G., Puls J., Najarro F., 2011, A&A, 536, A58

Roman-Duval J., et al., 2025, ApJ, 985, 109

Romano D., Karakas A. I., Tosi M., Matteucci F., 2010, A&A, 522, A32

Royer P., et al., 2024, A&A, 681, A107

Rubio-Díez M. M., Sundqvist J. O., Najarro F., Traficante A., Puls J., Calzoletti L., Figer D., 2022, A&A, 658, A61

Russell S. C., Dopita M. A., 1990, ApJS, 74, 93

Sana H., Gosset E., Nazé Y., Rauw G., Linder N., 2008, MNRAS, 386, 447

Sana H., et al., 2012, Science, 337, 444

Sana H., et al., 2024, A&A, 688, A104

Sana H., et al., 2025, Nature Astronomy, 9, 1337

Sánchez-Sanjuán S., Hernández J., Pérez-Villegas Á., Román-Zúñiga C., Aguilar L., Ballesteros-Paredes J., Bonilla-Barroso A., 2024, MNRAS, 534, 2566

Sander A. A. C., Vink J. S., 2020, MNRAS, 499, 873

Sander A., Shenar T., Hainich R., Gímenez-García A., Todt H., Hamann W. R., 2015, A&A, 577, A13

Sander A. A. C., et al., 2024, A&A, 689, A30

Sanders N. E., Caldwell N., McDowell J., Harding P., 2012, ApJ, 758, 133

Schild R. E., 1966, ApJ, 146, 142

Schmidt-Kaler T., Gochermann J., Oestreicher M. O., Grothues H. G., Tappert C., Zaum A., Berghöfer T., Brugger H. R., 1999, MNRAS, 306, 279

Schmutz W., 1997, A&A, 321, 268

Schmutz W., Hamann W. R., Wessolowski U., 1989, A&A, 210, 236

Schneider F. R. N., Langer N., de Koter A., Brott I., Izzard R. G., Lau H. H. B., 2014a, A&A, 570, A66

Schneider F. R. N., et al., 2014b, ApJ, 780, 117

Schneider F. R. N., Podsiadlowski P., Langer N., Castro N., Fossati L., 2016, MNRAS, 457, 2355

Schneider F. R. N., et al., 2018, A&A, 618, A73

Schootemeijer A., Langer N., 2018, A&A, 611, A75

Schootemeijer A., Langer N., Grin N. J., Wang C., 2019, A&A, 625, A132

Schootemeijer A., et al., 2024, A&A, 689, A157

Schwarzschild M., Härm R., 1958, ApJ, 128, 348

Scowcroft V., Freedman W. L., Madore B. F., Monson A., Persson S. E., Rich J., Seibert M., Rigby J. R., 2016, ApJ, 816, 49

Searle S. C., Prinja R. K., Massa D., Ryans R., 2008, A&A, 481, 777

Sedlmayr E., Dominik C., 1995, Space Sci. Rev., 73, 211

Senchyna P., Stark D. P., Mirocha J., Reines A. E., Charlot S., Jones T., Mulchaey J. S., 2020, MNRAS, 494, 941

Senchyna P., Hawcroft C., Garcia M., Wofford A., Lee J. C., Evans C., 2025, arXiv e-prints, p. arXiv:2511.03715

Shao Y., Li X.-D., 2019, ApJ, 885, 151

Shaviv G., Salpeter E. E., 1973, ApJ, 184, 191

Shenar T., Gilkis A., Vink J. S., Sana H., Sander A. A. C., 2020, A&A, 634, A79

Shenar T., et al., 2024, A&A, 690, A289

Simón-Díaz S., 2020, in , Reviews in Frontiers of Modern Astrophysics; From Space Debris to Cosmology. pp 155–187, doi:10.1007/978-3-030-38509-5_6

Simón-Díaz S., Herrero A., 2014a, A&A, 562, A135

Simón-Díaz S., Herrero A., 2014b, A&A, 562, A135

Simón-Díaz S., Garcia M., Herrero A., Maíz Apellániz J., Negueruela I., 2011a, in Stellar Clusters & Associations: A RIA Workshop on Gaia. pp 255–259 (arXiv:1109.2665), doi:10.48550/arXiv.1109.2665

Simón-Díaz S., Castro N., Garcia M., Herrero A., Markova N., 2011b, Bulletin de la Societe Royale des Sciences de Liege, 80, 514

Simón-Díaz S., Castro N., Herrero A., Puls J., Garcia M., Sabín-Sanjulián C., 2011c, in Journal of Physics Conference Series. IOP, p. 012021 (arXiv:1111.1341), doi:10.1088/1742-6596/328/1/012021

Simón-Díaz S., et al., 2015, in Cenarro A. J., Figueras F., Hernández-Monteagudo C., Trujillo Bueno J., Valdivielso L., eds, Highlights of Spanish Astrophysics VIII. pp 576–581 (arXiv:1504.04257), doi:10.48550/arXiv.1504.04257

Skrutskie M. F., et al., 2006, AJ, 131, 1163

Smartt S. J., 2009, ARA&A, 47, 63

Smartt S. J., 2015, Publ. Astron. Soc. Australia, 32, e016

Smith N., 2014, ARA&A, 52, 487

Smith N., 2017, Philosophical Transactions of the Royal Society of London Series A, 375, 20160268

Smith R. K., Brickhouse N. S., Liedahl D. A., Raymond J. C., 2001, ApJ, 556, L91

Smith N., Vink J. S., de Koter A., 2004, ApJ, 615, 475

Smith N., Li W., Silverman J. M., Ganeshalingam M., Filippenko A. V., 2011, MNRAS, 415, 773

Sobolev V. V., 1960, Moving Envelopes of Stars, doi:10.4159/harvard.9780674864658.

Sota A., Maíz Apellániz J., Walborn N. R., Alfaro E. J., Barbá R. H., Morrell N. I., Gamen R. C., Arias J. I., 2011, ApJS, 193, 24

Stacy A., Bromm V., 2014, ApJ, 785, 73

Sternberg A., Hoffmann T. L., Pauldrach A. W. A., 2003, ApJ, 599, 1333

Stevens I. R., Blondin J. M., Pollock A. M. T., 1992, ApJ, 386, 265

Sundqvist J. O., Owocki S. P., 2013, MNRAS, 428, 1837

Sundqvist J. O., Puls J., Feldmeier A., 2010, A&A, 510, A11

Sundqvist J. O., Puls J., Owocki S. P., 2014, A&A, 568, A59

Sundqvist J. O., et al., 2025, A&A, 703, A284

Susa H., Hasegawa K., Tominaga N., 2014, ApJ, 792, 32

Sweet P. A., 1950, MNRAS, 110, 548

Telford G., et al., 2023, A Legacy Far-Ultraviolet Spectral Atlas of Extremely Metal-Poor O Stars, HST Proposal. Cycle 31, ID. #17491

Telting J. H., et al., 2014, Astronomische Nachrichten, 335, 41

Thornton K., Gaudlitz M., Janka H. T., Steinmetz M., 1998, ApJ, 500, 95

Tobin J., 1958, Econometrica, 26, 24

Toribio San Cipriano L., Domínguez-Guzmán G., Esteban C., García-Rojas J., Mesa-Delgado A., Bresolin F., Rodríguez M., Simón-Díaz S., 2017, MNRAS, 467, 3759

Trundle C., Lennon D. J., 2005a, A&A, 434, 677

Trundle C., Lennon D. J., 2005b, A&A, 434, 677

Trundle C., Lennon D. J., Puls J., Dufton P. L., 2004a, A&A, 417, 217

Trundle C., Lennon D. J., Puls J., Dufton P. L., 2004b, A&A, 417, 217

Trundle C., Dufton P. L., Hunter I., Evans C. J., Lennon D. J., Smartt S. J., Ryans R. S. I., 2007, The VLT-FLAMES survey of massive stars: evolution of surface N abundances and effective temperature scales in the Galaxy and Magellanic Clouds, Astronomy and Astrophysics, Volume 471, Issue 2, August IV 2007, pp.625-643 (arXiv:0706.1731), doi:10.1051/0004-6361:20077838

Tsamis Y. G., Barlow M. J., Liu X.-W., Danziger I. J., Storey P. J., 2003, MNRAS, 338, 687

Urbaneja M. A., et al., 2005, ApJ, 622, 862

Urbaneja M. A., Kudritzki R.-P., Bresolin F., Przybilla N., Gieren W., Pietrzyński G., 2008, ApJ, 684, 118

Urbaneja M. A., Kudritzki R. P., Gieren W., Pietrzyński G., Bresolin F., Przybilla N., 2017, AJ, 154, 102

Varghese A., Ratnasingam R. P., Vanon R., Edelmann P. V. F., Rogers T. M., 2023, ApJ, 942, 53

Vassiliadis E., Wood P. R., 1993, ApJ, 413, 641

Venn K. A., 1999, ApJ, 518, 405

Verhamme O., et al., 2024, A&A, 692, A91

Verhamme O., Sundqvist J., XShootU Collaboration 2025, A&A

Vernet J., et al., 2011, A&A, 536, A105

Villaseñor J. I., et al., 2025, A&A, 698, A41

Vink J. S., Sander A. A. C., 2021, MNRAS, 504, 2051

Vink J. S., de Koter A., Lamers H. J. G. L. M., 1999, A&A, 350, 181

Vink J. S., de Koter A., Lamers H. J. G. L. M., 2000, A&A, 362, 295

Vink J. S., de Koter A., Lamers H. J. G. L. M., 2001, A&A, 369, 574

Vink J. S., Muijres L. E., Anthonisse B., de Koter A., Gräfener G., Langer N., 2011, A&A, 531, A132

Vink J. S., et al., 2023, A&A, 675, A154

Vink J. S., Sabhahit G. N., Sander A. A. C., 2026, A&A, 711, L4

Vourlidas A., Howard R. A., Esfandiari E., Patsourakos S., Yashiro S., Michalek G., 2010, ApJ, 722, 1522

Walborn N. R., 1971, ApJS, 23, 257

Walborn N. R., Fitzpatrick E. L., 1990, PASP, 102, 379

Walborn N. R., Fitzpatrick E. L., 2000, PASP, 112, 50

Walborn N. R., Lennon D. J., Heap S. R., Lindler D. J., Smith L. J., Evans C. J., Parker J. W., 2000, PASP, 112, 1243

Walborn N. R., Fullerton A. W., Crowther P. A., Bianchi L., Hutchings J. B., Pellerin A., Sonneborn G., Willis A. J., 2002, ApJS, 141, 443

Walborn N. R., Gamen R. C., Morrell N. I., Barbá R. H., Fernández Lajús E., Angeloni R., 2017, AJ, 154, 15

Walter R., Zurita Heras J., 2007, A&A, 476, 335

Weaver R., McCray R., Castor J., Shapiro P., Moore R., 1977, ApJ, 218, 377

Weis K., Chu Y. H., Duschl W. J., Bomans D. J., 1997, A&A, 325, 1157

Willett E., et al., 2023, Monthly Notices of the Royal Astronomical Society, 526, 2141

Woodgate B. E., et al., 1998, PASP, 110, 1183

Woods T. E., Heger A., Whalen D. J., Haemmerlé L., Klessen R. S., 2017, ApJ, 842, L6

Woosley S., Janka T., 2005, Nature Physics, 1, 147

Woosley S. E., Weaver T. A., 1995, ApJS, 101, 181

Wright A. E., Barlow M. J., 1975, MNRAS, 170, 41

Yoon S.-C., Cantiello M., 2010, ApJ, 717, L62

Yoon S. C., Langer N., Norman C., 2006, A&A, 460, 199

Zahn J.-P., 1992, A&A, 265, 115

Zapartas E., et al., 2017, A&A, 601, A29

Zhang D., 2018, Galaxies, 6, 114

de Burgos A., Keszthelyi Z., Simón-Díaz S., Urbaneja M. A., 2024a, A&A, 687, L16

de Burgos A., Simón-Díaz S., Urbaneja M. A., Puls J., 2024b, A&A, 687, A228

de Mink S. E., Langer N., Izzard R. G., Sana H., de Koter A., 2013, ApJ, 764, 166

de Mink S. E., Sana H., Langer N., Izzard R. G., Schneider F. R. N., 2014, ApJ, 782, 7

van Leeuwen F., 2007, A&A, 474, 653

von Zeipel H., 1924, MNRAS, 84, 665

Appendix A

LMC appendix

A.1 Omitted objects

Sk −69° 83 For this star, we find a sign of binarity in He II λ4686, where it is blue shifted relative to all the other lines, indicating the existence of an emission from a primary hotter object combined with the emission of a cooler object. We also find signs of two components in He II λ5411 and Hγ

Sk −67° 197, Sk −66° 152, Sk −67° 168, Sk −70° 50 These objects were omitted from the analysis due to Hα and He II λ4686 having two symmetrical emission peaks with a narrow absorption feature in the line centre, which is indicative of a non-spherically symmetric geometry such as a circumstellar disk.

Sk −66° 50 The spectrum of this object showed clear binary signatures in the form of double-peaked absorption in Hβ, Hϵ and Hγ in addition to the odd morphology of Hα.

A.2 $v_{\rm black}$ and $v_{\rm edge}$

In Table A.1 we present the measured $v_{\rm edge}$ and $v_{\rm black}$ from each line for our entire sample. Single velocity measurements from each line are subject to an uncertainty $\Delta v = 30$ km s^{-1}, which takes into account the velocity resolution of the UV spectra and the uncertainty in the radial velocity correction, which were added in quadrature.

Table A.1: $v_{\rm black}$ for the stars in our sample.

	$v_{\rm edge}$							
Target	Si IV 1393Å	Si IV 1403Å	C IV 1548Å	Al III 1855Å	Al III 1863Å	Mg II 2769Å	Mg II 2903Å	$\overline{v_{\rm black}}/\overline{v_{\rm edge}}$
Sk −66° 171	2135	-	2119	-	-	-	-	0.83
Sk −68° 155	1860	-	1799	-	-	-	-	0.81
Sk −69° 279	866	-	-	-	-	-	-	0.72
Sk −71° 41	1729	-	1737	-	-	-	-	-
Sk −68° 135	1247		1226	-	-	-	-	0.71
Sk −67° 5	1651	-	1629	-	-	-	-	0.75
Sk −68° 52	1583	1441	1581	-	-	-	-	0.75
Sk −69° 43	1059	1075	-	-	-	-	-	0.80
Sk −68° 140	1333	1419	1328	-	-	-	-	0.74
Sk −67° 2	-	505	-	465	464	-	-	0.79
Sk −67° 14	1005	1059	1081	-	-	-	-	0.77
Sk −69° 52	608	570	613	-	-	-	-	0.78
Sk −67° 78	473	-	441	-	-	-	-	-
Sk −70° 16	304	-	275	-	-	-	-	-
Sk −68° 8	256	258	262	255	257	-	-	-
Sk −67° 195	-	-	-	-	-	263	261	0.82
	$v_{\rm black}$							
Target	Si IV 1393Å	Si IV 1403Å	C IV 1548Å	Al III 1855Å	Al III 1863Å	Mg II 2769Å	Mg II 2903Å	$\overline{v_{\rm black}}$
Sk −66° 171	1704	-	1846	-	-	-	-	1775
Sk −68° 155	-	1485	1482	-	-	-	-	1520
Sk −69° 279	613	640	-	-	-	-	-	630
Sk −71° 41	-	-	-	-	-	-	-	-
Sk −68° 135	855	909	-	-	-	-	-	880
Sk −67° 5	1231	-	1237	-	-	-	-	1230
Sk −68° 52	1050	1097	-	-	-	-	-	1150
Sk −69° 43	790	-	914	-	-	-	-	825
Sk −68° 140	1005	984	1016	-	-	-	-	1000
Sk −67° 2	377	361	-	384	381	-	-	380
Sk −67° 14	796	796	839	-	-	-	-	810
Sk −69° 52	473	457	-	-	-	-	-	465
Sk −67° 78	-	-	-	-	-	-	-	-
Sk −70° 16	-	-	-	-	-	-	-	-
Sk −68° 8	-	-	-	-	-	-	-	-
Sk −67° 195	-	-	-	-	-	218	211	215

A.3 Comparison to literature

We show Table A.2, in which we present our obtained values for $T_{\rm eff}$, $\log g$, $\log \dot{M}$, $f_{\rm vol}$, and β in comparison to values presented in other previous studies. The volume-filling factor for studies that used the optically thick clumping is calculated from the equation introduced in Sander et al. (2024) following:

$$f_{\rm vol} = \frac{(1 - f_{\rm ic})^2}{f_{\rm cl} - 2f_{\rm ic} + f_{\rm ic}^2}, \tag{A.1}$$

where $f_{\rm cl} = \langle\rho^2\rangle/\langle\rho\rangle^2$ describes the contrast between the density in the clump and the mean density, and $f_{\rm ic}$ describes the contrast between the clump density and the density of the inter-clump medium.

Table A.2: Comparison of derived parameters to previous studies.

Target Sk −	$T_{\rm eff}$ kK	$\log g$ cm s^{-2}	$\log L$ $L_\odot$	$\log \dot{M}$ $M_\odot$ yr^{-1}	$f_{\rm vol}$	β	Ref.	wavelength	Code
66° 171	$29.9^{+1.2}_{-1.2}$	$3.12^{+0.14}_{-0.19}$	$5.66^{+0.08}_{-0.08}$	$-5.99^{+0.85}_{-0.23}$	0.1	1.00	JB25	Opt	F
	$32.3^{+0.70}_{-1.75}$	$3.20^{+0.47}_{-0.12}$	$5.80^{+0.03}_{-0.07}$	$-6.18^{+0.55}_{-0.07}$	0.021	1.60	SB25	UV+Opt	F
	$29.9^{+1.0}_{-1.0}$	$3.11^{+0.20}_{-0.20}$	$5.67^{+0.11}_{-0.11}$	$-6.07^{+0.33}_{-0.33}$	0.03	1.70	This study	UV+Opt	C
68° 155	$29.9^{+1.2}_{-1.2}$	$3.12^{+0.14}_{-0.19}$	$5.70^{+0.08}_{-0.08}$	$-6.19^{+0.23}_{-0.23}$	0.1	1.00	JB25	Opt	F
	$31.5^{+0.75}_{-0.25}$	$3.20^{+0.20}_{-0.05}$	$5.81^{+0.03}_{-0.02}$	$-5.85^{+0.12}_{-0.10}$	0.037	1.65	SB25	UV+Opt	F
	$32.5^{+0.25}_{-2.00}$	$3.25^{+0.10}_{-0.05}$	$5.77^{+0.04}_{-0.04}$	$-6.00^{+0.05}_{-0.15}$	0.002	1.35	V24	UV+Opt	F
	$29.0^{+1.0}_{-1.0}$	$3.06^{+0.2}_{-0.2}$	$5.64^{+0.11}_{-0.11}$	$-6.19^{+0.25}_{-0.25}$	0.03	1.50	This study	UV+Opt	C
69° 279	$(15.1^{+0.4}_{-0.8})$	$(1.50^{+0.10}_{-0.00})$	$(2.37^{+0.07}_{-0.10})$	$(-7.75^{+0.30}_{-0.22})$	0.1	1.00	JB25	Opt	F
	$29.5^{+0.5}_{-0.5}$	-	$5.54^{+0.06}_{-0.06}$	$-5.26^{+0.04}_{-0.04}$	0.5	3.00	G18	UV+Opt	C
	$28.5^{+2.0}_{-2.0}$	$2.95^{+0.22}_{-0.22}$	$5.63^{+0.11}_{-0.11}$	$-5.70^{+0.39}_{-0.39}$	0.10	2.70	This study	UV+Opt	C
71° 41	$29.9^{+1.2}_{-1.2}$	$3.31^{+0.14}_{-0.14}$	$5.60^{+0.08}_{-0.08}$	$-6.22^{+0.23}_{-0.23}$	0.1	1.00	JB25	Opt	F
	$31.0^{+1.00}_{-1.25}$	$3.12^{+0.23}_{-0.07}$	$5.65^{+0.04}_{-0.05}$	$-6.55^{+0.10}_{-0.05}$	0.019	2.90	SB25	UV+Opt	F
	$30.0^{+2.0}_{-2.0}$	$3.40^{+0.20}_{-0.20}$	$5.50^{+0.10}_{-0.10}$	$-6.09^{+0.10}_{-0.10}$	0.10	1.00	R18	UV+Opt	P
	$29.2^{+1.0}_{-1.0}$	$3.12^{+0.20}_{-0.20}$	$5.53^{+0.11}_{-0.11}$	$-6.03^{+0.25}_{-0.25}$	0.10	1.20	This work	UV+Opt	C
68° 135	$(22.3^{+0.8}_{-1.2})$	$(2.31^{+0.14}_{-0.14})$	$(5.09^{+0.08}_{-0.10})$	$(-5.94^{+0.30}_{-0.23})$	0.1	1.00	JB25	Opt	F
	27.5	2.70	6.97	−5.12	-	3.50	E04	UV+Opt	C
	$26.9^{+1.5}_{-1.5}$	$2.82^{+0.21}_{-0.21}$	$6.10^{+0.12}_{-0.12}$	$-5.70^{+0.31}_{-0.31}$	0.10	2.30	This study	UV+Opt	C
67° 5	$26.8^{+1.2}_{-1.2}$	$3.22^{+0.14}_{-0.33}$	$5.96^{+0.09}_{-0.15}$	$-5.95^{+0.23}_{-0.23}$	0.1	1.00	JB25	Opt	F
	$27.5^{+1.00}_{-1.00}$	$2.98^{+0.10}_{-0.15}$	$5.40^{+0.04}_{-0.04}$	$-6.64^{+0.15}_{-0.12}$	0.020	2.25	SB25	UV+Opt	F
	$25.6^{+1.0}_{-1.0}$	$2.81^{+0.20}_{-0.20}$	$5.89^{+0.12}_{-0.12}$	$-6.05^{+0.14}_{-0.14}$	0.10	1.30	This study	UV+Opt	C
68° 52	$25.2^{+1.2}_{-1.2}$	$2.88^{+0.19}_{-0.14}$	$5.86^{+0.09}_{-0.09}$	$-6.03^{+0.23}_{-0.23}$	0.1	1.00	JB25	Opt	F
	$28.3^{+0.75}_{-0.75}$	$3.10^{+0.25}_{-0.10}$	$5.96^{+0.02}_{-0.02}$	$-6.28^{+0.25}_{-0.25}$	0.084	1.95	V24	UV+Opt	F
	24.5	2.70	5.76	−5.49	-	2.75	E04	UV+Opt	C
	$26.0^{+1.0}_{-1.0}$	$2.85^{+0.20}_{-0.20}$	$5.87^{+0.12}_{-0.12}$	$-6.28^{+0.25}_{-0.25}$	0.03	2.00	This study	UV+Opt	C
69° 43	$23.7^{+1.2}_{-3.5}$	$2.69^{+0.14}_{-0.33}$	$5.62^{+0.10}_{-0.23}$	$-6.34^{+0.23}_{-0.23}$	0.1	1.00	JB25	Opt	F
	$25.0^{+0.75}_{-2.00}$	$2.85^{+0.05}_{-0.25}$	$5.62^{+0.02}_{-0.09}$	$-6.30^{+0.05}_{-0.25}$	0.235	2.45	V24	UV+Opt	F
	$22.8^{+0.25}_{-0.22}$	$2.60^{+0.02}_{-0.02}$	5.48	-	-	-	U17	Opt	F
	$22.4^{+1.0}_{-1.0}$	$2.71^{+0.21}_{-0.21}$	$5.55^{+0.11}_{-0.11}$	$-6.49^{+0.25}_{-0.25}$	0.10	2.00	This study	UV+Opt	C

U17: (Urbaneja et al., 2017), G18: (Gvaramadze et al., 2018), R18: (Ramachandran et al., 2018), E04: (Evans et al., 2004), M15: (McEvoy et al., 2015), V24: (Verhamme et al., 2024), SB25: (Brands et al., 2025), JB25: (Bestenlehner et al., 2025). F: FASTWIND, P: PoWR, C: CMFGEN, T: TLUSTY. The mass-loss rates are not corrected for clumping.

Table A.2: Continued

Target Sk −	$T_{\rm eff}$ kK	$\log g$ cm s^{-2}	$\log L$ $L_\odot$	$\log \dot{M}$ $M_\odot$ yr^{-1}	$f_{\rm vol}$	β	Ref.	wavelength	Code
68° 140	$23.7^{+1.2}_{-2.0}$	$3.12^{+0.19}_{-0.29}$	$5.29^{+0.10}_{-0.27}$	$-6.18^{+0.23}_{-0.52}$	0.1	1.00	JB25	Opt	F
	$23.5^{+1.00}_{-1.00}$	$2.75^{+0.10}_{-0.10}$	$5.64^{+0.10}_{-0.10}$	-	-	-	M15	Opt	T
	$24.1^{+1.0}_{-1.0}$	$2.81^{+0.21}_{-0.21}$	$5.52^{+0.11}_{-0.11}$	$-6.46^{+0.25}_{-0.25}$	0.10	2.20	This study	UV+Opt	C
67° 2	$21.3^{+0.8}_{-1.2}$	$2.50^{+0.14}_{-0.14}$	$5.96^{+0.06}_{-0.09}$	$-6.03^{+0.85}_{-0.23}$	0.1	1.00	JB25	Opt	F
	$19.9^{+0.36}_{-0.39}$	$2.30^{+0.03}_{-0.02}$	5.81	-	-	-	U17	Opt	F
	$18.8^{+1.0}_{-1.0}$	$2.31^{+0.21}_{-0.21}$	$5.76^{+0.12}_{-0.12}$	$-6.21^{+0.26}_{-0.26}$	0.14	3.00	This study	UV+Opt	C
67° 14	$22.5^{+0.8}_{-1.2}$	$2.50^{+0.14}_{-0.14}$	$5.60^{+0.08}_{-0.10}$	$-6.24^{+0.23}_{-0.24}$	0.1	1.00	JB25	Opt	F
	$23.3^{+1.50}_{-0.75}$	$2.55^{+0.35}_{-0.50}$	$5.53^{+0.06}_{-0.03}$	$-6.25^{+0.05}_{-0.30}$	0.003	1.65	V24	UV+Opt	F
	$22.9^{+0.12}_{-0.13}$	$2.70^{+0.01}_{-0.01}$	5.62	-	-	-	U17	Opt	F
	$21.1^{+1.0}_{-1.0}$	$2.51^{+0.21}_{-0.21}$	$5.58^{+0.11}_{-0.11}$	$-6.33^{+0.29}_{-0.29}$	0.10	2.00	This study	UV+Opt	C
69° 52	$20.1^{+3.5}_{-1.2}$	$2.31^{+0.38}_{-0.48}$	$5.58^{+0.26}_{-0.11}$	$-6.89^{+0.34}_{-0.30}$	0.1	1.00	JB25	Opt	F
	$22.5^{+0.25}_{-1.75}$	$2.60^{+0.05}_{-0.10}$	$5.73^{+0.00}_{-0.08}$	$-6.70^{+0.10}_{-0.05}$	0.001	2.60	V24	UV+Opt	F
	$18.8^{+1.0}_{-1.0}$	$2.31^{+0.21}_{-0.21}$	$5.60^{+0.11}_{-0.11}$	$-6.62^{+0.38}_{-0.38}$	0.14	2.50	This study	UV+Opt	C
67° 78	$16.6^{+0.8}_{-1.2}$	$2.31^{+0.14}_{-0.33}$	$5.45^{+0.09}_{-0.13}$	$-6.72^{+0.23}_{-0.51}$	0.1	1.00	JB25	Opt	F
	$17.8^{+1.50}_{-0.25}$	$2.35^{+0.05}_{-0.25}$	$5.62^{+0.06}_{-0.08}$	$-6.82^{+0.05}_{-0.03}$	0.036	3.45	V24	UV+Opt	F
	$16.2^{+0.98}_{-0.18}$	$2.20^{+0.01}_{-0.02}$	5.36	-	-	-	U17	Opt	F
	$15.5^{+1.0}_{-1.0}$	$2.10^{+0.21}_{-0.21}$	$5.47^{+0.11}_{-0.11}$	$-6.70^{+0.40}_{-0.40}$	0.20	3.00	This study	UV+Opt	C
70° 16	$20.1^{+0.5}_{-1.6}$	$2.69^{+0.14}_{-0.24}$	$4.93^{+0.06}_{-0.14}$	$-8.15^{+1.06}_{-0.73}$	0.1	1.00	JB25	Opt	F
	$20.9^{+2.60}_{+0.70}$	$2.85^{+0.25}_{-0.20}$	$4.92^{+0.14}_{-0.04}$	$-7.70^{+0.3}_{-1.150}$	0.031	2.90	V24	UV+Opt	F
	$18.4^{+1.0}_{-1.0}$	$2.61^{+0.21}_{-0.21}$	$4.88^{+0.10}_{-0.10}$	$-7.60^{+0.34}_{-0.34}$	0.10	1.00	This study	UV+Opt	C
68° 8	$13.5^{+1.2}_{-0.8}$	$1.50^{+0.29}_{-0.00}$	$5.23^{+0.13}_{-0.10}$	$-6.85^{+0.24}_{-0.37}$	0.1	1.00	JB25	Opt	F
	$14.8^{+2.00}_{-0.75}$	$1.95^{+0.25}_{-0.25}$	$5.56^{+0.00}_{-0.11}$	$-6.90^{+0.60}_{-0.05}$	0.006	2.00	V24	UV+Opt	F
	$14.1^{+1.0}_{-1.0}$	$1.81^{+0.21}_{-0.21}$	$5.57^{+0.11}_{-0.11}$	$-6.50^{+0.26}_{-0.26}$	0.10	1.00	This study	UV+Opt	C
67° 195	$12.0^{+0.4}_{-0.4}$	$1.88^{+0.19}_{-0.14}$	$4.55^{+0.08}_{-0.08}$	$-7.58^{+0.36}_{-0.29}$	0.1	1.00	JB25	Opt	F
	$14.2^{+0.90}_{-0.50}$	$2.45^{+0.20}_{-0.20}$	$4.72^{+0.06}_{-0.03}$	$-7.45^{+0.60}_{-1.50}$	0.027	0.65	V24	UV+Opt	F
	$12.6^{+1.0}_{-1.0}$	$2.11^{+0.22}_{-0.22}$	$4.65^{+0.10}_{-0.10}$	$-7.50^{+0.35}_{-0.35}$	0.10	1.00	This study	UV+Opt	C

U17: (Urbaneja et al., 2017), G18: (Gvaramadze et al., 2018), R18: (Ramachandran et al., 2018), E04: (Evans et al., 2004), M15: (McEvoy et al., 2015), V24: (Verhamme et al., 2024), SB25: (Brands et al., 2025), JB25: (Bestenlehner et al., 2025). F: FASTWIND, P: PoWR, C: CMFGEN, T: TLUSTY. The mass-loss rates are not corrected for clumping.

A.4 Comments on fitting issues

Sk −66° 171, Fig. A.2, Fig. A.18 When considering helium lines other than He I λ4471 He II λ4542, one might prefer a model with a slightly higher temperature. The other glaring issue is with the Hα, although the morphology of the model line is similar to the observation, we do find that the centre of the emission in the observation is slightly redshifted relative to all other lines. In the UV and FUV the model fits the observations very well. Fig. A.18 shows the fit for the entire spectrum, where for this object include a fit for the absorption profiles for $Ly\alpha$ through $Ly\eta$, which were calculated using H I column density $\log N(HI) = 20.7$ cm^{-2} (Fitzpatrick, 1985). The observed He II λ4686 emission is predicted in absorption.

Sk −68° 155, Fig. A.3, Fig. A.19 This star with $v \sin i = 80$ km/s is the fastest rotator in our sample, which is reflected in the relatively broad metal and helium lines. The small dip in the centre of the emission in Hα could be an indication of an optically thick disk forming around the star, other than that the overall quality of the fit is very good. The model overpredicts the He II λ4686 absoprtion.

Sk −69° 279, Fig. A.4, Fig. A.20 This is one of two hypergiants in our sample, which is classified as such by the extremely strong emission in Hα and the P Cygni shape in higher Balmer lines and in He I λ4471 , therefore, we use Hη for estimating $\log g$, as all other Balmer lines are contaminated by winds and take He I λ4026 and He II λ5411 as primary diagnostics to obtain the temperature. The overall fit is quite good considering all the challenges that come with fitting the spectra of emission line objects, with the exception of He II λ4686 line, where the predicted emission is weaker than the observed.

Sk −71° 41, Fig. A.5, Fig. A.21 For this object, we were not able to reproduce the observed unsaturated silicon lines Si IV $\lambda\lambda 1393-1403$ even with models with extremely clumped winds $f_{\rm vol} = 0.03 - 0.02$. We note two other peculiarities, first of which is the large discrepancy between v_∞ obtained from the C IV $\lambda\lambda 1548-1551$ (≈ 1500 km s^{-1})and Si IV $\lambda\lambda 1394-1403$ (≈ 1300 km s^{-1}). The other peculiarity is the unexplicably broad O III $\lambda 5592$ line.

Sk −68° 135, Fig. A.6, Fig. A.22 This is second hypergiant in our sample. Just as for Sk −69° 279, we estimate $\log g$ from Hη. But unlike the other hypergiant, we obtain a more reliable value for $T_{\rm eff}$ because the helium lines do are less contaminated by the extreme winds. We obtain decent fits for most lines, with the exception of the strong He II $\lambda 4686$ emission, which is predicted in absorption in the model.

Sk −67° 5, Fig. A.7, Fig. A.23 For this object, we were not able to replicate the morphology of Hα. The most glaring issue in this fit is the helium abundance, and therefore the hydrogen abundance as well.

Sk −68° 52, Fig. A.8, Fig. A.24 This is one of the early B0 supergiants that shows weak He II lines. We chose not to fit He II lines, as increasing the temperature of the model by a mere 500 K does indeed give a better fit for He II lines but drastically weakens S III lines. Overall, we obtain an excellent fit for most lines.

Sk −69° 43, Fig. A.9, Fig. A.25 In the case of this object, as for Sk −67° 2, we were able to accurately reproduce the emission in Hα but not the braod, blueshifted absorption.

Sk −68° 140, Fig. A.10, Fig. A.26 The unsaturated Si IV $\lambda\lambda 1393-1403$ lines, which suggests clumpier winds, were not reproduced by our models even with much smaller

volum filling factors. The fit for this stars serves as a good example of the consequences of excluding X-rays from our models, as seen on Fig. A.26, the strong P Cygni C IV λ1550 in the observations is much weaker in the model, this is because in this temeperature range C III dominates the ionization structure, but due to X-rays generated by shocks, we observe the enhanced C IV line.

Sk −67° 2, Fig. A.11, Fig. A.27 The overall fit for this object is very good. In this case, we obtain a good fit for Hα emission, but we were unable to fit the blueshifted absorption.

Sk −67° 14, Fig. A.12, Fig. A.28 We notice on this object that Si IV $\lambda\lambda 1393-1403$ would suggest less emissive winds (higher $f_{\rm vol}$), whereas Al III $\lambda\lambda 1856-1860$ would suggest more emissive winds (lower $f_{\rm vol}$).

Sk −69° 52, Fig. A.13, Fig. A.29 For this star, we were not able to reproduce the odd morphology of Hα, which seem to have a sudden cut-off and the peak of the emission.

Sk −67° 78, Fig. A.14, Fig. A.30 The most noticeable issue with the fit of this object is the extended wings and the blue shifted absorption of the model Hα, which we could not eliminate. Although, we were able to obtain a good match to the emission in Hα.

Sk −70° 16, Fig. A.15, Fig. A.31 For this object we obtain a very good fit, except for Hα, where we could not reproduce the weak, but broad absorption.

Sk −68° 8, Fig. A.16, Fig. A.32 For this object, we were able to obtain a good fit for Hα emission and to the general morphology. We do note the infilling of the Hγ line core, which could be due to nebular contamination. The Si II $\lambda\lambda 6347-6371$ lines in

the model match the observations quite well. This can be used as a sanity check for determining the effective temperature for mid and late B-supergiants.

Sk −67° 195, Fig. A.17, Fig. A.33 For this low luminosity late B-supergiant we do not find any vaiable oxygen lines, therefore we do not change the oxygen mass fraction when applying our pipline to this star. We consider the mass-loss rate of this object to be an upper limit due to Hα being fully in absorption. We note that the predicted Si II $\lambda\lambda 6347 - 6371$ lines excellently match the observed, albeit we did not use them as diagnostics.

A.5 Spectral energy distribution (SED)

In Fig. A.1 we present the SED fits for the entire sample.

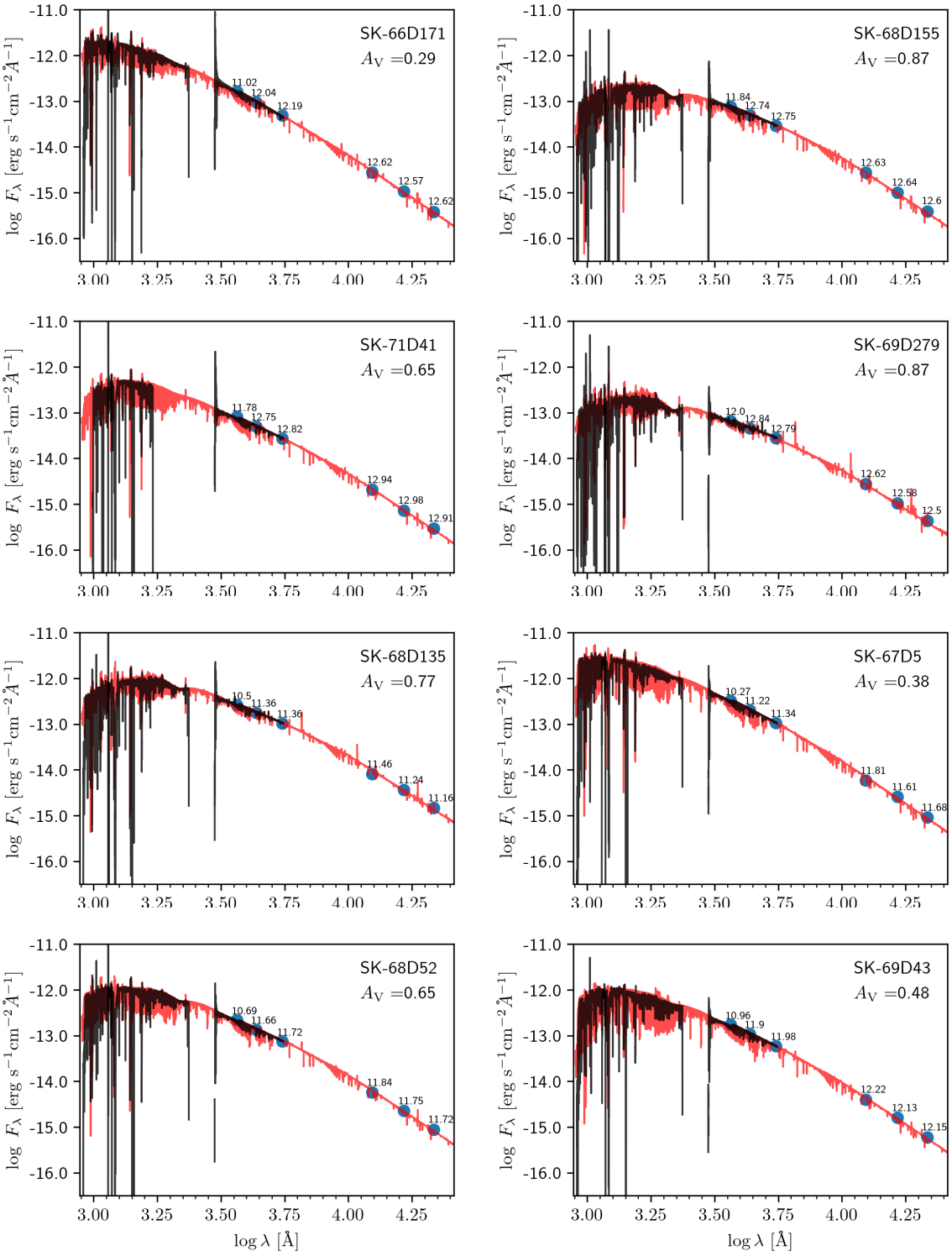


Figure A.1: Spectral energy distribution for all the stars in our sample. Red solid line: model SED, Black solid line: observed SED. The photometric points are indicated as blue circles.

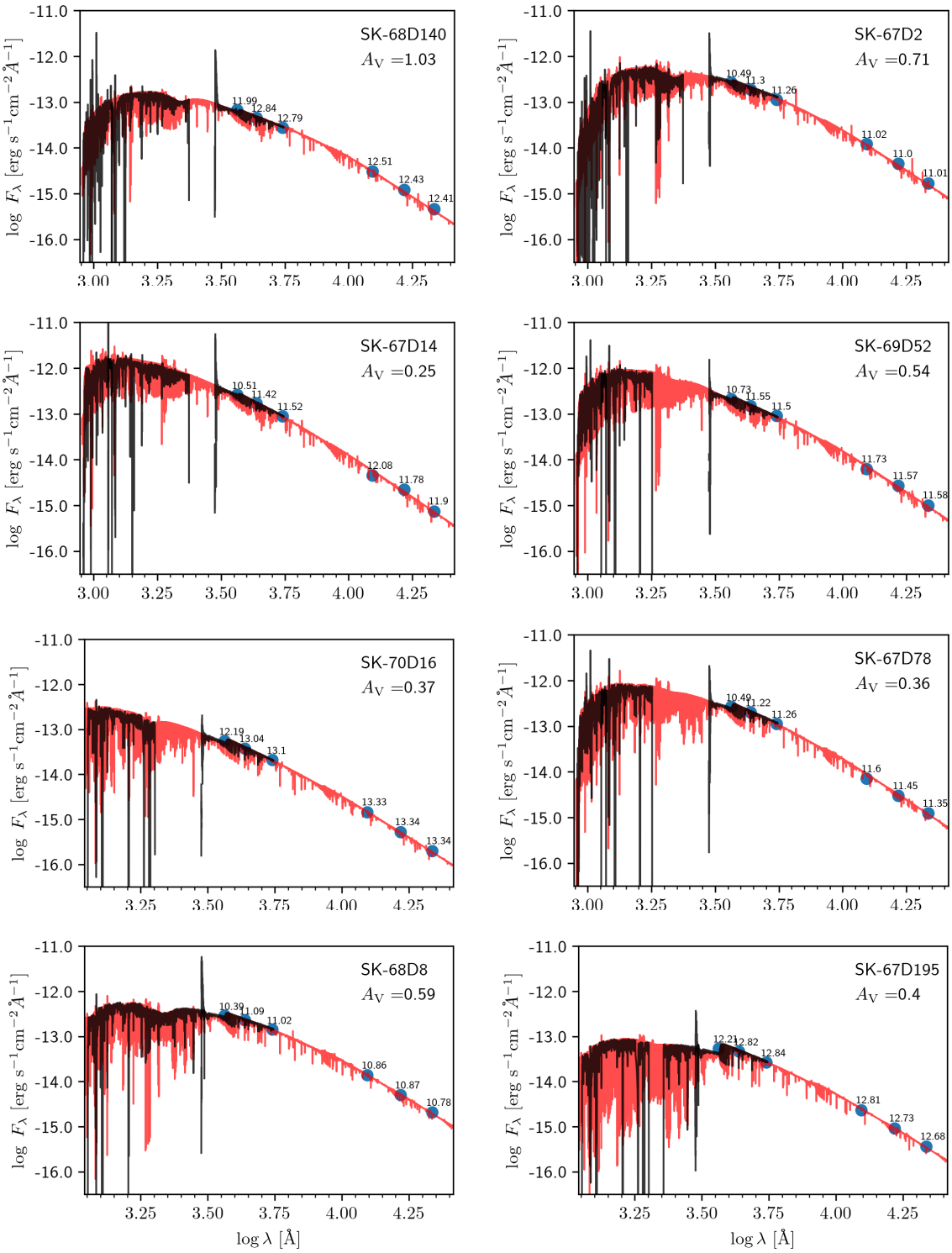


Figure A.1: continued

A.6 Line fitting for individual stars

Fig. A.2-A.17 are the individual diagnostic line fits for each star in our sample. On each row, from top to bottom, are the diagnostic lines used to determine the effective temperature, the effective surface gravity, the wind density parameters (mass-loss rate, β, clumping parameters), the helium abundance, the nitrogen abundance, the carbon abundance, and the oxygen abundance, respectively.

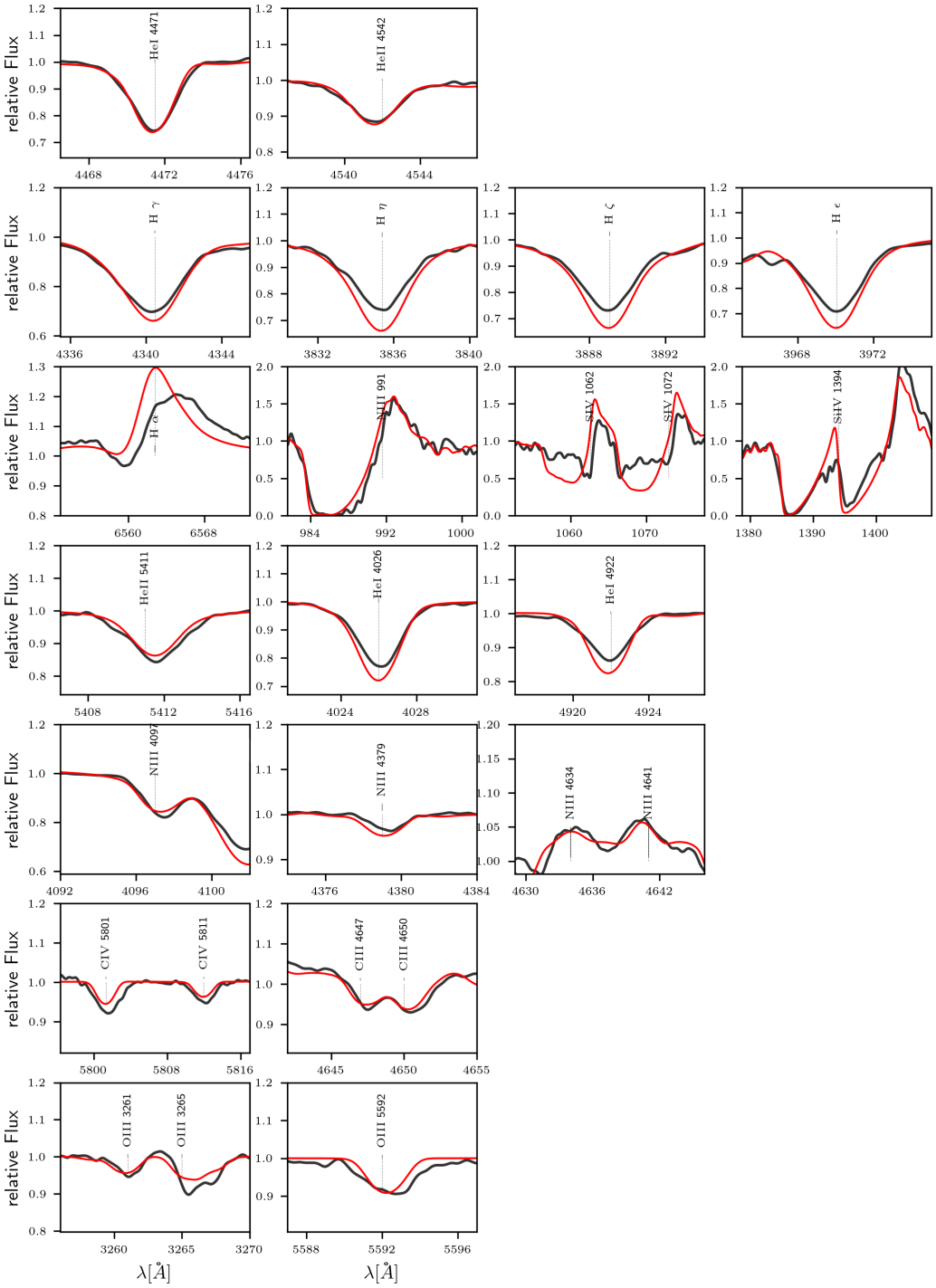


Figure A.2: Individual line fits for Sk −66° 171. Black solid line: observed spectrum. Red solid line: spectrum of the best fitting model. The observed spectrum is corrected for $v_{\rm rad} = 410 {\rm km\,s^{-1}}$

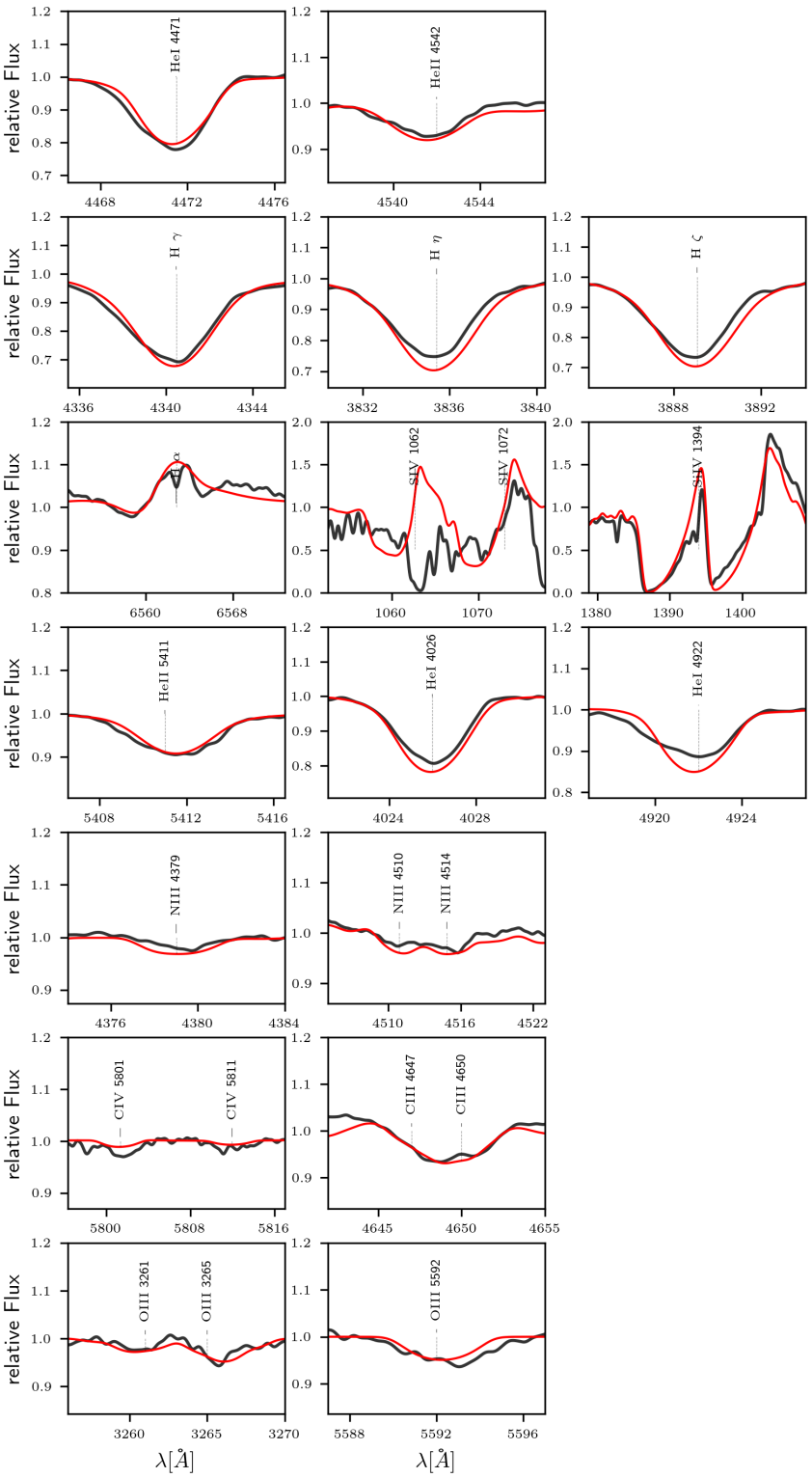


Figure A.3: Individual line fits for Sk −68° 155. Black solid line: observed spectrum. Red solid line: spectrum of the best fitting model. The observed spectrum is corrected for $v_{\rm rad} = 240 {\rm km\,s^{-1}}$

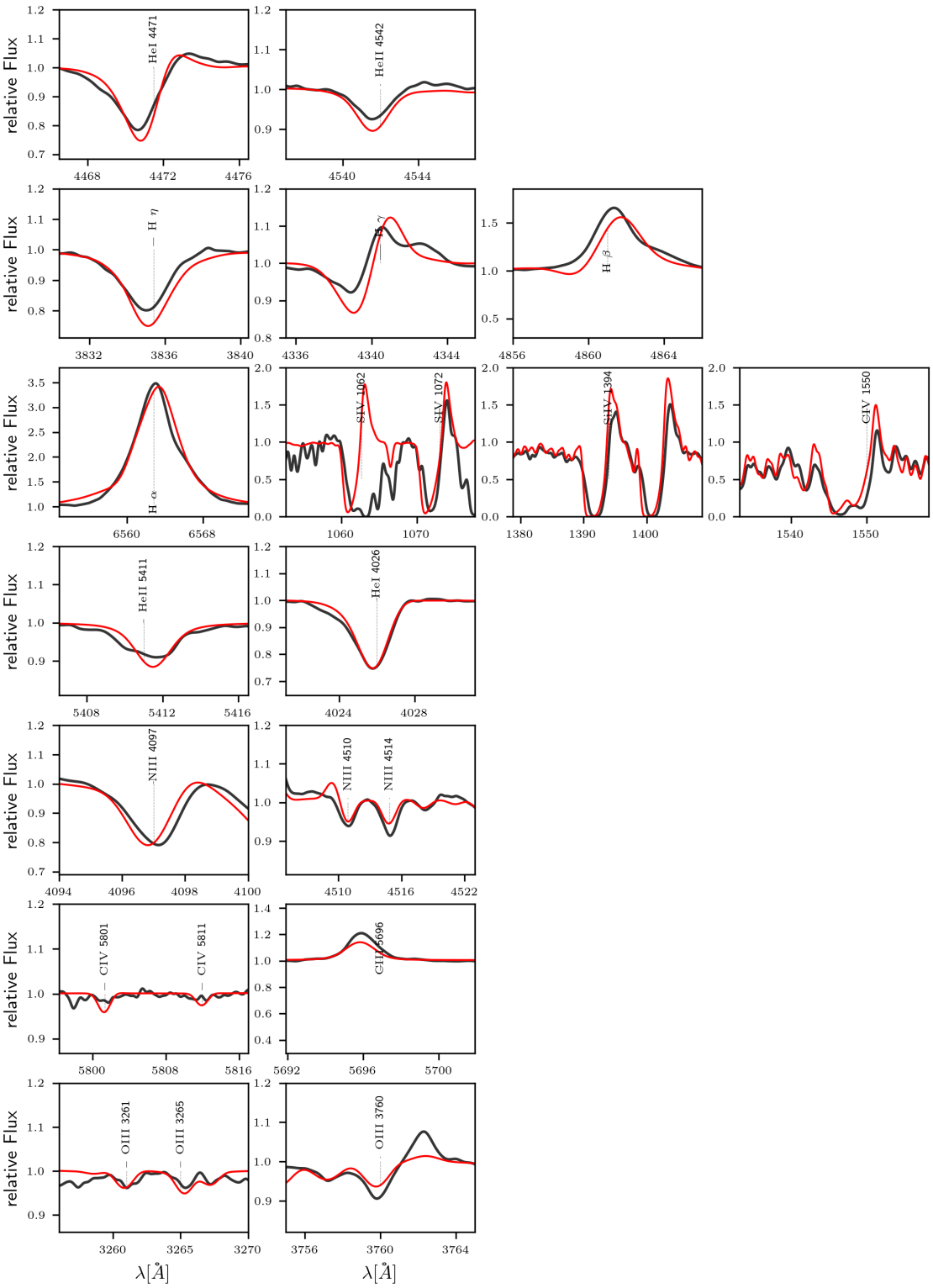


Figure A.4: Individual line fits for Sk −69° 279. Black solid line: observed spectrum. Red solid line: spectrum of the best fitting model. The observed spectrum is corrected for $v_{\rm rad} = 230 {\rm km\,s^{-1}}$

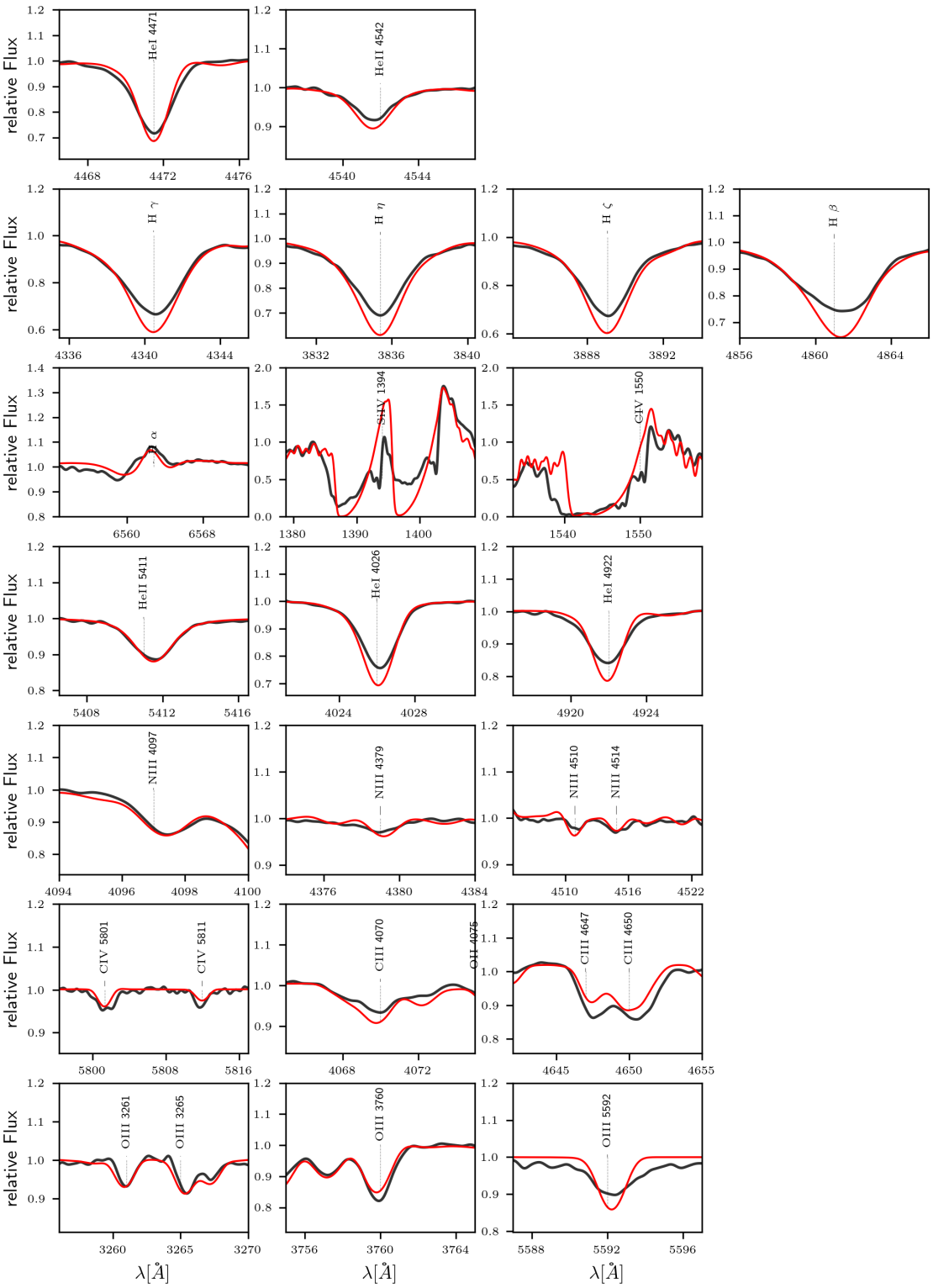


Figure A.5: Individual line fits for Sk −71° 41. Black solid line: observed spectrum. Red solid line: spectrum of the best fitting model. The observed spectrum is corrected for $v_{\rm rad} = 260 {\rm km\,s^{-1}}$

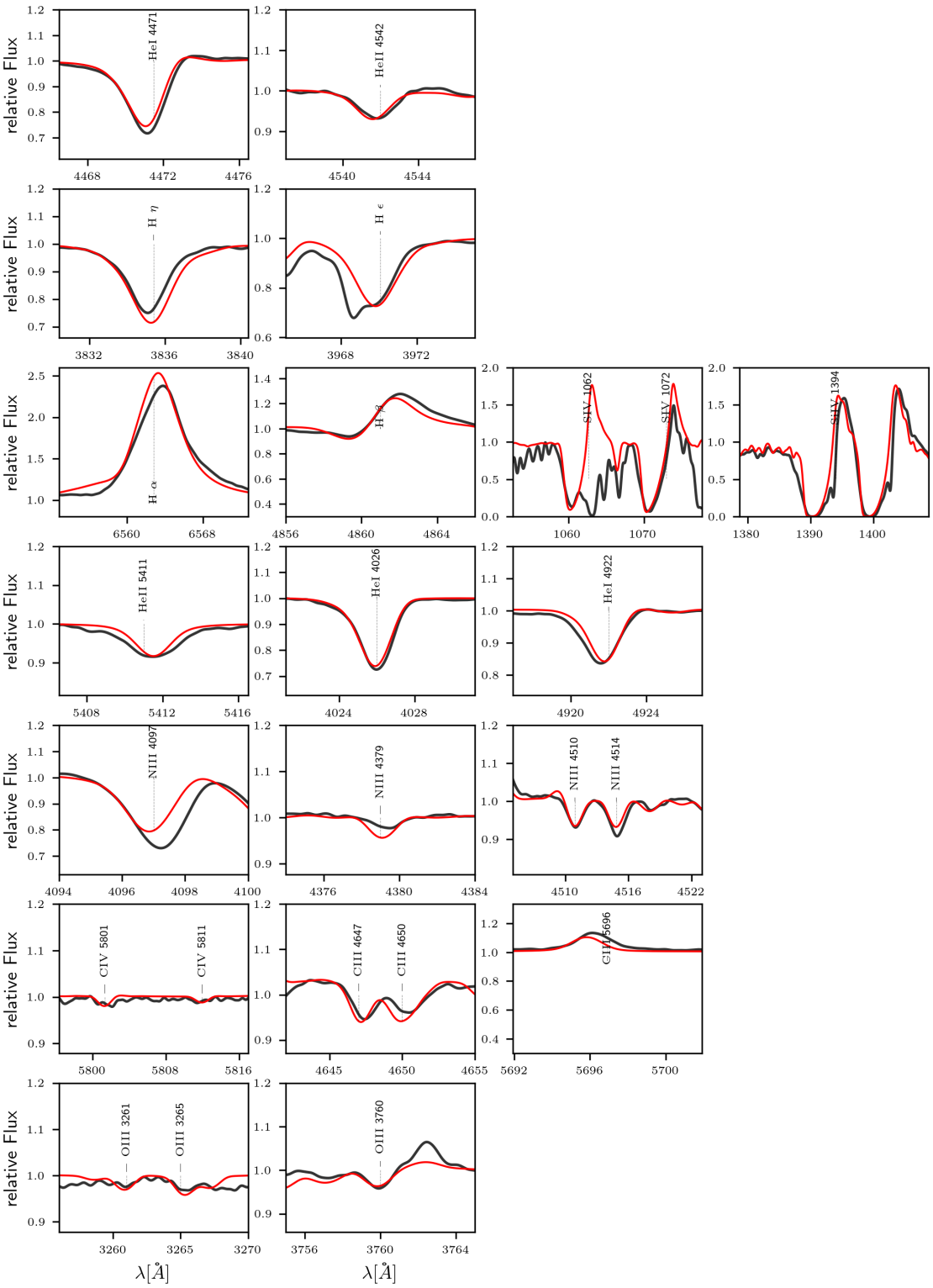


Figure A.6: Individual line fits for Sk −68° 135. Black solid line: observed spectrum. Red solid line: spectrum of the best fitting model. The observed spectrum is corrected for $v_{\rm rad} = 270 {\rm km\,s^{-1}}$

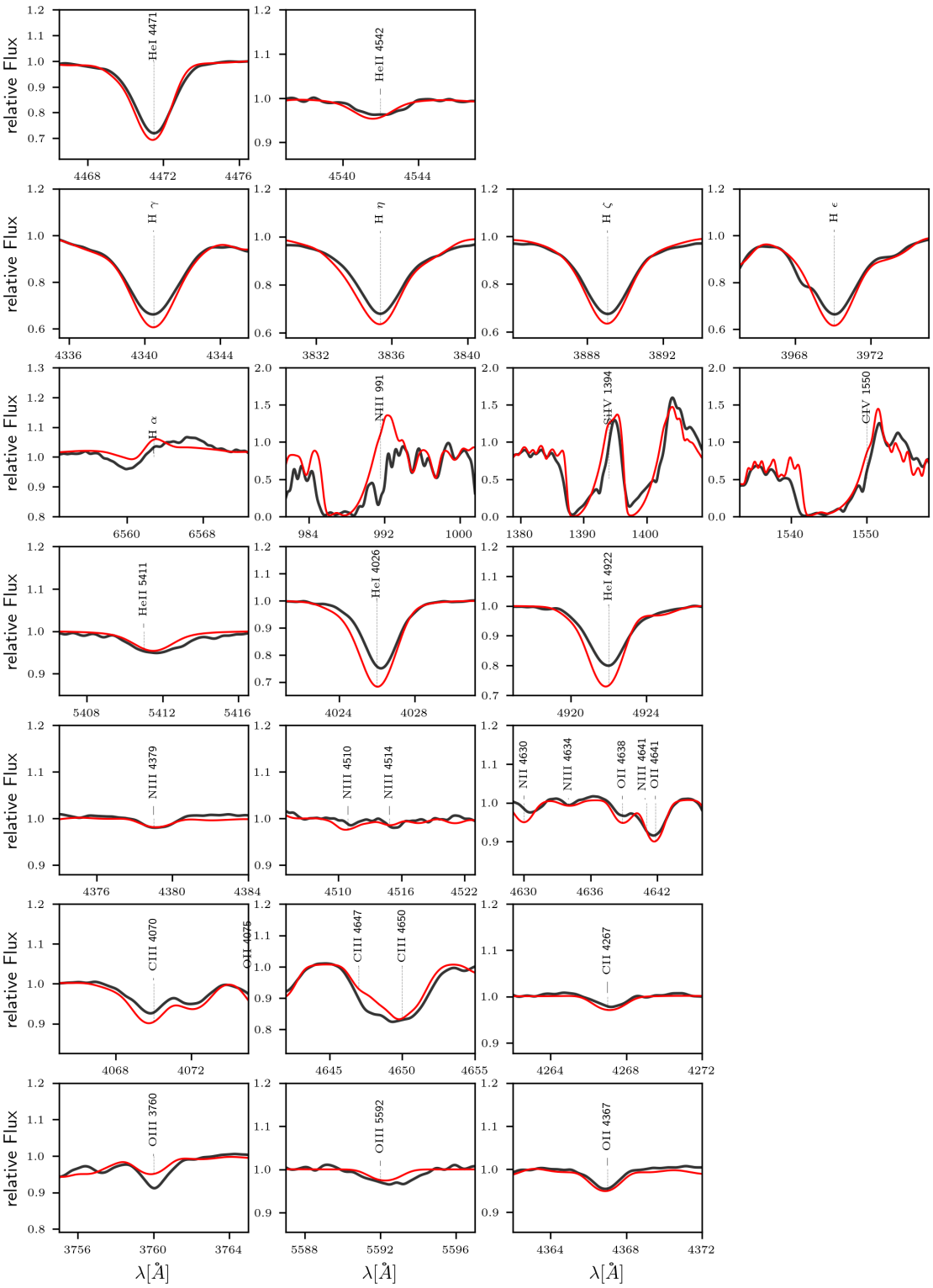


Figure A.7: Individual line fits for Sk −67° 5. Black solid line: observed spectrum. Red solid line: spectrum of the best fitting model. The observed spectrum is corrected for $v_{\rm rad} = 295 {\rm km\,s^{-1}}$

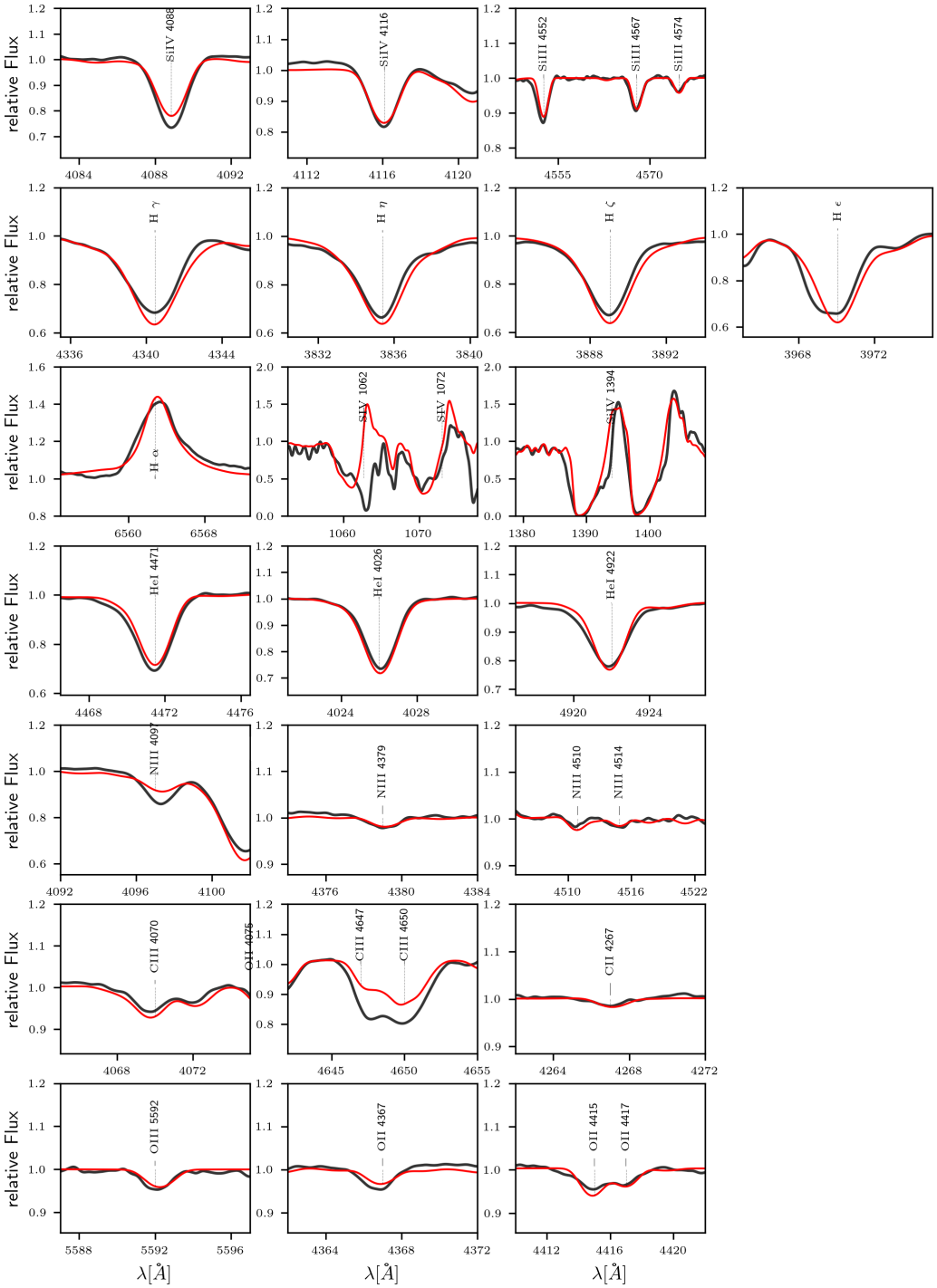


Figure A.8: Individual line fits for Sk −68° 52. Black solid line: observed spectrum. Red solid line: spectrum of the best fitting model. The observed spectrum is corrected for $v_{\rm rad} = 255 {\rm km\,s^{-1}}$

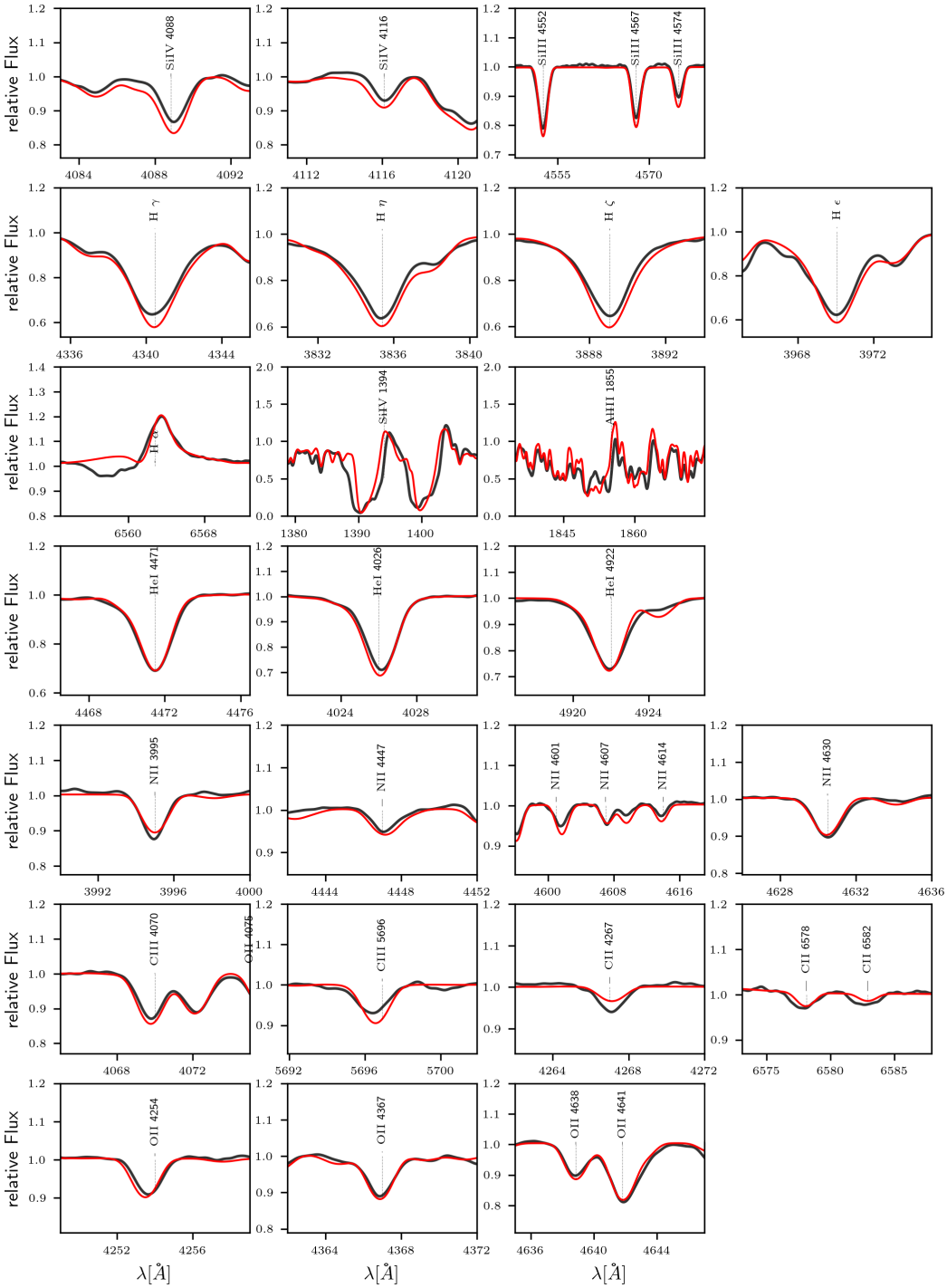


Figure A.9: Individual line fits for Sk −69° 43. Black solid line: observed spectrum. Red solid line: spectrum of the best fitting model. The observed spectrum is corrected for $v_{\rm rad} = 255 {\rm km\,s^{-1}}$

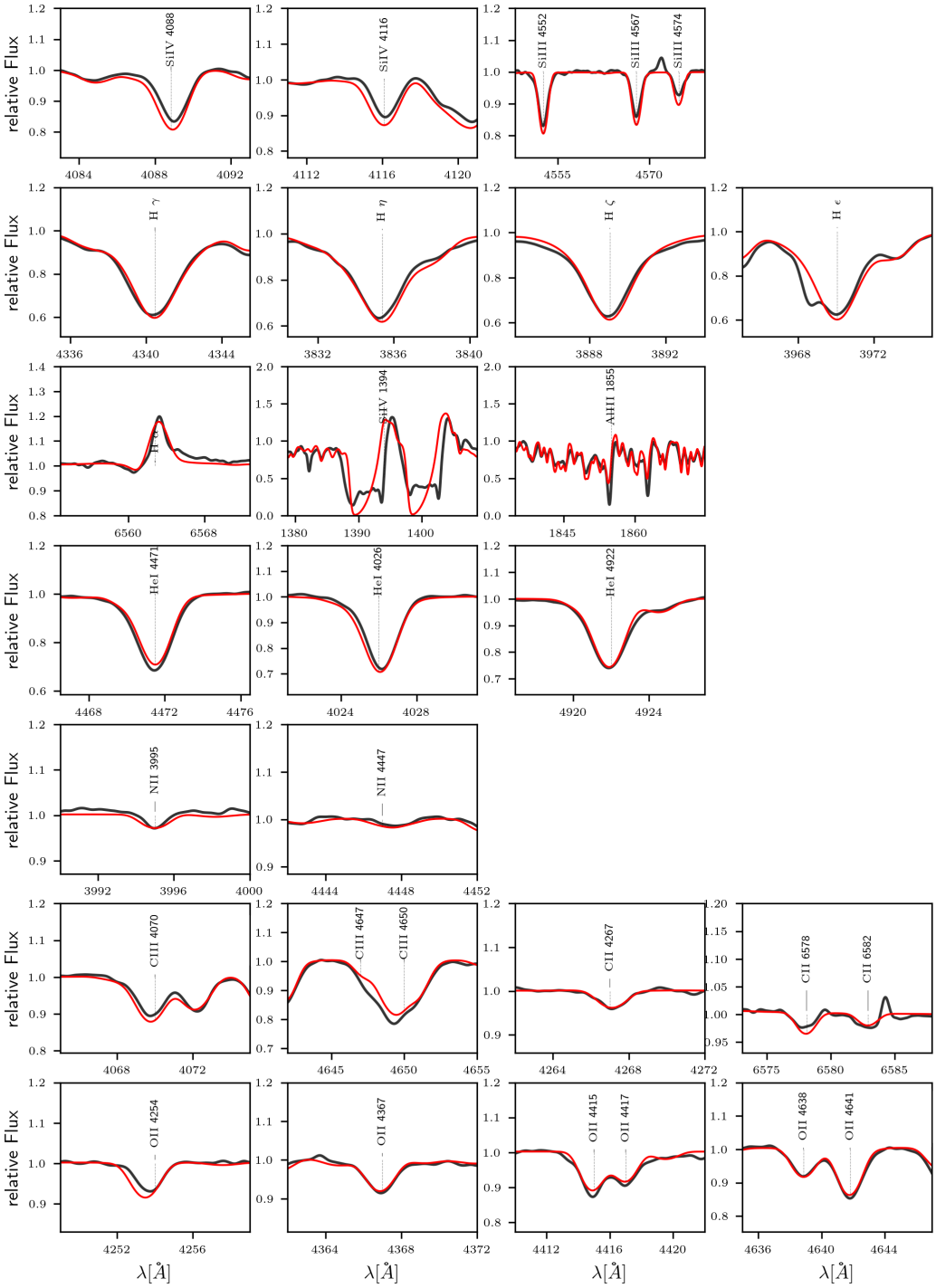


Figure A.10: Individual line fits for Sk −68° 140. Black solid line: observed spectrum. Red solid line: spectrum of the best fitting model. The observed spectrum is corrected for $v_{\rm rad} = 260 {\rm km\,s^{-1}}$

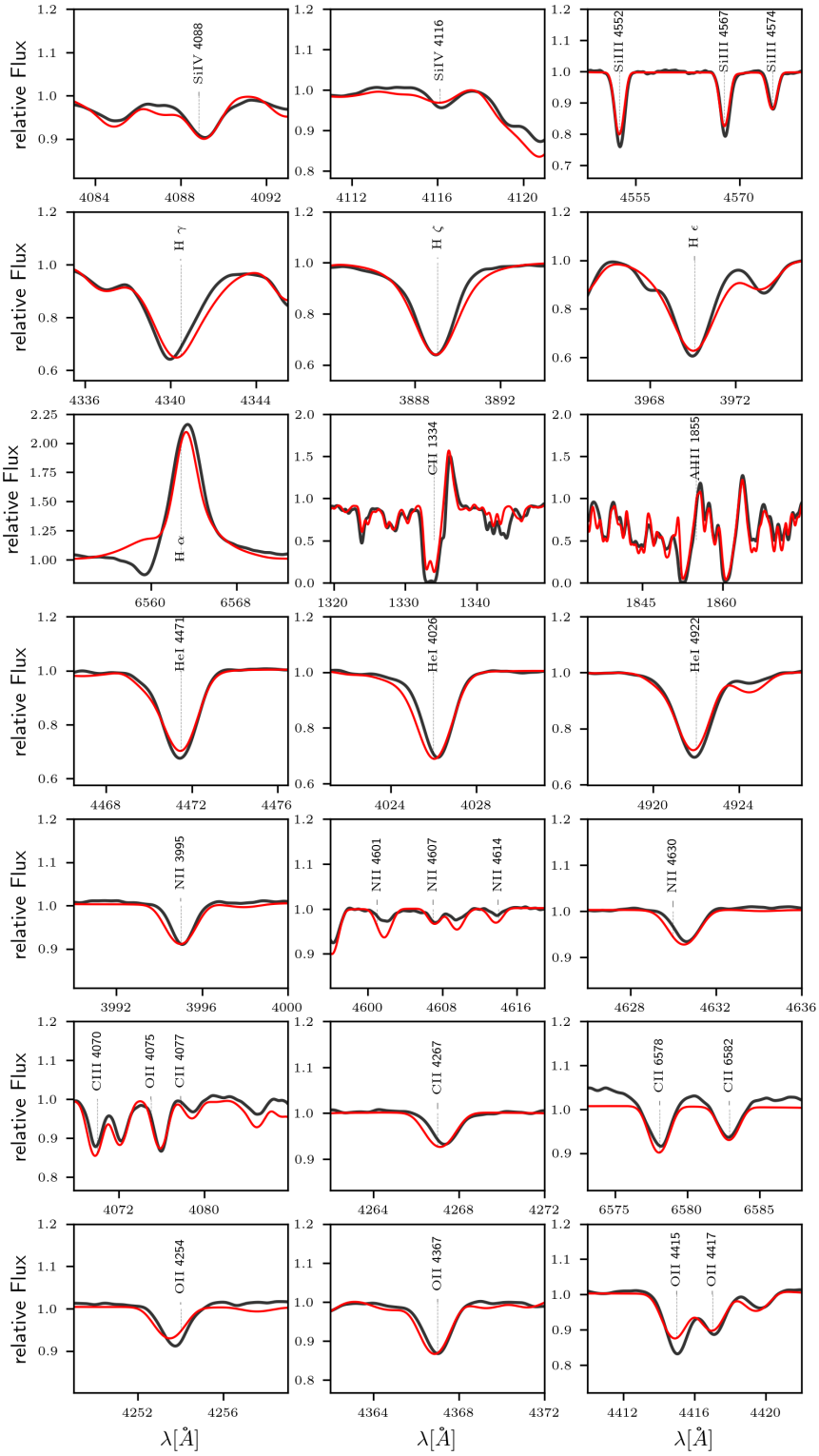


Figure A.11: Individual line fits for Sk −67° 2. Black solid line: observed spectrum. Red solid line: spectrum of the best fitting model. The observed spectrum is corrected for $v_{\rm rad} = 320 {\rm km\,s^{-1}}$

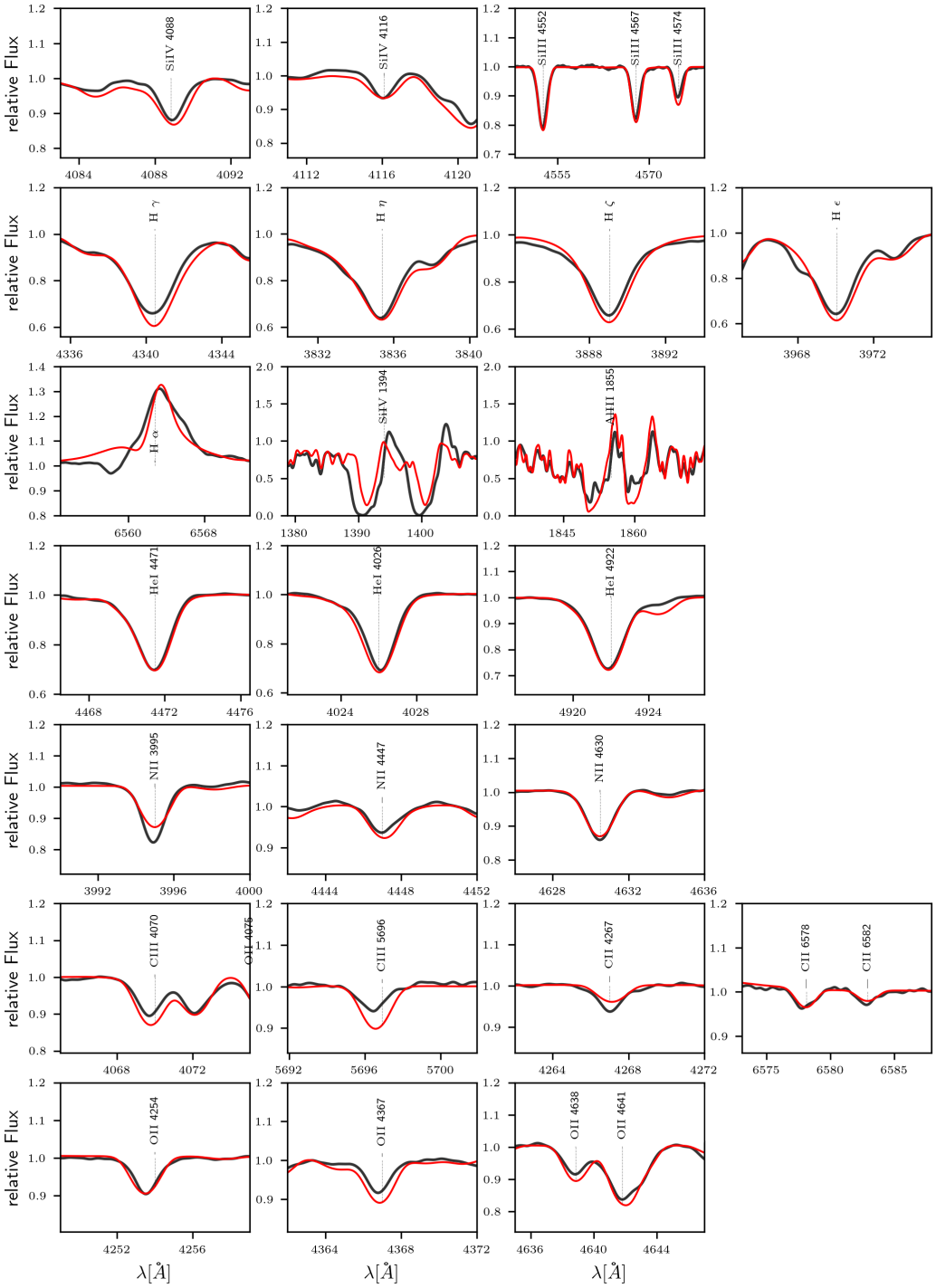


Figure A.12: Individual line fits for Sk −67° 14. Black solid line: observed spectrum. Red solid line: spectrum of the best fitting model. The observed spectrum is corrected for $v_{\rm rad} = 300 {\rm km\,s^{-1}}$

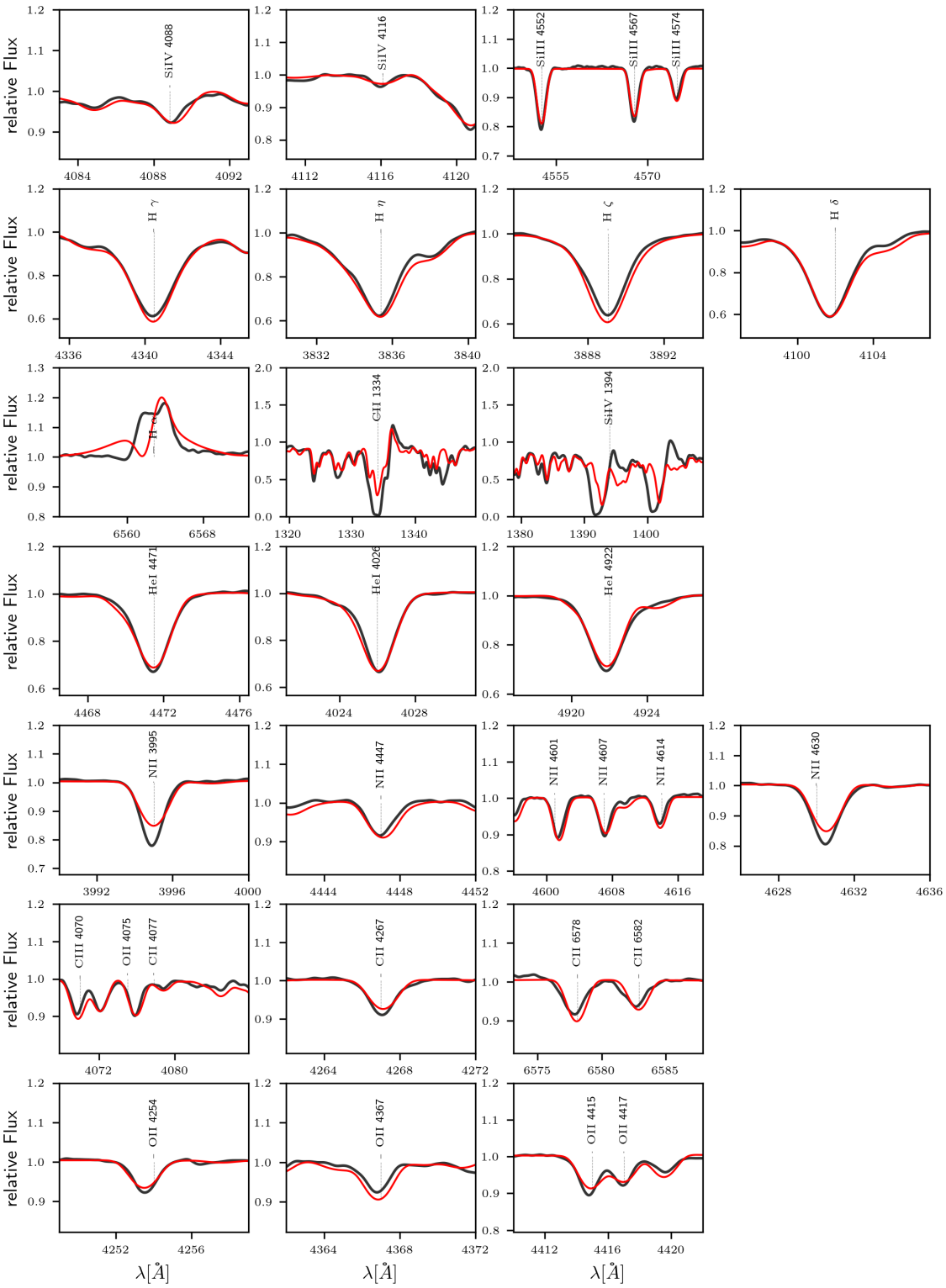


Figure A.13: Individual line fits for Sk −69° 52. Black solid line: observed spectrum. Red solid line: spectrum of the best fitting model. The observed spectrum is corrected for $v_{\rm rad} = 260 {\rm km\,s^{-1}}$

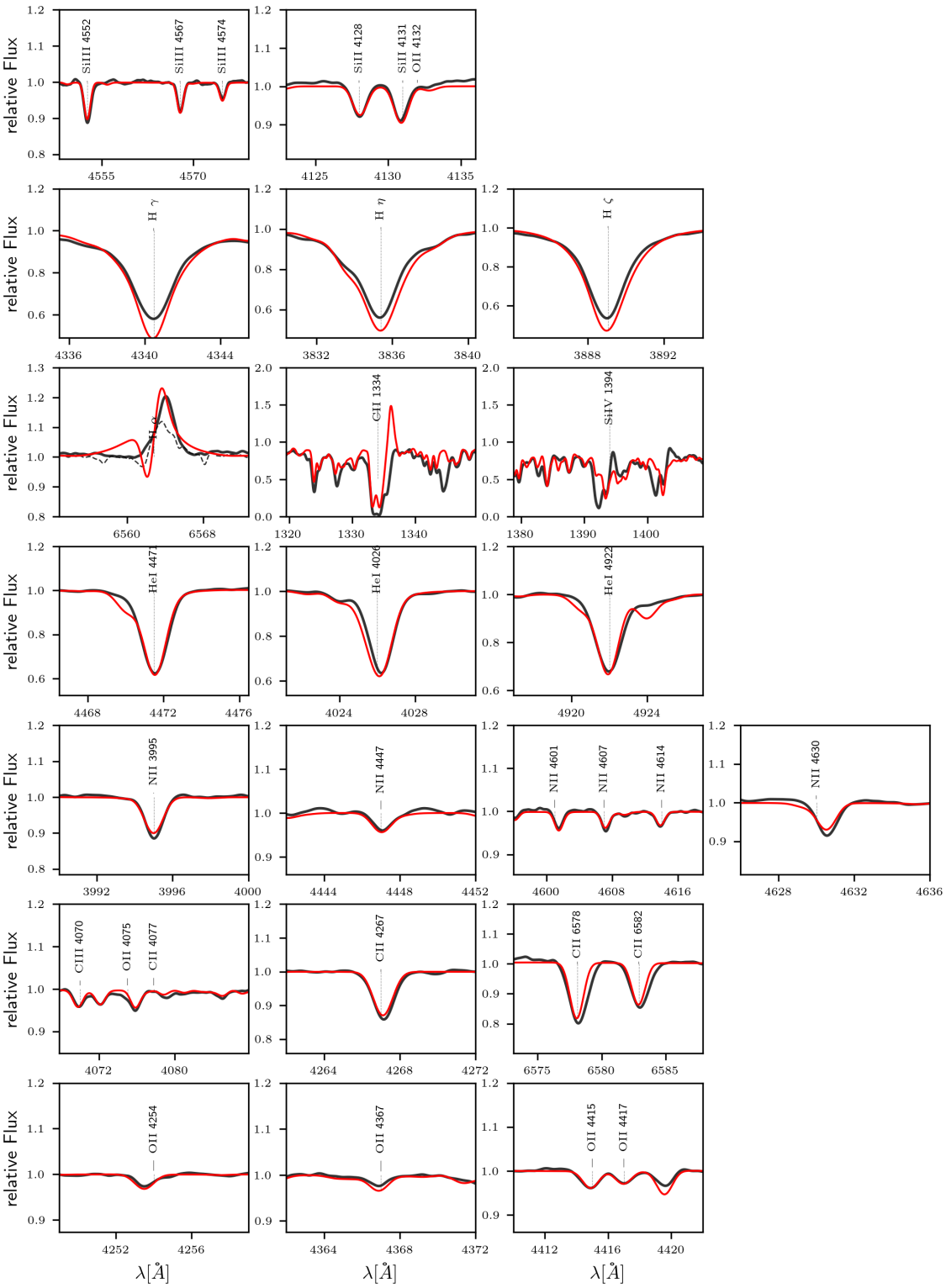


Figure A.14: Individual line fits for Sk −67° 78. Black solid line: observed spectrum. Red solid line: spectrum of the best fitting model. The observed spectrum is corrected for $v_{\rm rad} = 310 {\rm km\,s^{-1}}$

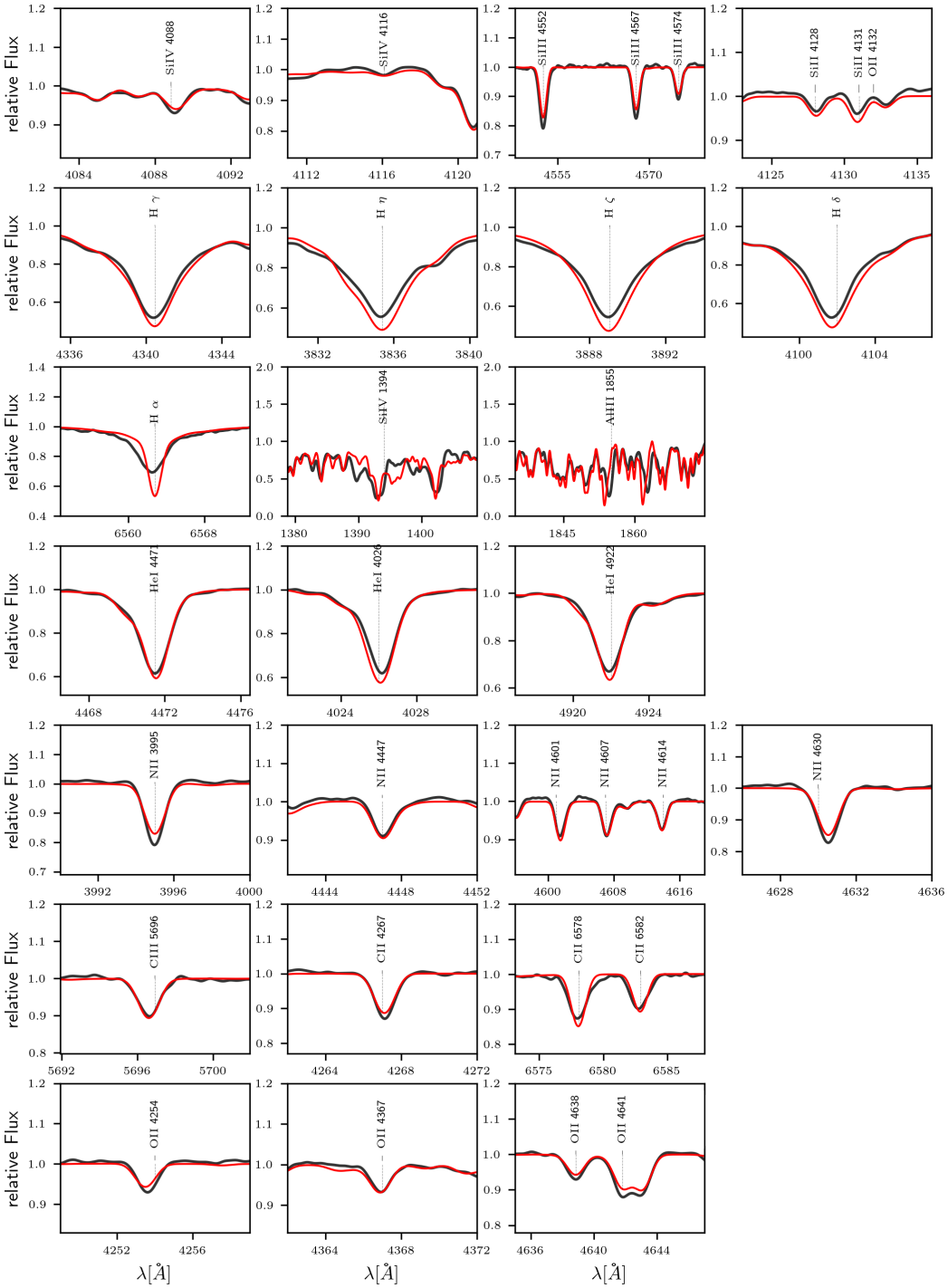


Figure A.15: Individual line fits for Sk −70° 16. Black solid line: observed spectrum. Red solid line: spectrum of the best fitting model. The observed spectrum is corrected for $v_{\rm rad} = 265 {\rm km\,s^{-1}}$

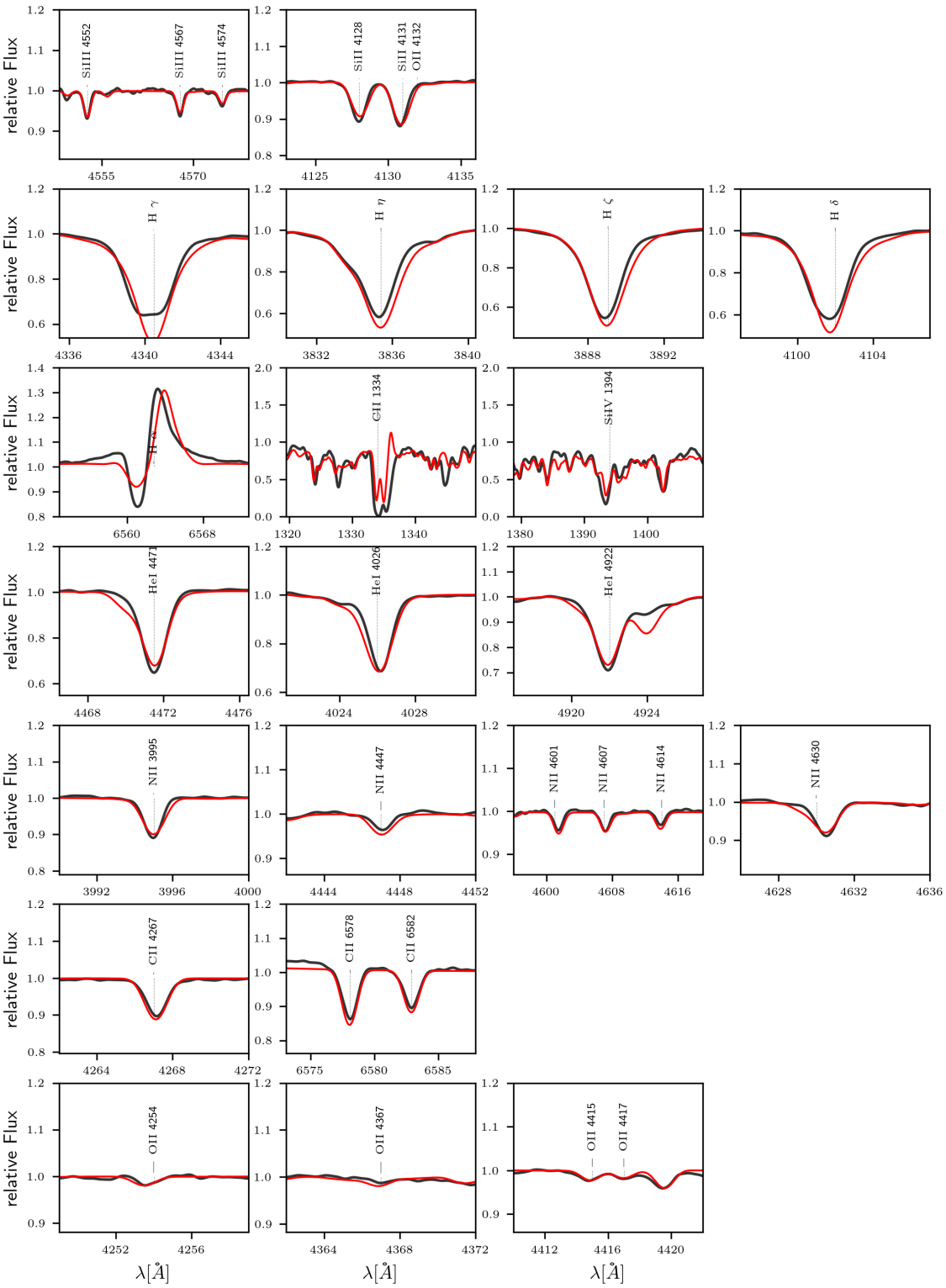


Figure A.16: Individual line fits for Sk −68° 8. Black solid line: observed spectrum. Red solid line: spectrum of the best fitting model. The observed spectrum is corrected for $v_{\rm rad} = 250 {\rm km\,s^{-1}}$

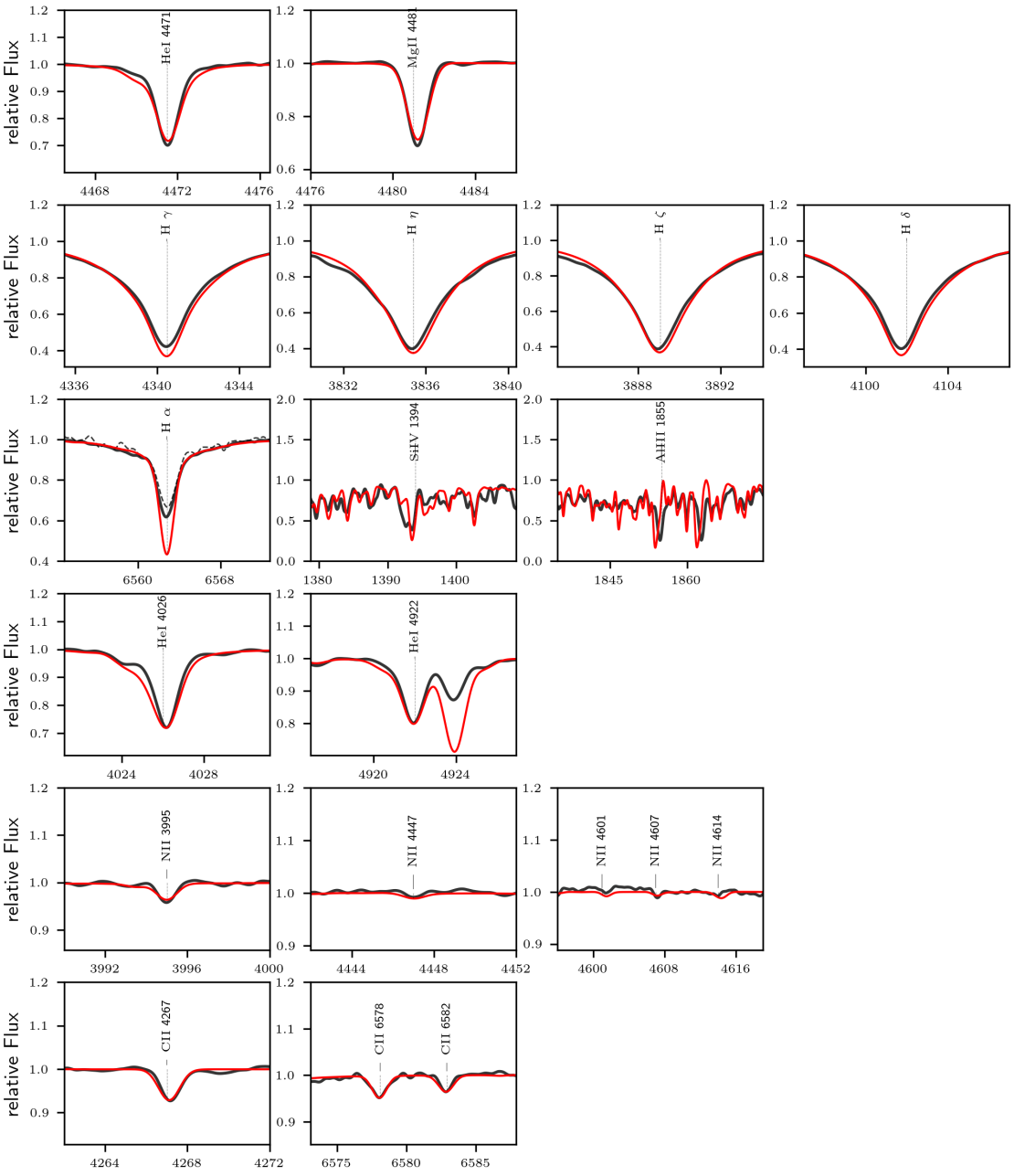


Figure A.17: Individual line fits for Sk −67° 195. Black solid line: observed spectrum. Red solid line: spectrum of the best fitting model. The observed spectrum is corrected for $v_{\rm rad} = 300 {\rm km\,s^{-1}}$

A.7 Overall spectral fits

Fig. A.18-A.33 are the fits for the overall spectrum of each star in our sample.

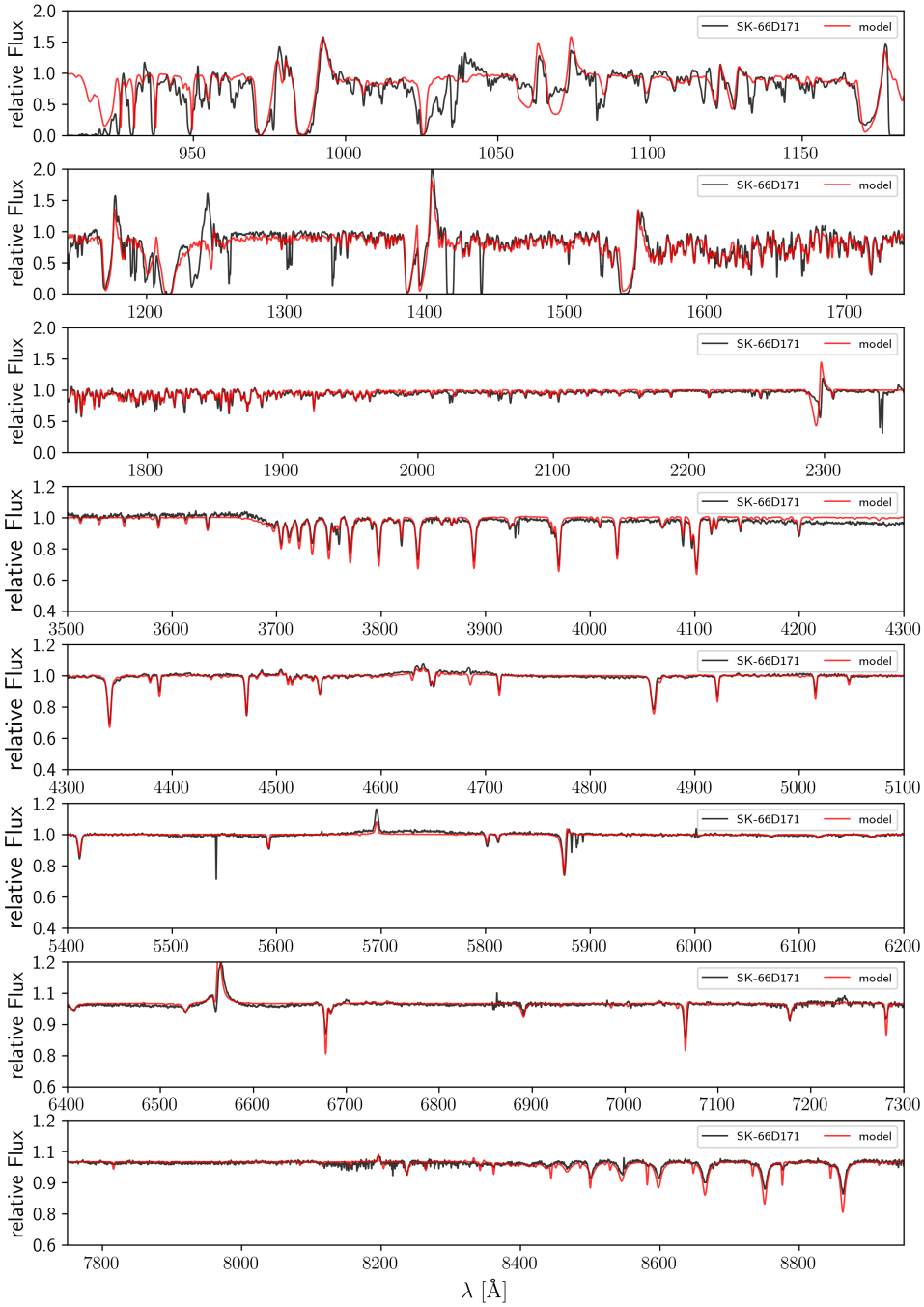


Figure A.18: An overall view of the best fit (red solid line) to key regions of the observed spectrum (black solid line) of Sk −66° 171. From the top, the first panel is the FUV FUSE range, containing interstellar features such as *Lyδ* λ950, *Lyγ* λ973, and *Lyβ* λ1026. Second and third panels are STIS E140M FUV and STIS E230M NUV spectral ranges, respectively, and we note some interstellar features: *Lyα* λ1216, O I + P II λ1302, C II λ1335, Si II λ1527, and Al IIλ1671. The rest of the panels are the UBV and VIS XShooter spectra, with the break between the two arms at ≈ 5600 Å. The lines Ca II H + K and Na I D are interstellar features. For this star, we fit the absorption profiles for *Lyα* through *Lyη*, which were calculated using H I column density $\log N(HI) = 20.7$ cm^{-2} (Fitzpatrick, 1985).

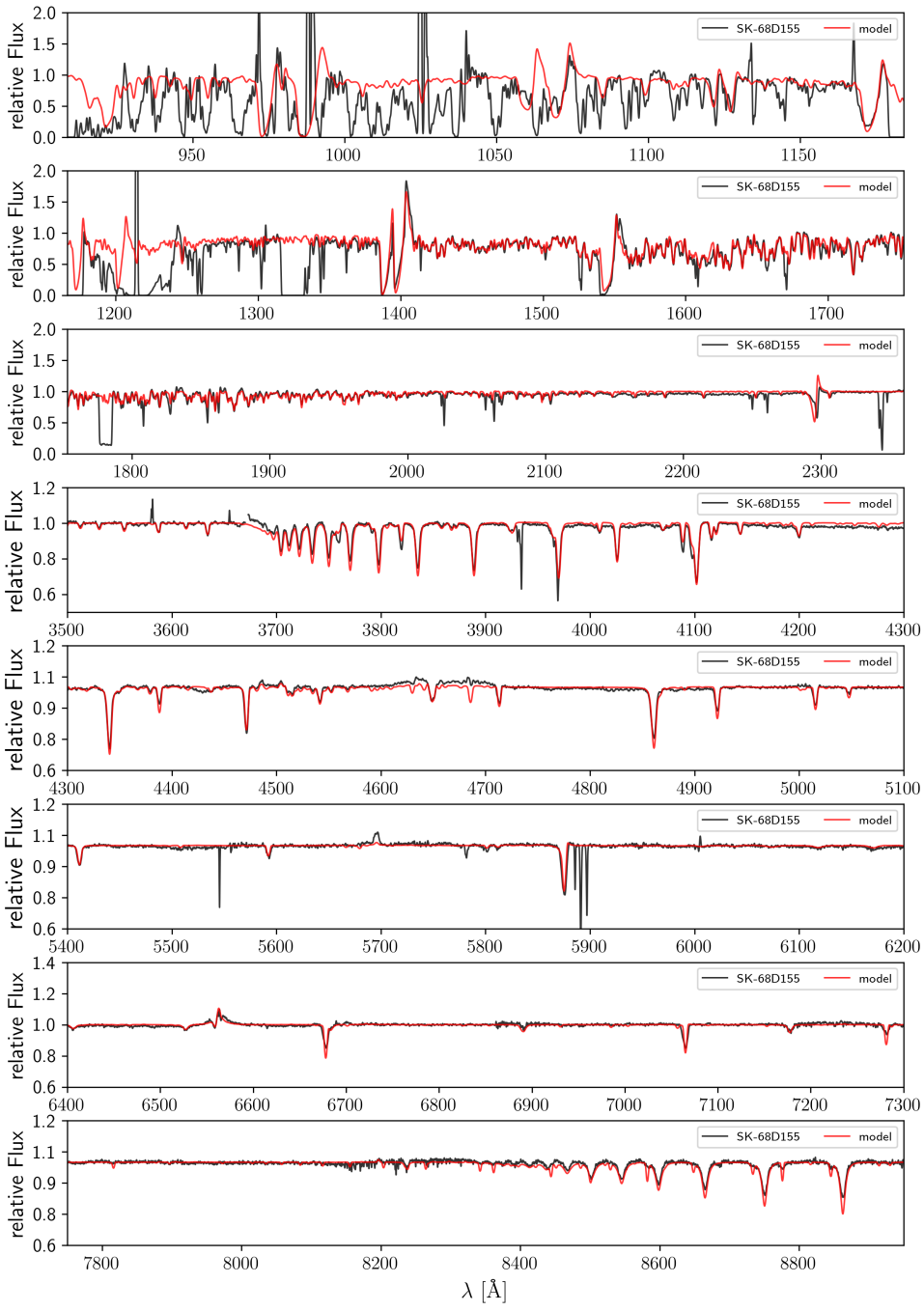


Figure A.19: An overall view of the best fit (red solid line) to key regions of the observed spectrum (black solid line) of Sk −68° 155. From the top, the first panel is the FUV FUSE range, containing interstellar features such as *Lyδ* λ950, *Lyγ* λ973, and *Lyβ* λ1026. The second and third panels are the COS G130M+G160M FUV and STIS E230M NUV spectral ranges, respectively, and we note some interstellar features: *Lyα* λ1216, O I + P II λ1302, C II λ1335, Si II λ1527, and Al IIλ1671. The rest of the panels are the UBV and VIS XShooter spectra, with the break between the two arms at ≈ 5600 Å. The lines Ca II H + K and Na I D are interstellar features.

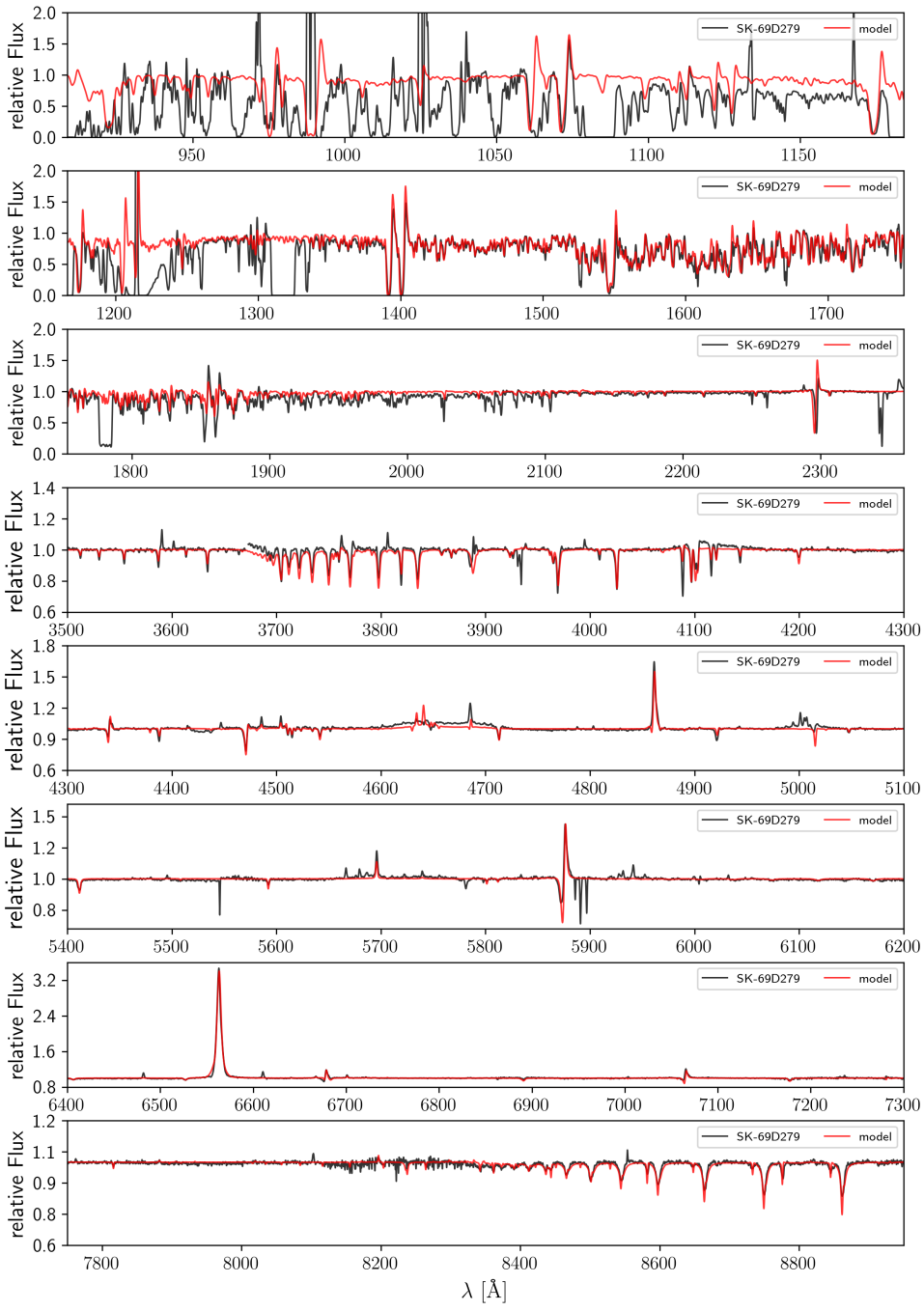


Figure A.20: An overall view of the best fit (red solid line) to key regions of the observed spectrum (black solid line) of Sk −69° 279. From the top, the first panel is the FUV FUSE range, containing interstellar features such as *Lyδ* λ950, *Lyγ* λ973, and *Lyβ* λ1026. Second and third panels are STIS E140M FUV and STIS E230M NUV spectral ranges, respectively, and we note some interstellar features: *Lyα* λ1216, O I + P II λ1302, C II λ1335, Si II λ1527, and Al II λ1671. The rest of the panels are the UBV and VIS XShooter spectra, with the break between the two arms at ≈ 5600 Å. The lines Ca II H + K and Na I D are interstellar features.

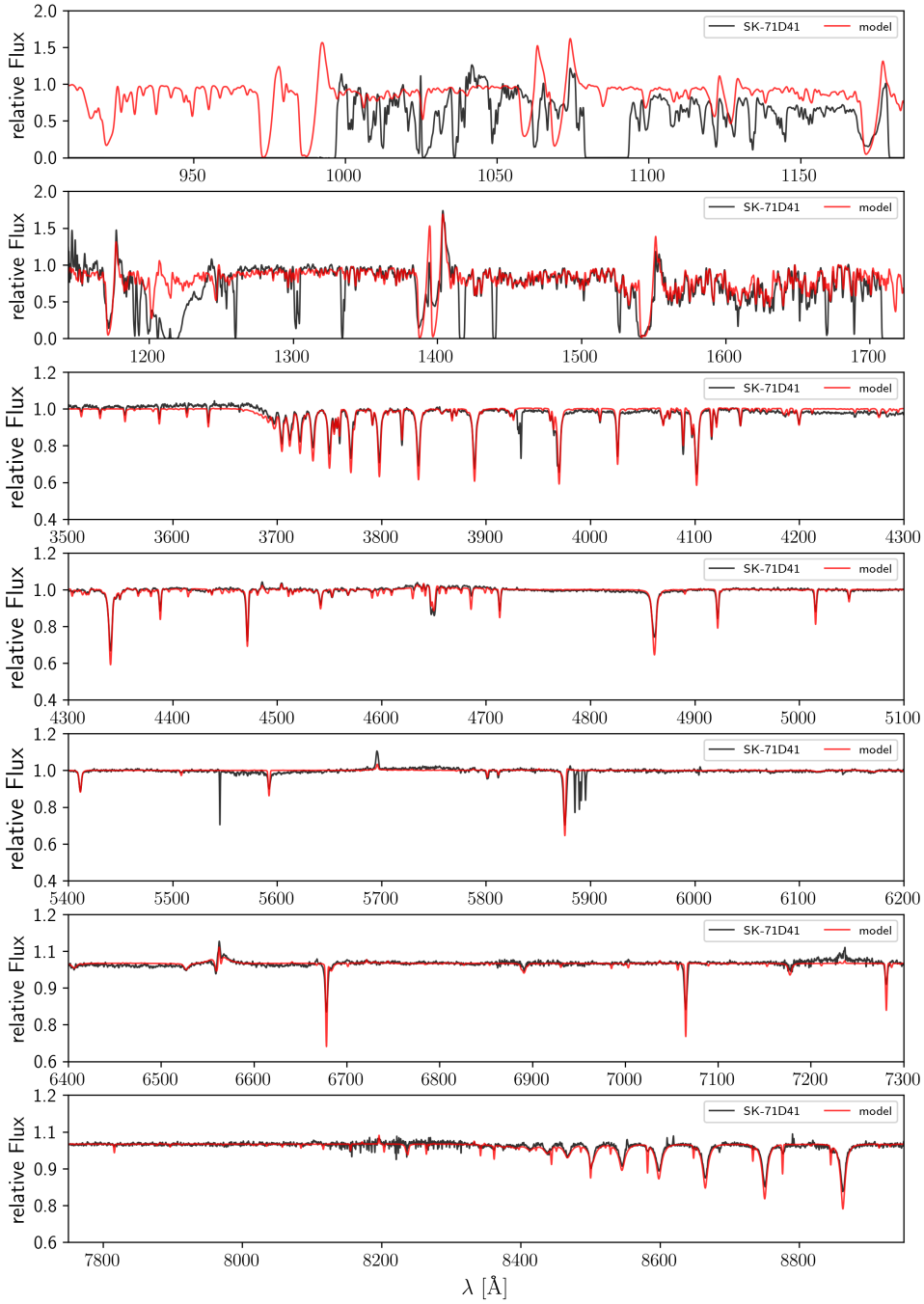


Figure A.21: An overall view of the best fit (red solid line) to key regions of the observed spectrum (black solid line) of Sk −71° 41. From the top, the first panel is the FUV FUSE range, containing interstellar features such as *Lyδ* λ950, *Lyγ* λ973, and *Lyβ* λ1026. Second panel is STIS E140M FUV, and we note some interstellar features: *Lyα* λ1216, O I + P II λ1302, C II λ1335, Si II λ1527, and Al IIλ1671. The rest of the panels are the UBV and VIS XShooter spectra, with the break between the two arms at ≈ 5600 Å. The lines Ca II H + K and Na I D are interstellar features.

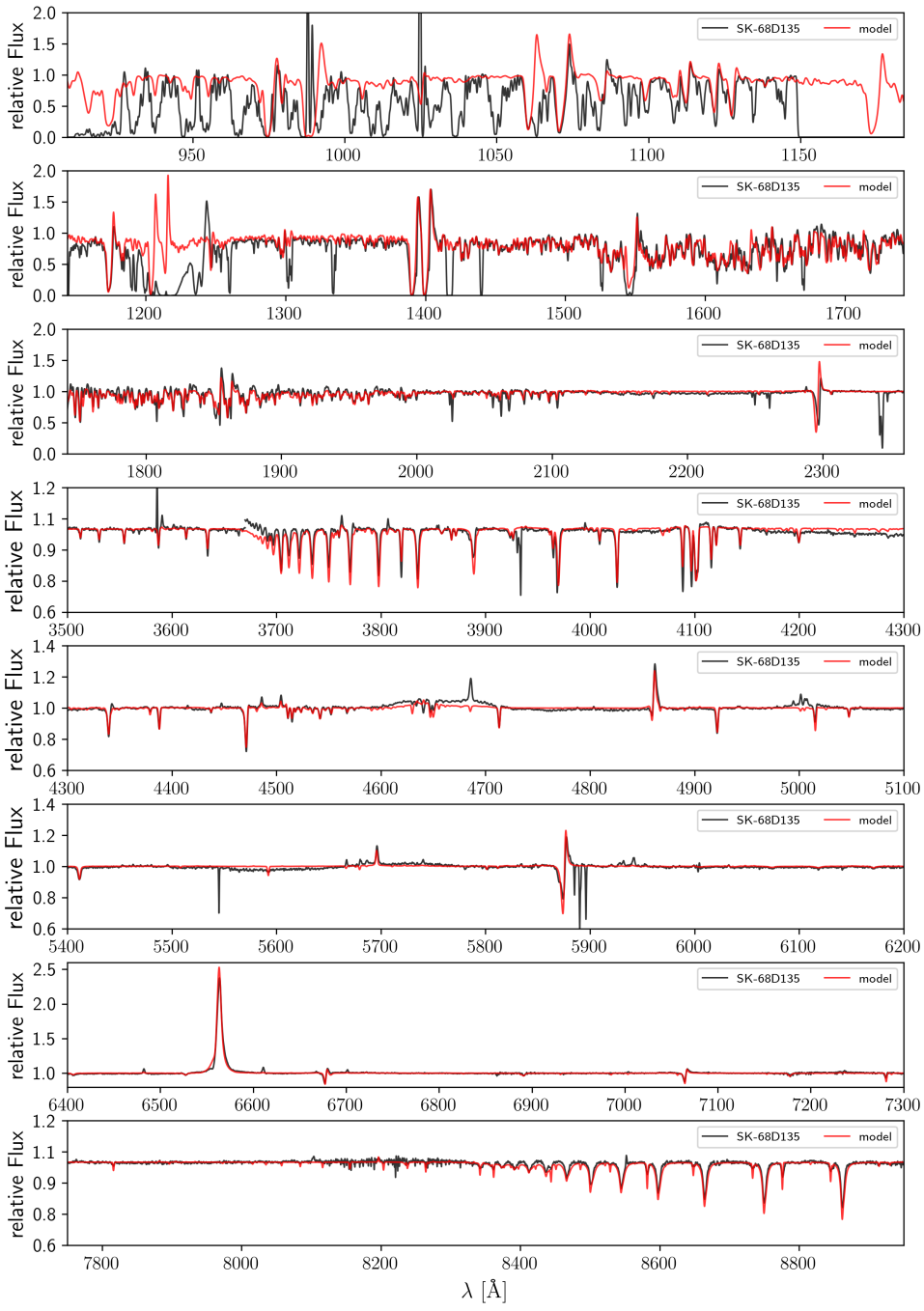


Figure A.22: An overall view of the best fit (red solid line) to key regions of the observed spectrum (black solid line) of Sk −68° 135. From the top, the first panel is the FUV FUSE range, containing interstellar features such as *Lyδ* λ950, *Lyγ* λ973, and *Lyβ* λ1026. Second and third panels are STIS E140M FUV and STIS E230M NUV spectral ranges, respectively, and we note some interstellar features: *Lyα* λ1216, O I + P II λ1302, C II λ1335, Si II λ1527, and Al IIλ1671. The rest of the panels are the UBV and VIS XShooter spectra, with the break between the two arms at ≈ 5600 Å. The lines Ca II H + K and Na I D are interstellar features.

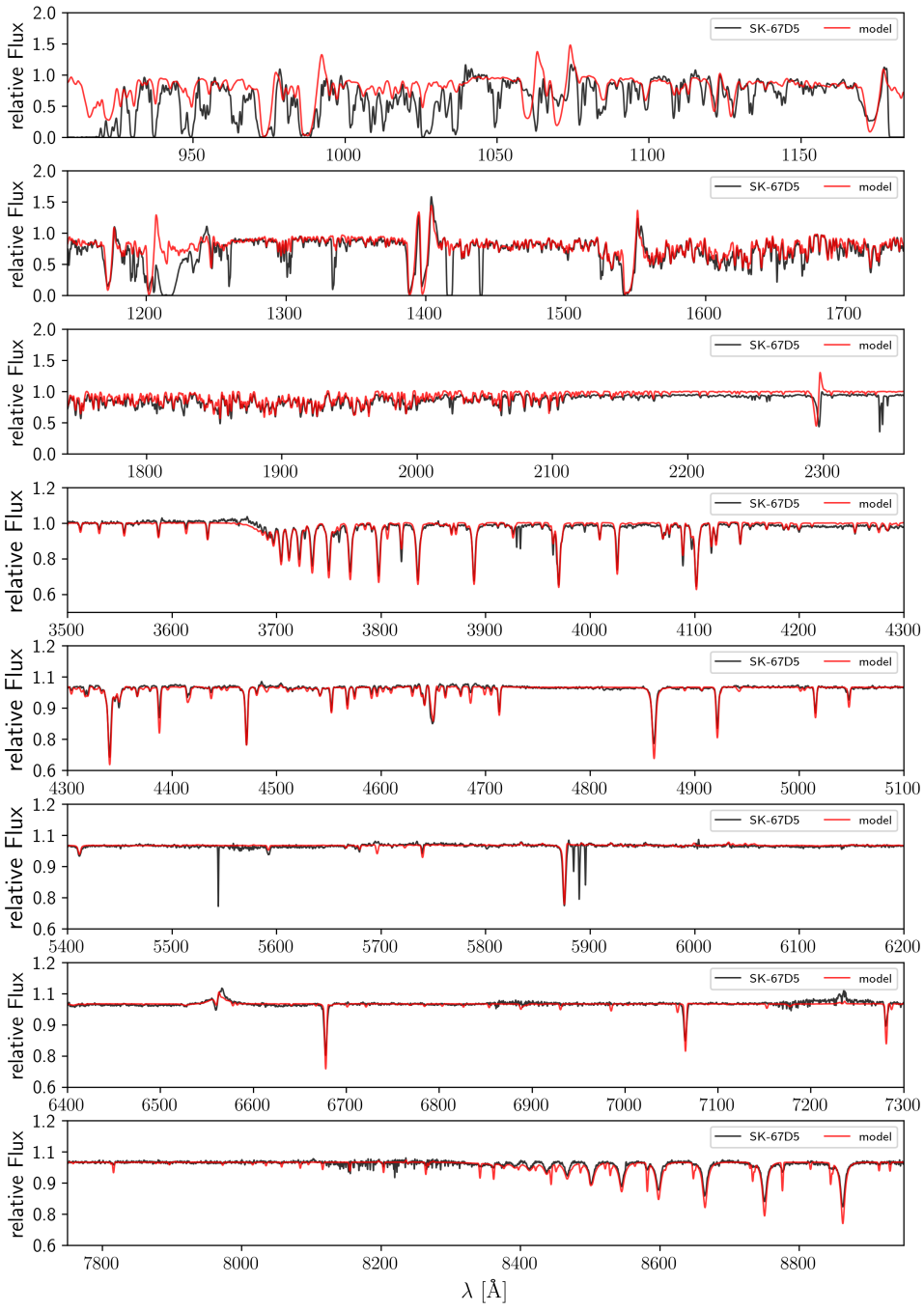


Figure A.23: An overall view of the best fit (red solid line) to key regions of the observed spectrum (black solid line) of Sk −67° 5. From the top, the first panel is the FUV FUSE range, containing interstellar features such as *Lyδ* λ950, *Lyγ* λ973, and *Lyβ* λ1026. Second and third panels are STIS E140M FUV and STIS E230M NUV spectral ranges, respectively, and we note some interstellar features: *Lyα* λ1216, O I + P II λ1302, C II λ1335, Si II λ1527, and Al IIλ1671. The rest of the panels are the UBV and VIS XShooter spectra, with the break between the two arms at ≈ 5600 Å. The lines Ca II H + K and Na I D are interstellar features.

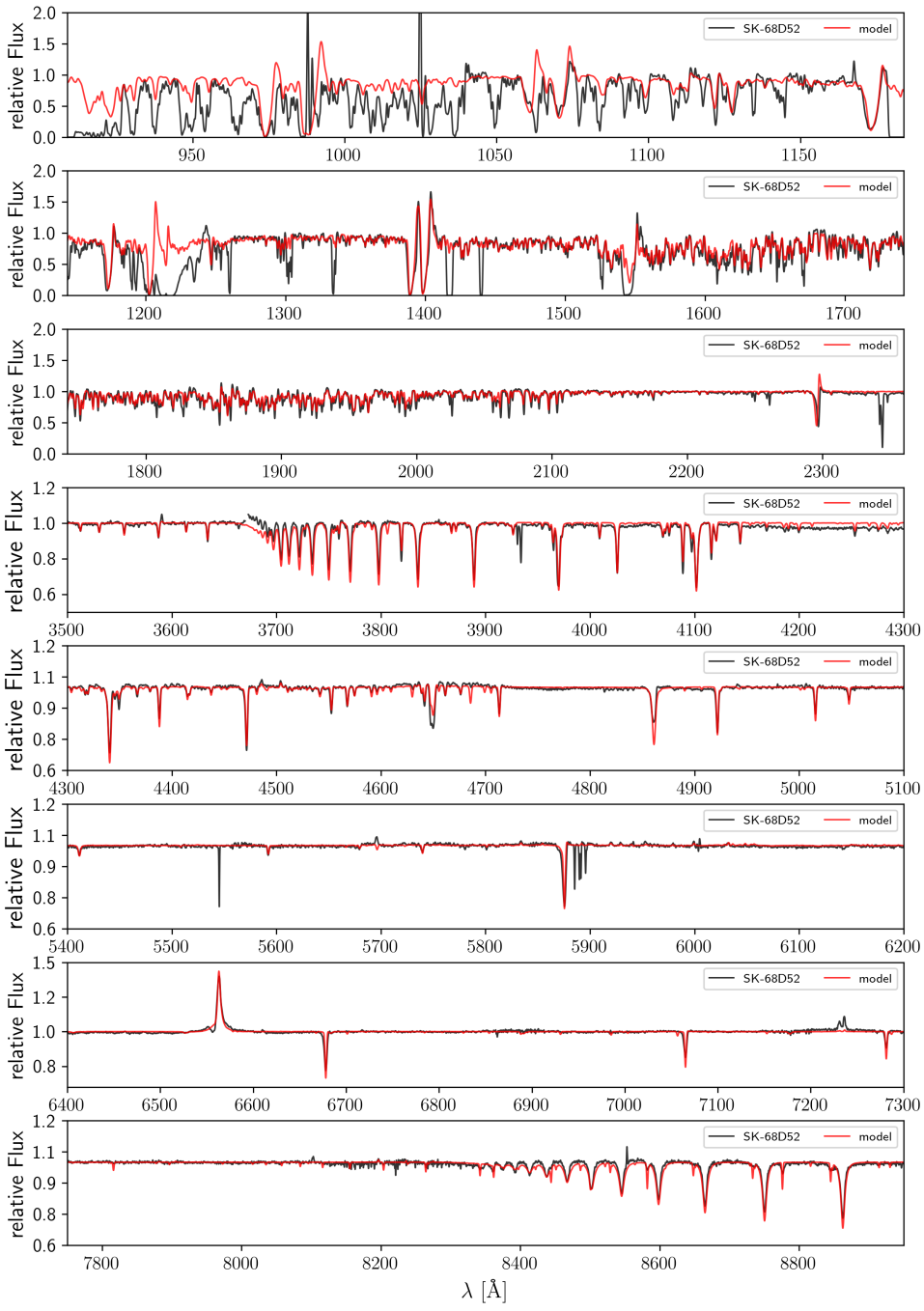


Figure A.24: An overall view of the best fit (red solid line) to key regions of the observed spectrum (black solid line) of Sk −68° 52. From the top, the first panel is the FUV FUSE range, containing interstellar features such as *Lyδ* λ950, *Lyγ* λ973, and *Lyβ* λ1026. Second and third panels are STIS E140M FUV and STIS E230M NUV spectral ranges, respectively, and we note some interstellar features: *Lyα* λ1216, O I + P II λ1302, C II λ1335, Si II λ1527, and Al IIλ1671. The rest of the panels are the UBV and VIS XShooter spectra, with the break between the two arms at ≈ 5600 Å. The lines Ca II H + K and Na I D are interstellar features.

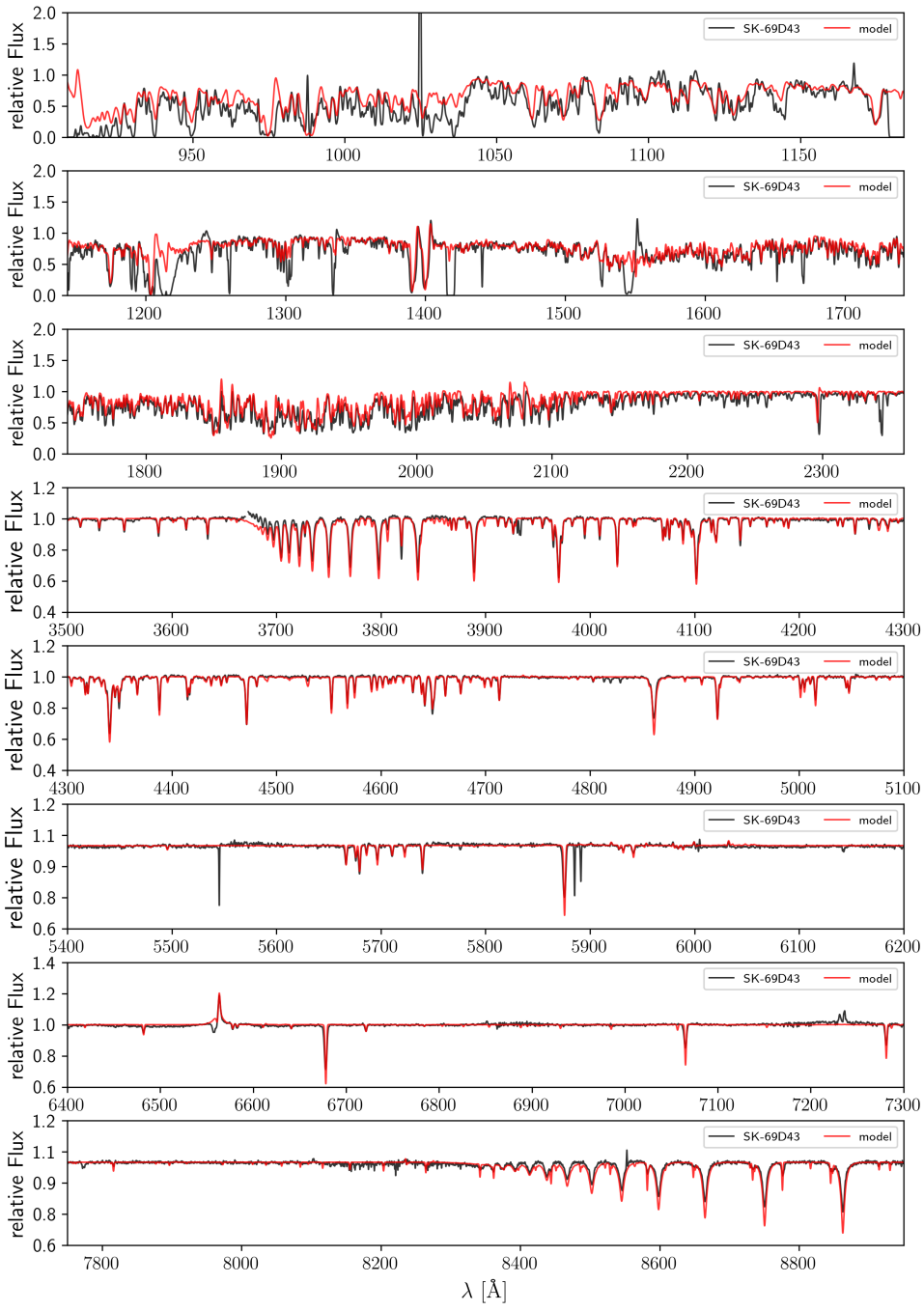


Figure A.25: An overall view of the best fit (red solid line) to key regions of the observed spectrum (black solid line) of Sk −69° 43. From the top, the first panel is the FUV FUSE range, containing interstellar features such as *Lyδ* λ950, *Lyγ* λ973, and *Lyβ* λ1026. Second and third panels are STIS E140M FUV and STIS E230M NUV spectral ranges, respectively, and we note some interstellar features: *Lyα* λ1216, O I + P II λ1302, C II λ1335, Si II λ1527, and Al IIλ1671. The rest of the panels are the UBV and VIS XShooter spectra, with the break between the two arms at ≈ 5600 Å. The lines Ca II H + K and Na I D are interstellar features.

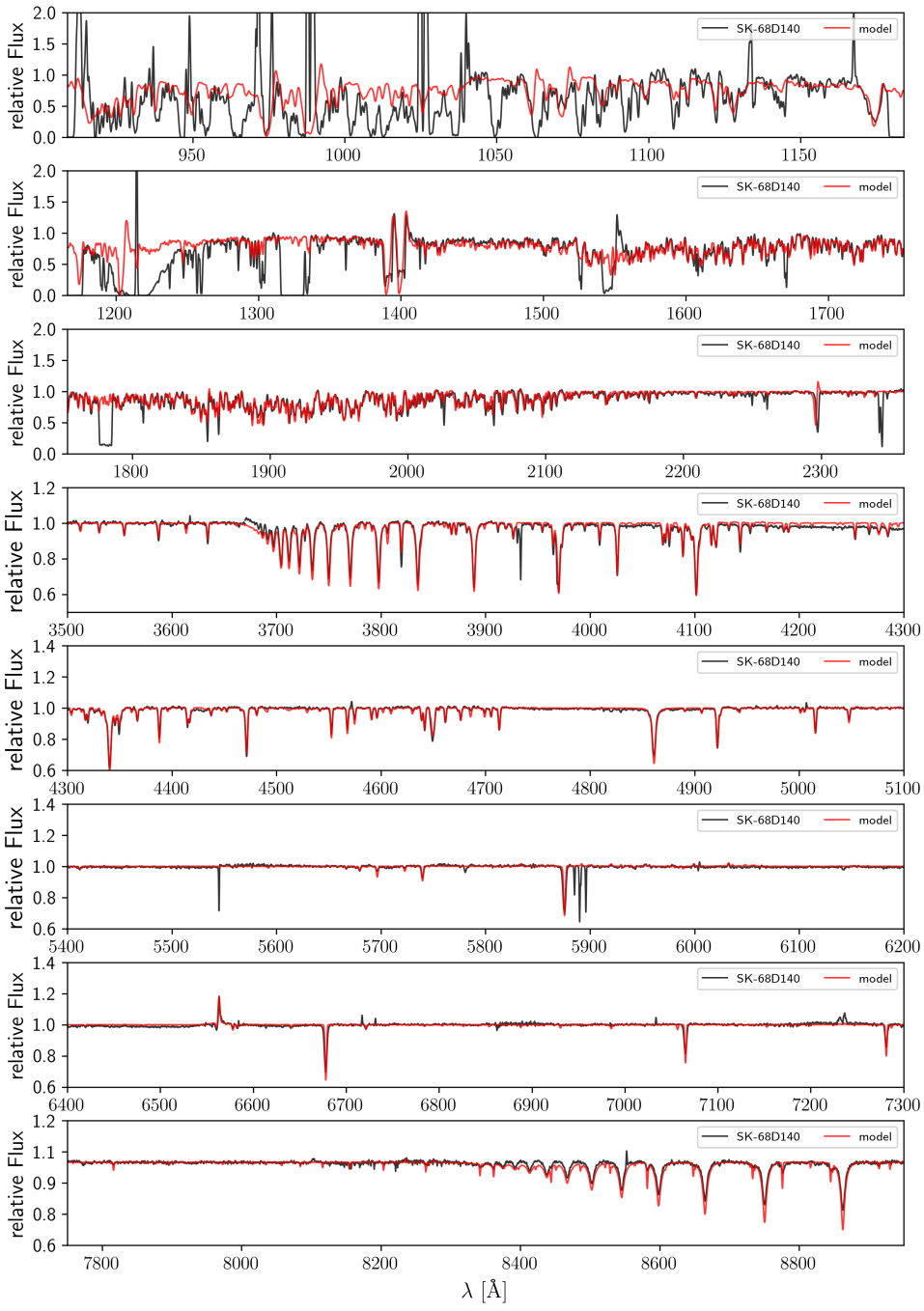


Figure A.26: An overall view of the best fit (red solid line) to key regions of the observed spectrum (black solid line) of Sk −68° 140. From the top, the first panel is the FUV FUSE range, containing interstellar features such as *Lyδ* λ950, *Lyγ* λ973, and *Lyβ* λ1026. Second and third panels are COS G130M+G160M FUV and STIS E230M NUV spectral ranges, respectively, and we note some interstellar features: *Lyα* λ1216, O I + P II λ1302, C II λ1335, Si II λ1527, and Al IIλ1671. The rest of the panels are the UBV and VIS XShooter spectra, with the break between the two arms at ≈ 5600 Å. The lines Ca II H + K and Na I D are interstellar features.

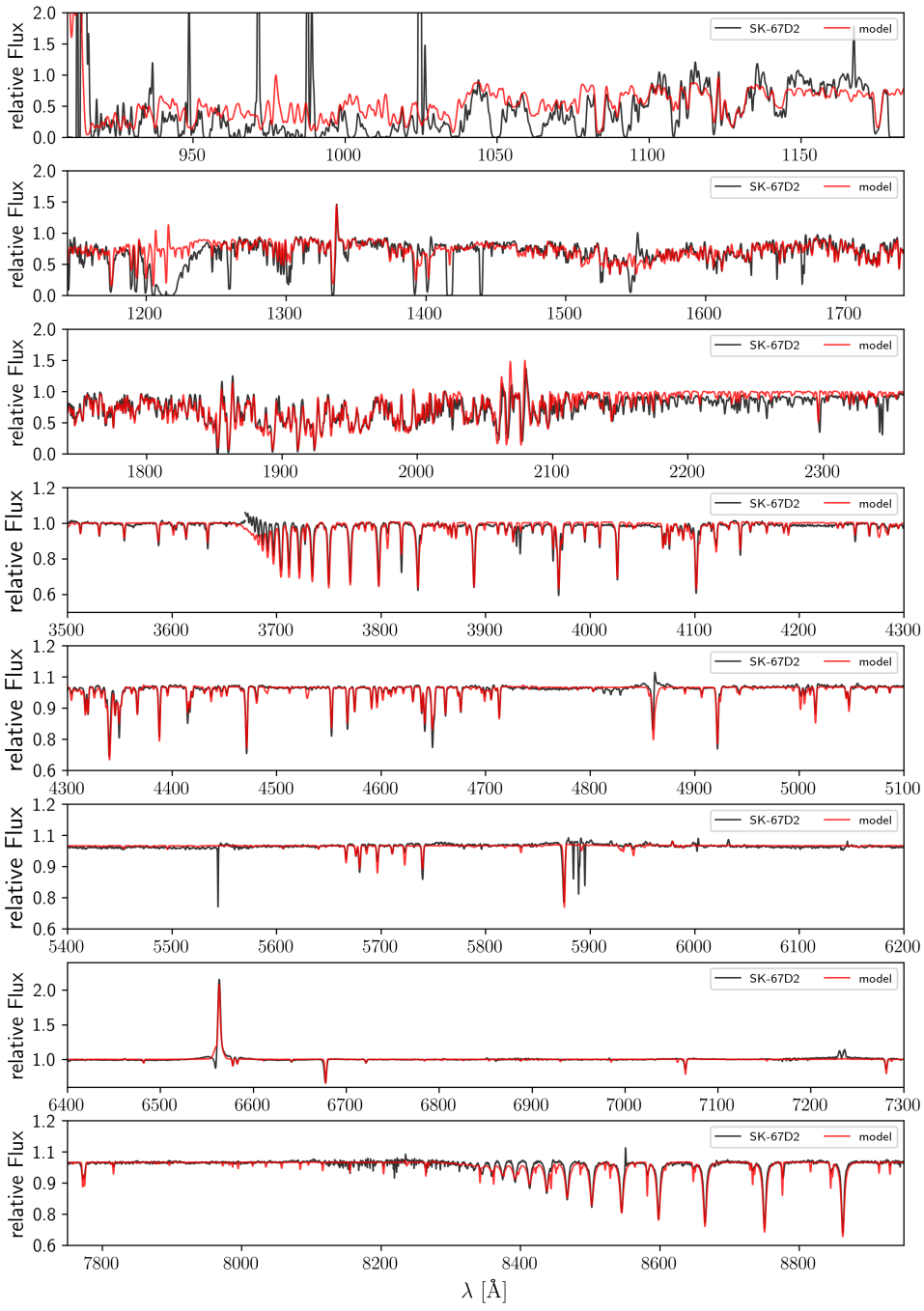


Figure A.27: An overall view of the best fit (red solid line) to key regions of the observed spectrum (black solid line) of Sk −67° 2. From the top, the first panel is the FUV FUSE range, containing interstellar features such as *Lyδ* λ950, *Lyγ* λ973, and *Lyβ* λ1026. Second and third panels are STIS E140M FUV and STIS E230M NUV spectral ranges, respectively, and we note some interstellar features: *Lyα* λ1216, O I + P II λ1302, C II λ1335, Si II λ1527, and Al IIλ1671. The rest of the panels are the UBV and VIS XShooter spectra, with the break between the two arms at ≈ 5600 Å. The lines Ca II H + K and Na I D are interstellar features.

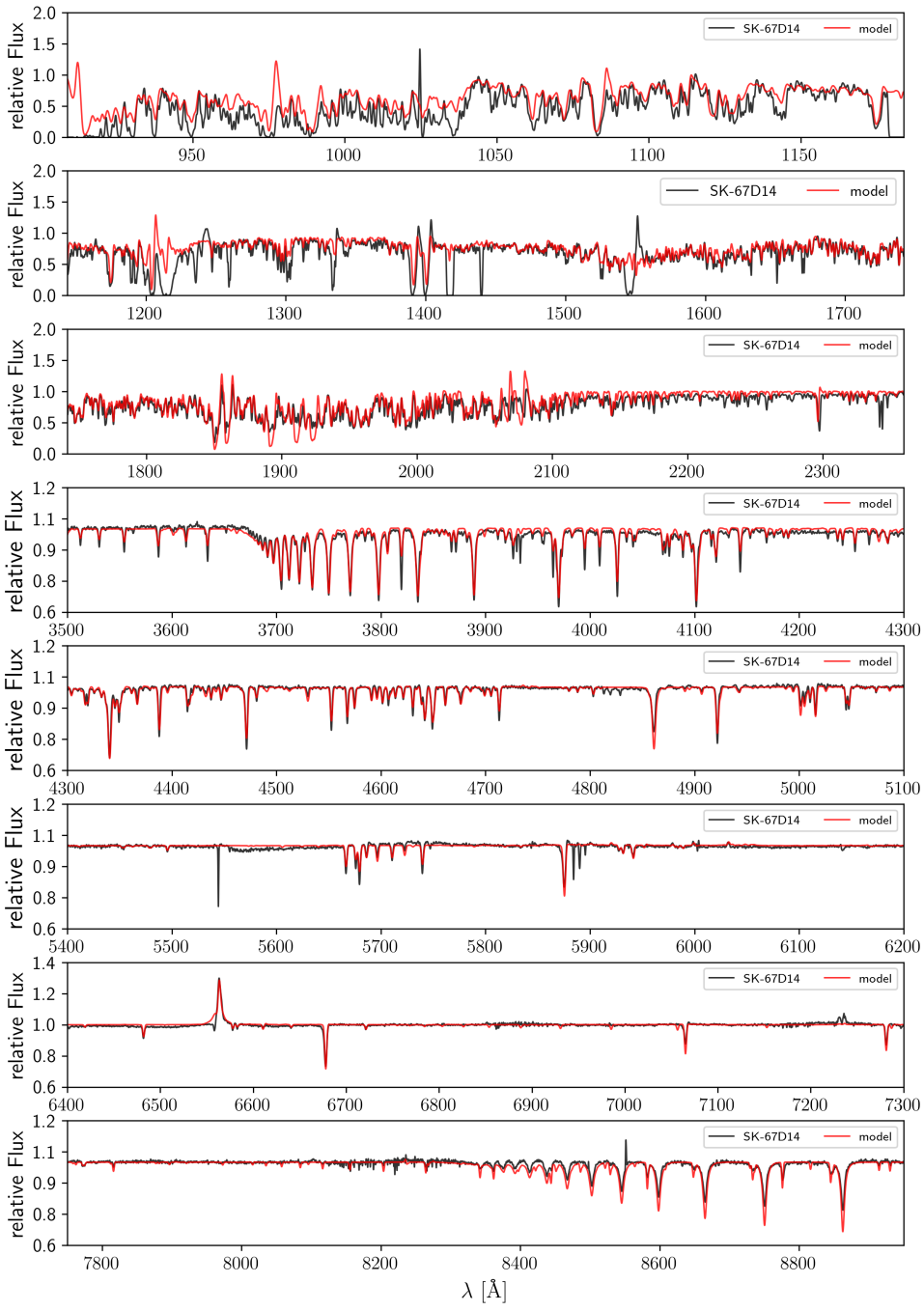


Figure A.28: An overall view of the best fit (red solid line) to key regions of the observed spectrum (black solid line) of Sk −67° 14. From the top, the first panel is the FUV FUSE range, containing interstellar features such as *Lyδ* λ950, *Lyγ* λ973, and *Lyβ* λ1026. Second and third panels are COS G130M+G160M FUV and STIS E230M NUV spectral ranges, respectively, and we note some interstellar features: *Lyα* λ1216, O I + P II λ1302, C II λ1335, Si II λ1527, and Al IIλ1671. The rest of the panels are the UBV and VIS XShooter spectra, with the break between the two arms at ≈ 5600 Å. The lines Ca II H + K and Na I D are interstellar features.

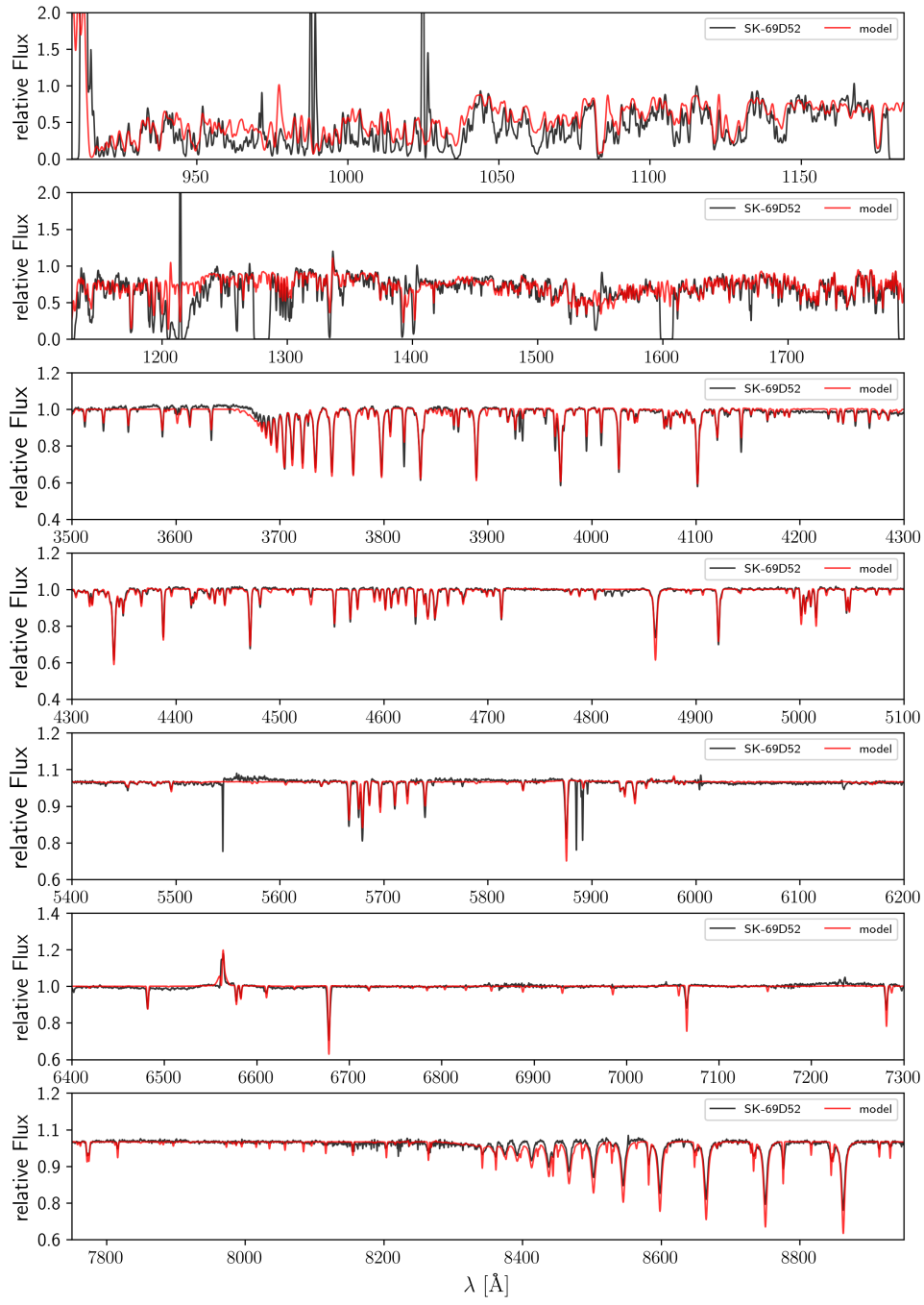


Figure A.29: An overall view of the best fit (red solid line) to key regions of the observed spectrum (black solid line) of Sk −69° 52. From the top, the first panel is the FUV FUSE range, containing interstellar features such as *Lyδ* λ950, *Lyγ* λ973, and *Lyβ* λ1026. Second and third panels are COS G130M+G160M FUV and STIS E230M NUV spectral ranges, respectively, and we note some interstellar features: *Lyα* λ1216, O I + P II λ1302, C II λ1335, Si II λ1527, and Al II λ1671. The rest of the panels are the UBV and VIS XShooter spectra, with the break between the two arms at ≈ 5600 Å. The lines Ca II H + K and Na I D are interstellar features.

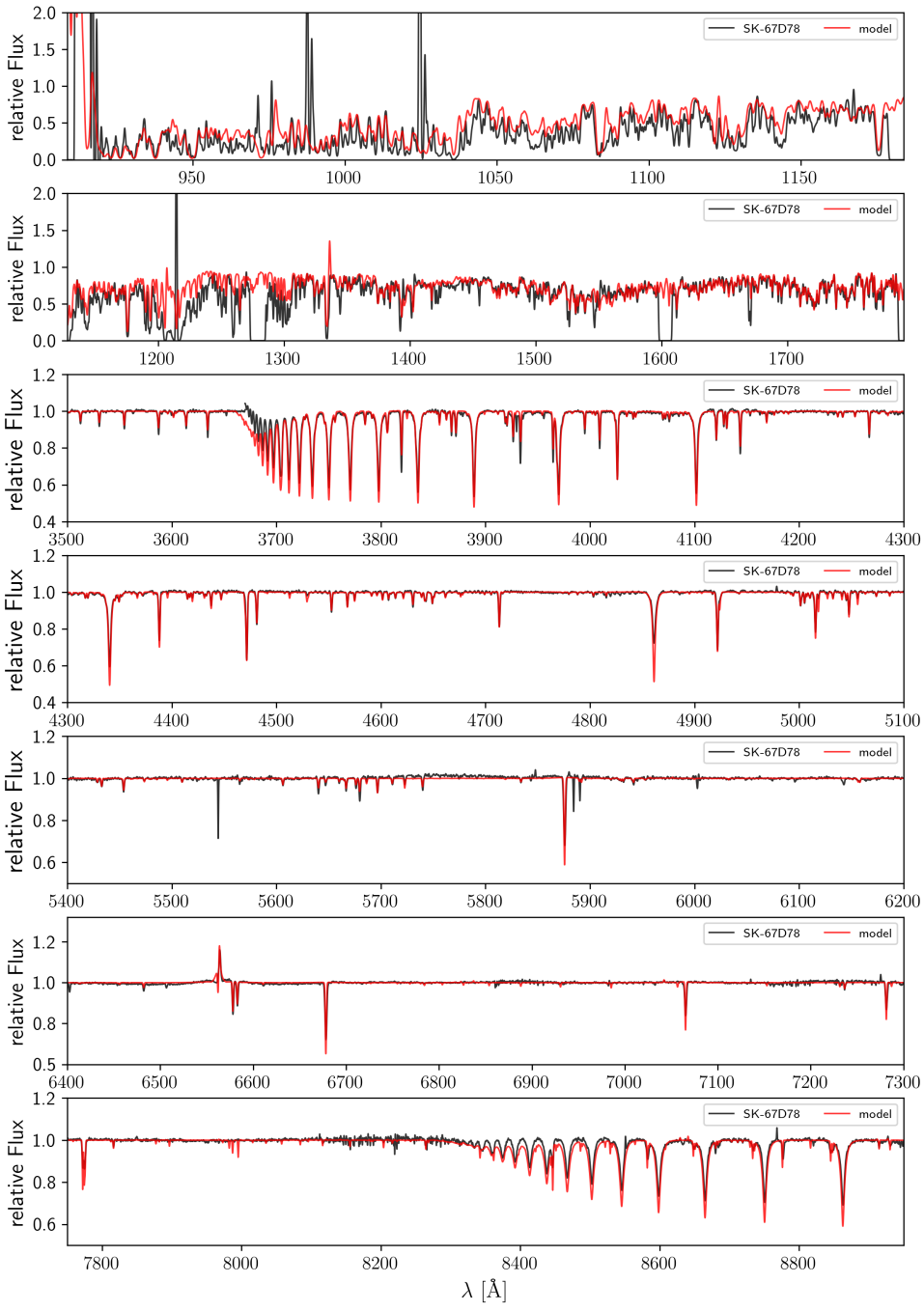


Figure A.30: An overall view of the best fit (red solid line) to key regions of the observed spectrum (black solid line) of Sk −67° 78. From the top, the first panel is the FUV FUSE range, containing interstellar features such as *Lyδ* λ950, *Lyγ* λ973, and *Lyβ* λ1026. Second and third panels are COS G130M+G160M FUV and STIS E230M NUV spectral ranges, respectively, and we note some interstellar features: *Lyα* λ1216, O I + P II λ1302, C II λ1335, Si II λ1527, and Al II λ1671. The rest of the panels are the UBV and VIS XShooter spectra, with the break between the two arms at ≈ 5600 Å. The lines Ca II H + K and Na I D are interstellar features.

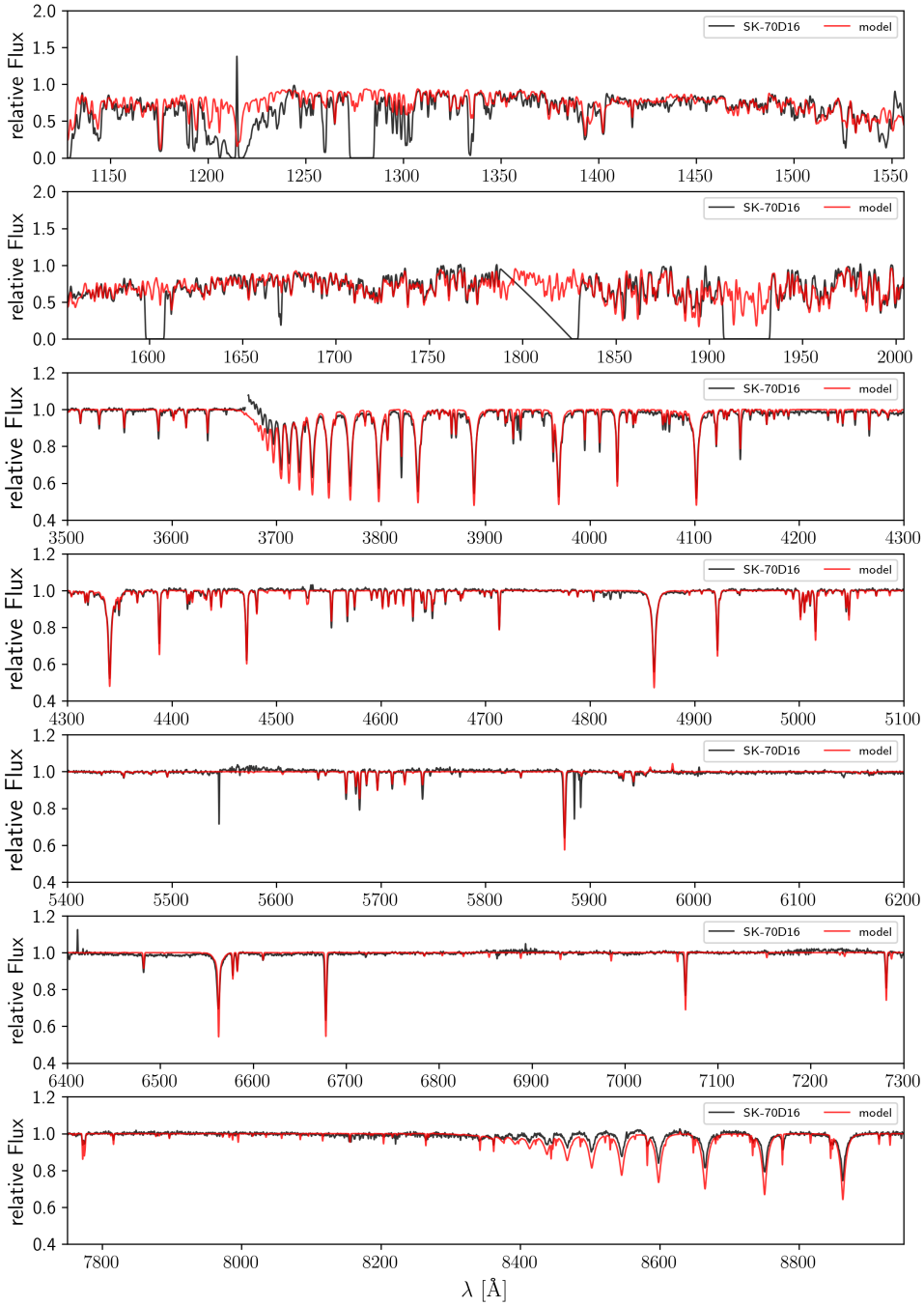


Figure A.31: An overall view of the best fit (red solid line) to key regions of the observed spectrum (black solid line) of Sk −70° 16. From the top, the first and second panels are COS G130M+G160M FUV and COS G160M+G185M NUV spectral ranges, respectively, and we note some interstellar features: *Lyα* λ1216, O I + P II λ1302, C II λ1335, Si II λ1527, and Al II λ1671. The rest of the panels are the UBV and VIS XShooter spectra, with the break between the two arms at ≈ 5600 Å. The lines Ca II H + K and Na I D are interstellar features.

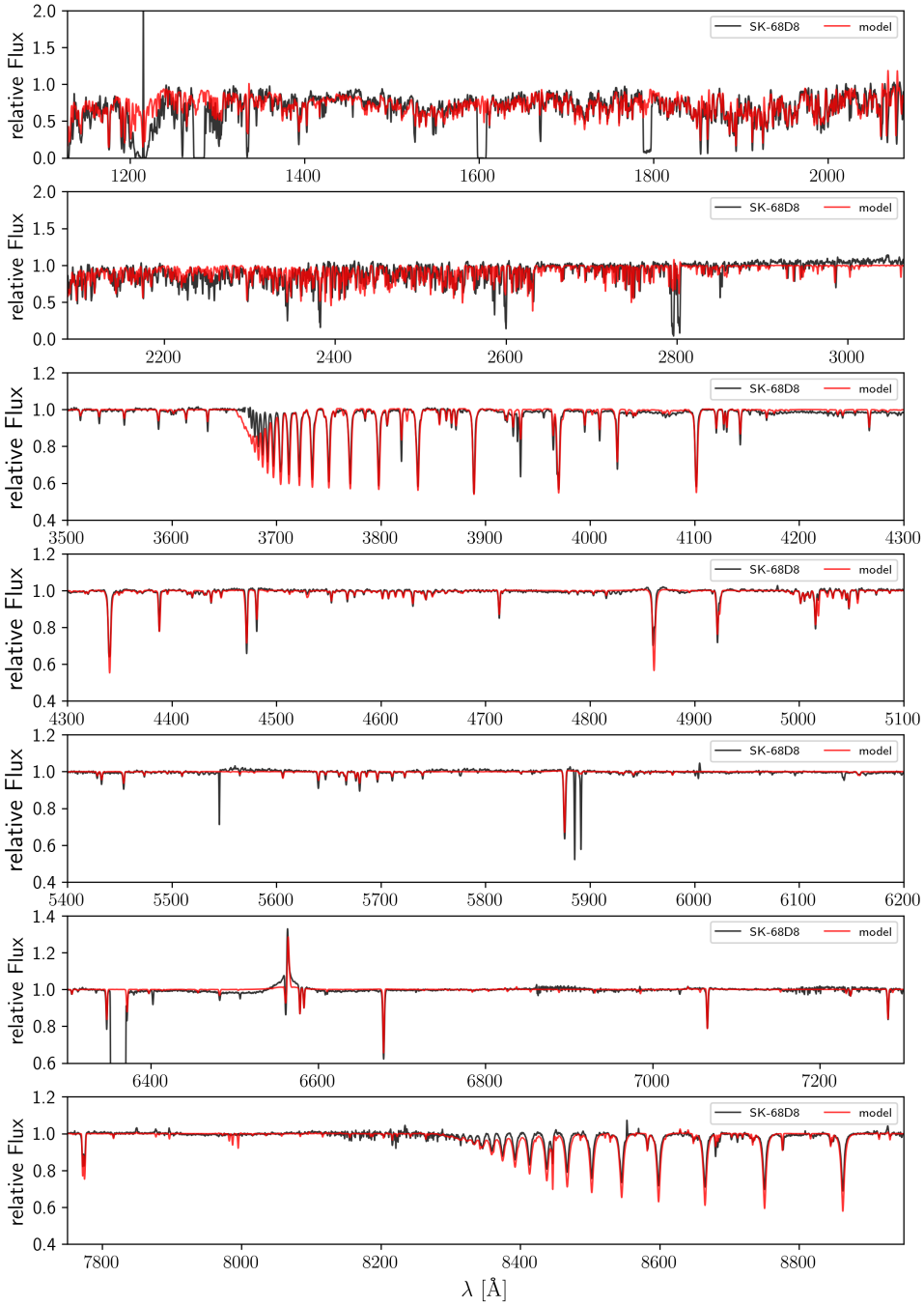


Figure A.32: An overall view of the best fit (red solid line) to key regions of the observed spectrum (black solid line) of Sk −68° 8. From the top, the first and second panels are COS G130M+G160M FUV and STIS E230M NUV spectral ranges, respectively, and we note some interstellar features: *Lyα* λ1216, O I + P II λ1302, C II λ1335, Si II λ1527, and Al IIλ1671. The rest of the panels are the UBV and VIS XShooter spectra, with the break between the two arms at ≈ 5600 Å. The lines Ca II H + K and Na I D are interstellar features.

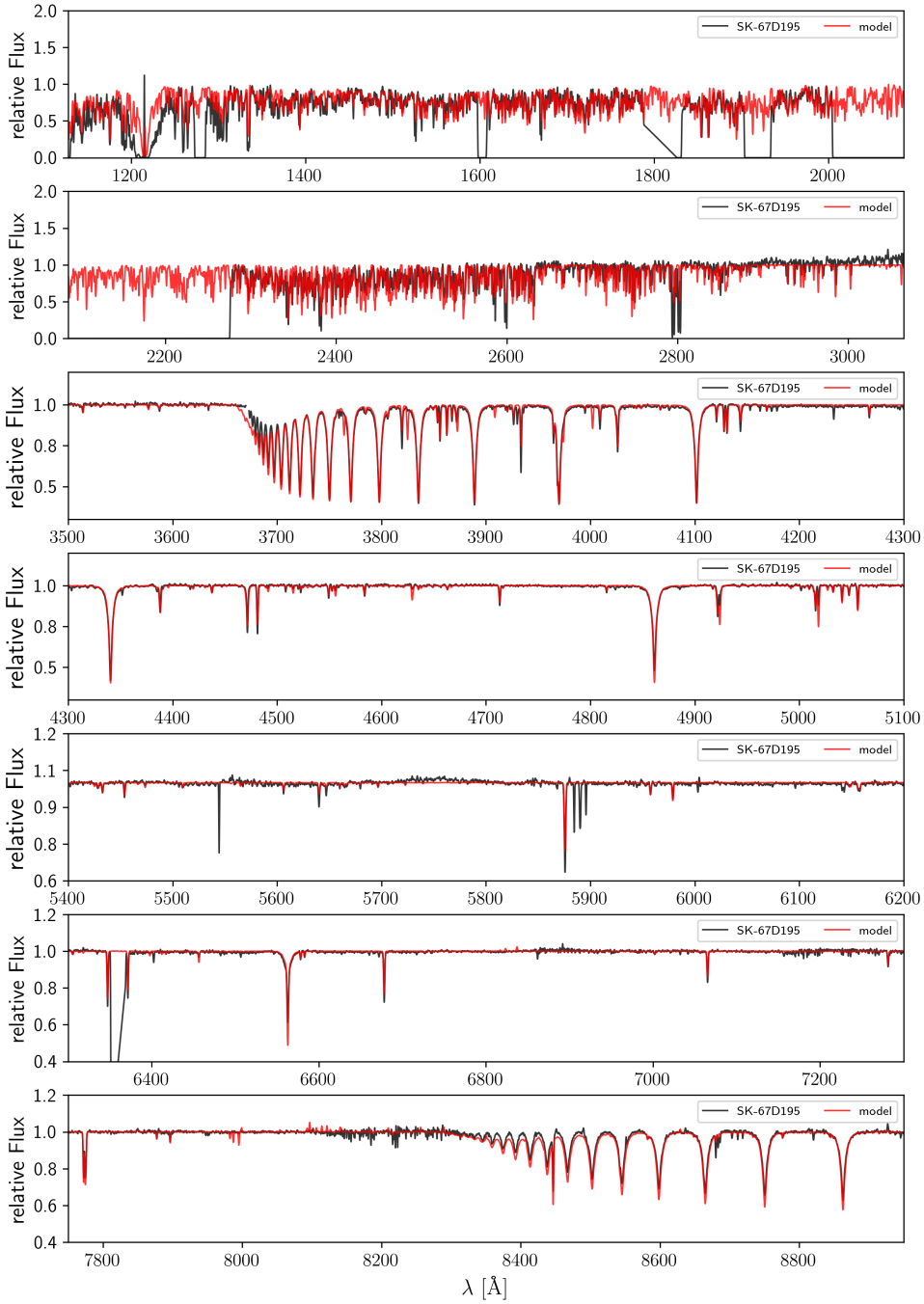


Figure A.33: An overall view of the best fit (red solid line) to key regions of the observed spectrum (black solid line) of Sk −67° 195. From the top, the first and second panels are COS G130M+G160M FUV and STIS E230M NUV spectral ranges, respectively, and we note some interstellar features: *Lyα* λ1216, O I + P II λ1302, C II λ1335, Si II λ1527, and Al II λ1671. The rest of the panels are the UBV and VIS XShooter spectra, with the break between the two arms at ≈ 5600 Å. The lines Ca II H + K and Na I D are interstellar features.

A.8 FM90 parameters

Table A.3: Fitting parameters of the UV reddening law.

Target	c_1	c_2	c_3	c_4	x_0	γ
Sk −66° 171	-2.50	1.33	1.10	0.10	4.63	0.90
Sk −68° 155	-1.85	1.41	1.20	0.16	4.62	0.80
Sk −69° 279	-1.50	1.25	1.20	0.14	4.62	0.80
Sk −71° 41	-1.00	1.04	0.90	0.30	4.69	1.15
Sk −68° 135	-2.50	1.41	1.05	0.16	4.65	0.90
Sk −67° 5	-1.80	1.18	0.60	0.10	4.63	0.69
Sk −68° 52	-2.50	1.30	0.93	0.05	4.63	0.82
Sk −69° 43	-1.90	1.12	1.20	0.17	4.63	0.90
Sk −68° 140	-2.30	1.37	1.60	0.14	4.62	1.00
Sk −67° 2	-2.20	1.55	1.95	0.60	4.65	0.90
Sk −67° 14	-2.10	1.55	0.50	0.35	4.63	0.90
Sk −69° 52	-2.10	1.10	1.20	0.30	4.60	0.90
Sk −67° 78	-1.90	1.23	1.20	0.40	4.70	0.90
Sk −70° 16	-1,90	1.08	2.80	0.18	5.13	0.90
Sk −68° 8	-2.00	1.14	4.90	0.58	4.69	1.15
Sk −67° 195	-2.70	1.54	1.35	0.90	4.67	0.90

Appendix B

SMC Appendix

B.1 $v_{\rm black}$ and $v_{\rm edge}$

In Table B.1 we present the measured $v_{\rm edge}$ and $v_{\rm black}$ from each line for all our samples. We obtain $v_{\rm edge}$ and v_{∞} from all the available P Cygni line profiles in the UV. Single velocity measurement from each line is subject to an uncertainty $\Delta v = 30$ km s^{-1} which takes into account the velocity resolution of the UV spectra and the uncertainty in the radial velocity correction, which were added in quadrature.

Table B.1: $v_{\rm edge}$ and $v_{\rm black}$ for the stars in our sample.

	$v_{\rm edge}$					
Target	Si IV 1393Å	Si IV 1403Å	C IV 1548Å	Al III 1855Å	Al III 1863Å	$\overline{v_{\rm black}}/\overline{v_{\rm edge}}$
AzV 469	2190	-	2133	-	-	0.84
AzV 372	1944	-	-	-	-	0.78
AzV 456	1655	-	2327	-	-	-
AzV 327	1935	-	1976	-	-	-
AzV 235	1653	-	1633	-	-	-
AzV 215	1935	-	2060	-	-	-
AzV 104	-	-	1255	-	-	-
AzV 410	1218	-	1280	-	-	-
AzV 242	1105	-	1270	-	-	-
AzV 96	972	-	956	-	-	-
AzV 264	827	-	-	-	-	-
AzV 175	222	-	224	-	-	-
Sk 191	620	594	600	582	-	0.76
AzV 18	507	-	472	-	-	-
NG330-ELS-04	515	-	-	-	-	-
AzV 187	589	588	575	-	-	-
AzV 22	190	173	206	222	230	-
AzV 393	319	-	279	-	-	-
AzV 343	285	251	282	-	-	-
AzV 324	259	207	220	210	-	-
	$v_{\rm black}$					
Target	Si IV 1393Å	Si IV 1403 Å	C IV 1548Å	Al III 1855Å	Al III 1863Å	$\overline{v_{\rm black}}$ km s^{-1}
AzV 469	-	-	1814	-	-	1814
AzV 372	-	-	1516	-	-	1516
Sk 191	474	440	451	-	-	455

B.2 Comparison to literature

The volume-filling factor for studies that used the optically thick clumping implementation in FASTWIND is calculated from the equation introduced in Sander et al. (2024) following:

$$f_{\mathrm{vol},\infty} = \frac{(1 - f_{\mathrm{ic}})^2}{f_{\mathrm{cl}} - 2f_{\mathrm{ic}} + f_{\mathrm{ic}}^2}, \tag{B.1}$$

where $f_{\mathrm{cl}} = \langle\rho^2\rangle/\langle\rho\rangle^2$ describes the contrast between the density in the clump and the mean density, and f_{ic} describes the contrast between the clump density and the density of the inter-clump medium.

Table B.2: Comparison of derived parameters to previous studies.

Target	$T_{\rm eff}$ kK	$\log g$ cm s^{-2}	$\log L$ $L_\odot$	$\log \dot{M}$ $M_\odot$ yr^{-1}	$f_{\rm vol,\infty}$	β	Ref.	wavelength	Code
AzV 469	32.0	3.30	5.55	-7.00	0.2	1.0	This study	UV+OPT	C
	$31.9^{+1.2}_{-1.6}$	$3.12^{+0.1}_{-0.2}$	$5.51^{+0.1}_{-0.1}$	$-6.61^{+0.2}_{-0.2}$	0.1	1.0	JB+25	OPT	F
	$34.5^{+1.0}_{-1.0}$	$3.36^{+0.1}_{-0.1}$	$5.67^{+0.0}_{-0.0}$	$-6.27^{+0.2}_{-0.1}$	0.34	1.1	FB+24	UV+OPT	F
	-	-	-	-6.46	-	-	LIME	-	-
AzV 372	29.2	3.02	5.68	-6.76	0.1	1.0	This study	UV+OPT	C
	$28.3^{+1.2}_{-1.2}$	$2.88^{+0.2}_{-0.1}$	$5.56^{+0.1}_{-0.1}$	$-6.23^{+0.2}_{-0.2}$	0.1	1.0	JB+25	OPT	F
	$30.8^{+1.5}_{-1.2}$	$3.1^{+0.2}_{-0.1}$	$5.76^{+0.1}_{-0.0}$	$-6.02^{+0.3}_{-0.2}$	0.42	1.8	FB+24	UV+OPT	F
	-	-	-	-6.4	-	-	LIME	-	-
AzV 456	30.7	3.35	5.91	-7.57	0.1	1.0	This study	UV+OPT	C
	$29.9^{+1.2}_{-1.2}$	$3.31^{+0.1}_{-0.1}$	$5.87^{+0.1}_{-0.1}$	$-6.32^{+0.2}_{-0.3}$	0.1	1.0	JB+25	OPT	F
	-	-	-	-6.27	-	-	LIME	-	-
AzV 327	30.5	3.32	5.47	-8.12	0.03	1.0	This study	UV+OPT	C
	$29.9^{+1.2}_{-1.2}$	$3.31^{+0.1}_{-0.1}$	$5.40^{+0.1}_{-0.1}$	$-7.1^{+0.4}_{-1.5}$	0.1	1.0	JB+25	OPT	F
	$29.5^{+0.2}_{-1.0}$	$3.28^{+0.2}_{-0.1}$	$5.41^{+0.0}_{-0.0}$	$-7.41^{+0.2}_{-0.4}$	0.67	0.8	FB+24	UV+OPT	F
	-	-	-	-6.65	-	-	LIME	-	-
AzV 235	27.1	2.99	5.86	-6.66	0.05	1.5	This study	UV+OPT	C
	$28.3^{+1.2}_{-1.6}$	$3.5^{+0.2}_{-0.1}$	$6.01^{+0.1}_{-0.1}$	$-5.65^{+0.8}_{-0.2}$	0.1	1.0	JB+25	OPT	F
	27.5	3.05	5.82	-6.17	0.02	2.4	BP+24	UV+OPT	C
	-	-	-	-6.39	-	-	LIME	-	-
AzV 215	27.1	2.96	5.62	-7.17	0.1	1.7	This study	UV+OPT	C
	$25.2^{+2.3}_{-1.2}$	$2.69^{+0.3}_{-0.1}$	$5.51^{+0.2}_{-0.1}$	$-6.11^{+0.2}_{-0.2}$	0.1	1.0	JB+25	OPT	F
	27.0	2.9	5.63	-6.44	0.2	2.8	BP+24	UV+OPT	C
	$27.0^{+1.0}_{-1.0}$	$2.9^{+0.1}_{-0.1}$	5.63	-5.87	1	1.4	T+04	OPT	F
	-	-	-	-6.58	-	-	LIME	-	-
AzV 104	28.0	3.25	5.42	-7.75	0.1	1.0	This study	UV+OPT	C
	$25.2^{+1.2}_{-1.2}$	$2.88^{+0.2}_{-0.1}$	$5.23^{+0.1}_{-0.1}$	$-7.56^{+0.3}_{-0.2}$	0.1	1.0	JB+25	OPT	F
	26.5	3.05	5.45	-6.96	0.6	0.5	BP+24	UV+OPT	C
	$27.5^{1.0}_{-1.0}$	$3.1^{0.1}_{-0.1}$	5.31	-6.4	1	1.0	T+04	OPT	F
	-	-	-	-6.87	-	-	LIME	-	-
AzV 410	25.1	3.12	5.26	-7.65	0.1	1.0	This study	UV+OPT	C
	$25.2^{+1.2}_{-2.3}$	$2.88^{+0.2}_{-0.1}$	$5.22^{+0.1}_{-0.2}$	$-7.26^{+0.3}_{-0.6}$	0.1	1.0	JB+25	OPT	F
	-	-	-	-7.21	-	-	LIME	-	-

JB+25: (Bestenlehner et al., 2025). FB+24: (Backs et al., 2024), BP+24: Bernini-Peron et al. (2024), T+05: (Trundle & Lennon, 2005a), T+04: (Trundle et al., 2004a) Obtained using F: FASTWIND, C: CMFGEN. The mass-loss rates are not corrected for clumping.

Table B.2: Continued.

Target	$T_{\rm eff}$ kK	$\log g$ cm s^{-2}	$\log L$ $L_\odot$	$\log \dot{M}$ $M_\odot$ yr^{-1}	$f_{\rm vol,\infty}$	β	Ref.	wavelength	Code
AzV 242	23.2	2.66	5.71	-7.47	0.03	3.1	This study	UV+OPT	C
	$22.5^{+0.8}_{-0.8}$	$2.31^{+0.1}_{-0.1}$	$5.28^{+0.1}_{-0.1}$	$-6.34^{+0.2}_{-0.2}$	0.1	1.0	JB+25	OPT	F
	23.0	2.65	5.62	-6.39	0.2	1.8	BP+24	UV+OPT	C
	$25.0^{+1.5}_{-1.5}$	$2.85^{+0.2}_{-0.2}$	5.67	-6.08	1	2.0	T+05	OPT	F
	-	-	-	-6.56	-	-	LIME	-	-
AzV 96	21.7	2.66	5.41	-7.43	0.1	2.6	This study	UV+OPT	C
	$21.3^{+1.6}_{-1.2}$	$2.31^{+0.3}_{-0.2}$	$5.23^{+0.1}_{-0.1}$	$-6.81^{+0.2}_{-0.3}$	0.1	1.0	JB+25	OPT	F
	-	-	-	-6.99	-	-	LIME	-	-
AzV 264	21.1	2.51	5.44	-7.32	0.1	3.0	This study	UV+OPT	C
	$21.3^{+0.8}_{-1.2}$	$2.31^{+0.1}_{-0.1}$	$5.3^{+0.1}_{-0.1}$	$-6.88^{+0.2}_{-0.3}$	0.1	1.0	JB+25	OPT	F
	21.5	2.5	5.43	-6.66	0.2	1.8	BP+24	UV+OPT	C
	$22.5^{+1.5}_{-1.5}$	$2.55^{+0.2}_{-0.2}$	5.44	-6.54	1	2.5	T+05	OPT	F
	-	-	-	-6.92	-	-	LIME	-	-
AzV 175	20.0	2.80	4.97	-7.55	0.2	1.0	This study	UV+OPT	C
	$19.0^{+1.6}_{-0.8}$	$2.5^{+0.3}_{-0.1}$	$4.84^{+0.1}_{-0.1}$	$-8.52^{+0.5}_{-1.1}$	0.1	1.0	JB+25	OPT	F
	-	-	-	-7.19	-	-	LIME	-	-
Sk 191	21.1	2.47	5.67	-6.81	0.2	2.5	This study	UV+OPT	C
	$22.5^{+0.8}_{-1.2}$	$2.5^{+0.1}_{-0.1}$	$5.79^{+0.1}_{-0.1}$	$-6.34^{+0.2}_{-0.2}$	0.1	1.0	JB+25	OPT	F
	19.0	2.25	5.67	-6.02	0.8	2.8	BP+24	UV+OPT	C
	$22.5^{1.5}_{-1.5}$	$2.55^{0.2}_{-0.2}$	5.77	-6.17	1	2.0	T+04	OPT	F
	-	-	-	-6.62	-	-	LIME	-	-
AzV 18	18.5	2.27	5.45	-7.19	0.1	3.5	This study	UV+OPT	C
	$23.7^{+1.2}_{-2.0}$	$2.69^{+0.1}_{-0.3}$	$5.75^{+0.1}_{-0.1}$	$-6.63^{+0.2}_{-0.2}$	0.1	1.0	JB+25	OPT	F
	19.0	2.35	5.45	-6.66	1.0	1.5	BP+24	UV+OPT	C
	$19.0^{+2.0}_{-2.0}$	$2.3^{+0.2}_{-0.2}$	5.44	-6.64	1	3.0	T+04	OPT	F
	-	-	-	-6.6	-	-	LIME	-	-
NGC330-ELS-04	17.1	2.36	4.93	-7.71	0.2	1.0	This study	UV+OPT	C
	$17.8^{+2.0}_{-0.8}$	$2.31^{+0.3}_{-0.2}$	$4.96^{+0.2}_{-0.1}$	$-7.77^{+0.3}_{-0.2}$	0.1	1.0	JB+25	OPT	F
	-	-	-	-7.31	-	-	LIME	-	-
AzV 187	16.8	2.21	5.37	-7.77	0.2	1.0	This study	UV+OPT	C
	16.5	2.2	5.33	-7.22	0.3	2.2	BP+24	UV+OPT	C
	-	-	-	-6.84	-	-	LIME	-	-

JB+25: (Bestenlehner et al., 2025). FB+24: (Backs et al., 2024), BP+24: Bernini-Peron et al. (2024), T+05: (Trundle & Lennon, 2005a), T+04: (Trundle et al., 2004a) Obtained using F: FASTWIND, C: CMFGEN. The mass-loss rates are not corrected for clumping.

Table B.2: Continued.

Target	$T_{\rm eff}$ kK	$\log g$ cm s^{-2}	$\log L$ $L_\odot$	$\log \dot{M}$ $M_\odot$ yr^{-1}	$f_{\rm vol,\infty}$	β	Ref.	wavelength	Code
AzV 22	14.2	1.81	5.22	-6.75	0.1	2.5	This study	UV+OPT	C
	$15.9^{+0.8}_{-0.8}$	$2.12^{+0.1}_{-0.6}$	$5.28^{+0.1}_{-0.1}$	$-7.38^{+0.3}_{-0.2}$	0.1	1.0	JB+25	OPT	F
	14.0	1.9	5.27	-7.15	0.1	3.7	BP+24	UV+OPT	C
	$14.5^{+1.5}_{-1.5}$	$1.9^{+0.2}_{-0.2}$	5.04	-6.64	1	1.0	T+04	OPT	F
	-	-	-	-7.6	-	-	LIME	-	-
AzV 393	13.3	1.61	5.53	-5.94	0.1	2.5	This study	UV+OPT	C
	-	-	-	-7.51	-	-	LIME	-	-
AzV 343	12.0	2.00	4.65	-8.2	0.1	1.0	This study	UV+OPT	C
	$12.7^{+0.4}_{-0.4}$	$1.88^{+0.2}_{-0.1}$	$4.67^{+0.1}_{-0.1}$	$-8.17^{+0.4}_{-0.9}$	0.1	1	JB+25	OPT	F
	12.5	2.05	4.72	-8.0	1.0	2.0	BP+24	UV+OPT	C
	-	-	-	-8.83	-	-	LIME	-	-
AzV 324	12.5	2.21	4.70	-8.05	0.1	1.0	This Study	UV+OPT	C
	$12.7^{+0.4}_{-0.4}$	$1.88^{+0.2}_{-0.3}$	$4.65^{+0.1}_{-0.1}$	$-8.67^{+0.7}_{-0.6}$	0.1	1	JB+25	OPT	F
	-	-	-	-8.78	-	-	LIME	-	-

JB+25: (Bestenlehner et al., 2025). FB+24: (Backs et al., 2024), BP+24: Bernini-Peron et al. (2024), T+05: (Trundle & Lennon, 2005a), T+04: (Trundle et al., 2004a) Obtained using F: FASTWIND, C: CMFGEN. The mass-loss rates are not corrected for clumping.

B.3 Comments on fitting issues

AzV 469, Figures B.2 and B.22. The fit quality of this star is very good. The only oddity is the shape of the core of Hα, which could be the result of wind contamination. It is unlikely that the morphology is the result of two components.

AzV 372, Figures B.3 and B.23. A problem in this fit is with the He I λ4922, which is over-predicted in the model. This issue could be resolved by increasing the temperature or decreasing the helium mass fraction. However, this would ruin the fit to other helium lines.

AzV 456, Figures B.4 and B.24. The most glaring issue for this star is the morphology of Hα, which we were unable to replicate with our models.

AzV 327, Figures B.5 and B.25. The fit for this star is good in general, with no major issues. The SED of this star shows abnormally high fluxes in the FUSE range. This is due to a nearby, UV-bright object, the light of which was included in the large FUSE aperture.

AzV 235, Figures B.6 and B.26. We note one major discrepancy between the predicted and observed Si IV$\lambda\lambda$1394 − 1403 P Cygni profile. Our estimated wind density parameters yield a satisfactory fit for other wind features. Our attempts to fit the silicon lines using models with clumpier winds had little effect of the fit of the silicon lines, but it lowered the quality of the fit for the other wind lines.

AzV 215, Figures B.7 and B.27. The line fits for this object are of high quality with no major issues.

AzV 104, Figures B.8 and B.28. The notable issue with this star is the fit for the absorption core of Hα. Attempting to remedy the discrepancy, we tried fitting this line with models that possess clumpier winds, which yielded better results, which made fitting the carbon P Cygni profile impossible.

AzV 410, Figures B.9 and B.29. The line fits of photospheric lines are satisfactory. The UV lines show a discrepancy between predictions and observations, specifically the silicon lines. The lines are predicted as strong P Cygni profiles with strong redshifted emission, while they lack any emission features in the observations. In the SED fitting of this star, we make use of the HST COS G230LB archival observation to constrain the reddening law parameters.

AzV 242, Figures B.10 and B.30. The overall line fits for this object are satisfactory with no notable discrepancies.

AzV 96, Figures B.11 and B.31. The only issue in this fit is that the predicted blue-shifted absorption of Hα is much narrower than the observed. Overall, the line fits are satisfactory.

AzV 264, Figures B.12 and B.32. Similar to AzV 96, the blue-shifted absorption of Hα in the model is much narrower than in the observations.

AzV 175, Figures B.13 and B.33. Satisfactory fits for all lines with no notable discrepancies.

Sk 191, Figures B.14 and B.34. In Hα, there is a moderate, but significant velocity shift. In addition, the predicted Si IV$\lambda\lambda$1394 − 1403 lines, which are seemingly photospheric, do not match the strong P Cygni observations. Finally, the red He I λ6678 and He I λ7065 lines are much broader than other helium lines, suggesting higher rotational broadening parameters are required to obtain a satisfactory fit. These issues all point towards this star being a potential binary.

AzV 18, Figures B.15 and B.35. Similar to AzV 96, the extremely broad blue-shifted absorption of the observed Hα is not matched by the model.

NGC330-ELS-04, Figures B.16 and B.36. The observed line diagnostics are generally well reproduced, except for the absorption strength Hα. The small peak in the left wing of Hα could be an artifact of normalisation.

AzV 187, Figures B.17 and B.37. The fit is generally satisfactory. Similar to NGC330-ELS-04, the absorption strength of Hα is exaggerated in the model.

AzV 22, Figures B.18 and B.38. Overall satisfactory line fits. Although we do not employ the O I $\lambda\lambda\lambda$7772 − 7774 − 7775 multiplet in obtaining the oxygen abundance for

this object, we include it to show that fitting these lines would require a significantly lower oxygen abundance compared to fitting O II lines.

AzV 393, Figures B.19 and B.39. This star is the sole hypergiant in our sample. We get satisfactory fits for most lines. The emission components in Hα and Hβ are well-matched by the model. However, we were unable to decrease the strength of the predicted absorption to match the observation without affecting the fits of other lines.

AzV 343, Figures B.20 and B.40. The quality of the fits in general is satisfactory. We note that for this star, due to the lack of O II lines, we obtain the oxygen mass fraction by fitting the O I $\lambda\lambda\lambda 7772 - 7774 - 7775$ multiplet.

AzV 324, Figures B.21 and B.41. Similar to AzV 343, for the determination of the oxygen mass fraction, we resorted to fitting the O I $\lambda\lambda\lambda 7772 - 7774 - 7775$ multiplet. No major issues in the fits of this objects, and the quality of the fits in general is satisfactory.

B.4 Spectral energy distribution (SED)

In Fig. B.1 we present the SED fits for the entire sample.

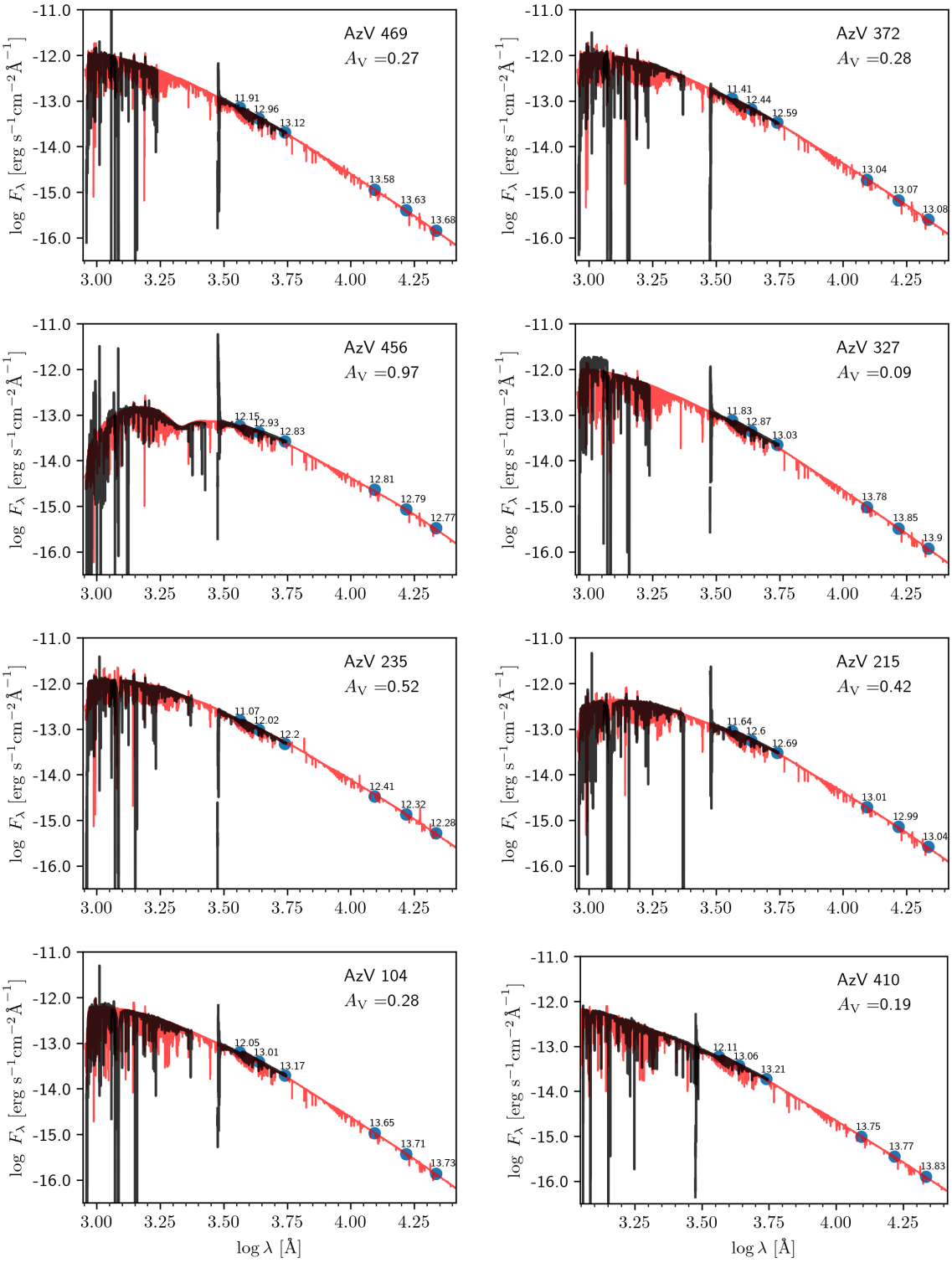


Figure B.1: Spectral energy distribution for all the stars in our sample. Red solid line: model SED, Black solid line: observed SED. The photometric points are indicated as blue circles.

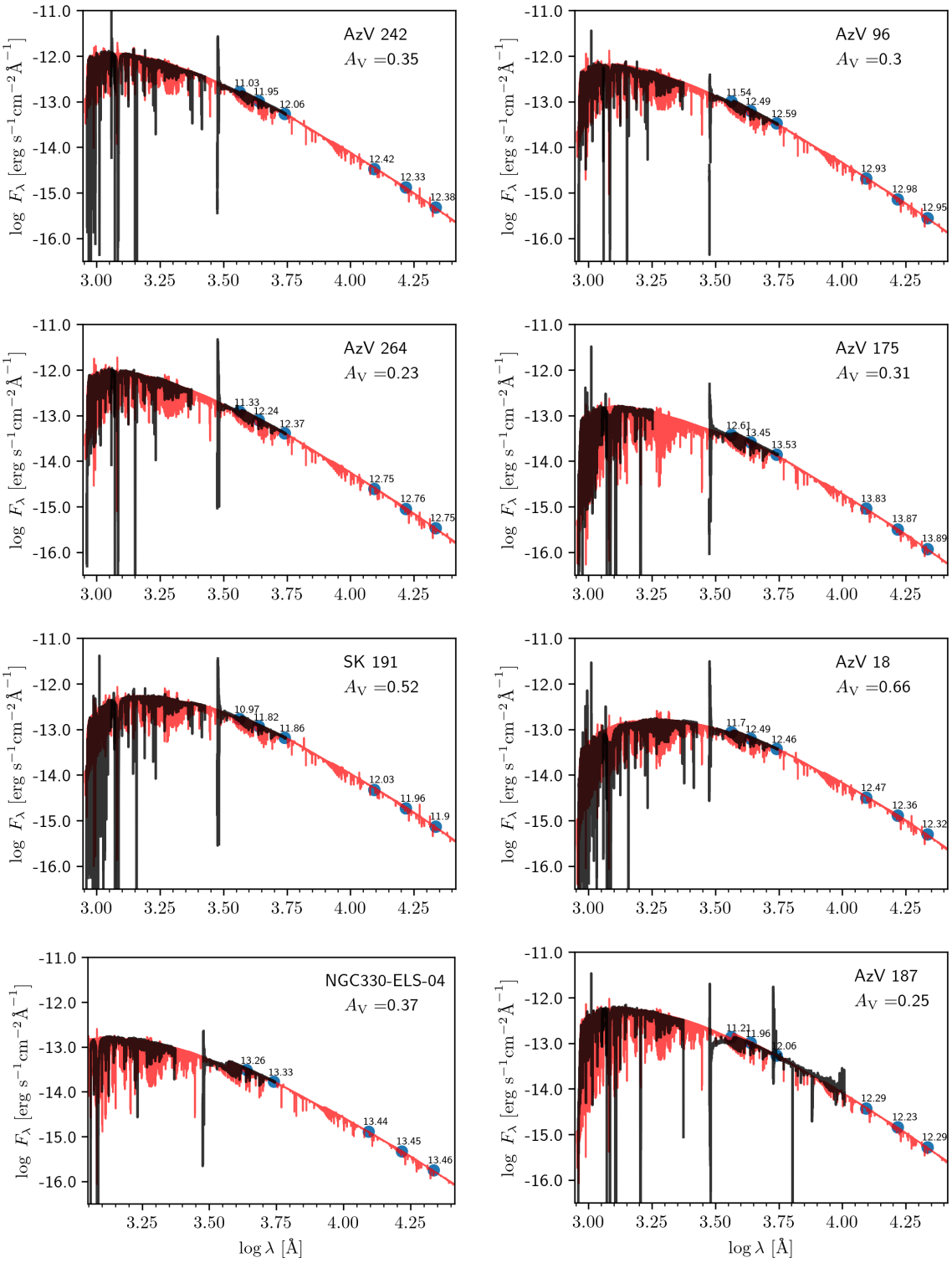


Figure B.1: continued

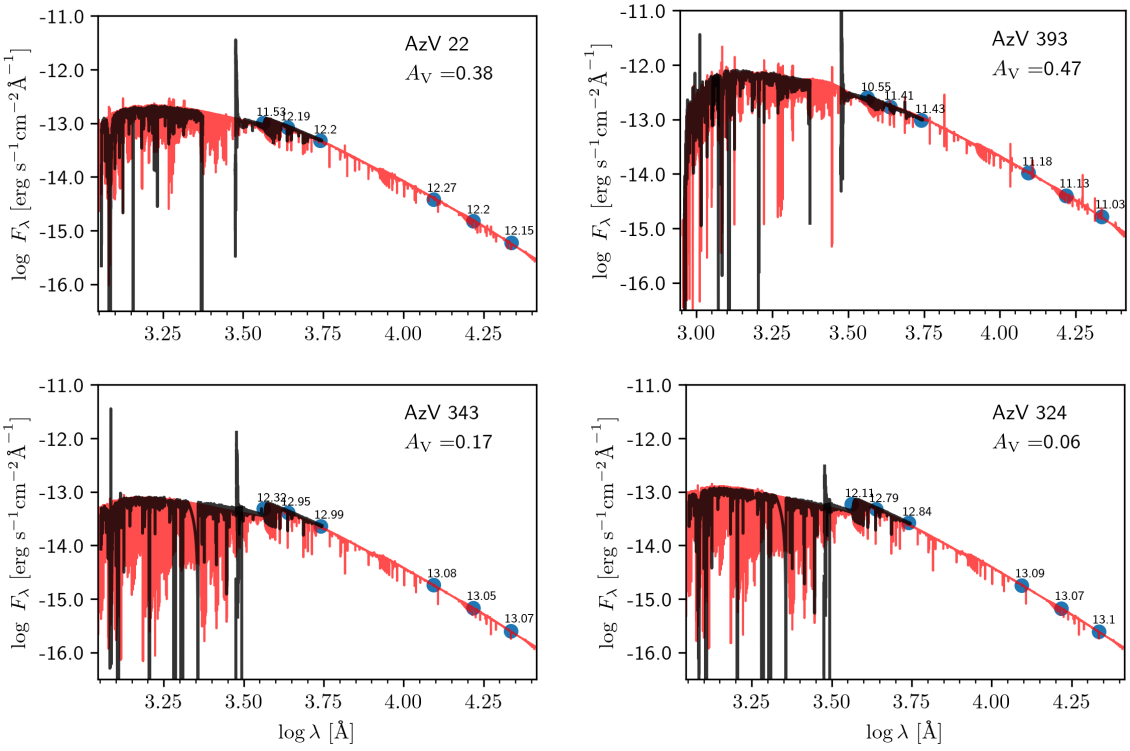


Figure B.1: continued

B.5 Line fitting for individual stars

Fig. B.2-B.21 are the individual diagnostic line fits for each star in our sample. In each row, from top to bottom, the diagnostic lines are used to determine the effective temperature, the effective surface gravity, the wind density parameters (mass loss rate, β, clumping parameters), the helium abundance, the nitrogen abundance, the carbon abundance, and the oxygen abundance, respectively.

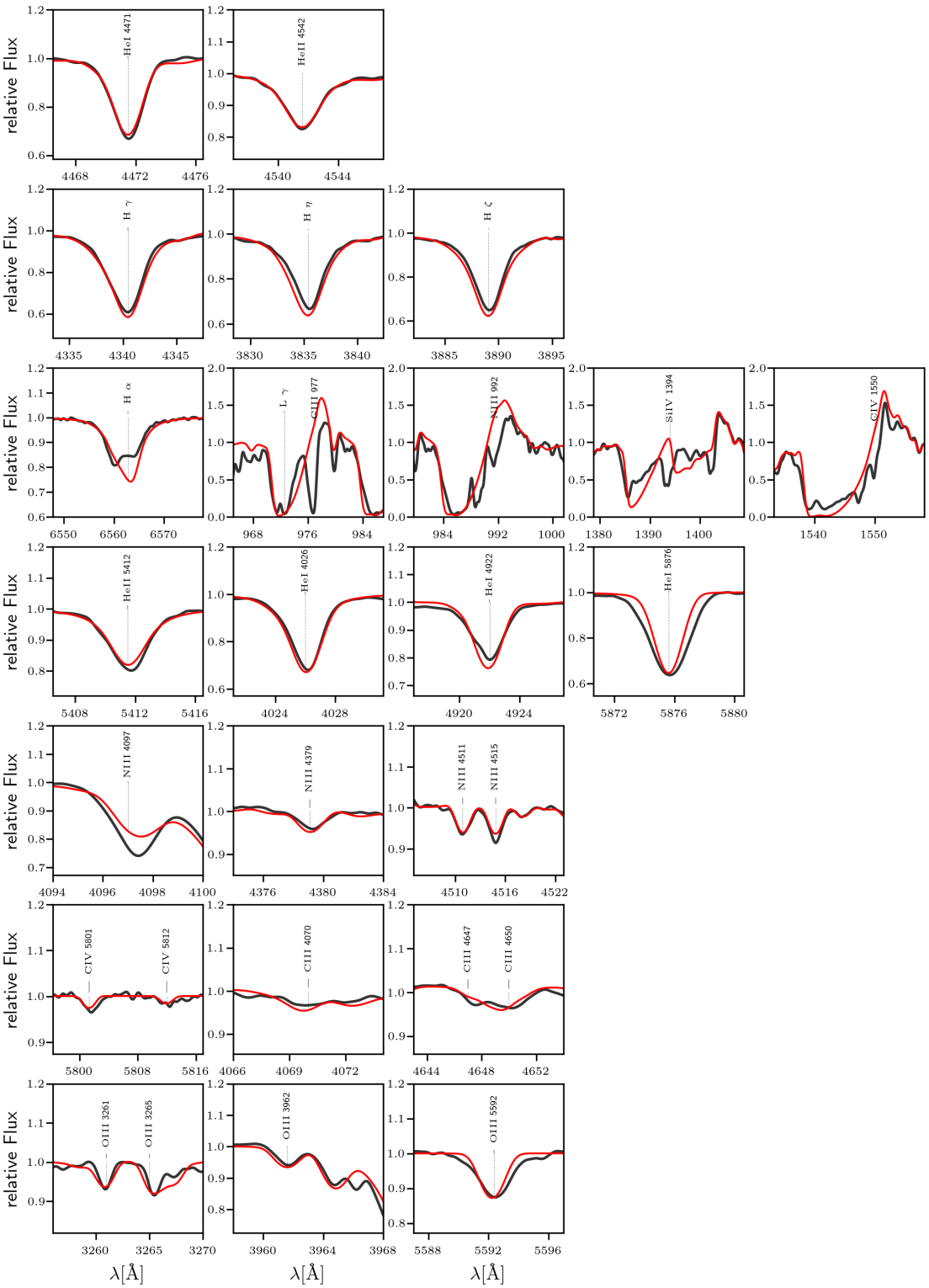


Figure B.2: Individual line fits for AzV 469 (O9 Iab(f)). Black solid line: observed spectrum. Red solid line: spectrum of the best fitting model.

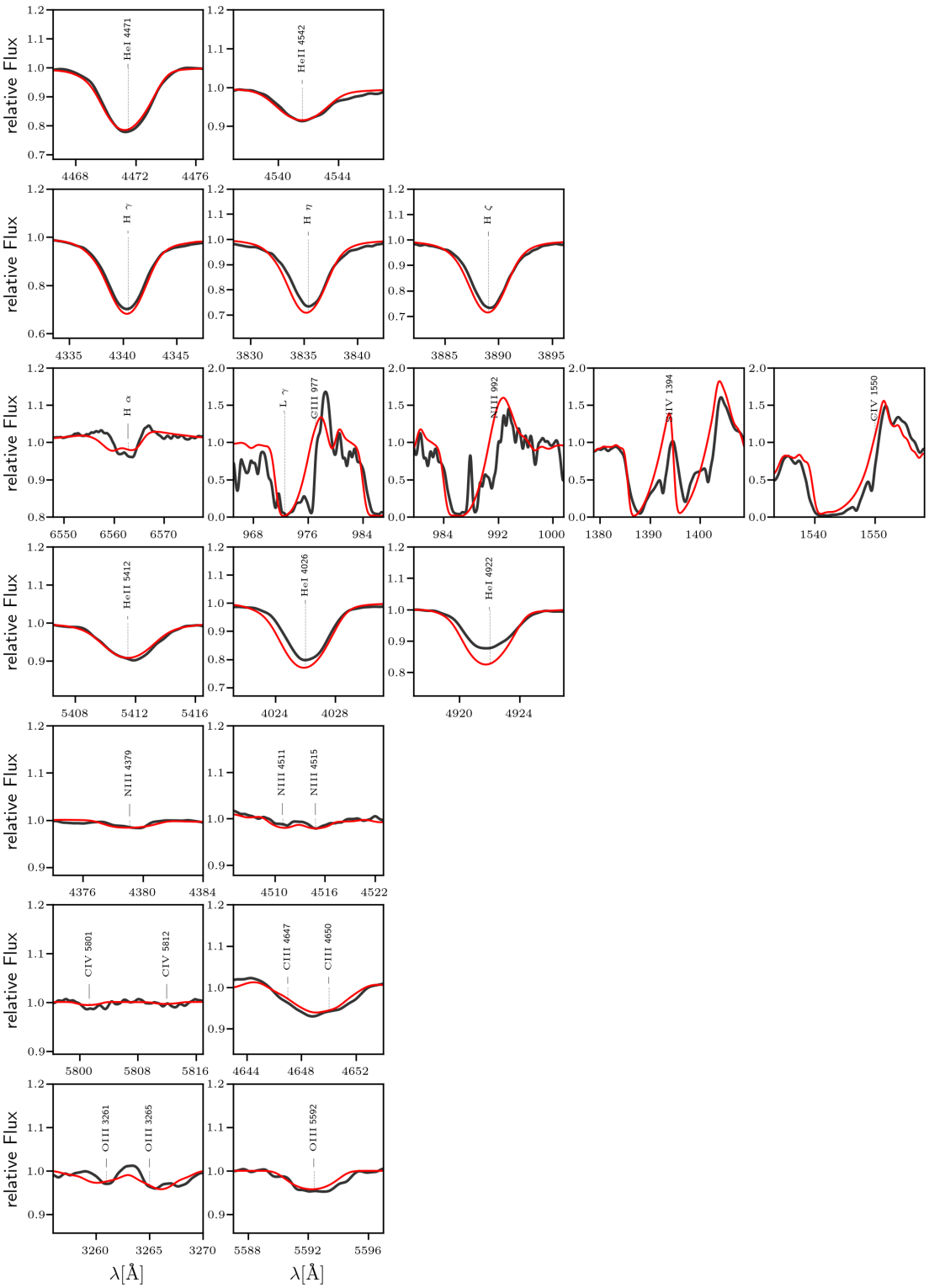


Figure B.3: Individual line fits for AzV 372 (O9.2 Iab). Black solid line: observed spectrum. Red solid line: spectrum of the best fitting model.

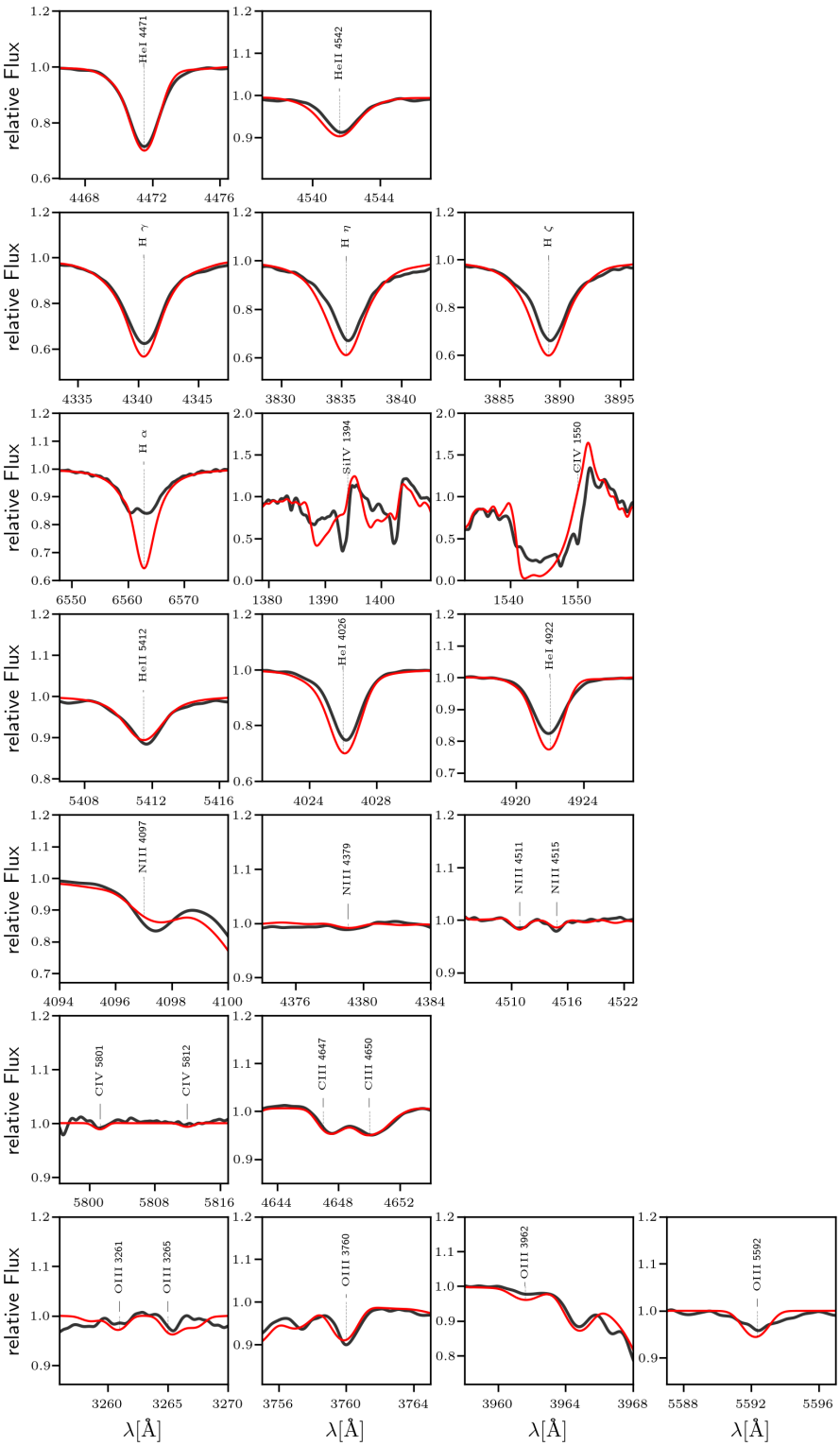


Figure B.4: Individual line fits for AzV 456 (O9.5 Iab). Black solid line: observed spectrum. Red solid line: spectrum of the best fitting model.

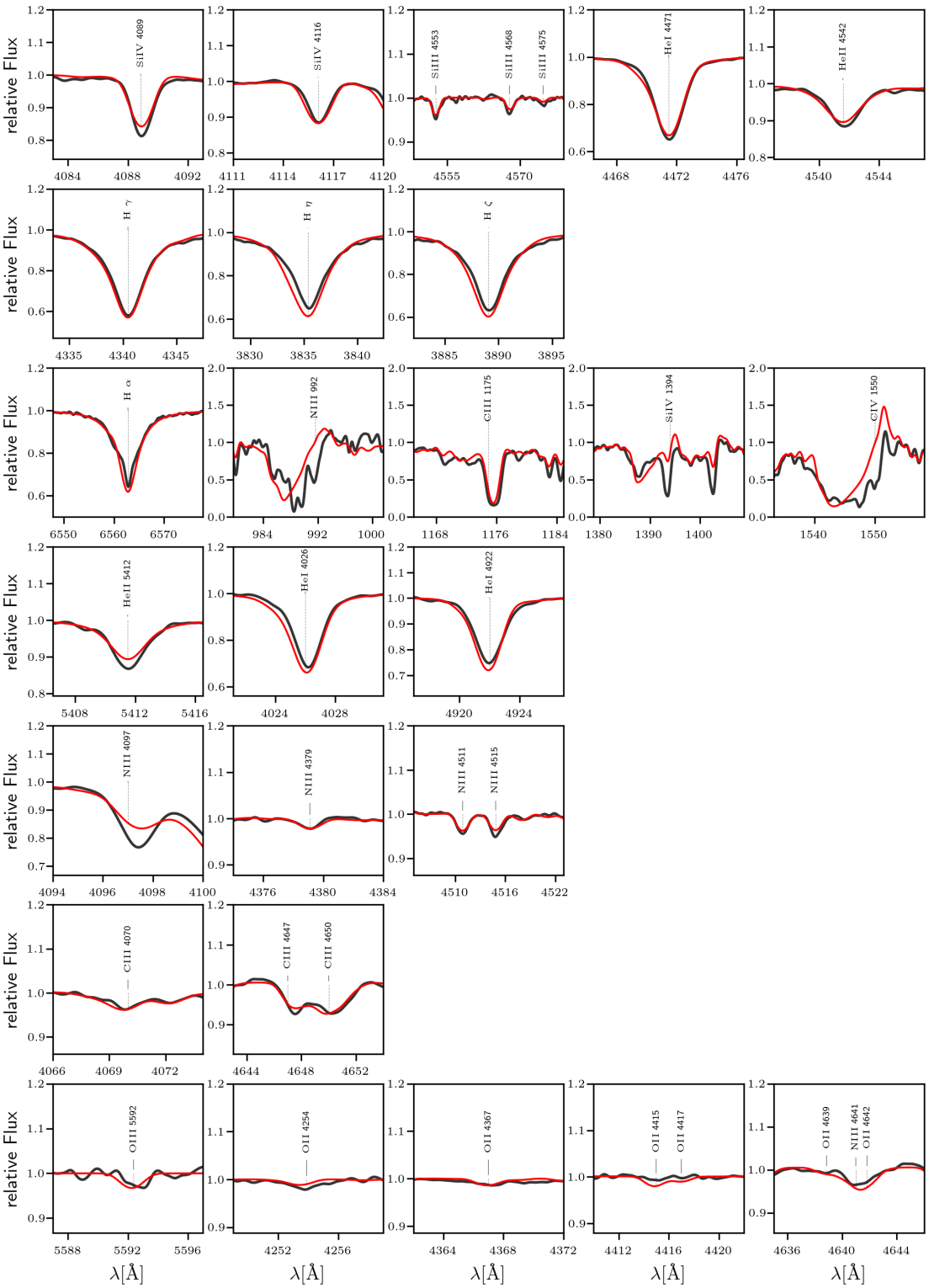


Figure B.5: Individual line fits for AzV 327 (O9.7 Ib). Black solid line: observed spectrum. Red solid line: spectrum of the best fitting model.

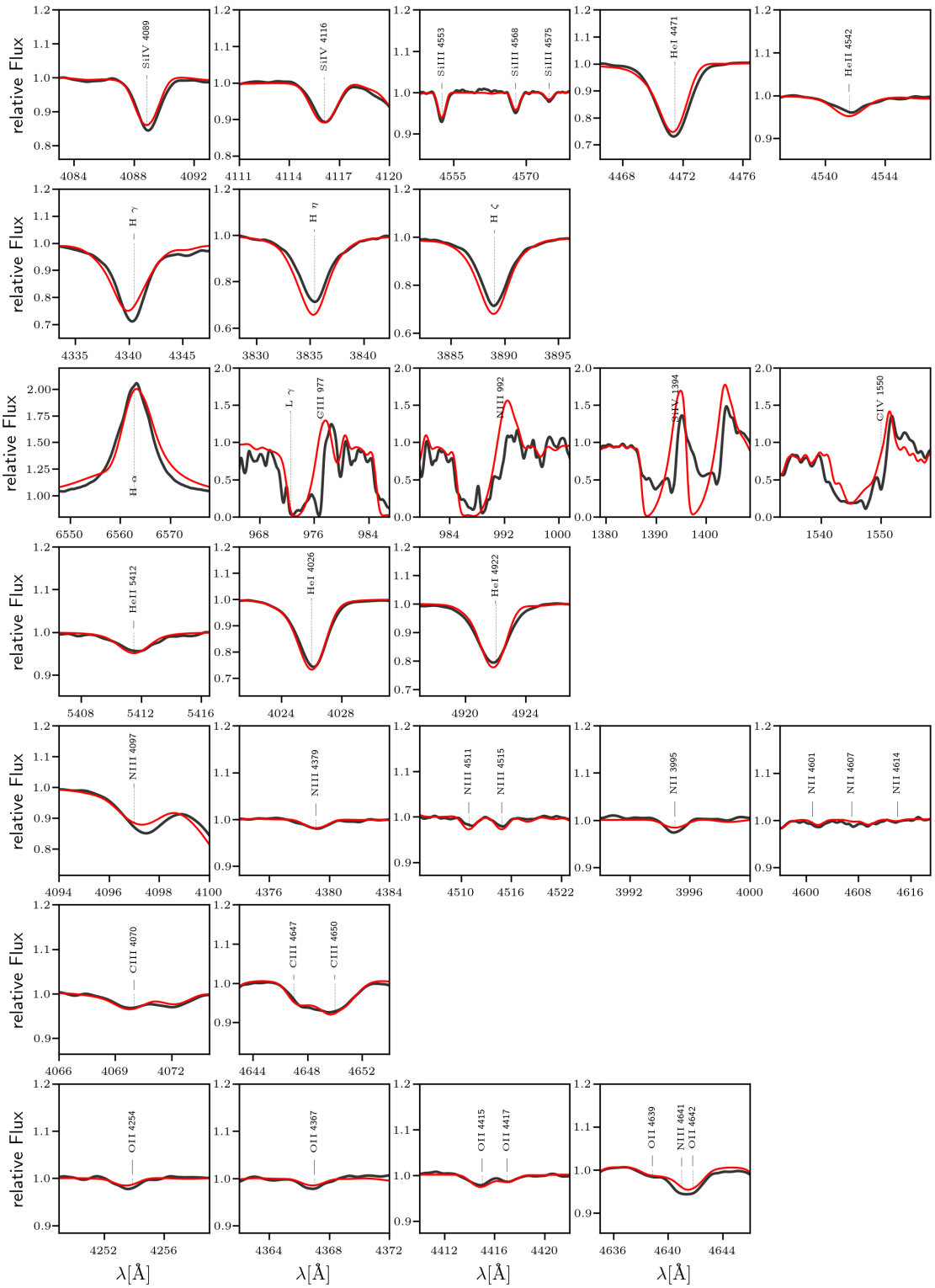


Figure B.6: Individual line fits for AzV 235 (B0 Ia). Black solid line: observed spectrum. Red solid line: spectrum of the best fitting model.

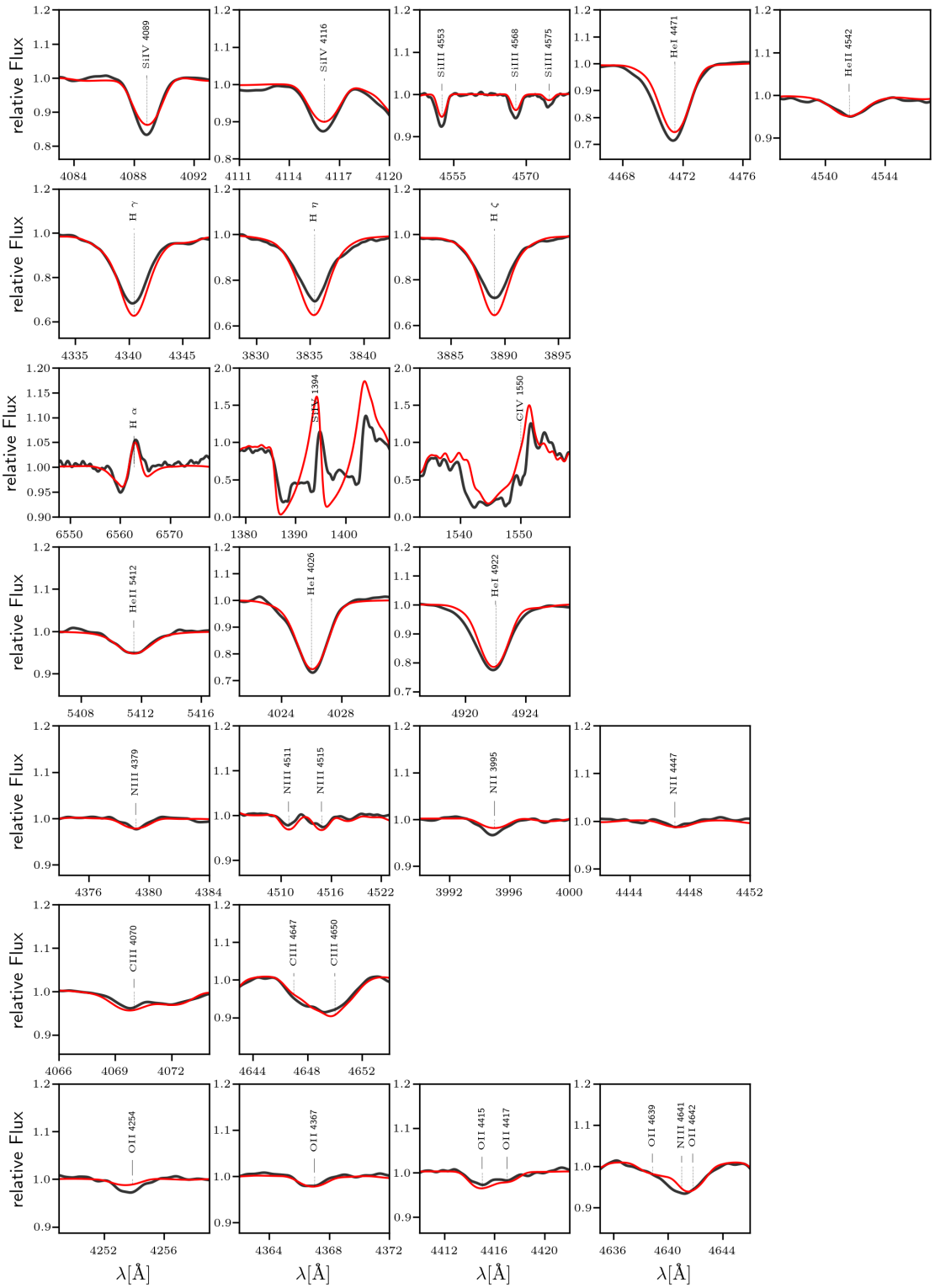


Figure B.7: Individual line fits for AzV 215 (B0 Ia). Black solid line: observed spectrum. Red solid line: spectrum of the best fitting model.

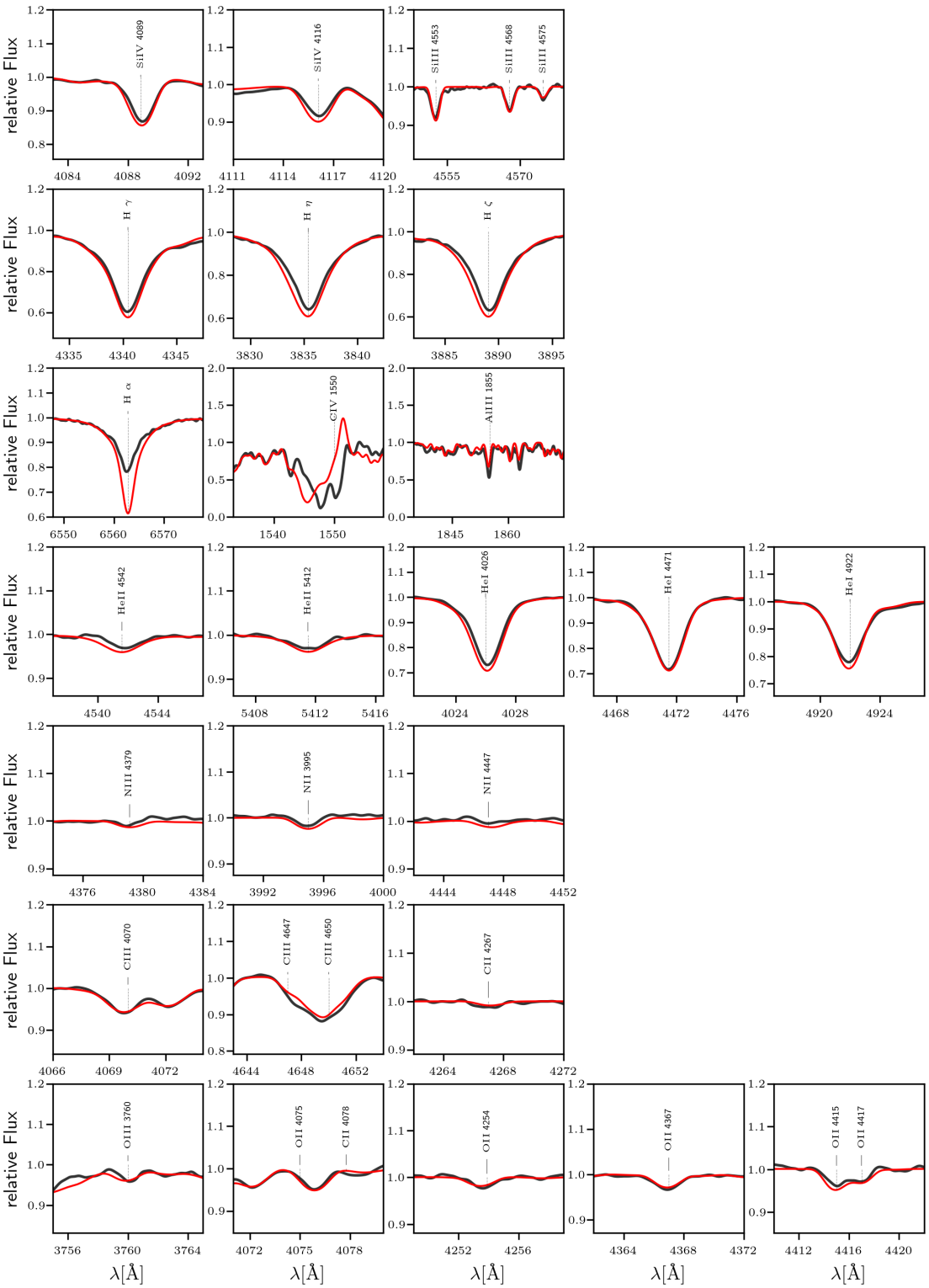


Figure B.8: Individual line fits for AzV 104 (B0.5 Ia). Black solid line: observed spectrum. Red solid line: spectrum of the best fitting model.

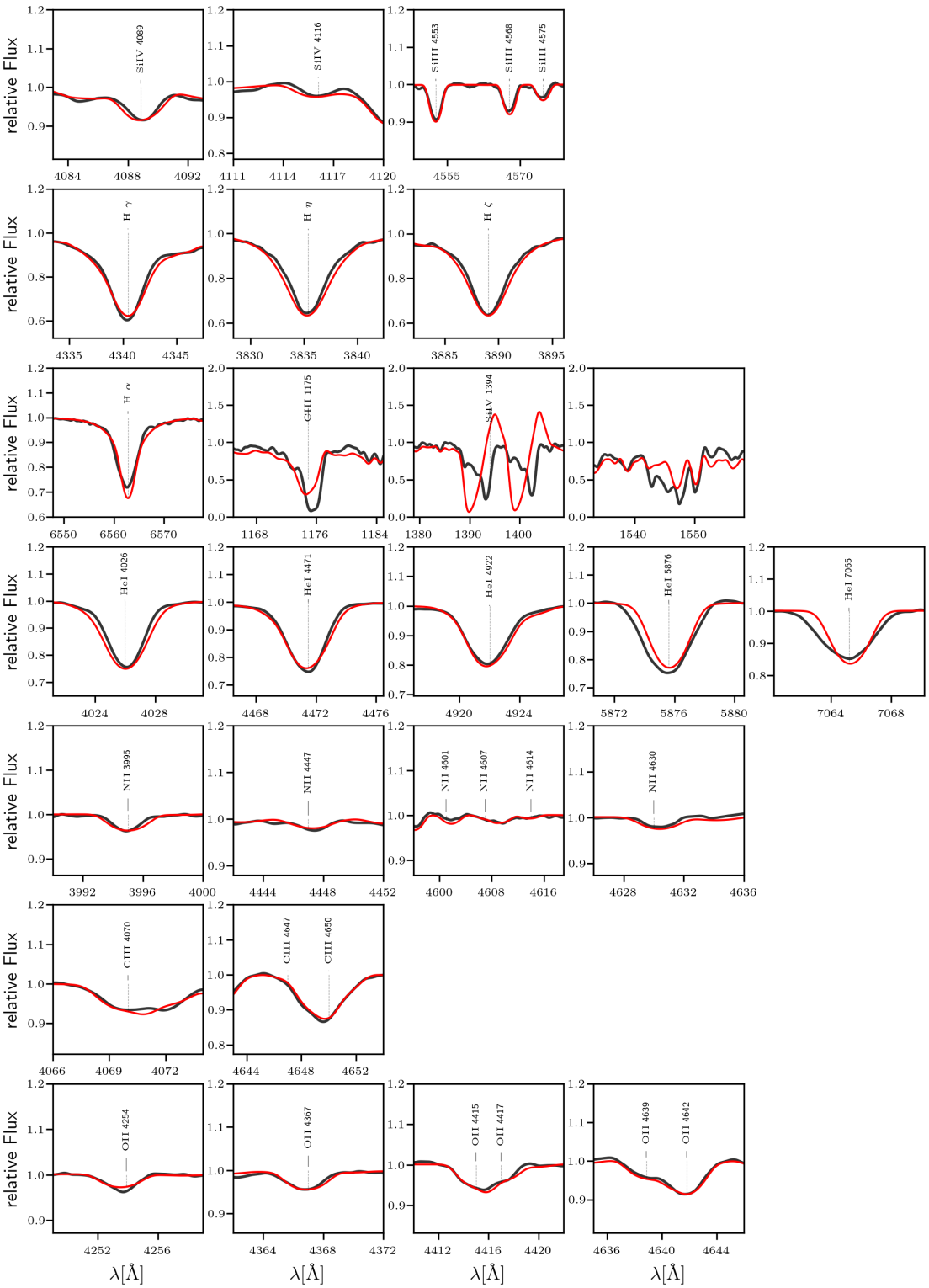


Figure B.9: Individual line fits for AzV 410 (B0.7 Iab). Black solid line: observed spectrum. Red solid line: spectrum of the best fitting model.

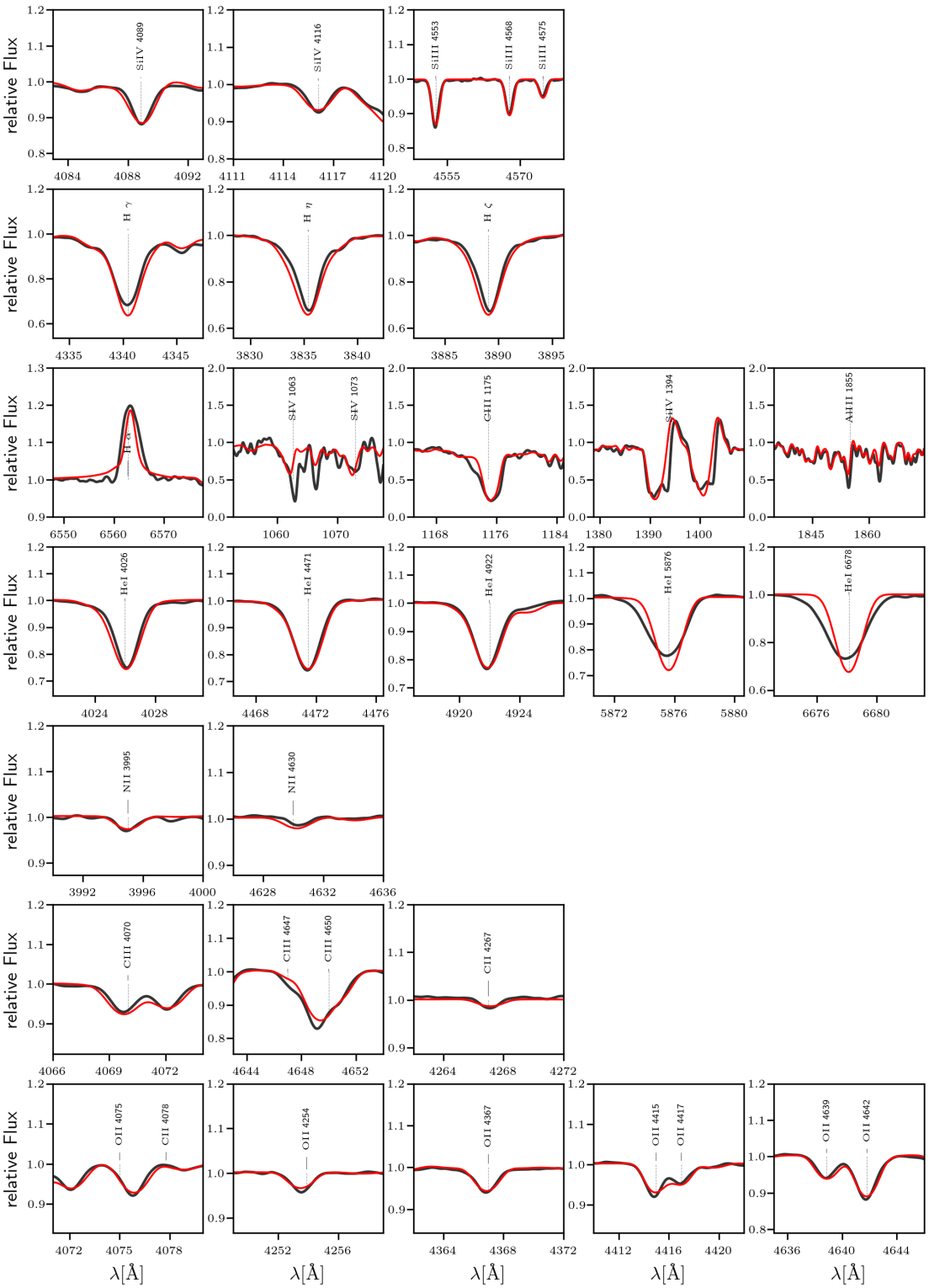


Figure B.10: Individual line fits for AzV 242 (B0.5 Ia). Black solid line: observed spectrum. Red solid line: spectrum of the best fitting model.

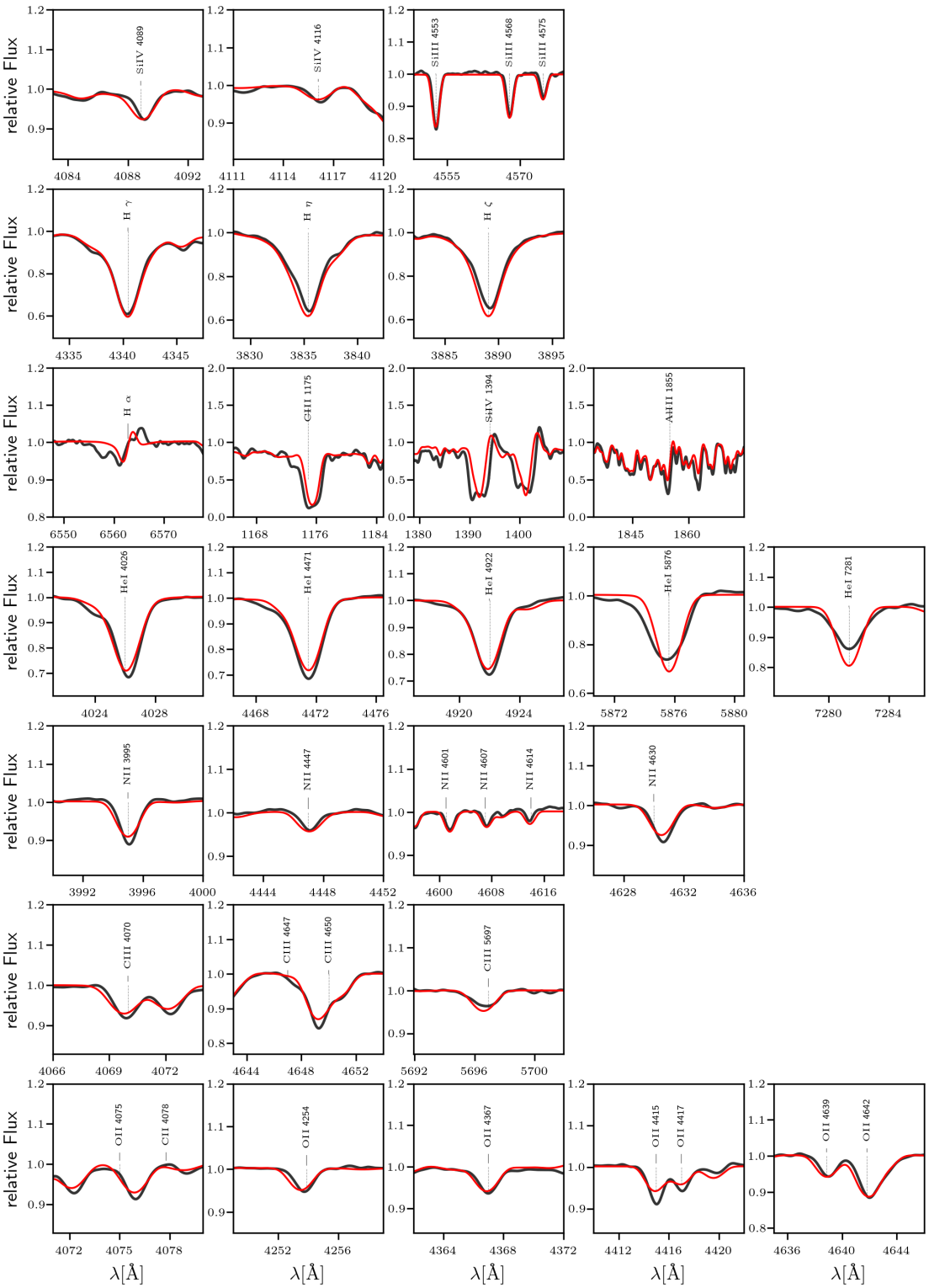


Figure B.11: Individual line fits for AzV 96 (B1 Iab). Black solid line: observed spectrum. Red solid line: spectrum of the best fitting model.

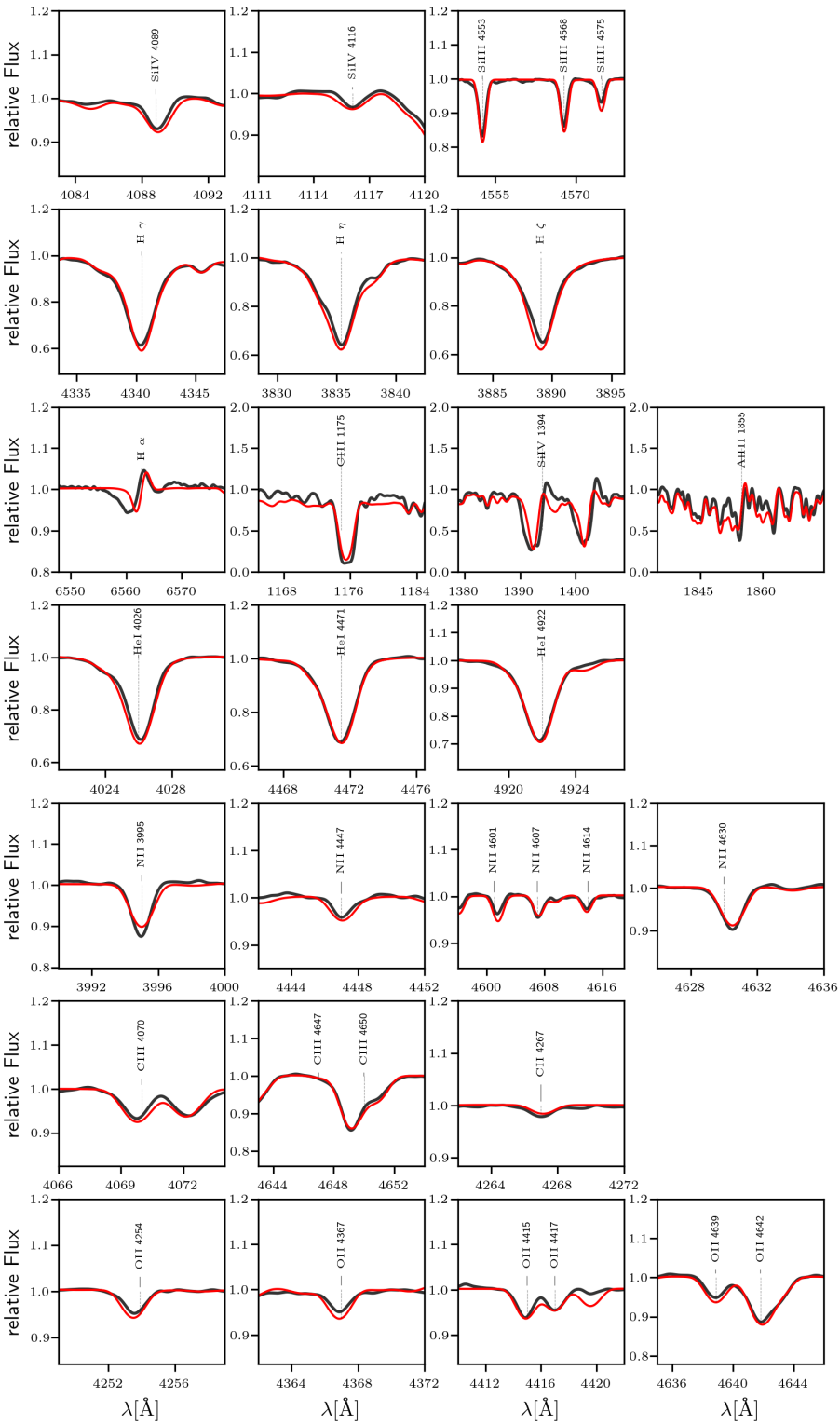


Figure B.12: Individual line fits for AzV 264 (B1 Ia). Black solid line: observed spectrum. Red solid line: spectrum of the best fitting model.

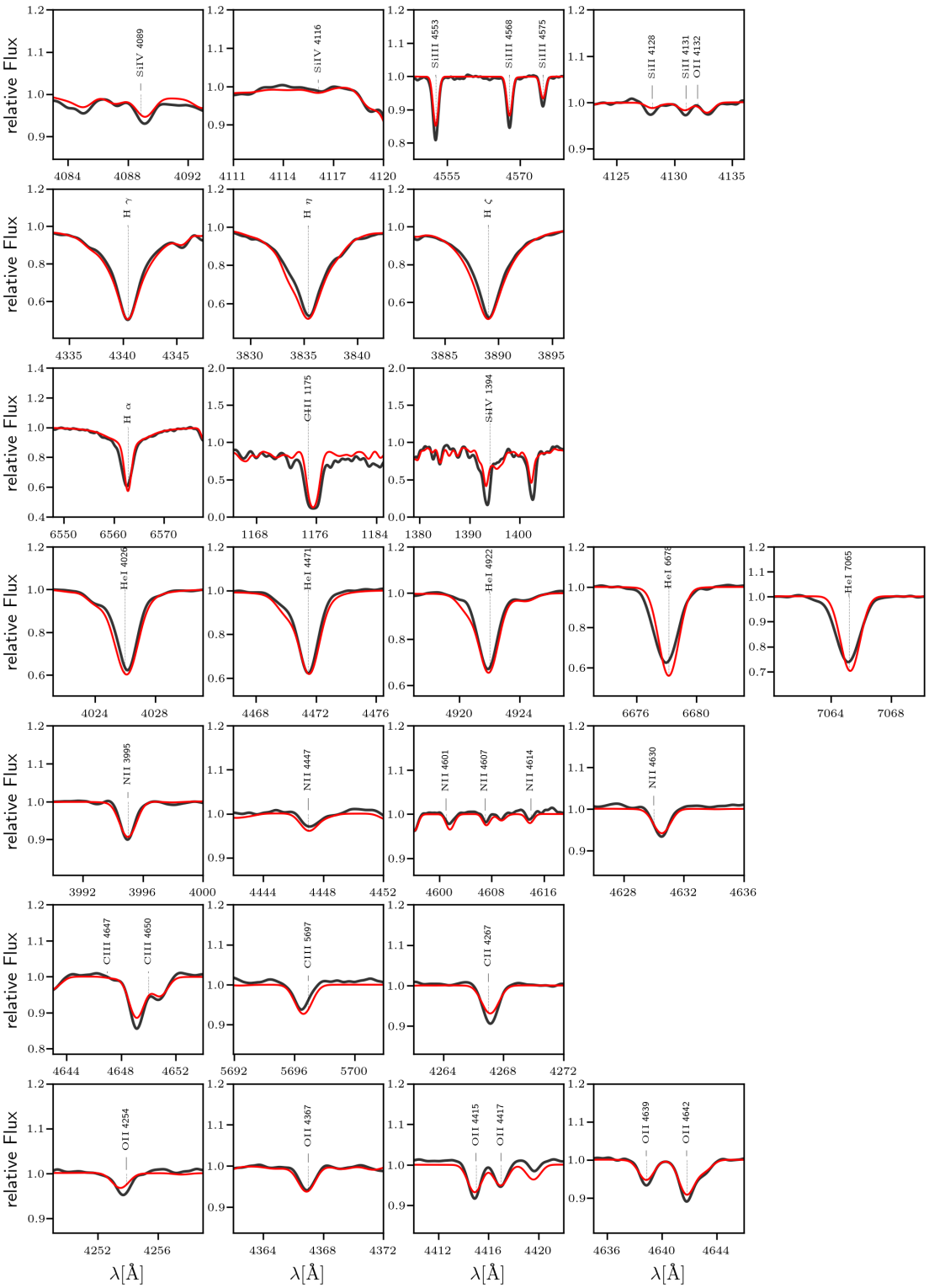


Figure B.13: Individual line fits for AzV 175 (B1.5 Ib). Black solid line: observed spectrum. Red solid line: spectrum of the best fitting model.

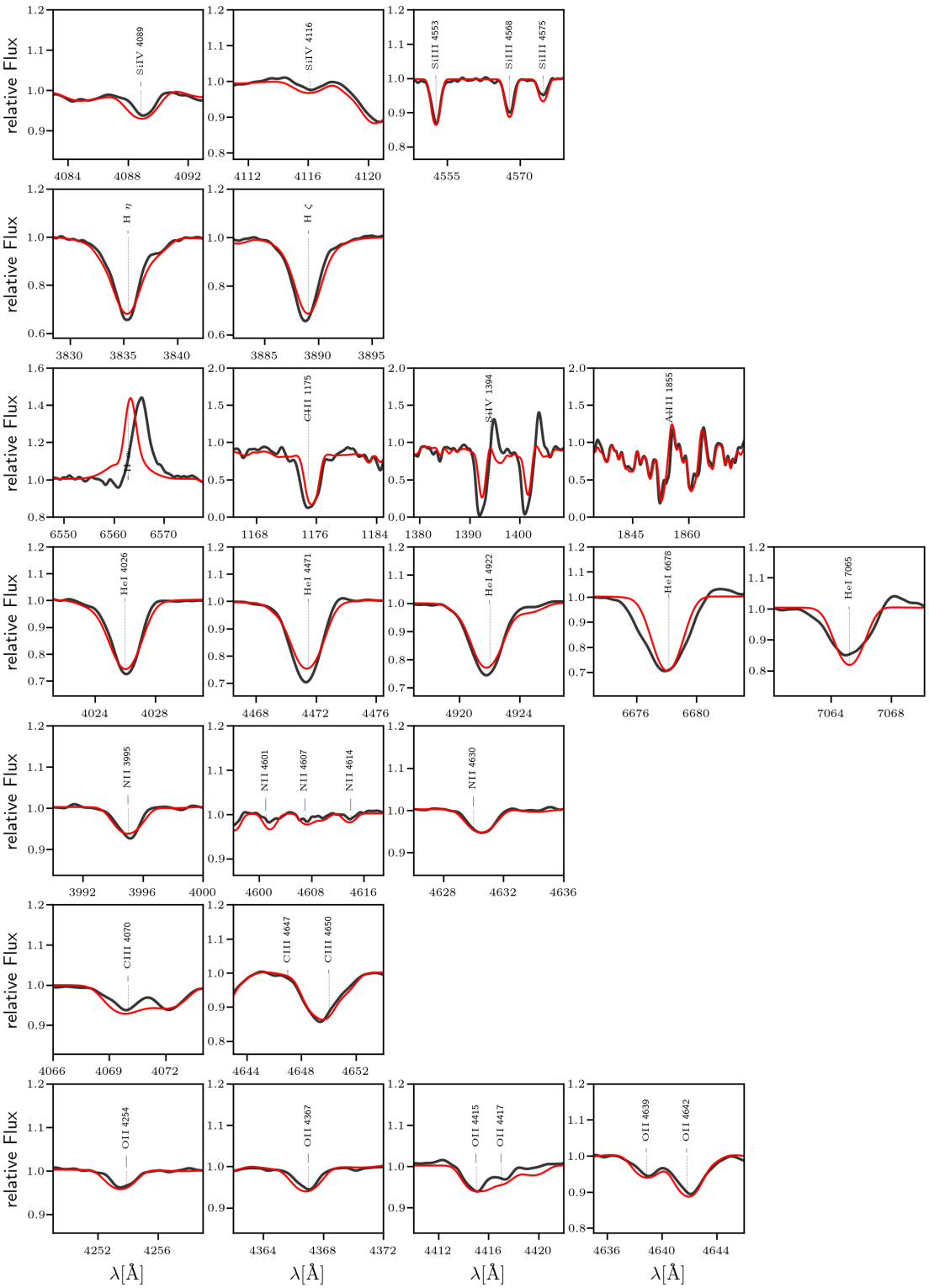


Figure B.14: Individual line fits for Sk 191 (B1.5 Ia). Black solid line: observed spectrum. Red solid line: spectrum of the best fitting model.

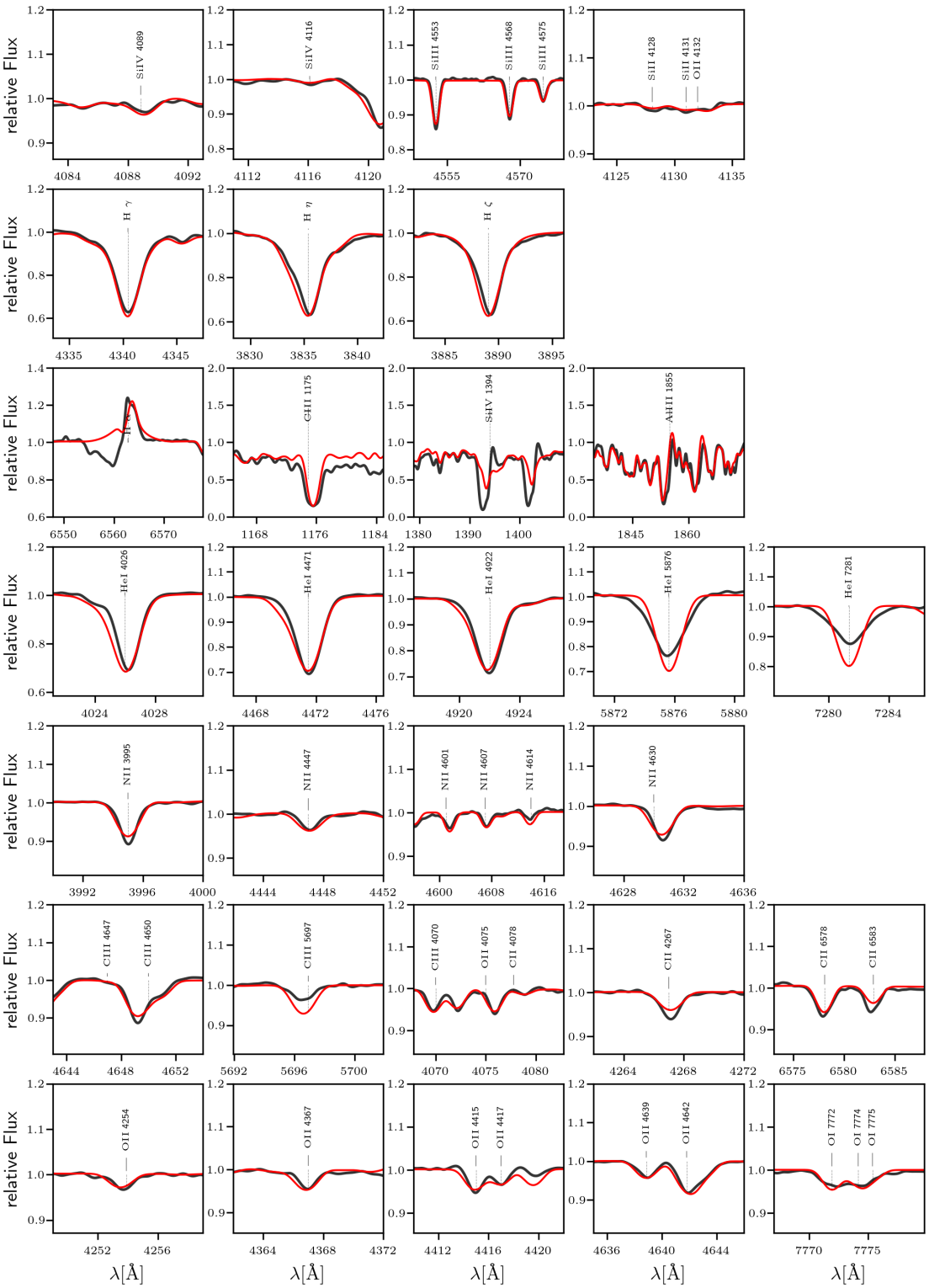


Figure B.15: Individual line fits for AzV 18 (B2 Ia). Black solid line: observed spectrum. Red solid line: spectrum of the best fitting model.

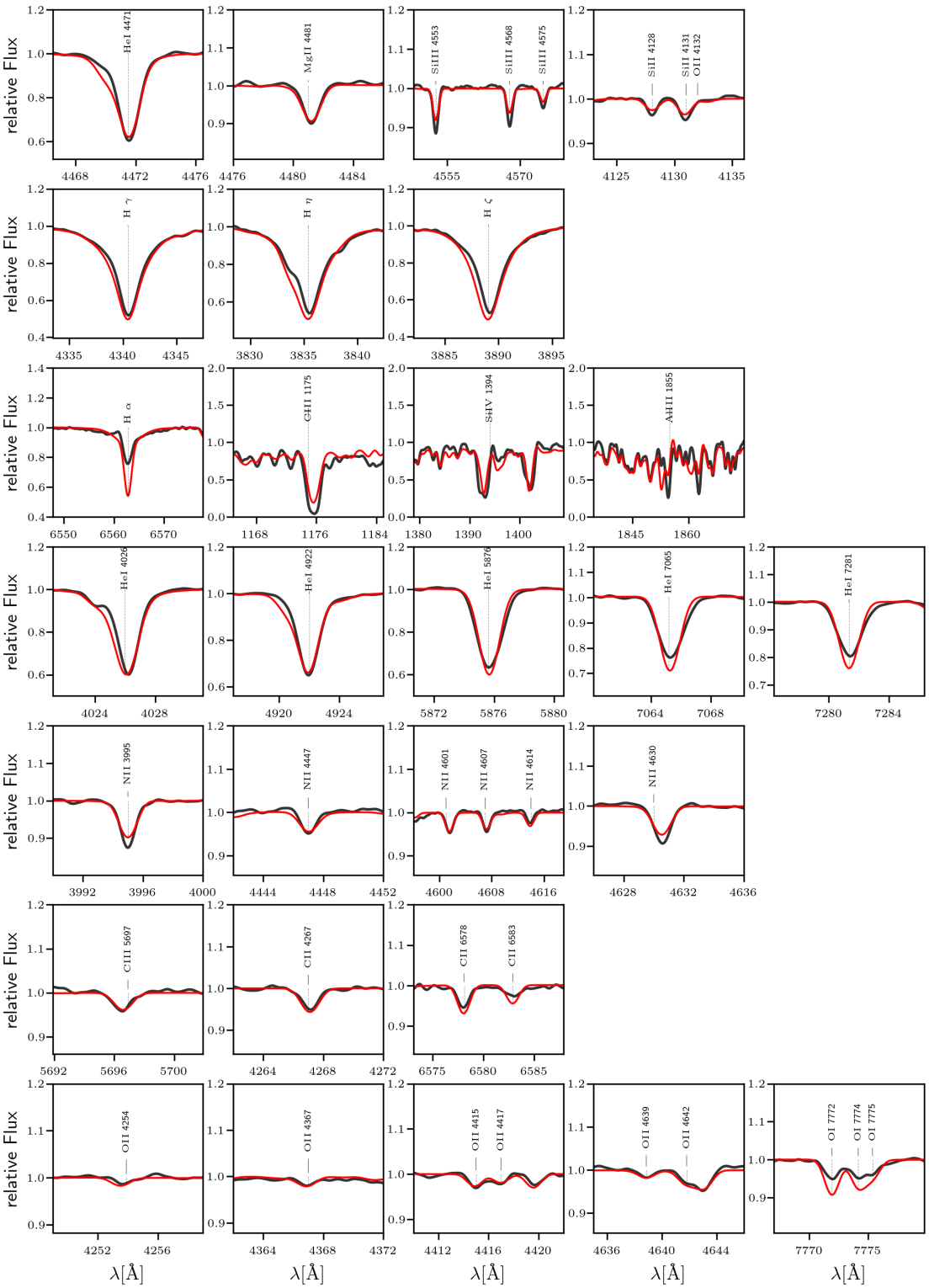


Figure B.16: Individual line fits for NGC330 ELS 04 (B2.5 Ib). Black solid line: observed spectrum. Red solid line: spectrum of the best fitting model.

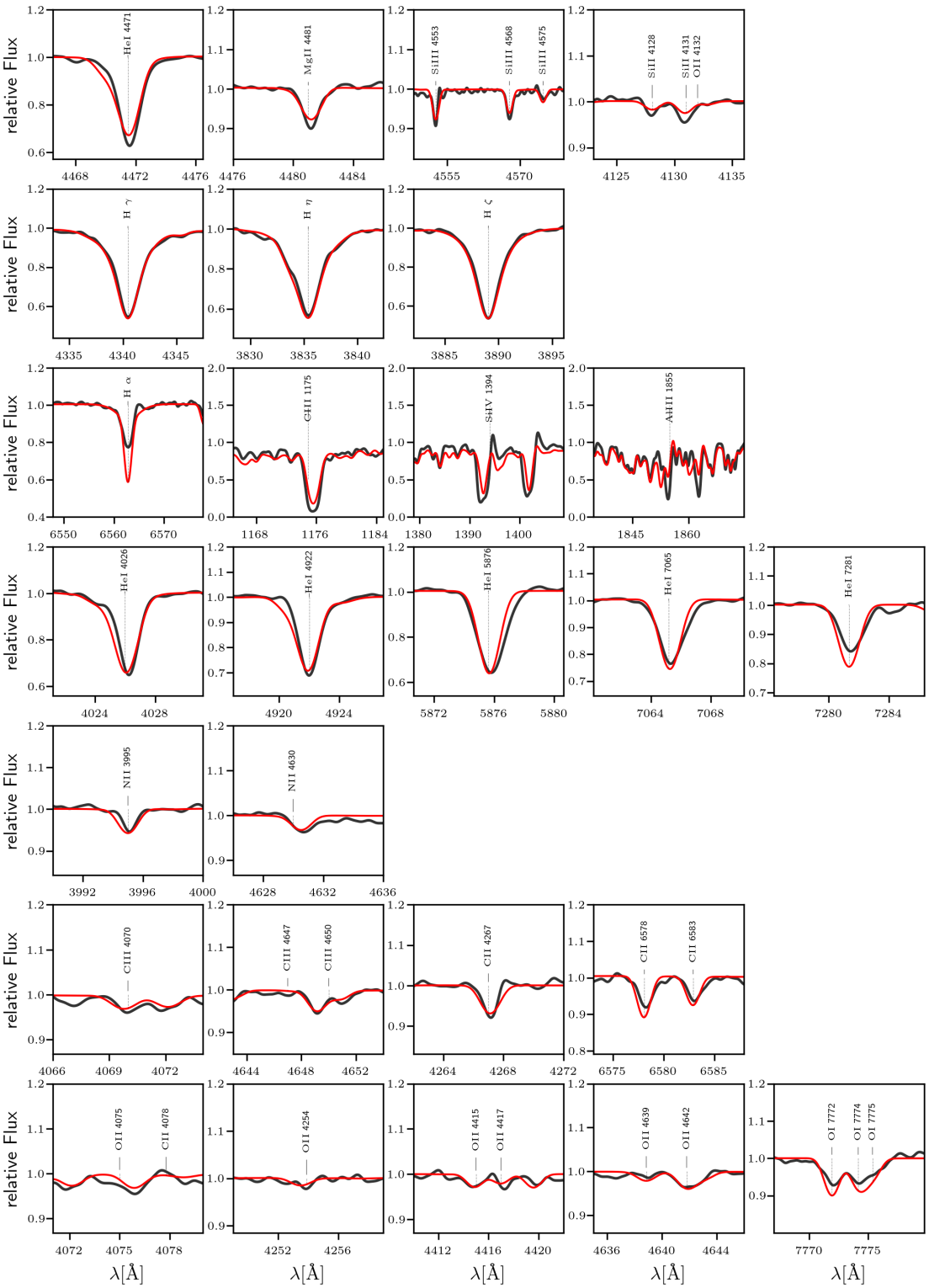


Figure B.17: Individual line fits for AzV 187 (B2.5 Ia). Black solid line: observed spectrum. Red solid line: spectrum of the best fitting model.

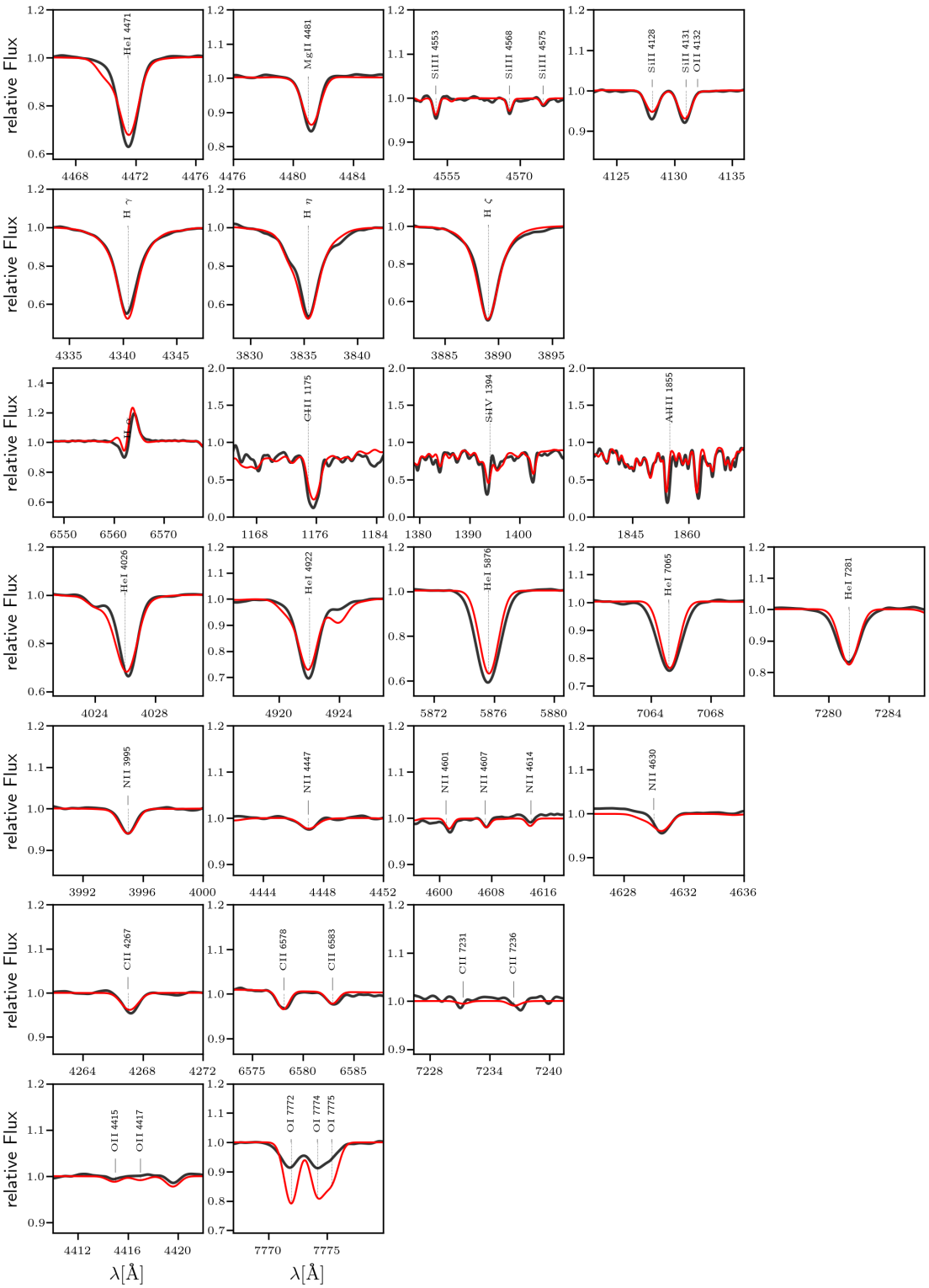


Figure B.18: Individual line fits for AzV 22 (B3 Ia). Black solid line: observed spectrum. Red solid line: spectrum of the best fitting model.

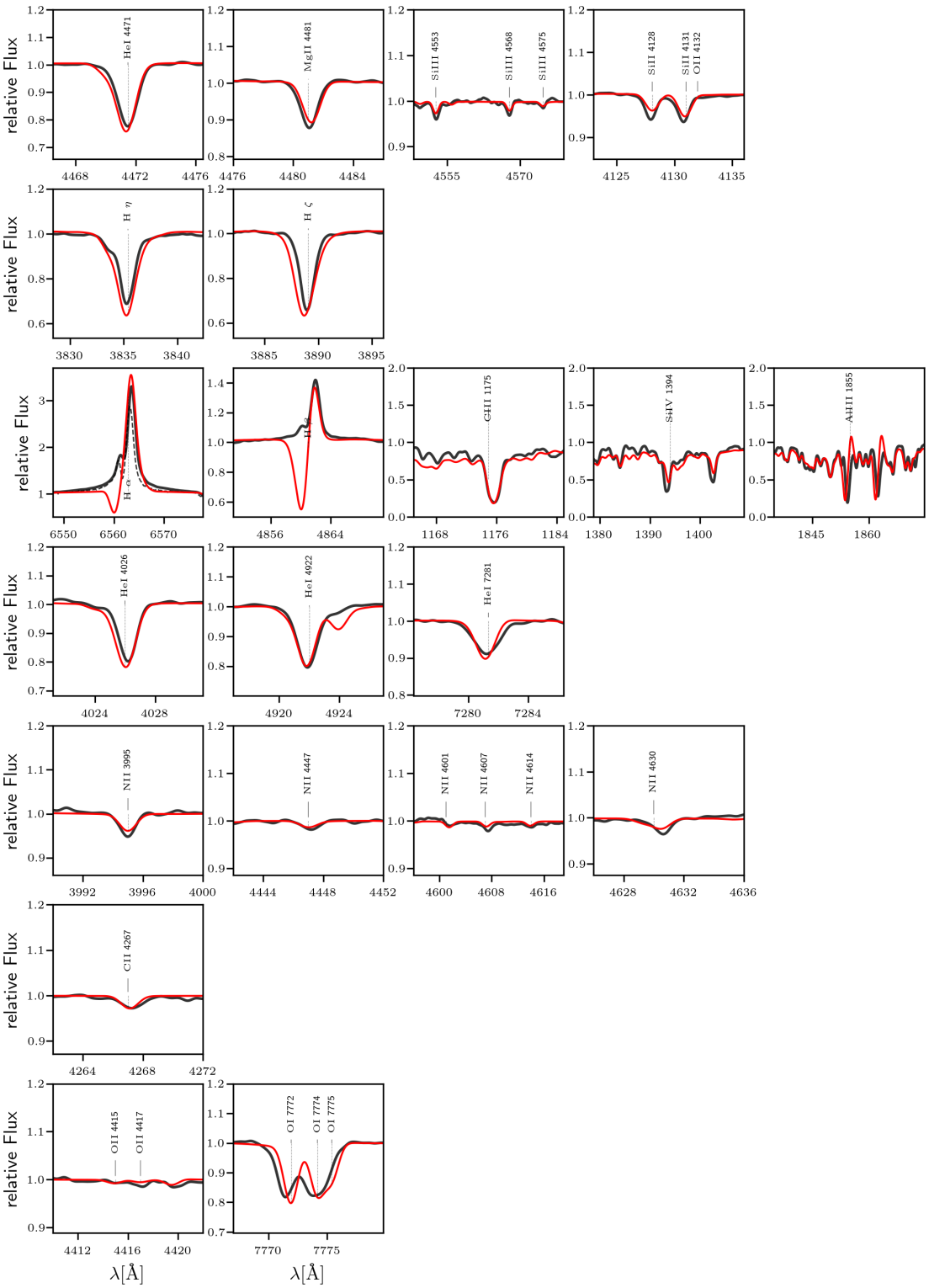


Figure B.19: Individual line fits for AzV 393 (B3 Ia$^+$). Black solid line: observed spectrum. Red solid line: spectrum of the best fitting model.

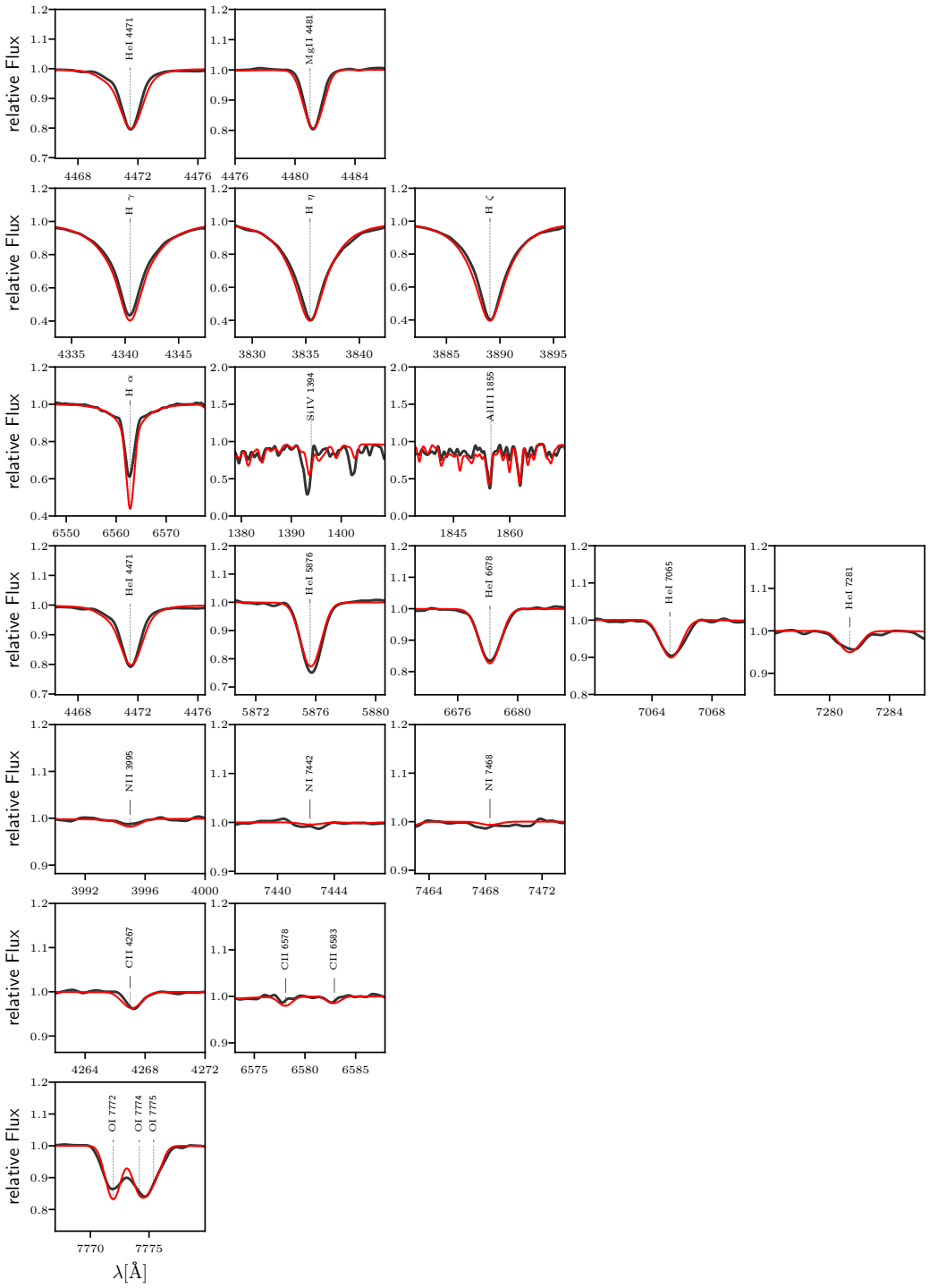


Figure B.20: Individual line fits for AzV 343 (B8 Iab). Black solid line: observed spectrum. Red solid line: spectrum of the best fitting model.

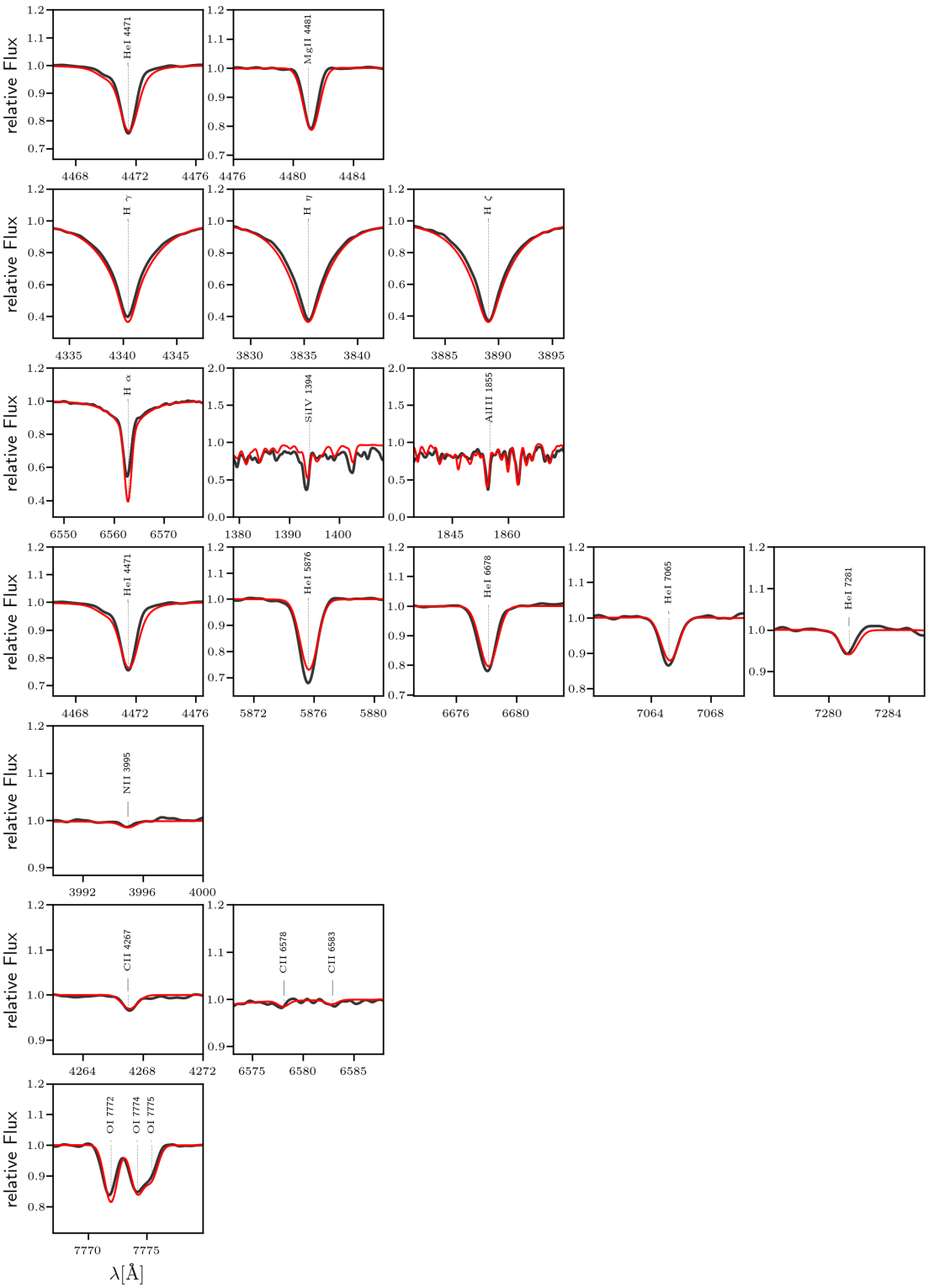


Figure B.21: Individual line fits for AzV 324 (B8 Ib). Black solid line: observed spectrum. Red solid line: spectrum of the best fitting model.

B.6 Overall spectral fits

Fig. B.22-B.41 are the fits for the overall spectrum of each star in our sample.

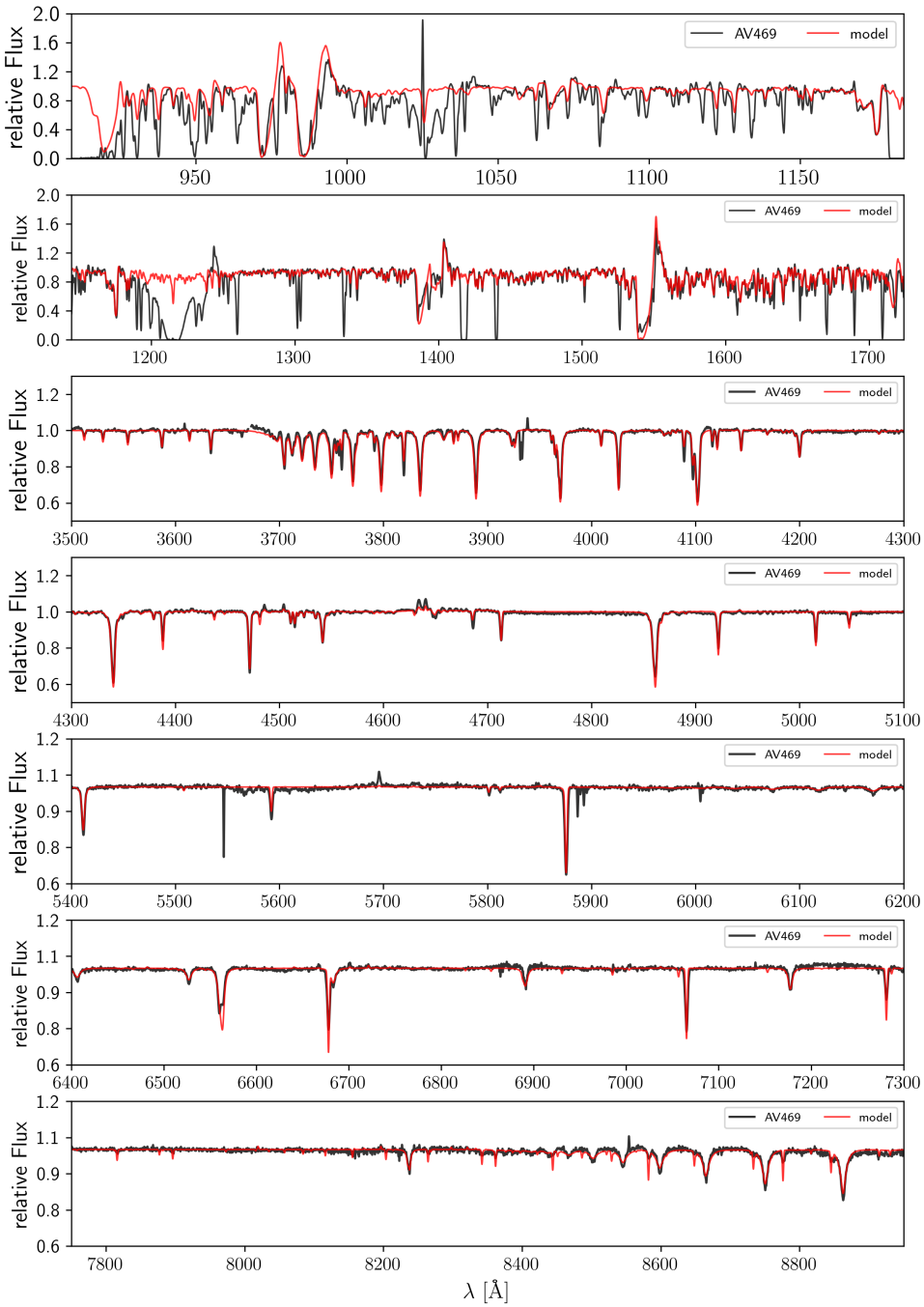


Figure B.22: An overall view of the best fit (red solid line) to key regions of the observed spectrum (black solid line) of AzV 469 (O9 Iab(f)). From the top, the first panel displays the FUV FUSE range, which contains interstellar features such as *Lyδ* λ950, *Lyγ* λ973, and *Lyβ* λ1026. The second panel is the STIS E140M FUV range. We note some interstellar features: *Lyα* λ1216, O I + P II λ1302, C II λ1335, Si II λ1527, and Al IIλ1671. The rest of the panels are the UBV and VIS XShooter spectra, with the break between the two arms at ≈ 5600 Å. The lines Ca II H + K and Na I D are interstellar features.

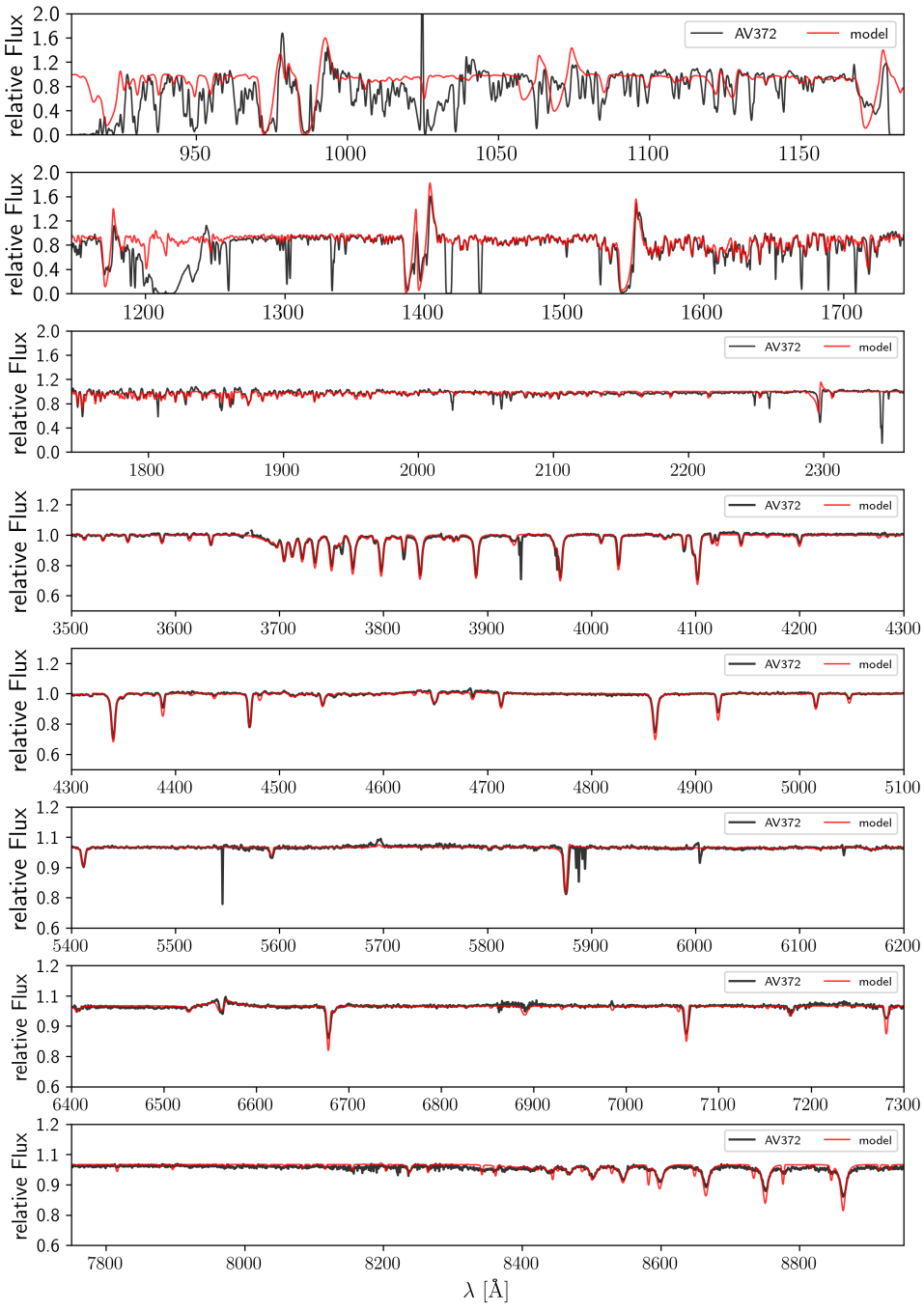


Figure B.23: An overall view of the best fit (red solid line) to key regions of the observed spectrum (black solid line) of AzV 372 (O9.2 Iab). From the top, the first panel displays the FUV FUSE range, which contains interstellar features such as *Lyδ* λ950, *Lyγ* λ973, and *Lyβ* λ1026. The second and third panels are STIS E140M FUV and STIS E230M UV, respectively. We note some interstellar features: *Lyα* λ1216, O I + P II λ1302, C II λ1335, Si II λ1527, and Al IIλ1671. The rest of the panels are the UBV and VIS XShooter spectra, with the break between the two arms at ≈ 5600 Å. The lines Ca II H + K and Na I D are interstellar features.

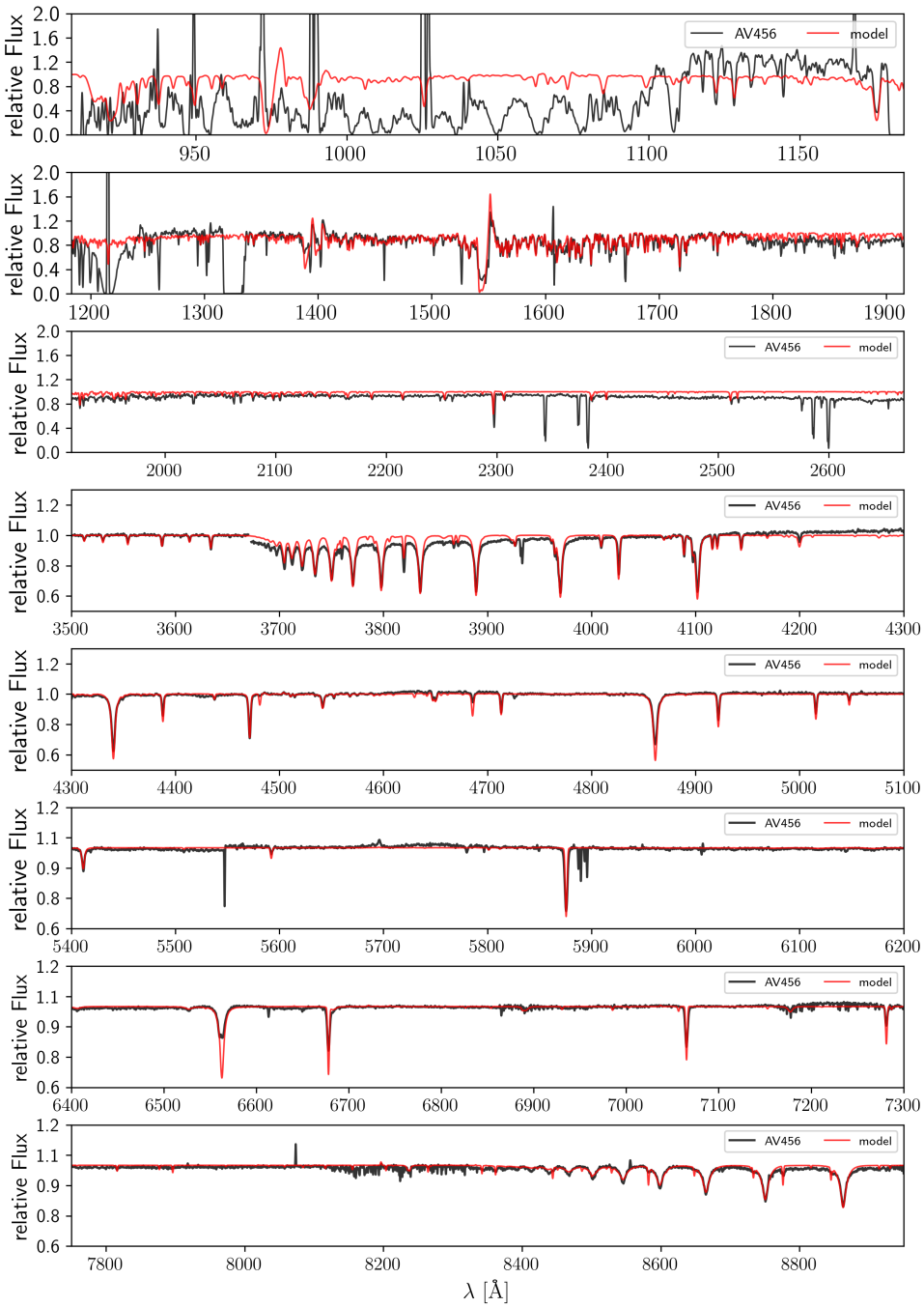


Figure B.24: An overall view of the best fit (red solid line) to key regions of the observed spectrum (black solid line) of AzV 456 (O9.5 Iab). From the top, the first panel displays the FUV FUSE range, which contains interstellar features such as *Lyδ* λ950, *Lyγ* λ973, and *Lyβ* λ1026. The second and third panels are STIS E140M FUV and STIS E230M UV, respectively. We note some interstellar features: *Lyα* λ1216, O I + P II λ1302, C II λ1335, Si II λ1527, and Al IIλ1671. The rest of the panels are the UBV and VIS XShooter spectra, with the break between the two arms at ≈ 5600 Å. The lines Ca II H + K and Na I D are interstellar features.

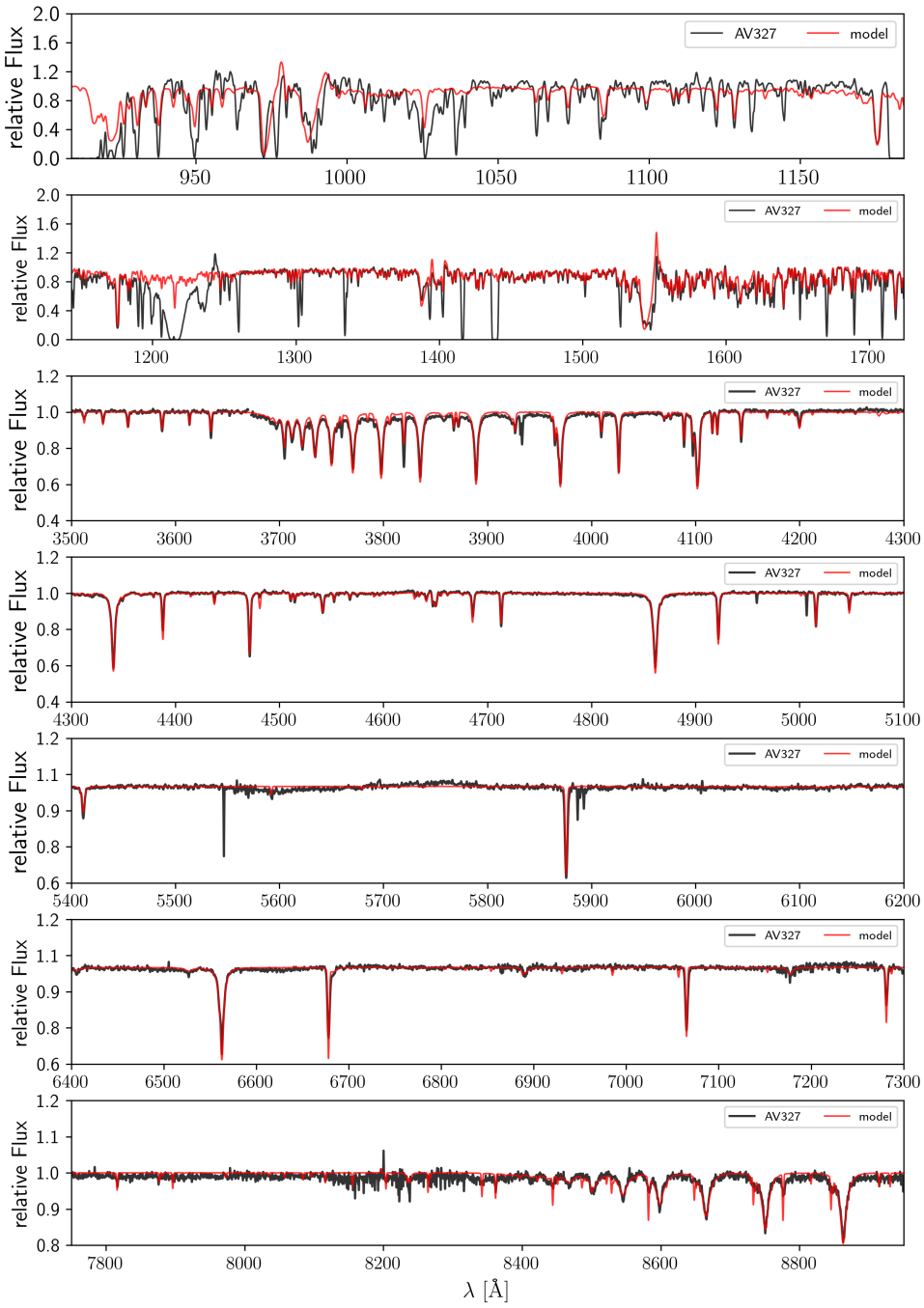


Figure B.25: An overall view of the best fit (red solid line) to key regions of the observed spectrum (black solid line) of AzV 327 (O9.7 Ib). From the top, the first panel displays the FUV FUSE range, which contains interstellar features such as *Lyδ* λ950, *Lyγ* λ973, and *Lyβ* λ1026. The second and third panels are COS G130M + Cos G160M FUV and STIS E230M UV, respectively. We note some interstellar features: *Lyα* λ1216, O I + P II λ1302, C II λ1335, Si II λ1527, and Al IIλ1671. The rest of the panels are the UBV and VIS XShooter spectra, with the break between the two arms at ≈ 5600 Å. The lines Ca II H + K and Na I D are interstellar features.

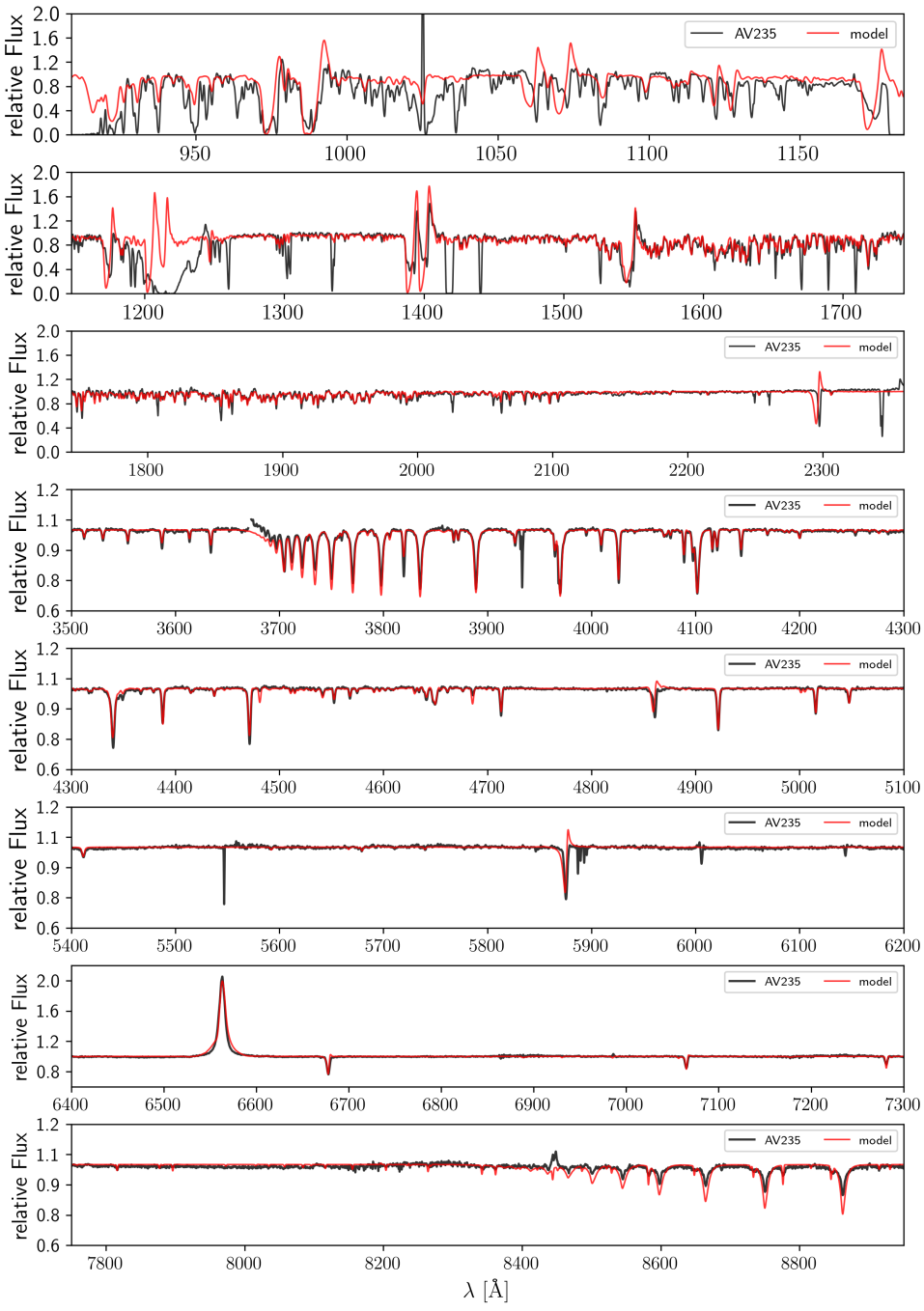


Figure B.26: An overall view of the best fit (red solid line) to key regions of the observed spectrum (black solid line) of AzV 235 (B0 Ia). From the top, the first panel displays the FUV FUSE range, which contains interstellar features such as *Lyδ* λ950, *Lyγ* λ973, and *Lyβ* λ1026. The second and third panels are STIS E140M FUV and STIS E230M UV, respectively. We note some interstellar features: *Lyα* λ1216, O I+P II λ1302, C II λ1335, Si II λ1527, and Al IIλ1671. The rest of the panels are the UBV and VIS XShooter spectra, with the break between the two arms at ≈ 5600 Å. The lines Ca II H + K and Na I D are interstellar features.

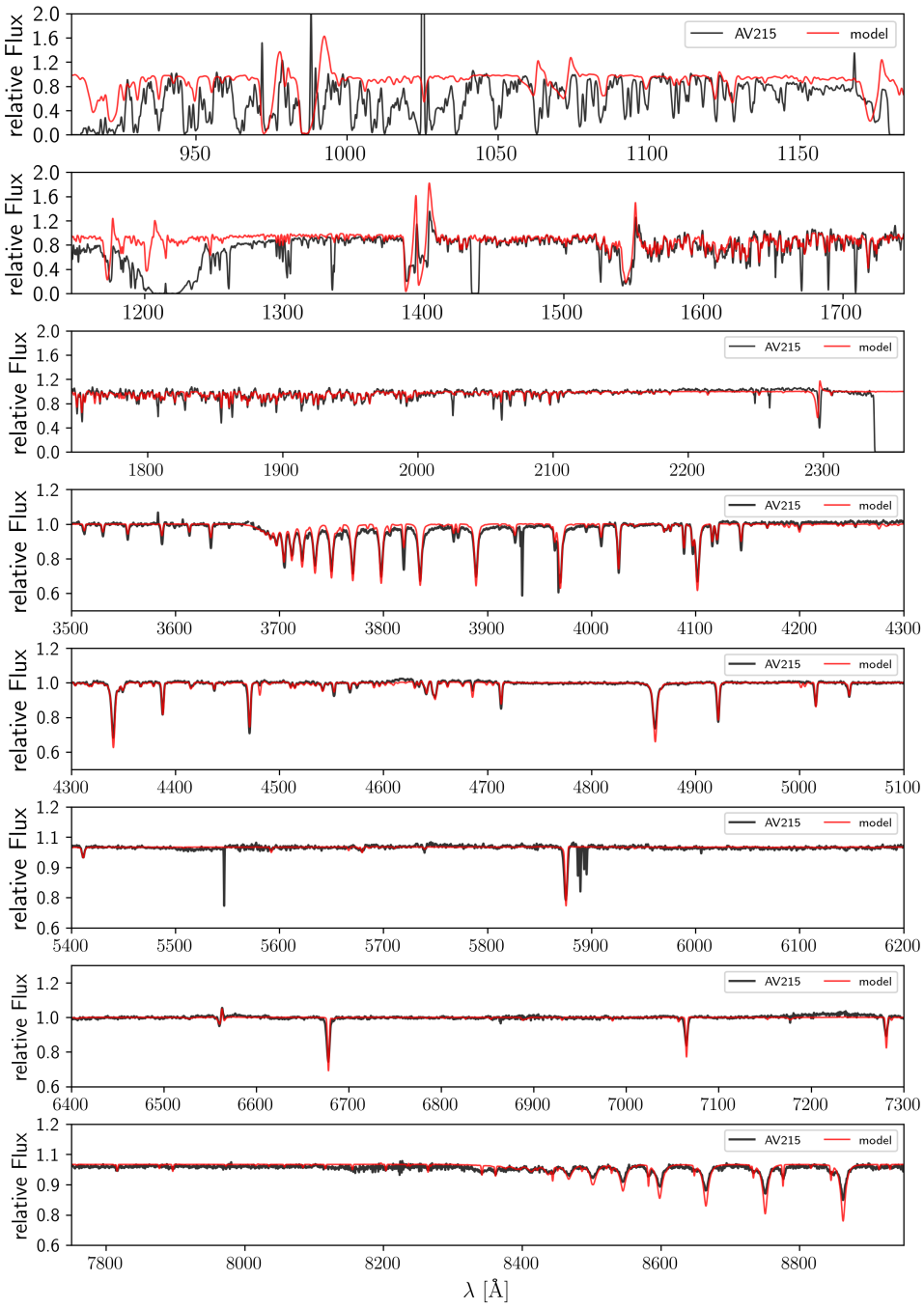


Figure B.27: An overall view of the best fit (red solid line) to key regions of the observed spectrum (black solid line) of AzV 215 (B0 Ia). From the top, the first panel displays the FUV FUSE range, which contains interstellar features such as *Lyδ* λ950, *Lyγ* λ973, and *Lyβ* λ1026. The second and third panels are STIS E140M FUV and STIS E230M UV, respectively. We note some interstellar features: *Lyα* λ1216, O I+P II λ1302, C II λ1335, Si II λ1527, and Al IIλ1671. The rest of the panels are the UBV and VIS XShooter spectra, with the break between the two arms at ≈ 5600 Å. The lines Ca II H + K and Na I D are interstellar features.

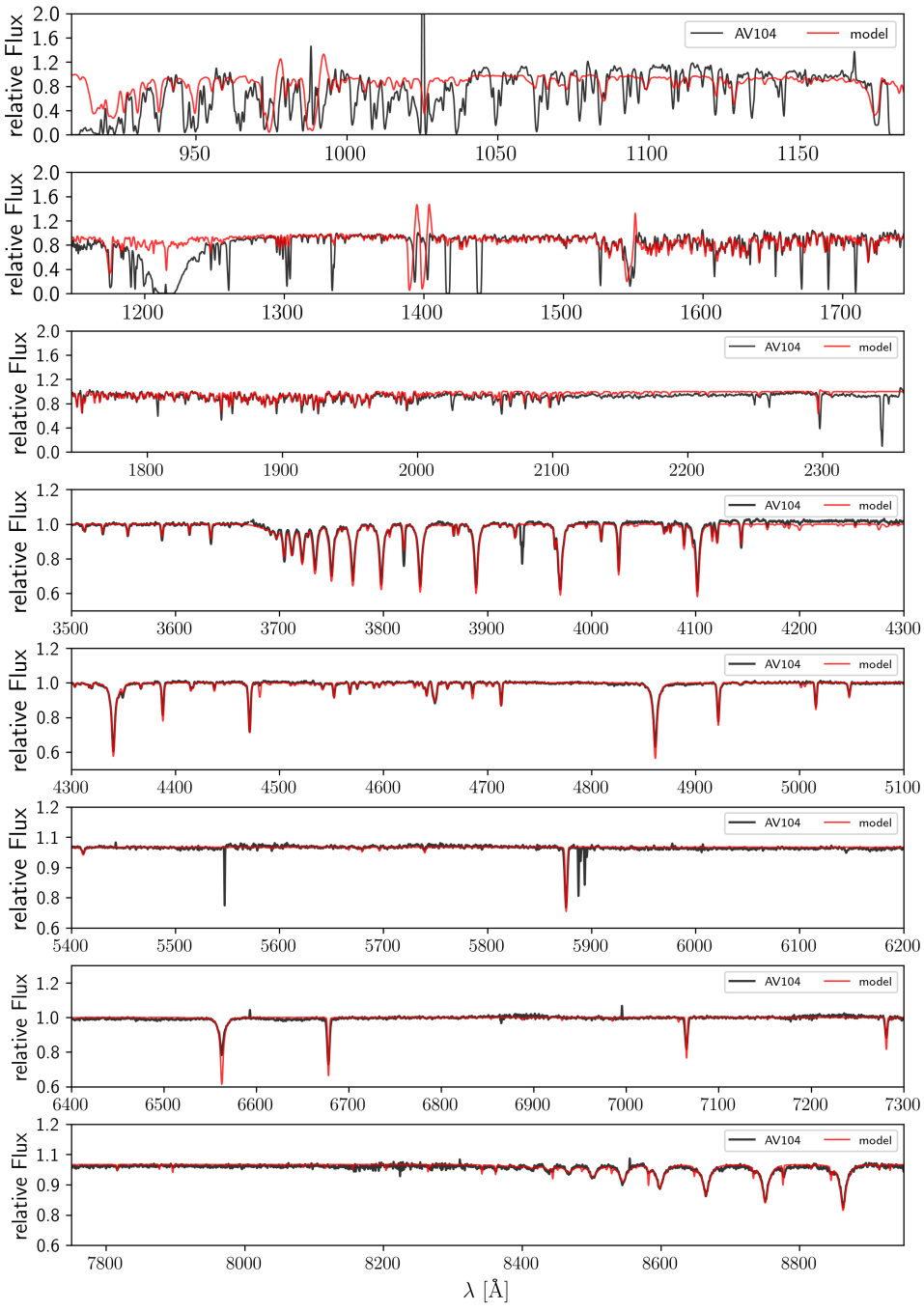


Figure B.28: An overall view of the best fit (red solid line) to key regions of the observed spectrum (black solid line) of AzV 104 (B0.5 Ia). From the top, the first panel displays the FUV FUSE range, which contains interstellar features such as *Lyδ* λ950, *Lyγ* λ973, and *Lyβ* λ1026. The second and third panels are STIS E140M FUV and STIS E230M UV, respectively. We note some interstellar features: *Lyα* λ1216, O I+P II λ1302, C II λ1335, Si II λ1527, and Al IIλ1671. The rest of the panels are the UBV and VIS XShooter spectra, with the break between the two arms at ≈ 5600 Å. The lines Ca II H + K and Na I D are interstellar features.

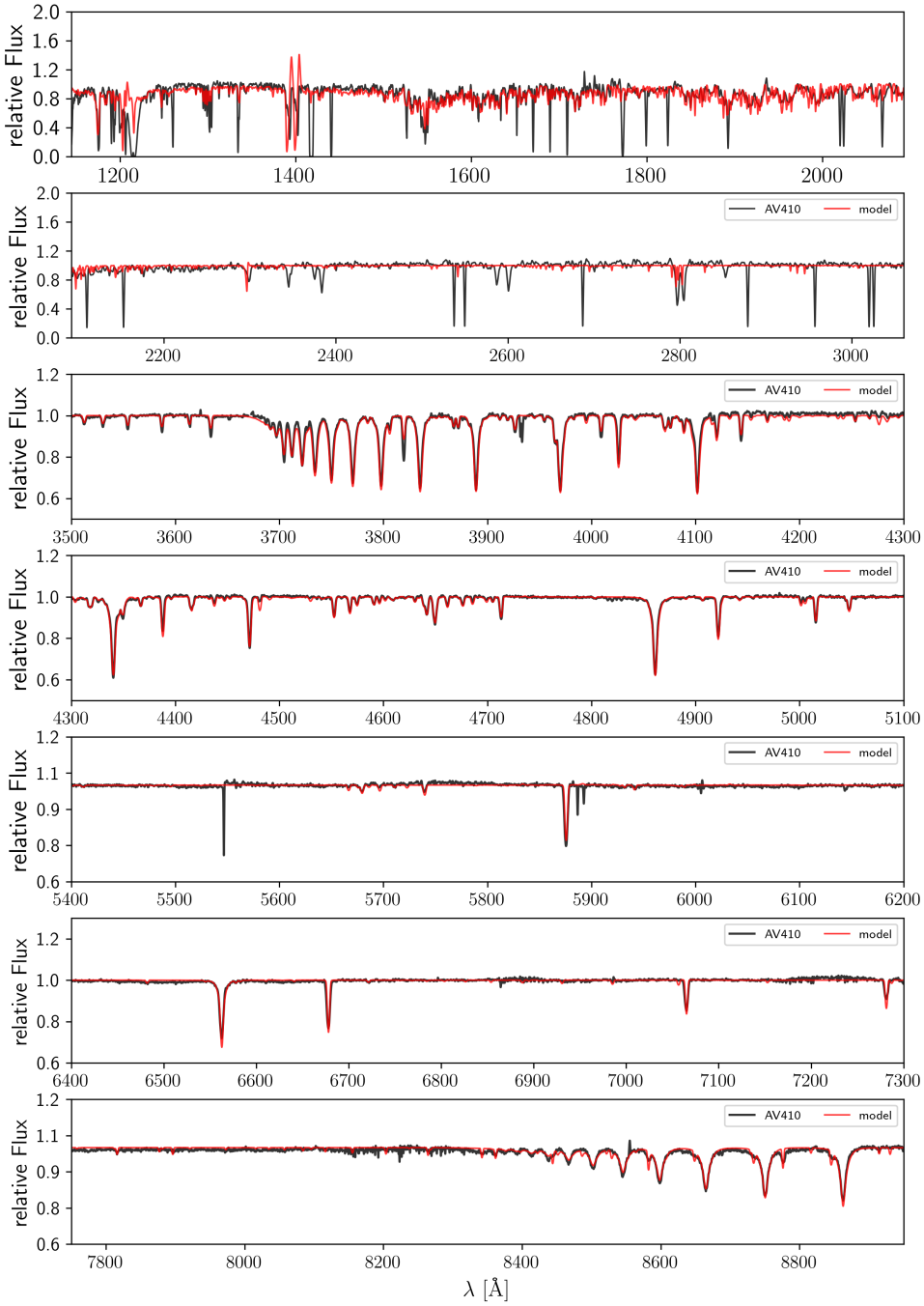


Figure B.29: An overall view of the best fit (red solid line) to key regions of the observed spectrum (black solid line) of AzV 410 (B0.7 Iab). From the top, the first and second panels are STIS E140M FUV and COS G230MLB UV, respectively. We note some interstellar features: *Lyα* λ1216, O I + P II λ1302, C II λ1335, Si II λ1527, and Al II λ1671. The rest of the panels are the UBV and VIS XShooter spectra, with the break between the two arms at ≈ 5600 Å. The lines Ca II H + K and Na I D are interstellar features.

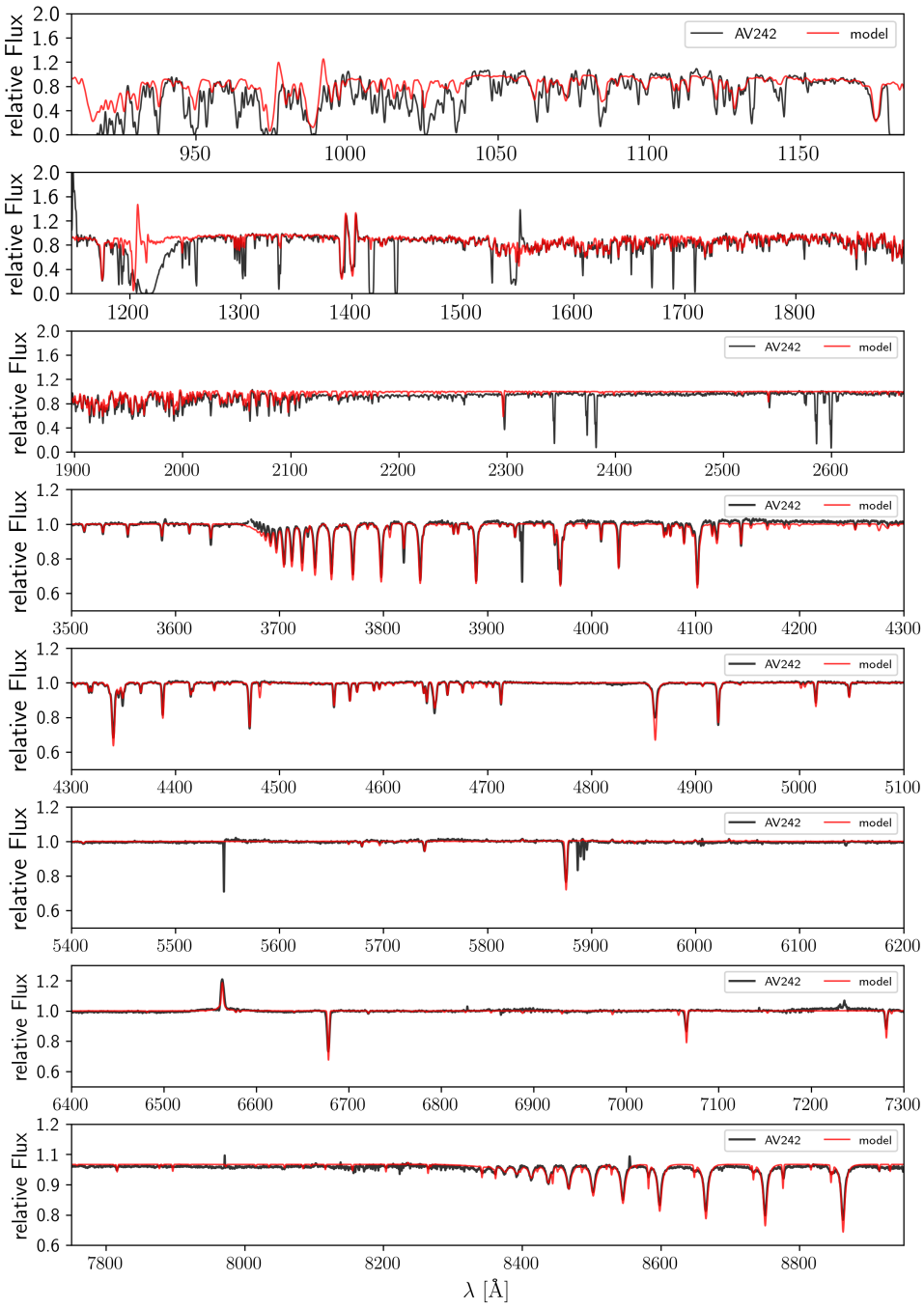


Figure B.30: An overall view of the best fit (red solid line) to key regions of the observed spectrum (black solid line) of AzV 242 (B0.7 Ia). From the top, the first panel displays the FUV FUSE range, which contains interstellar features such as *Lyδ* λ950, *Lyγ* λ973, and *Lyβ* λ1026. The second and third panels are STIS E140M FUV and STIS E230M UV, respectively. We note some interstellar features: *Lyα* λ1216, O I+P II λ1302, C II λ1335, Si II λ1527, and Al IIλ1671. The rest of the panels are the UBV and VIS XShooter spectra, with the break between the two arms at ≈ 5600 Å. The lines Ca II H + K and Na I D are interstellar features.

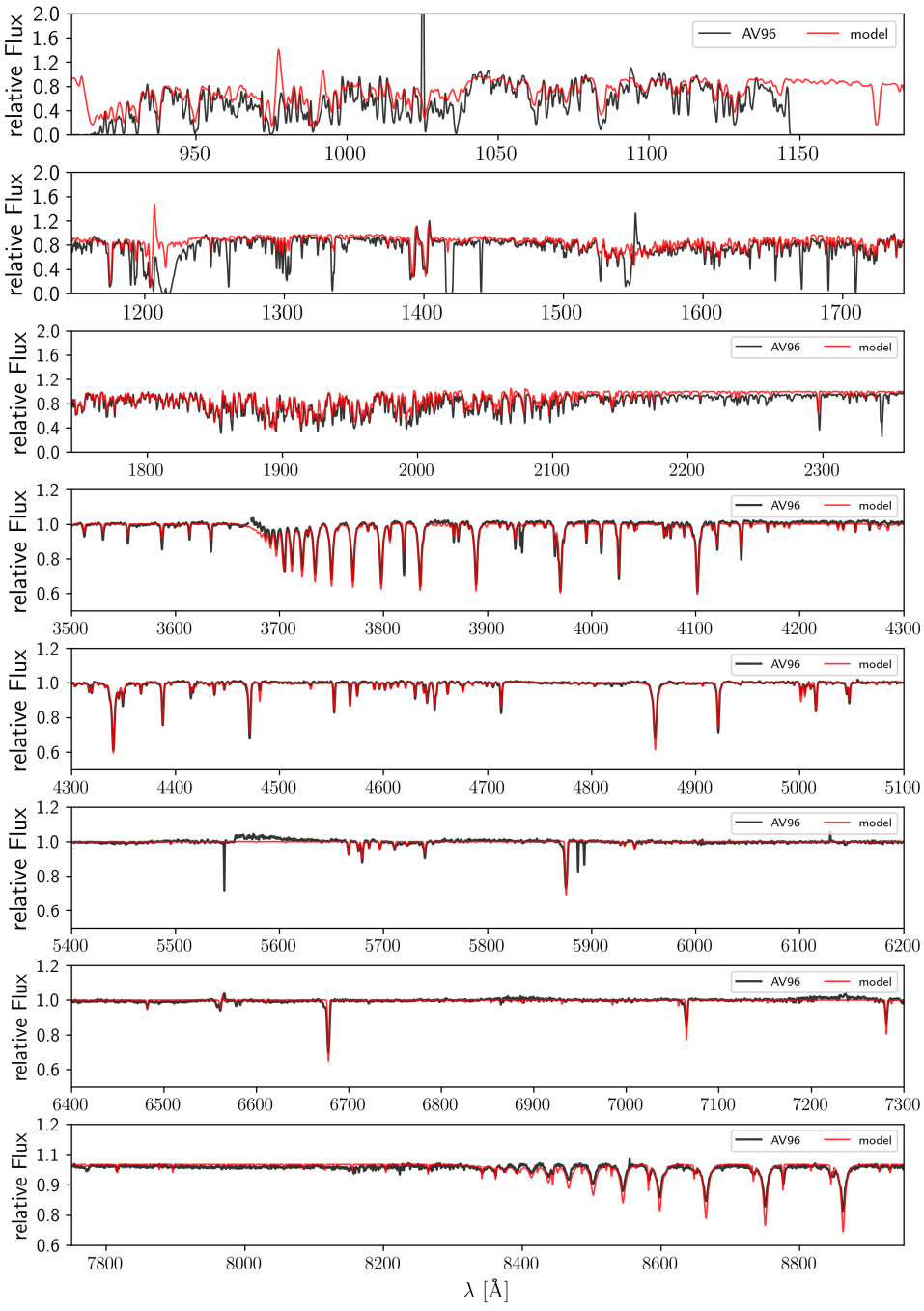


Figure B.31: An overall view of the best fit (red solid line) to key regions of the observed spectrum (black solid line) of AzV 96 (B1 Iab). From the top, the first panel displays the FUV FUSE range, which contains interstellar features such as *Lyδ* λ950, *Lyγ* λ973, and *Lyβ* λ1026. The second and third panels are STIS E140M FUV and STIS E230M UV, respectively. We note some interstellar features: *Lyα* λ1216, O I+P II λ1302, C II λ1335, Si II λ1527, and Al IIλ1671. The rest of the panels are the UBV and VIS XShooter spectra, with the break between the two arms at ≈ 5600 Å. The lines Ca II H + K and Na I D are interstellar features.

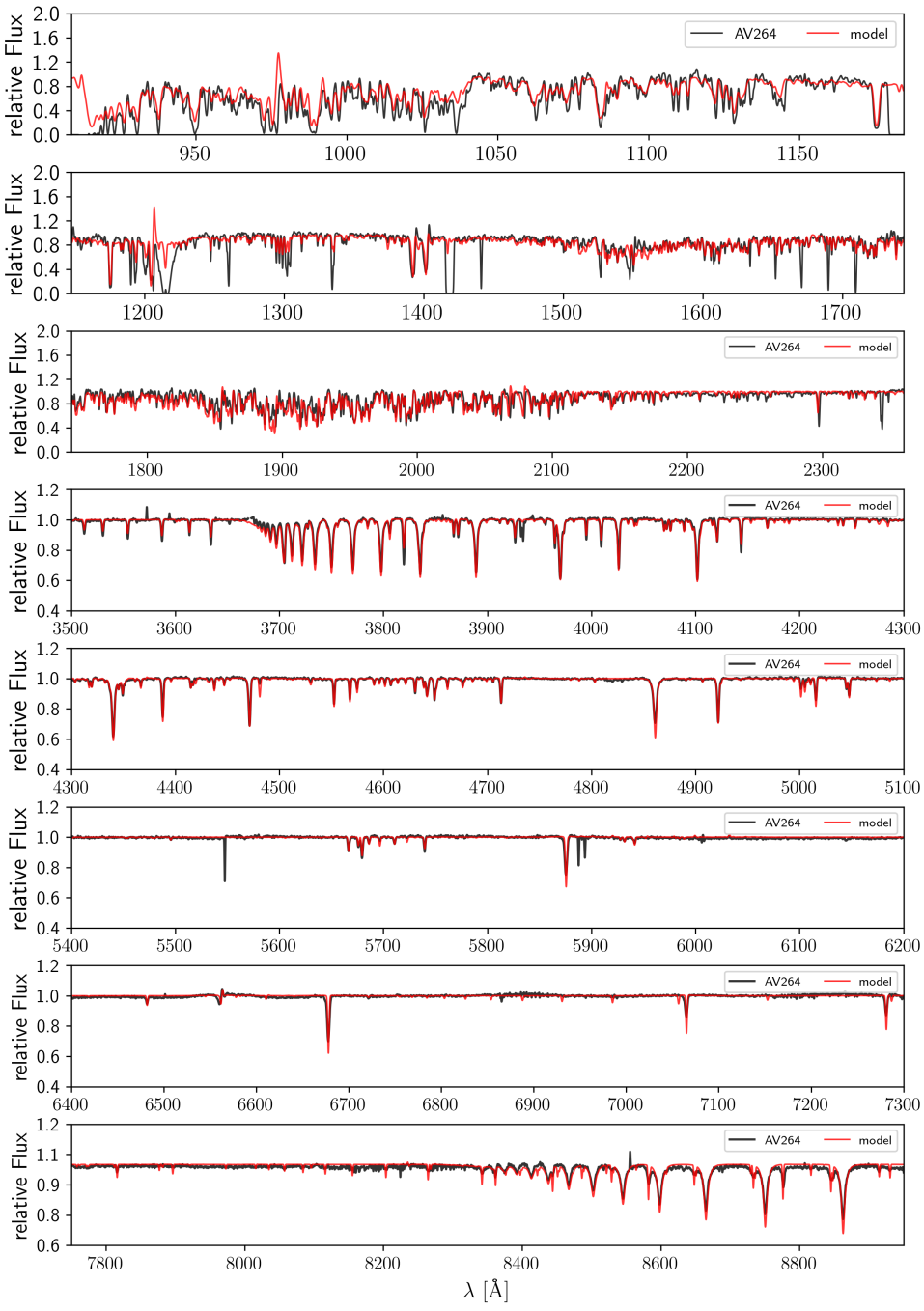


Figure B.32: An overall view of the best fit (red solid line) to key regions of the observed spectrum (black solid line) of AzV 264 (B1 Ia). From the top, the first panel displays the FUV FUSE range, which contains interstellar features such as *Lyδ* λ950, *Lyγ* λ973, and *Lyβ* λ1026. The second and third panels are STIS E140M FUV and STIS E230M UV, respectively. We note some interstellar features: *Lyα* λ1216, O I+P II λ1302, C II λ1335, Si II λ1527, and Al IIλ1671. The rest of the panels are the UBV and VIS XShooter spectra, with the break between the two arms at ≈ 5600 Å. The lines Ca II H + K and Na I D are interstellar features.

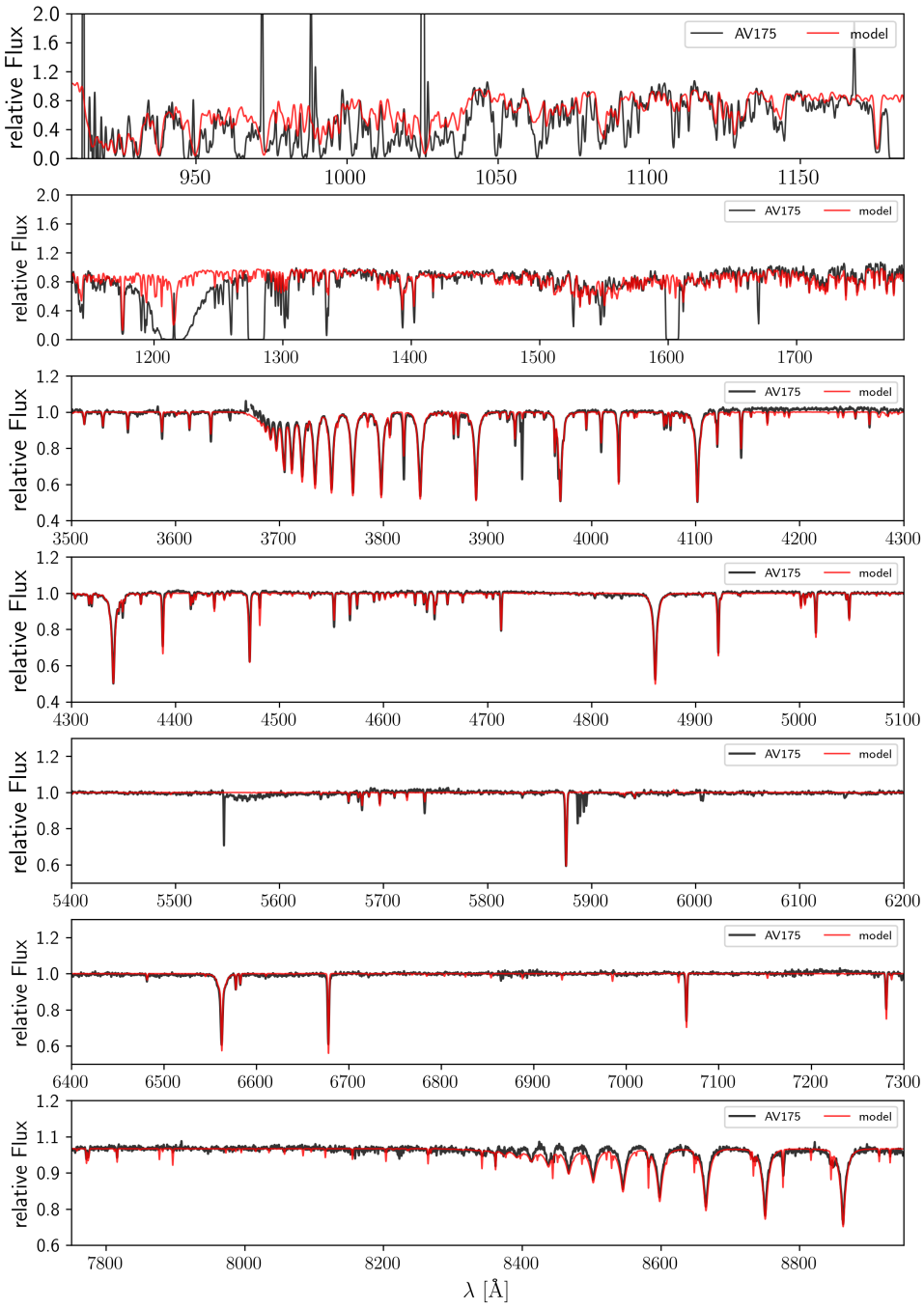


Figure B.33: An overall view of the best fit (red solid line) to key regions of the observed spectrum (black solid line) of AzV 175 (B1.5 Ib). From the top, the first panel displays the FUV FUSE range, which contains interstellar features such as *Lyδ* λ950, *Lyγ* λ973, and *Lyβ* λ1026. The second panel is the COS G130M + COS G160M FUV. We note some interstellar features: *Lyα* λ1216, O I + P II λ1302, C II λ1335, Si II λ1527, and Al IIλ1671. The rest of the panels are the UBV and VIS XShooter spectra, with the break between the two arms at ≈ 5600 Å. The lines Ca II H + K and Na I D are interstellar features.

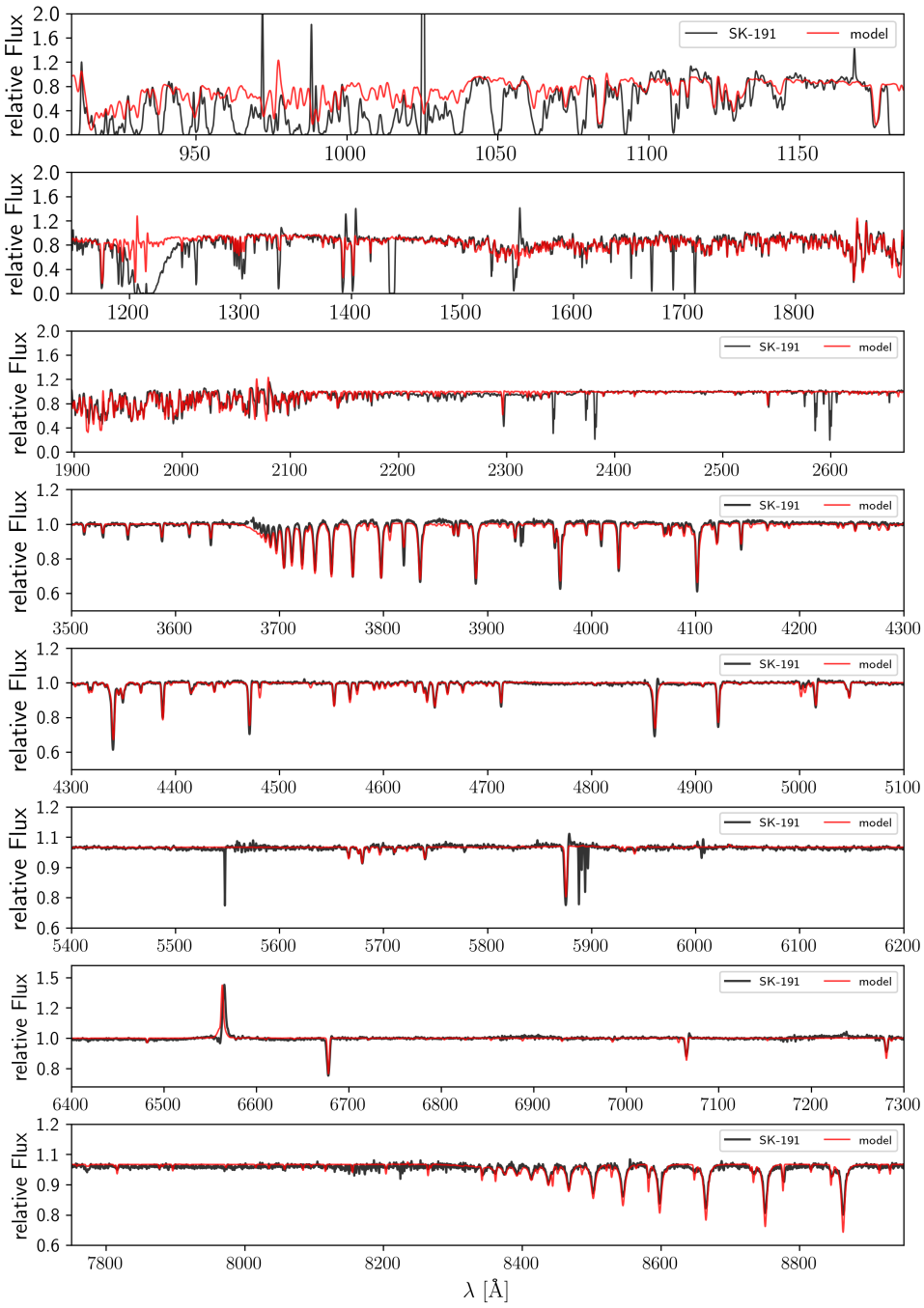


Figure B.34: An overall view of the best fit (red solid line) to key regions of the observed spectrum (black solid line) of Sk 191 (B1.5 Ia). From the top, the first panel displays the FUV FUSE range, which contains interstellar features such as *Lyδ* λ950, *Lyγ* λ973, and *Lyβ* λ1026. The second and third panels are STIS E140M FUV and STIS E230M UV, respectively. We note some interstellar features: *Lyα* λ1216, O I+P II λ1302, C II λ1335, Si II λ1527, and Al IIλ1671. The rest of the panels are the UBV and VIS XShooter spectra, with the break between the two arms at ≈ 5600 Å. The lines Ca II H + K and Na I D are interstellar features.

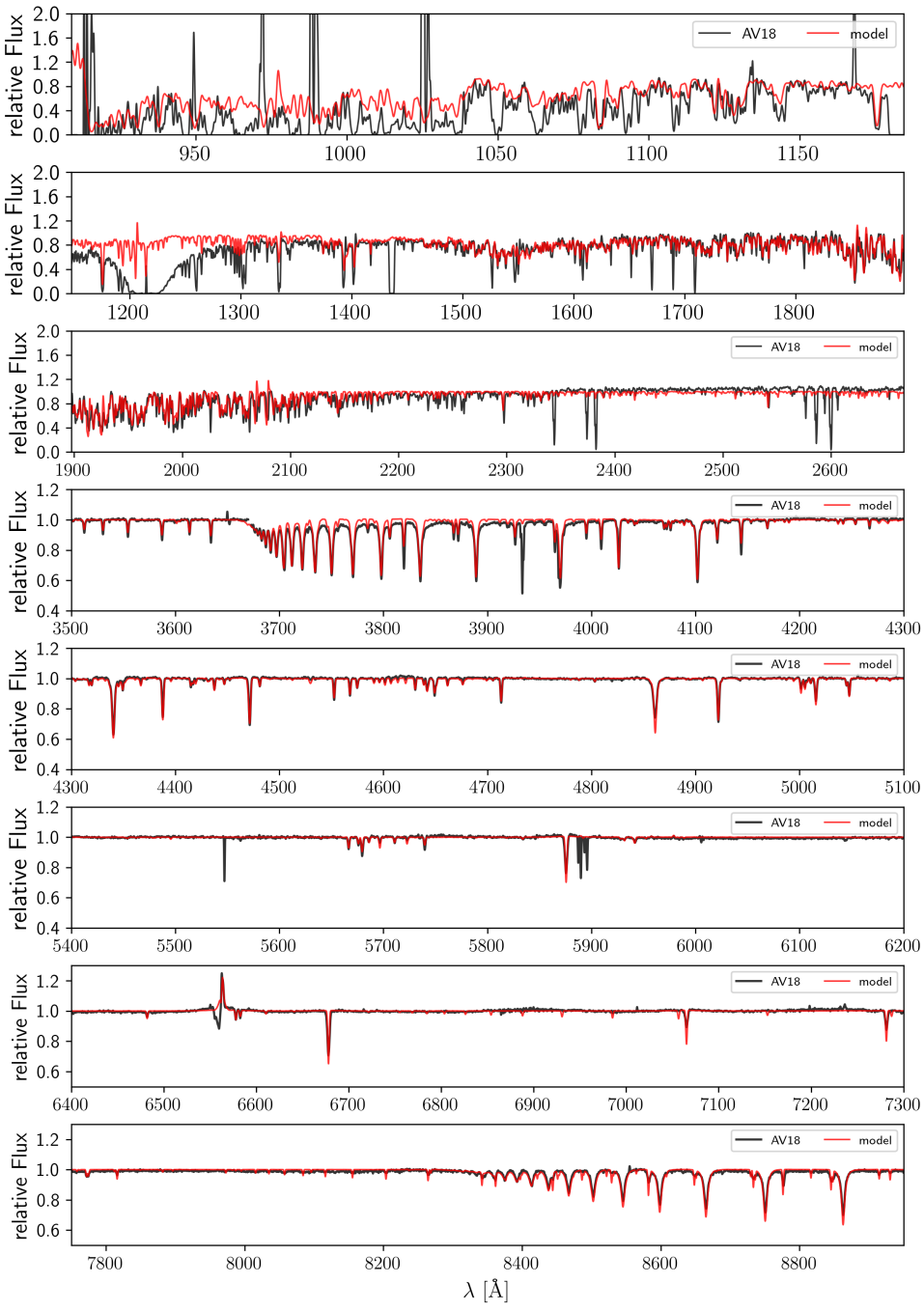


Figure B.35: An overall view of the best fit (red solid line) to key regions of the observed spectrum (black solid line) of AzV 18 (B2 Ia). From the top, the first panel displays the FUV FUSE range, which contains interstellar features such as *Lyδ* λ950, *Lyγ* λ973, and *Lyβ* λ1026. The second and third panels are STIS E140M FUV and STIS E230M UV, respectively. We note some interstellar features: *Lyα* λ1216, O I+P II λ1302, C II λ1335, Si II λ1527, and Al IIλ1671. The rest of the panels are the UBV and VIS XShooter spectra, with the break between the two arms at ≈ 5600 Å. The lines Ca II H + K and Na I D are interstellar features.

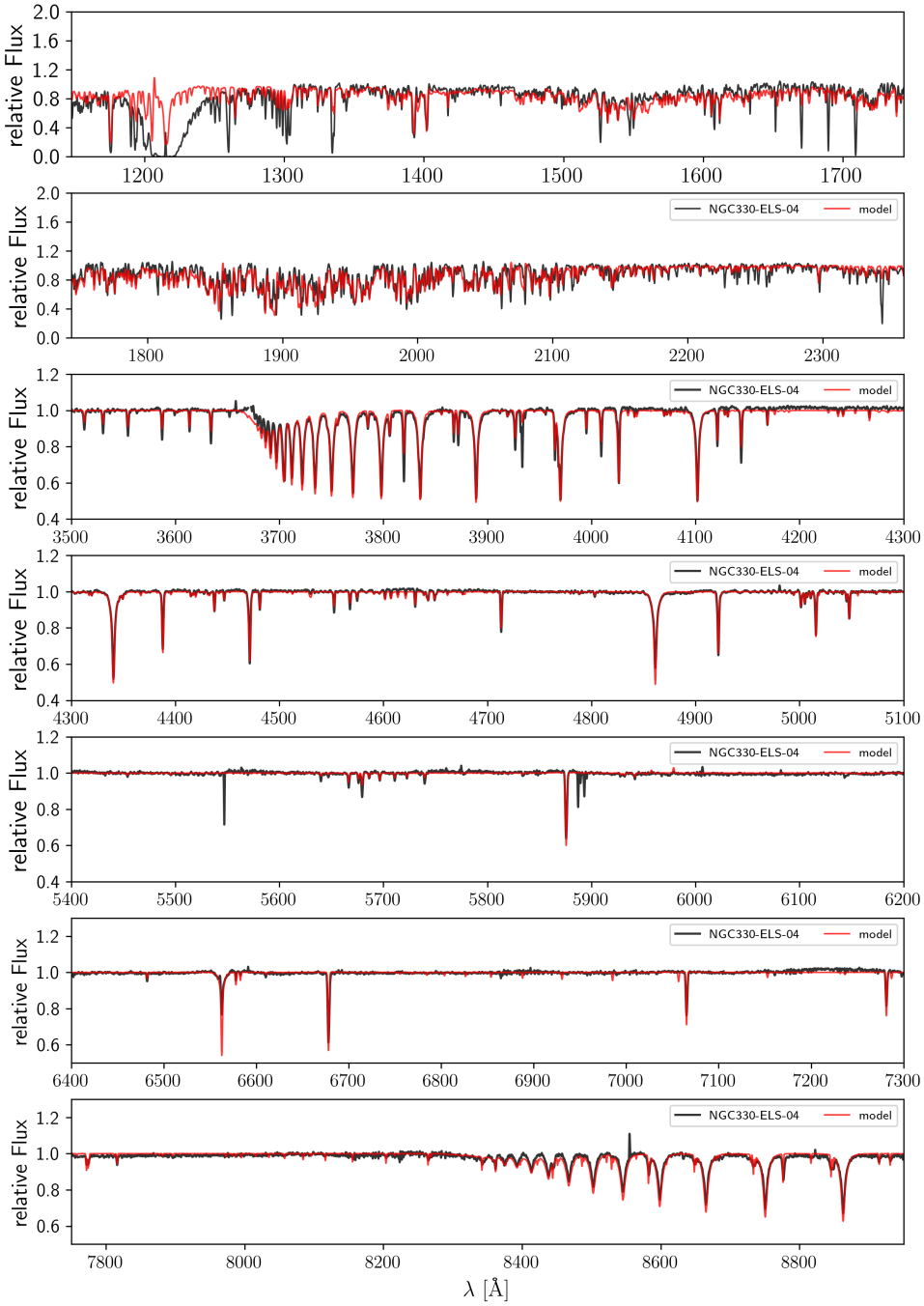


Figure B.36: An overall view of the best fit (red solid line) to key regions of the observed spectrum (black solid line) of NGC330 ELS 04 (B2.5 Ib). From the top, the first panel and second panels are STIS E140M FUV and STIS E230M UV, respectively. We note some interstellar features: *Lyα* λ1216, O I + P II λ1302, C II λ1335, Si II λ1527, and Al II λ1671. The rest of the panels are the UBV and VIS XShooter spectra, with the break between the two arms at ≈ 5600 Å. The lines Ca II H + K and Na I D are interstellar features.

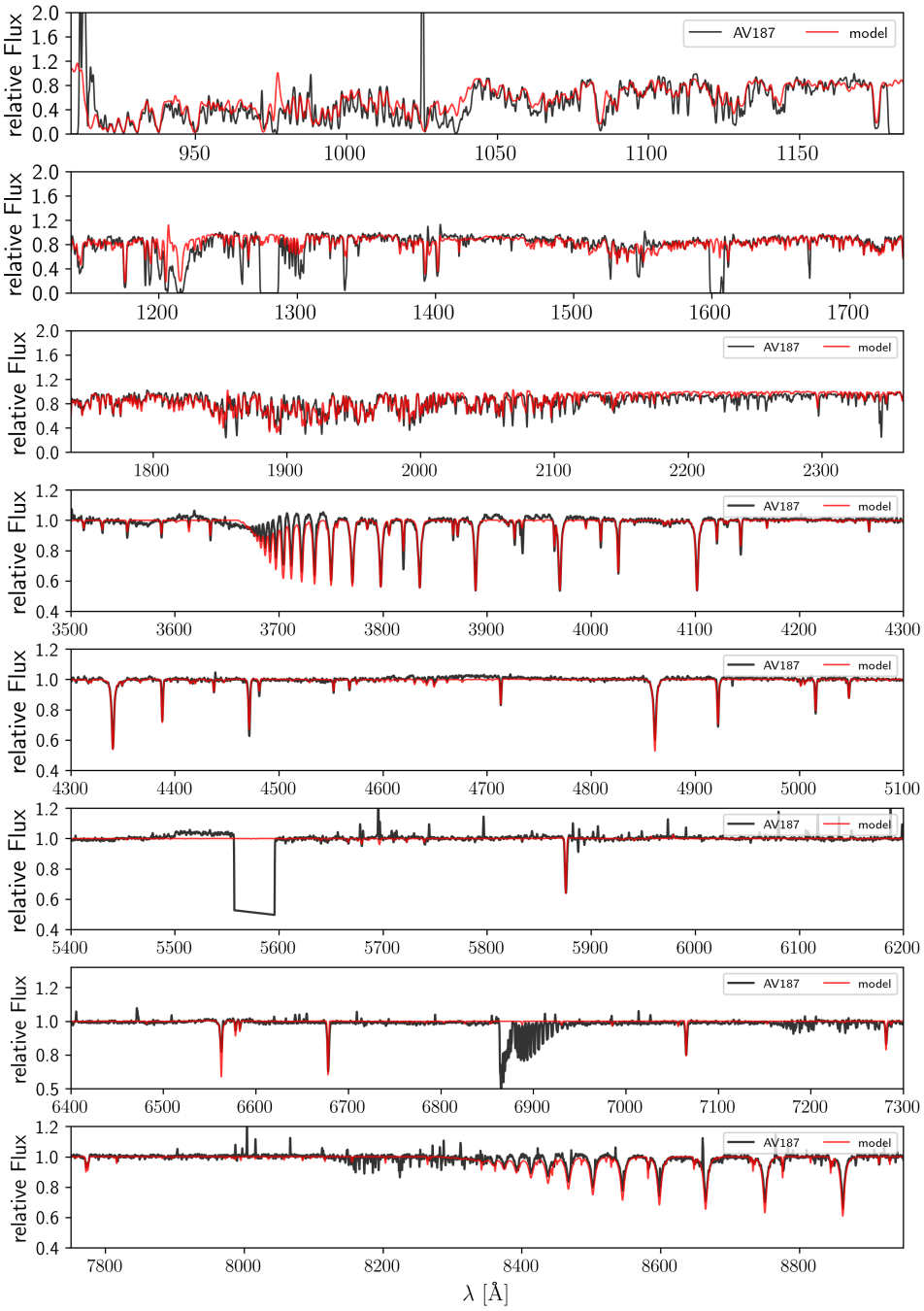


Figure B.37: An overall view of the best fit (red solid line) to key regions of the observed spectrum (black solid line) of AzV 187 (B2.5 Ia). From the top, the first panel displays the FUV FUSE range, which contains interstellar features such as *Lyδ* λ950, *Lyγ* λ973, and *Lyβ* λ1026. The second and third panels are COS G130M + COS G160M FUV and STIS E230M UV, respectively. We note some interstellar features: *Lyα* λ1216, O I + P II λ1302, C II λ1335, Si II λ1527, and Al IIλ1671. The rest of the panels are the UBV and VIS XShooter spectra, with the break between the two arms at ≈ 5600 Å. The lines Ca II H + K and Na I D are interstellar features.

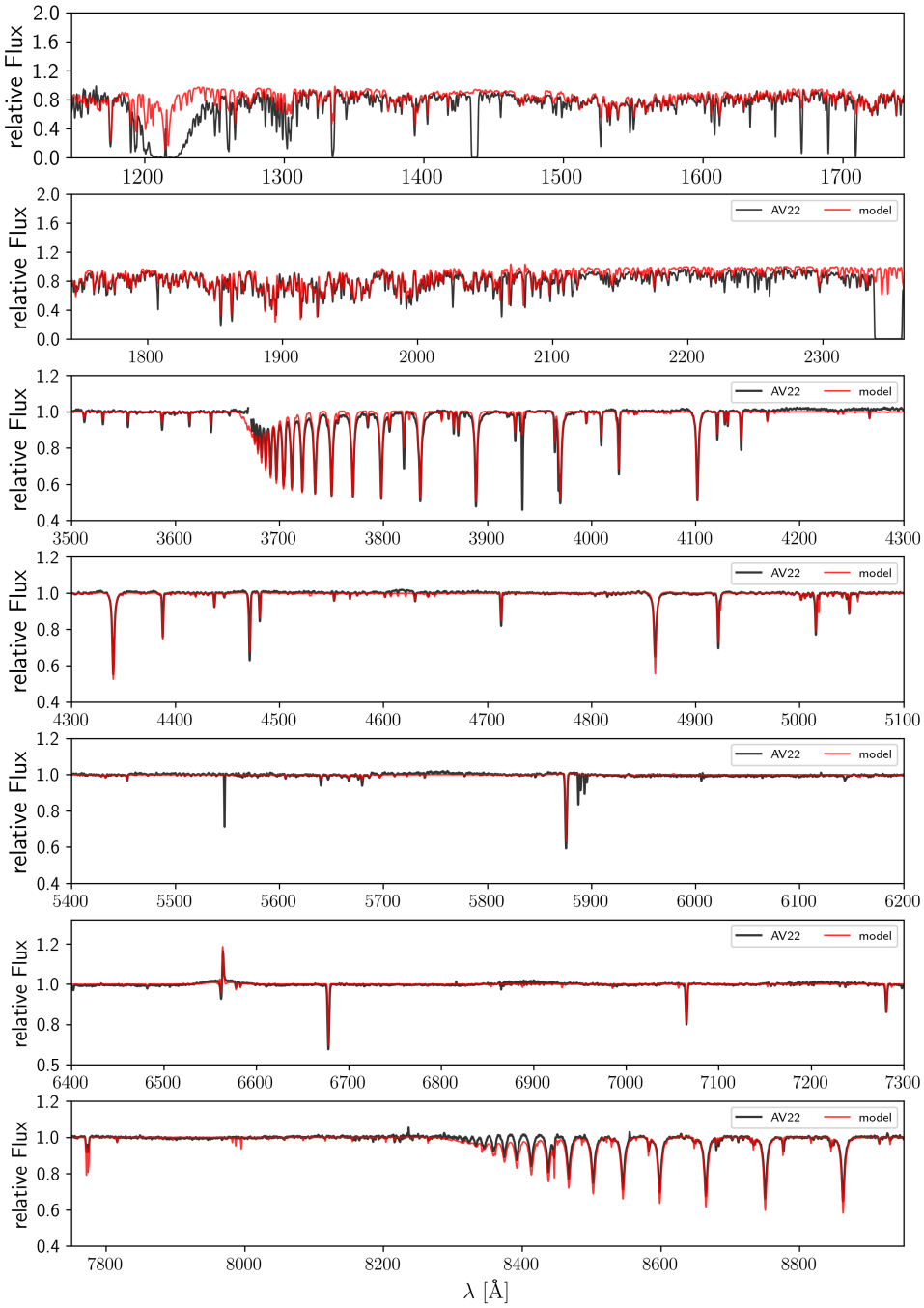


Figure B.38: An overall view of the best fit (red solid line) to key regions of the observed spectrum (black solid line) of AzV 22 (B3 Ia). From the top, the first and second panels are the STIS E140M FUV and STIS E230M UV, respectively. We note some interstellar features: *Lyα* λ1216, O I + P II λ1302, C II λ1335, Si II λ1527, and Al IIλ1671. The rest of the panels are the UBV and VIS XShooter spectra, with the break between the two arms at ≈ 5600 Å. The lines Ca II H + K and Na I D are interstellar features.

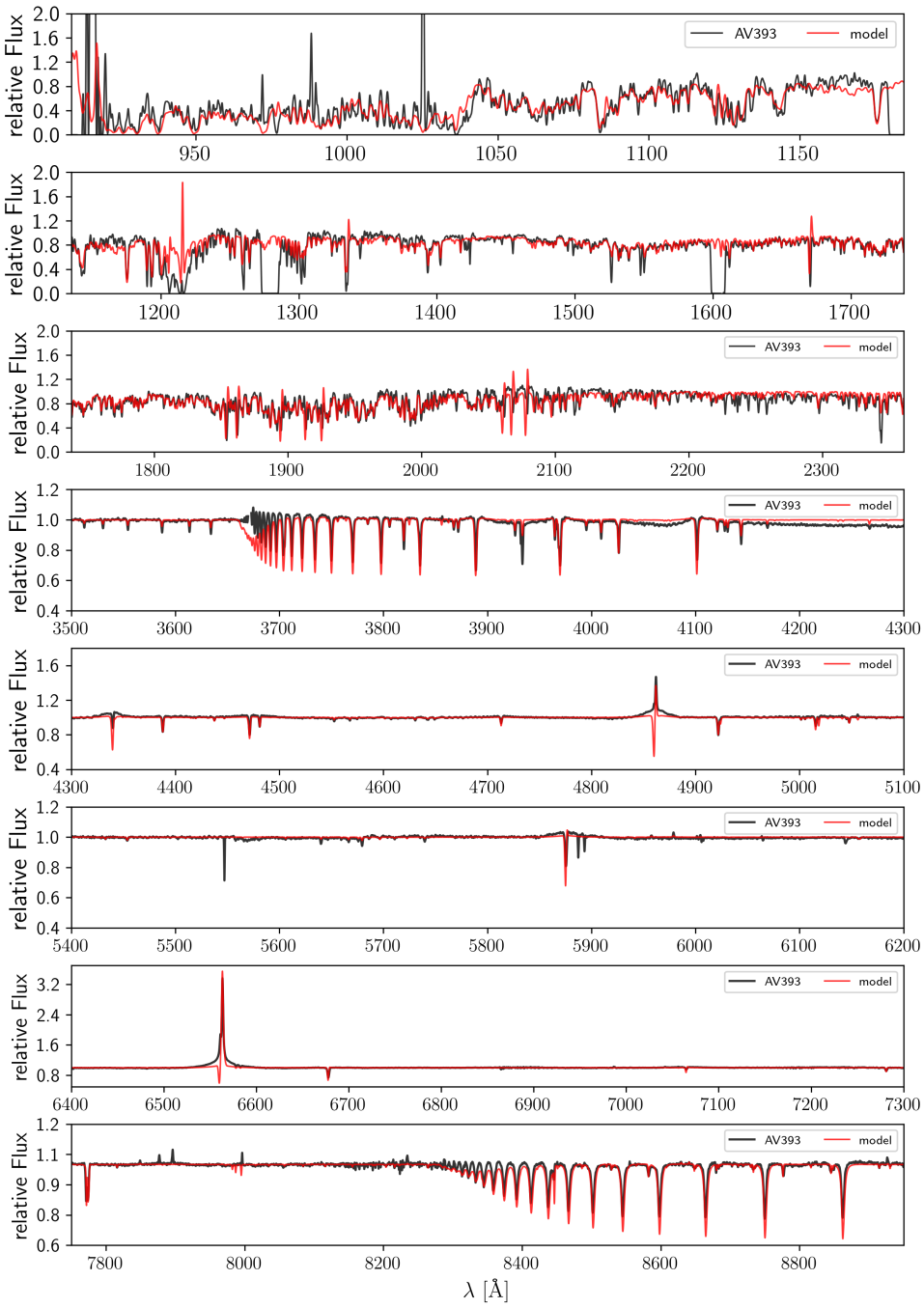


Figure B.39: An overall view of the best fit (red solid line) to key regions of the observed spectrum (black solid line) of AzV 393 (B3 Ia$^+$). From the top, the first panel is the FUV FUSE range, containing interstellar features such as *Lyδ* λ950, *Lyγ* λ973, and *Lyβ* λ1026. The second and third panels are COS G130M + COS G160M FUV and STIS E230M UV, respectively. We note some interstellar features: *Lyα* λ1216, O I + P II λ1302, C II λ1335, Si II λ1527, and Al IIλ1671. The rest of the panels are the UBV and VIS XShooter spectra, with the break between the two arms at ≈ 5600 Å. The lines Ca II H + K and Na I D are interstellar features.

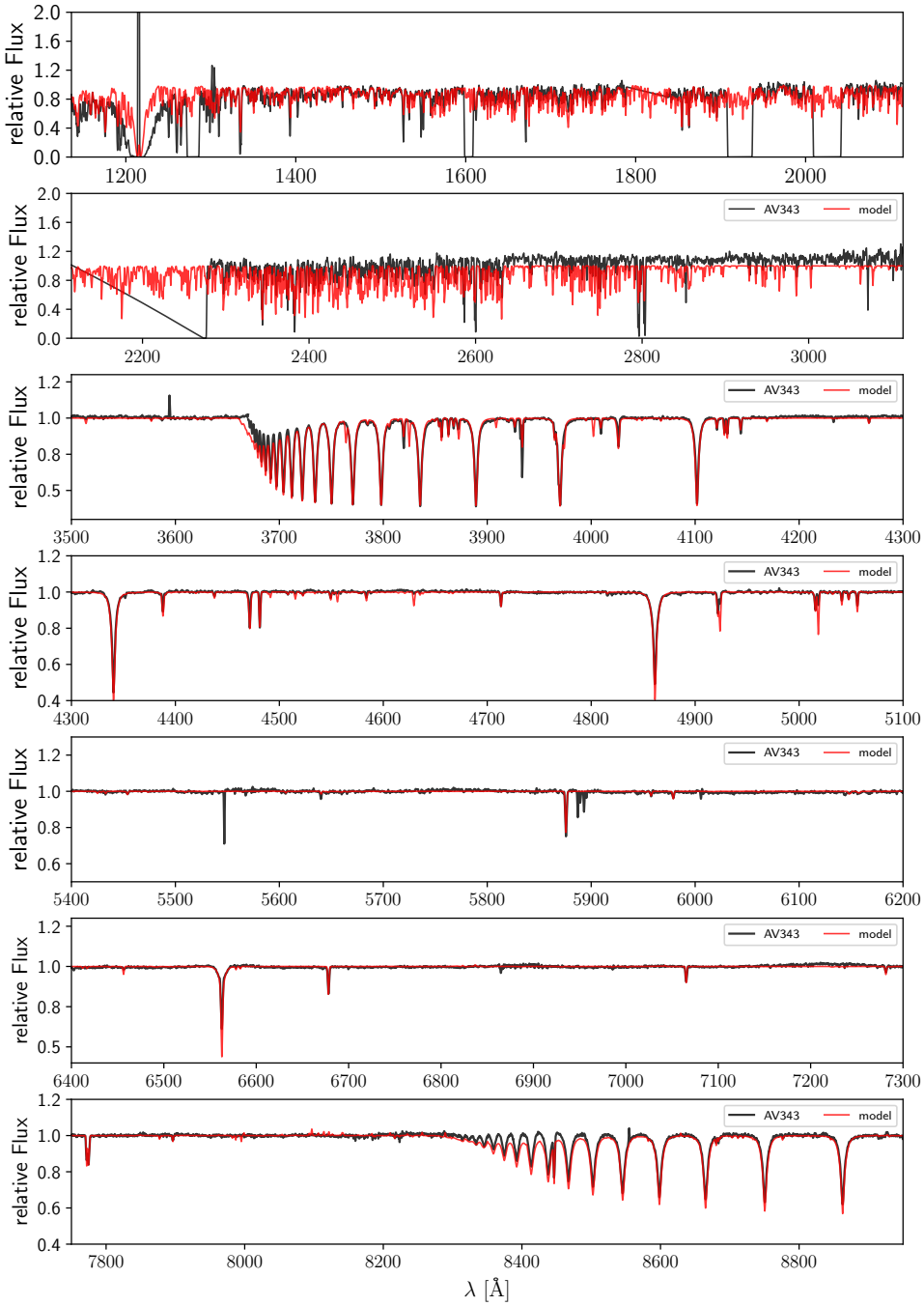


Figure B.40: An overall view of the best fit (red solid line) to key regions of the observed spectrum (black solid line) of AzV 343 (B8 Iab). From the top, the first panel and second panels are COS G130M + COS G160M FUV and STIS E230M UV, respectively. We note some interstellar features: *Lyα* λ1216, O I + P II λ1302, C II λ1335, Si II λ1527, and Al IIλ1671. The rest of the panels are the UBV and VIS XShooter spectra, with the break between the two arms at ≈ 5600 Å. The lines Ca II H + K and Na I D are interstellar features.

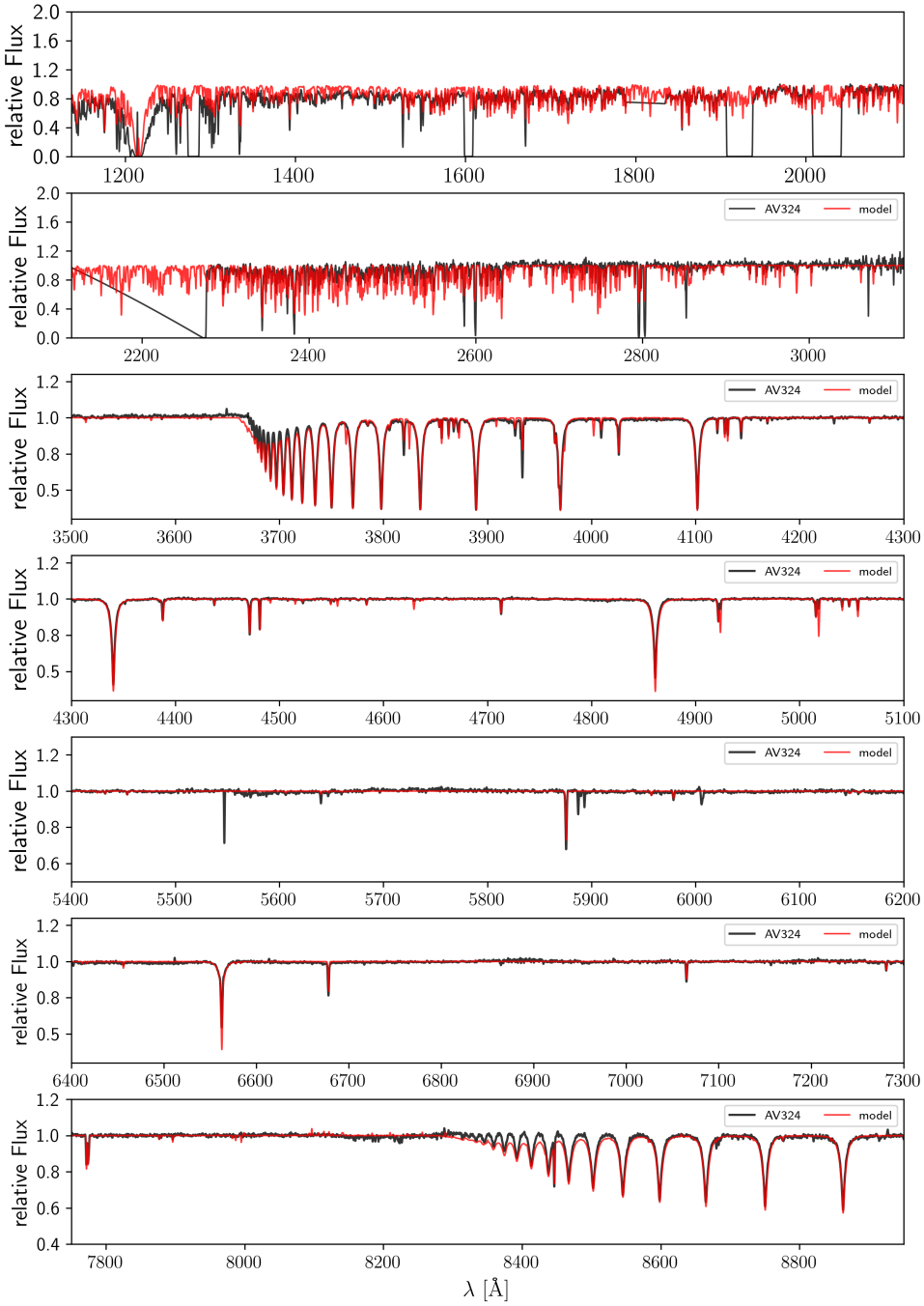


Figure B.41: An overall view of the best fit (red solid line) to key regions of the observed spectrum (black solid line) of AzV 324 (B8 Ib). From the top, the first and second panels are COS G130M + COS G160M FUV and STIS E230M UV, respectively. We note some interstellar features: *Lyα* λ1216, O I + P II λ1302, C II λ1335, Si II λ1527, and Al II λ1671. The rest of the panels are the UBV and VIS XShooter spectra, with the break between the two arms at ≈ 5600 Å. The lines Ca II H + K and Na I D are interstellar features.

B.7 FM90 parameters

Table B.3: Fitting parameters of the UV reddening law.

Target	R_V	$E(B-V)$	c_1	c_2	c_3	c_4	x_0	γ
AzV 469	1.60	0.17	−1.50	1.30	0.10	0.02	4.4	0.95
AzV 372	1.80	0.16	−2.30	1.55	0.10	0.05	4.4	0.95
AzV 456	2.25	0.43	−0.86	1.20	4.51	0.30	4.7	1.25
AzV 327	0.50	0.17	−4.00	4.25	1.01	0.00	4.7	0.90
AzV 235	4.10	0.13	−2.07	1.15	0.50	0.01	4.4	0.95
AzV 215	2.00	0.21	−1.50	1.60	0.10	0.13	4.4	0.95
AzV 104	1.70	0.17	−2.07	1.70	0.20	0.01	4.4	0.95
AzV 410	1.19	0.16	−1.86	1.70	1.22	0.05	4.7	1.25
AzV 242	2.10	0.17	−1.75	1.17	0.50	0.10	4.8	0.95
AzV 96	1.75	0.17	−1.75	1.23	0.50	0.20	4.8	0.95
AzV 264	1.75	0.13	−1.75	1.15	0.50	0.20	4.8	0.95
AzV 175	1.70	0.18	−1.35	1.60	0.50	0.25	4.8	0.95
SK-191	2.40	0.22	−3.35	1.70	0.80	0.20	4.8	0.95
AzV 18	2.50	0.26	−2.90	1.70	0.10	0.09	4.8	0.95
NGC330-ELS-04	2.30	0.16	−2.90	1.30	0.30	0.10	4.8	0.95
AzV 187	2.05	0.12	−2.90	1.40	0.40	0.15	4.8	0.95
AzV 22	2.30	0.16	−1.07	1.20	0.10	0.85	4.4	0.95
AzV 393	4.00	0.12	−2.75	0.62	1.50	0.20	4.8	0.95
AzV 343	1.70	0.10	−0.75	1.55	0.10	0.85	4.4	0.95
AzV 324	0.60	0.10	−0.16	2.27	4.01	2.50	4.7	1.25

Appendix C

Milky Way

C.1 $v_{\rm black}$ and $v_{\rm edge}$

In Table C.1 we present the measured $v_{\rm edge}$ and $v_{\rm black}$ from each line for all stars in our Galactic sample. Single velocity measurement from each line is subject to an uncertainty $\Delta v = 30$ km s^{-1}, which takes into account the velocity resolution of the UV spectra and the uncertainty in the radial velocity correction, which were added in quadrature.

Table C.1: $v_{\rm black}$ for the stars in our Galactic sample.

	$v_{\rm edge}$			
HD	Si IV 1393Å	C IV 1548Å	Al III 1855Å	$\overline{v_{\rm black}}/\overline{v_{\rm edge}}$
30614	2017	2083	-	0.75
210809	2309	2398	-	-
209975	2301	2392	-	0.84
154368	2294	2339	-	0.77
76968	2369	2331	-	-
105056	1117	968	935	-
37128	1978	2059	-	0.76
204172	2237	2329	-	-
38771	1802	1623	-	0.72
192422	1612	-	-	-
190066	1532	1583	-	0.83
169454	960	875	-	-
13854	1176	1321	1086	0.76
24398	-	1294	-	-
190603	-	604	-	0.62
13841	1480	1387	-	0.75
41117	871	871	-	-
206165	966	1008	-	0.64
198478	712	719	-	-
42087	899	930	-	-
53138	650	655	-	-
51309	-	795	-	0.76
58350	527	465	419	-
199478	382	381	392	-
34085	-	370	-	-
12301	614	632	-	-

	$v_{\rm black}$			
HD	Si IV 1393Å	C IV 1548Å	Al III 1855Å	$\overline{v_{\rm black}}$
30614	1502	1579	-	1540
209975	-	1978	-	1978
154368	1725	1860	-	1793
37128	-	1532	-	1532
38771	-	1231	-	1231
190066	-	1294	-	1294
13854	923	881	-	902
190603	390	375	354	375
13841	-	1076	-	1076
206165	-	631	-	631
51309	-	607	-	607

C.2 Comparison to literature

Table C.2: Comparison of derived parameters to previous studies.

HD	$T_{\rm eff}$	$\log g$	$\log L$	$\log \dot{M}^{\rm smooth}$	β	Ref.	wavelength	Code
	kK	$\rm cm\,s^{-2}$	$L_\odot$	$M_\odot\,\rm yr^{-1}$				
30614	28.3	2.96	6.04	−5.47	1.0	This study	UV+Opt	C
	29.0	3.0	5.63	−5.30	1.5	C06	UV+Opt	T+C
	29.0	3.0	5.44	−5.82	1.2	RD22	Opt+IR+Radio	P06
105056	28.2	3.11	5.25	−5.61	2.6	This study	UV+Opt	C
	25.0	2.7	5.75	−5.40	3.0	L07	Opt	F
37128	29.5	3.22	6.01	−5.86	1.3	This study	UV+Opt	C
	27.0	2.9	5.44	−5.60	1.5	C06	UV+Opt	T+C
	27.5	3.13	5.73	−5.72	1.1	S08	UV+Opt	T+C
	27.0	2.9	5.44	−5.60	1.5	RD22	Opt+IR+Radio	P06
204172	28.3	3.16	5.45	−6.11	1.0	This study	UV+Opt	C
	28.5	3.13	5.48	−6.24	1.0	S08	UV+Opt	T+C
38771	27.2	3.12	4.80	−5.92	1.0	This study	UV+Opt	C
	26.5	2.9	5.35	−6.05	1.5	C06	UV+Opt	T+C
	26.0	3.0	5.48	−5.92	1.1	S08	UV+Opt	T+C
	25.0	2.7	4.78	−6.85	1.5	H18	Opt	F
	26.5	2.9	5.34	−6.05	1.5	RD22	Opt+IR+Radio	P06
190066	24.2	2.96	5.09	−6.54	1.0	This study	UV+Opt	C
	21.0	2.88	5.54	−6.15	1.5	S08	UV+Opt	T+C
169454	19.4	2.41	5.90	−5.57	3.0	This study	UV+Opt	C
	20.4	2.35	5.93	−4.22	2.1	RD22	Opt+IR+Radio	P06
13854	20.9	2.61	5.39	−6.33	3.0	This study	UV+Opt	C
	21.5	2.55	5.43	−6.07	2.0	C06	UV+Opt	T+C
	20.0	2.5	5.54	−5.82	1.2	S08	UV+Opt	T+C
24398	21.8	2.79	4.80	−6.72	1.0	This study	UV+Opt	C
	20.3	2.9	4.91	−6.64	1.5	RD22	Opt+IR+Radio	P06
190603	20.4	2.51	5.89	−5.40	1.4	This study	UV+Opt	C
	18.5	2.25	5.57	−5.60	3.0	C06	UV+Opt	T+C
	19.5	2.38	5.41	−5.62	1.2	S08	UV+Opt	T+C

C06: (Crowther et al., 2006). L07: (Lefever et al., 2007), S08: (Searle et al., 2008), H18: (Haucke et al., 2018), RD22: (Rubio-Díez et al., 2022), BP23: Bernini-Peron et al. (2023). Obtained using F: FASTWIND, C: CMFGEN, T: TLUSTY, P06: (Puls et al., 2006). The mass-loss rates are corrected for clumping.

Table C.2: Continued.

Target	$T_{\rm eff}$ kK	$\log g$ cm s^{-2}	$\log L$ $L_\odot$	$\log \dot{M}^{\rm smooth}$ $M_\odot$ yr^{-1}	β	Ref.	wavelength	Code
41117	19.3	2.3	5.53	−5.95	3.5	This study	UV+Opt	C
	19.0	2.35	5.65	−6.05	2.0	C06	UV+Opt	T+C
	19.0	2.3	4.84	−6.77	2.0	H18	Opt	F
	19.0	2.35	5.65	−6.05	2.0	RD22	Opt+IR+Radio	P06
206165	17.8	2.47	5.21	−6.23	1.0	This study	UV+Opt	C
	18.0	2.5	5.18	−6.30	1.5	S08	UV+Opt	T+C
	18.0	2.45	5.07	−6.67	2.0	BP23	UV+Opt	C
198478	15.9	2.06	5.67	−6.24	4.3	This study	UV+Opt	C
	16.5	2.15	5.03	−6.64	2.0	C06	UV+Opt	T+C
	17.5	2.25	5.26	−6.30	1.2	S08	UV+Opt	T+C
	17.5	2.12	5.31	−6.51	1.3	RD22	Opt+IR+Radio	P06
	16.0	2.15	5.57	−6.14	2.0	BP23	UV+Opt	C
42087	17.6	2.46	5.51	−6.47	1.0	This study	UV+Opt	C
	18.0	2.5	5.11	−6.30	1.2	S08	UV+Opt	T+C
	16.5	2.45	5.31	−6.24	2.0	H18	Opt	F
53138	15.6	2.11	5.56	−6.37	4.0	This study	UV+Opt	C
	15.5	2.05	5.34	−6.44	2.0	C06	UV+Opt	T+C
	17.0	2.15	5.27	−6.51	2.5	L07	Opt	F
	16.5	2.25	5.3	−6.35	1.2	S08	UV+Opt	T+C
	18.0	2.25	5.31	−6.66	2.0	H18	Opt	F
	15.5	2.05	5.34	−6.44	2.0	RD22	Opt+IR+Radio	P06
	16.0	2.15	5.14	−6.48	2.0	BP23	UV+Opt	C
58350	14.5	2.12	5.09	−5.98	2.5	This study	UV+Opt	C
	13.5	1.75	5.1	−6.85	2.5	L07	Opt	F
	15.0	2.13	5.18	−6.15	1.0	S08	UV+Opt	T+C
	15.5	2.0	5.18	−6.89	3.0	H18	Opt	F
34085	12.2	1.91	5.11	−5.72	1.0	This study	UV+Opt	C
	12.7	1.7	5.09	−6.64	2.6	H18	Opt	F

C06: (Crowther et al., 2006). L07: (Lefever et al., 2007), S08: (Searle et al., 2008), H18: (Haucke et al., 2018), RD22: (Rubio-Díez et al., 2022), BP23: Bernini-Peron et al. (2023). Obtained using F: FASTWIND, C: CMFGEN, T: TLUSTY, P06: (Puls et al., 2006). The mass-loss rates are corrected for clumping.

C.3 Comments on individual stars

HD30614, Figures C.28 and C.28. The fit quality of this star is very good in general. However, our preferred model predicts a P Cygni morphology in He I λ5876, which is not seen in the observations.

HD210809, Figures C.29 and C.29. For this star, we obtain good fits for photospheric lines. However, we were unable to match the exact morphology of Hα, particularly the strong absorption component. Additionally, as with HD30614, the model predicts a P Cygni He I λ5876 feature that does not match the observations.

HD209975, Figures C.30 and C.30. The preferred model matches the observation well. The most glaring discrepancy is in Hα, where the observations show a wind-filled line core that we were unable to reproduce.

HD154368, Figures C.31 and C.31. The fit quality for this star is very good. We note that the preferred model does not match the observed saturated C IV $\lambda\lambda 1548-1551$ line, which is likely a product of the lack of X-rays in our models that can increase the population of higher ionisation levels.

HD76968, Figures C.32 and C.32. The fit quality of this star is excellent with no major issues to report.

HD105056, Figures C.33 and C.33. The fitting quality for this hypergiant is good for most diagnostic lines, apart from the Balmer lines that are used to determine the surface gravity (Hη, Hζ, Hγ). This is due to strong wind contamination in their red wings. Therefore, we resorted to fitting H12 (Hμ), and using the blue wing of other Balmer lines as a sanity check. We also note that we were not able to exactly match the emission feature in Hβ.

HD37128, Figures C.34 and C.34. The observed optical line diagnostics are well matched by our preferred model. We note that using helium lines instead of silicon lines as temperature diagnostics yields a model that is cooler by $\approx$ 1000 K. However, our model overpredicts the saturation of both C III λ1175 and Si IV $\lambda\lambda 1393-1403$. Our tests showed that varying the mass-loss rate and clumping factor cannot reproduce these lines without degrading the quality of the fit to Hα and C IV $\lambda\lambda 1548-1551$.

HD209975, Figures C.30 and C.30. The preferred model for this star predicts the optical lines very well. The UV predictions suffer from a similar issue to that in HD37128, in which the model shows higher saturation in C III λ1175 and Si IV $\lambda\lambda 1393-1403$, and varying the mass-loss rate and clumping factor did not help resolve this issue.

HD38771, Figures C.36 and C.36. The overall quality of the fit is very good for this star. The only issue is the oversaturation of Si IV $\lambda\lambda 1393-1403$ in the predictions, and the slight undersaturation of C IV $\lambda\lambda 1548-1551$, which is likely due to the lack of X-rays in the model.

HD192422, Figures C.11 and C.37. The fit quality for this star is very good. We note that the issue is similar to that in HD38771, where the observed Si IV $\lambda\lambda 1393-1403$ is less saturated than the model predicts, likely due to the lack of X-rays.

HD190066, Figures C.12 and C.38. The fit quality for this star is very good. We note that the observed Si IV $\lambda\lambda 1393-1403$ is less saturated than the model predicts due to the lack of X-rays, similar to the issue in HD38771 and HD192422.

HD169454, Figures C.13 and C.39. This is the second hypergiant in our sample. The overall quality of the fit is good for this star. We rely on fitting only the blue wings of Hη, Hζ, and Hγ to determine the surface gravity, as the red wings of these lines are

wind-contaminated. As with the hypergiant HD105056, we were unable to match the strength of the emission feature in Hβ.

HD13854, Figures C.14 and C.40. The fit quality of this star is excellent with no major issues to report.

HD24398, Figures C.15 and C.41. The fit quality of this star is very good. The only issue is in Si IV $\lambda\lambda 1393 - 1403$, where the model predicts more saturation than observed.

HD190603, Figures C.16 and C.16. This is the third hypergiant in our sample. The overall quality of the fit is good for this star, apart from Hη, Hζ, Hγ. As for the hypergiant HD169454, we fit only the blue wings of these lines to obtain the surface gravity. Our preferred model predicts Hβ to be fully in absorption, unlike the observations that show a P Cygni Hβ.

HD13841, Figures C.17 and C.17. The fit quality of this star is excellent with no major issues to report.

HD41117, Figures C.18 and C.18. The fit quality of this star is excellent with no major issues to report.

HD206165, Figures C.19 and C.19. The fit quality of this star is good. We note that the observed Hα shows a weak, redshifted emission feature. However, this is likely due to incorrect normalisation and not genuine emission, which could indicate a much stronger wind. N III λ3995 shows a second, blue-shifted component that could be indicative of a binary. However, no secondary component is seen in any other spectral lines.

HD198478, Figures C.20 and C.20. The overall quality of the fit for this star is very good. One noticeable discrepancy is in Si IV $\lambda\lambda 1393-1403$, which is predicted to be completely photospheric in the model. This could also be a case where including X-rays could increase the population in this level of the wind, producing a more saturated line. We also note the blueward velocity shift observed in Hα. This is an odd issue, as no other lines present a similar velocity shift.

HD42087 , Figures C.21 and C.21. The fit quality of this star is good. A discrepancy is seen in Al III $\lambda\lambda 1855-1863$, which the model predicts to be more saturated than in the observations.

HD53138 , Figures C.22 and C.22. The fit quality of this star is very good. We note that we were not able to match the strength of the absorption feature in Hα. Another discrepancy is in C II $\lambda\lambda 1334$, which is predicted to exhibit a P Cygni profile, but the emission feature is absent in the observations.

HD51309, Figures C.23 and C.23. The fit quality of this star is excellent with no major issues to report.

HD58350, Figures C.24 and C.24. The fit quality of this star is excellent with no major issues to report. We know that using silicon lines or Hlium and magnesium lines to obtain the temperature yields similar results.

HD199478, Figures C.25 and C.25. The fit quality of this star is good. The blueshift seen in Hα is discussed in Section 5.2.3. The most glaring discrepancy is in Hα, where observations do not show the strong absorption feature (P Cygni) predicted by the model.

HD34085, Figures C.26 and C.26. The fit quality of this star is very good. We were not able to match the in-filled Hα - even when varying the mass loss rates and clumping parameters - without ruining the fits to other lines, particularly in the UV. We also find that the model over-predicts the emission strength in C II $\lambda\lambda$1334.

HD34085, Figures C.26 and C.26. The fit quality of this star is very good. the model predicts a strong emission feature in C II $\lambda\lambda$1334 that is not seen in the observations.

C.4 Spectral energy distribution (SED)

In Fig. C.1 we present the SED fits for the entire sample.

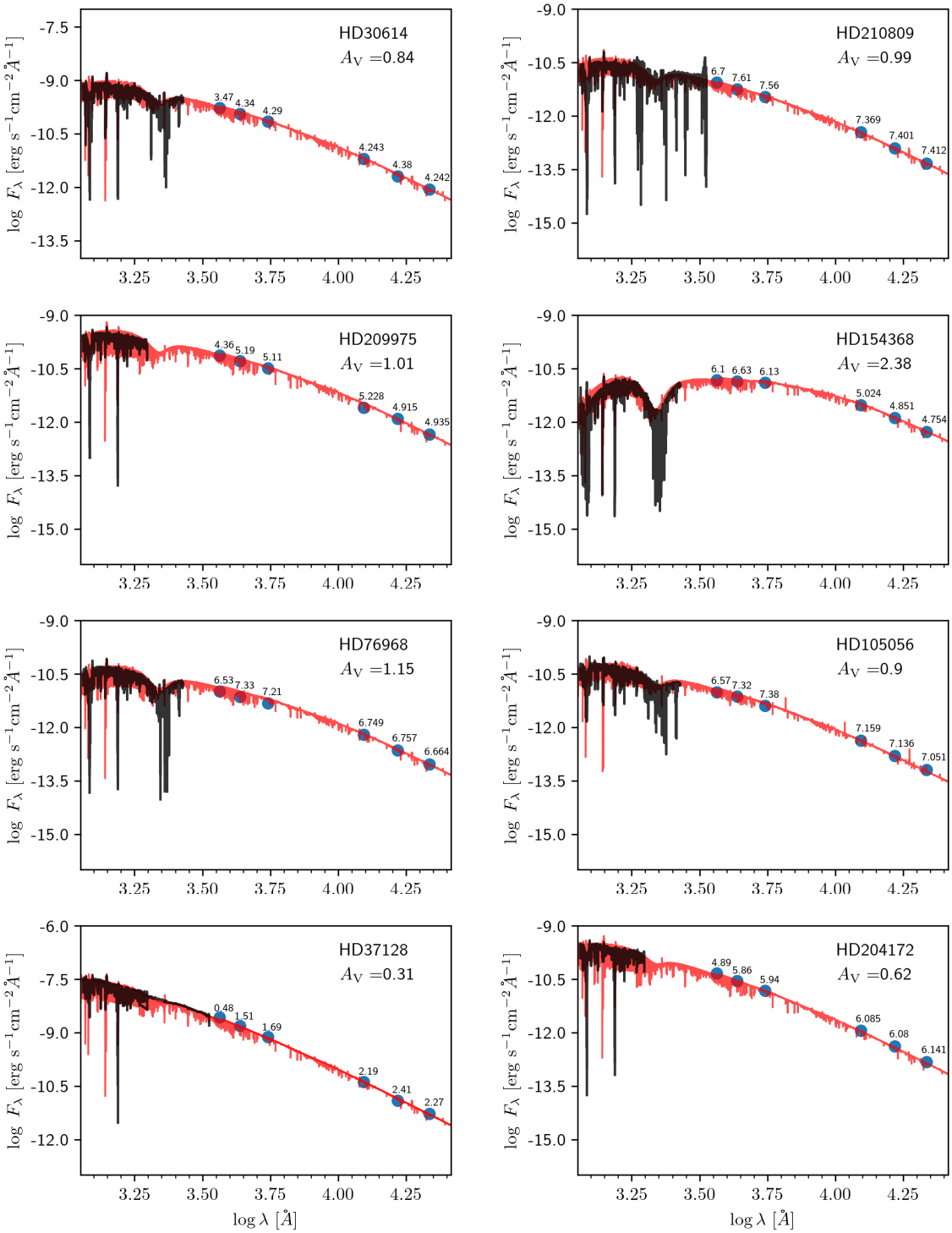


Figure C.1: Spectral energy distribution for all the stars in our Galactic sample. Red solid line: model SED, Black solid line: observed SED. The photometric points are indicated as blue circles.

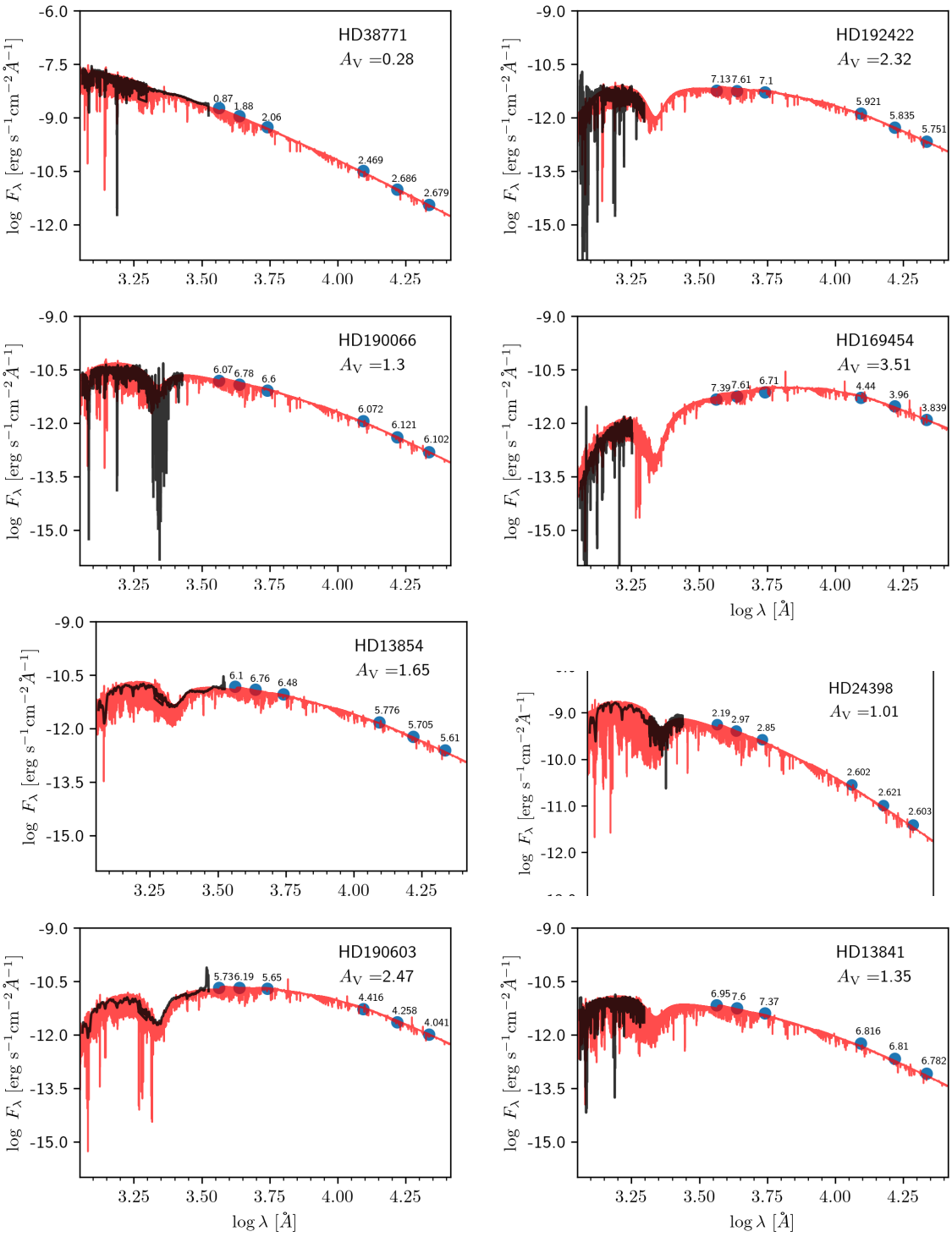


Figure C.1: continued

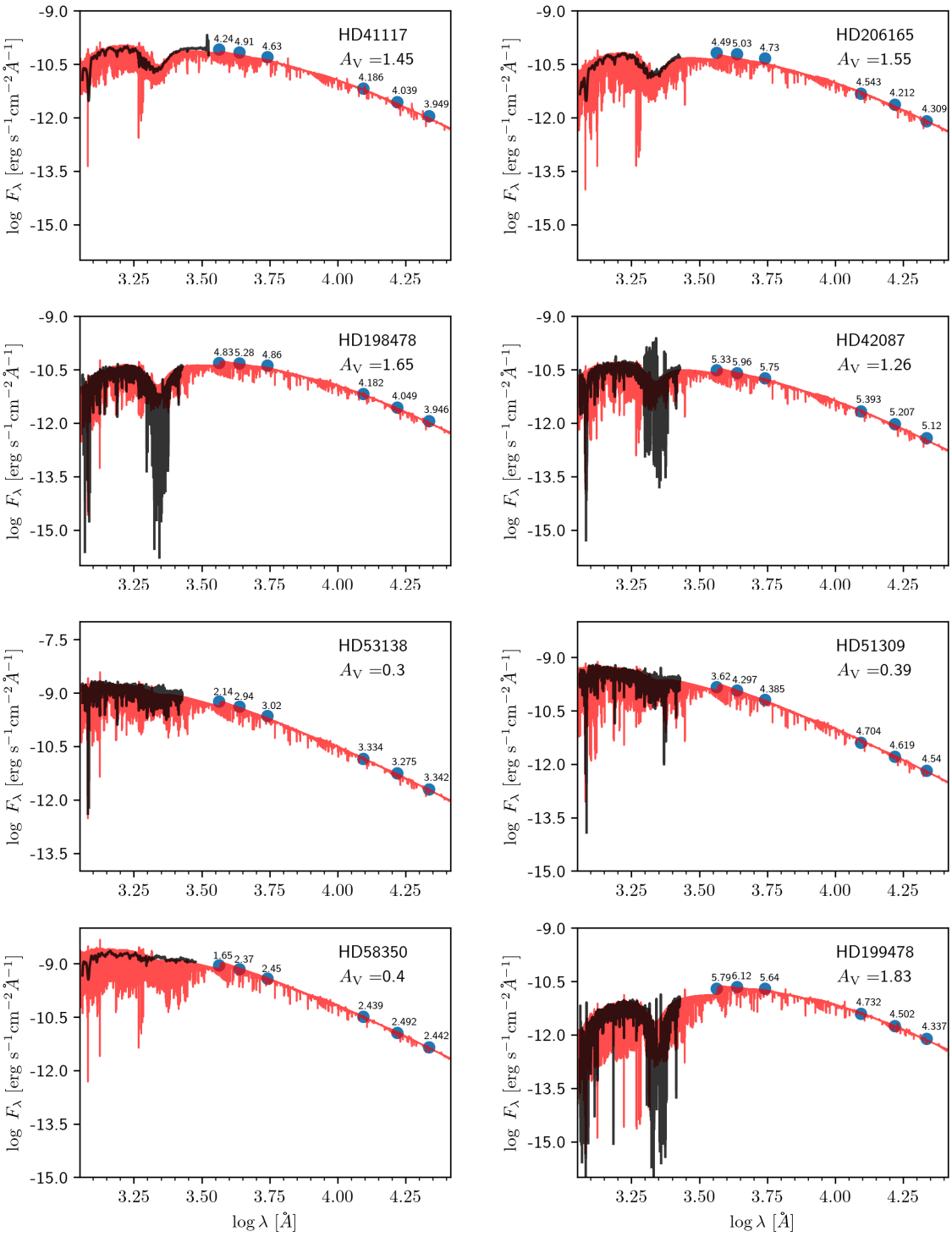


Figure C.1: continued

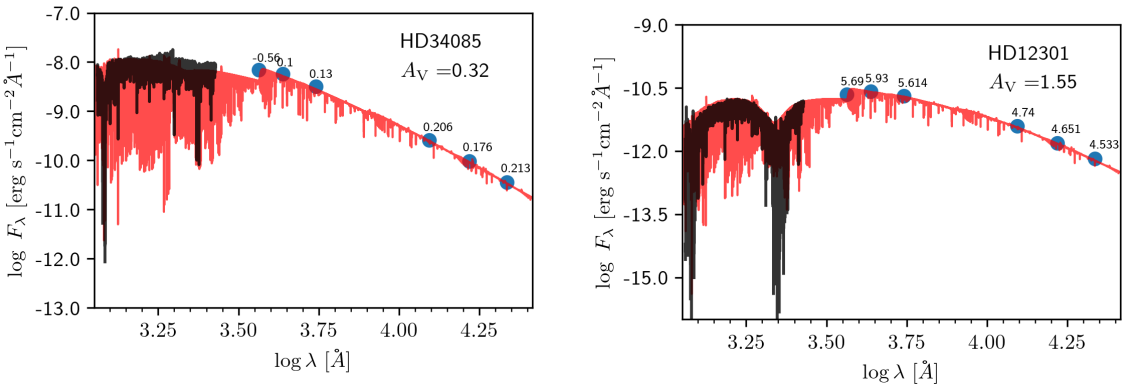


Figure C.1: continued

C.5 Line fitting for individual stars

Fig. C.2-C.27 are the individual diagnostic line fits for each star in our sample. On each row, from top to bottom, are the diagnostic lines used to determine the effective temperature, the effective surface gravity, the wind density parameters (mass-loss rate, β, clumping parameters), the helium abundance, the nitrogen abundance, the carbon abundance, and the oxygen abundance, respectively.

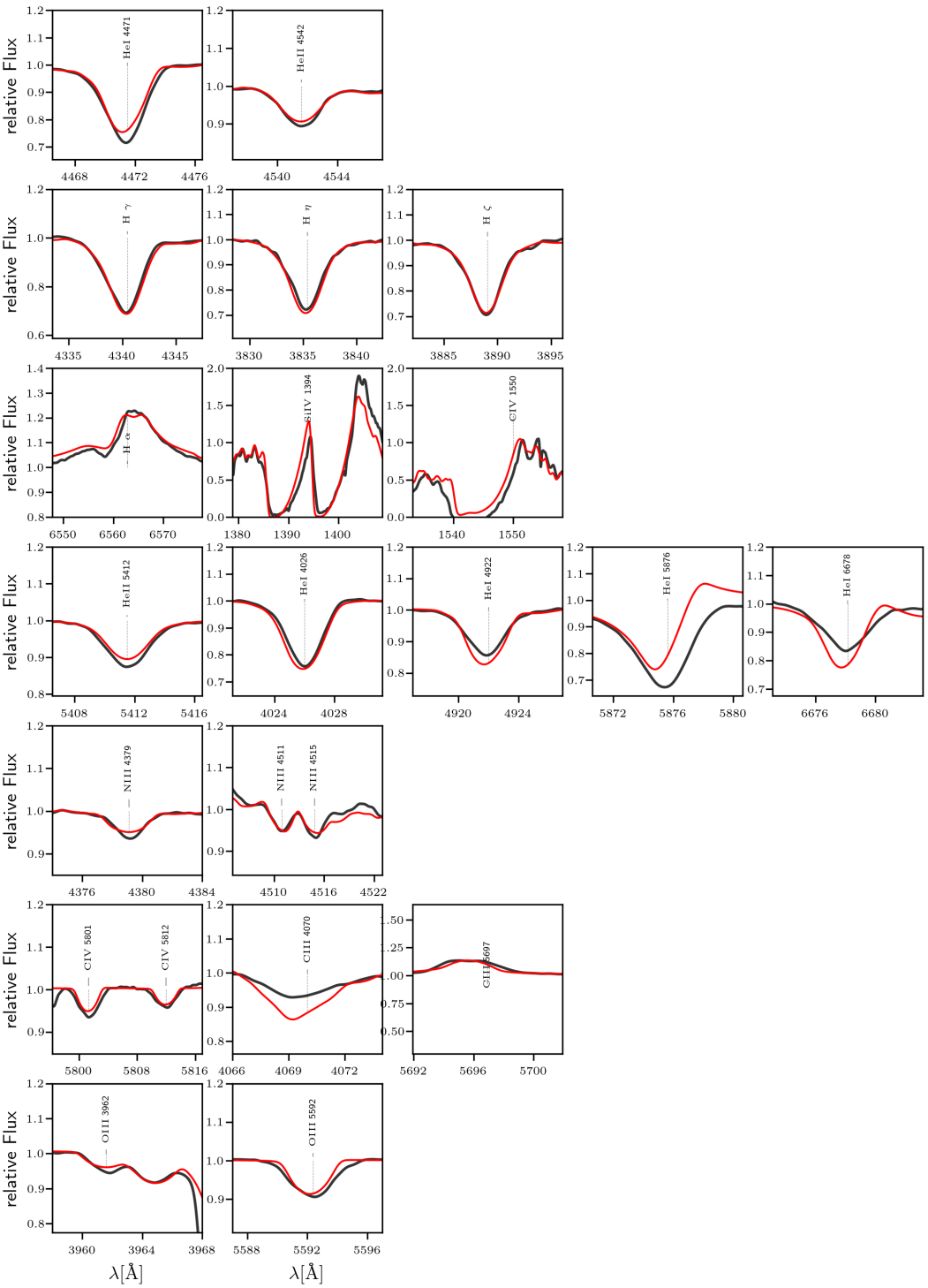


Figure C.2: Individual line fits for HD30614 (O9 Ia). Black solid line: observed spectrum. Red solid line: spectrum of the best fitting model.

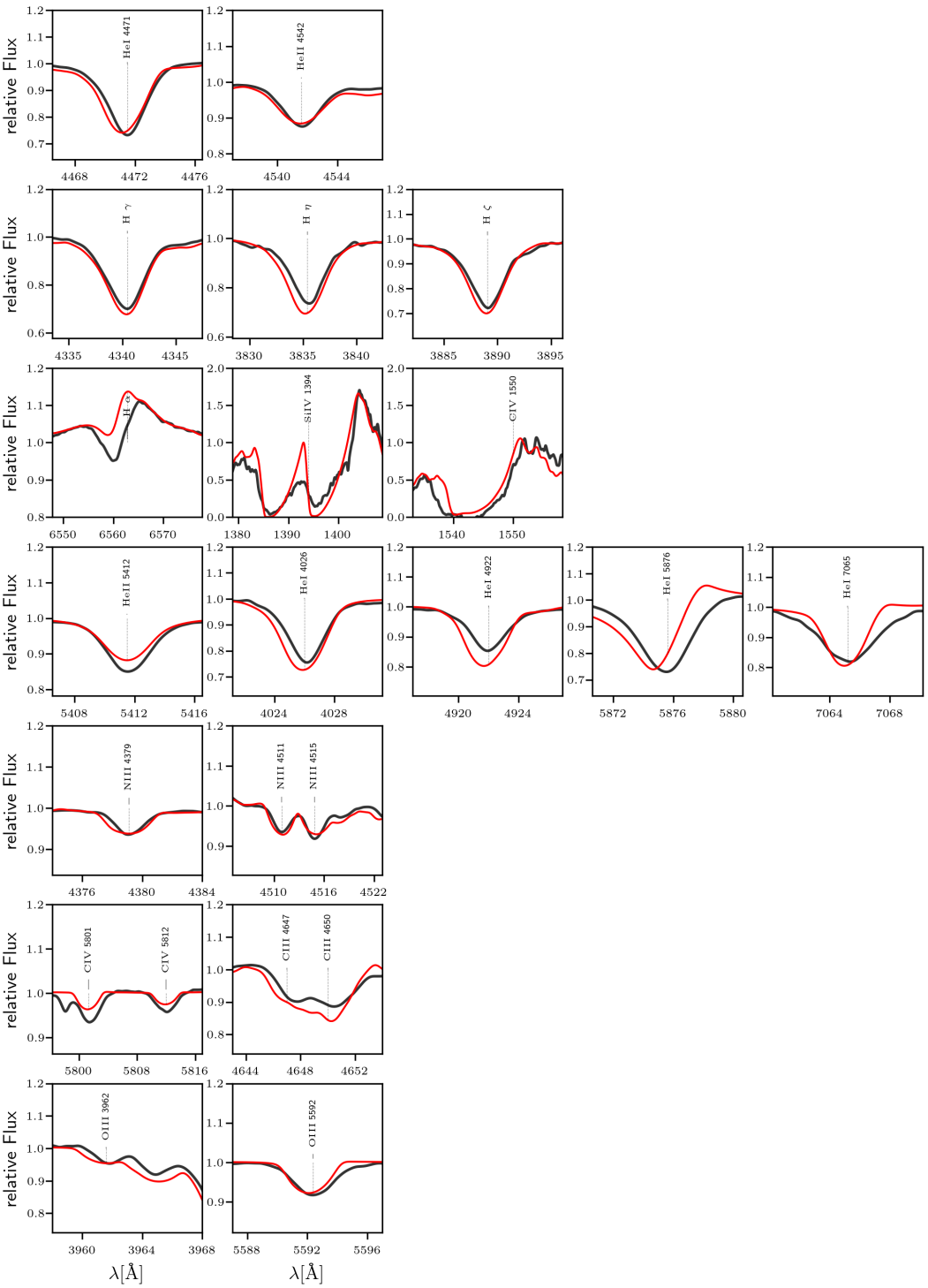


Figure C.3: Individual line fits for HD210809 (O9 Iab). Black solid line: observed spectrum. Red solid line: spectrum of the best fitting model.

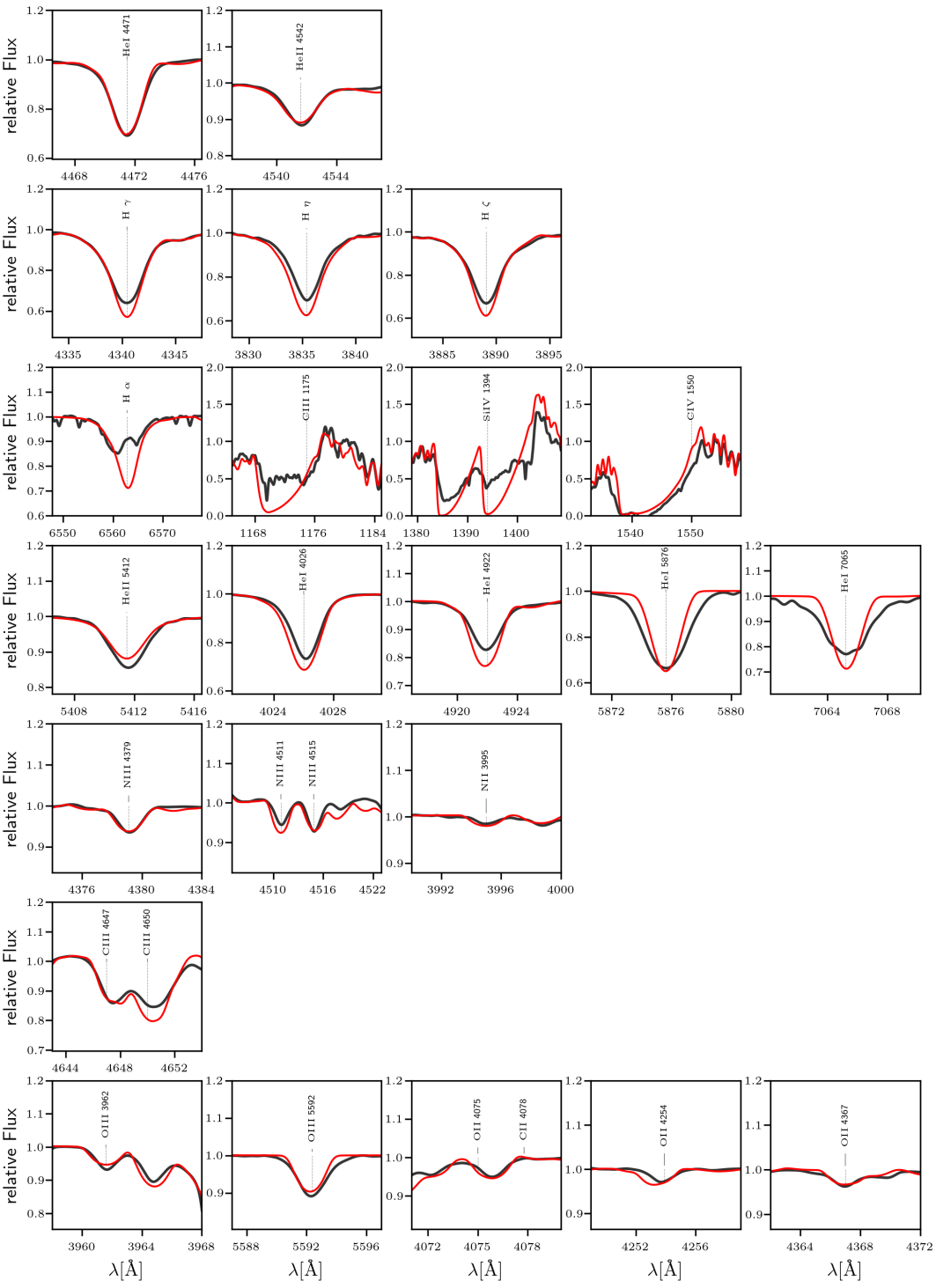


Figure C.4: Individual line fits for HD209975 (O9 Ib). Black solid line: observed spectrum. Red solid line: spectrum of the best fitting model. The observed spectrum is corrected for

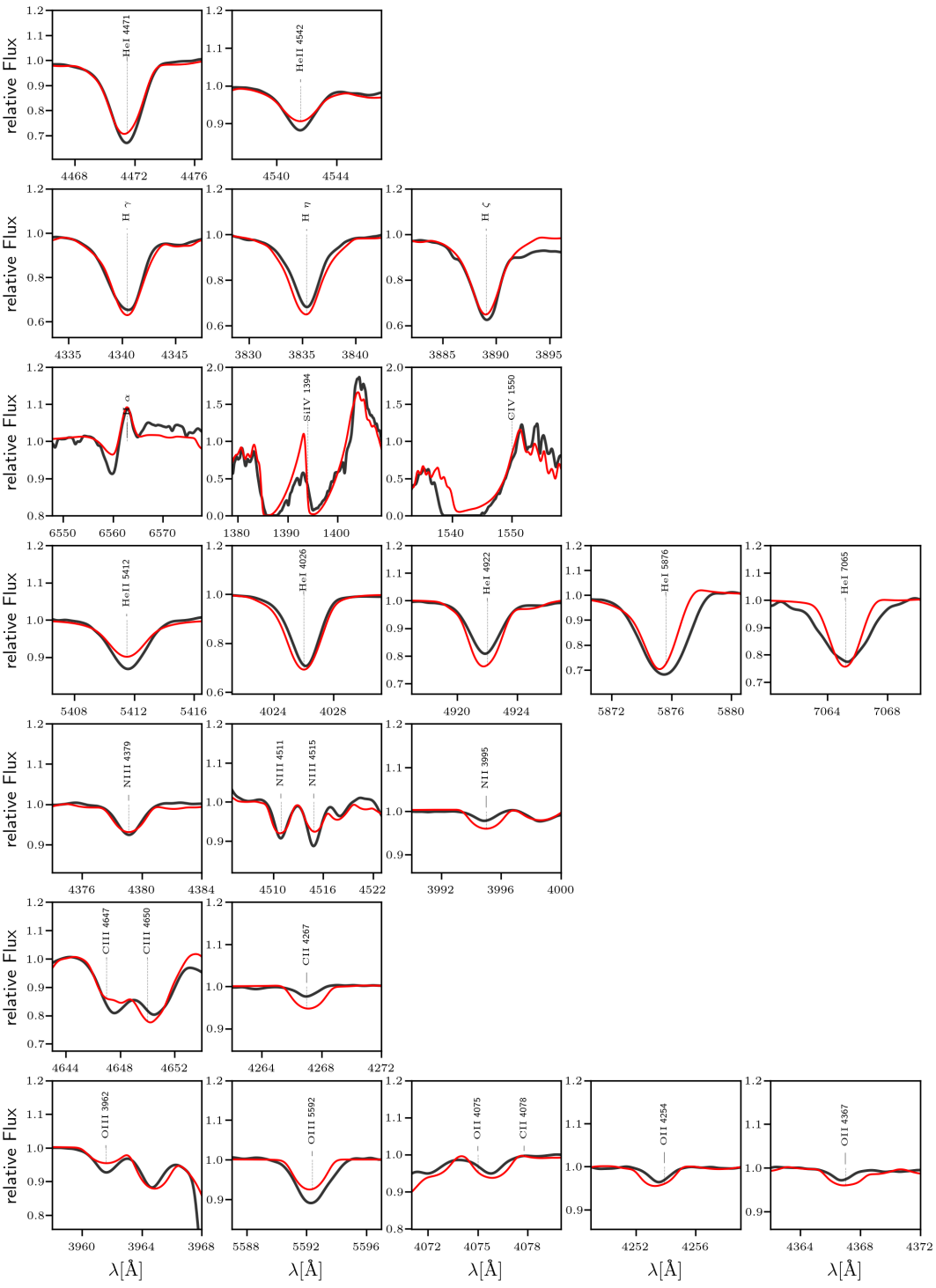


Figure C.5: Individual line fits for HD154368 (O9.2 Iab). Black solid line: observed spectrum. Red solid line: spectrum of the best fitting model. The observed spectrum is corrected for

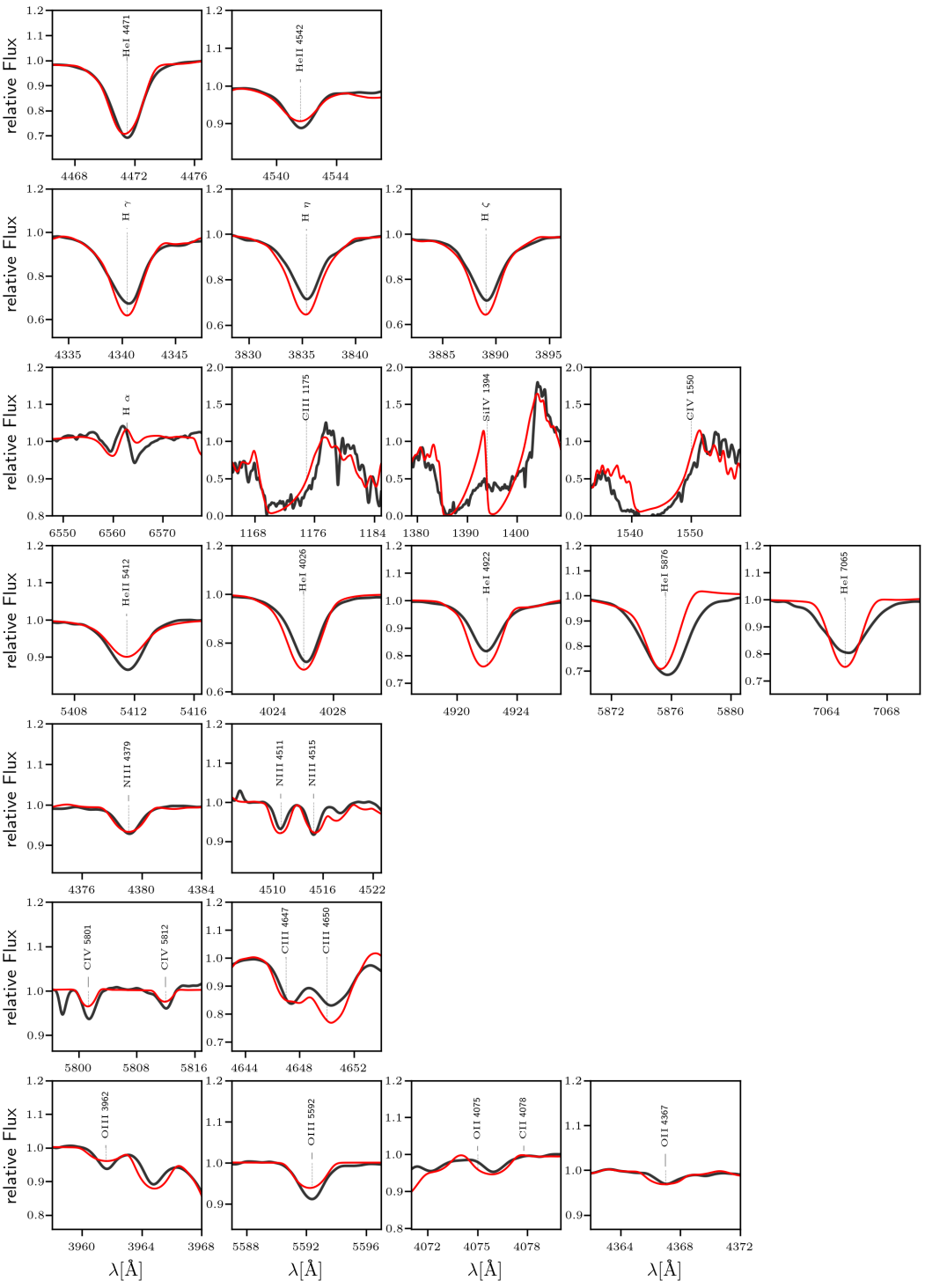


Figure C.6: Individual line fits for HD76968 (O9.2 Ib). Black solid line: observed spectrum. Red solid line: spectrum of the best fitting model. The observed spectrum is corrected for

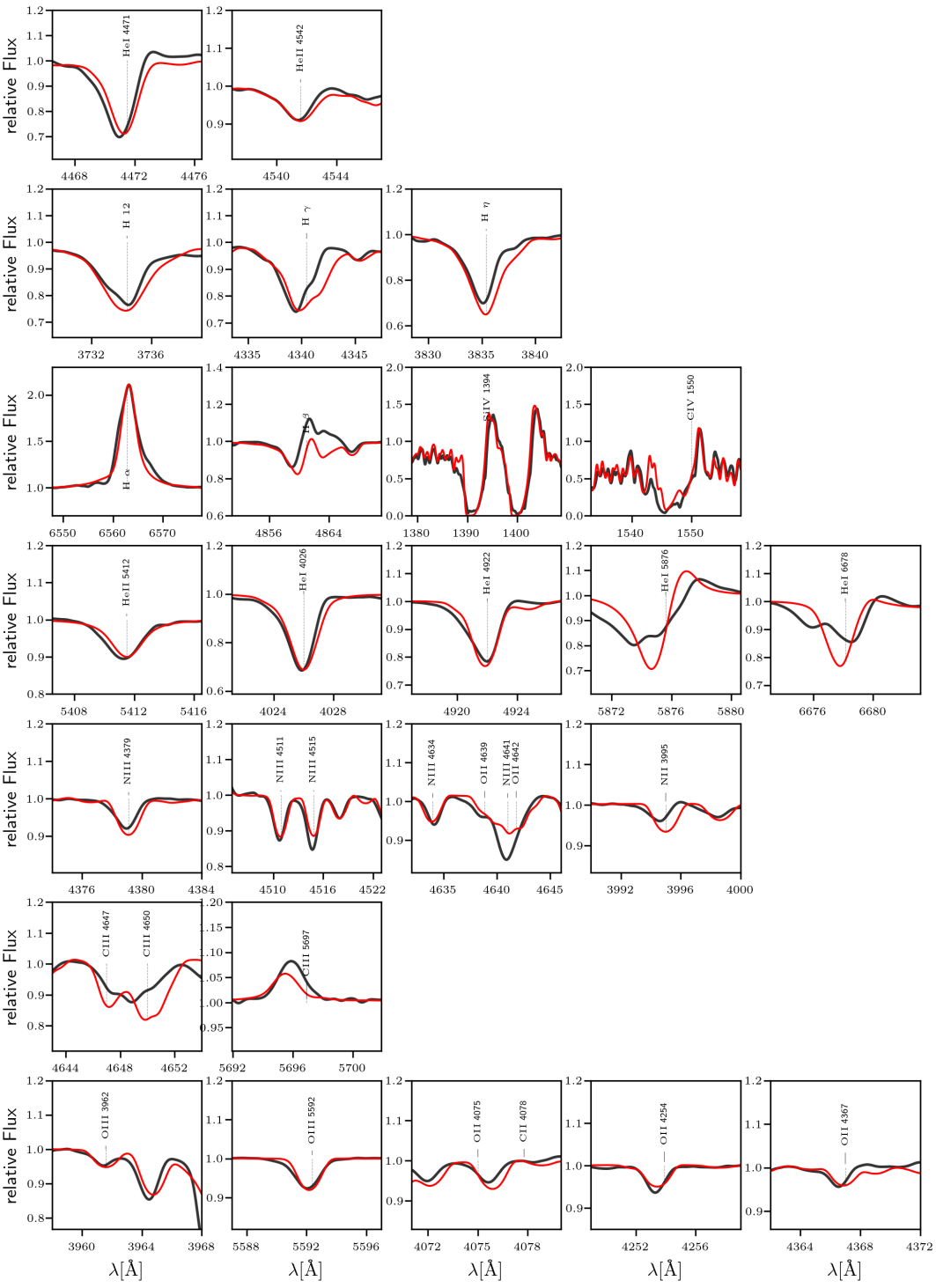


Figure C.7: Individual line fits for HD105056 (ON9.7 Ia$^+$). Black solid line: observed spectrum. Red solid line: spectrum of the best fitting model. The observed spectrum is corrected for

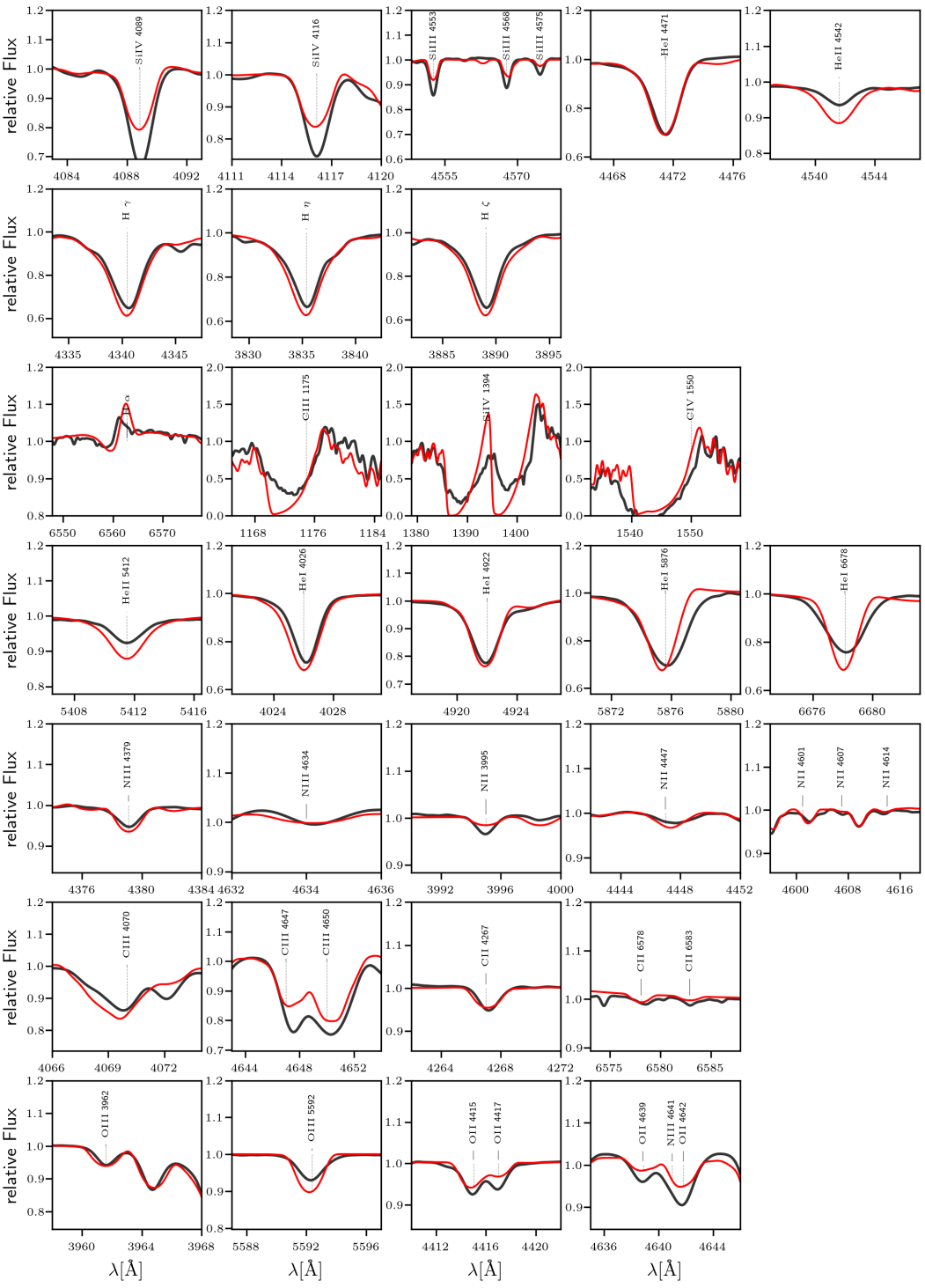


Figure C.8: Individual line fits for HD37128 (B0 Ia). Black solid line: observed spectrum. Red solid line: spectrum of the best fitting model. The observed spectrum is corrected for

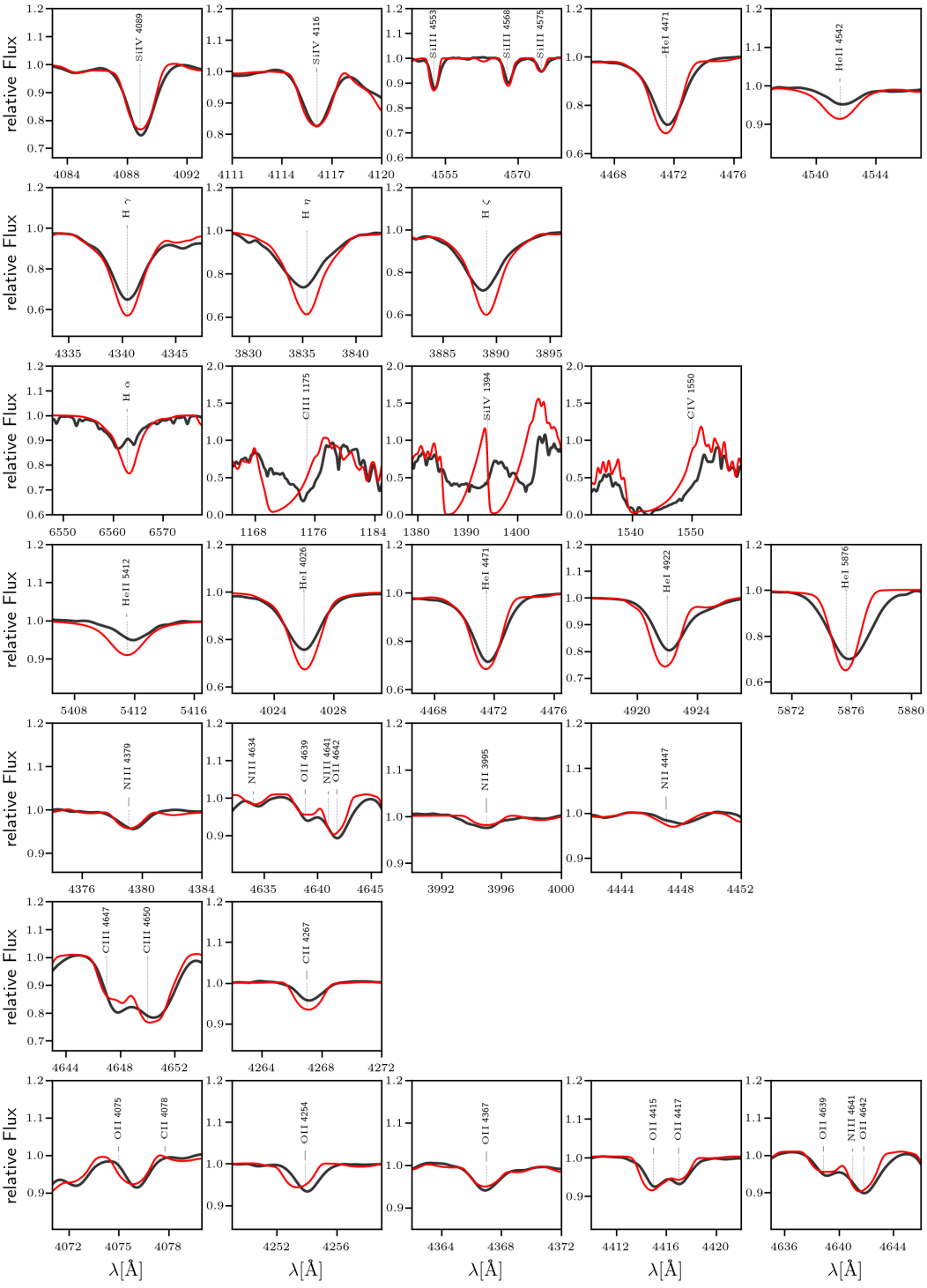


Figure C.9: Individual line fits for HD209975 (B0.2 Iab). Black solid line: observed spectrum. Red solid line: spectrum of the best fitting model. The observed spectrum is corrected for

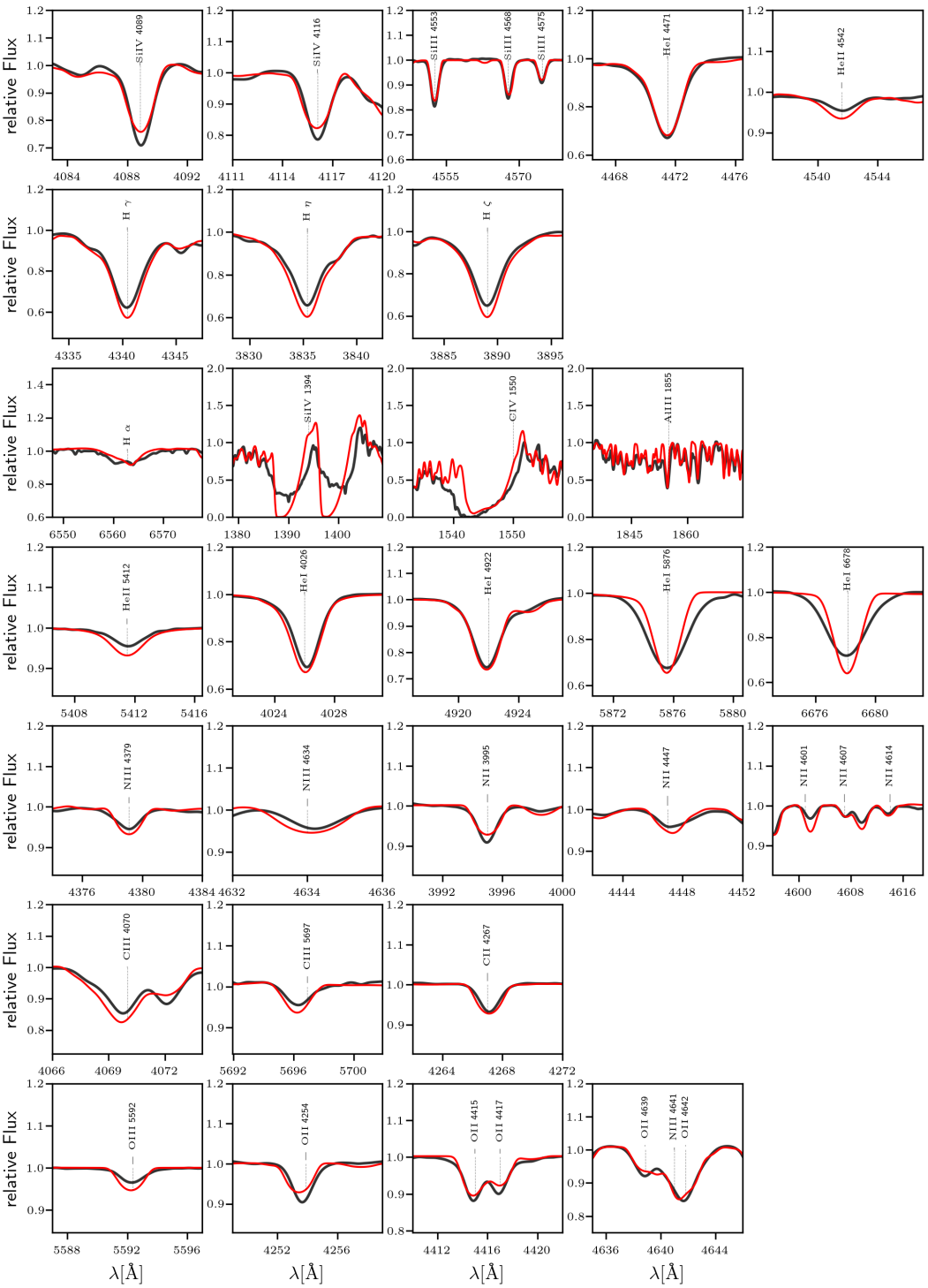


Figure C.10: Individual line fits for HD38771 (B0.5 Ia). Black solid line: observed spectrum. Red solid line: spectrum of the best fitting model.

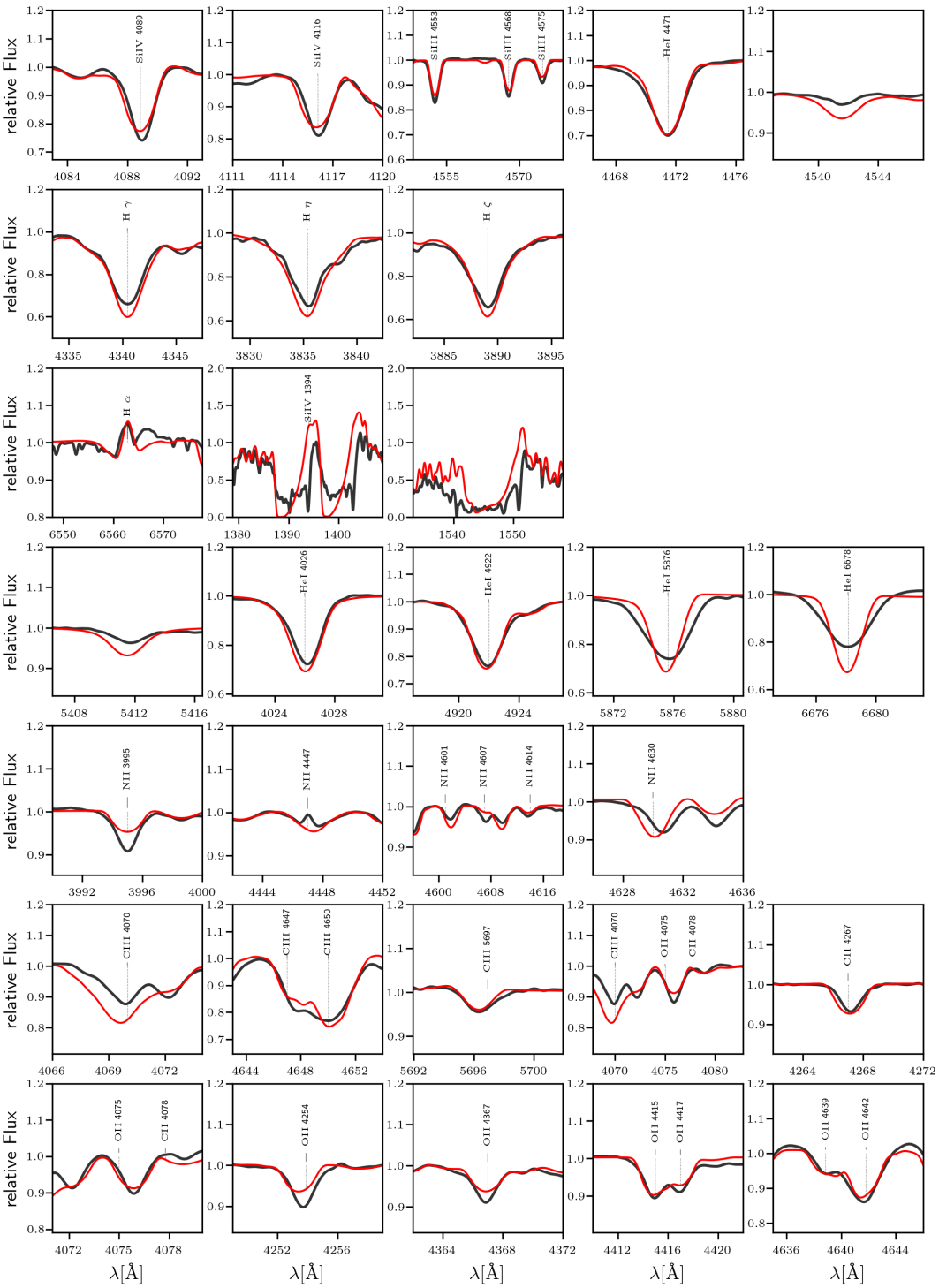


Figure C.11: Individual line fits for HD192422 (B0.5 Ib). Black solid line: observed spectrum. Red solid line: spectrum of the best fitting model.

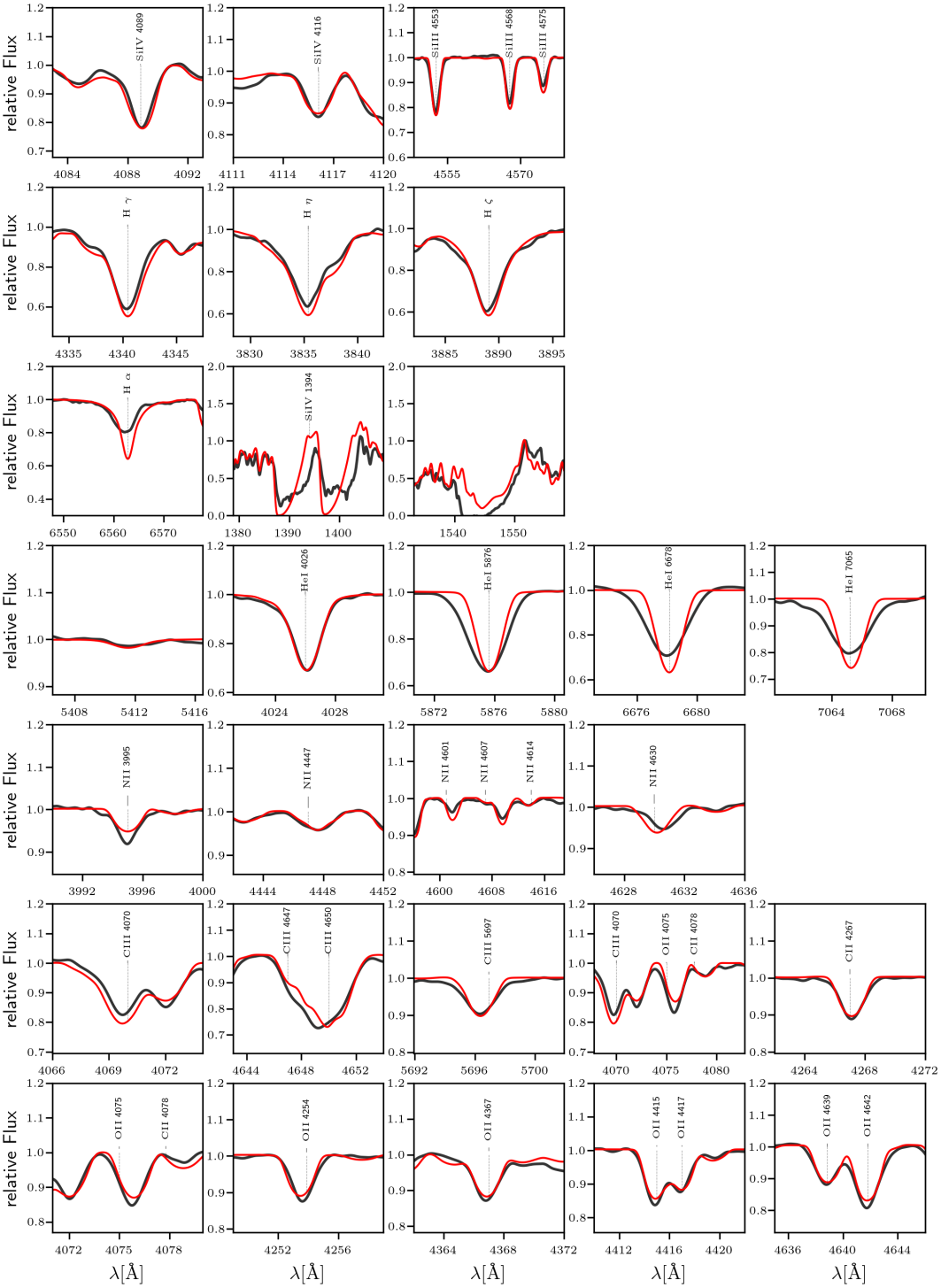


Figure C.12: Individual line fits for HD190066 (B0.7 Ib). Black solid line: observed spectrum. Red solid line: spectrum of the best fitting model.

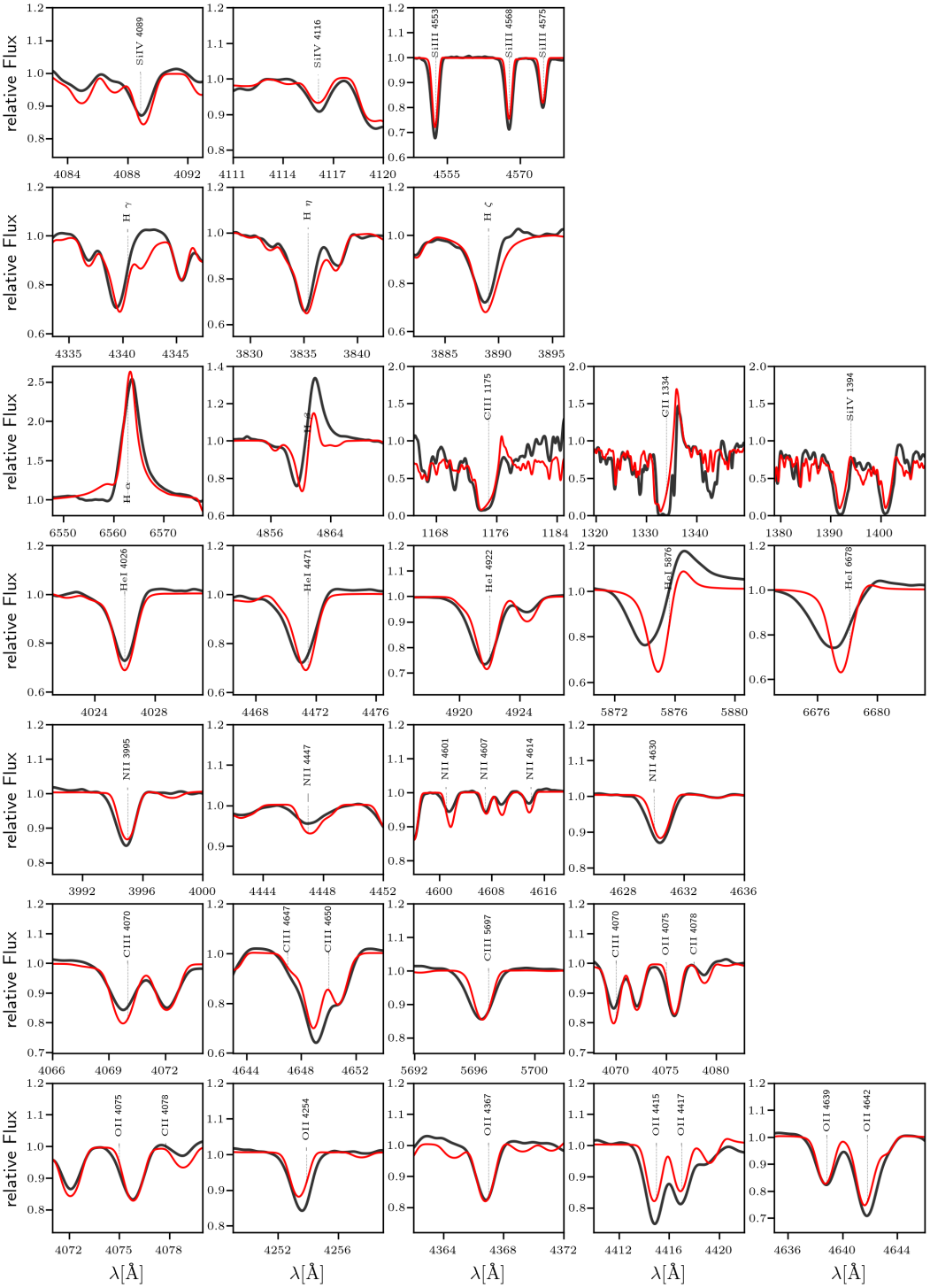


Figure C.13: Individual line fits for HD169454 (B1 Ia$^+$). Black solid line: observed spectrum. Red solid line: spectrum of the best fitting model.

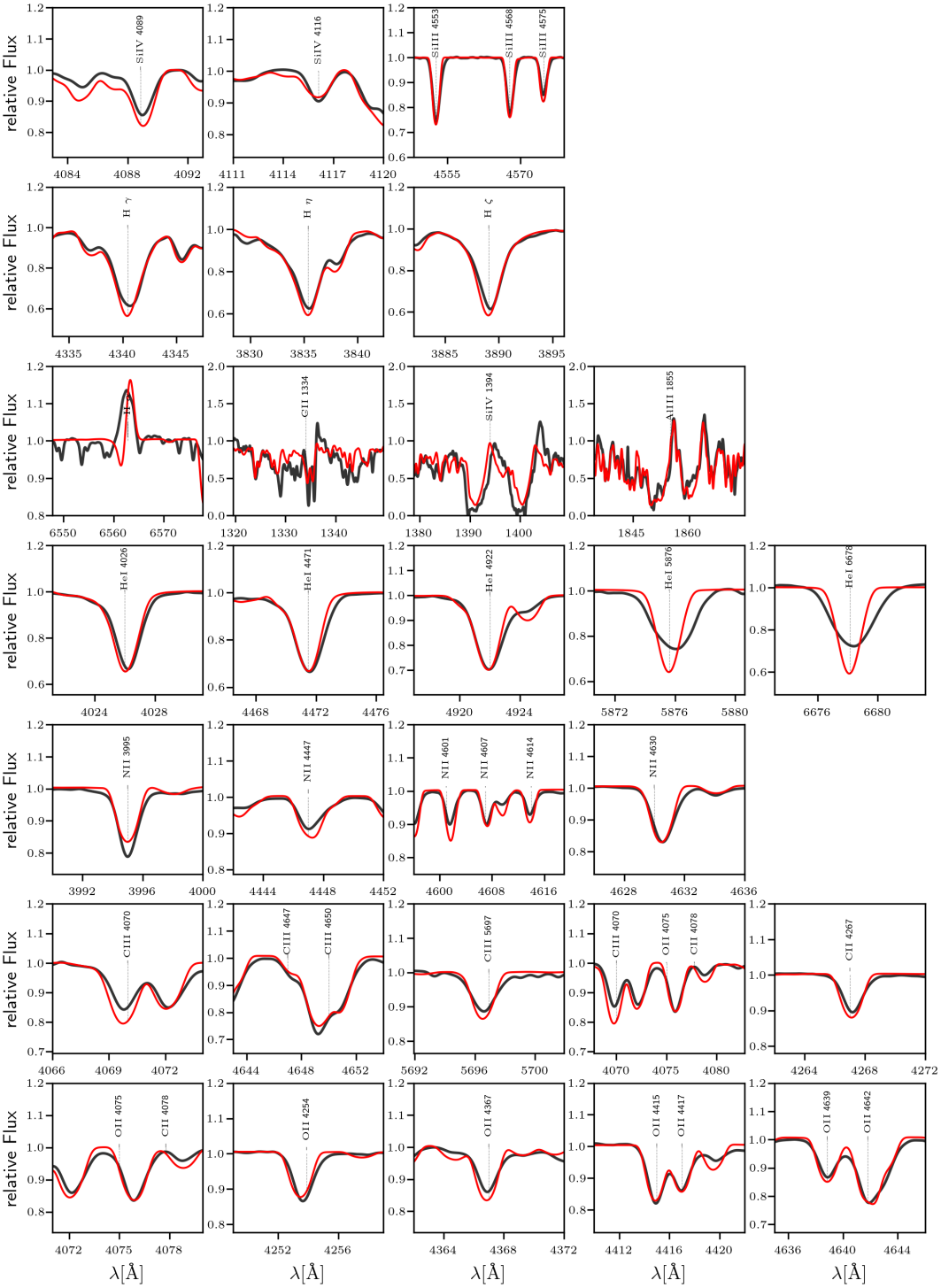


Figure C.14: Individual line fits for HD13854 (B1 Iab). Black solid line: observed spectrum. Red solid line: spectrum of the best fitting model.

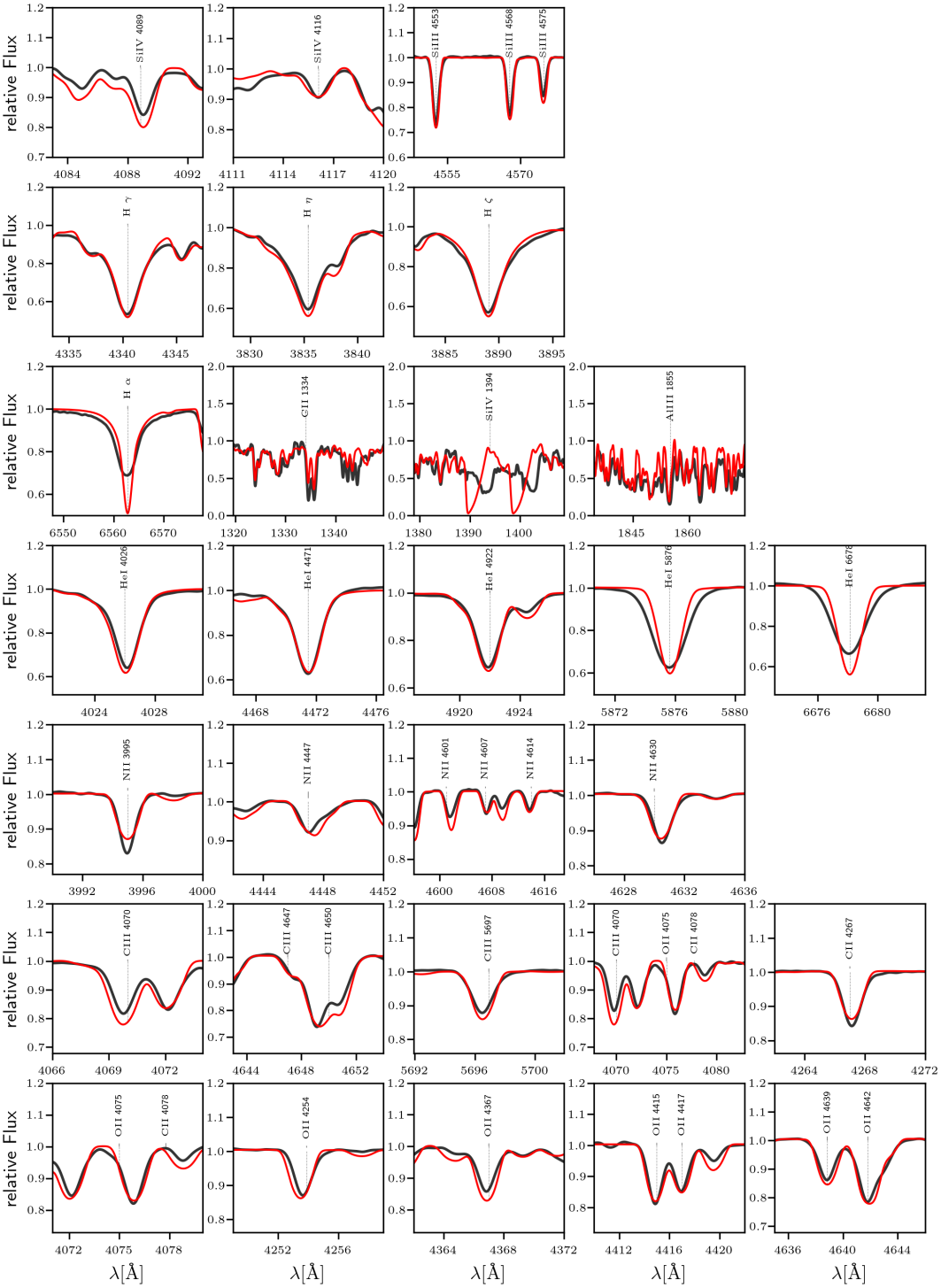


Figure C.15: Individual line fits for HD24398 (B1 Ib). Black solid line: observed spectrum. Red solid line: spectrum of the best fitting model.

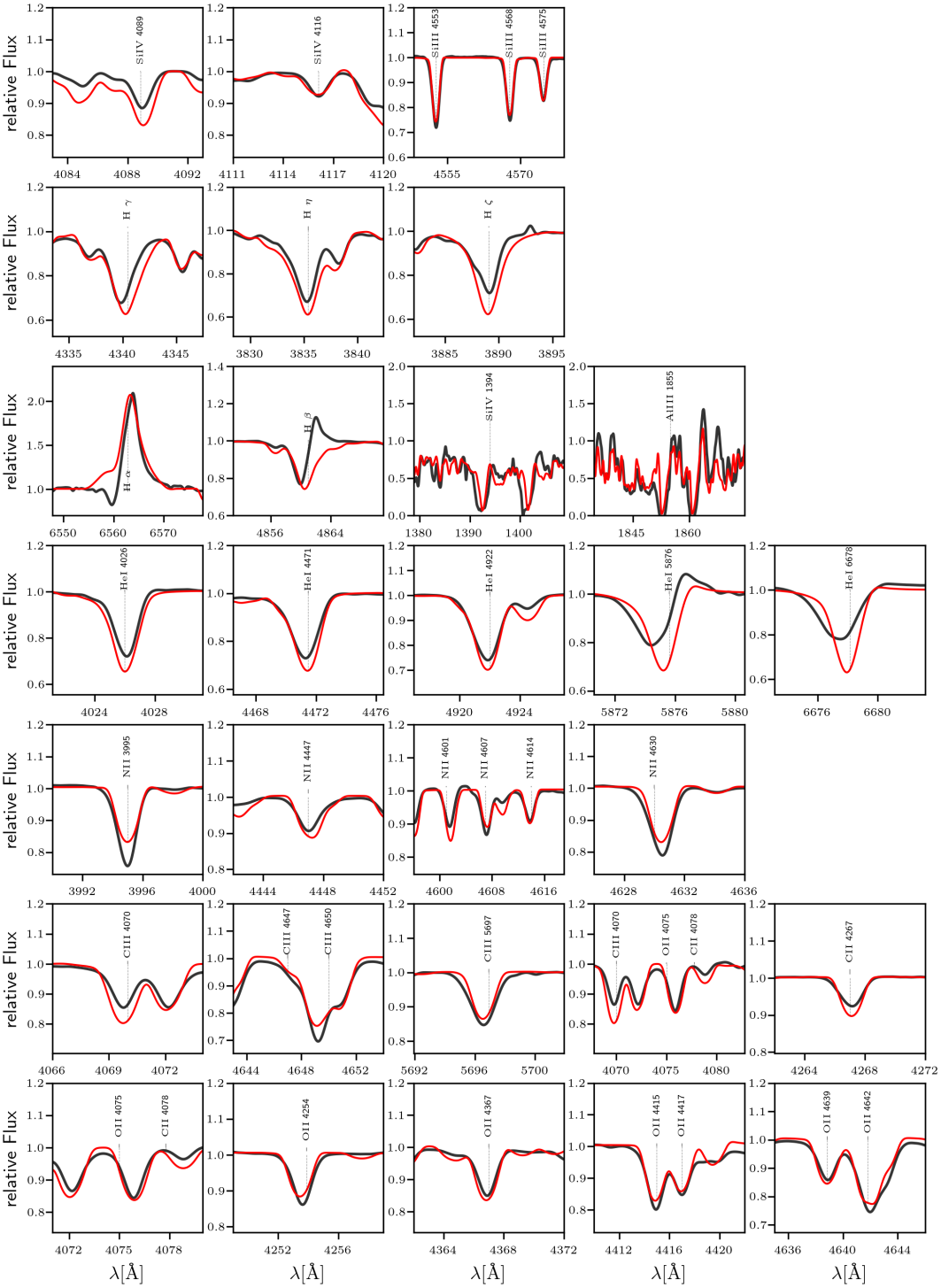


Figure C.16: Individual line fits for HD190603 (B1.5 Ia$^+$). Black solid line: observed spectrum. Red solid line: spectrum of the best fitting model.

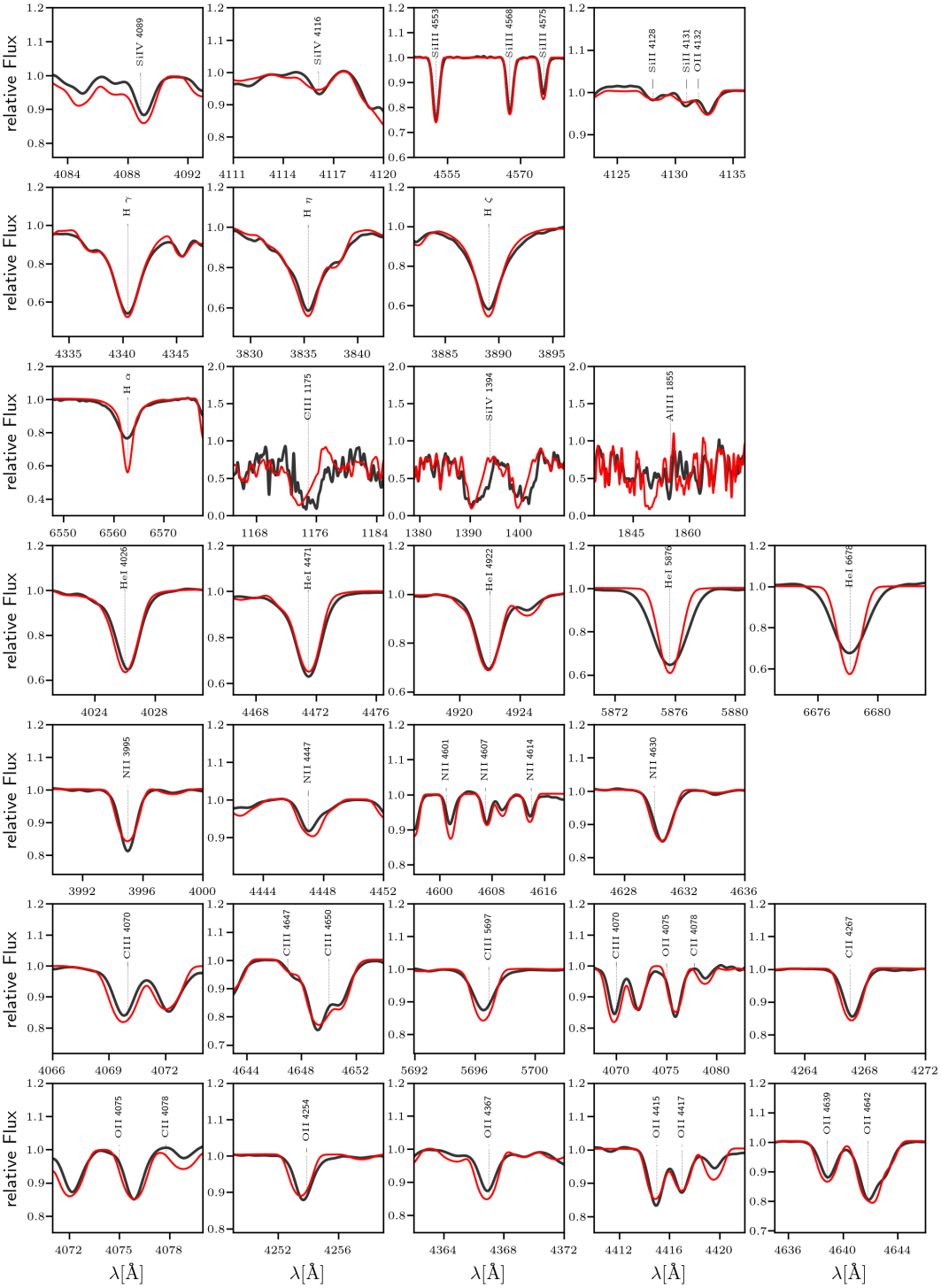


Figure C.17: Individual line fits for HD13841 (B1.5 Ib). Black solid line: observed spectrum. Red solid line: spectrum of the best fitting model.

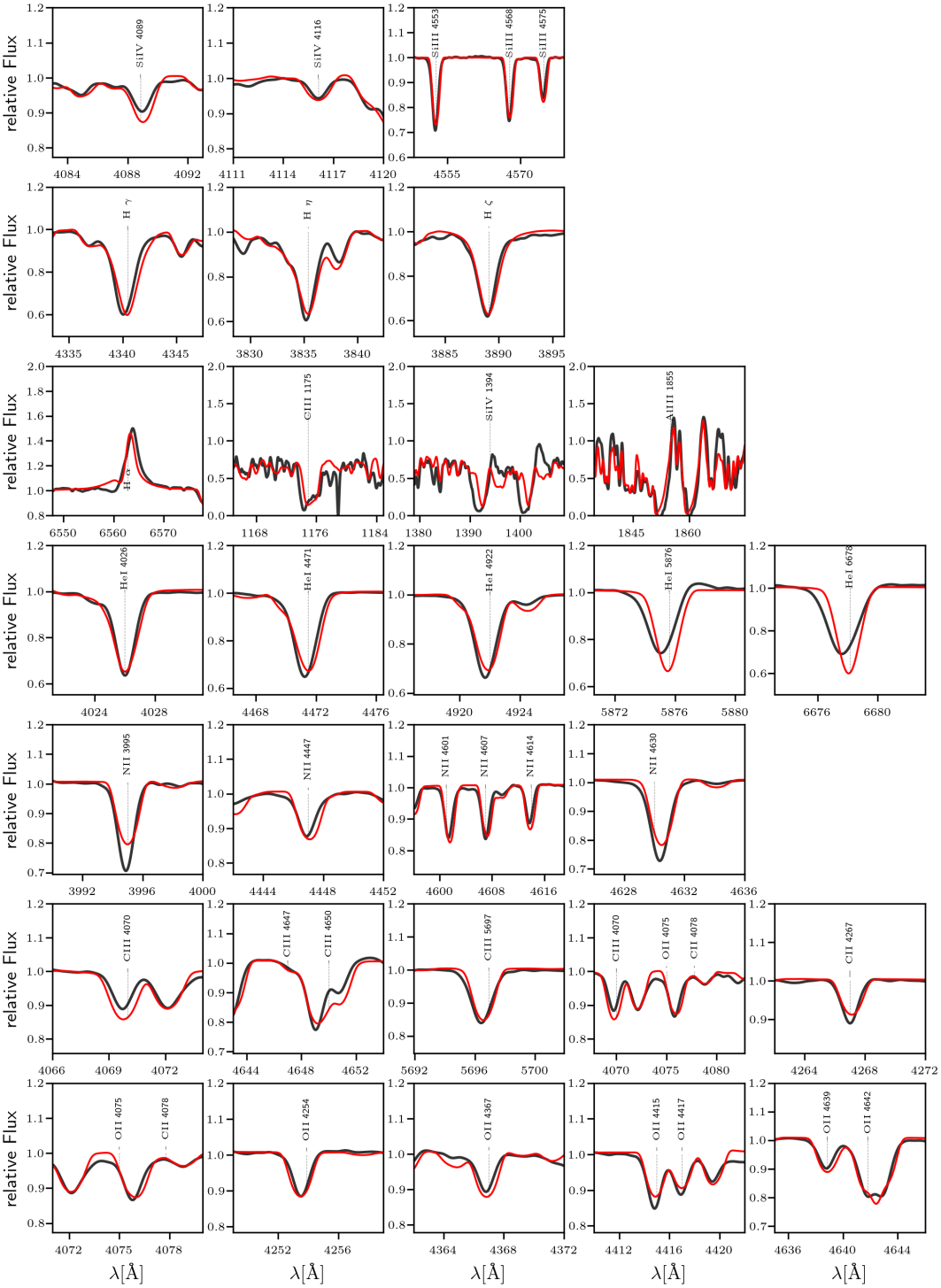


Figure C.18: Individual line fits for HD41117 (B2 Ia). Black solid line: observed spectrum. Red solid line: spectrum of the best fitting model.

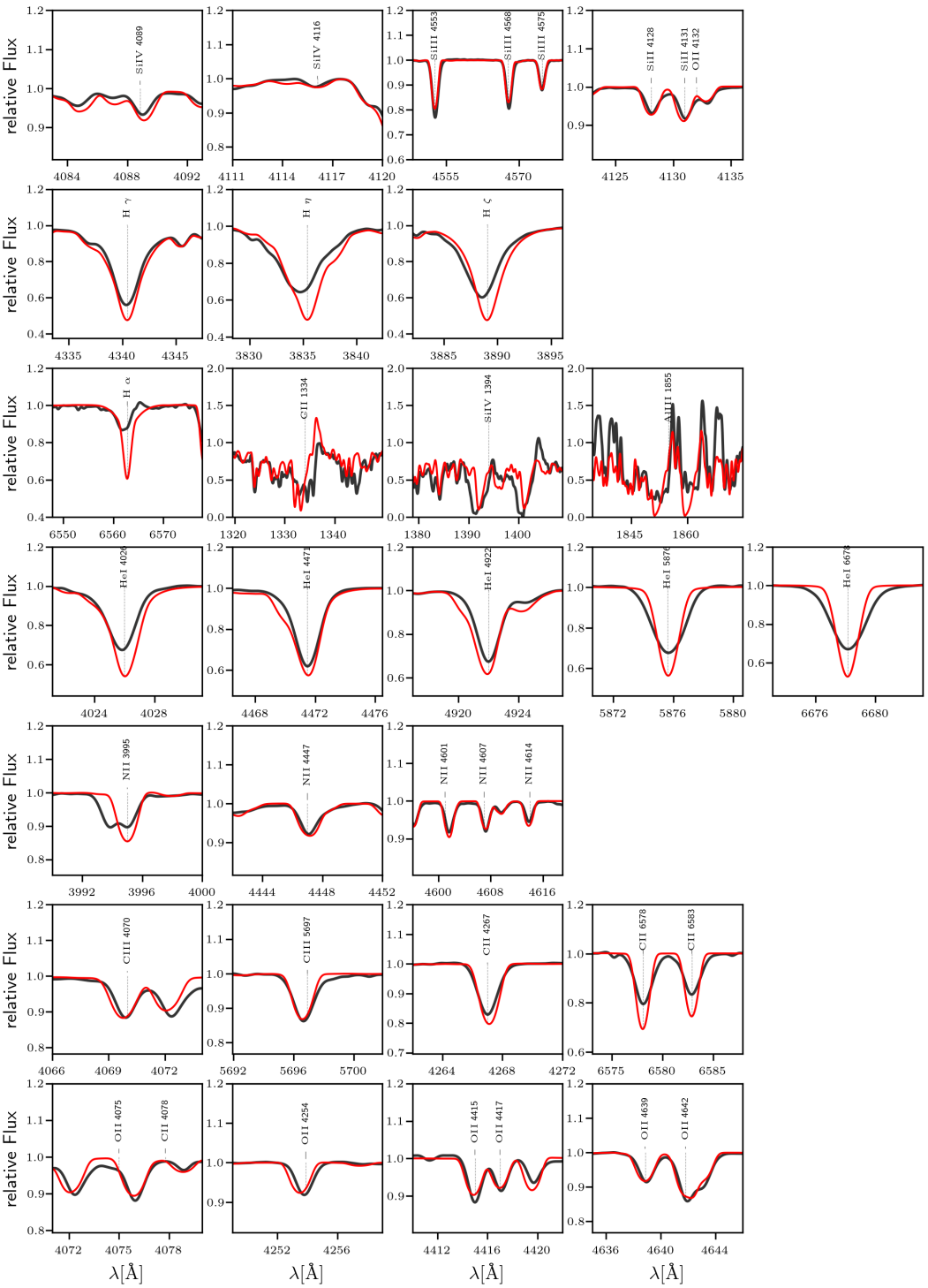


Figure C.19: Individual line fits for HD206165 (O9 Ia). Black solid line: observed spectrum. Red solid line: spectrum of the best fitting model.

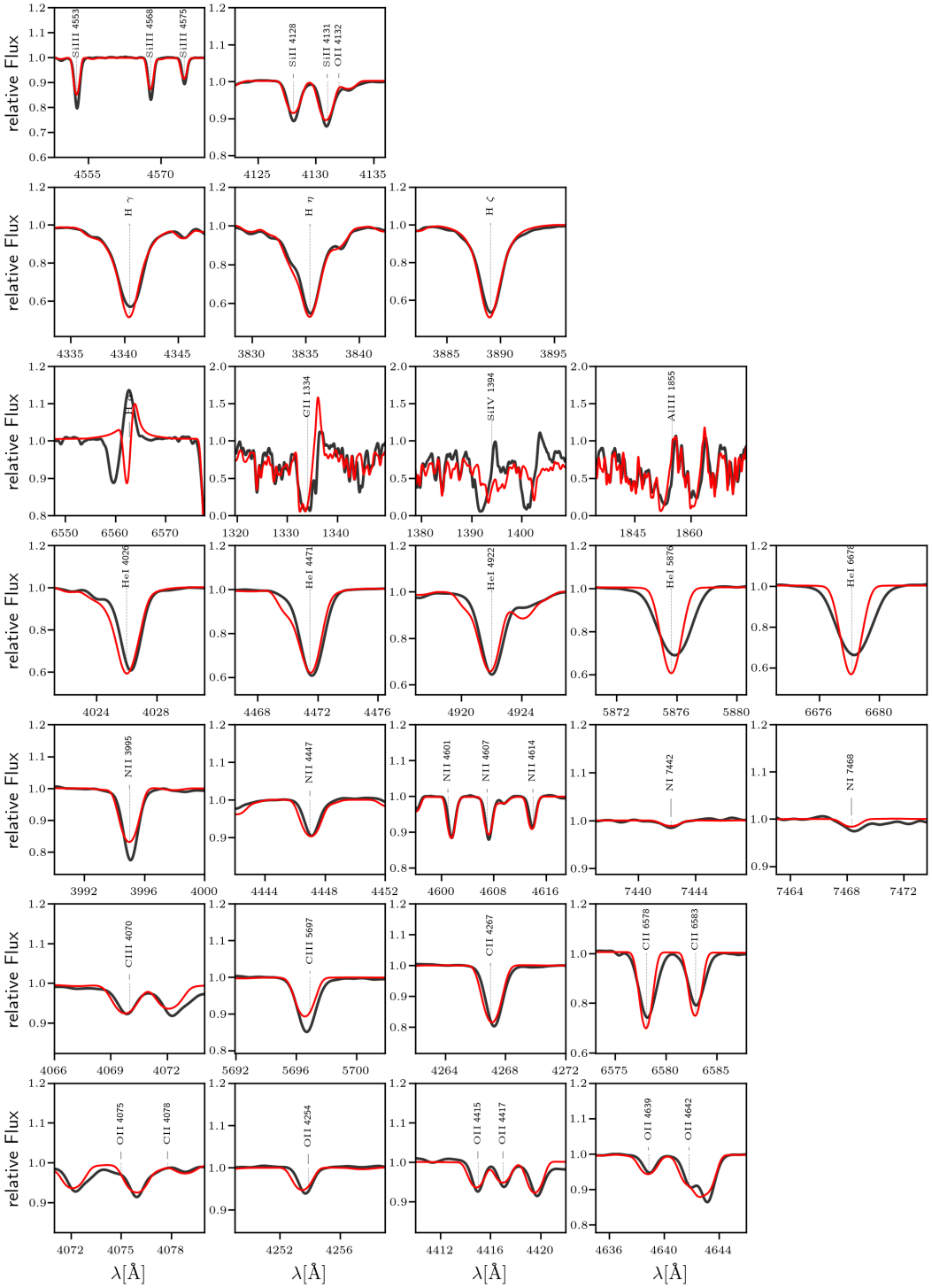


Figure C.20: Individual line fits for HD198478 (B2.5 Ia). Black solid line: observed spectrum. Red solid line: spectrum of the best fitting model.

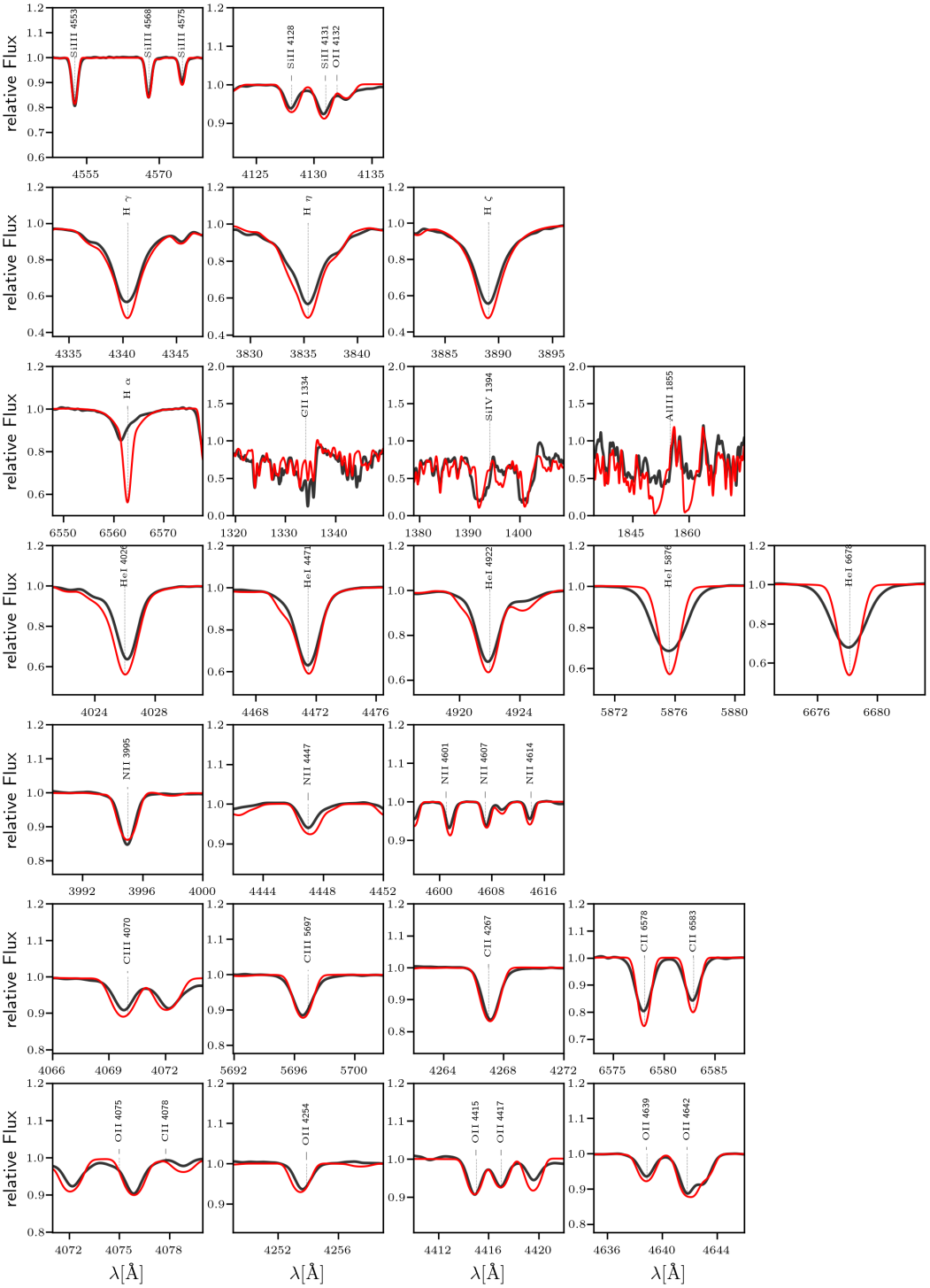


Figure C.21: Individual line fits for HD42087 (B2.5 Ib). Black solid line: observed spectrum. Red solid line: spectrum of the best fitting model.

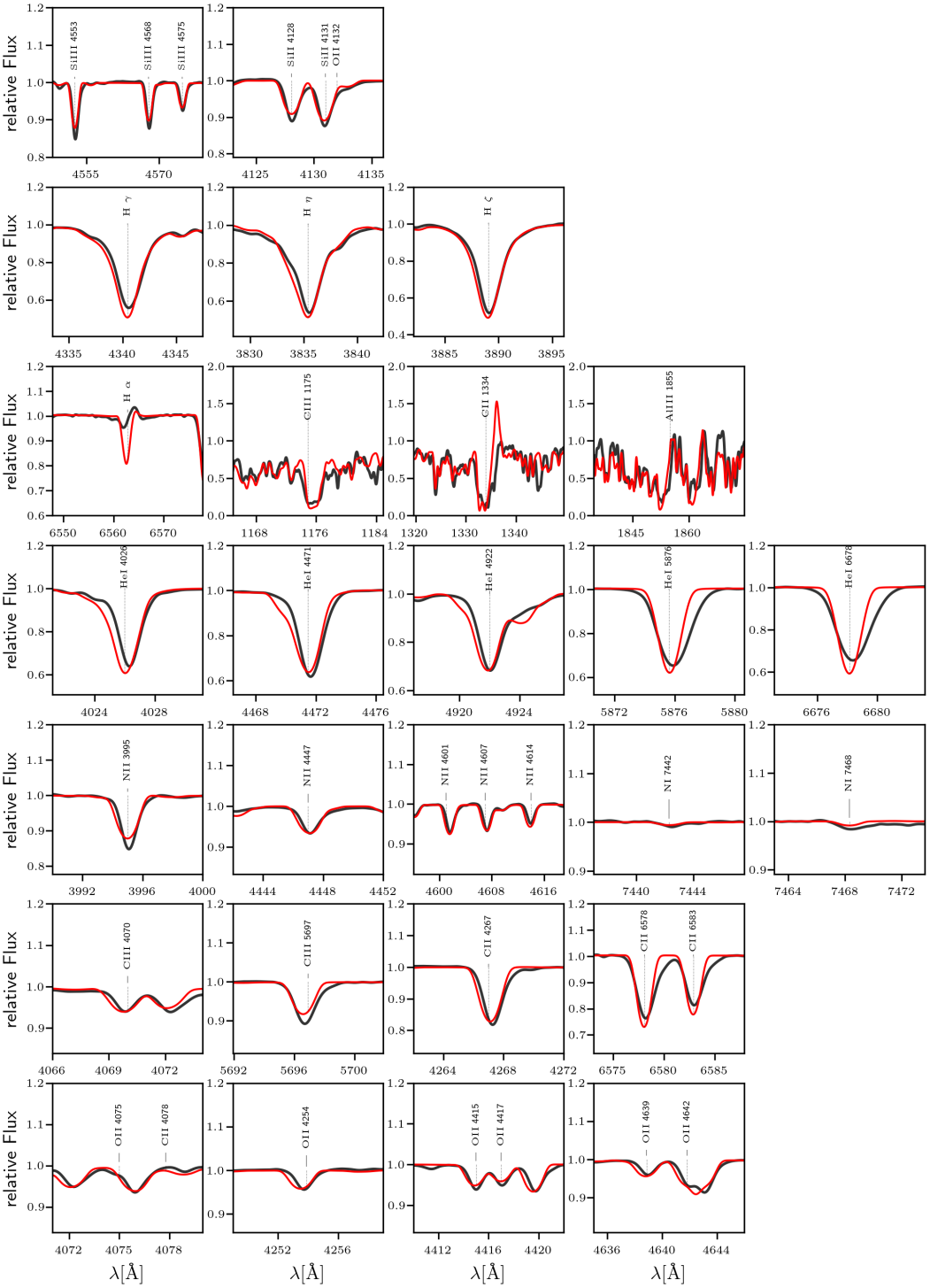


Figure C.22: Individual line fits for HD53138 (B3 Ib). Black solid line: observed spectrum. Red solid line: spectrum of the best fitting model.

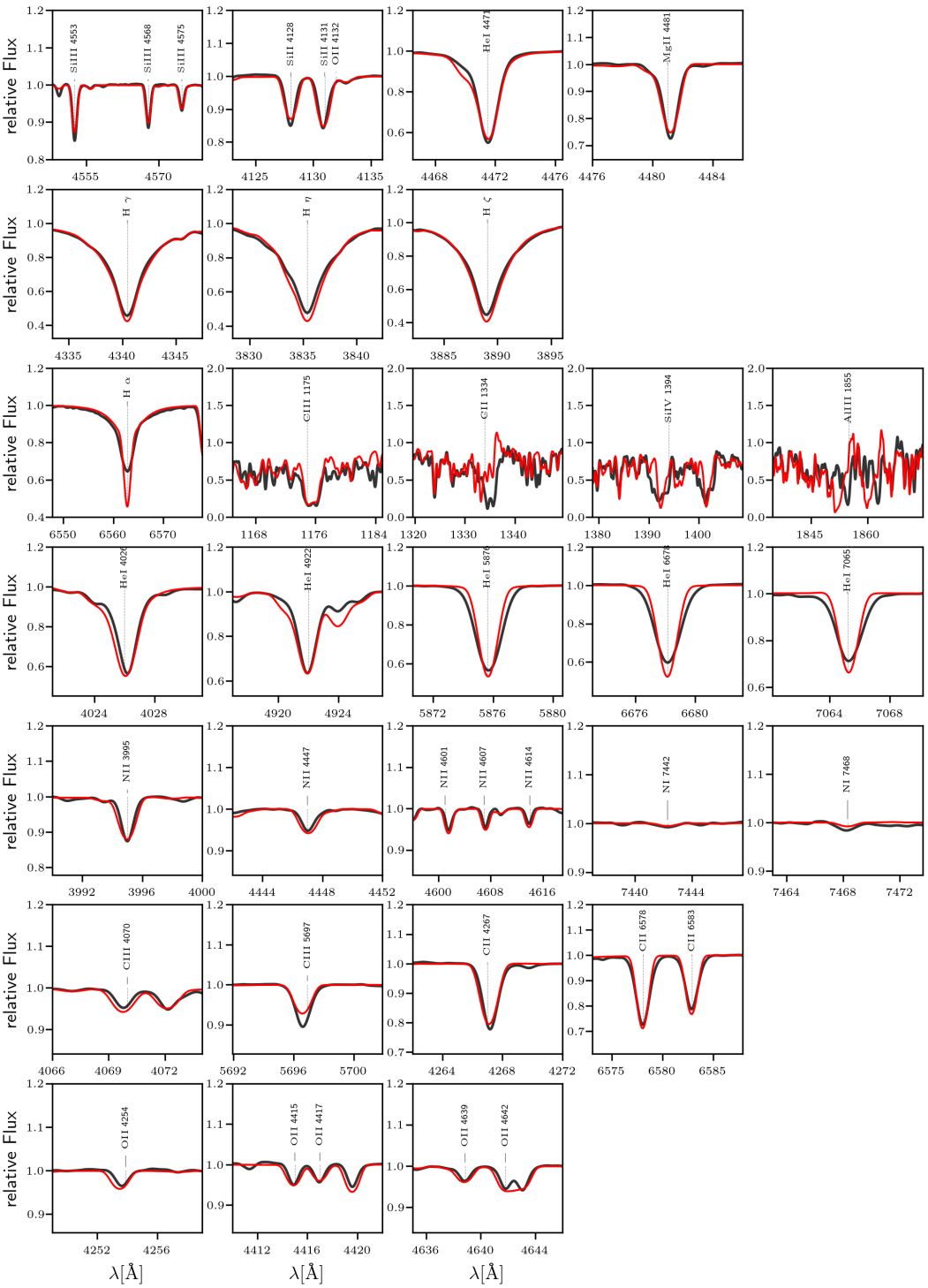


Figure C.23: Individual line fits for HD51309 (B3 Ib). Black solid line: observed spectrum. Red solid line: spectrum of the best fitting model.

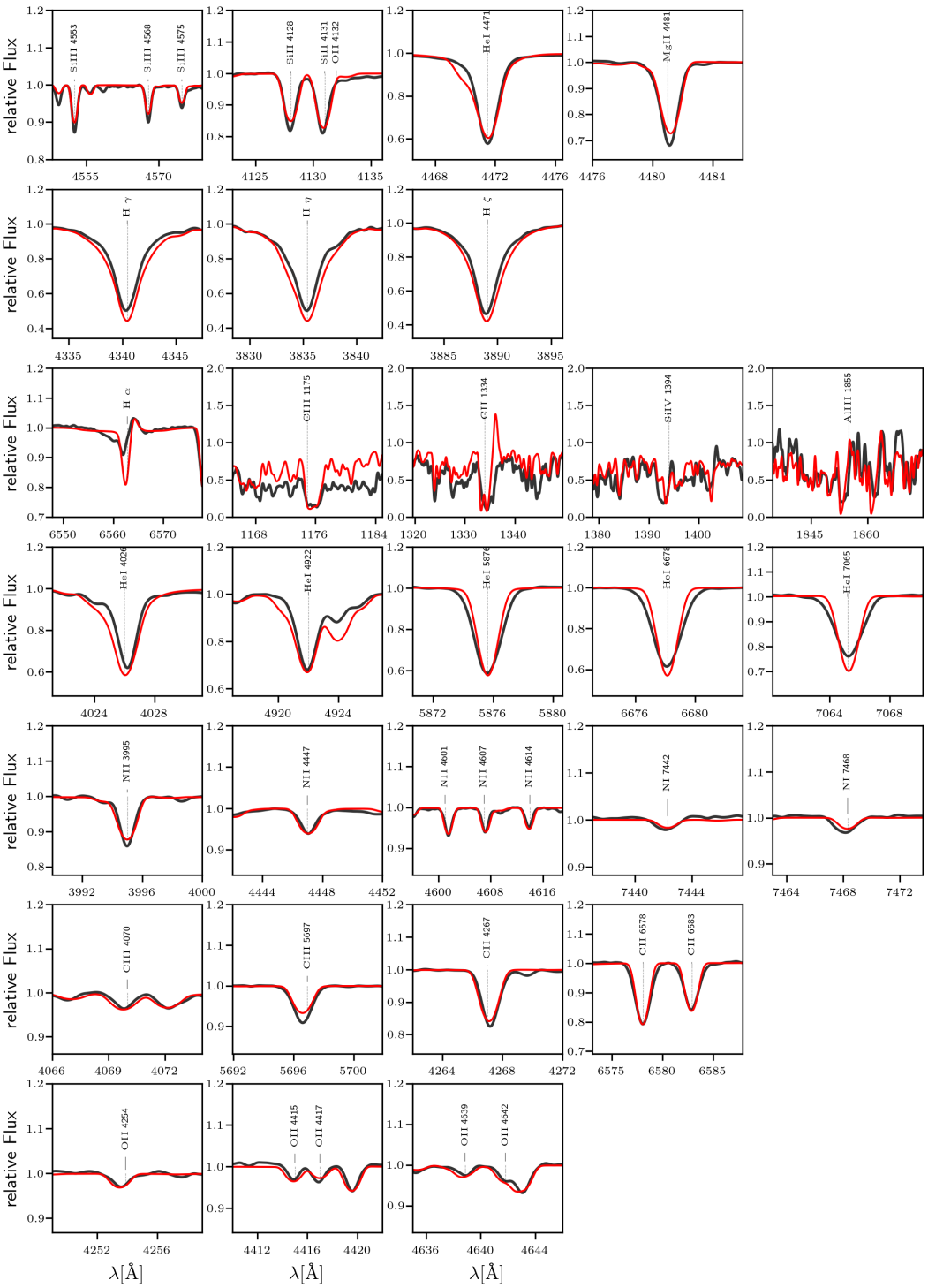


Figure C.24: Individual line fits for HD58350 (B5 Ia). Black solid line: observed spectrum. Red solid line: spectrum of the best fitting model.

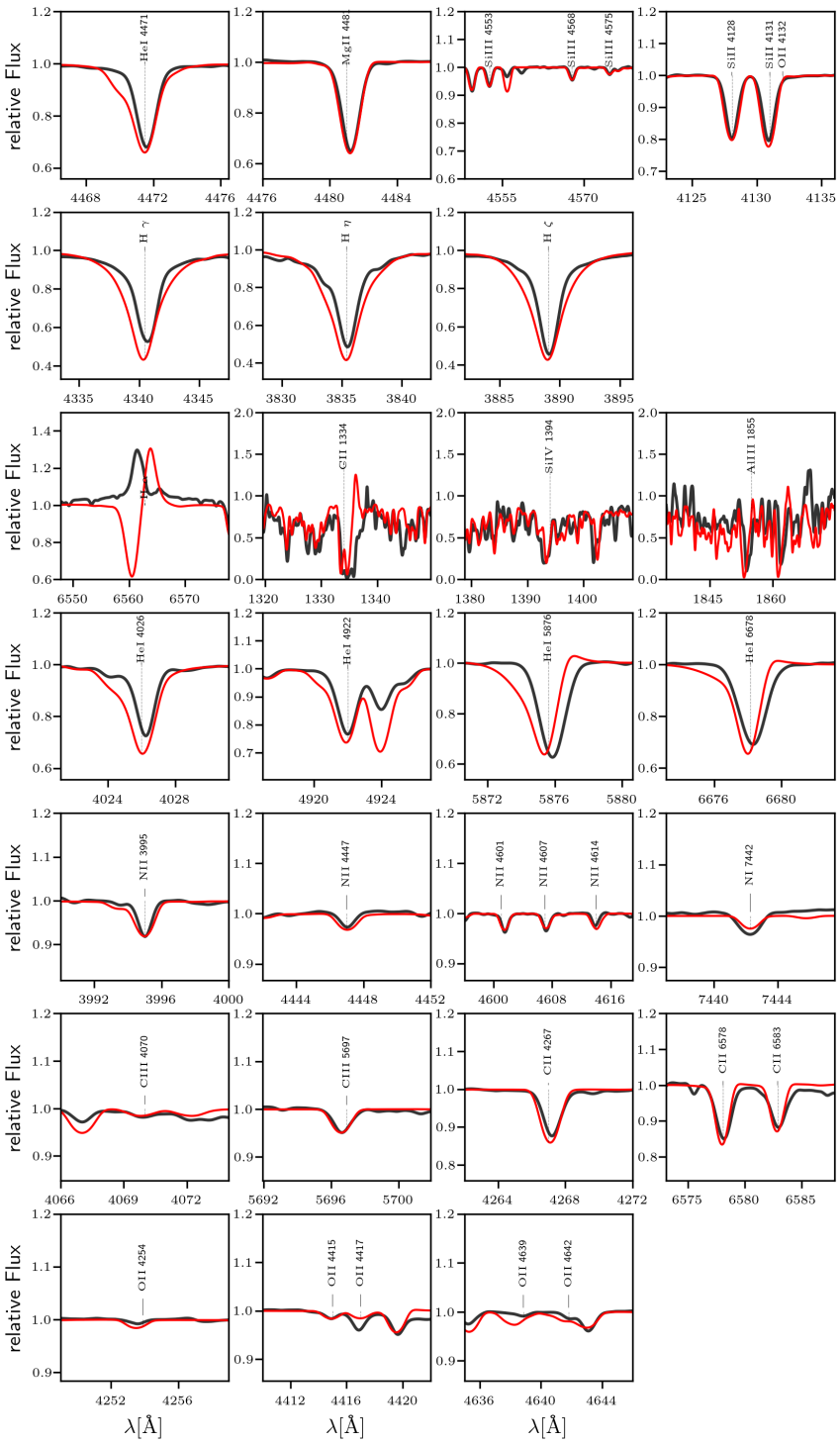


Figure C.25: Individual line fits for HD199478 (B7 Ia). Black solid line: observed spectrum. Red solid line: spectrum of the best fitting model.

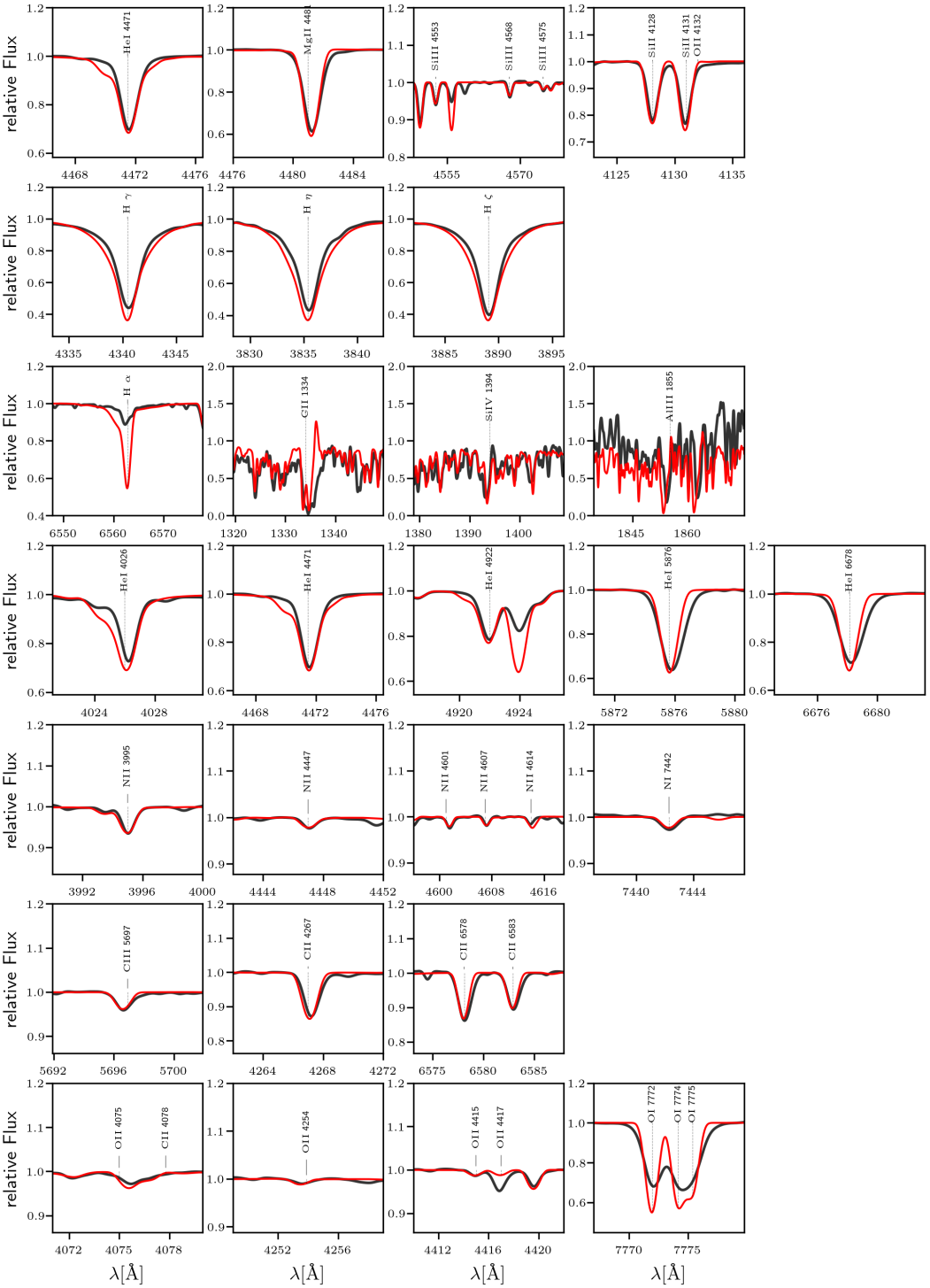


Figure C.26: Individual line fits for HD34085 (B8 Ia). Black solid line: observed spectrum. Red solid line: spectrum of the best fitting model.

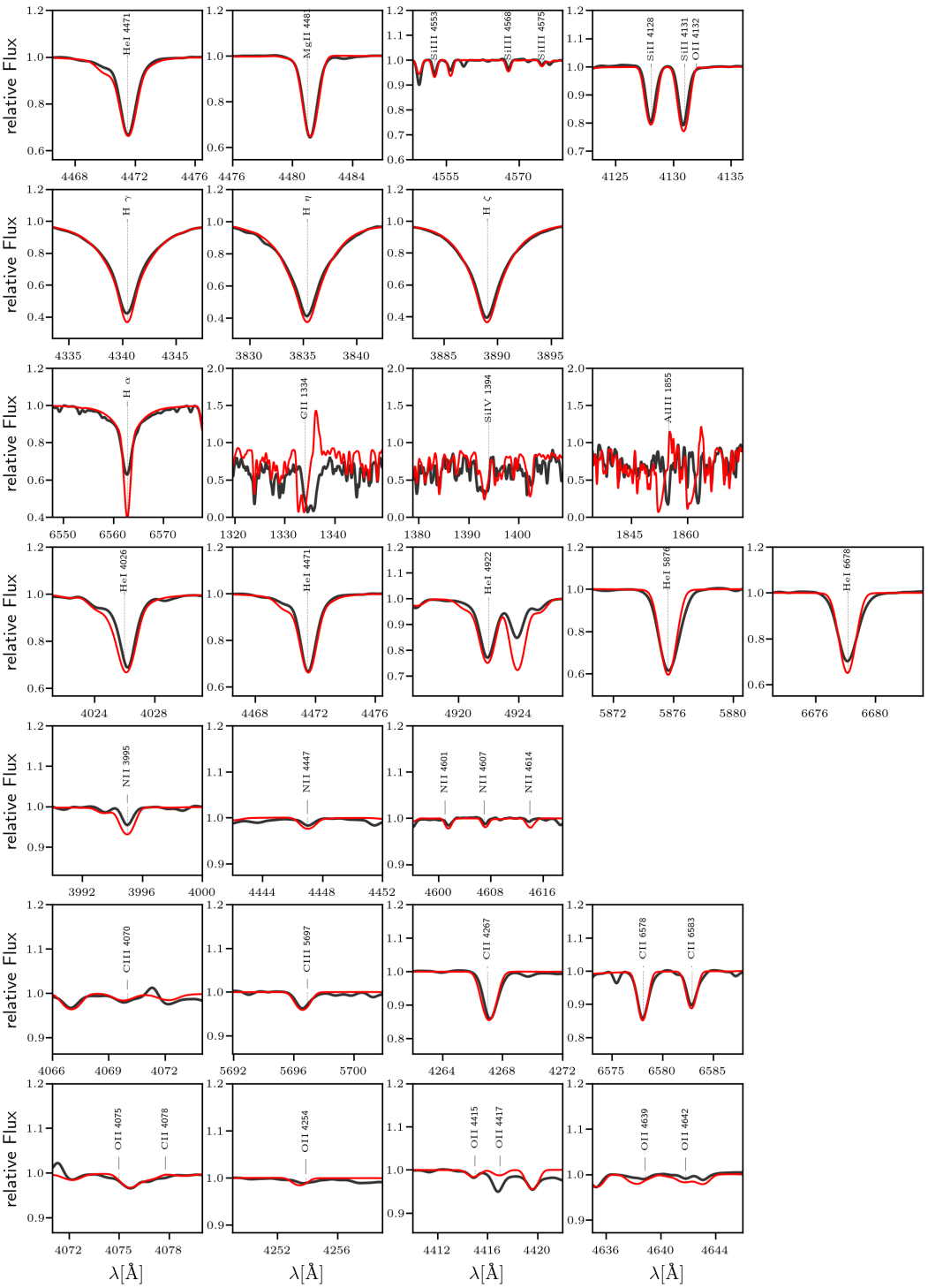


Figure C.27: Individual line fits for HD12301 (B8 Ib). Black solid line: observed spectrum. Red solid line: spectrum of the best fitting model.

C.6 Overall spectral fits

Fig. C.28-C.53 are the fits for the overall spectrum of each star in our sample.

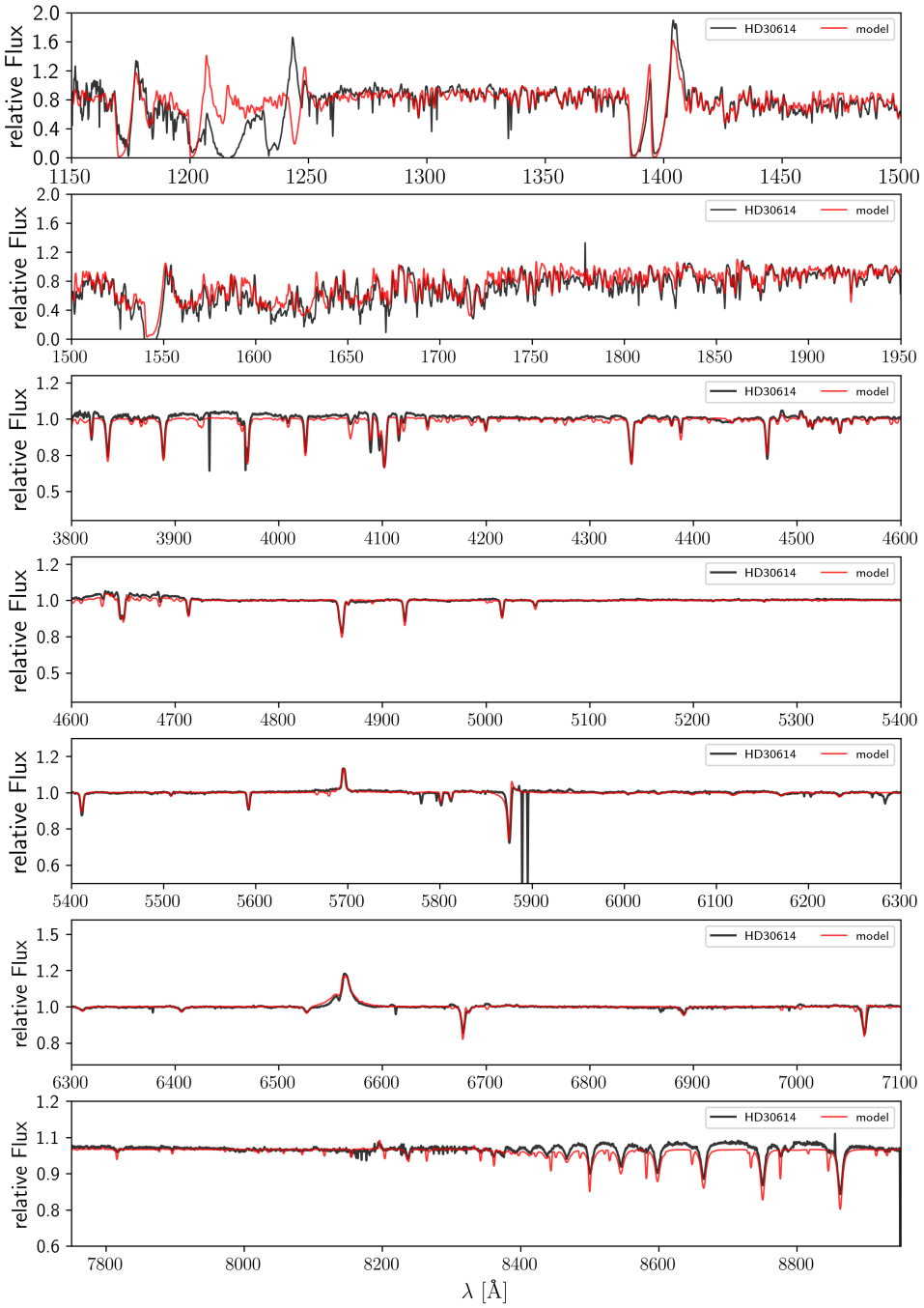


Figure C.28: An overall view of the best fit (red solid line) to key regions of the observed spectrum (black solid line) of HD30614. From top to bottom, the first two panels show the IUE SWP FUV range. We note some interstellar features: *Lyα* λ1216, O I + P II λ1302, C II λ1335, Si II λ1527, and Al II λ1671. The remaining panels show the Mercator/HERMES spectrum from the Melchiors spectroscopic library. The lines Ca II H + K and Na I D are interstellar features.

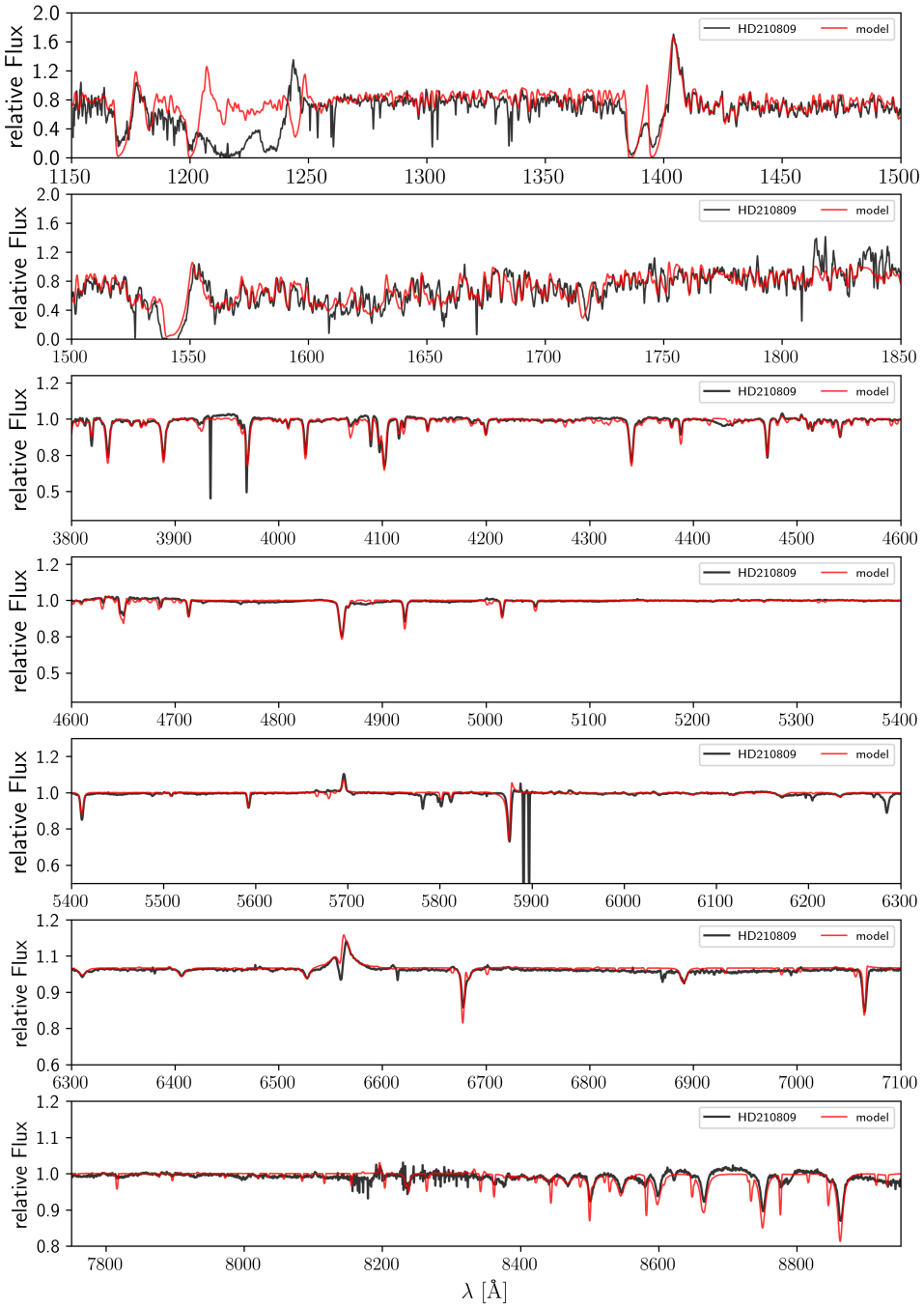


Figure C.29: An overall view of the best fit (red solid line) to key regions of the observed spectrum (black solid line) of HD210809. From top to bottom, the first two panels show the IUE SWP FUV range. We note some interstellar features: *Lyα* λ1216, O I + P II λ1302, C II λ1335, Si II λ1527, and Al II λ1671. The remaining panels show the Mercator/HERMES spectrum from the Melchiors spectroscopic library. The lines Ca II H + K and Na I D are interstellar features.

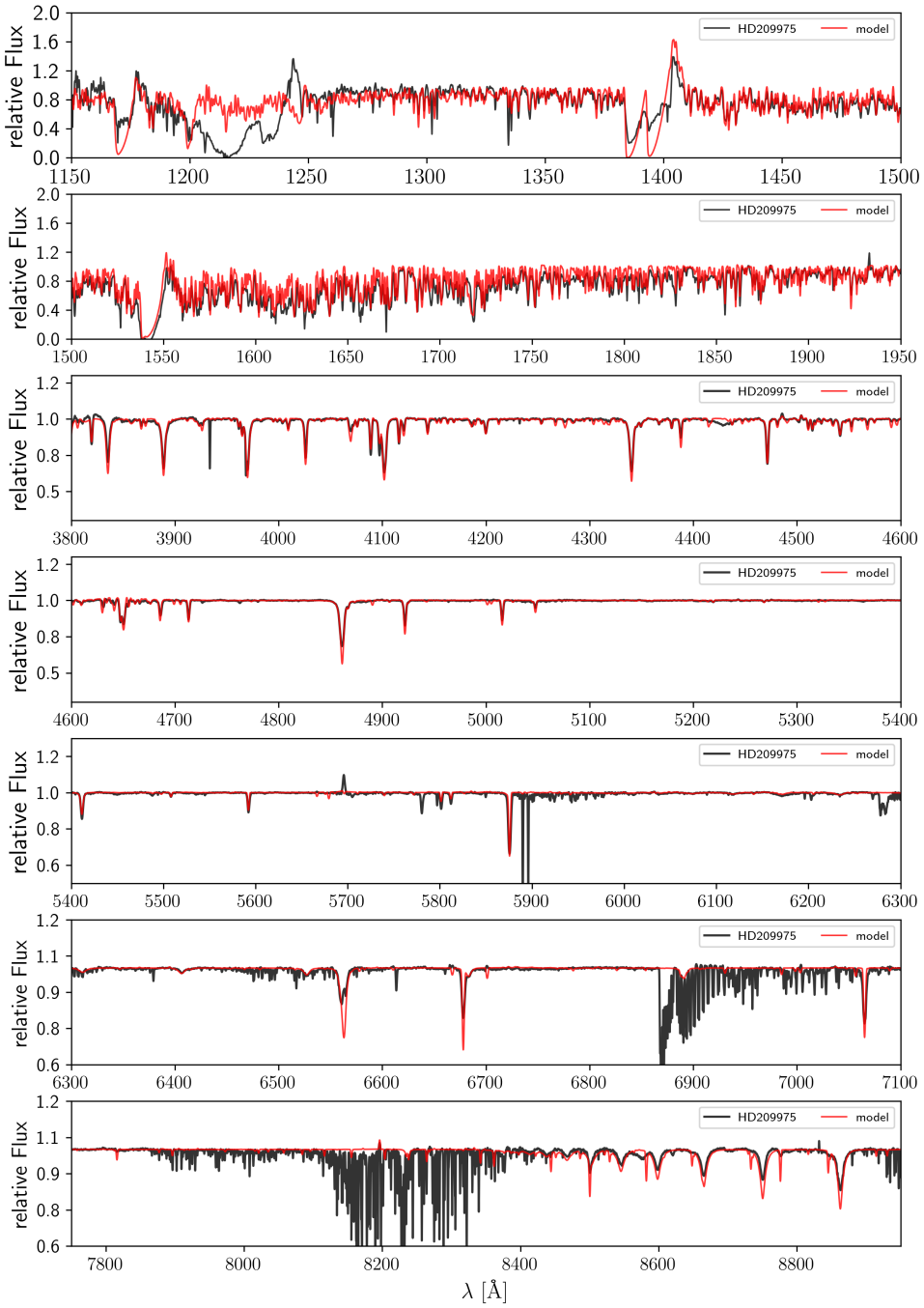


Figure C.30: An overall view of the best fit (red solid line) to key regions of the observed spectrum (black solid line) of HD209975. From top to bottom, the first two panels show the IUE SWP FUV range. We note some interstellar features: *Lyα* λ1216, O I + P II λ1302, C II λ1335, Si II λ1527, and Al II λ1671. The remaining panels show the Mercator/HERMES spectrum from the IACOB spectroscopic library. The lines Ca II H + K and Na I D are interstellar features.

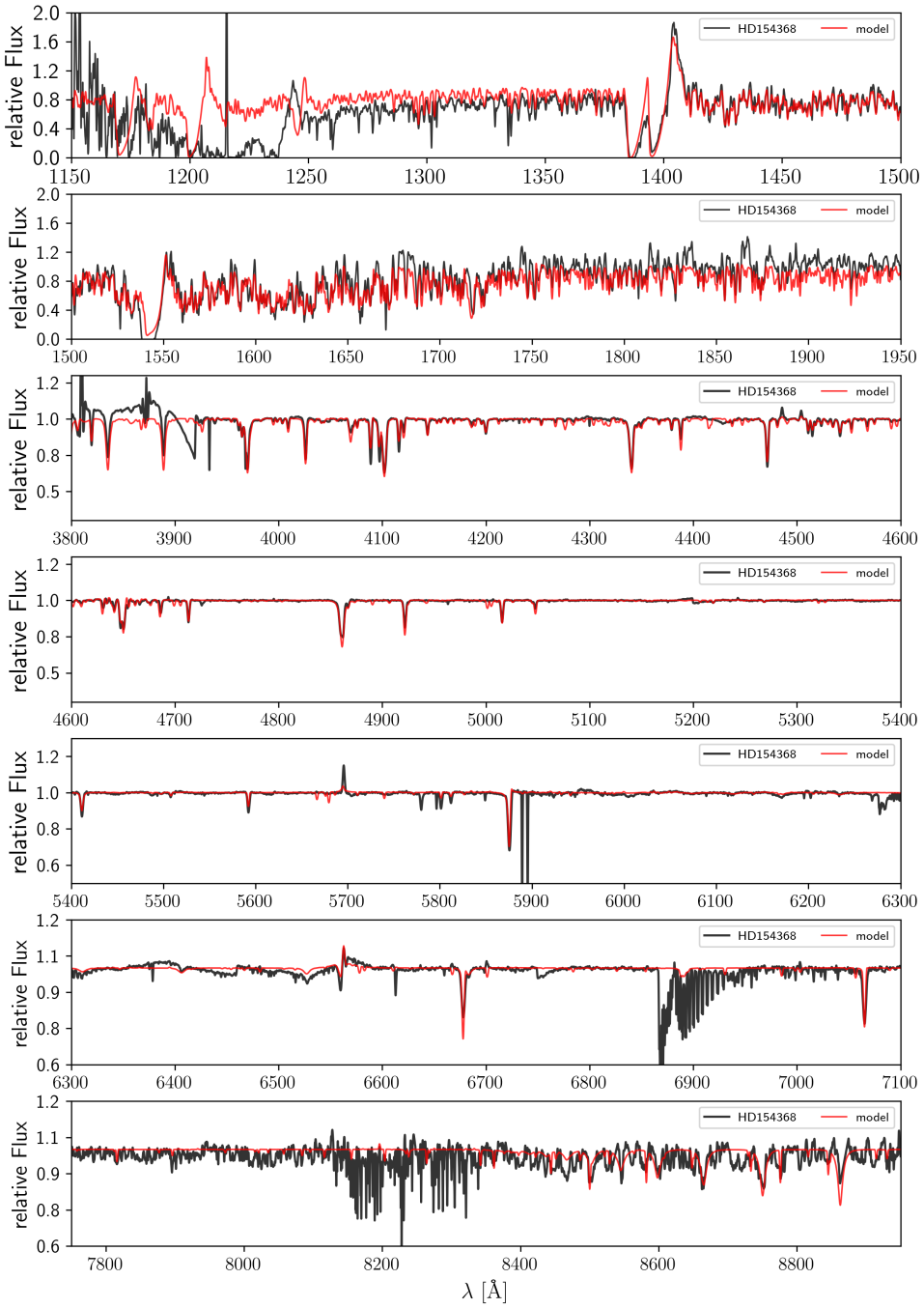


Figure C.31: An overall view of the best fit (red solid line) to key regions of the observed spectrum (black solid line) of HD154368. From top to bottom, the first two panels show the IUE SWP FUV range. We note some interstellar features: *Lyα* λ1216, O I + P II λ1302, C II λ1335, Si II λ1527, and Al II λ1671. The remaining panels show the MPG/FEROS spectrum from the IACOB spectroscopic library. The lines Ca II H + K and Na I D are interstellar features.

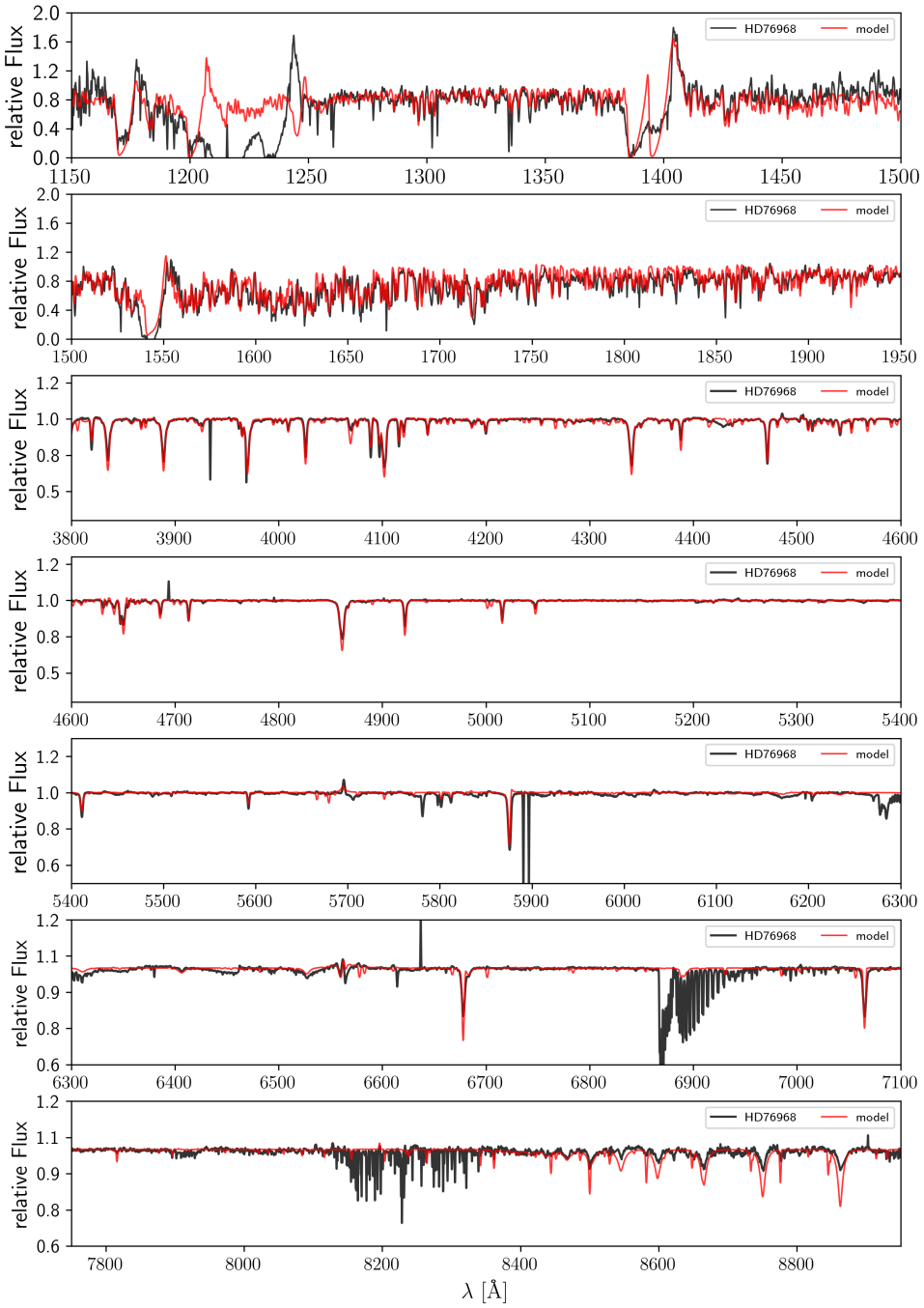


Figure C.32: An overall view of the best fit (red solid line) to key regions of the observed spectrum (black solid line) of HD76968. From top to bottom, the first two panels show the IUE SWP FUV range. We note some interstellar features: *Lyα* λ1216, O I + P II λ1302, C II λ1335, Si II λ1527, and Al II λ1671. The remaining panels show the MPG/FEROS spectrum from the IACOB spectroscopic library. The lines Ca II H + K and Na I D are interstellar features.

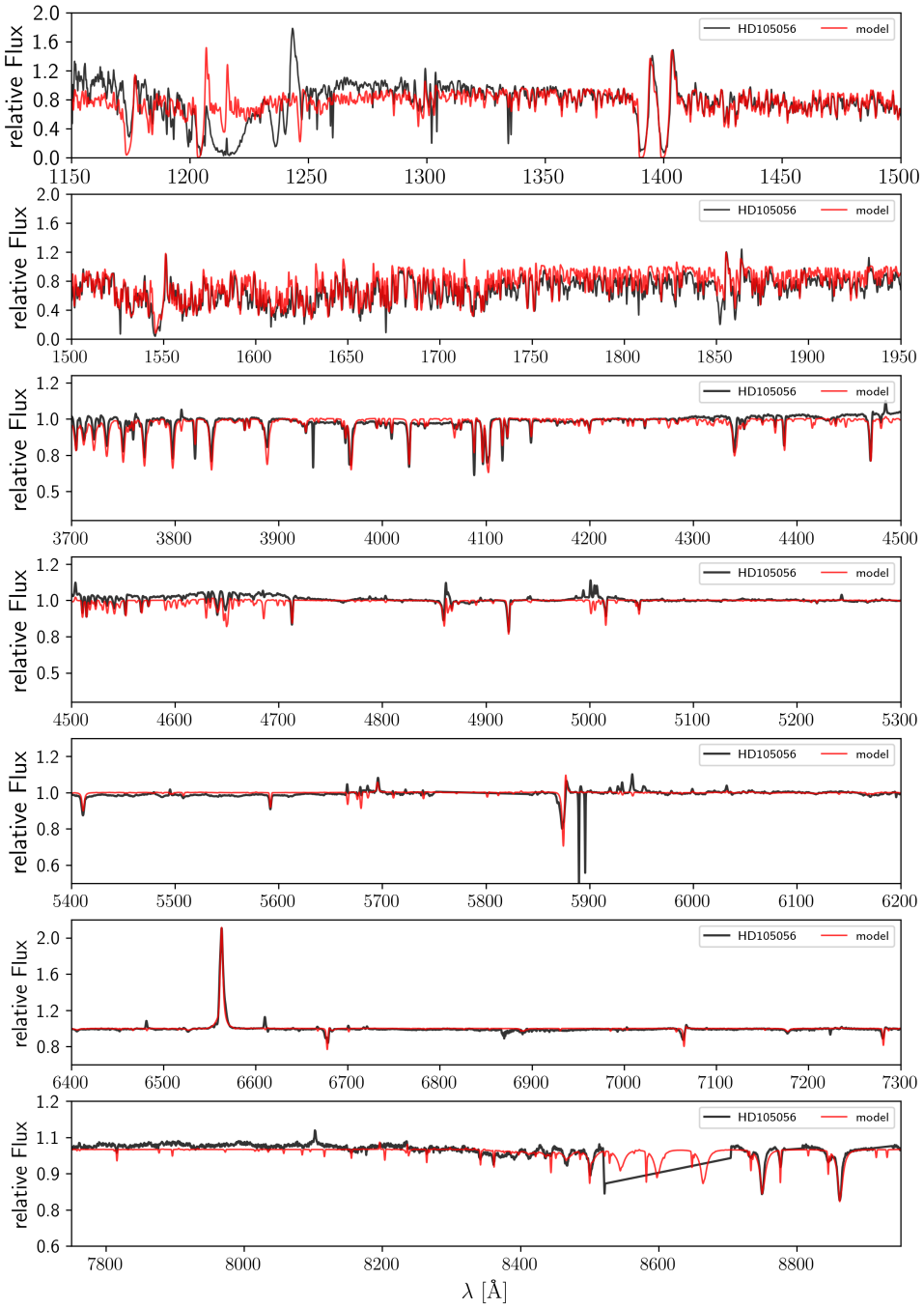


Figure C.33: An overall view of the best fit (red solid line) to key regions of the observed spectrum (black solid line) of HD105056. From top to bottom, the first two panels show the IUE SWP FUV range. We note some interstellar features: *Lyα* λ1216, O I + P II λ1302, C II λ1335, Si II λ1527, and Al II λ1671. The remaining panels show the VLT/UVES spectrum from the UVES-POP spectroscopic library. The lines Ca II H + K and Na I D are interstellar features.

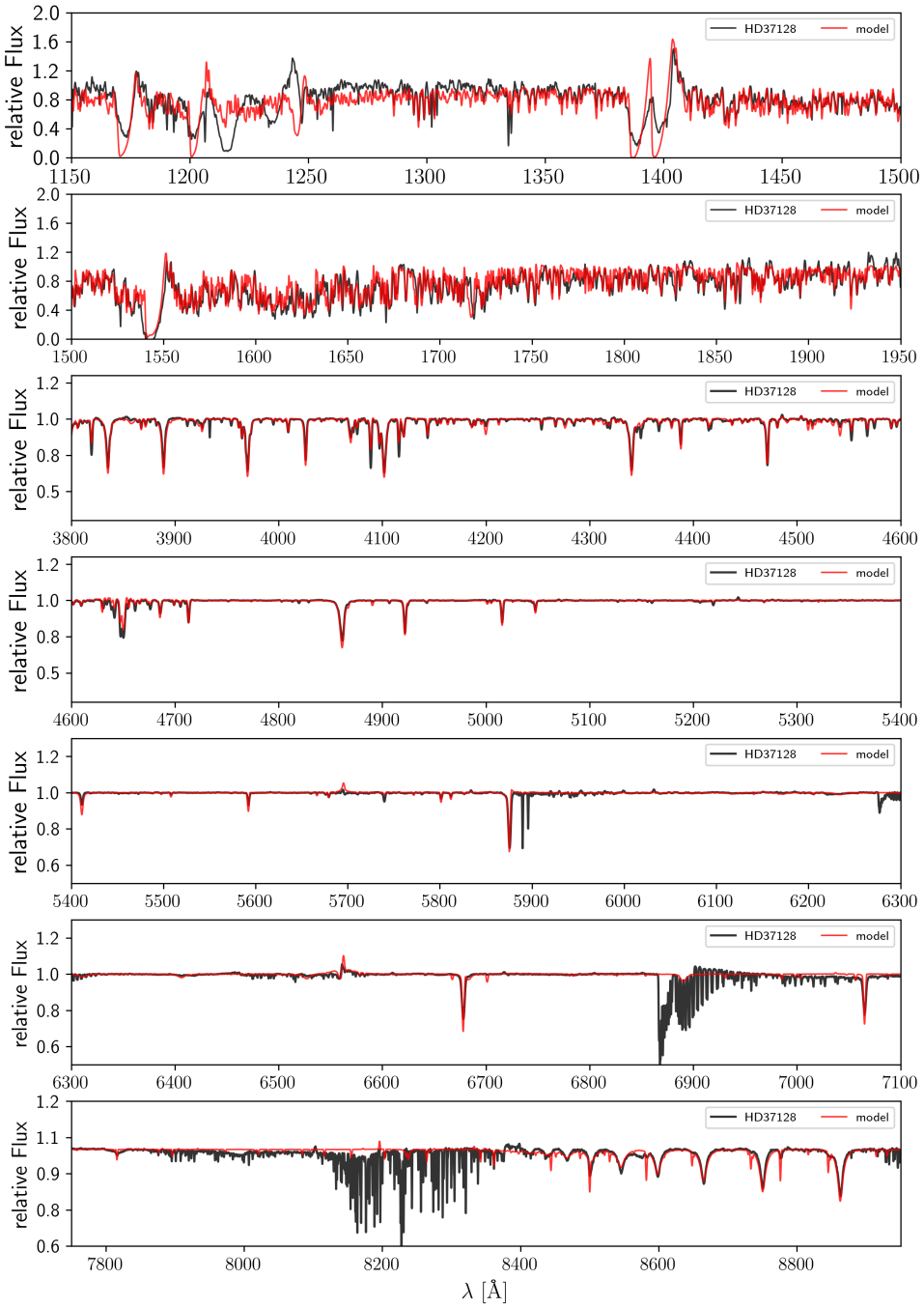


Figure C.34: An overall view of the best fit (red solid line) to key regions of the observed spectrum (black solid line) of HD37128. From top to bottom, the first two panels show the IUE SWP FUV range. We note some interstellar features: *Lyα* λ1216, O I + P II λ1302, C II λ1335, Si II λ1527, and Al II λ1671. The remaining panels show the Mercator/HERMES spectrum from the IACOB spectroscopic library. The lines Ca II H + K and Na I D are interstellar features.

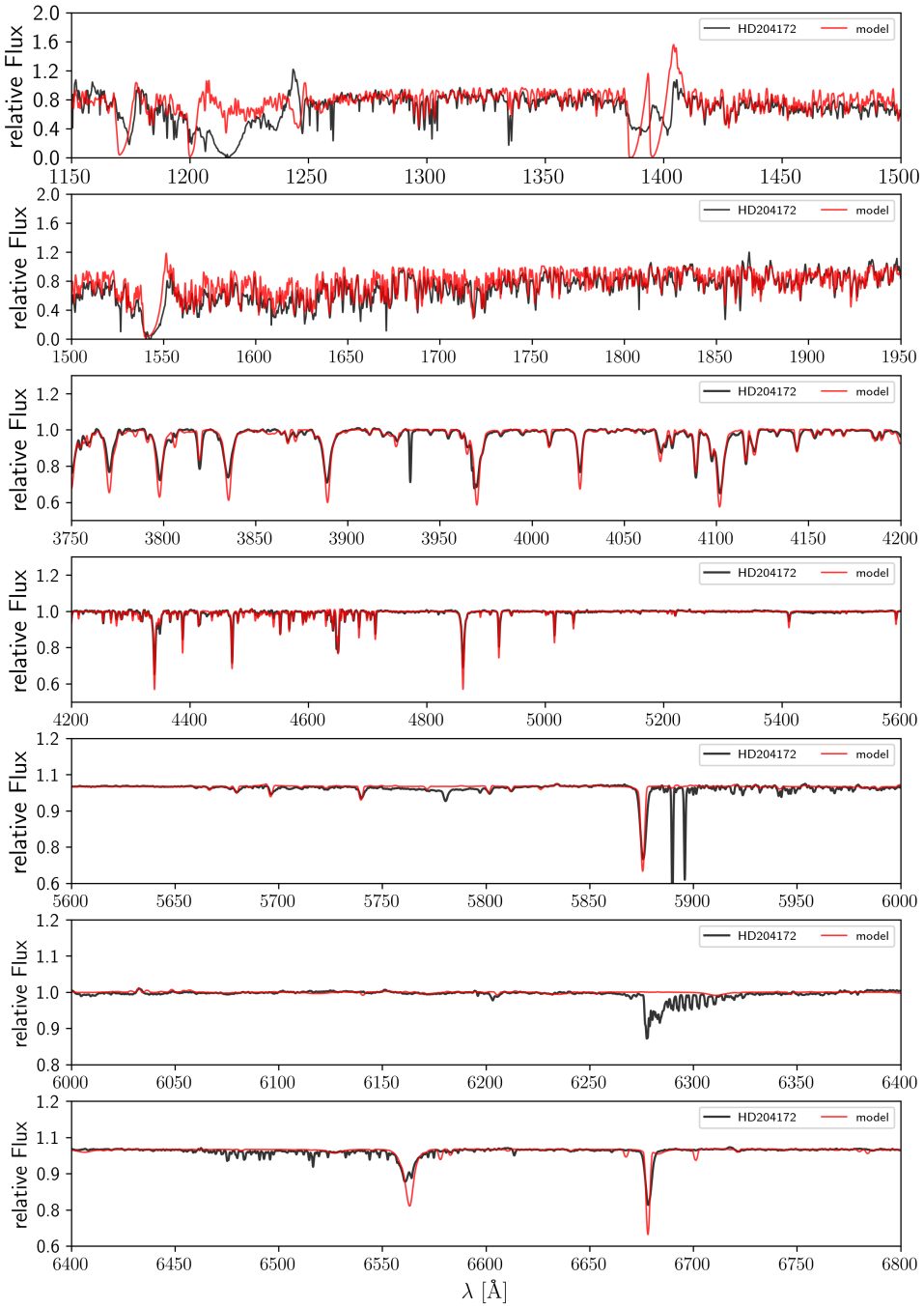


Figure C.35: An overall view of the best fit (red solid line) to key regions of the observed spectrum (black solid line) of HD204172. From top to bottom, the first two panels show the IUE SWP FUV range. We note some interstellar features: *Lyα* λ1216, O I + P II λ1302, C II λ1335, Si II λ1527, and Al II λ1671. The remaining panels show the NOT/FIES spectrum from the IACOB spectroscopic library. The lines Ca II H + K and Na I D are interstellar features.

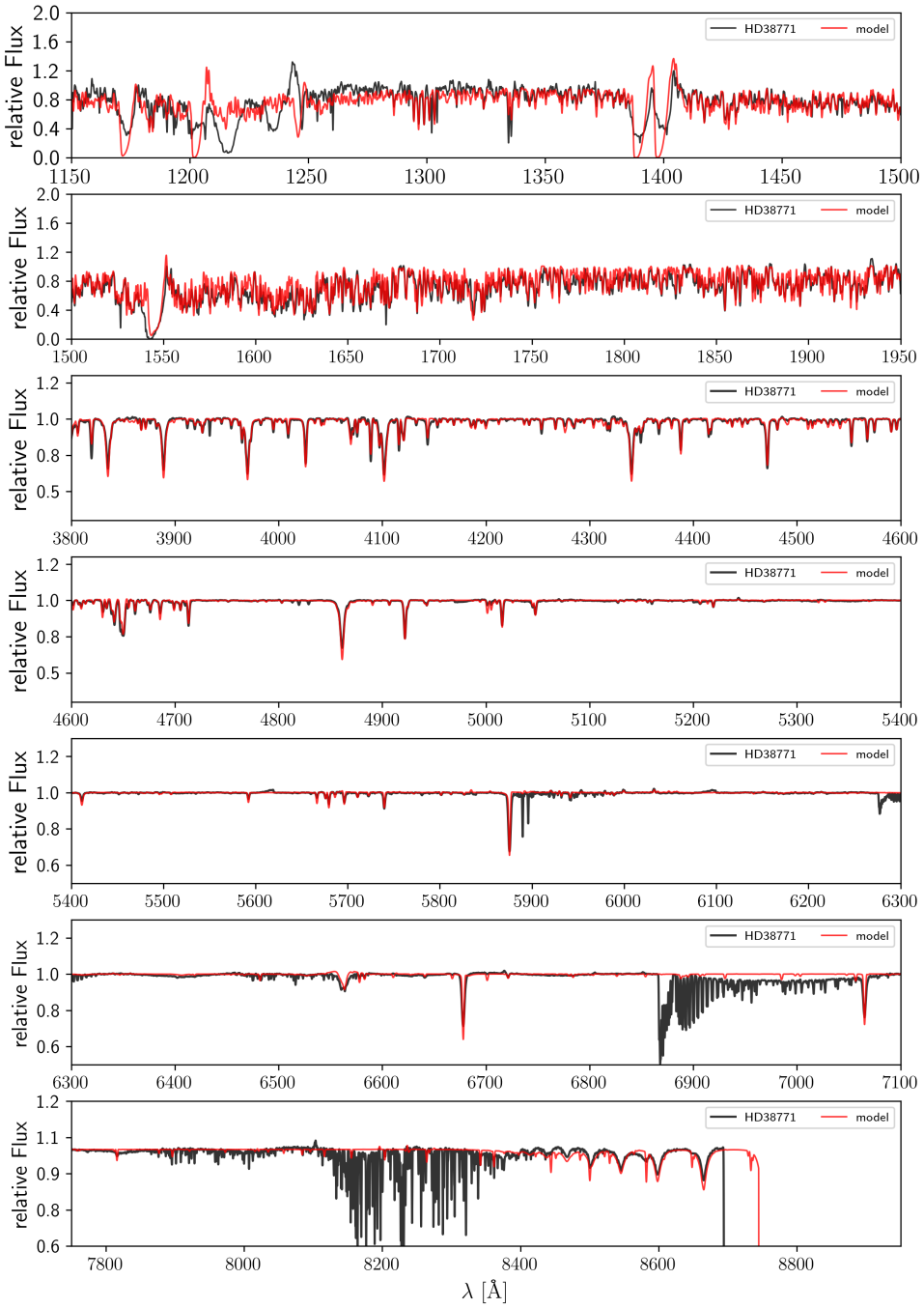


Figure C.36: An overall view of the best fit (red solid line) to key regions of the observed spectrum (black solid line) of HD38771. From top to bottom, the first two panels show the IUE SWP FUV range. We note some interstellar features: *Lyα* λ1216, O I + P II λ1302, C II λ1335, Si II λ1527, and Al II λ1671. The remaining panels show the Mercator/HERMES spectrum from the IACOB spectroscopic library. The lines Ca II H + K and Na I D are interstellar features.

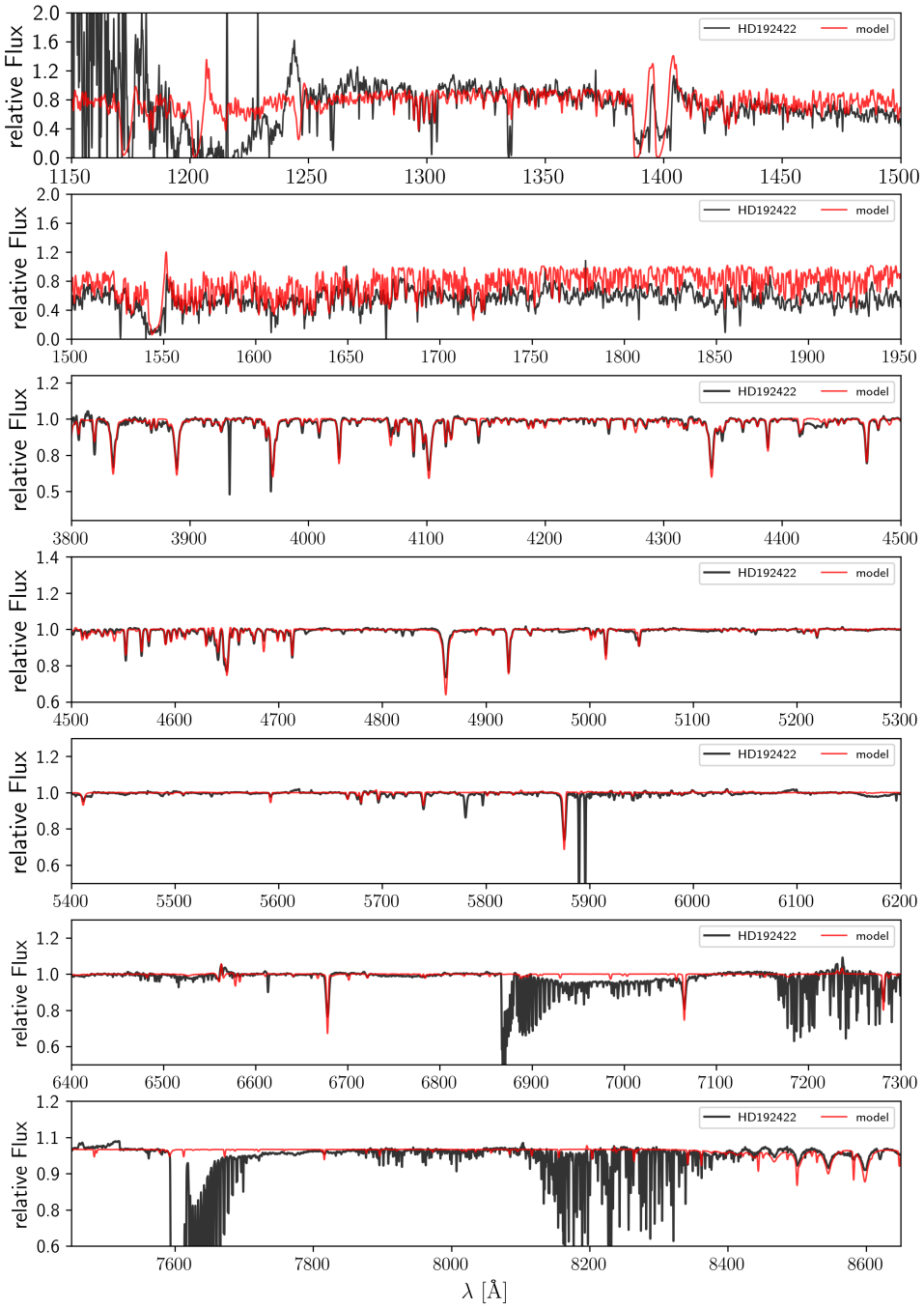


Figure C.37: An overall view of the best fit (red solid line) to key regions of the observed spectrum (black solid line) of HD192422. From top to bottom, the first two panels show the IUE SWP FUV range. We note some interstellar features: *Lyα* λ1216, O I + P II λ1302, C II λ1335, Si II λ1527, and Al II λ1671. The remaining panels show the Mercator/HERMES spectrum from the IACOB spectroscopic library. The lines Ca II H + K and Na I D are interstellar features.

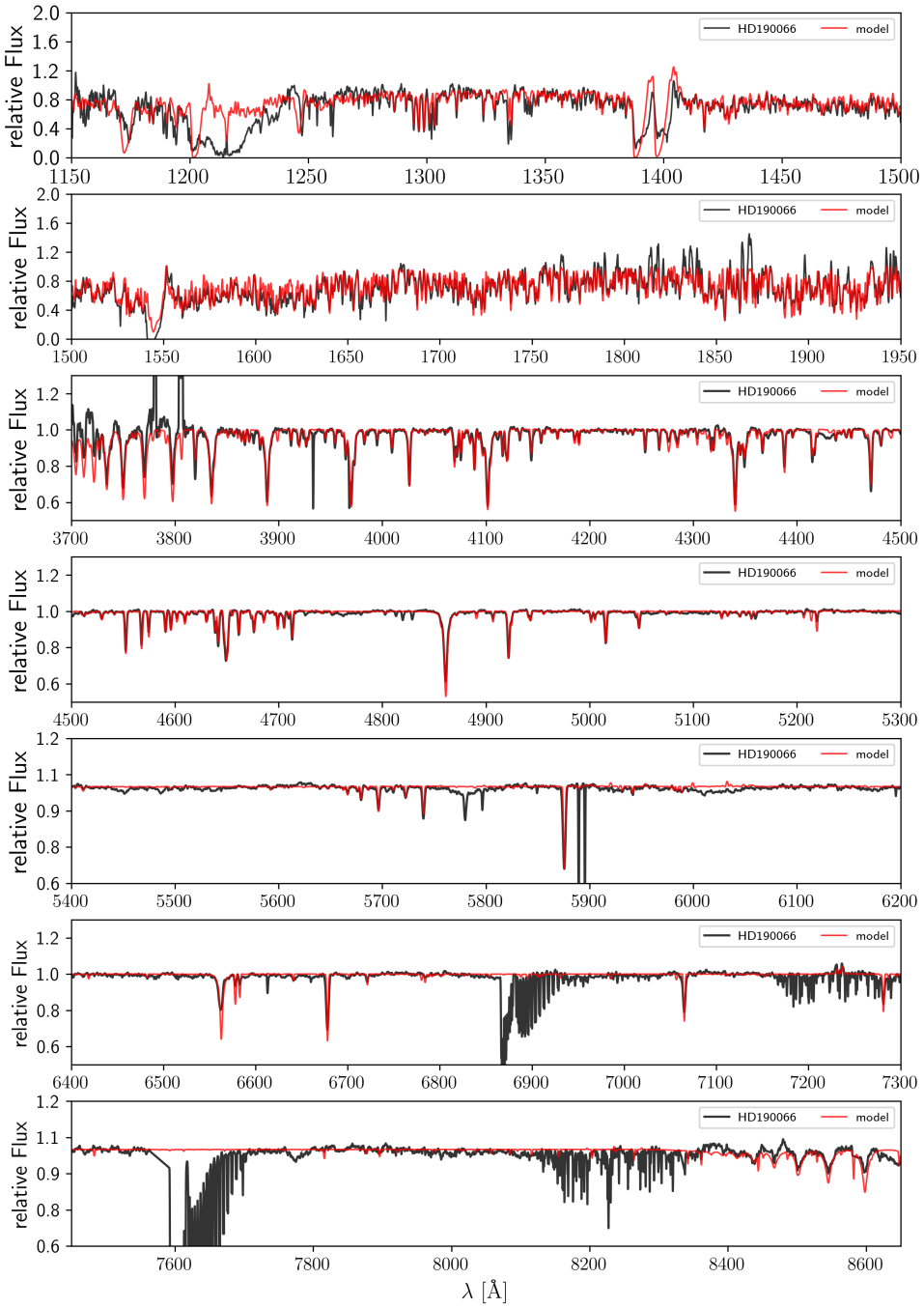


Figure C.38: An overall view of the best fit (red solid line) to key regions of the observed spectrum (black solid line) of HD190066. From top to bottom, the first two panels show the IUE SWP FUV range. We note some interstellar features: *Lyα* λ1216, O I + P II λ1302, C II λ1335, Si II λ1527, and Al II λ1671. The remaining panels show the NOT/FIES spectrum from the IACOB spectroscopic library. The lines Ca II H + K and Na I D are interstellar features.

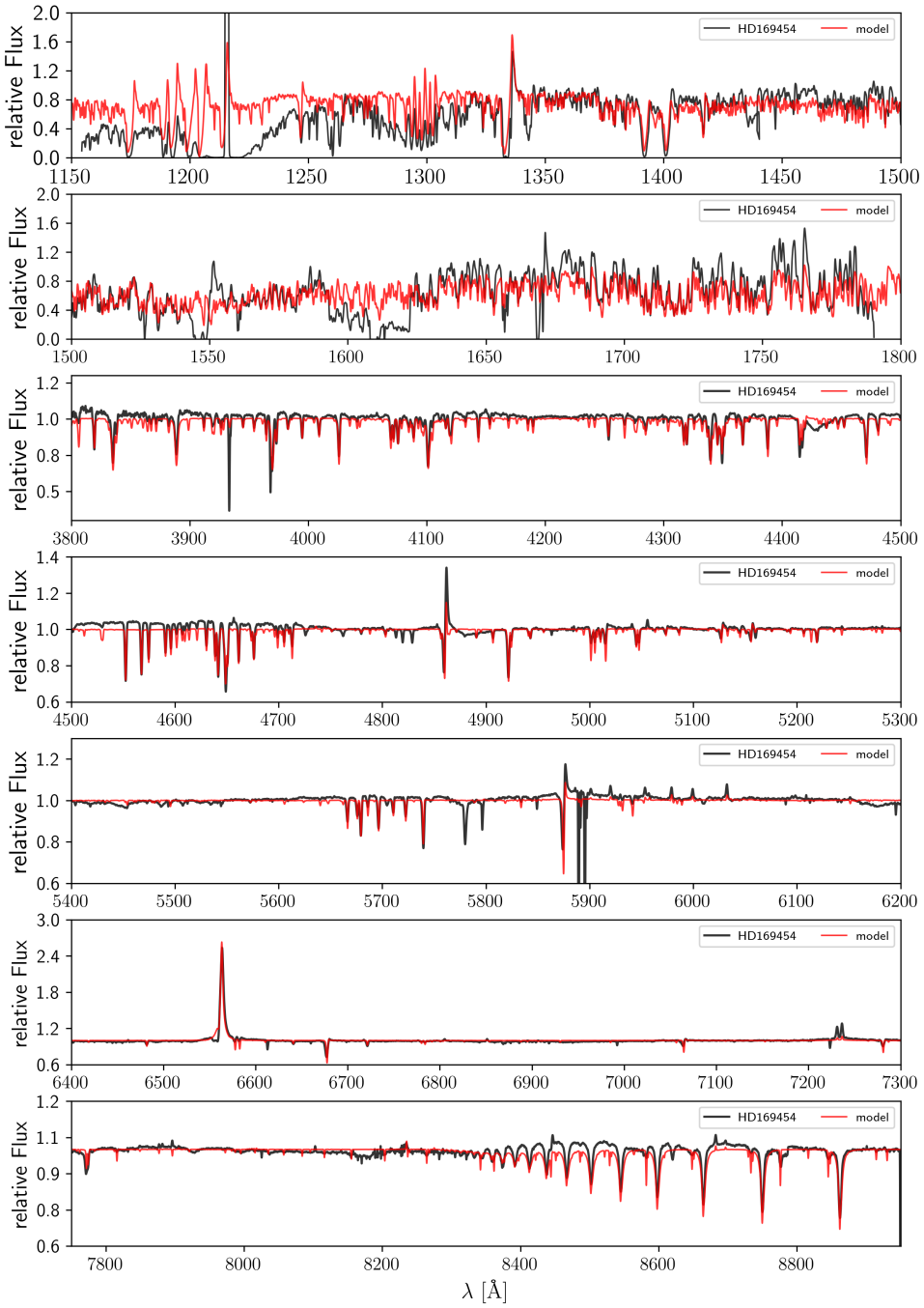


Figure C.39: An overall view of the best fit (red solid line) to key regions of the observed spectrum (black solid line) of HD169454. From top to bottom, the first two panels show the IUE SWP FUV range. We note some interstellar features: *Lyα* λ1216, O I + P II λ1302, C II λ1335, Si II λ1527, and Al II λ1671. The remaining panels show the Mercator/HERMES spectrum from the Melchiors spectroscopic library. The lines Ca II H + K and Na I D are interstellar features.

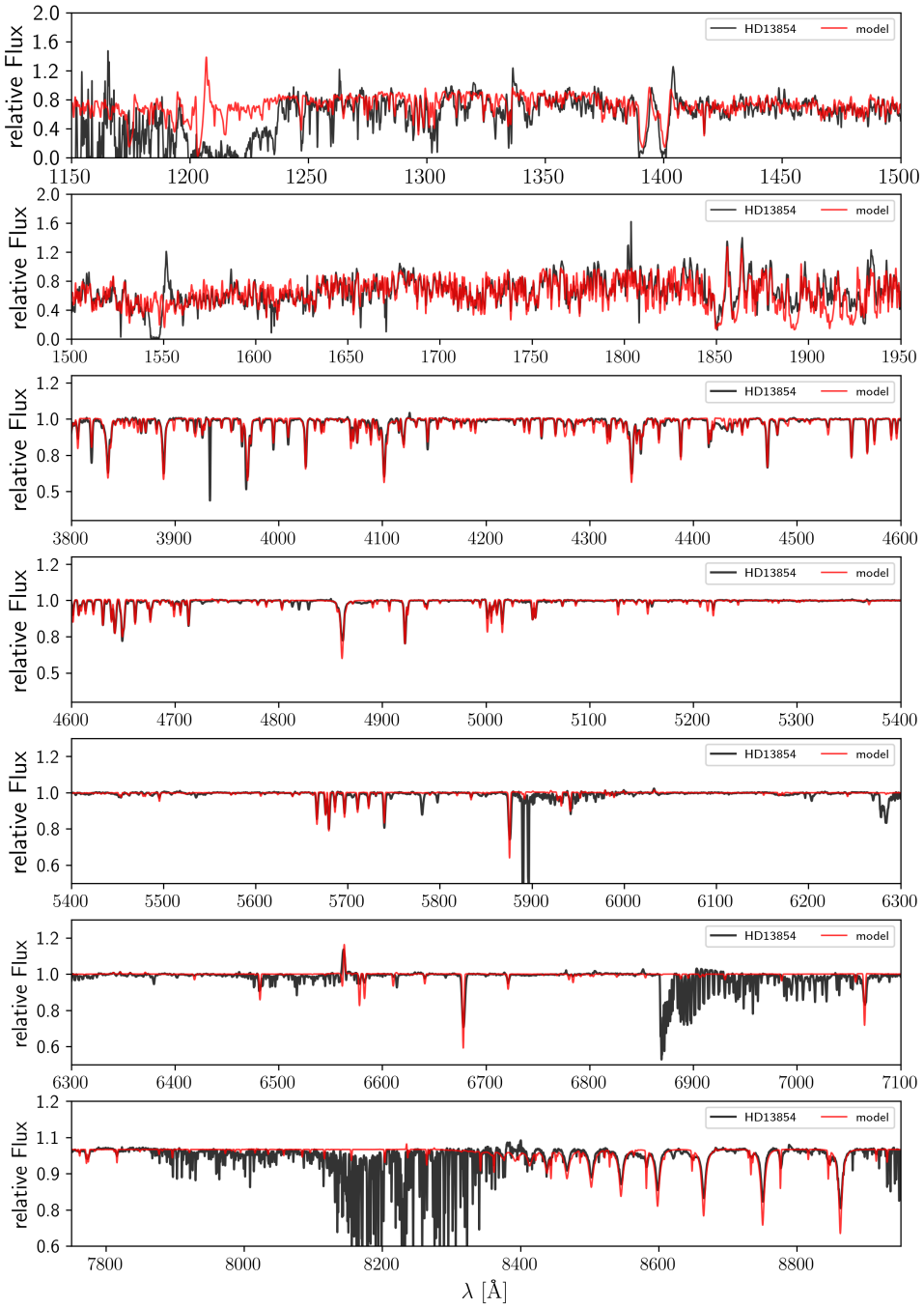


Figure C.40: An overall view of the best fit (red solid line) to key regions of the observed spectrum (black solid line) of HD13854. From top to bottom, the first two panels show the IUE SWP FUV range. We note some interstellar features: *Lyα* λ1216, O I + P II λ1302, C II λ1335, Si II λ1527, and Al II λ1671. The remaining panels show the Mercator/HERMES spectrum from the IACOB spectroscopic library. The lines Ca II H + K and Na I D are interstellar features.

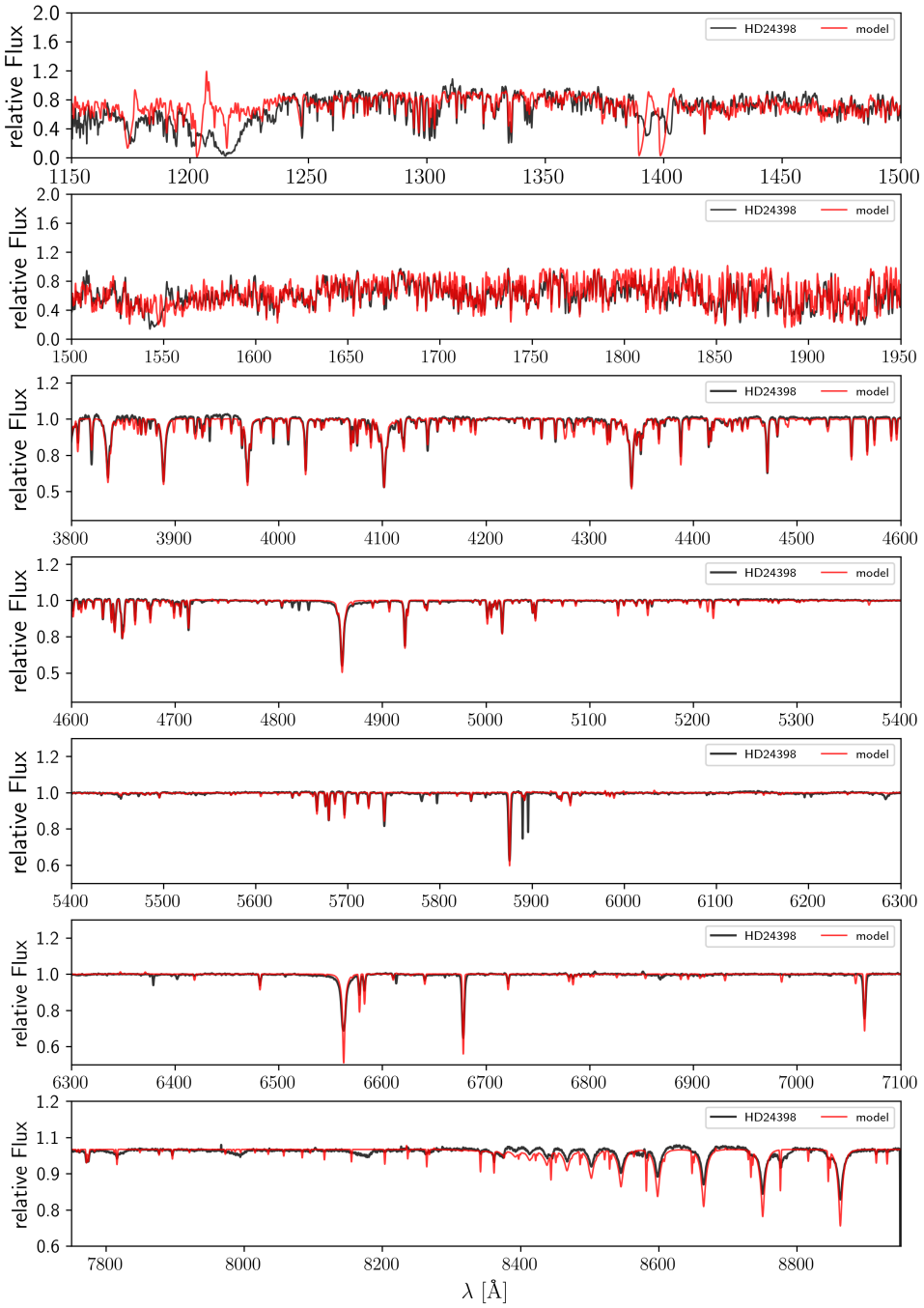


Figure C.41: An overall view of the best fit (red solid line) to key regions of the observed spectrum (black solid line) of HD24398. From top to bottom, the first two panels show the IUE SWP FUV range. We note some interstellar features: *Lyα* λ1216, O I + P II λ1302, C II λ1335, Si II λ1527, and Al II λ1671. The remaining panels show the Mercator/HERMES spectrum from the Melchiors spectroscopic library. The lines Ca II H + K and Na I D are interstellar features.

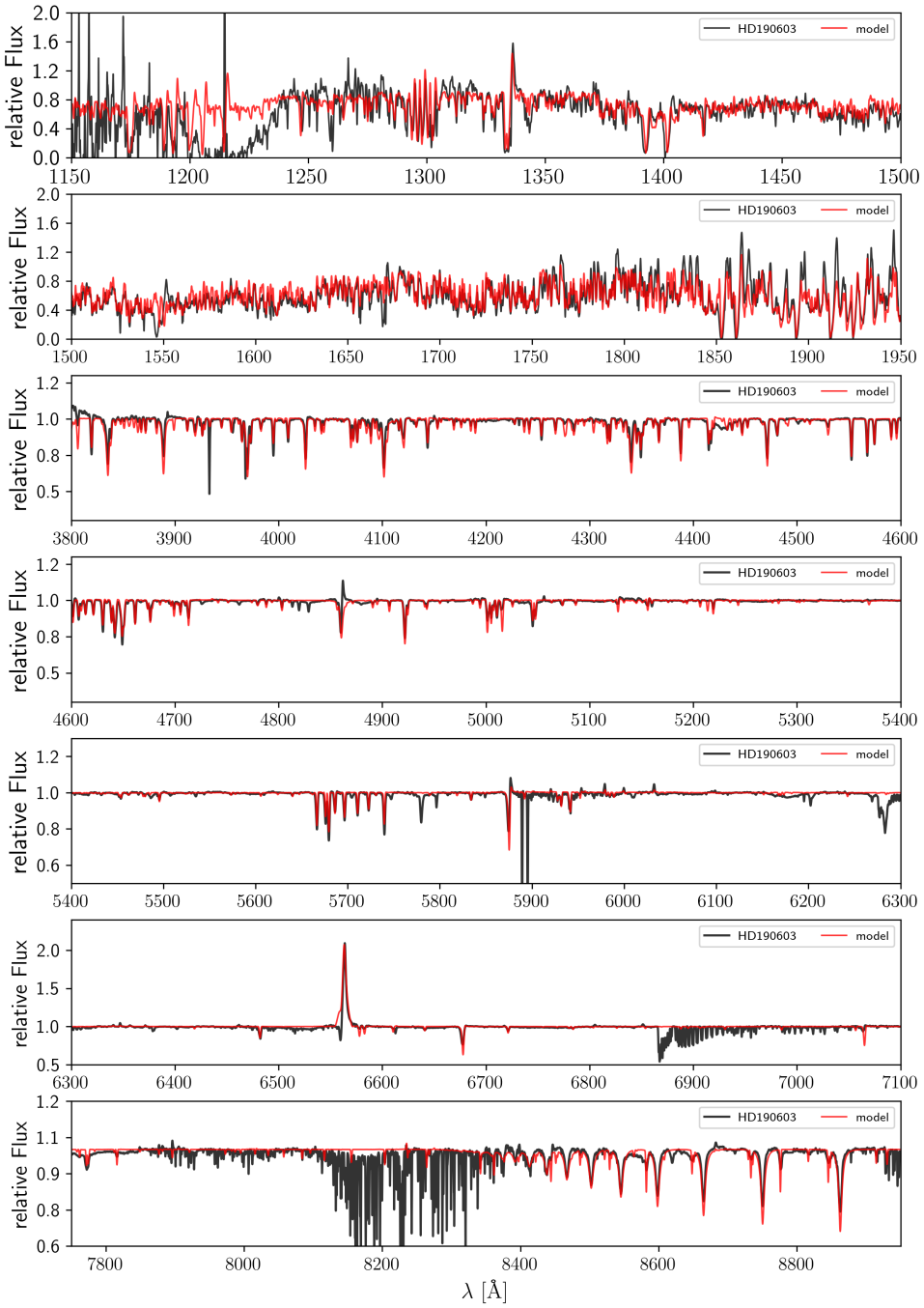


Figure C.42: An overall view of the best fit (red solid line) to key regions of the observed spectrum (black solid line) of HD190603. From top to bottom, the first two panels show the IUE SWP FUV range. We note some interstellar features: *Lyα* λ1216, O I + P II λ1302, C II λ1335, Si II λ1527, and Al II λ1671. The remaining panels show the Mercator/HERMES spectrum from the IACOB spectroscopic library. The lines Ca II H + K and Na I D are interstellar features.

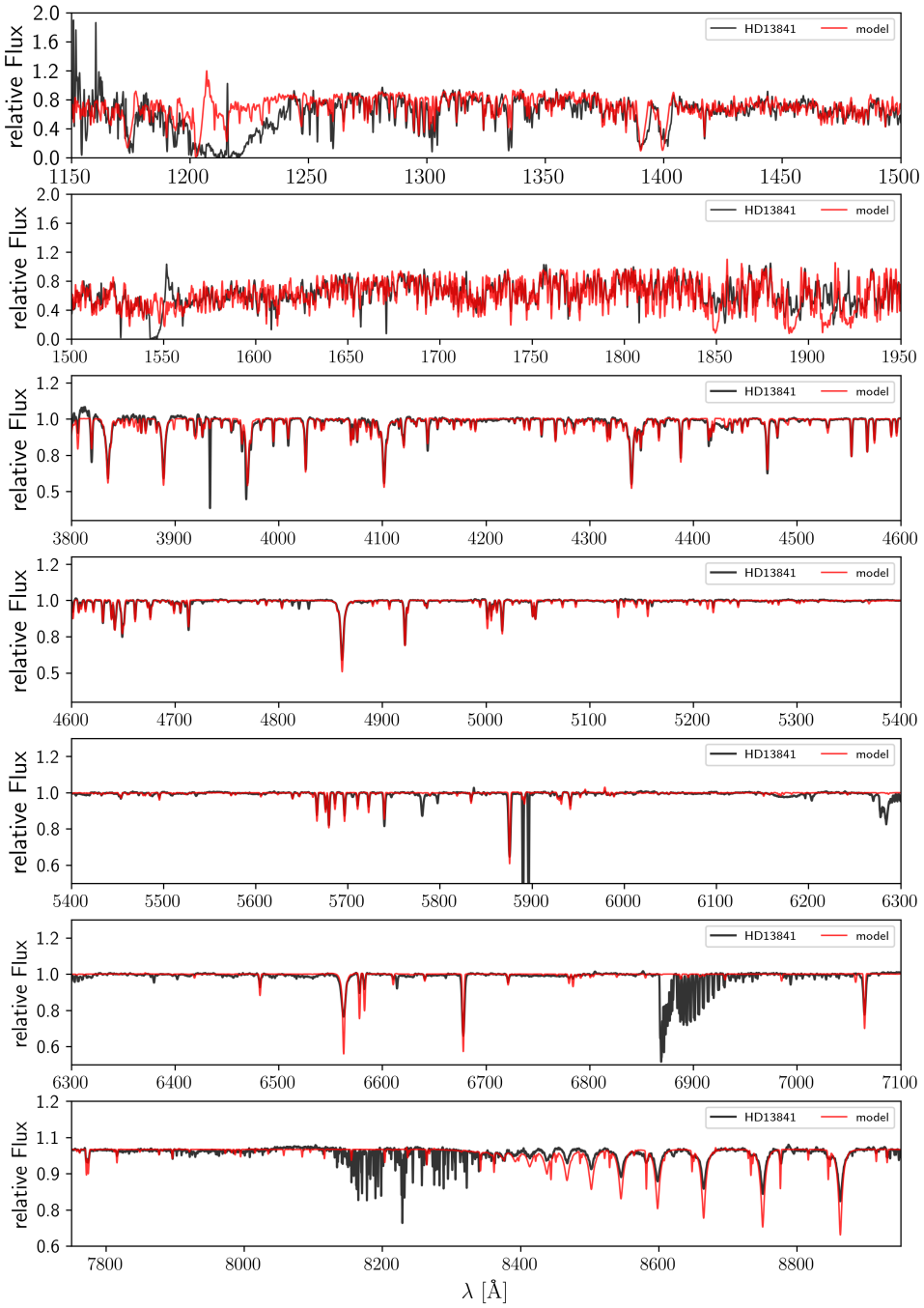


Figure C.43: An overall view of the best fit (red solid line) to key regions of the observed spectrum (black solid line) of HD13841. From top to bottom, the first two panels show the IUE SWP FUV range. We note some interstellar features: *Lyα* λ1216, O I + P II λ1302, C II λ1335, Si II λ1527, and Al II λ1671. The remaining panels show the Mercator/HERMES spectrum from the IACOB spectroscopic library. The lines Ca II H + K and Na I D are interstellar features.

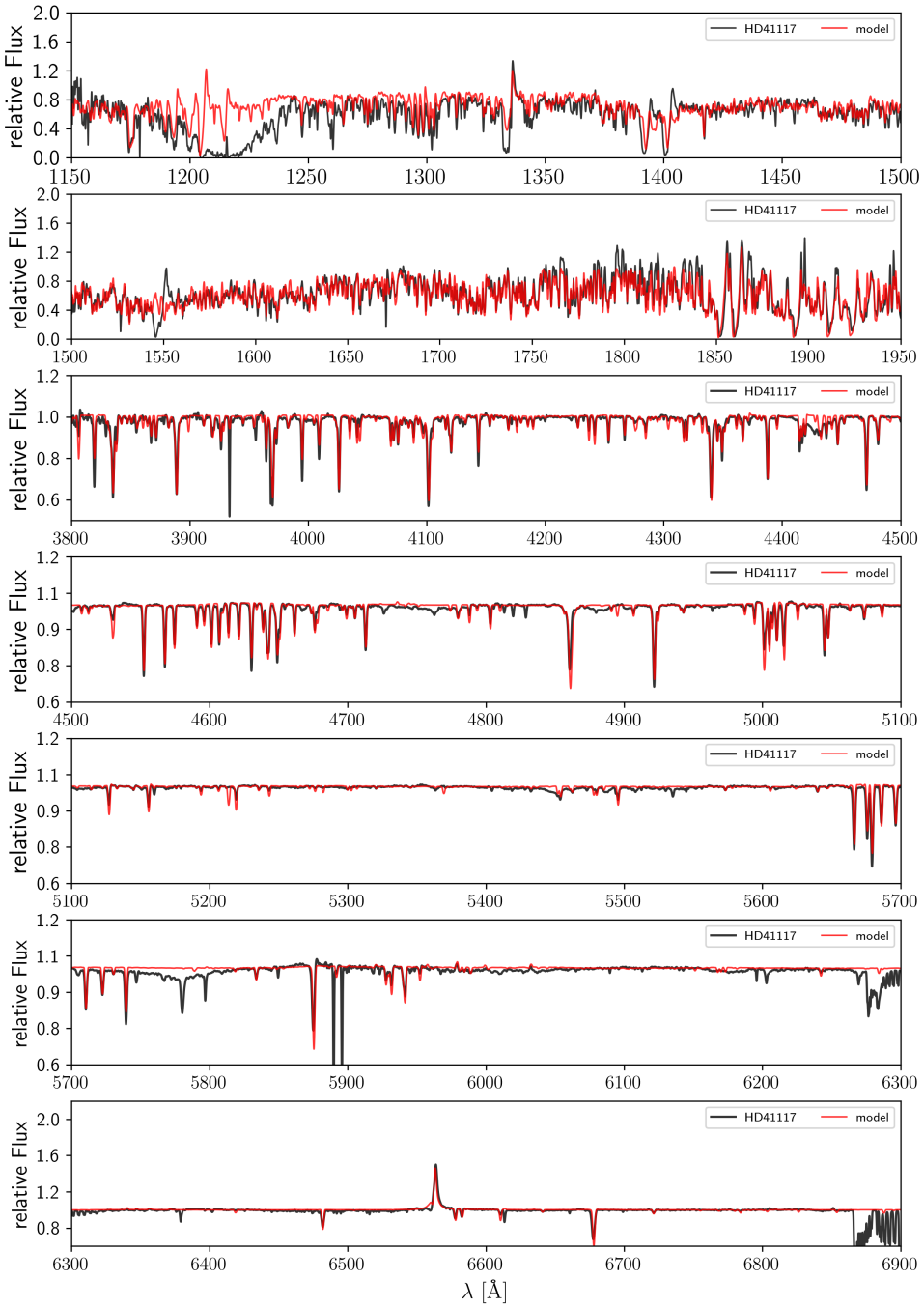


Figure C.44: An overall view of the best fit (red solid line) to key regions of the observed spectrum (black solid line) of HD41117. From top to bottom, the first two panels show the IUE SWP FUV range. We note some interstellar features: *Lyα* λ1216, O I + P II λ1302, C II λ1335, Si II λ1527, and Al II λ1671. The remaining panels show the NOT/FIES spectrum from the IACOB spectroscopic library. The lines Ca II H + K and Na I D are interstellar features.

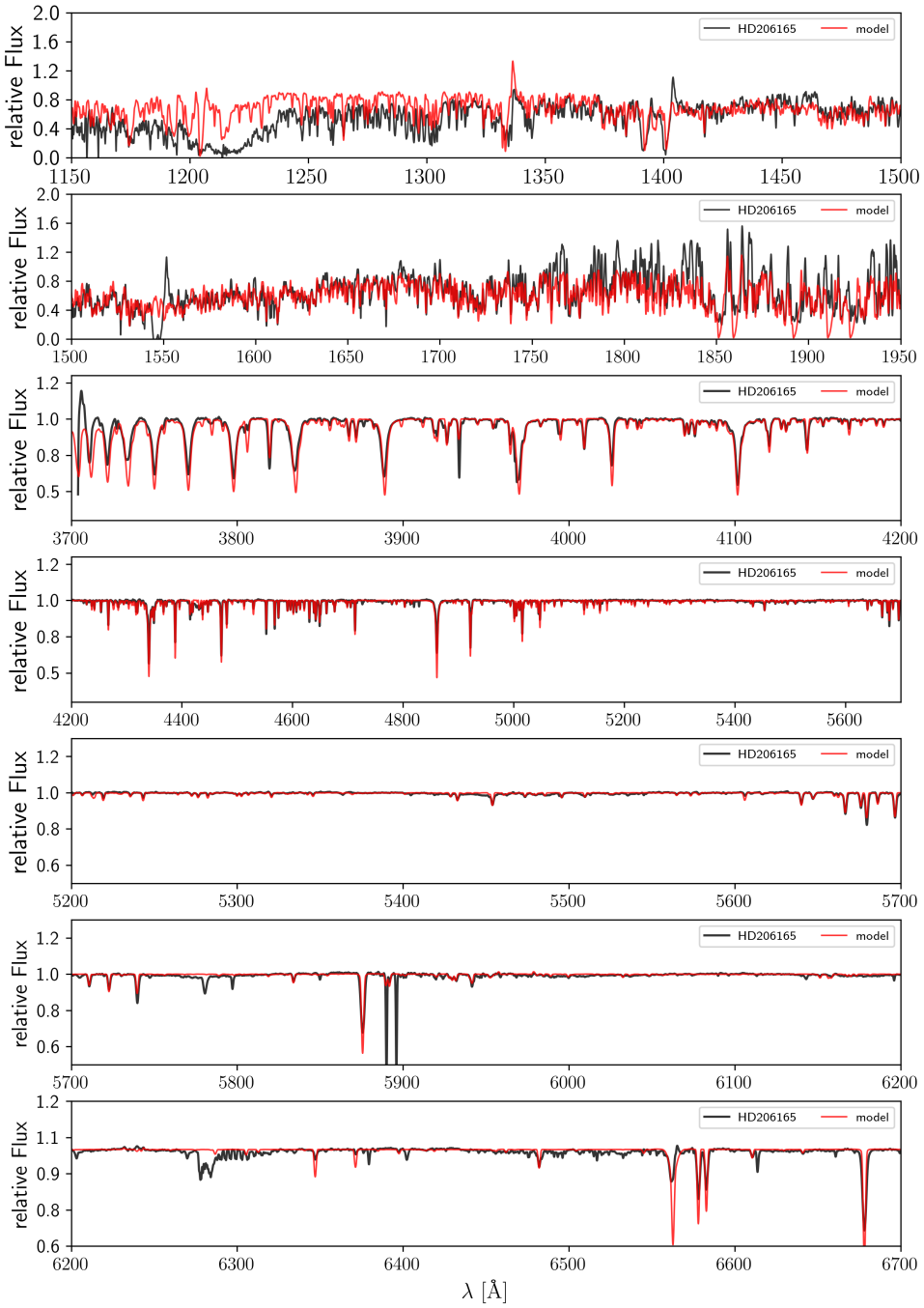


Figure C.45: An overall view of the best fit (red solid line) to key regions of the observed spectrum (black solid line) of HD206165. From top to bottom, the first two panels show the IUE SWP FUV range. We note some interstellar features: *Lyα* λ1216, O I + P II λ1302, C II λ1335, Si II λ1527, and Al II λ1671. The remaining panels show the NOT/FIES spectrum from the IACOB spectroscopic library. The lines Ca II H + K and Na I D are interstellar features.

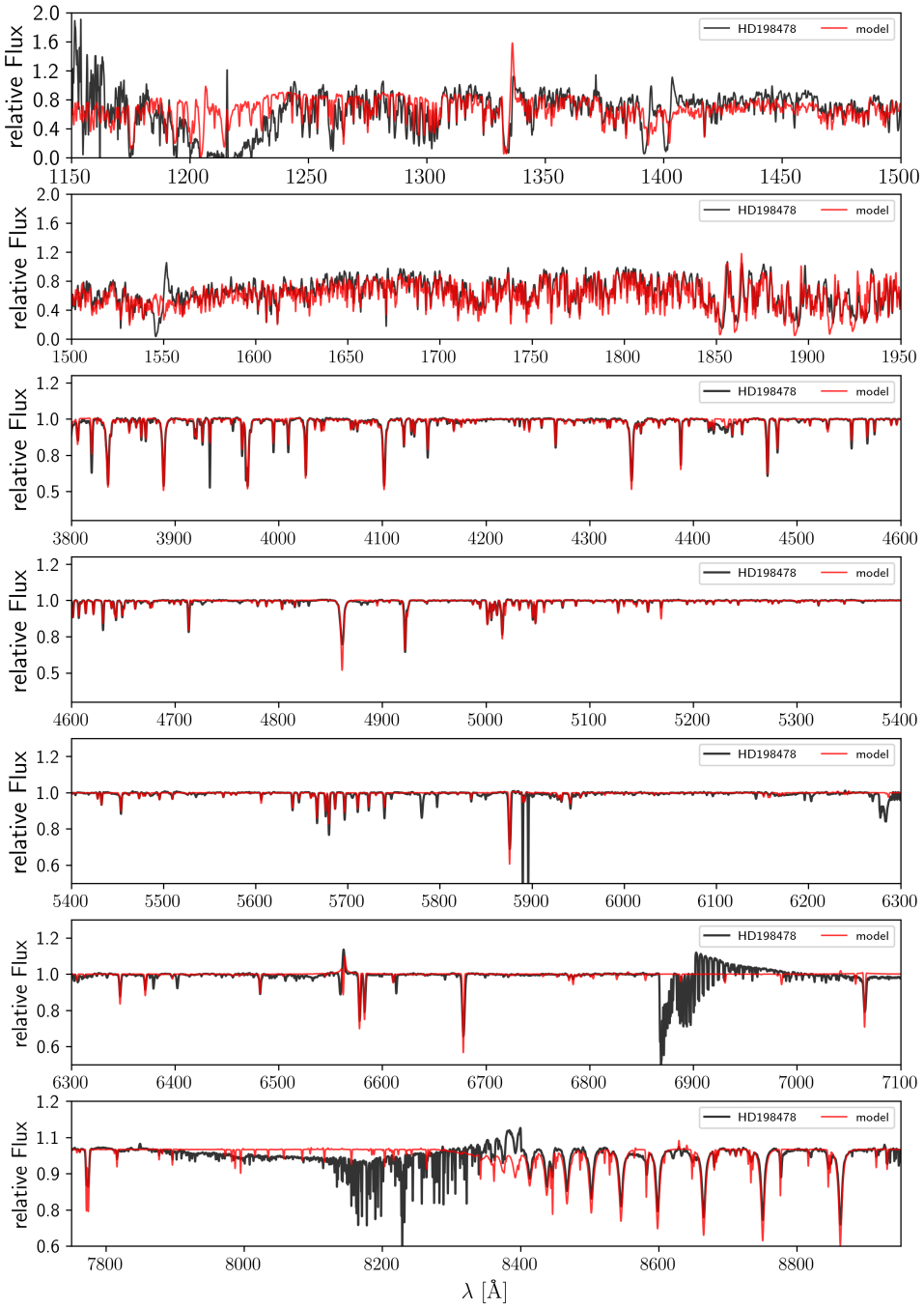


Figure C.46: An overall view of the best fit (red solid line) to key regions of the observed spectrum (black solid line) of HD198478. From top to bottom, the first two panels show the IUE SWP FUV range. We note some interstellar features: *Lyα* λ1216, O I + P II λ1302, C II λ1335, Si II λ1527, and Al II λ1671. The remaining panels show the Mercator/HERMES spectrum from the IACOB spectroscopic library. The lines Ca II H + K and Na I D are interstellar features.

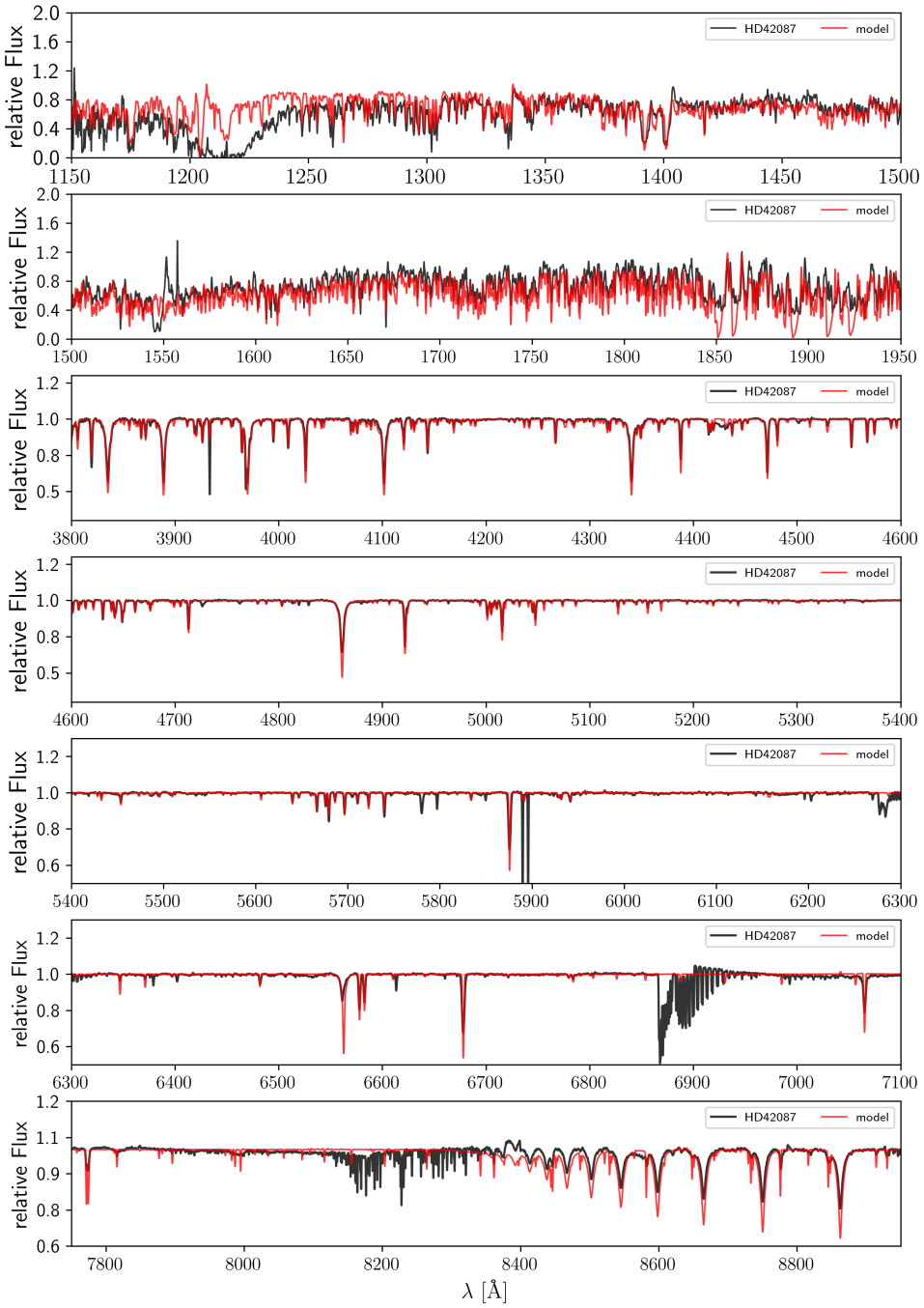


Figure C.47: An overall view of the best fit (red solid line) to key regions of the observed spectrum (black solid line) of HD42087. From top to bottom, the first two panels show the IUE SWP FUV range. We note some interstellar features: *Lyα* λ1216, O I + P II λ1302, C II λ1335, Si II λ1527, and Al II λ1671. The remaining panels show the Mercator/HERMES spectrum from the IACOB spectroscopic library. The lines Ca II H + K and Na I D are interstellar features.

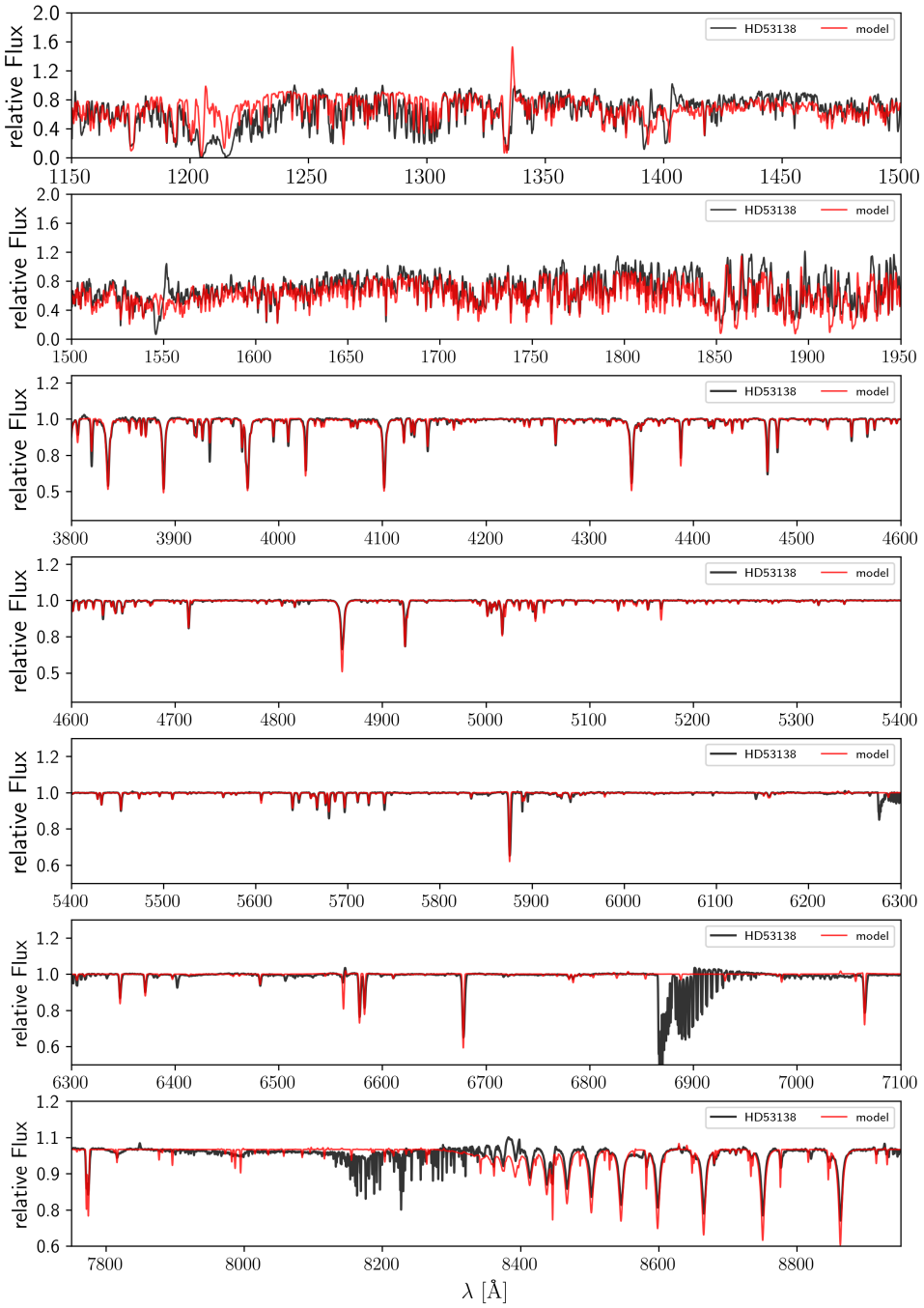


Figure C.48: An overall view of the best fit (red solid line) to key regions of the observed spectrum (black solid line) of HD53138. From top to bottom, the first two panels show the IUE SWP FUV range. We note some interstellar features: *Lyα* λ1216, O I + P II λ1302, C II λ1335, Si II λ1527, and Al II λ1671. The remaining panels show the Mercator/HERMES spectrum from the IACOB spectroscopic library. The lines Ca II H + K and Na I D are interstellar features.

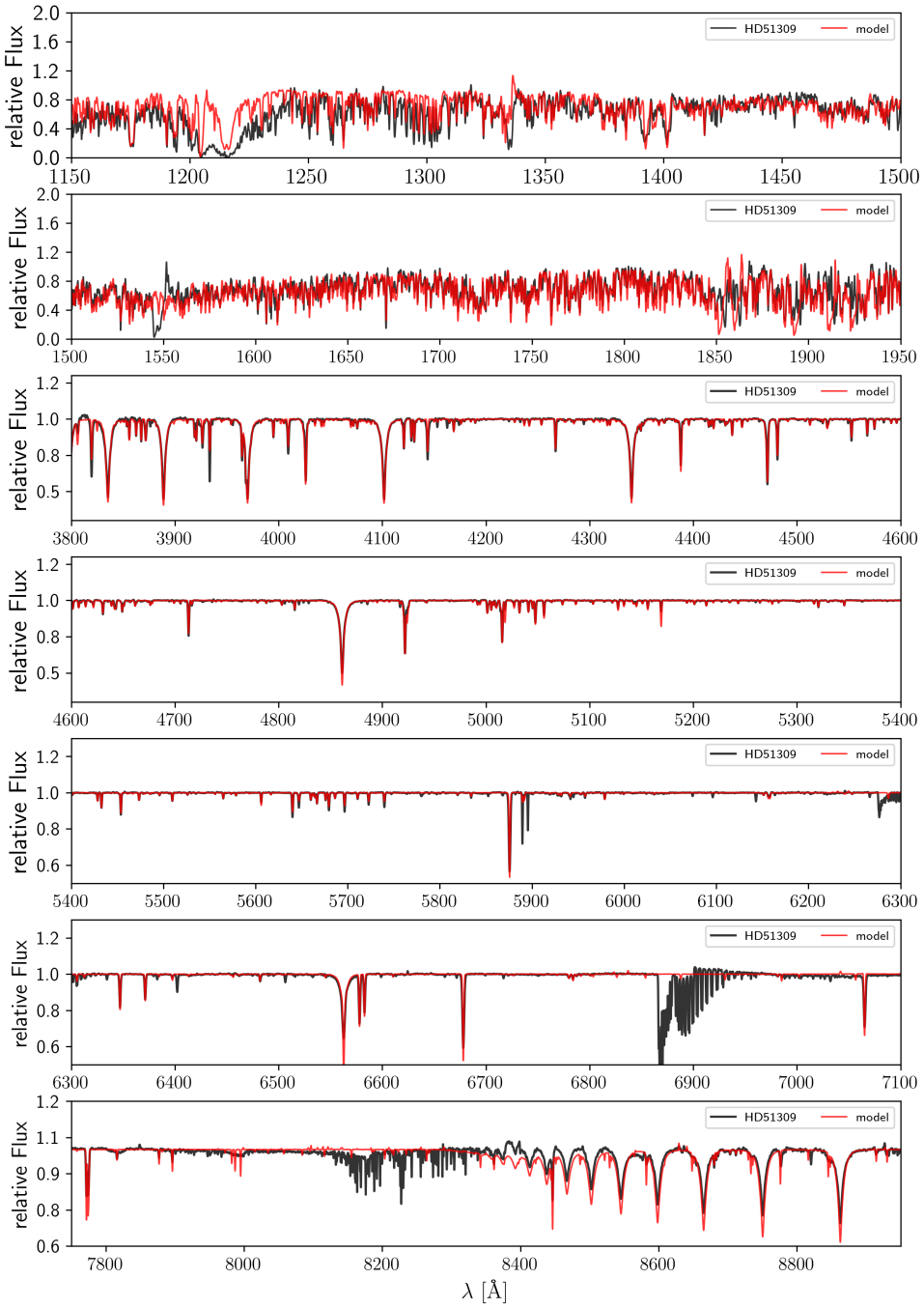


Figure C.49: An overall view of the best fit (red solid line) to key regions of the observed spectrum (black solid line) of HD51309. From top to bottom, the first two panels show the IUE SWP FUV range. We note some interstellar features: *Lyα* λ1216, O I + P II λ1302, C II λ1335, Si II λ1527, and Al II λ1671. The remaining panels show the Mercator/HERMES spectrum from the IACOB spectroscopic library. The lines Ca II H + K and Na I D are interstellar features.

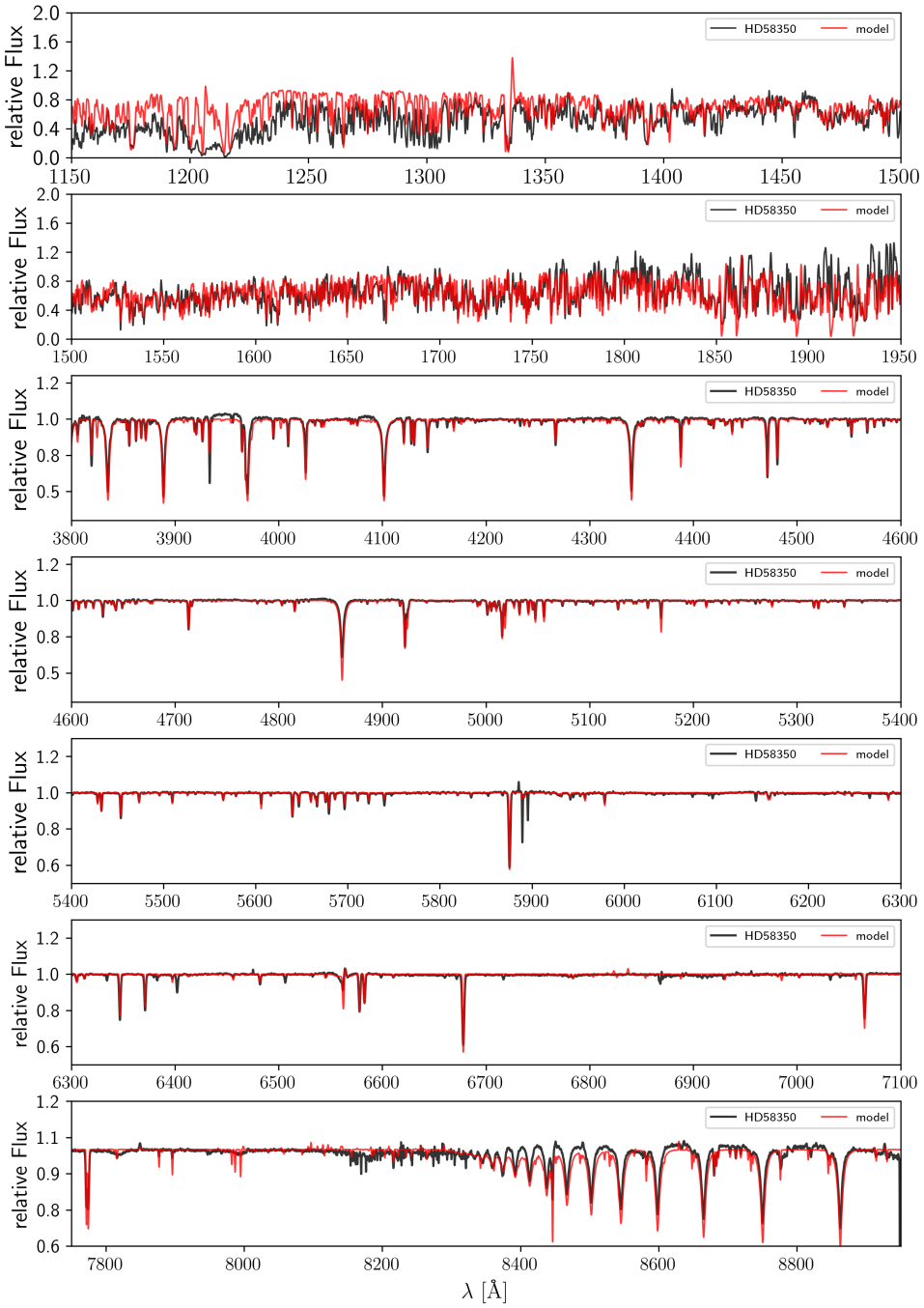


Figure C.50: An overall view of the best fit (red solid line) to key regions of the observed spectrum (black solid line) of HD58350. From top to bottom, the first two panels show the IUE SWP FUV range. We note some interstellar features: *Lyα* λ1216, O I + P II λ1302, C II λ1335, Si II λ1527, and Al II λ1671. The remaining panels show the Mercator/HERMES spectrum from the Melchiors spectroscopic library. The lines Ca II H + K and Na I D are interstellar features.

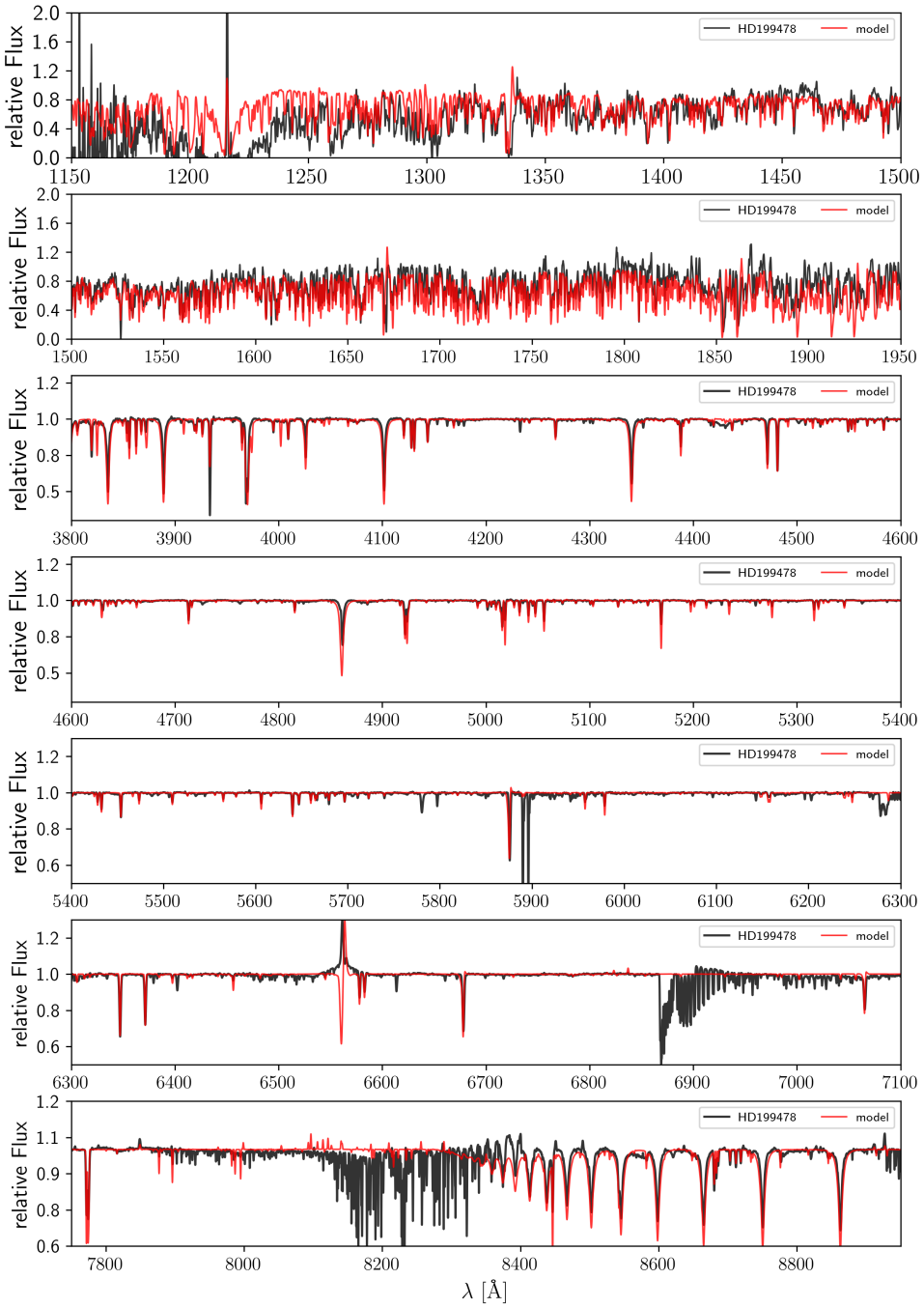


Figure C.51: An overall view of the best fit (red solid line) to key regions of the observed spectrum (black solid line) of HD199478. From top to bottom, the first two panels show the IUE SWP FUV range. We note some interstellar features: *Lyα* λ1216, O I + P II λ1302, C II λ1335, Si II λ1527, and Al II λ1671. The remaining panels show the Mercator/HERMES spectrum from the IACOB spectroscopic library. The lines Ca II H + K and Na I D are interstellar features.

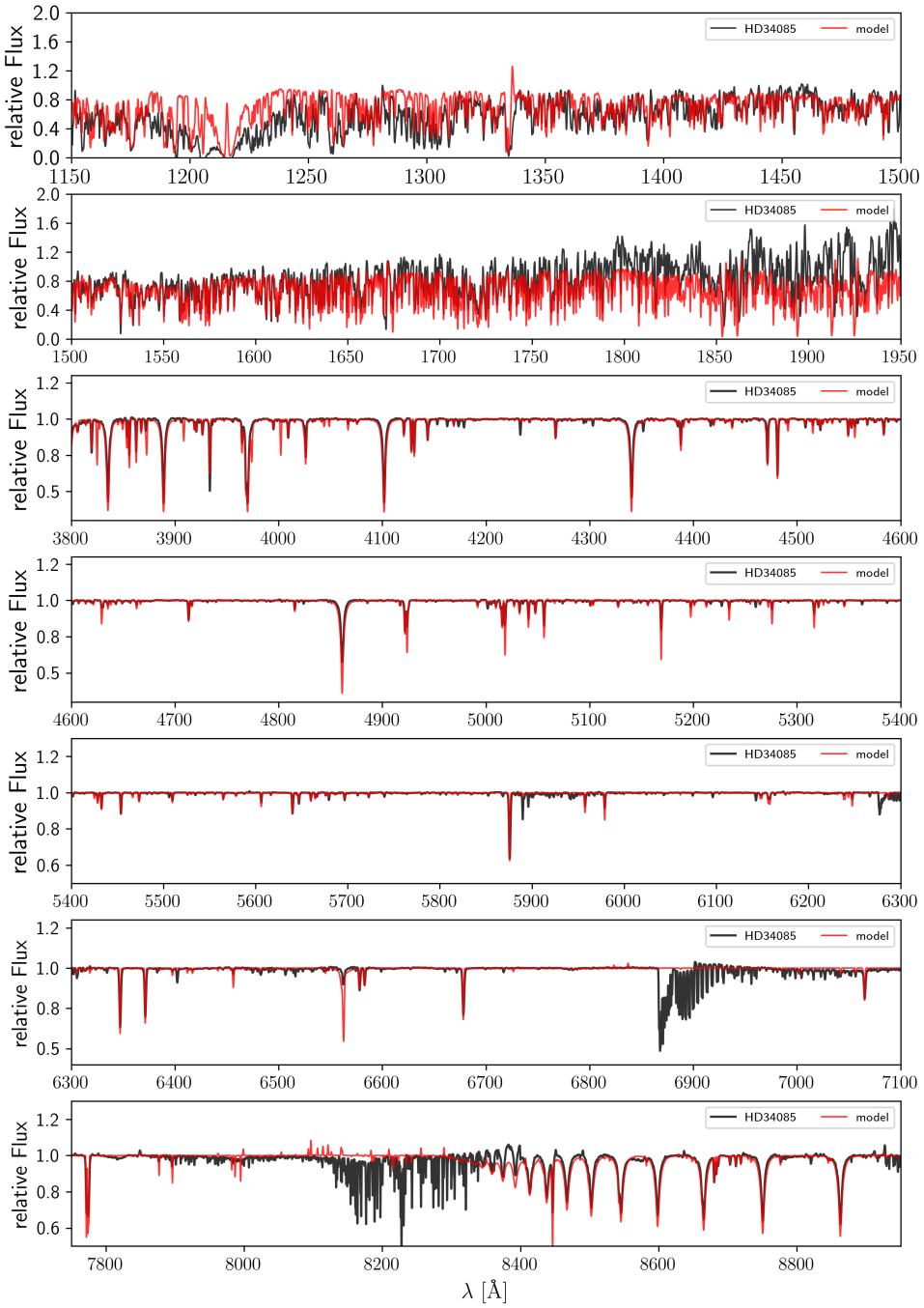


Figure C.52: An overall view of the best fit (red solid line) to key regions of the observed spectrum (black solid line) of HD34085. From top to bottom, the first two panels show the IUE SWP FUV range. We note some interstellar features: *Lyα* λ1216, O I + P II λ1302, C II λ1335, Si II λ1527, and Al II λ1671. The remaining panels show the Mercator/HERMES spectrum from the IACOB spectroscopic library. The lines Ca II H + K and Na I D are interstellar features.

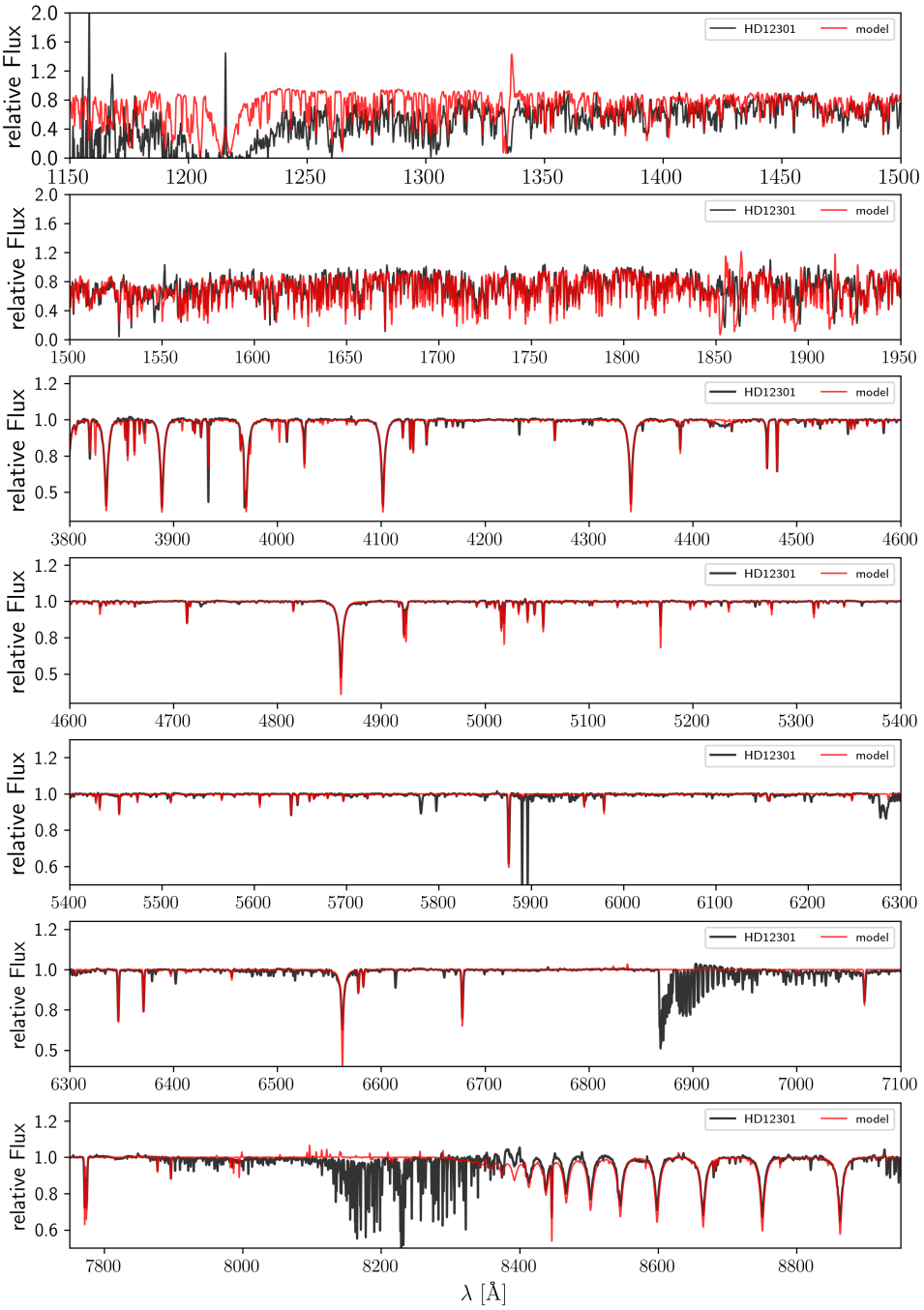


Figure C.53: An overall view of the best fit (red solid line) to key regions of the observed spectrum (black solid line) of HD12301. From top to bottom, the first two panels show the IUE SWP FUV range. We note some interstellar features: *Lyα* λ1216, O I + P II λ1302, C II λ1335, Si II λ1527, and Al II λ1671. The remaining panels show the Mercator/HERMES spectrum from the IACOB spectroscopic library. The lines Ca II H + K and Na I D are interstellar features.